Surface Chemistry of N-Heterocyclic Carbenes and the Self-Assembly, Structure, and Properties of Polymer Metal-Organic Cage Gels

By

Aleksandr V. Zhukhovitskiy

B.A., Northwestern University (2011)
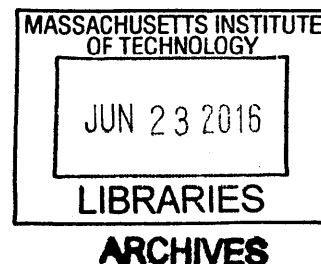Joint B.A./M.S. in Chemistry, Northwestern University (2011)

Submitted to the Department of Chemistry
in Partial Fulfillment of the Requirements for the Degree of

Doctor of Philosophy in Organic Chemistry

at the

MASSACHUSETTS INSTITUTE OF TECHNOLOGY

June 2016

Signature of Author: **Signature redacted**

Department of Chemistry
May 23, 2016

Certified by: **Signature redacted**

Jeremiah A. Johnson
Firmenich Career Development Assistant Professor of Chemistry
Thesis Supervisor

Accepted by: **Signature redacted**

Robert W. Field
Haslam and Dewey Professor of Chemistry
Chairman, Departmental Committee on Graduate Students

This doctoral thesis has been examined by a committee of the Department of Chemistry as follows:

Professor Timothy M. Swager:

Signature redacted

Thesis Committee Chair

Professor Jeremiah A. Johnson:

Signature redacted

Thesis Supervisor

Professor Mohammad Movassaghi:

Signature redacted

Surface Chemistry of N-Heterocyclic Carbenes and the Self-Assembly, Structure, and Properties of Polymer Metal-Organic Cage Gels

By

Aleksandr V. Zhukhovitskiy

Submitted to the Department of Chemistry on May 25, 2016
in Partial Fulfillment of the Requirements for the Degree of Doctor of Philosophy
in Organic Chemistry at the Massachusetts Institute Of Technology

Abstract

Chapter 1. Introduction to Carbene Ligands in Surface Chemistry: From Stabilization of Discrete Elemental Allotropes to Modification of Nanoscale and Bulk Substrates
In this chapter, we review the development of carbene surface chemistry from its inception through 2015, covering elemental allotrope substrates, nanomaterials, and bulk surfaces, as well as persistent and non-persistent carbenes. We synthesize from the reviewed reports a mechanistic understanding of this chemistry and outline the road ahead in this field.

Chapter 2. Addressable Carbene Anchors for Gold Surfaces
New strategies to access functional monolayers could augment current surface modification methods. Here we present addressable N-heterocyclic carbene (ANHC) anchors for gold surfaces and provide experimental and theoretical characterization of ANHC monolayers. Additionally, we demonstrate grafting of highly fluorinated polymers from surface-bound ANHCs.

Chapter 3. Reactions of Persistent Carbenes with Hydrogen-Terminated Silicon Surfaces
We report here the use of persistent aminocarbenes to functionalize via Si-H insertion reactions a range of hydrogen-terminated silicon surfaces: from model compounds, to nanoparticles, and planar Si(111) wafers. In particular, a cyclic(alkyl)(amino)carbene and an acyclic diaminocarbene underwent Si-H insertion, forming persistent C-Si linkages and thereby installing amine or aminal functionality in proximity to the surface. Our results pave the way for the further development of persistent carbenes as universal ligands for silicon and potentially other non-metallic substrates.

Chapter 4. Cycloelimination of Imidazolidin-2-Ylidene N-Heterocyclic Carbenes: Mechanism and Insights into the Synthesis of Stable "NHC-CDI" Amidinates
We report the discovery that 1,3-bis(aryl)imidazolidin-2-ylidenes, one of the most widely studied classes of N-heterocyclic carbenes (NHCs), undergo quantitative conversion to zwitterionic "NHC-CDI" amidinates upon heating to 100 °C in solution. The mechanism of this novel NHC decomposition process was studied in detail and enabled the rational synthesis of a new class of bench stable amidinates.

Chapter 5. Toward Dynamic and Hierarchically Structured Polymer Gels: An Introduction to Polymer Metal-Organic Cage Gels
Key challenges in polymer network/gel chemistry are overviewed. Polymer metal-organic cage

gels capable of addressing some of these key challenges are introduced.

Chapter 6. Highly Branched and Loop-Rich Gels Via Formation of Metal-Organic Cages Linked by Polymers

We report here a new class of gels (called 'polyMOC' gels) assembled from polymeric ligands and metal-organic cages (MOCs) as junctions with M_2L_4 or $M_{12}L_{24}$ stoichiometries. The latter features increased branch functionality and large shear moduli, but also an abundance of elastically inactive loop defects that allow via ligand exchange the introduction of function at no cost to the gel's mechanical properties.

Thesis Supervisor: Jeremiah A. Johnson
Title: Firmenich Career Development Assistant Professor of Chemistry

To my parents – for my roots

and

to my wife – for my sunshine

ACKNOWLEDGEMENTS

outstanding collaborator – productive, thoughtful, and always positive – and a good friend otherwise. I am also grateful to Michael Campion, Frank Leibfarth, and Erik Dreaden from whom I learned a great deal about numerous things, and who were likewise great friends to me out of the lab. And of course I am grateful to all of the fellow scientists at MIT, who have always been generous with advice, instrumentation, glassware, and chemicals.

Additionally, I could not have been a productive graduate student without the help of many of the MIT staff. Specifically, I am thankful to Gang Liu, Jeff Simpson, Anne Rachupka, and Deb Bass, Li Li, Libby Shaw (and Neal Fairley at CasaXPS), Yong Zhang, Alan Schwartzman, and Peter Müller. I am grateful for and admire their knowledge, professionalism, and passion for science. Finally, I would like to thank Jennifer Weisman and Lynn Marie-Guthrie for answering my non-scientific questions on all things graduate school; Tyler Brezler for helping to coordinate so many critical aspects of our lab and for being a good friend; and Scott Ide and Scott Wade for helping to keep our lab safe and sound.

Outside of MIT, I have had the pleasure of working with a number of tremendous collaborators, and I would like to thank Professor Rudolf Faust and Ren Li at UMass Lowell; Hui Li and Professor Tianbo Liu at the University of Akron; Jessie Sun and Professor Darrin Pochan at University of Delaware; Professor Michael Hore at Case Western Reserve University; and Professor K. T. Queeney at Smith College for their enthusiasm for our joint work and for all that they have taught me over the years.

In the Johnson group, I was lucky to get to know and work with all of my labmates, some of whom have become my close friends. I would first like to thank my labmates from year 1 in the Johnson lab – Alan Burts, Alexandra Cok, Jenny Liu, Jessica McCombs, Jiyeon Woo, and Huaxing Zhou, who have been an extremely supportive group of people, and who helped to establish a tone of mutual help and respect in our group. Next, I would like to thank all of my collaborators in the group for their camaraderie and all that they have taught me – in particular, Michelle MacLeod, Yufeng Wang, Mao Chen, Julia Zhao, and of course Mingjiang Zhong, one of my closest collaborators in the lab, who has been an extraordinarily valuable source of information for all things polymer chemistry: over the years of collaborating, traveling together, and being desk neighbors, he and I have found that we share an incredible number of common views and experiences, and I am happy to count him among my close friends. I am also thankful to Ken Kawamoto, one of my closest friends at MIT, for being one of the most conscientious labmates around, for all of our interesting conversations ranging from chemistry to politics and culture, for his mentorship in powerlifting, and many memorable times we shared at MIT and on our joint trip. I am also thankful to Jonathan Barnes, who has become a great friend to me during his time in our lab – his advice and support have meant a lot – and to Matt Golder for our camaraderie in the recent months. I'd also like to especially thank Deborah Ehrlich for her devotion to her labmates, and Longyan Liao, Molly Sowers, Angela Gao, Gihan Hewage, Yuwei Gu, Hung Nguyen, Yivan Jiang, and Qixian, as well as all of the visiting students and scientists, for being great labmates. Lastly, I'd like to thank my mentees – Katherine Mizrahi, Julie Geng, Vivian Tian, and Julia Zhao – for entrusting me with their chemistry laboratory training. Julia Zhao is a current first-year graduate student in the Johnson lab and a terrific collaborator and labmate with a bright future.

Additionally, I would be remiss not to thank the chemistry graduate students from my entering class with whom we shared numerous ups and downs as fellow TAs, classmates, and researchers. In particular, I want to thank several individuals, who have come to mean a lot to me over the last fiver years: Kolby White, Joe Azzarelli, and Dave Song. Kolby has become a

7

close friend to my wife Martha and me, and I am grateful to her for being there for both of us. Joe Azzarelli and Dave Song have in the past five years become among my very closest friends. Their friendship and support have been among the most important positive influences during my graduate school. I am grateful to them for all the adventures, heart-to-heart conversations, shared dreams, and a brotherly union, which I have no doubt will last for our lifetimes.

Aside from my close friends at MIT, I want to thank many other friends (including Sean Sanders, Erick Bennett, and Justin Derbas) for helping me remain connected to life outside of the laboratory. Most of all, I want to thank Stephen Guerin, John Regan, Karoline Röderer, Michael Tremmel and Carrie Templeton, whose enduring and close friendship in the face of distance and time has meant the world to me. Our reunions and communication in all of its forms have been sources of pure happiness for me.

I would next like to thank all of my teachers and mentors, without whose instruction and dedication I would not make it this far. In particular, I would like to thank Professor SonBinh Nguyen at Northwestern University for providing me with research opportunities in chemistry, thoughtful advising, and support during much of my undergraduate career. In the same vein, I am grateful to Professor Omar Farha, Professor Emily Pentzer, Hakan Üsta and Professor Tobin Marks for supervising my early research experiences. I would also like to thank Professor Jared Wunsch for his supervision of my independent study in mathematics, and who was and remains one of my role model educators. I would also like to highlight Dennis Wyatt, my high school English teacher and coach, whose support of me has evolved into a friendship through the years. I am also in lifelong debt of gratitude to Dr. Siegel, who has taken me under her wing soon after I immigrated to the U.S. and invested so much of her time to help me overcome numerous barriers to achieving success. Finally, I would like to thank all of my teachers and friends from the Ukraine, who helped to shape my worldview.

Most importantly, I would like to thank my family. I have strived to continue their long tradition of hard work and strength of character, a heritage I am proud of, and I am thankful to them for their love and support through the good times and the bad. In particular, I often think with gratitude and pride of my grandmothers Tamara and Polina, as well as my cousin Yulia and aunt Liuda. I am also grateful to my brother Vova, who, despite our age difference, has included me among his closest friends, and with whom we have been through some tough times, and I am thankful to have a great sister-in-law in Polina and sweet nephew Danik and niece Alyssa. I look forward to spending much more time with them in the future. I am also extremely grateful for my parents-in-law Janek and Ania and Polish relatives-in-law (and Abby), who have adopted me as their own. Their hospitality, thoughtfulness, and love have been a source of strength and comfort for me during my graduate studies at MIT.

Most of all I am thankful to my parents Vadym and Svetlana and my wife Martha, to whom this thesis is dedicated. My parents are incredible people, who have taught me by example my most important lessons in life. Their love and loyalty to their family and friends, and their thoughtfulness, hard work, and courage have been models which I am incredibly fortunate to have, and thanks to which I have the luxury to live in the U.S. and attend MIT. I am grateful to my parents for teaching me how to think creatively and critically and for encouraging curiosity in me. My father in particular invested many years in teaching me mathematics, chemistry, and physics, and in fact, my interest in chemistry originated from listening to him tutor chemistry students at home. Moreover, my father in many ways blazed the trail for me as a PhD in chemistry in his own right, and I cherish all of the chemistry and graduate school-related conversations we have had over the years. Thank you for everything Mom and Dad!

Lastly, I would like to thank Martha, who has been not only my wife, but also my closest friend and confidant and strongest supporter. Her presence in my life has given me confidence in myself and in a bright future; thanks to Martha, I feel a profound happiness even during times of hardship, and I feel excitement even during days that seem otherwise mundane. I look up to Martha in many ways, and motivated by her, I strive to become a wiser, more judicious, and overall a better person. I am also thankful to Martha for the lion's share of the work that she did to sustain our young family and ensure its stability during my graduate studies. I am incredibly fortunate to love and be loved by such an amazing person. Thank you for everything Martha!

PREFACE

This thesis has been adapted from the following published or submitted articles co-written by the author:

- Peer-Reviewed Publications
Zhukhovitskiy, A. V.; Mavros, M. G.; Van Voorhis, T.; Johnson, J. A. Addressable Carbene Anchors for Gold Surfaces. *J. Am. Chem. Soc.* **2013**, *135,* 7418–7421.

Zhukhovitskiy, A. V.; Geng, J.; Johnson, J. A. Cycloelimination of Imidazolidin-2-Ylidene N-Heterocyclic Carbenes: Mechanism and Insights into the Synthesis of Stable "NHC-CDI" Amidinates. *Chem. Eur. J.* **2015**, *21,* 5685–5688.

Zhukhovitskiy A. V.; MacLeod, M. J.; Johnson, J. A. Carbene Ligands in Surface Chemistry: From Stabilization of Discrete Elemental Allotropes to Modification of Nanoscale and Bulk Substrates. *Chem. Rev.* **2015**, *115,* 11503–11532.

Zhukhovitskiy A. V.; Zhong, M.; Keeler, E. G.; Michaelis, V. K.; Sun, J. E. P.; Hore, M. J. A.; Pochan, D. J.; Griffin, R. G.; Willard, A. P.; Johnson, J. A. Highly Branched and Loop-Rich Gels via Formation of Metal-Organic Cages Linked by Polymers. *Nat. Chem.* **2016**, *8,* 33-41.

- Submitted for Publication
Zhukhovitskiy, A. V.; Mavros, M. G.; Queeney, K. T.; Wu, T.; Van Voorhis, T.; Johnson, J. A. Reactions of Persistent Carbenes with Hydrogen-Terminated Silicon Surfaces. *J. Am. Chem. Soc.* **2016**, *Submitted.*

RESPECTIVE CONTRIBUTIONS

This thesis describes work, which resulted from collaborative efforts of the author with other colleagues at MIT, Smith College, University of Delaware, and Case Western Reserve University. The specific contributions of the author and collaborators are delineated below.

The review presented in **Chapter 1** was a collaborative effort between Michelle J. MacLeod and the author. Ms. MacLeod prepared half of the figures and wrote a section on the PEGylated gold nanoparticles in this review. The author prepared the remainder of the figures and wrote the remainder of the review.

The work in **Chapter 2** was a collaborative effort between Dr. Michael G. Mavros and the author. Dr. Mavros performed the computations. The author carried out the experimental work described in this chapter.

The work in **Chapter 3** was a collaborative effort between Dr. Michael G. Mavros, Prof. K. T. Queeney (Smith College), Mr. Tony Wu, and the author. Dr. Mavros performed the computations. Prof. Queeney and the author jointly carried out the FTIR characterization and analysis of the Si(111) wafers. Mr. Wu etched all of the Si(111) wafers. The author initiated this project and carried out all of the synthetic and surface functionalization studies and spectroscopic analysis.

The work in **Chapter 4** was a collaborative effort between Ms. Julie Geng and the author. With the assistance of the author, Ms. Geng prepared the reported NHC-CDIs via direct addition. The author initiated this project and is responsible for the remainder of the synthetic work, and all of the mechanistic, and computational studies.

The overview in **Chapter 5** of the challenges in the field of polymer networks/gels was written by the author.

The work in **Chapter 6** was a collaborative effort between the author and Dr. Mingjiang Zhong, Dr. Vladimir K. Michaelis, Mr. Eric G. Keeler, Dr. Jessie E. P. Sun, Prof. Darrin J. Pochan, Prof. Michael J. A. Hore, and Prof. Adam P. Willard. The author conducted the synthesis and characterization experiments. The author and Dr. Zhong conducted mechanical testing experiments. The author, Mr. Keeler, and Dr. Michaelis conducted MAS NMR experiments. Dr. Sun and Prof. Pochan conducted SANS experiments and analyzed the SANS data. Prof. Hore provided the SANS model. Prof. Willard developed simulations. All authors analyzed data.

TABLE OF CONTENTS

CHAPTER 1. Introduction to Carbene Ligands in Surface Chemistry: From Stabilization of Discrete Elemental Allotropes to Modification of Nanoscale and Bulk Substrates

1.1 Introduction

Carbenes are perhaps the most versatile reactive intermediates in chemistry. Since the original visions of "methylene" by Dumas[1] in 1835 and a generalization of this vision by Nef[2] in 1897 (Figure 1), these formally divalent carbon species[3] have found broad application in organic synthesis,[4,5] organometallic chemistry and specifically transition metal catalysis,[6,7] organocatalysis,[8,9] biochemistry,[10,11] and materials chemistry.[12] Much like free radical and carbocation chemistry were forever impacted by the discoveries of the persistent trityl radical by Gomberg[13] and stable ion media for carbocations by Olah,[14-17] respectively, the field of carbene chemistry was dramatically influenced by Bertrand and coworkers' 1988 report of the first isolable carbene[18] and Arduengo and coworkers' 1991 report[19] of the first isolable, *crystalline* carbene – an imidazolylidene based *N*-heterocyclic carbene (NHC) IAd (Figure 2A). The latter seminal work, which showed that the traditionally highly reactive and unstable carbene could be tamed, crystallized, and bottled like ordinary persistent chemical reagents, led the same group to later report the first use of a free NHC as a donor ligand to form an organometallic complex.[20] Thus, a new era began wherein carbenes began to be studied in a wide range of unprecedented applications.[21,22] Perhaps the most prominent examples of the impact of carbene ligands emerged in the field of transition metal catalyzed olefin metathesis (Figure 2B).[23,24,25,26] The ubiquitous second[27,28] and third[29-31] generation Grubbs catalysts and Hoveyda-Grubbs[32,33] catalysts, and several more recent Ru-based catalysts[26,34-38] feature NHC ligands. Furthermore, all of the well-defined olefin metathesis catalysts contain an alkylidene carbene ligand.[23,39-42] Thus, carbenes have played a critical role in the development of the field of olefin metathesis for which Schrock, Grubbs, and Chauvin shared the 2005 Nobel Prize in chemistry. Now, NHCs such as IMes, SIMes, Dipp, and DippH$_2$ (Figure 2A) can be purchased directly from major chemical suppliers. Furthermore, alternative NHCs with a much broader range of properties such as triazolylidenes,[43] cyclic (alkyl)(amino) carbenes (CAACs),[44,45] and diamidocarbenes (DACs)[46,47] have been developed for specific applications (Figure 2C).

By 2005, the broader chemistry community had become well aware of the virtues of NHCs as ligands for transition metal species. Hence, it should come as no surprise that NHCs would soon find applications outside the realm of transition metal catalysis. For example, an entire field of NHC organocatalysis has emerged; NHCs opened umpolung reactivity pathways that enable otherwise difficult transformations.[43,48-73] NHCs have also been used extensively for the
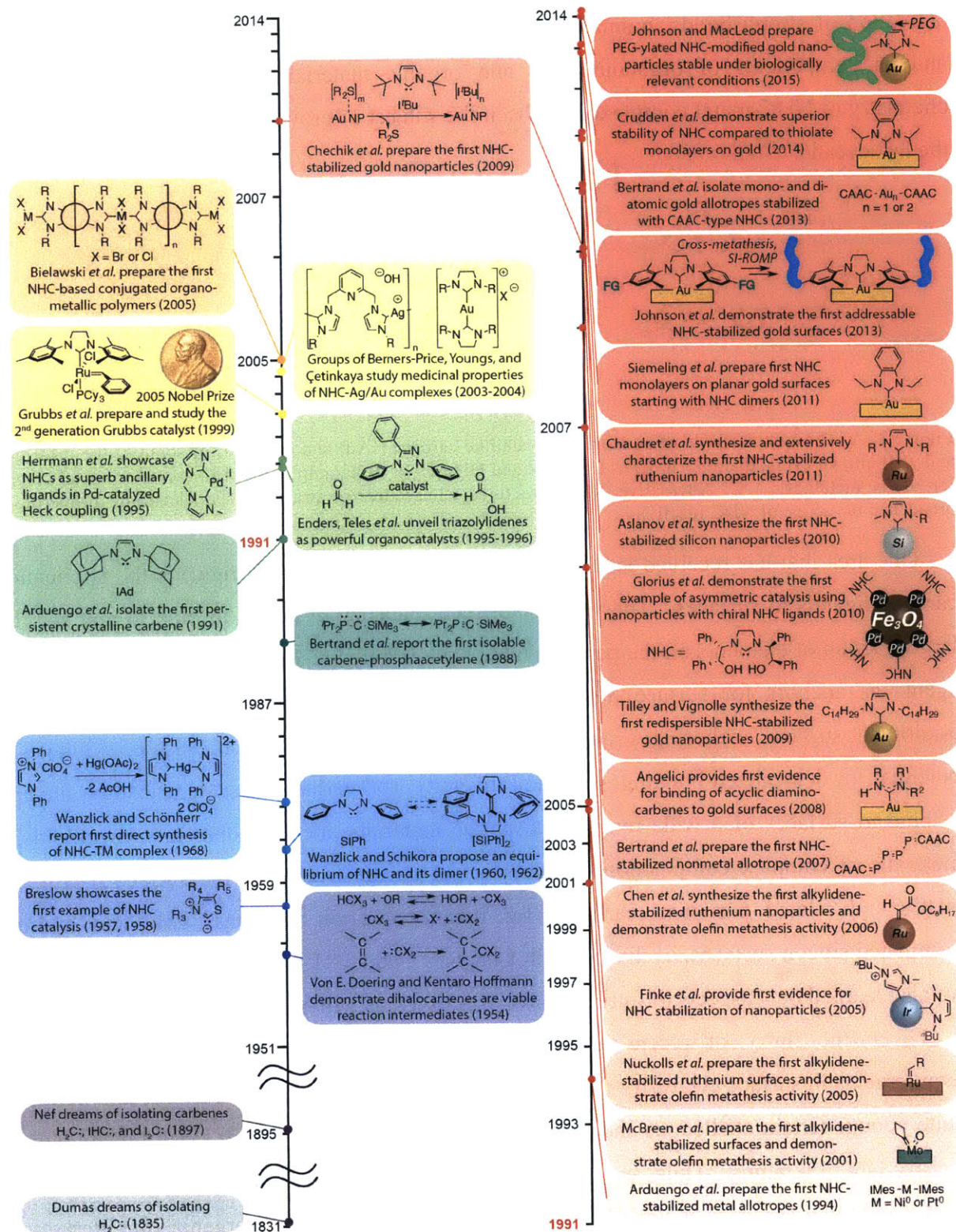
Figure 1. Timelines depicting major milestones in the development of carbene chemistry and its major applications. Key examples of carbenes in surface chemistry from 1994-2015 are shown at right.

17

activation of strong bonds in small molecules (e.g., B–H,[74] C–H,[75] and N–H,[76] among others) and as components of organometallic and organic materials.[12,77-81] Finally, the medicinal chemistry of NHC-metal complexes has been the subject of growing interest during the course of the last decade.[12,82-84]
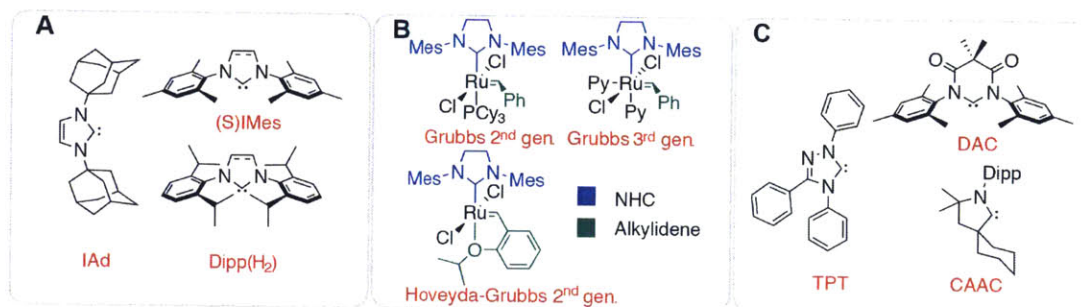
Figure 2. A. The first example of an isolable crystalline carbene (IAd) and examples of some of the most utilized and well-known cyclic diaminocarbenes ((S)IMes and Dipp(H₂)). **B.** Examples of NHC-transition metal complexes for olefin metathesis. **C.** Alternative NHC structures whose diverse structural and electronic properties have broadened the scope of NHC reactivity.

One area that has received less attention until recently (Figure 1, right) is the application of carbene ligands to surfaces. The well-established tendency of NHCs to bind to and stabilize a large fraction of elements on the periodic table have inspired researchers to utilize these versatile agents as anchors for surface modification. NHCs offer several potential advantages over traditional surface anchoring groups, such as enhanced stabilization, ease-of-synthesis, the potential for delocalized bonding, structural diversity, and perhaps most significantly, the ability to bind to surfaces of a wide range of disparate materials: metals, nonmetals, metalloids, and materials of complex composition. Hence we set out to investigate the surface chemistry of NHCs and related persistent carbenes for functionalization of planar gold and hydrogen-terminated silicon surfaces, as discussed in Chapters 2 and 3. During the course of these studies we also learned new aspects of intrinsic NHC reactivity, as will be discussed in Chapter 4.

Given the flurry of recent activity in this field, our understanding of NHC design requirements in surface chemistry continues to increase at a rapid pace. Though this field is still quite young, certain challenges and patterns have begun to emerge from careful examination of the available literature. Thus, we begin by providing a comprehensive account of the use of NHCs and other carbenes as ligands for surfaces. Our main goal is to organize the literature and illuminate challenges, patterns, and paths forward in this nascent field. This overview is roughly organized by surface size scale. We start with a brief discussion of NHC stabilization of molecular elemental allotrope species; these complexes represent the smallest possible fragments

of a metal surface. We then describe examples of NHC ligands bound to nanoparticles (NPs) and then move to the formation of NHC monolayers on planar surfaces. We conclude with a summary of the application of other types of carbenes to surface stabilization.

1.2 Elemental allotropes stabilized by NHCs

Aside from noble gases, elements with an oxidation state of 0 are unstable in monoatomic form due to their unfilled valence orbitals. Consequently, many elements exist in diatomic, oligoatomic, or polyatomic form; some have multiple allotropes.[85-87] Notably, advances in allotrope chemistry (as in the stabilization of elemental species with oxidation state 0) often lead to major paradigm shifts in chemistry. For example, the discovery of C_{60} inaugurated the field of carbon nanotechnology;[88-91] the discovery of graphene revolutionized electronic materials science;[92-99] the invention of soluble forms of Pd^0 facilitated the development and application of Pd-catalyzed cross-coupling.[100-110] Each of these three developments was recognized with a Nobel Prize. Shortly after their discovery, NHCs have had a profound impact on allotrope chemistry. Since NHC-stabilized allotropes and metal^0 species represent the smallest possible fragments of NHC-functionalized surfaces, we have chosen to include key examples here. The insights gained from these studies inspire and inform studies in surface chemistry.

In 1994, Arduengo and coworkers reported the first examples of NHC complexes with elements in their atomic form: monoatomic Ni^0 and Pt^0 complexes with IMes (**1** and **2**, respectively, Figure 3).[20] In 2000, Herrmann and coworkers reported similar NHC-Pd^0 complexes.[108] At the time, the fact that Ni^0, Pd^0, and Pt^0 complexes were isolated was not by itself remarkable; these metals had previously been isolated as complexes with other L-type ligands – *e.g.*, dibenzylideneacetone (dba),[111,112] CO,[113] and PPh_3.[114-117] However, these reports suggested that NHCs have the right combination of steric and electronic properties to complement these canonical ligands. Furthermore, the unique properties[45,118] and synthetic flexibility of NHCs hinted that maybe they could be used to isolate other elusive species.

In 2007, the first example that proved this notion emerged. Bertrand and coworkers were able to stabilize a neutral linear P_4 phosphorus allotrope with a CAAC ligand (**3**, Figure 3).[44,119] Shortly thereafter they achieved controlled trimerization of P_4 to a novel P_{12} phosphorus allotrope stabilized by $DippH_2$.[120] In the following years, the Robinson and Bertrand groups independently prepared P_2 stabilized by Dipp (or IMes)[121] and a CAAC,[122] respectively (**4** and **5**,
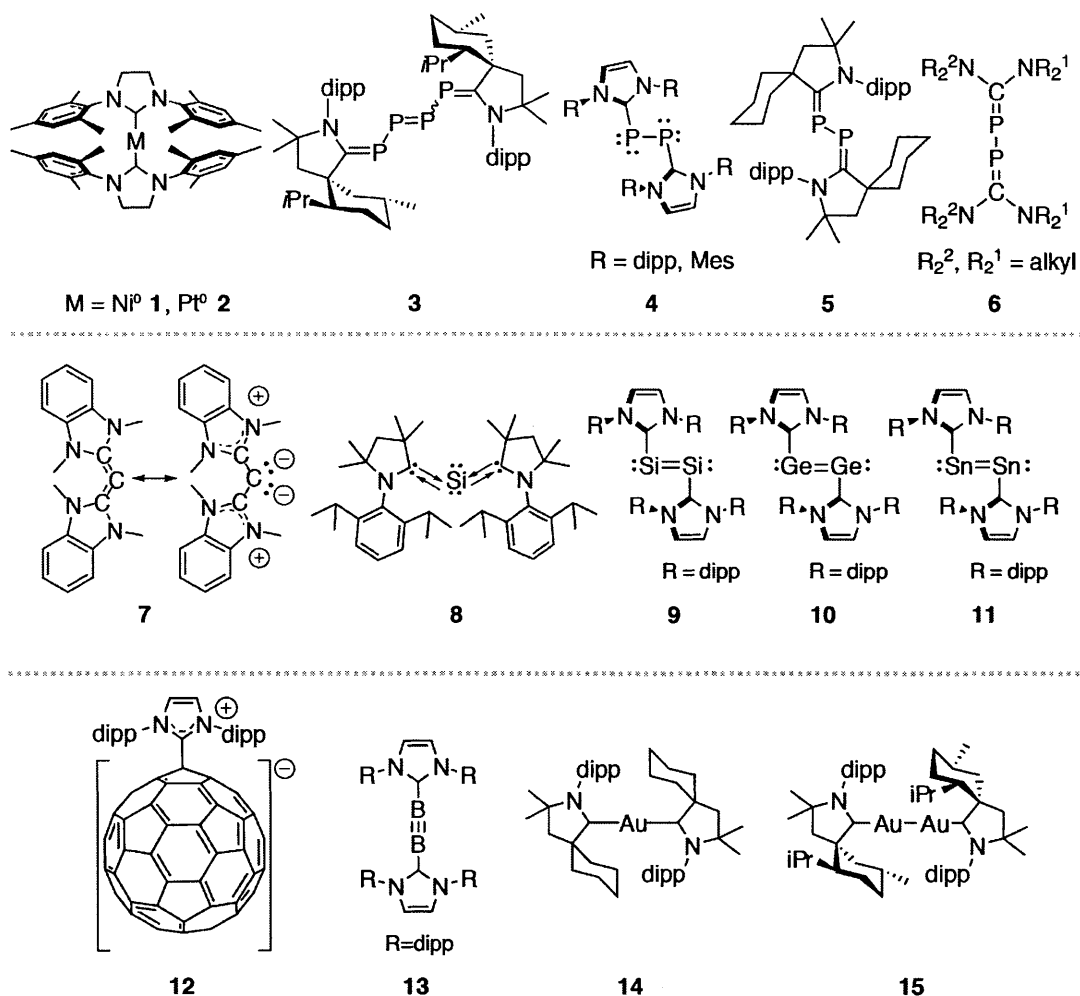
Figure 3. NHCs and one example of an acyclic diaminocarbene as stabilizing ligands for elemental allotropes (dipp = 2,6-diisopropylphenyl, Mes = 2,4,6-trimethylphenyl). The selected structures highlight the ability of NHCs to bind to and, in many cases, stabilize a diverse set of elements that in some cases could not otherwise be isolated. The structural differences between cyclic diaminocarbenes and CAACs have proven essential for defining their electronic properties and stabilizing abilities.

Figure 3). Both groups noted the strong contribution of the diphosphabutadiene resonance form as well as an NHC→P dative bond resonance contribution, leading to an effective P-P bond order of 1. In its "unstabilized" form, P_2 has a P-P bond order of 3. Among the pnictogens, Robinson, Schleyer, and coworkers also prepared the NHC-stabilized As_2, which exhibited similar properties to the P_2 analog.[123] It should be noted that the first carbene-stabilized P_2 species was reported by Markovskii and coworkers[124] over two decades before the work of Bertrand and Robinson, though in Markovskii's case the carbene was acyclic and the free carbene was not explicitly handled (**6**, Figure 3) as isolable free carbenes were not known at the time. One is again reminded of the significance of Arduengo's discovery of persistent, isolable NHCs.

The successful stabilization of phosphorus allotropes with NHCs propelled chemists to attempt to stabilize even more exotic species. In 2008, Bertrand and coworkers reported the isolation of a single carbon atom stabilized by two NHCs (7, Figure 3).[125] In contrast to other well-known examples of "carbodicarbenes" – *i.e.*, allenes – this $(NHC)_2C$ is more appropriately classified as a carbone[126] with a C-C-C bond angle of 134.8°. Its reactivity was also remarkably different from typical allenes and more characteristic of carbones: upon reacting with $[RhCl(CO)_2]_2$, it formed an h^1 complex with Rh, which exhibited an unusually low average CO stretch frequency in its infrared spectrum, indicating that the isolated $(NHC)_2C$ was a stronger electron-donor than most NHCs. More recently, the Stalke group reported a Si^0 atom stabilized by two CAAC molecules (8, Figure 3).[127] The C-Si-C bond angle of 117.7° was even smaller than that of Bertrand's carbon analog 7. Theoretical treatment was most consistent with Si having two non-bonding electron pairs – *i.e.*, that it is a silylone.

In 2008, Robinson and coworkers expanded the scope of elements stabilized in their neutral form by NHCs with their report of Si_2 stabilized by two units of Dipp (9, Figure 3).[128] Analogously to their previous synthesis of $Dipp\,P_2\,Dipp$,[121] they obtained $Dipp\,Si_2\,Dipp$ by reduction of the $Dipp\,SiCl_4$ adduct with potassium graphite. This singlet, doubly bonded Si_2 species was the first such structure in which Si atoms had a formal oxidation state of 0 *and* that was soluble in organic solvents,[129-131] stable at room temperature, and isolable in pure form. Since then, this type of stabilization (though not via the same synthetic route) has been extended to Ge_2[132] (10, Figure 3) and Sn_2[133] (11, Figure 3). These compounds also exhibited a singlet double-bonded ground state. Though computational studies predicted that the Pb_2 analog should be stable,[134] attempts to synthesize it via approaches that were employed for its congeners proved unsuccessful.[133]

With NHC allotrope stabilization now having securely gripped the imagination of chemists, other intriguing NHC-element^0 complexes began to emerge. For example, in 2011 a stable Dipp-C_{60} adduct was reported (12, Figure 3, admittedly, C_{60} is quite stable and soluble in organic solvents on its own).[135] The same year, diboryne (triply bonded B_2) stabilized by two units of Dipp was reported by Braunschweig and coworkers (13, Figure 3).[136] This structure was another first of its kind: an isolable, stable-at-room-temperature molecule that possessed several characteristics of a boron-boron triple bond. We must note here, however, that considerations of bond force constants and thermodynamics of NHC addition to B_2* (excited state of B_2 in the gas

phase) compelled Schnöckel and Köppe to question this assignment and propose that the B_2 bond order in **13** is, in fact, 1.5.[137] Yet, molecular orbital analysis, as well as a host of structural and spectroscopic evidence (including an alternate interpretation of experimentally evaluated bond force constants), favors the original assignment by Braunschweig and coworkers.[136,138-140] Moreover, the same group demonstrated that the B_2 bond order could be reduced to two if one uses the simultaneously more nucleophilic and more electrophilic CAAC-type NHCs.[139] This dramatic distinction in the mode of stabilization provided by CAACs, as well as Stalke's success with these ligands in uniquely stabilizing Si^0, illuminated their potential to stabilize other species for which cyclic diaminocarbenes may be inadequate.

Several groups have demonstrated the validity of this supposition: in a matter of two years, isolable, CAAC-stabilized monoatomic Au^0 (**14**, Figure 3),[141] Mn^0,[142] Fe^0,[143] Co^0,[143] Ni^0,[144] Cu^0,[145] and Zn^0,[146] as well as the diatomic Au_2^0 (**15**,[141] Figure 3) and Sb_2^0,[147] complexes have been reported. The isolation by Bertrand and coworkers of the Au^0 and Au_2^0 complexes – the smallest possible "fragments" of Au – is a particularly impressive, milestone achievement[141]: these complexes are stable at room temperature, soluble in organic solvents (*e.g.*, THF and benzene), and crystalline, which provides crucial, but previously inaccessible, experimental characterization of bonding that may exist in neutral Au nanoclusters and planar gold surfaces stabilized by NHCs. With these findings in mind, and given the recent isolation of NHC-stabilized Au_3^+ clusters by the Sadighi[148] and Bertrand[149] groups, the next anticipated breakthroughs will likely come from the crystallization of larger Au^0 and other metal clusters[150,151] stabilized by NHCs. For example, during the preparation of this review, Szczepura and coworkers reported that they were able to isolate and crystallize small rhenium sulfide and selenide clusters (with $[Re_6S_8]^{2+}$ and $[Re_6Se_8]^{2+}$ cores) with NHC ligands (SIMes and IMes).[152] The NHC-Re bond lengths in these clusters were 2.203(14) Å and 2.248(16) Å, respectively, indicating relatively weak interactions of the NHC with the metal center. Nonetheless, the incorporation of NHC ligands resulted in significantly altered photophysical cluster properties: namely, a blue- or red-shift in emission maximum, a reduced quantum yield, and a shortened excited-state lifetime.[152] Perhaps more significantly, this advance will help to guide future attempts to crystallize other types of NHC-stabilized clusters.

1.3 Metal nanoparticles stabilized by NHCs (NHC@metal NPs)

NHC@Ir NPs: Early clues about NHC binding to metal surfaces
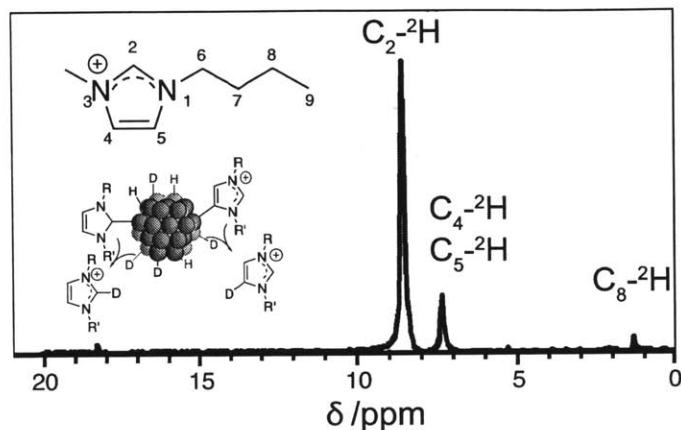
Figure 4. ^{2}H NMR of an imidazolium based ionic liquid after its exposure to Ir NPs formed by the reduction of Ir(I) precursors with ^{2}H$_2$.[153] The exposure of ionic liquid to the deuterium labeled Ir NP lead to deuterium incorporation. This demonstrated that the imidazolium was coordinating to the surface, likely through oxidative addition. Exchange of ^{1}H and ^{2}H occurred on the surface during reductive elimination as depicted. This supported the hypothesis that carbenes, Arduengo-type (C$_2$-^{2}H) and abnormal (C$_4$-^{2}H and C$_5$-^{2}H), were binding to and desorbing from the surface.

While NHC-stabilized mono/oligo-atomic elemental species had been synthesized and characterized as early as 1994,[20] the first hypothesis and evidence for NHC-NP interactions were reported in 2005 and 2007 by Finke and coworkers.[153,154] The hypothesis of NHC binding to an Ir NP surface was advanced based on observation of ^{1}H/^{2}H exchange (Figure 4) observed at C2, C4, C5 and C8 of imidazolium-based ligands in the presence of Ir NPs formed by reduction of Ir(I) precursors with ^{2}H$_2$ (*i.e.*, D$_2$).[153] The mechanism for this exchange likely proceeds through reversible oxidative addition of the imidazolium C–H bond to an Ir surface site, a process with precedent among molecular Ir^I complexes,[155,156] as well as other TM species,[157-159] though not general across all transition metals (*e.g.*, there is no such precedent for Au^0). Finke and coworkers were unable to definitively confirm that NHCs were directly bound to the Ir NP surface, however.[154] It was stated that the number of NHC-bound surface sites was likely small, and that the analytical techniques available to characterize the NHC@Ir NP surface (NMR, IR, etc.) might be much less informative than in the case of traditional complexes.[154] Since then, the use of alternative NHC structures, different NP materials, and a wider range of characterization tools have enabled the confirmation that NHCs indeed bind to surfaces.

23
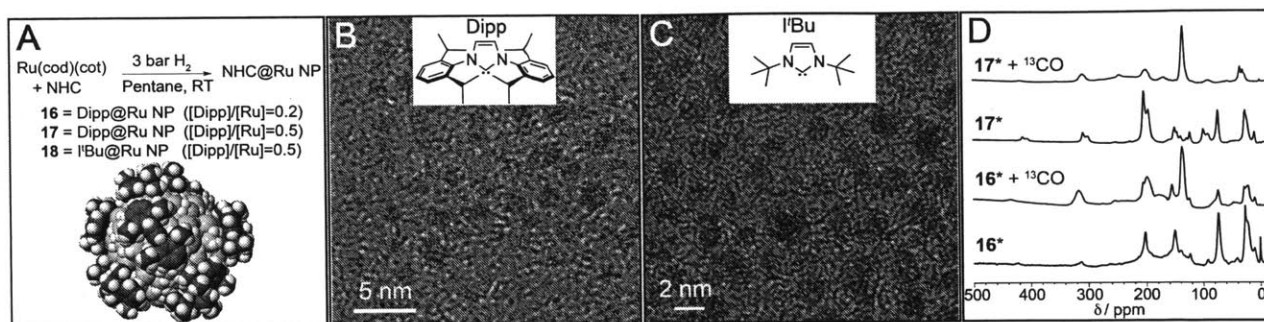
Figure 5. Characterization of NHC@Ru NPs by Chaudret and coworkers.[160] **A.** Synthesis of NHC@Ru NPs **16–18** from different NHCs and using different ratios of NHC to ruthenium, as shown in the figure. Below: simulation of eight Dipp ligands bound to a 1.8 nm-diameter hcp Ru NP, which shows the availability of possible hydride binding sites on the NP surface. **B.** HR TEM of **16**. Inset: structure of Dipp. **C.** HR TEM of **18**. Inset: structure of I'Bu. **D.** ^{13}C CP-MAS of **16*** and **17*** (analogues of **16** and **17** synthesized using ^{13}C-labeled NHCs) before and after exposure to ^{13}CO. The spectra before exposure reveal that there is a correlation between the concentration of Dipp and the binding sites of the carbene. Exposure to ^{13}CO revealed that **17*** had NHCs bound to the faces and edges, while **16*** was mainly bound to just the edges. The peak at 205 ppm observed in both **16*** and **17*** was attributed to NHC binding to Ru NP edges. The peak 195 in **17*** is attributed to the binding to NP faces. Reprinted with permission from reference 160. Copyright 2011 John Wiley and Sons.

Much of our current understanding of NHC@metal NP systems comes from the seminal contribution of Chaudret and coworkers in 2011.[160] These authors reported the formation of NHC-stabilized Ru NPs via hydrogenative decomposition of (1,5-cyclooctadiene)(1,3,5-cyclooctatriene)ruthenium(0) in the presence of either Dipp or I'Bu (Figure 5A). The authors found that Dipp was a better NP stabilizer: Dipp-Ru NPs (**16** and **17**), when protected from air, were quite stable to aggregation in pentane and toluene. In contrast, I'Bu-stabilized Ru NPs (**18**) precipitated after ~1 d in solution. Furthermore, the authors found that at higher relative NHC concentrations, slightly smaller NPs were formed; ultimately, when the relative amount of the NHC was sufficiently large, predominantly molecular species were formed. Thus, for [Dipp]/[Ru] = 0.2, the NP diameter was 1.7(0.2) nm (**16**), and for [Dipp]/[Ru] = 0.5, the NP diameter was 1.5(0.2) nm (**17**). High resolution TEM (HRTEM, Figure 5B and 5C) and wide-angle X-ray scattering (WAXS) indicated that the NPs in all cases were single-crystalline with hexagonal close-packed structures. The well-defined, crystalline and re-dispersible nature of these Ru NPs was certainly exciting, and offered an opportunity to investigate NHC binding to the NP surface in more detail.

Perhaps the most definitive evidence for binding of NHCs to the Ru NP surface was obtained from solution- and solid-state ^{1}H and ^{13}C NMR spectroscopy. The only non-solvent resonances observed in the ^{1}H NMR spectra corresponded to the Dipp and I'Bu methyl protons of **16** and **18**,

respectively. Furthermore, the aryl, benzylic (for **16**), and imidazolylidene backbone ^{1}H resonances of surface-bound Dipp and I[r]Bu (for **16** and **18**, respectively) were absent in the spectra due to the slow tumbling of the NPs and the heterogeneity of the surface magnetic environments. These data suggested that both NHCs were rigidly and tightly bound to the surface. The authors also proposed that the proximity of the aryl groups of **16** (and by extension, **17**) to the NP surface (suggested by the above ^{1}H NMR data) could play a role in the NP stabilization (*vide infra*).

Addition of diphenylphosphinobutane to **16–18** led to neither ligand exchange nor additional ligand attachment, which suggested that the NHCs were strongly bound and densely packed on the NP surface. Comparison of the ^{13}C solid state magic angle spinning (MAS) NMR spectra of these NPs with and without a ^{13}C label at the carbene carbon demonstrated that the NHCs were indeed bound via the carbene carbon: in all three ^{13}C-labeled NP samples (**16*–18***), the labeled carbon had a chemical shift indicative of the corresponding carbene carbon (190 ppm for **18***, and 205 ppm for **16*** and **17***) bound to a transition metal.[161] Curiously, while **16*** and **18*** exhibited only one peak corresponding to the carbene carbon, the analogous NPs prepared with more Dipp (**17***) exhibited two peaks, one of which matched the peak for **16*** (205 ppm), and another, which was even more upfield than the free carbene (Figure 5D). This observation suggested the presence of at least two types of binding sites on the Ru NPs, which was consistent with the results derived from hydride-titration experiments carried out to quantify the number of Ru-H species on the NP surfaces (see Figure 5A for a model of such a surface). Namely, titration experiments showed an anomalous ~2-fold greater H density for **17*** than for the **16***, which was deemed to be an artifact of insertion of Ru into the 3° C-H bonds of the NHC. The fact that this insertion was evident only in Ru NPs exposed to the greater amount of Dipp (*i.e.*, **17***) suggested that in the more densely NHC-coated Ru NPs, more NHCs were proximal to surface sites disposed toward C-H insertion.

To further probe the various possible surface sites, ^{13}C solid-state NMR studies were conducted on NHC@Ru NPs treated with [13]CO (Figure 5D). These elegant experiments revealed the presence of both terminal (non-diffusing) and bridging carbonyl groups in colloids **18** and **16**, while only the terminal [13]CO was observed in colloid **17**, which confirmed that the binding sites accessible to bridging [13]CO were occupied/blocked by NHCs in **17**. Carrying out the solid-state NMR with and without [1]H-^{13}C cross-polarization (CP) further indicated that the terminal

carbonyl groups were located in close proximity to the NHCs. The different chemical reactivity toward air of the three colloids exposed to CO was also used to comment on the surface coverage by the NHCs: **18** + CO was pyrophoric, **16** + CO decomposed rapidly in air, and **17** + CO reacted only slowly with dioxygen in air. Hence, I^{r}Bu, as well as Dipp at low relative amount, appeared to bind to the more exposed apical and edge sites of the Ru NPs, which left room for other species to bind to the surface. In contrast, the NHC binding in colloid **17** was sufficiently dense to render these NPs less accessible to other species. Finally, all three colloids were active catalysts for hydrogenation of styrene to ethylcyclohexane, though the reaction rate was much slower than for one catalyzed by the less sterically encumbered Ru/PVP system. More extensive investigation[162] later revealed that **16** with the more "accessible" NP surface compared to **17** is the optimal hydrogenation catalyst among the three NHC-stabilized NPs. Why **18** – seemingly possessing equally accessible surface sites as colloid **16** based on ^{13}CO experiments – is much less active in hydrogenation is not yet well understood. These fundamental studies provided a clear understanding that steric effects play an important role in selective stabilization of the Ru NP surface by NHCs, and confirm that NHCs – even ones possessing large steric bulk – are not intrinsically incapable of stabilizing transition metal NPs; in fact the stabilization can be sufficiently effective so as to poison otherwise catalytically active NPs.

Chaudret and coworkers also recently reported that aggregation-stable and catalytically active NHC-stabilized Pt NPs, analogously to Ru NPs, could be synthesized by reductive decomposition of molecular Pt species in the presence of NHCs.[163] Thus, NHC@Pt NPs derived from Pt(dba)$_2$ and supported by Dipp or I^{i}Pr$_2$Me$_2$ ligands were found to be highly active (TOF on the order of 10^3 h^{-1}) and chemoselective in the reduction of nitroarenes to anilines under rather mild conditions (1 atm H$_2$, 30 °C, 0.2 mol % Pt, [substrate] = 0.75 M in THF).[163] As observed in their work on NHC@Ru NPs, increasing the concentration of the NHC during the Pt NP preparation led to diminished catalytic activity, likely due to a reduced number of available sites for substrate binding. Furthermore, Pt NPs stabilized with Dipp were ~5 times more active in nitroarene reduction compared to Pt NPs stabilized with I^{i}Pr$_2$Me$_2$, suggesting that steric bulk and potentially other factors – *e.g.*, non-covalent interactions, the density of ligand packing and NHC electronics – contribute to the nuanced nature of NHC binding to a metal surface and its resulting catalytic activity. However, even with little ligand optimization, the potential of NHC@Pt NPs as catalysts was apparent.

Expanding on this first example of NHC@Pt NPs, Chaudret and coworkers unveiled a class of water-dispersible NHC-stabilized Pt NPs, which was subjected to a much more thorough structural characterization that provided several important new details regarding NHC-surface binding (Figure 6).[164] In this work, the authors found that Pt NPs stabilized by NHCs can be prepared by reductive decomposition of NHC-bearing Pt complexes. The use of an anionic sulfonate-based NHC (Figure 6) provided Pt-NPs that were air-stable, aggregation stable, and water-dispersible. The direct bond between the Pt and the carbene carbon of the NHC was definitively confirmed by the observation of (1) a resonance in the ^{1}H–^{13}C CP-MAS NMR spectrum with a chemical shift characteristic of the surface-bound carbene carbon and (2) ^{195}Pt–^{13}C coupling with a magnitude of 940 ± 20 Hz, consistent with a ^{195}Pt–^{13}C (Figure 6A). This value is significantly higher than the ^1J scalar coupling constant in the analogous molecular Pt(II)-NHC complex (767 Hz), but also significantly lower than that in known molecular Pt^0 complexes (1365 Hz).[165] The coupling magnitude is certainly indicative of direct bonding of the carbene carbon and a surface Pt atom; however, while the formal oxidation state of the NHC-bearing surface Pt atom is likely to be 0, further evidence to confirm this is required. Lastly, the
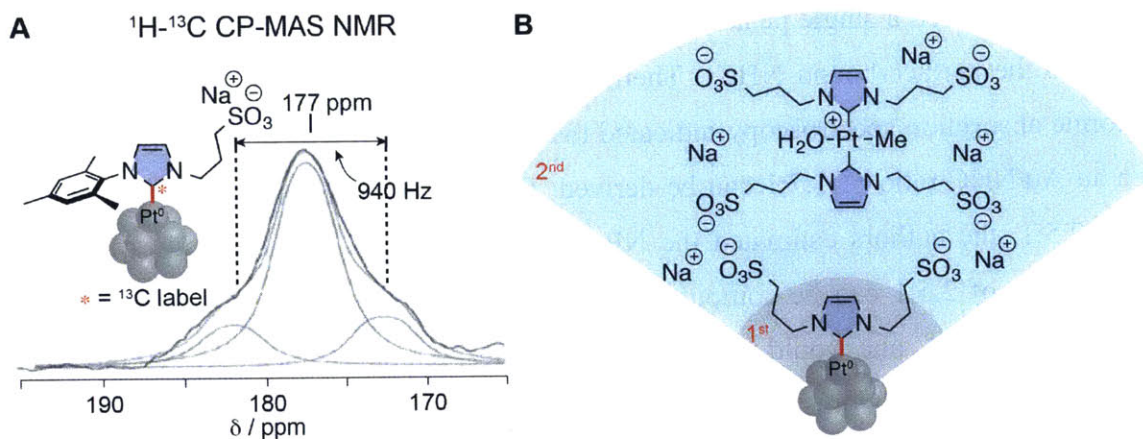
Figure 6. (A) The characteristic "metallated carbene (NHC)" region of the ^{1}H-^{13}C CP-MAS NMR spectrum obtained by Chaudret et al. for their novel water-soluble NHC@Pt NPs, a cartoon of which is depicted alongside the spectrum (NHC-Pt surface bond is shown in red).[164] The carbene carbon is ^{13}C-labeled, and the corresponding resonance appears at 177 ppm, with a characteristic splitting due to J-coupling with Pt with a magnitude of 940 Hz. (B) Cartoon of another type of water soluble Pt NPs prepared by Chaudret et al., which exhibited a second layer of stabilization by bis(NHC)Pt(II) complexes in addition to direct attachment of NHCs to the NP surface (NHC-Pt surface bond is shown in red). Reprinted with permission from reference 164. Copyright 2014 John Wiley and Sons.

authors found that when both of the NHC *N*-substituents were ^{n}propylsulfonate, the NHC-stabilized NPs could not be separated from a shell of corresponding bis(NHC)Pt(II) complexes due to a proposed strong electrostatic complex-NP attraction (Figure 6B). This observation is

analogous to the possible involvement of bis(NHC)Au$^+$ complexes in Au NP stabilization discussed in section 1.4 (*vide infra*).

While a great deal of information has been gathered to date about NHC interactions with Ru and Pt surfaces, one must be cautious about the extrapolation of Ru/Pt-specific conclusions to other metal surfaces due to differences in valence, coordination geometry, and reactivity. Thus, we will discuss the current understanding of NHC binding to other types of surfaces below separately for each type.

NHC@Au NPs: Synthetic routes and derived insights into NHC binding

In 2009, the Chechik group reported[166] the preparation of Au and Pd NPs coated with bis(tert-butylimidazol)-2-ylidene (I^{t}Bu) via ligand exchange (Figure 7A), beginning with didodecylthioether- or trioctylphosphine-stabilized Au and Pd NPs, respectively. Both types of NPs exhibited a number of similar characteristics after treatment with NHC. These NPs remained unchanged in size after ligand exchange as determined by TEM. X-ray photoelectron spectroscopy (XPS) revealed an absence of thioether ligands in the case of Au NPs; in the N 1s region there appeared a single peak at 400.3 eV (slightly below 400 eV for Pd NPs), which was assigned to the surface-bound NHC. Thermal gravimetric analysis (TGA), elemental analysis and atomic absorption spectroscopy indicated that Au comprised 65—66 wt.% of the NPs, from which an Au/NHC ratio of 1.7:1 can be derived; from these values and the XPS-derived Au:N ratio of 2.5:1, the authors estimated the NP composition to be Au$_{840}$(I^{t}Bu)$_{340}$, from which an Au/NHC ratio of 2.5:1 can be computed. Given a 2.9 Å Au-Au bond length (or 1.44 Å Au covalent radius),[151,167] one would estimate for a spherical 2.6 nm-diameter Au NP the ratio of all Au atoms to surface Au atoms to be ~1.9:1[168] (another computation method[169] afforded a similar ratio of ~2.3:1); an experimentally-derived Au/NHC ratio of 1.7—2.5:1 suggests that >75% of the surface atoms had an NHC attached (less if two NHCs are bound to some surface gold atoms). Despite – or perhaps because of – this high degree of NHC attachment, as well as the relatively strong NHC-Au bond (TGA-MS indicated the onset of ligand loss at 230 °C), the NHC@Au NPs (and likewise, the NHC@Pd NPs) were unstable in solution, forming insoluble precipitate after approximately 12 h. The authors observed mono- and bis-NHC Au (or Pd) complexes as degradation products. Based on these results they hypothesized that the mechanism of NP instability was desorption of these complexes from the surface leading to NP aggregation.

They further proposed that the NHC stabilization of NPs could be viewed as stabilization of NP cores by NHC-metal complexes, which is consistent with dissociation of these complexes in solution. With this model in mind, Chechik and coworkers hypothesized that NHC coated NPs would be inherently prone to leaching NHC-metal complexes and subsequent aggregation.
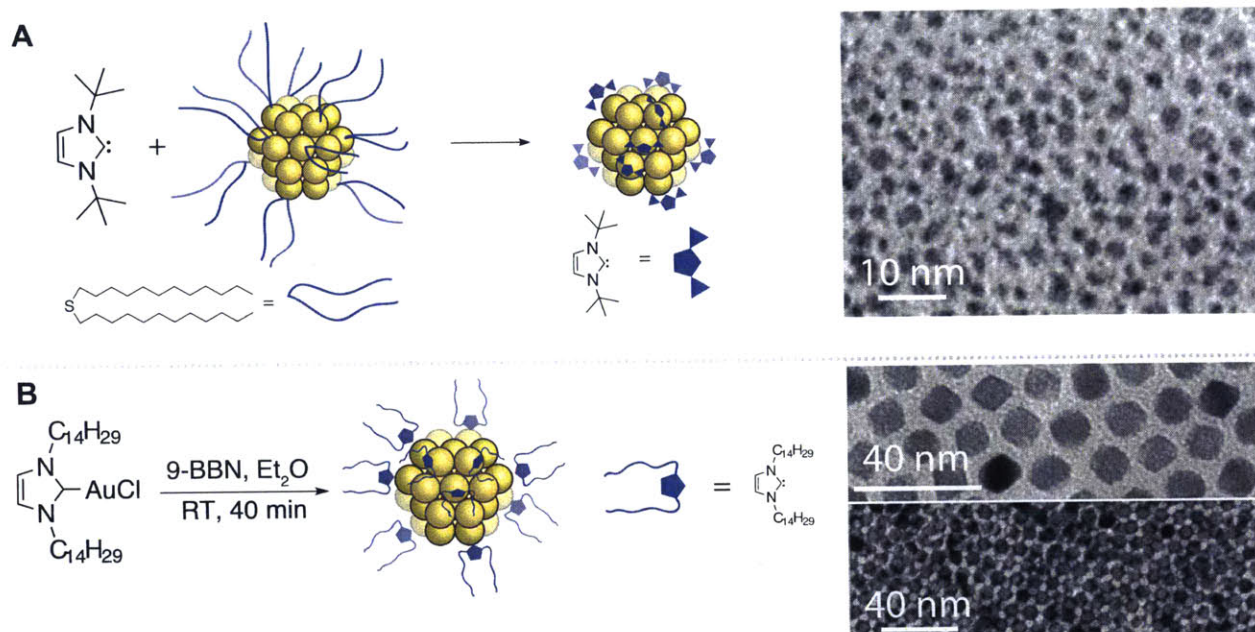
Figure 7. A depiction of the first syntheses of NHC-stabilized Au NPs. **A.** Chechik and coworkers reported I'Bu-stabilized Au NPs via ligand exchange of thioether protected NPs.[166] The size of the I'Bu-stabilized NPs, 2.6 ± 0.5 nm, was reported to be the same as that of the starting thioether-stabilized NPs. After ~12 hours in solution, aggregation of the NHC@Au NPs was observed. Reprinted with permission from reference 166. Copyright 2009 Royal Society of Chemistry. **B.** Tilley and coworkers reported the synthesis of NHC-stabilized Au NPs via reduction of NHC-AuCl complexes.[170] The utilization of long alkyl N-substituents led to high NP stability in solution. Reprinted with permission from reference 170. Copyright 2009 Royal Society of Chemistry.

This hypothesis was disproven a few months after Chechik's seminal report, when Tilley and coworkers prepared NHC-stabilized Au NPs with different NHCs (*vide infra*) and via a different method: namely, by reduction of well-defined NHC-Au(I) complexes (Figure 7B).[170] This method worked best when the N-substituents of the NHC were long alkyl chains, producing monocrystalline 5—7 nm NPs (by TEM and X-ray diffractometry) that were stable for months in organic solvents. UV-visible (UV-vis) absorption spectroscopy revealed the expected plasmon resonance peak at 525 or 535 nm, and other characterization methods (^{1}H NMR and MS) were consistent with NHC stabilization of the Au NPs (*e.g.*, Tilley observed $(NHC)_2Au^+$ complexes via fast atom bombardment MS of the formed Au NPs). TEM also revealed self-assembly of the NHC@Au NPs into a 2D hcp superlattice; an fcc 3D superlattice could be achieved by slow evaporation of the NHC@Au NP dispersion in THF. Interdigitation of the long alkyl chains was

proposed as the driving force behind the observed self-assembly. Harking back to Chechik's hypothesis, one is led to wonder if such inter-nanoparticle and, more importantly for solution stability, intra-nanoparticle alkyl chain van der Waals interactions played an important role in the stabilization of Tilley's NPs. Similar stabilization is well known for alkanethiol-stabilized gold surfaces.[171] While the end-result was highly encouraging, Tilley's report did not address the mode and geometry of NHC binding and the mechanism of NP stabilization.

More recently (in 2014), Glorius, Ravoo and coworkers demonstrated that, indeed, introduction of long alkyl chains at C4 and C5 of the imidazolylidene ligand *and* use of small or flexible *N*-substituents allows one to prepare air-stable and aggregation-stable NHC@Au NPs (and NHC@Pd NPs, *vide infra*).[172] Notably, these NPs were prepared via ligand exchange on thioether-stabilized NPs, confirming the viability of this method in preparing stable NHC@NPs Figure 8A).
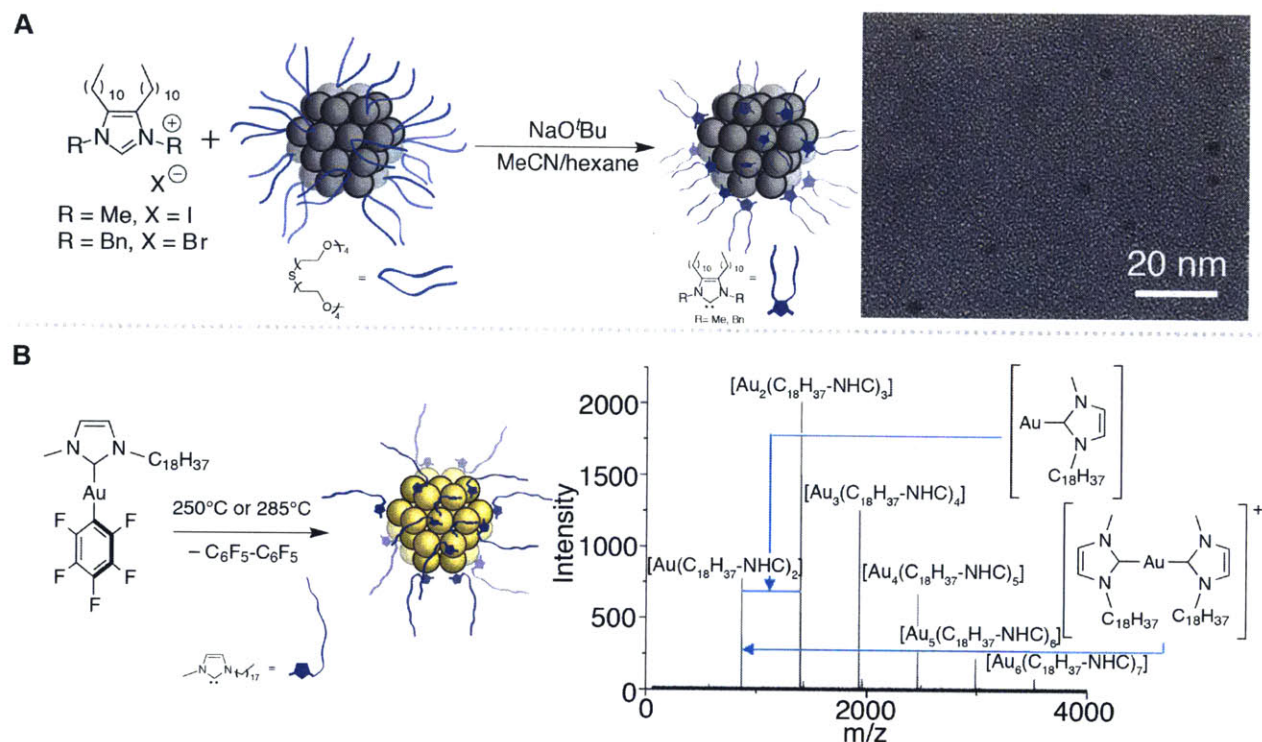
Figure 8. Examples of NHC-stabilized Au and Pd NP. **A.** Glorius, Ravoo, and coworkers utilized ligand exchange to form NHC@Pd and Au NPs (depicted as clusters of gray spheres).[172] They found small nitrogen substituents (methyl and benzyl) were best-suited for the formation of stable NPs. TEM image reprinted with permission from reference 172. Copyright 2014 Royal Society of Chemistry. **B.** Novel thermolysis route for the preparation of NHC-stabilized ultra-small Au NPs reported by Monge, Guarí and coworkers. These NHC@Au NPs were formed from the *in situ* generated Au[I] NHC complex The presence of NHCs on the NP surface was verified through MALDI-TOF mass spectrometry, which detected fragments $[Au_n(NHC)_{n+1}]^+$ with $n>1$.[173] Mass spectrum reprinted with permission from reference 173. Copyright 2014 Royal Society of Chemistry.

Also in 2014, Monge, Guarí and coworkers disclosed a novel route toward NHC-stabilized Au NPs: namely, solvent-free thermolysis (250 °C or 285 °C) of preformed or *in situ*-generated NHC-Au(C$_6$F$_5$) complexes (Figure 8B).[173] This method was enabled by the long alkyl (^{n}C$_{18}$H$_{37}$) *N*-substituents of the NHC (or imidazolium precursor), which reduced the melting point of the complex (or imidazolium salt) and allowed for the thermolysis to proceed in the melt. Remarkably, MALDI-TOF of the resulting NHC@Au NPs revealed, for the first time in the NHC@NP field, an extended series of peaks corresponding to [Au$_n$(NHC)$_{n+1}$]$^+$ species (n = 1—6, Figure 8B). Previously, complexes of NHCs with only a single gold atom were observed by mass spectrometry of Au NPs.[166,170] In combination with NMR spectroscopy – consistent with previous reports of NHC@metal NPs[160,166,170,172] – these results were strong evidence for binding of NHCs to the NP surface as well as for the viability of thermolysis for the synthesis of NHC-stabilized Au NPs.

A convenient approach was reported for the synthesis of NHC@Au NPs via deprotonation of imidazolium haloaurate salts followed by their *in situ* reduction. This route was first reported by Beer and coworkers[174] and later expanded upon by Pileni, Roland and coworkers.[175] Though this route is very straightforward and practical, it should be noted that ^{1}H NMR characterization of the resulting particles suggests the presence of some unidentified NHC-derived impurities.[174,175]

In addition to these six reports and the report by Crudden and Horton[176] (which mainly focused on planar Au surfaces and is therefore discussed in the planar surfaces section of this review), to the best of our knowledge, there have been four other published examples of NHC@Au NPs stabilized in organic media,[177-180] one in aqueous media (*vide infra*),[181] and one example dealing with Au NP degradation by NHCs via formation of NHC-Au(I) complexes.[182] Two of the former four reports utilized reduction of *ex situ* generated NHC-Au complexes.[177,178] The third report utilized disproportionation of Au(I) to Au(III) and Au^0, with concomitant reduction of Au(III) by oxidatively-coupling bithiophenes linked to the NHC ligands in the Au(I) complexes.[179] The fourth report utilized combinations of citrate-stabilized Au NPs and preformed macrocyclic bis(NHC)Ag$^+$ or bis(NHC)Au$^+$ complexes: the former combination led to Au NP aggregation, and the latter led to stabilization of Au NPs toward acidic media or Cu(I) species through presumed aurophilic interactions between the macrocyclic complexes and the Au NP surface and inter-NP electrostatic repulsion.[180]
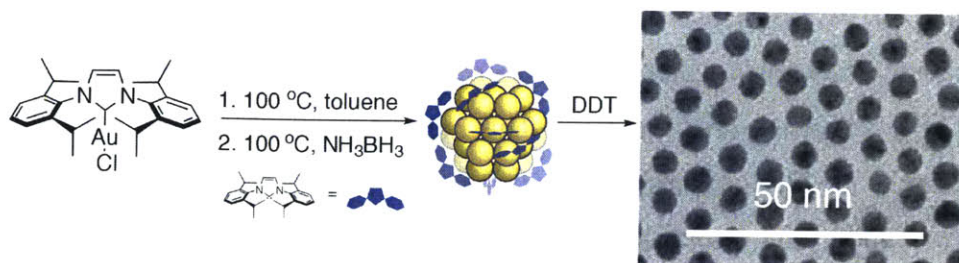
Figure 9. Pileni, Roland, and coworkers used amine-borane complexes to reduce NHC-AuCl complexes to afford NHC@Au NPs.[177] The NP were subsequently treated with 1-dodecanethiol (DDT) prior to TEM analysis. The authors found that the identity of the NHC *N*-substituents was important for the success of NP formation.

It is also worth noting that in their report on NHC@Au NPs in organic media, Pileni, Roland, and coworkers presented[177] new and rather mild conditions for the reduction of NHC-Au complexes (Figure 9) that allowed them to make Au NPs from Dipp-AuCl, a substrate that Tilley and coworkers had been unable to convert to Au NPs. 1-Dodecanethiol (DDT) was subsequently used to stabilize the formed NPs. While admittedly, Pileni, Roland, and coworkers did not spectroscopically identify Dipp ligands attached to the Au NPs, the absence of free Dipp or its derivatives aside from Dipp-AuCl, as well as a decrease in the Dipp-AuCl : DDT ratio after NP formation suggested to us that a few Dipp ligands were likely bound to NP surfaces.[177]

Since Chechik's and Tilley's reports, NHCs with large steric bulk (*e.g.*, I^{t}Bu or Dipp) have carried a stigma of being inadequate for the formation or stabilization of AuNPs. However, while some NHCs with small *N*-substituents may indeed provide enhanced stabilization, as Glorius and Ravoo showcased,[172] others lead to NP etching.[182] Furthermore, Pileni and Roland's findings compel us to reserve assumptions related to steric effects until we have a clearer picture of NHC binding to Au NPs. Crystallization of small gold clusters stabilized by NHCs would provide the desired information, but this is certainly no simple task: aside from the obvious challenges associated with crystallization of such very large molecules and solving of their crystal structures, at present there is no known way to synthesize precisely monodisperse Au$_n$ clusters (n > 3) with NHC ligands. Nonetheless, the recent reports by Bertrand and coworkers[141] on Au^0 and Au$_2^0$ and by Sadighi and coworkers[148] on Au$_3^+$ stabilized by NHCs, as well as the reports of crystallization of monodisperse small gold clusters stabilized by thiolate,[151,167,183-192] selenolate,[193] phosphine,[194-198] mixed phosphine/thiolate,[199,200] mixed phosphine/alkynyl,[201,202] and mixed phosphine/aryl[203] ligands, leave us hopeful that we will witness this milestone in the near future.

Development of NHC@Au NP for catalysis and biomedical applications

Catalysis utilizing NHC-Au(I) complexes is well established.[204] Yet, it wasn't until 2014 that the catalytic activity of NHC-stabilized Au NPs was tested.[173,179] Two cases (both discussed above in the context of NP stabilization with NHCs) showed evidence that NHC@Au NPs could be used to reduce 4-nitrophenol to 4-aminophenol with sodium borohydride. The first study, utilized NHC@Au NPs stabilized by thiophene-functionalized NHCs as the catalyst for 4-nitrophenol reduction, and the authors computed a corresponding reaction rate constant of 6.3 x 10^{-3} s^{-1}.[179] In the second study, due to the insolubility of the NHC-functionalized Au NPs in water, they were loaded onto aminopropyl-functionalized silica support; the observed rate constant for nitrophenol reduction in this case was 2.3 x 10^{-3} s^{-1}.[173] To date no other substrates have been tested, nor have the reaction conditions been optimized. The catalytic activity of these first-generation systems indicates there is promise for the utilization of NHC-stabilized Au NPs as catalysts, as has been observed in other NHC stabilized NP systems.[160,162-164,172,205,206]
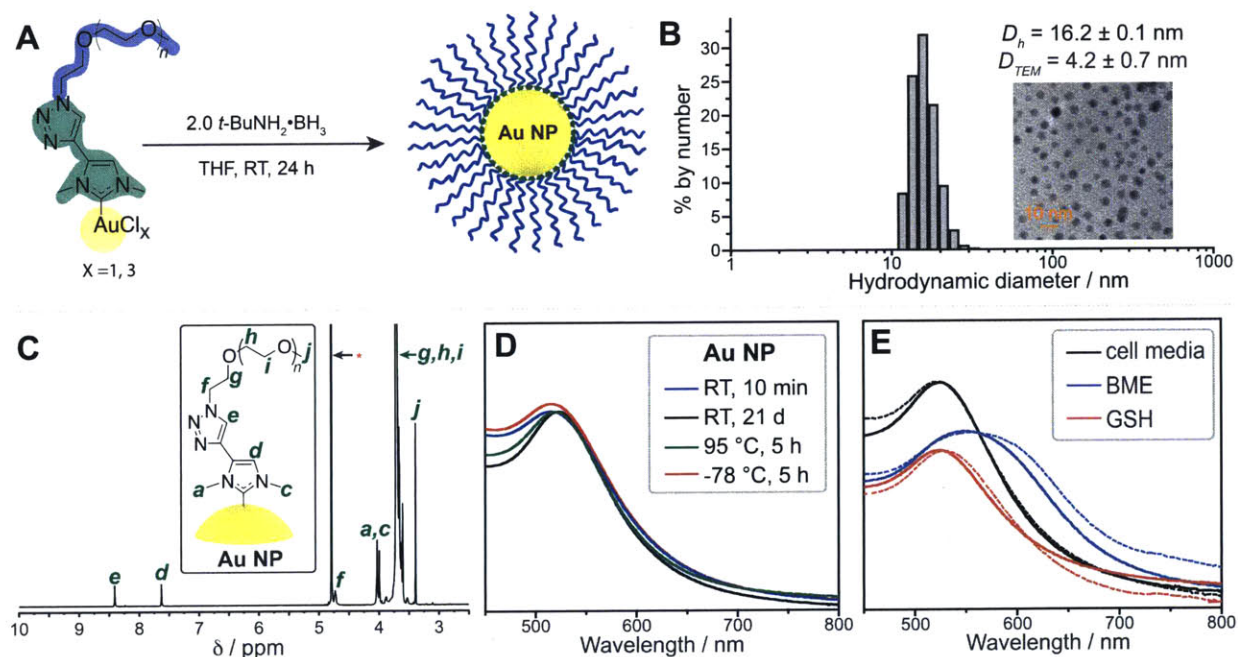
Figure 10. Water-soluble NHC-stabilized Au NP. **A.** Synthetic scheme of gold complex reduction to form Au NP. **B.** Dynamic light scattering (DLS) histogram for aqueous solution of PEGylated NHC@Au NP. Inset: TEM image of these Au NP. **C.** ^{1}H NMR spectrum of PEGylated NHC@Au NP. "*" = residual solvent peak. **D.** UV-vis spectra showing the surface plasmon band (SPB) for PEGylated NHC@Au NP(aq) after exposure to various conditions. **E.** UV-vis spectra showing SPBs for PEGylated NHC@Au NPs exposed to various conditions: "cell media" = cell culture media with fetal bovine serum for 5 min (solid) and 6 h (dashed) at 37 °C, "BME" = 15.8 mM 2-mercaptoethanol for 5 min (solid) and 3 h (dashed) at RT, "GSH" = 2 mM glutathione for 5 min (solid) and 3 h (dashed).

NHC-Au(I) complexes have also been thoroughly studied in the context of biomedicine, particularly for their application as cancer drugs;[11,82-84] yet, no examples of NHC-stabilized Au NPs were explored in biomedically relevant conditions until very recently. Meanwhile, Au NPs are ubiquitous in biomedicine, where they serve as versatile scaffolds for drug/gene delivery, imaging, and photothermal therapy.[207-209] Our group recently reported PEGylated NHC-stabilized water-soluble Au NPs (Figure 10A).[181] Dissimilar to the previous reports of NHC@Au NPs dispersible in organic media, the ultimate goal of the study was the viability of the NHC@Au NPs in biologically relevant systems.

En route to the target NP system, we also gleaned a number of valuable insights into the synthetic strategy and structural features of these NHC@Au NPs. For instance, the NHC ligands were derived in short order from commercially available starting materials, linked in a key step via the modular copper-catalyzed azide-alkyne cycloaddition (CuAAC), a strategy that enables broad diversification of the NHC core.[210] The triazole moiety thus obtained was noted to be coplanar with the imidazolylidene ring and engaged in intermolecular π-stacking interactions in the crystal structure of the closely related triethylene glycol (TEG)-modified NHC-AuCl complex; the TEG units were also aligned in a lamellar morphology. These observations suggested that similar interactions could contribute to the stabilization of analogous PEGylated NHC@Au NPs.

The PEGylated NHC@Au NPs were prepared via reduction of the preformed NHC-Au complexes (Figure 10A). A difference in the diameter of the gold core (TEM) and the hydrodynamic radius (dynamic light scattering) of the NPs confirmed the presence of a polymeric shell around the gold core (Figire 10B), and ^{1}H NMR spectroscopy indicated that the polymeric shell was attached to the Au NPs via NHC ligands (Figure 10C). UV-vis spectroscopy of these PEGylated NHC@Au NPs revealed that the Au NPs were stable for at least 3 months in aqueous solution, could be heated to 95 °C or frozen and cooled to -78 °C for 5 hours (Figure 10D), and were similarly stable in NaCl solutions below 250 mM, and above pH 3. The Au NPs remained dispersed in cell media at 37 °C for days, and the surface plasmon band (SPB) was essentially unaffected after 6 hours. The effect of thiols on the PEGylated NHC@Au NPs was monitored by UV-vis spectroscopy (Figure 10E) and ^{1}H NMR, and different rates of reactivity and induced aggregation were observed.

The stability studies of these PEGylated NHC@Au NPs support their potential utility in biological applications. Moreover, the facile synthesis of imidazolium salts and NHCs presents ample opportunity to modulate the reactivity of the NPs for desired applications.

NHC@Ag and Cu NPs: A conspicuous absence of precedent

While significant progress has been made towards the stabilization of gold NPs with NHCs, the situation is markedly different for its congeners Ag and Cu. For example, there are three reports of silver NPs derived from NHC-Ag(I) complexes, but in all three cases, the NHC@NPs are either not stable or never isolated in pure form, the NHC binding to the nanoparticle is not confirmed, or the NHC is verified to be absent in the resulting nanoparticles.[177,211,212] To date, there are no reports on the preparation of NHC-stabilized copper NPs, though there is one example of CuSe nanodiscs, whose shape-control was proposed to arise from the hypothesized presence of an NHC-Cu adlayer.[213] While the situation with copper NPs is not clear, we can theorize as to why no stable NHC@Ag NP system has been prepared to date. One notable factor is the significantly reduced Ag(I)-NHC bond dissociation energy compared to Au(I)-NHCs: in NHC-AgX complexes, the NHC-Ag BDE has been calculated to be 54.1–62.2 kcal/mol, which is ~25 kcal/mol less than the values calculated for similar gold complexes.[118] In fact, NHC-AgX complexes readily undergo transmetallation with Au(I) species (and other metals) at room temperature,[214] which attests to both the bond strength difference, and the relatively low energy barrier for NHC transfer from Ag(I). Furthermore, ligand exchange takes places in the presence of DDT for NHC-Ag(I) complexes, while NHC-Au(I) complexes are perfectly stable in the presence of DDT.[177] The already relatively low NHC-Ag(I) BDE is likely reduced even further for Ag^0. Additionally, Ag NPs are known to be readily oxidized in aerobic conditions with concomitant leaching of Ag^+ ions, which could serve as another mode of NHC@Ag NP decomposition.[215] Hence, the paucity of reports on NHC@Ag NPs is not surprising.

NHC@Pd and Ni NPs: Current structural understanding and applications in catalysis

The extent of our understanding of NHC attachment to Pd surfaces has until recently been limited primarily to the picture presented by Chechik and coworkers in their 2009 report.[166] In the following years, Beer and coworkers discussed the preparation of NHC@Pd NPs, but they did not provide new characterization data for these species.[174] Shafir, Pleixats, and Planellas

reported a ^{13}C CP-MAS NMR spectrum of putative NHC@Pd NPs; the spectrum exhibited a resonance with a chemical shift consistent with a Pd-bound carbene carbon, but the assignment was not definitive.[216] Nevertheless, the authors found their NHC@Pd NPs to be active catalysts for Suzuki cross-coupling reactions, though the effect of NHC ligation on catalysis was not investigated in detail.

In 2014, Glorius, Ravoo, and coworkers reported a significant advance in our understanding of how NHCs bind to and stabilize Pd NPs (Figure 8A).[172] The authors were able to prepare, for the first time, NHC@Pd NPs that were air-stable and stable towards aggregation in solution for >4 months. In this system, the NHCs were introduced to the Pd NP surface via ligand exchange with a thioether (Figure 8A), similarly to the procedure first carried out by Chechik and coworkers. However, Glorius, Ravoo, and coworkers had additional insights that allowed them to stabilize the Pd (and also Au) NPs from aggregation and etching-related degradation: they used small (methyl) or flexible (benzyl) NHC N-substituents to minimize repulsive interactions between the ligand and the NP surface; moreover, they introduced long alkyl chains on the periphery of the ligand (C4 and C5 of the imidazolylidene) to inhibit NP aggregation. It is also possible that the long alkyl chains could have contributed to NP stabilization via inter-ligand van der Waals interactions (illustrated in section 1.4, *vide infra*). The authors reported that they could not prepare re-dispersible Dipp@Pd NPs, which provided justification for their design.

With their new ligand design, Ravoo, Glorius and coworkers were able to provide several key pieces of characterization data that advanced our understanding of NHC-Pd NP interactions. For example, the direct linkage of the carbene to the Pd surface was verified through ^{13}C CP-MAS NMR experiments. The carbene carbon resonance was assigned via ^{13}C-labeling; a chemical shift of 168.2 ppm, which is reasonably consistent with typical values for metal-bound imidazolylidenes (~170-195 ppm[161]), was observed. The authors also noted that while bis(tetraethylene glycol mono-methyl ether)sulfide was unable to displace the NHC from the Pd NP surface, exposure of the NHC@Pd NPs to excess 2,5,8,11-tetraoxatridecane-13-thiol resulted in complete ligand exchange. The ligand exchange mechanism in the latter case was not discussed in the original report, though it likely involves – and may be driven by – the oxidation of the Pd^0 surface. The resultant NHC@Pd NPs proved to be chemoselective catalysts for olefin hydrogenation.

Ketone	Aryl Halide	Yield [%][a,b]	ee[%][c]
(tetralone)	Ph-Cl	56	61
	Ph-Br	74	53
	Ph-I	70	45
	(2-methylphenyl)-Cl	58	33
	(3-dioxolanyl)phenyl-Br	90	61
	(4-methylphenyl)-Br	83	60
	NC-phenyl-Br	78	57
(indanone)	Ph-Br	61	35
	(3-dioxolanyl)phenyl-Br	66	40
	(2-Cl, naphthyl amide, N-Bn)	91[d,e]	81[e]
	(2-Br, naphthyl amide, N-)	68[d]	85
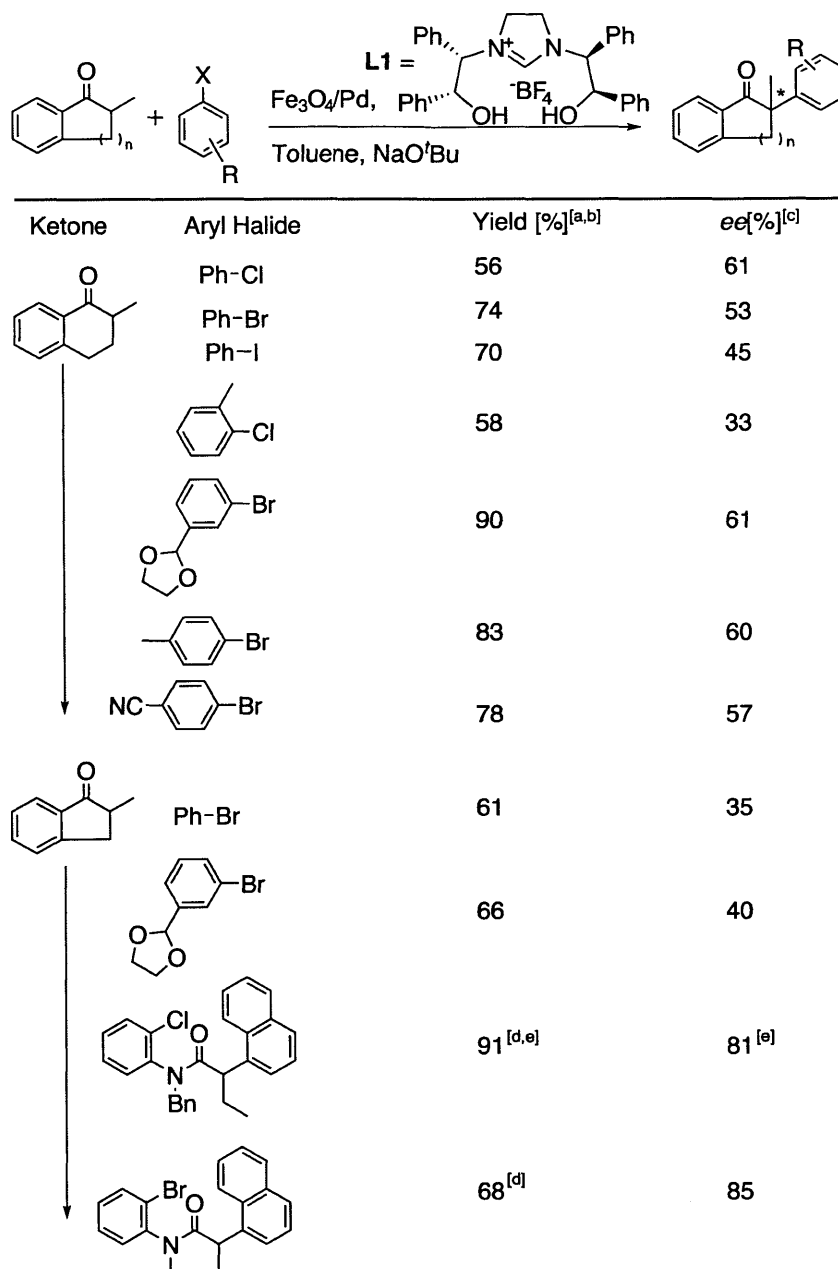
[a] Reaction conditions: Ketone (0.3 mmol), aryl halide (0.6 mmol), NaO'Bu (0.6 mmol), Fe$_3$O$_4$/Pd NP (50 mg), ligand **L1** (2.5 mol%). [b] Yield of isolated product. [c] Determined by HPLC on a chiral stationary phase. [d] Substrate (0.3 mmol), NaO'Bu (0.6 mmol), Fe$_3$O$_4$/Pd modified with **L1** (50 mg), PhMe (3.0 mL). [e] Under homogeneous conditions ([{Pd(allyl)Cl}$_2$] (5.0 mol%), ligand **L1** (10 mol%), substrate (0.3 mmol), NaO'Bu (2.0 equiv), PhMe (3.0 mL)); the product was formed in 32% yield with 24% ee.

Figure 11. Demonstration of asymmetric catalysis using chiral NHC bound to Pd NP by Glorius and coworkers.[205] The Pd NP was attached to magnetic Fe$_3$O$_4$ for facile catalyst removal. The moderate ee indicates the involvement of the chiral NHC in the catalytic process.

Despite limited information on the details of surface binding, several interesting examples of NHC-stabilized Pd and Ni NP catalysts have been reported. In 2010, Glorius and coworkers

reported an enantioselective a-arylation of ketones catalyzed by Pd NPs stabilized by chiral NHCs (Figure 11, Note: the NHC-stabilized Pd NPs were embedded in magnetic Fe_3O_4 NPs to facilitate catalyst recovery).[205] Though the exact nature of the NHC-Pd bond was not studied, the presence of the NHCs on the Pd surface was verified by XPS (using the N 1s region). Furthermore, the significant enantiomeric excesses (ee = 33-85%) observed in the products of the studied reactions suggested that the chiral NHCs influenced the reactions. Admittedly, the possibility of homogeneous catalysis due to NHC-Pd complex leaching could not be completely ruled out, because a small but significant amount of Pd (0.232 ppm) was observed in solution upon completion of the reaction. While the mercury-poisoning test resulted in loss of catalytic activity for the NP system but not for a model NHC-Pd complex, the employed model complex was not necessarily representative of the leached Pd species; moreover, "false-positives" have been shown to be possible in mercury-poisoning tests.[217-219] Nonetheless, this work presented the tantalizing possibility that chiral NHC surface modifiers could be used for stereoselective heterogeneous catalysis. Finally, the utility and recyclable nature of their catalytic system[205] encouraged the authors to explore similar catalysts in other contexts. In 2011, Glorius and coworkers reported a similar catalyst system that was shown to be active for the enantioselective allylation of aldehydes.[206]

To our knowledge, the only published example of NHC@Ni NPs was reported by Kobayashi and coworkers.[220] In this work, NHC stabilized Ni NPs were employed in the catalysis of the Corriu-Kumada-Tamao reaction. Field gradient swollen-resin magic angle spinning *Carr-Purcell-Meiboom-Gill* NMR confirmed that the imidazolium salt fragments were indeed converted to NHCs, suggesting that they were contributing to the stabilization of the Ni NPs. The catalyst showed useful activity and little Ni leaching. The potential utility of NHC-stabilized NPs in catalysis, as demonstrated in the examples above, provides motivation for future studies aimed towards a better understanding of NHC-surface interactions.

NHC@Si NPs and the road ahead

Si NPs are the only non-TM NPs to have received some attention in the context of NHC stabilization.[221] The optoelectronic characteristics of small (<10 nm) Si NPs make them useful materials in applications ranging from photovoltaics to cell biology.[222,223] NP stability (to air and

aggregation), well-defined nature, and surface functionality are critical in these applications; yet, the stabilization methods for Si NPs are limited. The state-of-the-art in this field consists of two general methods: modifying Si NP surfaces by addition of nucleophiles – in particular, alcohols, amines, and Grignard and organolithium reagents – to halide-terminated Si NPs, or radical addition of alkenes or alkynes to H-terminated Si NPs.[224-233] Given this relative scarcity of methods, complementary Si NP stabilization routes – *e.g.*, using NHCs – are desired. Recently, Yatsenko and coworkers reported the use of NHCs – specifically, 1,3-dialkylimidazol-2-ylidenes – to generate crystalline, though widely dispersed, Si NPs with putative NHC-surface layers.[221] Notably, the authors used sodium or zinc metal reduction of $SiBr_4$ at 110 °C in xylene or diglyme in the presence of *N*-alkyl substituted imidazolium iodides. The attachment of NHCs to the Si NP surface via the carbene carbon was proposed, although direct evidence for this interaction was not provided. The role of the imidazolium salts and their conversion to surface-bound NHCs was proposed based on observations of their effect on Si NP size: increasing the imidazolium salts' alkyl group size (from *N,N'*-dimethyl to *N*-butyl-*N'*-methyl to *N*-decyl-*N'*-methyl) led to a decrease in the average NP size; for the *N*-decyl-*N*-methyl derivative, no NPs were observed. Based on the Ru NP studies of Chaudret and coworkers,[160] one must also keep in mind that ligand concentration during NP synthesis can play an important role in the NP size. Furthermore, Yatsenko and coworkers noted that the strength of the reducing agent used to synthesize the Si NPs also affected the final NP size, with stronger reducing agents leading to smaller NPs.

Conclusions

The previous section highlights the application of NHCs for NP-surface stabilization. NHCs have proven capable of stabilizing Ru, Pt, Au, and Pd NPs; less information is available regarding the stabilization of Ir, Ni, and Si NPs with NHCs. The much more extensive range of elements with which NHCs form strong bonds in complexes foreshadows their use in the near future for the stabilization of NPs comprised of other main group elements (*e.g.*, C, P, S, As, Se, Sn, and Pb) and transition metals (*e.g.*, Cd, Cu, Co, Rh, Fe, Os, Mn, Re, Mo, W) and mixtures/alloys thereof – the just-reported small Re chalcogenide clusters with NHC ligands[152] are an exciting testament to this claim. Furthermore, none of the reported examples makes use of chemically addressable NHCs, which would facilitate further NP-surface functionalization.[234,235]

A clearer picture of the stabilization of all of the aforementioned NPs with NHCs will likely remain an important goal in this field for a number of years. Moreover, NHC are likely to impart novel and untapped electronic and structural properties to these nanoparticles – an exciting prospect with high potential for discovery. Truly, a new class of ligands makes a new surface, and a new surface, in turn, makes a new material.

1.4 Planar surfaces stabilized by *N*-heterocyclic carbenes (NHC@metal)

While thiol surface anchors were first studied in the context of planar surfaces[236-238] and then were translated to NPs,[239-241] NHC surface anchors took the opposite trajectory. This trend may have stemmed from the larger selection of direct techniques available to characterize the surface chemistry of NPs, as well as the availability of methods for the synthesis of NPs with other types of ligands. Nevertheless, NHCs have now been applied to planar surfaces, and the results suggest that they are a promising platform for further development in a range of applications where they could complement other ligand classes (*e.g.*, thiols).

<u>First examples of planar Au surfaces modified with acyclic diaminocarbenes and NHCs</u>

To the best of our knowledge, to date, there have only been three studies, all since 2011, on planar surface modification with NHCs; all of these examples focused on gold. Despite these recent reports, it should be noted that the binding of related acyclic diaminocarbenes to roughly planar (powdered gold) surfaces dates back to the work of Angelici.[242-244] In these studies, Angelici and coworkers postulated that amine additions to Au-bound isocyanides provided acyclic diaminocarbene intermediates transiently bound to the Au surface. These intermediates immediately formed either carbodiimides or ureas depending on the nature of the amine (1° vs. 2°, respectively), which is an intriguing finding in itself. However, the properties of the carbene intermediates were not explored further, as they were not readily isolable.

The first effort to generate stable NHC monolayers on planar gold was reported in 2011 by Siemeling and coworkers.[245] In this study, thin films derived from a mixture of the predominantly intact 1,3-diethylbenzimidazol- 2-ylidene dimer (BIEt)$_2$ and the monomeric BIEt were generated (Figure 12). The thermodynamics of the dimeric and the monomeric BIEt equilibrium were reported to be essentially identical to those reported by Lemal and coworkers,[246] despite the difference in the solvent used by Siemeling and coworkers (THF

instead of diglyme). From the thermodynamic parameters reported by Siemeling and coworkers (DH° = 17.6 ± 1.9 kcal/mol, DS°, 26.3 ± 3.3 cal/(mol·K)), one could calculate that less than 1% of the dimer was dissociated at 298 K (here we assume the same concentration of the dimer was used as in Lemal's study – i.e., 0.1 M). Moreover, Lemal and coworkers mention in a note that without catalysis by adventitious electrophilic species equilibrium could not be reached quickly[246]; numerous reports (with one exception[247]) attest to the requirement of catalysis to establish such an equilibrium[246,248-250], which was first proposed to exist by Wanzlick.[251,252] Thus, one is led to wonder if the monomeric NHC was indeed the active species binding to the gold surface in Siemeling's study, and the authors themselves admit that they are "not certain whether film formation is based on the chemisorption of the carbene or its dimer on the gold substrate."[245] With this in mind, Siemeling and coworkers proposed two mechanisms for how monolayers of BIEt could form on gold: (1) the dimer could coordinate to the surface and undergo fission similar to what is observed in solution in the presence of Au(I);[253,254] or (2) the dimer could be in depletive equilibrium with the less stable monomeric form, as the latter would bind to the gold surface, which would cause more dimer to dissociate.
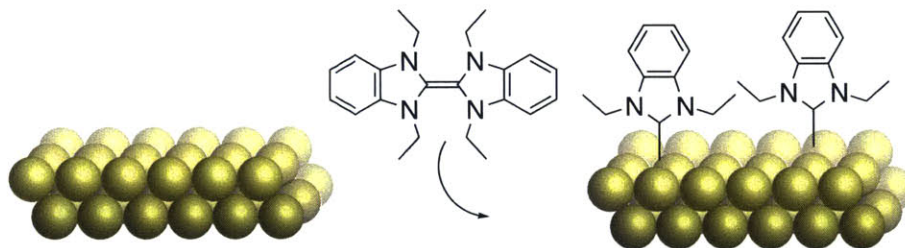
Figure 12. The first example of the utilization of NHC dimers (in equilibrium with free NHC) to modify planar gold surfaces.[245]

The primary analytical methods Siemeling and coworkers employed for NHC@Au monolayer characterization were XPS and C K-edge near edge X-ray absorption fine structure spectroscopy (NEXAFS). The former method provided a C:Au ratio of 1.3, which suggested that approximately a monolayer of NHC was added. The ratio of C to N was ~5.2:1, which was within experimental error of the expected 5.5:1; however, a component of the C 1s peak accounting for ~5% of the total carbon content had an energy characteristic of carbonyl carbons, suggesting the presence of urea species that are known to arise from the reaction of the NHC dimer with oxygen[255] (free NHCs of this type are generally stable to O_2[256]). While the authors ruled out the presence of these species based on the absence of a corresponding peak in the N 1s region, the signal-to-noise ratio in the N 1s region leaves room for this possibility. Notably, the

41

energy of the N 1s peak in this case was found to be 400.2 eV, almost identical to that observed by Chechik and coworkers in their I^{t}Bu-stabilized Au NPs (400.3 eV). Lastly, the NEXAFS analysis indicated that the molecules in the monolayer were oriented at ~30 ± 6° relative to the normal to the surface.

While this work set an important precedent for employing NHCs as stabilizing agents for planar gold surfaces, analogous to thiol-based self-assembled monolayers, the chemical nature of the monolayer – i.e., free carbene vs carbene dimer – was not verified, and characterization of carbene-gold bonding was not provided. As in the NP examples described above, the monolayers did not possess addressable functionality, rendering the surfaces inert to subsequent modification. Lastly, the authors mention the formation of unknown side-products that led to surface contamination. These products were likely due to NHC dimerization and decomposition, which would not be unexpected given the highly electron-rich nature of the tetraminoethylene fragment of the dimer.

Addressable NHC@Au monolayers

While much effort has been devoted to understanding the NHC@metal interfaces during the past decade, all of the examples prior to 2013 were of essentially non-functional structures, rendering the surfaces inert to further chemical modification. Yet, the ability to tune surface properties through chemical modification of the monolayer is required in many applications. We set out to develop new NHC ligands for planar gold surfaces that would provide stable, chemically addressable surfaces (Figure 13).[235] Furthermore, in an effort to gain a better understanding of the NHC@Au monolayer formation, we designed functional ("addressable") NHCs based on the SIMes scaffold, which are known to not dimerize. Finally, in order to extend the utility of NHCs for monolayer formation, we introduced the use of bench stable, yet thermally labile, CO_2-protected NHCs for surface coating.

The addressable derivatives of SIMes we studied included aryl-bromide and 2-methyl-styrene substituted NHCs (Figure 13). These structures were selected due to the breadth of reactions for which aryl bromides and styrenes are substrates. Indeed, XPS and quartz crystal microbalance with dissipation (QCM-D) gravimetry confirmed that the brominated NHC we had selected, as well as IMes, formed monolayers on Au surfaces, with areal mass densities (AMDs) of ~63 and ~56 ng/cm^2, respectively. The AMD values corresponded to a roughly ~74% surface
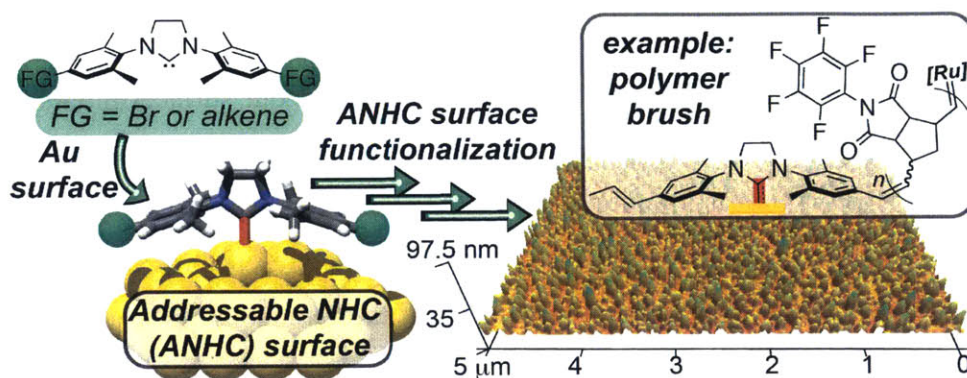
Figure 13. A depiction of the formation of binding of addressable NHCs to planar Au surface followed by functionalization via surface-initiated ROMP, which gave rise to a polymer-coated surface visualized by AFM (bottom right).[235]

coverage based on the dimensions of the NHC in the crystal structure of an isolated Au(I) complex – in other words, the monolayers were densely packed. The N 1s peak energy in XPS was consistent with that observed for Au NPs by Chechik and coworkers.[166] The NHCs could be generated by the typical treatment of the corresponding imidazolium salt with strong base (KHMDS, followed by filtration) or, as alluded to above, by thermal decarboxylation of the corresponding CO_2 adduct. In the former case, co-adsorption of KHMDS species present in trace amounts in solution was proposed to account for the larger values and larger variability of the AMD obtained via QCM-D.

The NHC@Au surface interaction was investigated for the first time using DFT. These studies suggested a carbene C-Au^0 bond length of 2.03 Å, which as expected, is slightly longer than the bond length of 1.98 Å observed in the crystal structure of an analogous Au(I) complex. Notably, the C-Au bond lengths in Bertrand's (CAAC)$_2$Au^0 and (CAAC)$_2$Au$_2$^{0} (*vide supra*) were 1.99 Å and 2.08—2.09 Å, respectively.[141] The overall consistency in the bond lengths between the crystal structures mentioned above and our calculated structure provide support for our calculated bond dissociation energy for the NHC-Au^0 bond of 67 kcal/mol, which is more than 20 kcal/mol greater than the bond dissociation energy for a typical thiolate-Au bond.[237] The NHC-Au bond strength in similar Au(I) complexes had been previously calculated to be as large as 76.3—82.8 kcal/mol[257,258]; the reduced bond strength observed in the less electrophilic Au^0 system is reasonable.

With dense, stable NHC@Au monolayers in hand, we turned our attention to subsequent functionalization via NHC-selective reactions. While cross-coupling reactions with the aryl bromide-functionalized NHC left large amounts of Cu and Pd residue on the gold surface, the

methylstyrene derivative underwent a clean cross-metathesis reaction, forming a surface-bound Ru(II) benzylidene species. The latter was utilized to carry out surface-initiated ring-opening metathesis polymerization (SIROMP)[259] of pentafluorophenyl-substituted *exo*-norbornene-imide. The sequence of reactions was monitored by QCM-D and the final surfaces were characterized by XPS and AFM (Figure 13); both methods confirmed the presence of polymer brushes on the surface, and demonstrated the remarkable stability of these monolayers to multistep on-surface synthetic sequences.

Enhanced stability of NHC@Au compared to thiolate@Au monolayers

In 2014, Crudden, Horton, and coworkers verified that the strong binding of NHCs to gold surfaces can provide NHC@Au monolayers that outperform thiols in a range of direct stability tests (Figure 14).[176] These authors showed that the NHCs N,N'-diisopropylbenzimidazolidene (^{i}Pr$_2$bimy), IMes, SIMes, Dipp, and TPT all form monolayers on either Au(111) surfaces or on Au NPs deposited on mica. It was found that certain NHC@Au monolayers were qualitatively much more kinetically stable than thiolate monolayers in a range of contexts with the exception of reduction, though monolayer stability was only reported for ^{i}Pr$_2$bimy and IMes. For example, ^{i}Pr$_2$bimy was not displaced from surfaces by dodecyl sulfide or DDT (Figure 14A). All of the NHCs above displaced dodecyl sulfide from Au NPs and Au(111) to some extent. Moreover, ^{i}Pr$_2$bimy was shown by XPS to be capable of displacing 100% of dodecylsulfide (Figure 14A), 60% of DDT, ~100% of benzenethiol, and all or most of the bidentate ligands benzene-1,2-dithiol and propane-1,3-dithiol.

The kinetic stability of NHC@Au monolayers was further tested under various conditions such as (a) exposure to water at room temperature (RT) for 1 month, (b) 100 °C water for 24 h, (c) 66 °C THF for 24 h, (d) 100 °C decalin for 24 h, (e) pH 2 at RT for 24 h, (f) pH 12 at RT for 24 h, (g) pH 2 at 100 °C for 24 h, (h) pH 12 at 100 °C for 24 h, (i) 1% H_2O_2 at RT for 24 h, (j) 3% H_2O_2 at RT for 24 h, as well as (k) electrochemical reduction and oxidation; the effects of conditions (b), (c), (h), and (i) for iPr$_2$bimy- modified surfaces are summarized in Figure 14B. Thus, while thiol monolayers are unstable even in THF at RT, in the case of ^{i}Pr$_2$bimy, the monolayers were virtually unchanged by all of listed conditions except conditions (i)-(k). Even in the latter cases, however, the ^{i}Pr$_2$bimy monolayers generally exhibited remarkable resistance: 80 ± 5% of the monolayer survives condition (i) and ~20-30% survives the harsher condition (j).
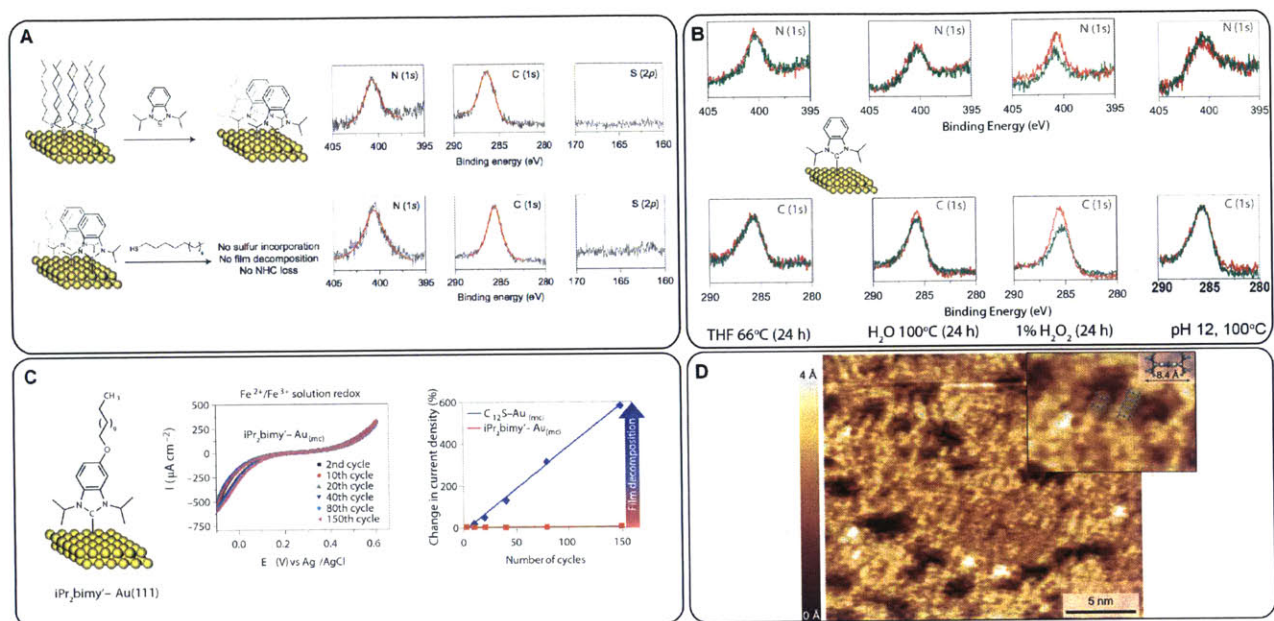
Figure 14. Stability studies of NHCs on planar gold by Crudden, Horton and coworkers.[176] (A) XPS data demonstrating the full surface exchange of dodecyl sulfide for ^{i}Pr$_2$bimy and no exchange of ^{i}Pr$_2$bimy for DDT on Au (111) surfaces. (B) XPS data demonstrating stability of ^{i}Pr$_2$bimy under various conditions. Based on the intensity before and after treatment, it was concluded that ^{i}Pr$_2$bimy was stable in 66 °C THF for 24 h, 100 °C water for 24 h, and pH 12 at RT for 24 h. The decline in intensity at 1% H$_2$O$_2$ at RT for 24 h indicated some NHC loss. (C) Cyclic voltammetry of an alkyl derivative of ^{i}Pr$_2$bimy on microcrystalline Au on Si. Over the course of 150 scans no change in peak current is observed. The film decomposition is compared to DDT films. (D) An STM image of ^{i}Pr$_2$bimy on Au (111) depicting the local order comprised by 5 to 10 stacked units of ^{i}Pr$_2$bimy on the surface. The inset is a to scale schematic representation of individual molecules overlaid. Reprinted with permission from reference 176. Copyright 2014 Nature Publishing Group.

Collectively, the results revealed that NHC monolayers were more resilient than thiolate monolayers under the studied conditions, with ^{i}Pr$_2$bimy monolayers exhibiting superior stability compared to IMes.

While no change was observed under oxidizing conditions for ^{i}Pr$_2$bimy monolayers (up to +0.6 eV vs Ag/AgCl) over 150 cycles (Figure 14C), the NHC@Au monolayers appeared to have a much lower stability under reducing conditions compared to dodecanethiolate monolayers; the reductive desorption potential for the latter is -1.1 eV, while for the former it is only -0.4 eV vs Ag/AgCl. Such a behavior is inconsistent with a much greater NHC-Au BDE compared to the thiolate-Au BDE. However, considering an approximate, molecular model of the surface, one might reasonably expect that the SOMO for the NHC-Au system would be lower in energy than the thiolate-Au LUMO, rendering the NHC monolayer less stable to reducing conditions. Furthermore, the surface charge of the NHC monolayer may be different from that in the case of thiolates (see section 1.4).

Scanning tunneling microscopy (STM) images of the NHC@Au monolayers revealed the

45

presence of dark pits that the authors attributed to restructuring or etching of the superficial layer of gold atoms (Figure 14D) – a phenomenon that has been linked to observation of adatoms in the monolayer (*vide infra*). These pits were much more abundant on IMes treated surfaces compared to ^{i}Pr$_2$bimy-treated ones, suggesting that the steric bulk of IMes induces greater surface restructuring. Moreover, the ^{i}Pr$_2$bimy-treated surfaces exhibited one-dimensional arrays with dimensions corresponding to those of the benzimidazolylidene positioned upright on the gold surface. In the case of IMes, no such ordering was observed. Lastly, the packing density of ^{i}Pr$_2$bimy was estimated to be 3.5 ± 0.5 molecules/nm^2 via electrochemical methods.

In the same report, Crudden, Horton and coworkers expanded on the addressable NHC concept by incorporating a reactive azide functionality on the backbone of their ^{i}Pr$_2$bimy scaffold. NHCs and azides are generally incompatible because they rapidly form triazine adducts at room temperature.[260] Evidence to exclude the formation of multilayers from step-growth polymerization of the azido-NHC on the surface was not provided, nor were the characterization data for the azido carbene. Nonetheless, XPS and contact angle measurements were used as evidence to support azido-NHC@Au monolayer modification via CuAAC.

In summary, the work of Crudden, Horton, and coworkers represents an important landmark in the development of NHC-surface anchors. The first STM analysis of NHC@Au monolayers and detailed stability studies of NHC@Au surfaces compared directly to thiols represent a highly valuable contribution to understanding the nature of NHC monolayers on metal surfaces.

Current understanding of NHC binding to Au(0)

We must admit that the nature of NHC binding to surfaces is still not understood in detail, and what understanding exists is predominantly qualitative and not general across different surfaces, as has been noted at times in the preceding sections. Yet, computational treatment of NHC-Au$_1^0$, (CAAC)$_2$Au$_1^0$, and (CAAC)$_2$Au$_2^0$, as well as crystal structures of the latter two complexes provide us with critical insights into the bond strength and orbital interactions in the molecular species, which may with future investigations prove to extend to bulk gold surfaces.

The frontier orbitals of a traditional cyclic diaminocarbene (*e.g.*, SIMes) are shown in Figure 15A; the orbitals of a single Au^0 atom bound to such an NHC were computed by M. Mavros and reported by Johnson and coworkers.[235] The DFT calculations with the B3LYP functional[261] revealed that this complex has a singly-occupied molecular orbital (SOMO) with 48.7%

contribution from Au 6s, 19.1% from C 2s, 8.1% from C $2p_z$, 8.8% from Au $6p_z$, and 7.6% Au from $5dz^2$ plus minor contributions from other Au d orbitals. In other words, the SOMO is sigma-symmetric, and delocalized primarily between the Au 6s and carbene carbon 2s orbitals. The SOMO-1 orbital is also constructed primarily from the Au $6s/5dz^2$ and the carbene 2s orbitals. The NHC-Au interaction is thus a two-center three-electron bond. The calculated NHC-Au bond dissociation energy was 67 kcal/mol.[235]

Compared to cyclic diaminocarbenes, Bertrand's CAACs are both nucleophilic and more electrophilic (*i.e.*, have a significantly lower LUMO *and* an elevated HOMO), as depicted in Figure 15B.[141,262,263] This key difference explains the much greater contribution of the C $2p_x$ orbital (LUMO) to the overall bonding of CAACs with a single Au^0 atom – for simplicity, in Figure 15B we demonstrate this orbital interaction for a single CAAC with a Au^0 atom. Thus, Bertrand and coworkers find through EDA-NOCV theory with BP86/TZ2P+//M05-2X/SVP that 35.6% of the bonding between Au^0 and the two CAACs in their $(CAAC)_2Au$ complex is due to the Au $p(\pi)$ back-donation into the LUMO of the carbenes. To enable this back-donation, the authors suggest that the Au_1^0 binds to the CAACs in an excited electronic configuration, where the electron residing in the 6s orbital in the ground state is promoted to a 6p orbital. This orbital, in turn, overlaps more efficiently with the CAAC LUMO, affording a net stabilization. The dissociation energy of $(CAAC)_2Au$ into 2CAAC and Au was calculated to be 91.2 kcal/mol, or an average of 45.6 kcal/mol per each CAAC—Au bond. Elaboration and extension of these computations to the compare the binding in $(CAAC)_2Au$ with that in $(CAAC)_2Cu$ and $(CAAC)_2Ag$ revealed that Au $p(\pi)$ back-donation is a generally important phenomenon in the binding of neutral monoatomic coinage metals with CAACs.[264]
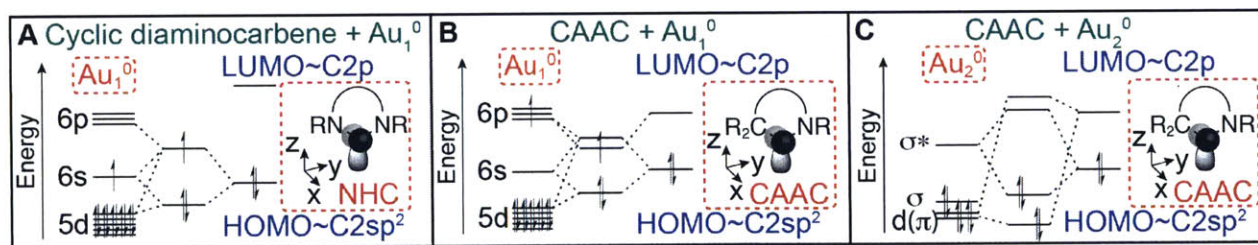
Figure 15. Qualitative frontier and near-frontier orbital diagrams of a cyclic diaminocarbene coordinated to Au_1^0 (A), a CAAC coordinated to Au_1^0 (Bertrand and coworkers propose the binding of Au_1^0 in this case to proceed from an excited state) (B), and a CAAC coordinated to Au_2^0 (C).

Bertrand and coworkers found that the bonding in a $(CAAC)_2Au_2^0$ cluster (bonding of one CAAC with Au_2^0 illustrated in Figure 15C) was quite different than that of the $(CAAC)_2Au_1^0$

cluster discussed above, which serves to caution one to consider the changes in the orbital structure of gold when extrapolating from Au^0 complexes to the bulk. In the $(CAAC)_2Au_2$ case, the authors described the bonding by mixing the orbitals of the gold dimer with those of the individual CAACs (as opposed to mixing of two CAAC-Au fragments).[141] In this complex, the LUMO of the CAAC interacts with one of the Au_2^0 $5d(\pi)$ orbitals. The CAAC HOMO orbital now mixes with the Au_2^0 s* orbital formed from the antibonding combination of the $6s/5dz^2$ hybrid orbitals of the two Au atoms. The average bond dissociation energy per CAAC remains virtually unchanged, however, at 45.3 kcal/mol.

Direct extension of a molecular orbitals picture of NHC binding to mono- or di-atomic Au to bulk gold would require that the surface states be representative of the bulk. This assumption is, strictly speaking, invalid given the unfulfilled valence of the surface atoms, but deviation from this assumption would not be expected to significantly perturb the qualitative picture of binding, especially if the surface gold atoms were all in their 0th oxidation state. However, the possible presence of gold *adatoms* – single gold atoms positioned upon the lattice surface often as a consequence of surface reconstruction[265] (Figure 16) – can restrict the hybridization of gold orbitals with the bulk. The importance of gold adatoms in the formation of thiol (sub)monolayers on planar and nanoparticle gold surfaces has been thrust into the spotlight in recent years,[151,167,171,183,185,186,192,266-273] and it may generalize to other, non-thiol monolayers on gold.

Furthermore, the relevant molecular orbitals (or energy bands) would likely be further perturbed if the surface atoms were oxidized to Au^+ (Figure 16) upon NHC binding to surface Au^0, a feasible scenario given the reported high air-sensitivity of $(CAAC)_2Au_2^0$.[141] In fact, binding of two NHCs to a single surface Au atom and dissociation of $(NHC)_2Au^+$ (or dissociation of $(NHC)Au^+$ followed by formation of $(NHC)_2Au^+$) is a mechanism that has been invoked in observed etching of gold nanoparticles by NHCs.[166,182] The latter observation gives credence to the proposed oxidation of some surface Au^0 atoms to Au^+, and suggests that at least a small fraction of the NHC monolayer may consist of NHC-Au^+ and bis(NHC)Au^+ complexes, attracted to bulk Au^0 surfaces via non-covalent (*e.g.*, aurophilic) interactions (Figure 16). These interactions may be persistent in "poor" solvent media that are incapable of solvating these ionic complexes; in "better" solvent media, such complexes may dissociate and contribute to the observed etching. Remarkably, Chaudret and coworkers recently observed persistent association of bis(NHC)Pt^+ complexes with Pt NPs (*vide supra*).[164]

48
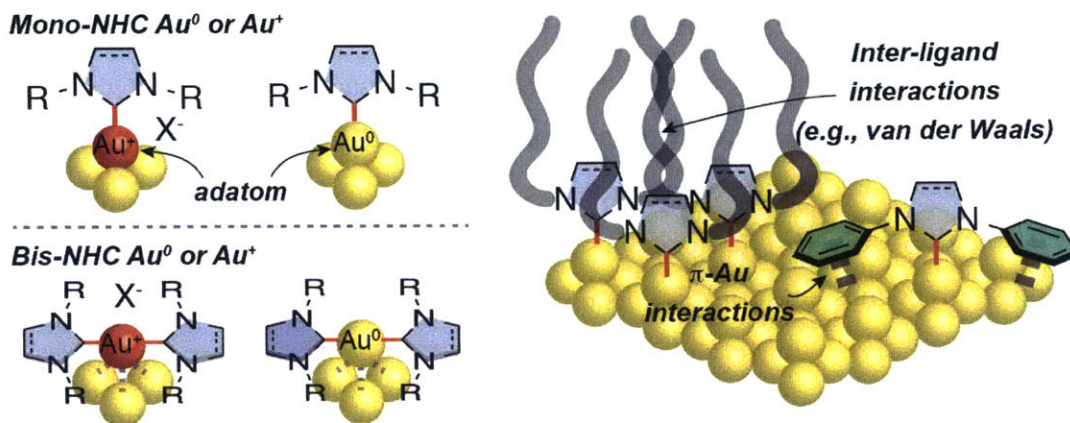
Figure 16. Depiction of different modes of NHC binding to the surface of bulk or nanoparticular gold, as well as the likely modes of additional monolayer stabilization. Top left: single NHC binding to a Au^+ ion or a Au^0 atom (these could be adatoms, as shown in the figure, or other sites on the gold surface). Bottom left: two NHCs binding to a Au^+ ion or a Au^0 atom, leading to disruption of the Au-Au delocalization; these complexes could still remain bound to the surface through non-covalent interactions. Right: inter-ligand interactions (*e.g.*, van der Waals interactions) and auxiliary interactions between the ligand and the surface (*e.g.*, π-Au interactions), which contribute to the stabilization of the monolayer.

Non-covalent interactions may also help to stabilize mono(NHC)-type monolayers on Au surfaces, and likely on other surfaces also. Thus, long *n*-alkyl or PEG substituents appended to the NHC core (on the *N* atoms as shown in Figure 16, or on the C4 and C5) have been shown to produce NHC-coated Au and Pd nanoparticles (NPs) with enhanced stability.[170,172,175,181] Presumably, this enhanced stabilization is afforded by the inter-ligand van der Waals interactions (Figure 16), similarly to alkylthiol monolayers on gold.[171] Aryl or benzyl substituents can also participate in stabilizing π-surface interactions, as has been demonstrated in the case of Ru and Pd surfaces.[160,172] Lastly, while large steric bulk (*e.g.*, in Dipp or IMes) does not prevent monolayer formation on metal surfaces,[160,235] small *N*-substituents (*i*Pr, Me, Bn) have been shown to impart greater stability to monolayers formed via ligand exchange on Au and Pd,[172,176] likely due to the relaxation of steric constraints for binding to the surface which enables the ligands to pack tightly in the monolayer, thereby augmenting the number of favorable inter-ligand interactions.

The road ahead

While laudable progress has been made in understanding the NHC@Au interface, numerous questions remain to be answered. For instance, one would like a clearer picture of the bonding geometry and experimental confirmation of orbital/band interactions (see Figure 16) and non-covalent interactions for different NHCs on gold, as well as experimental evidence for the nature

of the gold atoms (step edge sites vs adatoms vs lattice atoms, charged vs neutral, two NHCs vs one) bound to NHCs. Also, the effects of stereoelectronic parameters on NHC binding strength and density as well as on the stability of the monolayers to NHC-Au complex desorption are also still poorly understood, though some progress in the realm of steric effects has been made. Moreover, a variety of NHC types exist besides the benzimidazolylidenes, imidazolylidenes, and dihydroimidazolylidenes, and triazolylidenes explored by Siemeling, Johnson, and Crudden and Horton: CAACs, thiazolylidenes, oxazolylidenes, P-heterocyclic carbenes, diazacyclopropylidenes, and many others leave much room for future investigation. Finally, these gaps in understanding are just for the gold surface – many other material surfaces remain largely unexplored and in some cases present a formidable challenge but also immense potential. For example, one remarkable aspect of NHCs is that they could, in principle, bind to surfaces via completely disparate mechanisms compared to traditional ligands, and thus they could be applicable to a wider range of materials. We anticipate key advances in the near future in these areas.

1.5 Surfaces stabilized by alkylidene-type carbenes

NHCs certainly possess many merits as surface ligands, but they constitute only a subclass of carbenes within a broader structural group envisioned by J. U. Nef.[2] While species such as dichlorocarbene are too unstable to be stored in any practical way, they can be generated and utilized *in situ*. Other carbenes are conveniently transferred to the desired target from diazo-compounds with concomitant dinitrogen elimination, while others such as Schrock-type alkylidenes found in all of the olefin metathesis catalysts can be transferred *via* the olefin metathesis reaction. Thus, these carbenes present intriguing alternatives to NHCs in the context of surface stabilization, and merit discussion in the present review.

<u>Alkylidene polymerization on metal surfaces</u>

One of the earliest examples of alkylidene reactivity on metal surfaces was witnessed in 1955, when Saini and Nasini had observed that treatment of $AuCl_3$ with diazomethane immediately gave rise to Au NPs and led to complete conversion of diazomethane to polymethylene.[274] Within several years, Au NPs were confirmed to be an active catalyst in this decomposition of diazomethane and other diazoalkanes to dinitrogen and surface-bound

alkylidenes, which were subsequently converted into growing polymer chains.[275] Many other metals (though notably not Pd, Rh, Zr, and Ag) also exhibited similar reactivity.[275,276] The facile on-surface polymerization of alkylidenes and the fact that the produced polymer could be separated from the NPs[275] indicated that these alkylidene@metal surfaces were quite reactive, which likely precluded their isolation.

Nonetheless, this on-surface polymerization of alkylidenes was further advanced in later works initiated in 1997 by the groups of Tao and Allara[277,278] and in 2002 by Jennings and coworkers,[279] which led to a powerful method to prepare polymer-film coatings on metal surfaces. Specifically, Tao and Allara posited that decomposition of diazomethane at defect sites on the Au(111) surfaces forms weakly Au-bound methylene that undergoes radical chain growth polymerization into a hydrophobic crystalline polymethylene film (Figure 17); eventually (at thicknesses $\geq$ 20 nm), this film covers the entire Au(111) surface and can reach an ellipsometric thickness as high as 100 nm. Tao and coworkers demonstrated that these films could be patterned on a surface and subsequently serve as a resist for electrochemical growth of conducting polymers.[280,281] Allara, Guiseppi-Elie and coworkers further showed that selective blocking of defects on Au electrodes could be achieved using the growth of thin polymethylene films.[278] Finally, these films have been utilized to align organic small molecule semiconductors into oriented nanocrystalline thin films.[282,283]
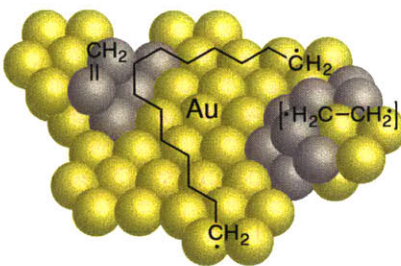
Figure 17. Depiction of diazomethane-derived methylidene undergoing polymerization at a Au surface. Polymerization is thought to initiate at defect sites (*e.g.*, step edge sites, highlighted in light-brown) via first dimerization of the carbene to form a surface-bound excited-state ethylene diradical followed by radical chain growth.[277]

Jennings and coworkers have introduced additional complexity and function in the above film deposition process. Firstly, Jennings and Guo reported that underpotentially deposited copper and silver on top of a gold surface provided effective means to control the kinetics of polymethylene formation and the resulting film properties.[279] For example, when the coverage of deposited Cu or Ag is 0.6, the growth rate of polymethylene is constant with time (in contrast

to the decreasing rate on plain Au); at coverages beyond 0.6, Ag is found to dramatically inhibit polymethylene growth, while Cu promotes it.[279] The relative orthorhombic crystallite content in the films can be controlled through this method as well.[279]

In another fruitful effort, Jennings and coworkers explored the copolymerization of diazomethane and ethyl diazoacetate on planar Au surfaces.[284] Despite not being able to incorporate more than 4% of the ethyl acetylidene into the produced polymer (and inability to homopolymerize ethyl diazoacetate), even this small fraction of ester functionality throughout the polymer backbone served as a valuable and powerful chemical handle to vary macroscopic film properties.[284-286] Namely, hydrolysis (partial or complete) of the ester moieties gives rise to carboxylic acid functionalities that become ionized at elevated pH and decrease the resistance to ion-transport by as much as 5 orders of magnitude.[285,286] Jennings and coworkers demonstrated the utility of these polymers through the fabrication of pH-responsive composite alumina/Au/polymeric membranes.[287]

Alkylidene-functionalized Mo- and Ru-based surfaces: An historical context

Parallel to the development of carbene polymerization on gold and other metal surfaces, reports of heterogeneous catalysts capable of mediating olefin metathesis reactions[288,289] appeared in the scientific literature as early as the mid-1960s, and these catalysts almost certainly operated *via* the mechanism proposed by Chauvin,[39] which also involved a metal alkylidene intermediate. Unbeknownst to the authors of those earliest reports on heterogeneous metathesis, they had likely prepared molybdenum-based surfaces coated with alkylidene ligands, which participated in their observed olefin metathesis reaction. Subsequent progress in the field of surface stabilization with alkylidenes had to await the maturation of our understanding of the olefin metathesis reaction, and only in 2001 did the first report appear on alkylidene surface anchors by McBreen and coworkers.[290] Since then, the McBreen laboratory, as well as those of Chen, Konopelski, and Nuckolls pioneered the field of alkylidene surface anchors; their contributions are presented sequentially below.
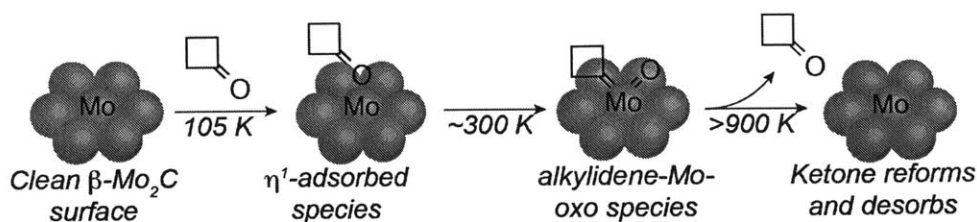
Figure 18. A depiction of the transformation of cyclobutanone at the β-Mo$_2$C surface discovered and studied by McBreen. At 105 K, cyclobutanone is predominantly η^1-coordinated to the surface (5:1 η^1 / η^2); upon warming to 300 K, the carbonyl group undergoes scission into a cyclobutylidene and oxo ligands bound to a Mo atom. Above 900 K, the reverse process takes place, leading to desorption of cyclobutanone.[290,291]

Alkylidene-modified β-Mo$_2$C surfaces pioneered by McBreen

In 2001, McBreen and coworkers described a pioneering study of molybdenum alkylidene monolayers (and simultaneous Mo=O formation) on β-Mo$_2$C (Figure 18).[290] In this study, the authors exposed β-Mo$_2$C surfaces to microTorr pressures of cycloketones (*e.g.*, cyclobutanone) at 105 K. Upon heating these surfaces to 300 K they obtained simultaneously oxo and cyclobutylidene functionalized molybdenum surfaces. The alkylidene monolayers were remarkably thermally stable below 900 K; between 900 and 1200 K they underwent ketone regeneration/desorption. Pretreating the surface with ^{18}O$_2$ followed by the cyclobutanone, resulted in ^{18}O incorporation into the cyclobutanone desorbed above 900 K, as indicated by temperature-programmed desorption mass spectrometry (m/z = 72) (TPD-MS), confirming the microscopic reverse of the original proposed carbonyl oxidative addition process.

At the same time, the monolayers were catalytically active in the olefin metathesis reaction at 105 K. The authors had at the time postulated that the metathesis reaction proceeded via the Hérisson-Chauvin mechanism established for the homogeneous systems and confirmed in 2006 to be operative in a heterogeneous system containing a molybdenum-aluminum alloy film.[292] In 2005[293], the same group used elegant isotopic labeling studies combined with reflection absorption infrared spectroscopy (RAIRS) to identify molybdenum ethylidene and methylidene species formed upon exposure of the cyclopentylidene-covered β-Mo$_2$C to D-labeled propene, as well as the byproducts of olefin metathesis (methylidene cyclopentane and ethylidene cyclopentane) via TPD-MS. These authors were even able to demonstrate cross-metathesis of butadiene[294] with the cyclopentylidene-coated surface, as well as surface-initiated polymerization at 500 K of norbornene[293] and cyclopentene[295]; the degree of polymerization was not quantified for the former, and was estimated to be small for the latter. Attempts to polymerize cyclooctatetraene in a later study met with little success, though the authors have hypothesized

that control over the surface morphology may be critical for the success of catalytic activity of the β-Mo$_2$C surface.[296] The authors further intimated that carbene junctions may make for conductive metal-polymer junctions, a vision that our laboratory has expanded to NHC-interfaces.[235]

In subsequent studies, McBreen and coworkers elaborated on the various aspects of the β-Mo$_2$C surface functionalization. They found that in parallel with Mo insertion into an alkanone carbonyl group to yield a Mo alkylidene and Mo=O, Mo also participates in C-H bond scission followed by H$_2$ elimination, as well as decarbonylation, which gives rise to a layer of carbon surrounding the alkylidene sites.[297,298] The deposited carbon layer thus protects the alkylidene sites from thermally activated molybdenum-mediated decomposition by passivation of the reactive molybdenum sites around the alkylidenes.[298] The alkylidene sites, however, are still reactive toward olefins in the metathesis reaction manifold.

In another study,[299] the same group established that aldehydes (in particular, acetaldehyde) undergo similar oxidative addition to the molybdenum atoms on the surface of β-Mo$_2$C. Furthermore, the used RAIRS to identify the first intermediate en route to the ethylidene-Mo-oxo species: the η^1-adsorbed acetaldehyde. In a follow-up study[291] that focused on cyclobutanone, the geometry of the intermediate was refined through XPS and RAIRS to that of a tilted η^1-adsorbed species, present at 105 K, and stable under annealing temperatures below 300 K. In addition to the tilted species, there was evidence for an η^2-adsorbed species, in which the π and π* orbitals of the carbonyl group are interacting with the Mo atoms in the surface. XPS examination of the oxygen 1s region indicated that the η^1 and η^2 species were present in a 5:1 ratio. The η^2 state upon heating past above 300 K presumably leads to the alkylidene-Mo-oxo species.

Thus, the McBreen laboratory has pioneered and furnished a plentitude of mechanistic evidence for the formation of alkylidene/"carbon" mixed monolayers on industrially relevant b-Mo$_2$C surfaces. Others following in their footsteps have demonstrated similar olefin metathesis reactivity on a MoAl alloy.[292] Beyond the immediate impact of McBreen's studies, his recognition that carbene@metal interfaces could form thermally stable and highly conductive junctions between metals and organic materials left a lasting impact on the field.

Following McBreen's work, and given the Mo (or W) / Ru dichotomy in olefin metathesis, the later development of analogous ruthenium alkylidene surfaces (*vide infra*) is logical. The first reports of ruthenium surfaces stabilized by alkylidenes (or benzylidenes) were actually

motivated by the study of the Fischer-Tropsch reaction, in which carbenes are presumed to insert into the metal-carbonyl bond to form ketenes. Evidence for this mechanism was in part supported by the finding of Woll and coworkers[300] that diphenylcarbene (generated from the corresponding diazo-precursor) reacts with carbonyl-coated Ru(0001) surface to form strongly adsorbed diphenylketene. In the process, they also found that diphenylcarbene forms a well-defined, upright-directed monolayer on a pristine Ru(0001) surface; however, the chemical reactivity (*e.g.*, ability to participate in olefin metathesis) and physical properties of these surfaces were not explored beyond the insertion into metal-carbonyl bonds and IRAS characterization.[300]

Alkylidene-functionalized Ru surfaces developed by Nuckolls
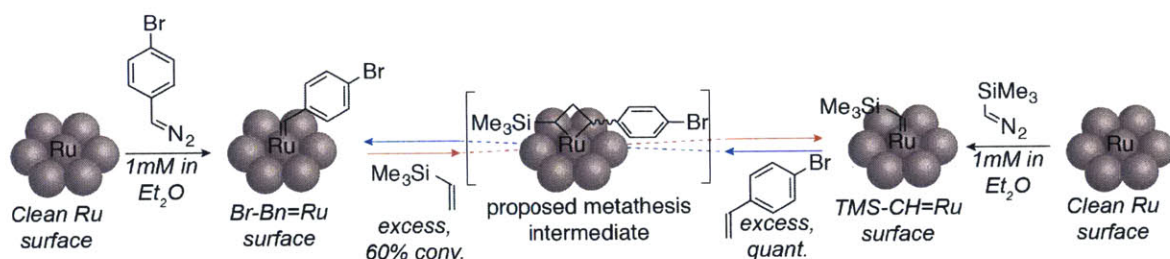
Figure 19. A depiction of planar Ru surface functionalization with TMS-methylidene or *p*-bromobenzylidene by Nuckolls and coworkers via the corresponding diazo-compounds in Et₂O, as well as the olefin metathesis reactivity of such surfaces.[301]

In a seminal report published in 2005,[301] the Nuckolls group explored the chemical reactivity of alkylidene functionalized Ru surfaces (prepared similarly from diazo-precursors) in olefin metathesis (Figure 19). These authors found that, as one might expect, trimethylsilyl methylidene-functionalized Ru films were air- and thermally stable (up to at least 160 °C) and capable of undergoing cross-metathesis with 4-bromostyrene to generate a 4-bromo-benzylidene-functionalized surface and vice-versa (though the conversion exhibited by the reverse reaction was much lower due to the claimed greater density of the 4-bromobenzylidene monolayers). Analogous carbene-functionalized Ru NPs provided additional support for the surface-catalyzed olefin metathesis reaction. These NPs underwent olefin metathesis to generate enough of the cross-metathesis byproduct (4-bromostyrene) to be detected by GC-MS. Notably, the authors show only one of two possible regioisomers of the metallocyclobutane intermediate (Figure 19); no comments on the possible formation of Ru-methylidene surfaces from the alternate regioisomer are offered. Furthermore, it is not clear if 4-bromostyrene is the sole product, or if

TMS-4-bromostyrene, 4,4'-dibromostilbene, and/or 1,2-bis(TMS)ethene are produced as well. Nevertheless, this work represents an important advance in the realm of catalytic carbene-Ru anchors.

Notably, Nuckolls and coworkers put forth an analogous proposal to the one expressed by McBreen: that the carbene anchor group could be used to form highly conductive contacts between the metal (in this case Ru) and the attached organic moiety. Furthermore, SI-ROMP could allow one to grow "conjugated molecular wires in electrical contact with a Ru metal particle or surface." Though this goal has yet to be accomplished, Nuckolls and coworkers employed DFT calculations to demonstrate that 1,3,5-pentatriene-Ru is a fully conjugated organometallic species. They also elaborate on alkylidyne-Ru species, but this discussion is outside the scope of our review.

Subsequently, Nuckolls and coworkers developed a more well-defined Ru NP system[302] than what they had used in their original study: instead of using Ru nanopowder for functionalization with alkylidene, they synthesized Ru NP from Ru(COD)(COT) in the presence of a diazo-precursor (they found that introduction of alkylidenes through ligand exchange with alcohols led to aggregated particles with poor ROMP performance). When TMS-diazomethane was used as the alkylidene source, the obtained Ru NPs were 10.3 nm in diameter (TEM), but precipitated from the 19:1 THF/MeOH crude reaction mixture after several hours (suggesting agglomeration), and were unstable in air, forming RuO_2. Nonetheless, the authors took advantage of the several-hour time window and were able to demonstrate reasonably good ROMP activity of these NPs. Notably, these Ru NPs mediated ROMP just as well in air as in inert atmosphere, suggesting that the polymers grown from the particle surface inhibited oxidation of Ru NPs to RuO_2.

With regard to the polymers produced from ROMP of norbornene after quenching the reactions with ethylvinyl ether and acetone, the yield depended heavily on the relative amount of Ru(COD)(COT) and the diazo-precursor used in the NP synthesis: when the former was in a four-fold excess of the latter, the yields were substantially lower (as low as 30%) than when the two were at least in a 1:1 stoichiometry ($\geq$ 95%). The cis/trans olefin ratio (0.21—0.38) was close to the expected thermodynamic ratio (0.16 $\div$ 0.84 = 0.19[303]), but varied slightly (for reasons that remain poorly understood) when different conditions were used. The polymer M_n was generally quite large, approaching 200 kDa in cases where monomer conversion was nearly

quantitative. The molar mass dispersity ($Đ_M$) was generally lower when the Ru NP was stabilized with TMS-methylidene (1.2—1.3) than when it was stabilized with 4-bromobenzylidene (1.35—1.68), suggesting that the former was faster-initiating. Assuming no chain transfer, and given the high conversion ($\geq$ 95%), high molecular weights (~200 kDa) and low NP loading (7 x 10^{-8} M), we calculate that on average, the Ru NPs must have ~2400 catalytically active sites per particle.[304] Given the diameter of the Ru NPs (~10 nm), and the atomic radius of Ru (0.134 nm), the expected number of atoms at the surface can be _roughly_ estimated by dividing the NP surface area by the cross-sectional area of the atom: ~5600. Following this reasoning, ~43% of the available Ru atoms on the surface are active SI-ROMP initiators, which is remarkable.

Among the exciting aspects of the Ru NP system developed in the Nuckolls laboratory are the relatively well-defined nature of the catalyst despite its colloid nature, the polymerization efficiency, and the potential to interface organic polymers with metal nanoparticles in a way that allows for charge delocalization over both through the carbene linkages. However, the latter aspect had yet to be tested experimentally, and the poor stability of the Ru NP was a significant limitation.

Alkylidene-functionalized R@NPs and thin films developed by Chen and Konopelski

Almost exactly one year prior to Nuckolls's Ru NP report, Chen and coworkers developed a ligand exchange method to synthesize small (~2.1 $\pm$ 0.7 nm diameter) Ru NPs functionalized with alkylidene ligands (Figure 20A).[305] There were three major differences between Chen and Nuckolls's NP synthesis approach that allowed the former authors to access small *air-stable* and non-agglomerating alkylidene-functionalized Ru NPs: (1) the alcohol-stabilized NPs were synthesized via a previously reported route known to result in small nanoparticles; (2) the alcohols were exchanged for alkylidenes in a biphasic solvent mixture containing an alpha-diazoester (not diazo-alkylidenes/benzylidenes) (3) the alkylidene ligand contained a long alkyl chain ($^nC_8H_{17}$) attached via an ester group to the alkylidene anchor group, and such alkyl chains are known to additionally stabilize the monolayer on metal surfaces through van der Waals interactions (*e.g.*, ~6 kcal/mol of additional stabilization for hexanethiol on Au[171]). These Ru NPs exhibited quantized charging, which had been observed previously in small coinage metal nanoparticles,[306-310] broadened ligand peaks in the ^{1}H NMR spectra (with greater broadening for

protons closer to the NP surface), and a greatly red-shifted (from 1698 cm^{-1} to 1640 cm^{-1}) carbonyl stretch, indicating delocalization of electron density from the metal to the carbonyl group. Lastly, the alkylidene-stabilized Ru NPs were also capable of undergoing ligand exchange via olefin metathesis with 11-bromo-1-undecene; by ^{1}H NMR, the conversion plateaued at 90% after 35 h at room temperature. The rate constant for the olefin metathesis ligand exchange was calculated to be 1.5×10^{-2} M^{-1} s^{-1}, which is ~twice that observed in Au-NP thiol exchange.[305] Again, the possible formation of methylidene ligands via olefin metathesis was not discussed.
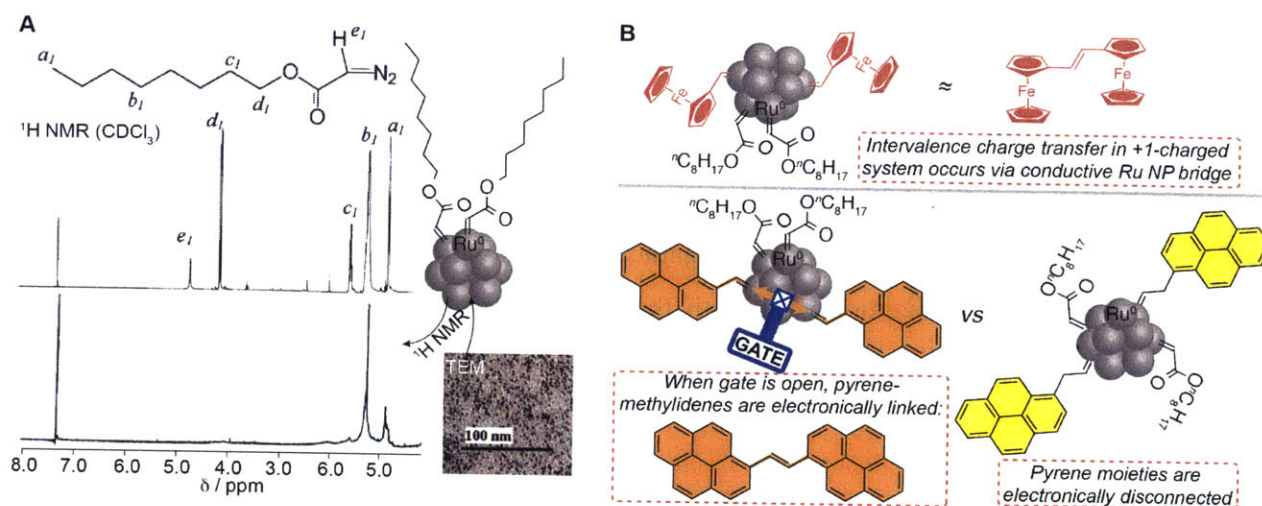
Figure 20. **A.** ^{1}H NMR and TEM evidence for the formation of *n*-octylacetylidene stabilized Ru NPs reported by Chen and coworkers.[305] **B.** Chen and coworkers subsequently demonstrate that analogous Ru NPs functionalized with ferrocenemethylidene or pyrenemethylidene exhibit, respectively, intervalence charge transfer or photophysical behavior characteristic of dimerized pyrenemethylidene (*i.e.*, (*E*)-1,2-di(pyren-1-yl)-ethene), and that this behavior could be ion-gated; in contrast, pyrene moieties in pyreneallylidene ligands are electronically disconnected.[311,313-315]

In a subsequent study, Chen, Wang, and coworkers established a more detailed picture of the electronic communication between Ru NPs and their ligands wired with alkylidene anchors.[311] Through olefin metathesis ligand exchange with either vinylferrocene or allylferrocene, they attached ferrocene to Ru NPs in a conjugated or conjugation-disrupted manner, respectively (Figure 20B). As a consequence, the former scenario led to observation of signatures of intraparticle intervalence charge transfer during square wave voltammetry as well as NIR spectroscopy of +1-charged Ru NPs obtained by treatment with an oxidant (Figure 20B). In short, the Ru NP behaved as highly conductive wires connecting carbene-anchored ferrocenes, resulting in spectroscopic features quite similar to bis(ferrocenyl)ethylene! In contrast, when the ferrocenes were separated by a saturated methylene unit from the carbene anchor (in the case of allylferrocene), no such signatures were present. Similar intervalence transfer was also observed

for Ru thin films with carbene-attached ferrocene moieties.[312]

Further evidence for the phenomenon described above came from fluorescence measurements of Ru NPs functionalized partially with pyrene moieties (Figure 20B).[313] In perfect analogy with the ferrocene-functionalized Ru NPs described above, when pyrene was attached directly to the carbene anchor, the fluorescence behavior of the particles was almost identical to that of pyrene dimers separated by a conjugated bridge (Figure 20B). In contrast, when the conjugation was broken by a methylene unit, the Ru NP system behaved as a collection of non-interacting pyrenes (Figure 20B). Intriguingly, in a later study, the Chen group demonstrated the ability to control the intraparticle delocalization via a through-bond gating mechanism with metal cation-binding benzo-crown ethers or histidine moieties on the NP periphery (Figure 20B).[314,315] One must also note that while the Ru NPs conjugated to pyrenes exhibited strikingly similar fluorescence spectrum to the conjugated pyrene dimers, the former had a pronounced increase in fluorescence lifetime at one of the emission wavelengths, suggesting that the pyrenemethylidene-functionalized Ru NPs might be more stable to photobleaching than their all-organic small molecule fluorophore counterparts. This improvement, in addition to their greater collisional cross-section area and ability to modulate the fluorescence through selective binding of metal ions could prove quite useful in the design of novel chemosensors.[315] Chen and coworkers provided additional experimental grounds for this idea in a study focusing on detecting nitroaromatics, infamous for their powerful explosive nature.[316] They found that, indeed, Ru-NPs conjugated to pyrenes via carbene anchors were extremely sensitive to nitroaromatic compounds (down to the nM concentration levels for TNT).

Thus, Chen's Ru NP alkylidene functionalization platform has enabled them to effectively manipulate the optical and red-ox properties of Ru NPs through tuning the structure of the carbene ligands. In 2011, the Chen group demonstrated that their ligand design platform could also be used to affect interparticle "communication" in thin films of NPs.[317] Thus, by introducing anthracene moieties via olefin metathesis ligand exchange with octyl acetylidene functionalized Ru NPs, they dramatically altered the charge transport behavior of Ru NP films: the original NP films exhibited a transition from semiconducting to metallic regime within the temperature range of 100—320 K (as inferred from the temperature dependence of conductivity), but the ligand-exchanged Ru NP films retained their semiconducting behavior in the same range of temperatures.

Current state of the art and understanding of the alkylidene-Ru NP interface

To summarize, much of the alkylidene-Ru NP interface is now well-understood thanks to the pioneering work predominantly by groups of Nuckolls and Chen. Inspired by the vision of McBreen for an electrically conductive interface between metals/alloys and organic materials through carbene anchors, Nuckolls and coworkers prepared the first well-defined alkylidene-functionalized planar Ru surfaces capable of participating in olefin metathesis.[301] In their original work, Nuckolls focused on planar bulk surfaces, employing Ru *nanopowder* only to assist in confirmation of the olefin metathesis mechanism. Building on Nuckolls's work, Chen and coworkers designed and constructed the first well-defined, air-stable(!) and nonpolar solvent-redispersible Ru NP system.[305] This platform proved to be exceedingly fruitful, yielding insight into the optoelectronic coupling of the Ru NP and its organic shell through alkylidene linkages. Further progress will likely come from expansion of the scope of metal and binary nanoparticles, as well as in types of carbenes capable of forming conductive junctions with them. Chen and coworkers recently reported a first study of vinylidene-carbene junctions obtained through isomerization of surface-bound alkynes, but these were again on Ru NP surfaces.[318] As discussed above, we think that the tenability and great variety of NHC types, their ability to bind strongly to a wide range of elements, and the significant p-component present in their bonding[118] make them ideal candidates to fill that niche, and work in our and others' laboratories is underway to test this hypothesis.

Dichlorocarbene-modified H-terminated Si(111) surfaces

We will end our review with mention of the recent, pioneering example of silicon surface functionalization with dichlorocarbene carried out in the Tilley group.[319] This selection is quite fitting for two reasons: (1) the chemical reactivity of what was in fact dichlorocarbene noted by J. G. A. Geuther in 1862[320] marked one of the earliest observations hinting at the existence of the carbene species; and (2) the Tilley group was also one of the pioneers of Au NP surface functionalization with NHCs.[170] In their latest work, Tilley and coworkers selected a Seyferth reagent, $PhHgCCl_2Br$, as the precursor for $:CCl_2$. Carbene-functionalized monolayers were prepared by thermal decomposition of the Seyferth reagent at 80 °C in the presence of H-terminate Si(111) surfaces. During the course of 4 h, $:CCl_2$ purportedly inserts into the Si-H

surface bonds. While all of the Si-H sites are consumed during the course of the functionalization, as indicated by the disappearance of the corresponding stretch in the ATR-IR spectra, the extent of the :CCl$_2$ insertion was quantified by XPS to be ~25 ± 4%. The remainder of the atop silicon sites were converted to Si-Cl (~26 ± 1%) and Si-Br (~41 ± 5%). The halogenation of the silicon surface was proposed to proceed via a radical-based mechanism, similar to one that takes place on heating (TMS)$_3$SiH in the presence of an alkyl halide.[321] While the Si-Hal (Hal = Cl or Br) sites were reported to selectively react with sodium azide to form Si-N$_3$ on the silicon surface (the presence of which was confirmed by XPS), it is also possible that the superficial azide could also be formed through S$_N$2 displacement of chlorides at the Si-CHCl$_2$ (carbene-functionalized) sites. Displacement of the latter occurs completely and non-selectively when the surfaces are instead treated with MeMgCl. Hence, this work on the use of carbene ligands for Si-surface functionalization sets an important and valuable precedent. However, several aspects could be improved upon: the use of a highly toxic Hg-containing precursor for a non-persistent carbene species is not desirable, and the presence of parallel reaction manifolds leads to a somewhat ill-defined surface. We believe that both of these shortcomings could potentially be overcome with the use of NHCs.

1.6 Conclusion

Herein, we have reviewed the entirety of work on surface functionalization and stabilization of predominantly inorganic bulk material, nanoparticles, and molecular elemental allotropes with NHCs and surface functionalization with alternative, non-persistent carbenes. We excluded less well-defined systems, in which highly reactive dihalocarbenes or methylene have been used in the functionalization of carbon-based materials (*e.g.*, carbon nanotubes and other organic materials). We have attempted to justly identify the strengths and weaknesses of various functionalization routes and to assess the maturity and potential of each subfield. At present, the alkylidene field is sufficiently mature to allow development of applications – particularly in the realm of electronics – though the scope of materials is to date limited to Ru and Mo-containing substrates. NHC functionalization of surfaces, however, is less well-defined, and more work is needed in both planar surface and NP functionalization to develop a crisper picture of NHC binding – in particular, crystallization of precisely-defined small metal clusters with NHC ligands would be a major step forward in understanding the structure of the NHC-functionalized

surfaces. Furthermore, the scope of material surfaces functionalized with NHCs remains small. Advances are likely to come from studies aimed in these directions. Furthermore, the experimental evidence collected by Chen and coworkers for the conductive nature of alkylidene bonds has yet to find analogous confirmation in the case of NHC ligands. With these advances in understanding, technological advances of global significance – particularly in the area of electronics – are sure to come. In particular, the bottleable nature of NHCs and their ability to form strong, stable bonds and potentially electrically conductive interfaces with a broad range of elements profess an exciting future for these unassuming small molecules containing carbon atoms with only six valence electrons: to paraphrase Robert Browning's famous quote, less can and may indeed prove to be more in this case.

1.7 References

(1)   Dumas, J. B.; Péligot, E. Mémoire Sur L'esprit De Bois Et Sur Les Divers Composés Ethérés Qui En Proviennent. *Ann. Chim. Phys.* **1835**, *58*.

(2)   Nef, J. U. Ueber Das Zweiwerthige Kohlenstoffatom. (Vierte Abhandlung.) Die Chemie Des Methylens. *Justus Liebigs Ann. Chem.* **1897**, *298*, 202-374.

(3)   Hine, J. *Divalent Carbon*; Ronald Press, 1964.

(4)   Nolan, S. P. *N-Heterocyclic Carbenes in Synthesis*; John Wiley & Sons, 2006.

(5)   Dörwald, F. Z. *Metal Carbenes in Organic Synthesis*; John Wiley & Sons, 2008.

(6)   Glorius, F. *N-Heterocyclic Carbenes in Transition Metal Catalysis*; Springer, 2007.

(7)   de Frémont, P.; Marion, N.; Nolan, S. P. Carbenes: Synthesis, Properties, and Organometallic Chemistry. *Coord. Chem. Rev.* **2009**, *253*, 862-892.

(8)   Enders, D.; Niemeier, O.; Henseler, A. Organocatalysis by *N*-Heterocyclic Carbenes. *Chem. Rev.* **2007**, *107*, 5606-5655.

(9)   Cazin, C. S. J. *N-Heterocyclic Carbenes in Transition Metal Catalysis and Organocatalysis*; Springer, 2011.

(10)   Dubinsky, L.; Krom, B. P.; Meijler, M. M. Diazirine Based Photoaffinity Labeling. *Bioorg. Med. Chem.* **2012**, *20*, 554-570.

(11)   Gautier, A.; Cisnetti, F. Advances in Metal-Carbene Complexes as Potent Anti-Cancer Agents. *Metallomics* **2012**, *4*, 23-32.

(12)   Mercs, L.; Albrecht, M. Beyond Catalysis: *N*-Heterocyclic Carbene Complexes as Components for Medicinal, Luminescent, and Functional Materials Applications. *Chem. Soc. Rev.* **2010**, *39*, 1903-1912.

(13)   Gomberg, M. An Instance of Trivalent Carbon Triphenylmethyl. *J. Am. Chem. Soc.* **1900**, *22*, 757-771.

(14)   Olah, G. G. A. Olah in C. D. Nenitzescu's 60th Birthday Issue. *Rev. Chim.* **1962**, *7*, 1139.

(15)   Olah, G. A.; Baker, E. B.; Kuhn, S. J.; Tolgyesi, W. S. Stable Carbonium Ions. II. Oxocarbonium (Acylium) Tetrafluoroborates, Hexafluorophosphates, Hexafluoroantimonates and Hexafluoroarsenates. Structure and Chemical Reactivity of Acyl Fluoride: Lewis Acid Fluoride Complexes. *J. Am. Chem. Soc.* **1962**, *84*, 2733-2740.

(16)   Olah, G. A.; Bastien, I. J.; Moffatt, M. E.; Kuhn, S. J.; Baker, E. B.; Tolgyesi, W. S. Stable Carbonium Ions. IV. Secondary and Tertiary Alkyl and Aralkyl Oxocarbonium Hexafluoroantimonates. Formation and Identification of the Trimethylcarbonium Ion by Decarbonylation of the *tert*-Butyl Oxocarbonium Ion. *J. Am. Chem. Soc.* **1963**, *85*, 1328-1334.

(17)   Olah, G. A. Stable Carbocations. CXVIII. General Concept and Structure of Carbocations Based on Differentiation of Trivalent (Classical) Carbenium Ions from 3-Center Bound Pentacoordinated or Tetracoordinated (Nonclassical) Carbonium-Ions. Role of Carbocations in Electrophilic Reactions. *J. Am. Chem. Soc.* **1972**, *94*, 808-820.

(18)   Igau, A.; Grutzmacher, H.; Baceiredo, A.; Bertrand, G. Analogous α,α'-Bis-Carbenoid, Triply Bonded Species: Synthesis of a Stable λ^3-Phosphino Carbene-λ^5-Phosphaacetylene. *J. Am. Chem. Soc.* **1988**, *110*, 6463-6466.

(19)   Arduengo, A. J.; Harlow, R. L.; Kline, M. A Stable Crystalline Carbene. *J. Am. Chem. Soc.* **1991**, *113*, 361-363.

(20)   Arduengo, A. J.; Gamper, S. F.; Calabrese, J. C.; Davidson, F. Low-Coordinate Carbene Complexes of Nickel(0) and Platinum(0). *J. Am. Chem. Soc.* **1994**, *116*, 4391-4394.

(21)   Arduengo, A. J.; Bertrand, G. Carbenes Introduction. *Chem. Rev.* **2009**, *109*, 3209-3210.

(22) Hopkinson, M. N.; Richter, C.; Schedler, M.; Glorius, F. An Overview of *N*-Heterocyclic Carbenes. *Nature* **2014**, *510*, 485-496.
(23) Grubbs, R. H. Olefin Metathesis. *Tetrahedron* **2004**, *60*, 7117-7140.
(24) Schrock, R. R.; Czekelius, C. Recent Advances in the Syntheses and Applications of Molybdenum and Tungsten Alkylidene and Alkylidyne Catalysts for the Metathesis of Alkenes and Alkynes. *Adv. Synth. Catal.* **2007**, *349*, 55-77.
(25) Bielawski, C. W.; Grubbs, R. H. Living Ring-Opening Metathesis Polymerization. *Prog. Polym. Sci.* **2007**, *32*, 1-29.
(26) Vougioukalakis, G. C.; Grubbs, R. H. Ruthenium-Based Heterocyclic Carbene-Coordinated Olefin Metathesis Catalysts. *Chem. Rev.* **2010**, *110*, 1746-1787.
(27) Scholl, M.; Trnka, T. M.; Morgan, J. P.; Grubbs, R. H. Increased Ring Closing Metathesis Activity of Ruthenium-Based Olefin Metathesis Catalysts Coordinated with Imidazolin-2-Ylidene Ligands. *Tetrahedron Lett.* **1999**, *40*, 2247-2250.
(28) Huang, J.; Stevens, E. D.; Nolan, S. P.; Petersen, J. L. Olefin Metathesis-Active Ruthenium Complexes Bearing a Nucleophilic Carbene Ligand. *J. Am. Chem. Soc.* **1999**, *121*, 2674-2678.
(29) Sanford, M. S.; Love, J. A.; Grubbs, R. H. A Versatile Precursor for the Synthesis of New Ruthenium Olefin Metathesis Catalysts. *Organometallics* **2001**, *20*, 5314-5318.
(30) Love, J. A.; Morgan, J. P.; Trnka, T. M.; Grubbs, R. H. A Practical and Highly Active Ruthenium-Based Catalyst That Effects the Cross Metathesis of Acrylonitrile. *Angew. Chem. Int. Ed.* **2002**, *41*, 4035-4037.
(31) Love, J. A.; Sanford, M. S.; Day, M. W.; Grubbs, R. H. Synthesis, Structure, and Activity of Enhanced Initiators for Olefin Metathesis. *J. Am. Chem. Soc.* **2003**, *125*, 10103-10109.
(32) Kingsbury, J. S.; Harrity, J. P. A.; Bonitatebus, P. J.; Hoveyda, A. H. A Recyclable Ru-Based Metathesis Catalyst. *J. Am. Chem. Soc.* **1999**, *121*, 791-799.
(33) Gessler, S.; Randl, S.; Blechert, S. Synthesis and Metathesis Reactions of a Phosphine-Free Dihydroimidazole Carbene Ruthenium Complex. *Tetrahedron Lett.* **2000**, *41*, 9973-9976.
(34) Endo, K.; Grubbs, R. H. Chelated Ruthenium Catalysts for Z-Selective Olefin Metathesis. *J. Am. Chem. Soc.* **2011**, *133*, 8525-8527.
(35) Keitz, B. K.; Endo, K.; Patel, P. R.; Herbert, M. B.; Grubbs, R. H. Improved Ruthenium Catalysts for Z-Selective Olefin Metathesis. *J. Am. Chem. Soc.* **2012**, *134*, 693-699.
(36) Keitz, B. K.; Fedorov, A.; Grubbs, R. H. Cis-Selective Ring-Opening Metathesis Polymerization with Ruthenium Catalysts. *J. Am. Chem. Soc.* **2012**, *134*, 2040-2043.
(37) Occhipinti, G.; Hansen, F. R.; Tornroos, K. W.; Jensen, V. R. Simple and Highly Z-Selective Ruthenium-Based Olefin Metathesis Catalyst. *J. Am. Chem. Soc.* **2013**, *135*, 3331-3334.
(38) Rosebrugh, L. E.; Herbert, M. B.; Marx, V. M.; Keitz, B. K.; Grubbs, R. H. Highly Active Ruthenium Metathesis Catalysts Exhibiting Unprecedented Activity and Z-Selectivity. *J. Am. Chem. Soc.* **2013**, *135*, 1276-1279.
(39) Jean-Louis Hérisson, P.; Chauvin, Y. Catalyse De Transformation Des Oléfines Par Les Complexes Du Tungstène. II. Télomérisation Des Oléfines Cycliques En Présence D'oléfines Acycliques. *Macromol. Chem. Phys.* **1971**, *141*, 161-176.
(40) McGinnis, J.; Katz, T. J.; Hurwitz, S. Selectivity in the Olefin Metathesis of Unsymmetrically Substituted Ethylenes. *J. Am. Chem. Soc.* **1976**, *98*, 605-606.

(41)   Schrock, R.; Rocklage, S.; Wengrovius, J.; Rupprecht, G.; Fellmann, J. Preparation and Characterization of Active Niobium, Tantalum and Tungsten Metathesis Catalysts. *J. Mol. Catal.* **1980**, *8*, 73-83.

(42)   Schrock, R. R.; Hoveyda, A. H. Molybdenum and Tungsten Imido Alkylidene Complexes as Efficient Olefin-Metathesis Catalysts. *Angew. Chem. Int. Ed.* **2003**, *42*, 4592-4633.

(43)   Enders, D.; Breuer, K.; Raabe, G.; Runsink, J.; Teles, J. H.; Melder, J. P.; Ebel, K.; Brode, S. Preparation, Structure, and Reactivity of 1,3,4-Triphenyl-4,5-Dihydro-1*H*-1,2,4-Triazol-5-Ylidene, a New Stable Carbene. *Angew. Chem. Int. Ed.* **1995**, *34*, 1021-1023.

(44)   Lavallo, V.; Canac, Y.; Prasang, C.; Donnadieu, B.; Bertrand, G. Stable Cyclic (Alkyl)(Amino) Carbenes as Rigid or Flexible, Bulky, Electron-Rich Ligands for Transition-Metal Catalysts: A Quaternary Carbon Atom Makes the Difference. *Angew. Chem. Int. Ed.* **2005**, *44*, 5705-5709.

(45)   Soleilhavoup, M.; Bertrand, G. Cyclic (Alkyl)(Amino)Carbenes (CAACs): Stable Carbenes on the Rise. *Acc. Chem. Res.* **2015**, *48*, 256-266.

(46)   Hudnall, T. W.; Bielawski, C. W. An *N,N'*-Diamidocarbene: Studies in C-H Insertion, Reversible Carbonylation, and Transition-Metal Coordination Chemistry. *J. Am. Chem. Soc.* **2009**, *131*, 16039-16041.

(47)   César, V.; Lugan, N.; Lavigne, G. Reprogramming of a Malonic *N*-Heterocyclic Carbene: A Simple Backbone Modification with Dramatic Consequences on the Ligand's Donor Properties. *Eur. J. Inorg. Chem.* **2010**, 361-365.

(48)   Ukai, T.; Tanaka, S.; Dokawa, S. Thiamin Catalysis of the Benzoin Condensation. *J. Pharm. Soc. Jpn.* **1943**, *63*, 269.

(49)   Breslow, R. Rapid Deuterium Exchange in Thiazolium Salts. *J. Am. Chem. Soc.* **1957**, *79*, 1762-1763.

(50)   Breslow, R. On the Mechanism of Thiamine Action. IV. Evidence from Studies on Model Systems. *J. Am. Chem. Soc.* **1958**, *80*, 3719-3726.

(51)   Sheehan, J. C.; Hunneman, D. H. Homogeneous Asymmetric Catalysis. *J. Am. Chem. Soc.* **1966**, *88*, 3666-3667.

(52)   Sheehan, J. C.; Hara, T. Asymmetric Thiazolium Salt Catalysis of the Benzoin Condensation. *J. Org. Chem.* **1974**, *39*, 1196-1199.

(53)   Enders, D.; Breuer, K.; Runsink, J.; Teles, J. H. The First Asymmetric Intramolecular Stetter Reaction. Preliminary Communication. *Helv. Chim. Acta* **1996**, *79*, 1899-1902.

(54)   Enders, D.; Breuer, K.; Teles, J. H. A Novel Asymmetric Benzoin Reaction Catalyzed by a Chiral Triazolium Salt. Preliminary Communication. *Helv. Chim. Acta* **1996**, *79*, 1217-1221.

(55)   Henrique Teles, J.; Melder, J.-P.; Ebel, K.; Schneider, R.; Gehrer, E.; Harder, W.; Brode, S.; Enders, D.; Breuer, K.; Raabe, G. The Chemistry of Stable Carbenes. Part 2. Benzoin-Type Condensations of Formaldehyde Catalyzed by Stable Carbenes. *Helv. Chim. Acta* **1996**, *79*, 61-83.

(56)   Enders, D.; Kallfass, U. An Efficient Nucleophilic Carbene Catalyst for the Asymmetric Benzoin Condensation. *Angew. Chem. Int. Ed.* **2002**, *41*, 1743-1745.

(57)   Kerr, M. S.; Read de Alaniz, J.; Rovis, T. A Highly Enantioselective Catalytic Intramolecular Stetter Reaction. *J. Am. Chem. Soc.* **2002**, *124*, 10298-10299.

(58)   Burstein, C.; Glorius, F. Organocatalyzed Conjugate Umpolung of α,β-Unsaturated Aldehydes for the Synthesis of γ-Butyrolactones. *Angew. Chem. Int. Ed.* **2004**, *43*, 6205-6208.

(59)   Sohn, S. S.; Rosen, E. L.; Bode, J. W. N-Heterocyclic Carbene-Catalyzed Generation of Homoenolates: γ-Butyrolactones by Direct Annulations of Enals and Aldehydes. *J. Am. Chem. Soc.* **2004**, *126*, 14370-14371.

(60)   Reynolds, N. T.; Rovis, T. Enantioselective Protonation of Catalytically Generated Chiral Enolates as an Approach to the Synthesis of α-Chloroesters. *J. Am. Chem. Soc.* **2005**, *127*, 16406-16407.

(61)   Maki, B. E.; Chan, A.; Phillips, E. M.; Scheidt, K. A. Tandem Oxidation of Allylic and Benzylic Alcohols to Esters Catalyzed by N-Heterocyclic Carbenes. *Org. Lett.* **2007**, *9*, 371-374.

(62)   Duguet, N.; Campbell, C. D.; Slawin, A. M. Z.; Smith, A. D. N-Heterocyclic Carbene Catalysed β-Lactam Synthesis. *Org. Biomol. Chem.* **2008**, *6*, 1108-1113.

(63)   He, J.; Tang, S.; Liu, J.; Su, Y.; Pan, X.; She, X. N-Heterocyclic Carbene Catalyzed Intramolecular Nucleophilic Addition of Carbonyl Anion Equivalents to Enol Ethers. *Tetrahedron* **2008**, *64*, 8797-8800.

(64)   Zhang, Y.-R.; He, L.; Wu, X.; Shao, P.-L.; Ye, S. Chiral N-Heterocyclic Carbene Catalyzed Staudinger Reaction of Ketenes with Imines: Highly Enantioselective Synthesis of N-Boc β-Lactams. *Org. Lett.* **2008**, *10*, 277-280.

(65)   Hirano, K.; Biju, A. T.; Piel, I.; Glorius, F. N-Heterocyclic Carbene-Catalyzed Hydroacylation of Unactivated Double Bonds. *J. Am. Chem. Soc.* **2009**, *131*, 14190-14191.

(66)   Jeong, W.; Shin, E. J.; Culkin, D. A.; Hedrick, J. L.; Waymouth, R. M. Zwitterionic Polymerization: A Kinetic Strategy for the Controlled Synthesis of Cyclic Polylactide. *J. Am. Chem. Soc.* **2009**, *131*, 4884-4891.

(67)   Kayaki, Y.; Yamamoto, M.; Ikariya, T. N-Heterocyclic Carbenes as Efficient Organocatalysts for CO_2 Fixation Reactions. *Angew. Chem. Int. Ed.* **2009**, *48*, 4194-4197.

(68)   Riduan, S. N.; Zhang, Y.; Ying, J. Y. Conversion of Carbon Dioxide into Methanol with Silanes over N-Heterocyclic Carbene Catalysts. *Angew. Chem. Int. Ed.* **2009**, *48*, 3322-3325.

(69)   Biju, A. T.; Wurz, N. E.; Glorius, F. N-Heterocyclic Carbene-Catalyzed Cascade Reaction Involving the Hydroacylation of Unactivated Alkynes. *J. Am. Chem. Soc.* **2010**, *132*, 5970-5971.

(70)   Gu, L.-Q.; Zhang, Y.-G. Unexpected CO_2 Splitting Reactions to Form CO with N-Heterocyclic Carbenes as Organocatalysts and Aromatic Aldehydes as Oxygen Acceptors. *J. Am. Chem. Soc.* **2010**, *132*, 914-915.

(71)   DiRocco, D. A.; Rovis, T. Catalytic Asymmetric α-Acylation of Tertiary Amines Mediated by a Dual Catalysis Mode: N-Heterocyclic Carbene and Photoredox Catalysis. *J. Am. Chem. Soc.* **2012**, *134*, 8094-8097.

(72)   Fu, Z.; Xu, J.; Zhu, T.; Leong, W. W. Y.; Chi, Y. R. β-Carbon Activation of Saturated Carboxylic Esters through N-Heterocyclic Carbene Organocatalysis. *Nature Chem.* **2013**, *5*, 835-839.

(73)   Flanigan, D. M.; Romanov-Michailidis, F.; White, N. A.; Rovis, T. Organocatalytic Reactions Enabled by N-Heterocyclic Carbenes. *Chem. Rev.* **2015**.

(74)   Frey, G. D.; Masuda, J. D.; Donnadieu, B.; Bertrand, G. Activation of Si–H, B–H, and P–H Bonds at a Single Nonmetal Center. *Angew. Chem. Int. Ed.* **2010**, *49*, 9444-9447.

(75)   Arduengo III, A. J.; Calabrese, J. C.; Davidson, F.; Rasika Dias, H. V.; Goerlich, J. R.; Krafczyk, R.; Marshall, W. J.; Tamm, M.; Schmutzler, R. C–H Insertion Reactions of Nucleophilic Carbenes. *Helv. Chim. Acta* **1999**, *82*, 2348-2364.

(76)   Hudnall, T. W.; Moerdyk, J. P.; Bielawski, C. W. Ammonia N-H Activation by a *N,N'*-Diamidocarbene. *Chem. Commun.* **2010**, *46*, 4288-4290.

(77)   Powell, A. B.; Bielawski, C. W.; Cowley, A. H. Electropolymerization of an *N*-Heterocyclic Carbene-Gold(I) Complex. *J. Am. Chem. Soc.* **2009**, *131*, 18232-18233.

(78)   Mercs, L.; Neels, A.; Stoeckli-Evans, H.; Albrecht, M. Main-Chain Organometallic Polymers Comprising Redox-Active Iron(II) Centers Connected by Ditopic *N*-Heterocyclic Carbenes. *Dalton Trans.* **2009**, 7168-7178.

(79)   Norris, B. C.; Bielawski, C. W. Structurally Dynamic Materials Based on Bis(*N*-Heterocyclic Carbene)s and Bis(Isothiocyanate)s: Toward Reversible, Conjugated Polymers. *Macromolecules* **2010**, *43*, 3591-3593.

(80)   Schuster, O.; Mercs, L.; Albrecht, M. The Potential of *N*-Heterocyclic Carbene Complexes as Components for Electronically Active Materials. *Chimia* **2010**, *64*, 184-187.

(81)   Powell, A. B.; Bielawski, C. W.; Cowley, A. H. Design, Synthesis, and Study of Main Chain Poly(*N*-Heterocyclic Carbene) Complexes: Applications in Electrochromic Devices. *J. Am. Chem. Soc.* **2010**, *132*, 10184-10194.

(82)   Teyssot, M.-L.; Jarrousse, A.-S.; Manin, M.; Chevry, A.; Roche, S.; Norre, F.; Beaudoin, C.; Morel, L.; Boyer, D.; Mahiou, R.; Gautier, A. Metal-NHC Complexes: A Survey of Anti-Cancer Properties. *Dalton Trans.* **2009**, 6894-6902.

(83)   Liu, W. K.; Gust, R. Metal N-Heterocyclic Carbene Complexes as Potential Antitumor Metallodrugs. *Chem. Soc. Rev.* **2013**, *42*, 755-773.

(84)   Oehninger, L.; Rubbiani, R.; Ott, I. *N*-Heterocyclic Carbene Metal Complexes in Medicinal Chemistry. *Dalton Trans.* **2013**, *42*, 3269-3284.

(85)   Singman, C. N. Atomic Volume and Allotropy of the Elements. *J. Chem. Educ.* **1984**, *61*, 137-142.

(86)   King, H. Crystal Structures and Lattice Parameters of Allotropes of the Elements. *CRC Handbook of Chemistry and Physics* **2005**.

(87)   Dyker, C. A.; Bertrand, G. Soluble Allotropes of Main-Group Elements. *Science* **2008**, *321*, 1050-1051.

(88)   Osawa, E. Superaromaticity. *Kagaku* **1970**, *25*, 854-863.

(89)   Kroto, H. W.; Heath, J. R.; Obrien, S. C.; Curl, R. F.; Smalley, R. E. C$_{60}$ - Buckminsterfullerene. *Nature* **1985**, *318*, 162-163.

(90)   Dai, L. *Carbon Nanotechnology: Recent Developments in Chemistry, Physics, Materials Science and Device Applications*; Elsevier, 2006.

(91)   25 Years of C60. *Nature Nanotech.* **2010**, *5*, 691-691.

(92)   Boehm, H. P.; Clauss, A.; Fischer, G. O.; Hofmann, U. Das Adsorptionsverhalten Sehr Dünner Kohlenstoff-Folien. *Z. Anorg. Allg. Chem.* **1962**, *316*, 119-127.

(93)   Novoselov, K. S.; Geim, A. K.; Morozov, S. V.; Jiang, D.; Zhang, Y.; Dubonos, S. V.; Grigorieva, I. V.; Firsov, A. A. Electric Field Effect in Atomically Thin Carbon Films. *Science* **2004**, *306*, 666-669.

(94)   Novoselov, K. S.; Geim, A. K.; Morozov, S. V.; Jiang, D.; Katsnelson, M. I.; Grigorieva, I. V.; Dubonos, S. V.; Firsov, A. A. Two-Dimensional Gas of Massless Dirac Fermions in Graphene. *Nature* **2005**, *438*, 197-200.

(95)   Novoselov, K. S.; Jiang, D.; Schedin, F.; Booth, T. J.; Khotkevich, V. V.; Morozov, S. V.; Geim, A. K. Two-Dimensional Atomic Crystals. *Proc. Natl. Acad. Sci. U. S. A.* **2005**, *102*, 10451-10453.

(96)   Meyer, J. C.; Geim, A. K.; Katsnelson, M. I.; Novoselov, K. S.; Booth, T. J.; Roth, S. The Structure of Suspended Graphene Sheets. *Nature* **2007**, *446*, 60-63.

(97)   Lin, Y. M.; Dimitrakopoulos, C.; Jenkins, K. A.; Farmer, D. B.; Chiu, H. Y.; Grill, A.; Avouris, P. 100-GHz Transistors from Wafer-Scale Epitaxial Graphene. *Science* **2010**, *327*, 662-662.

(98)   Palacios, T. Graphene Electronics: Thinking Outside the Silicon Box. *Nature Nanotech.* **2011**, *6*, 464-465.

(99)   Yung, K. C.; Wu, W. M.; Pierpoint, M. P.; Kusmartsev, F. V. Introduction to Graphene Electronics – a New Era of Digital Transistors and Devices. *Contemp. Phys.* **2013**, *54*, 233-251.

(100)   Cassar, L. Synthesis of Aryl-Substituted and Vinyl-Substituted Acetylene Derivatives by Use of Nickel and Palladium Complexes. *J. Organomet. Chem.* **1975**, *93*, 253-257.

(101)   Sekiya, A.; Ishikawa, N. Facile Synthesis of Aryl Cyanides from Iodides Catalyzed by Palladium Triphenylphosphine Complex. *Chem. Lett.* **1975**, 277-278.

(102)   Sonogashira, K.; Tohda, Y.; Hagihara, N. Convenient Synthesis of Acetylenes: Catalytic Substitutions of Acetylenic Hydrogen with Bromoalkenes, Iodoarenes, and Bromopyridines. *Tetrahedron Lett.* **1975**, 4467-4470.

(103)   Yamamura, M.; Moritani, I.; Murahashi, S. I. Reaction of σ-Vinylpalladium Complexes with Alkyllithiums. Stereospecific Syntheses of Olefins from Vinyl Halides and Alkyllithiums. *J. Organomet. Chem.* **1975**, *91*, C39-C42.

(104)   Baba, S.; Negishi, E. Novel Stereospecific Alkenyl-Alkenyl Cross-Coupling by a Palladium-Catalyzed or Nickel-Catalyzed Reaction of Alkenylalanes with Alkenyl Halides. *J. Am. Chem. Soc.* **1976**, *98*, 6729-6731.

(105)   Fauvarque, J. F.; Jutand, A. Action of Various Nucleophiles with Organopalladium Compounds. *B. Soc. Chim. Fr. II-Ch.* **1976**, 765-770.

(106)   Negishi, E.; Baba, S. Novel Stereoselective Alkenyl-Aryl Coupling Via Nickel-Catalyzed Reaction of Alkenylalanes with Aryl Halides. *J. Chem. Soc., Chem. Commun.* **1976**, 596-597.

(107)   Sekiya, A.; Ishikawa, N. Cross-Coupling of Aryl Halides with Grignard-Reagents Catalyzed by Iodo(Phenyl)Bis(Triphenylphosphine)-Palladium(II). *J. Organomet. Chem.* **1976**, *118*, 349-354.

(108)   Böhm, V. P. W.; Gstöttmayr, C. W. K.; Weskamp, T.; Herrmann, W. A. N-Heterocyclic Carbenes Part 26. N-Heterocyclic Carbene Complexes of Palladium(0): Synthesis and Application in the Suzuki Cross-Coupling Reaction. *J. Organomet. Chem.* **2000**, *595*, 186-190.

(109)   Fu, G. C. The Development of Versatile Methods for Palladium-Catalyzed Coupling Reactions of Aryl Electrophiles through the Use of P(t-Bu)$_3$ and PCy$_3$ as Ligands. *Acc. Chem. Res.* **2008**, *41*, 1555-1564.

(110) Martin, R.; Buchwald, S. L. Palladium-Catalyzed Suzuki-Miyaura Cross-Coupling Reactions Employing Dialkylbiaryl Phosphine Ligands. *Acc. Chem. Res.* **2008**, *41*, 1461-1473.

(111) Takahashi, Y.; Ito, T.; Sakai, S.; Ishii, Y. A Novel Palladium(0) Complex; Bis(Dibenzylideneacetone)Palladium(0). *J. Chem. Soc., Chem. Commun.* **1970**, 1065-&.

(112) Moseley, K.; Maitlis, P. M. Bis- and Tris-(Dibenzylideneacetone)Platinum and Stabilization of Zerovalent Complexes by an Unsaturated Ketone. *J. Chem. Soc., Chem. Commun.* **1971**, 982-&.

(113) Pinhas, A. R. In *Encyclopedia of Reagents for Organic Synthesis*; John Wiley & Sons, Ltd, 2001.

(114) Malatesta, L.; Cariello, C. Platinum(0) Compounds with Triarylphosphines and Analogous Ligands. *J. Chem. Soc.* **1958**, 2323-2328.

(115) Coulson, D. R.; Satek, L. C.; Grim, S. O. Tetrakis(Triphenylphosphine)Palladium(0). *Inorg. Synth.* **1972**, *13*, 121-124.

(116) Ittel, S. D.; Berke, H.; Dietrich, H.; Lambrecht, J.; Härter, P.; Opitz, J.; Springer, W. Complexes of Nickel(0). *Inorg. Synth.* **1990**, *28*, 98-104.

(117) Schunn, R. A.; Ashby, E. C.; Dilts, J. Tetrakis(Triphenylphosphine)Nickel(0). *Inorg. Synth.* **1972**, *13*, 124-126.

(118) Jacobsen, H.; Correa, A.; Poater, A.; Costabile, C.; Cavallo, L. Understanding the M-(NHC) (NHC = *N*-Heterocyclic Carbene) Bond. *Coord. Chem. Rev.* **2009**, *253*, 687-703.

(119) Masuda, J. D.; Schoeller, W. W.; Donnadieu, B.; Bertrand, G. Carbene Activation of P_4 and Subsequent Derivatization. *Angew. Chem. Int. Ed.* **2007**, *46*, 7052-7055.

(120) Masuda, J. D.; Schoeller, W. W.; Donnadieu, B.; Bertrand, G. NHC-Mediated Aggregation of P_4: Isolation of a P_{12} Cluster. *J. Am. Chem. Soc.* **2007**, *129*, 14180-14180.

(121) Wang, Y.; Xie, Y.; Wei, P.; King, R. B.; Schaefer, I. I. I. H. F.; Schleyer, P. v. R.; Robinson, G. H. Carbene-Stabilized Diphosphorus. *J. Am. Chem. Soc.* **2008**, *130*, 14970-14971.

(122) Back, O.; Kuchenbeiser, G.; Donnadieu, B.; Bertrand, G. Nonmetal-Mediated Fragmentation of P_4: Isolation of P_1 and P_2 Bis(Carbene) Adducts. *Angew. Chem. Int. Ed.* **2009**, *48*, 5530-5533.

(123) Abraham, M. Y.; Wang, Y.; Xie, Y.; Wei, P.; Schaefer III, H. F.; Schleyer, P. v. R.; Robinson, G. H. Carbene Stabilization of Diarsenic: From Hypervalency to Allotropy. *Chem. Eur. J.* **2010**, *16*, 432-435.

(124) Romanenko, V. D.; Kachkovskaya, L. S.; Markovskii, L. N. 1,1,4,4-Tetrakis(Dialkylamino)-2,3-Diphosphabutadienes. *Zh. Obshch. Khim.* **1985**, *55*, 2140-2141.

(125) Dyker, C. A.; Lavallo, V.; Donnadieu, B.; Bertrand, G. Synthesis of an Extremely Bent Acyclic Allene (a "Carbodicarbene"): A Strong Donor Ligand. *Angew. Chem. Int. Ed.* **2008**, *47*, 3206-3209.

(126) Celik, M. A.; Frenking, G.; Neumuller, B.; Petz, W. Exploiting the Twofold Donor Ability of Carbodiphosphoranes: Theoretical Studies of $[(PPh_3)_2C{\rightarrow}EH_2]^q$ (E^q = Be, B^+, C^{2+}, N^{3+}, O^{4+}) and Synthesis of the Dication $[(Ph_3P)_2C{=}CH_2]^{2+}$. *Chempluschem* **2013**, *78*, 1024-1032.

(127) Mondal, K. C.; Roesky, H. W.; Schwarzer, M. C.; Frenking, G.; Niepötter, B.; Wolf, H.; Herbst-Irmer, R.; Stalke, D. A Stable Singlet Biradicaloid Siladicarbene: (L:)$_2$Si. *Angew. Chem. Int. Ed.* **2013**, *52*, 2963-2967.

69

(128) Wang, Y.; Xie, Y.; Wei, P.; King, R. B.; Schaefer, H. F.; von R. Schleyer, P.; Robinson, G. H. A Stable Silicon(0) Compound with a Si=Si Double Bond. *Science* **2008**, *321*, 1069-1071.

(129) Previously, Si_2 was only observed in the gas phase and in frozen matrices.[130,131]

(130) Van Zee, R. J.; Ferrante, R. F.; Weltner, W. Si_2, SiH_3, and HSiO Molecules: ESR at 4 K. *J. Chem. Phys.* **1985**, *83*, 6181-6187.

(131) Zhou, M.; Jiang, L.; Xu, Q. Reactions of Silicon Atoms and Small Clusters with CO: Experimental and Theoretical Characterization of Si_nCO (n = 1–5), $Si_2(CO)_2$, c-$Si_2(\mu$-O)(μ-CSi), and c-$Si_2(\mu$-O)(μ-CCO) in Solid Argon. *J. Chem. Phys.* **2004**, *121*, 10474-10482.

(132) Sidiropoulos, A.; Jones, C.; Stasch, A.; Klein, S.; Frenking, G. *N*-Heterocyclic Carbene Stabilized Digermanium(0). *Angew. Chem. Int. Ed.* **2009**, *48*, 9701-9704.

(133) Jones, C.; Sidiropoulos, A.; Holzmann, N.; Frenking, G.; Stasch, A. An *N*-Heterocyclic Carbene Adduct of Diatomic Tin, Sn=Sn. *Chem. Commun.* **2012**, *48*, 9855-9857.

(134) Wilson, D. J. D.; Couchman, S. A.; Dutton, J. L. Are *N*-Heterocyclic Carbenes "Better" Ligands Than Phosphines in Main Group Chemistry? A Theoretical Case Study of Ligand-Stabilized E_2 Molecules, L-E-E-L (L = NHC, Phosphine; E = C, Si, Ge, Sn, Pb, N, P, as, Sb, Bi). *Inorg. Chem.* **2012**, *51*, 7657-7668.

(135) Li, H.; Risko, C.; Seo, J. H.; Campbell, C.; Wu, G.; Brédas, J.-L.; Bazan, G. C. Fullerene–Carbene Lewis Acid–Base Adducts. *J. Am. Chem. Soc.* **2011**, *133*, 12410-12413.

(136) Braunschweig, H.; Dewhurst, R. D.; Hammond, K.; Mies, J.; Radacki, K.; Vargas, A. Ambient-Temperature Isolation of a Compound with a Boron-Boron Triple Bond. *Science* **2012**, *336*, 1420-1422.

(137) Koppe, R.; Schnockel, H. The Boron-Boron Triple Bond? A Thermodynamic and Force Field Based Interpretation of the *N*-Heterocyclic Carbene (NHC) Stabilization Procedure. *Chem. Sci.* **2015**, *6*, 1199-1205.

(138) Holzmann, N.; Stasch, A.; Jones, C.; Frenking, G. Structures and Stabilities of Group 13 Adducts [(NHC)(EX_3)] and [$(NHC)_2(E_2X_n)$] (E=B to in; X = H, Cl; N = 4, 2, 0; NHC = *N*-Heterocyclic Carbene) and the Search for Hydrogen Storage Systems: A Theoretical Study. *Chem. Eur. J.* **2011**, *17*, 13517-13525.

(139) Böhnke, J.; Braunschweig, H.; Ewing, W. C.; Horl, C.; Kramer, T.; Krummenacher, I.; Mies, J.; Vargas, A. Diborabutatriene: An Electron-Deficient Cumulene. *Angew. Chem. Int. Ed.* **2014**, *53*, 9082-9085.

(140) Böhnke, J.; Braunschweig, H.; Constantinidis, P.; Dellermann, T.; Ewing, W. C.; Fischer, I.; Hammond, K.; Hupp, F.; Mies, J.; Schmitt, H. C.; Vargas, A. Experimental Assessment of the Strengths of B-B Triple Bonds. *J. Am. Chem. Soc.* **2015**, *137*, 1766-1769.

(141) Weinberger, D. S.; Melaimi, M.; Moore, C. E.; Rheingold, A. L.; Frenking, G.; Jerabek, P.; Bertrand, G. Isolation of Neutral Mono- and Dinuclear Gold Complexes of Cyclic (Alkyl)(Amino)Carbenes. *Angew. Chem. Int. Ed.* **2013**, *52*, 8964-8967.

(142) Samuel, P. P.; Mondal, K. C.; Roesky, H. W.; Hermann, M.; Frenking, G.; Demeshko, S.; Meyer, F.; Stuckl, A. C.; Christian, J. H.; Dalal, N. S.; Ungur, L.; Chibotaru, L. F.; Propper, K.; Meents, A.; Dittrich, B. Synthesis and Characterization of a Two-Coordinate Manganese Complex and Its Reaction with Molecular Hydrogen at Room Temperature. *Angew. Chem. Int. Ed.* **2013**, *52*, 11817-11821.

(143) Ung, G.; Rittle, J.; Soleilhavoup, M.; Bertrand, G.; Peters, J. C. Two-Coordinate Fe^0 and Co^0 Complexes Supported by Cyclic (Alkyl)(Amino) Carbenes. *Angew. Chem. Int. Ed.* **2014**, *53*, 8427-8431.

(144) Mondal, K. C.; Samuel, P. P.; Li, Y.; Roesky, H. W.; Roy, S.; Ackermann, L.; Sidhu, N. S.; Sheldrick, G. M.; Carl, E.; Demeshko, S.; De, S.; Parameswaran, P.; Ungur, L.; Chibotaru, L. F.; Andrada, D. M. A Catalyst with Two-Coordinate Nickel: Theoretical and Catalytic Studies. *Eur. J. Inorg. Chem.* **2014**, *2014*, 818-823.

(145) Weinberger, D. S.; Sk, N. A.; Mondal, K. C.; Melaimi, M.; Bertrand, G.; Stuckl, A. C.; Roesky, H. W.; Dittrich, B.; Demeshko, S.; Schwederski, B.; Kaim, W.; Jerabek, P.; Frenking, G. Isolation of Neutral Mononuclear Copper Complexes Stabilized by Two Cyclic (Alkyl)(Amino)Carbenes. *J. Am. Chem. Soc.* **2014**, *136*, 6235-6238.

(146) Singh, A. P.; Samuel, P. P.; Roesky, H. W.; Schwarzer, M. C.; Frenking, G.; Sidhu, N. S.; Dittrich, B. A Singlet Biradicaloid Zinc Compound and Its Nonradical Counterpart. *J. Am. Chem. Soc.* **2013**, *135*, 7324-7329.

(147) Kretschmer, R.; Ruiz, D. A.; Moore, C. E.; Rheingold, A. L.; Bertrand, G. One-, Two-, and Three-Electron Reduction of a Cyclic Alkyl-(Amino)Carbene-$SbCl_3$ Adduct. *Angew. Chem. Int. Ed.* **2014**, *53*, 8176-8179.

(148) Robilotto, T. J.; Bacsa, J.; Gray, T. G.; Sadighi, J. P. Synthesis of a Trigold Monocation: An Isolobal Analogue of $[H_3]^+$. *Angew. Chem. Int. Ed.* **2012**, *51*, 12077-12080.

(149) Jin, L. Q.; Weinberger, D. S.; Melaimi, M.; Moore, C. E.; Rheingold, A. L.; Bertrand, G. Trinuclear Gold Clusters Supported by Cyclic (Alkyl)(Amino)Carbene Ligands: Mimics for Gold Heterogeneous Catalysts. *Angew. Chem. Int. Ed.* **2014**, *53*, 9059-9063.

(150) Mednikov, E. G.; Eremenko, N. K.; Mikhailov, V. A.; Gubin, S. P.; Slovokhotov, Y. L.; Struchkov, Y. T. New Palladium Cluster Compounds - X-Ray Crystal-Structure of $Pd_{10}(CO)_{12}(PBu^n_3)_6$. *J. Chem. Soc., Chem. Commun.* **1981**, 989-990.

(151) Jadzinsky, P. D.; Calero, G.; Ackerson, C. J.; Bushnell, D. A.; Kornberg, R. D. Structure of a Thiol Monolayer-Protected Gold Nanoparticle at 1.1 Angstrom Resolution. *Science* **2007**, *318*, 430-433.

(152) Durham, J. L.; Wilson, W. B.; Huh, D. N.; McDonald, R.; Szczepura, L. F. Organometallic Rhenium(III) Chalcogenide Clusters: Coordination of *N*-Heterocyclic Carbenes. *Chem. Commun.* **2015**, *51*, 10536-10538.

(153) Ott, L. S.; Cline, M. L.; Deetlefs, M.; Seddon, K. R.; Finke, R. G. Nanoclusters in Ionic Liquids: Evidence for *N*-Heterocyclic Carbene Formation from Imidazolium-Based Ionic Liquids Detected by ^{2}H Nmr. *J. Am. Chem. Soc.* **2005**, *127*, 5758-5759.

(154) Ott, L. S.; Campbell, S.; Seddon, K. R.; Finke, R. G. Evidence That Imidazolium-Based Ionic Ligands Can Be Metal(0)/Nanocluster Catalyst Poisons in at Least the Test Case of Iridium(0)-Catalyzed Acetone Hydrogenation. *Inorg. Chem.* **2007**, *46*, 10335-10344.

(155) Viciano, M.; Mas-Marzá, E.; Poyatos, M.; Sanaú, M.; Crabtree, R. H.; Peris, E. An *N*-Heterocyclic Carbene/Iridium Hydride Complex from the Oxidative Addition of a Ferrocenyl–Bisimidazolium Salt: Implications for Synthesis. *Angew. Chem. Int. Ed.* **2005**, *44*, 444-447.

(156) Viciano, M.; Poyatos, M.; Sanaú, M.; Peris, E.; Rossin, A.; Ujaque, G.; Lledós, A. C−H Oxidative Addition of Bisimidazolium Salts to Iridium and Rhodium Complexes, and *N*-Heterocyclic Carbene Generation. A Combined Experimental and Theoretical Study. *Organometallics* **2006**, *25*, 1120-1134.

(157) McGuinness, D. S.; Cavell, K. J.; Yates, B. F.; Skelton, B. W.; White, A. H. Oxidative Addition of the Imidazolium Cation to Zerovalent Ni, Pd, and Pt: A Combined Density Functional and Experimental Study. *J. Am. Chem. Soc.* **2001**, *123*, 8317-8328.

(158) Grundemann, S.; Albrecht, M.; Kovacevic, A.; Faller, J. W.; Crabtree, R. H. Bis-Carbene Complexes from Oxidative Addition of Imidazolium C-H Bonds to Palladium(0). *J. Chem. Soc., Dalton Trans.* **2002**, 2163-2167.

(159) Clement, N. D.; Cavell, K. J.; Jones, C.; Elsevier, C. J. Oxidative Addition of Imidazolium Salts to Ni^0 and Pd^0: Synthesis and Structural Characterization of Unusually Stable Metal–Hydride Complexes. *Angew. Chem. Int. Ed.* **2004**, *43*, 1277-1279.

(160) Lara, P.; Rivada-Wheelaghan, O.; Conejero, S.; Poteau, R.; Philippot, K.; Chaudret, B. Ruthenium Nanoparticles Stabilized by *N*-Heterocyclic Carbenes: Ligand Location and Influence on Reactivity. *Angew. Chem. Int. Ed.* **2011**, *50*, 12080-12084.

(161) Dröge, T.; Glorius, F. The Measure of All Rings—*N*-Heterocyclic Carbenes. *Angew. Chem. Int. Ed.* **2010**, *49*, 6940-6952.

(162) Gonzalez-Galvez, D.; Lara, P.; Rivada-Wheelaghan, O.; Conejero, S.; Chaudret, B.; Philippot, K.; van Leeuwen, P. W. N. M. NHC-Stabilized Ruthenium Nanoparticles as New Catalysts for the Hydrogenation of Aromatics. *Catal. Sci. Tech.* **2013**, *3*, 99-105.

(163) Lara, P.; Suarez, A.; Colliere, V.; Philippot, K.; Chaudret, B. Platinum *N*-Heterocyclic Carbene Nanoparticles as New and Effective Catalysts for the Selective Hydrogenation of Nitroaromatics. *ChemCatChem* **2014**, *6*, 87-90.

(164) Baquero, E. A.; Tricard, S.; Flores, J. C.; de Jesús, E.; Chaudret, B. Highly Stable Water-Soluble Platinum Nanoparticles Stabilized by Hydrophilic *N*-Heterocyclic Carbenes. *Angew. Chem. Int. Ed.* **2014**, *53*, 13220-13224.

(165) Berthon-Gelloz, G.; Buisine, O.; Brière, J.-F.; Michaud, G.; Stérin, S.; Mignani, G.; Tinant, B.; Declercq, J.-P.; Chapon, D.; Markó, I. E. Synthetic and Structural Studies of NHC–Pt(Dvtms) Complexes and Their Application as Alkene Hydrosilylation Catalysts (NHC = *N*-Heterocyclic Carbene, Dvtms = Divinyltetramethylsiloxane). *J. Organomet. Chem.* **2005**, *690*, 6156-6168.

(166) Hurst, E. C.; Wilson, K.; Fairlamb, I. J. S.; Chechik, V. *N*-Heterocyclic Carbene Coated Metal Nanoparticles. *New J. Chem.* **2009**, *33*, 1837-1840.

(167) Heaven, M. W.; Dass, A.; White, P. S.; Holt, K. M.; Murray, R. W. Crystal Structure of the Gold Nanoparticle $[N(C_8H_{17})_4][Au_{25}(SCH_2CH_2Ph)_{18}]$. *J. Am. Chem. Soc.* **2008**, *130*, 3754-3755.

(168) This ratio was estimated by dividing the entire volume of the Au NP (without taking ligands into account) by the estimated volume of the outer shell of gold atoms: $(4 \cdot p \cdot (\text{radius of NP})^3/3)/[(4 \cdot p \cdot (\text{radius of NP})^3/3) - (4 \cdot p \cdot (\text{radius of inner core})^3/3)]$, where radius of NP = 2.6 nm/2, and radius of inner core equals to the radius of NP *minus* Au-Au bond length (= 0.29 nm).

(169) Lewis, D. J.; Day, T. M.; MacPherson, J. V.; Pikramenou, Z. Luminescent Nanobeads: Attachment of Surface Reactive Eu(III) Complexes to Gold Nanoparticles. *Chem. Commun.* **2006**, 1433-1435.

(170) Vignolle, J.; Tilley, T. D. *N*-Heterocyclic Carbene-Stabilized Gold Nanoparticles and Their Assembly into 3D Superlattices. *Chem. Commun.* **2009**, 7230-7232.

(171) Pensa, E.; Cortés, E.; Corthey, G.; Carro, P.; Vericat, C.; Fonticelli, M. H.; Benítez, G.; Rubert, A. A.; Salvarezza, R. C. The Chemistry of the Sulfur–Gold Interface: In Search of a Unified Model. *Acc. Chem. Res.* **2012**, *45*, 1183-1192.

(172) Richter, C.; Schaepe, K.; Glorius, F.; Ravoo, B. J. Tailor-Made *N*-Heterocyclic Carbenes for Nanoparticle Stabilization. *Chem. Commun.* **2014**, *50*, 3204-3207.

(173) Crespo, J.; Guari, Y.; Ibarra, A.; Larionova, J.; Lasanta, T.; Laurencin, D.; López-de-Luzuriaga, J. M.; Monge, M.; Olmos, M. E.; Richeter, S. Ultrasmall NHC-Coated Gold Nanoparticles Obtained through Solvent Free Thermolysis of Organometallic Au(I) Complexes. *Dalton Trans.* **2014**, *43*, 15713-15718.

(174) Serpell, C. J.; Cookson, J.; Thompson, A. L.; Brown, C. M.; Beer, P. D. Haloaurate and Halopalladate Imidazolium Salts: Structures, Properties, and Use as Precursors for Catalytic Metal Nanoparticles. *Dalton Trans.* **2013**, *42*, 1385-1393.

(175) Ling, X.; Roland, S.; Pileni, M. P. Supracrystals of *N*-Heterocyclic Carbene-Coated Au Nanocrystals. *Chem. Mater.* **2015**, *27*, 414-423.

(176) Crudden, C. M.; Horton, J. H.; Ebralidze, I. I.; Zenkina, O. V.; McLean, A. B.; Drevniok, B.; She, Z.; Kraatz, H. B.; Mosey, N. J.; Seki, T.; Keske, E. C.; Leake, J. D.; Rousina-Webb, A.; Wu, G. Ultra Stable Self-Assembled Monolayers of *N*-Heterocyclic Carbenes on Gold. *Nature Chem.* **2014**, *6*, 409-414.

(177) Ling, X.; Schaeffer, N.; Roland, S.; Pileni, M. P. Nanocrystals: Why Do Silver and Gold *N*-Heterocyclic Carbene Precursors Behave Differently? *Langmuir* **2013**, *29*, 12647-12656.

(178) Nigra, M. M.; Yeh, A. J.; Okrut, A.; DiPasquale, A. G.; Yeh, S. W.; Solovyov, A.; Katz, A. Accessible Gold Clusters Using Calix[4]Arene *N*-Heterocyclic Carbene and Phosphine Ligands. *Dalton Trans.* **2013**, *42*, 12762-12771.

(179) Song, S. G.; Satheeshkumar, C.; Park, J.; Ahn, J.; Premkumar, T.; Lee, Y.; Song, C. *N*-Heterocyclic Carbene-Based Conducting Polymer-Gold Nanoparticle Hybrids and Their Catalytic Application. *Macromolecules* **2014**, *47*, 6566-6571.

(180) Liu, H.-X.; He, X.; Zhao, L. Metallamacrocycle-Modified Gold Nanoparticles: A New Pathway for Surface Functionalization. *Chem. Commun.* **2014**, *50*, 971-974.

(181) MacLeod, M. J.; Johnson, J. A. PEGylated *N*-Heterocyclic Carbene Anchors Designed to Stabilize Gold Nanoparticles in Biologically Relevant Media. *J. Am. Chem. Soc.* **2015**, *137*, 7974-7977.

(182) Rodríguez-Castillo, M.; Laurencin, D.; Tielens, F.; van der Lee, A.; Clément, S.; Guari, Y.; Richeter, S. Reactivity of Gold Nanoparticles Towards *N*-Heterocyclic Carbenes. *Dalton Trans.* **2014**, *43*, 5978-5982.

(183) Zhu, M.; Aikens, C. M.; Hollander, F. J.; Schatz, G. C.; Jin, R. Correlating the Crystal Structure of a Thiol-Protected Au_{25} Cluster and Optical Properties. *J. Am. Chem. Soc.* **2008**, *130*, 5883-5885.

(184) Zeng, C. J.; Qian, H. F.; Li, T.; Li, G.; Rosi, N. L.; Yoon, B.; Barnett, R. N.; Whetten, R. L.; Landman, U.; Jin, R. C. Total Structure and Electronic Properties of the Gold Nanocrystal $Au_{36}(SR)_{24}$. *Angew. Chem. Int. Ed.* **2012**, *51*, 13114-13118.

(185) Das, A.; Li, T.; Nobusada, K.; Zeng, C. J.; Rosi, N. L.; Jin, R. C. Nonsuperatomic $[Au_{23}(SC_6H_{11})_{16}]^-$ Nanocluster Featuring Bipyramidal Au_{15} Kernel and Trimeric $Au_3(SR)_4$ Motif. *J. Am. Chem. Soc.* **2013**, *135*, 18264-18267.

(186) Zeng, C. J.; Li, T.; Das, A.; Rosi, N. L.; Jin, R. C. Chiral Structure of Thiolate-Protected 28-Gold-Atom Nanocluster Determined by X-Ray Crystallography. *J. Am. Chem. Soc.* **2013**, *135*, 10011-10013.

(187) Crasto, D.; Barcaro, G.; Stener, M.; Sementa, L.; Fortunelli, A.; Dass, A. $Au_{24}(SAdm)_{16}$ Nanomolecules: X-Ray Crystal Structure, Theoretical Analysis, Adaptability of

Adamantane Ligands to Form $Au_{23}(SAdm)_{16}$ and $Au_{25}(SAdm)_{16}$, and Its Relation to $Au_{25}(SR)_{18}$. *J. Am. Chem. Soc.* **2014**, *136*, 14933-14940.

(188) Crasto, D.; Malola, S.; Brosofsky, G.; Dass, A.; Hakkinen, H. Single Crystal XRD Structure and Theoretical Analysis of the Chiral $Au_{30}S(S\text{-}t\text{-}Bu)_{18}$ Cluster. *J. Am. Chem. Soc.* **2014**, *136*, 5000-5005.

(189) Das, A.; Li, T.; Li, G.; Nobusada, K.; Zeng, C.; Rosi, N. L.; Jin, R. Crystal Structure and Electronic Properties of a Thiolate-Protected Au_{24} Nanocluster. *Nanoscale* **2014**, *6*, 6458-6462.

(190) Das, A.; Liu, C.; Zeng, C. J.; Li, G.; Li, T.; Rosi, N. L.; Jin, R. C. Cyclopentanethiolato-Protected $Au_{36}(SC_5H_9)_{24}$ Nanocluster: Crystal Structure and Implications for the Steric and Electronic Effects of Ligand. *J. Phys. Chem. A* **2014**, *118*, 8264-8269.

(191) Zeng, C. J.; Liu, C.; Chen, Y. X.; Rosi, N. L.; Jin, R. C. Gold-Thiolate Ring as a Protecting Motif in the $Au_{20}(SR)_{16}$ Nanocluster and Implications. *J. Am. Chem. Soc.* **2014**, *136*, 11922-11925.

(192) Das, A.; Liu, C.; Byun, H. Y.; Nobusada, K.; Zhao, S.; Rosi, N.; Jin, R. Structure Determination of $[Au_{18}(SR)_{14}]$. *Angew. Chem. Int. Ed.* **2015**, *54*, 3140-3144.

(193) Song, Y. B.; Wang, S. X.; Zhang, J.; Kang, X.; Chen, S.; Li, P.; Sheng, H. T.; Zhu, M. Z. Crystal Structure of Selenolate-Protected $Au_{24}(SeR)_{20}$ Nanocluster. *J. Am. Chem. Soc.* **2014**, *136*, 2963-2965.

(194) Teo, B. K.; Shi, X. B.; Zhang, H. Pure Gold Cluster of 1-9-9-1-9-9-1 Layered Structure - a Novel 39-Metal-Atom Cluster $[(Ph_3P)_{14}Au_{39}Cl_6]Cl_2$ with an Interstitial Gold Atom in a Hexagonal Antiprismatic Cage. *J. Am. Chem. Soc.* **1992**, *114*, 2743-2745.

(195) Wan, X. K.; Lin, Z. W.; Wang, Q. M. Au_{20} Nanocluster Protected by Hemilabile Phosphines. *J. Am. Chem. Soc.* **2012**, *134*, 14750-14752.

(196) Chen, J.; Zhang, Q. F.; Bonaccorso, T. A.; Williard, P. G.; Wang, L. S. Controlling Gold Nanoclusters by Diphospine Ligands. *J. Am. Chem. Soc.* **2014**, *136*, 92-95.

(197) McKenzie, L. C.; Zaikova, T. O.; Hutchison, J. E. Structurally Similar Triphenylphosphine-Stabilized Undecagolds, $Au_{11}(PPh_3)_7Cl_3$ and $[Au_{11}(PPh_3)_8Cl_2]Cl$, Exhibit Distinct Ligand Exchange Pathways with Glutathione. *J. Am. Chem. Soc.* **2014**, *136*, 13426-13435.

(198) Wan, X. K.; Yuan, S. F.; Lin, Z. W.; Wang, Q. M. A Chiral Gold Nanocluster Au_{20} Protected by Tetradentate Phosphine Ligands. *Angew. Chem. Int. Ed.* **2014**, *53*, 2923-2926.

(199) Shichibu, Y.; Negishi, Y.; Watanabe, T.; Chaki, N. K.; Kawaguchi, H.; Tsukuda, T. Biicosahedral Gold Clusters $[Au_{25}(PPh_3)_{10}(SC_nH_{2n+1})_5Cl_2]^{2+}$ (n = 2–18): A Stepping Stone to Cluster-Assembled Materials. *J. Phys. Chem. C* **2007**, *111*, 7845-7847.

(200) Das, A.; Li, T.; Nobusada, K.; Zeng, Q.; Rosi, N. L.; Jin, R. C. Total Structure and Optical Properties of a Phosphine/Thiolate-Protected Au_{24} Nanocluster. *J. Am. Chem. Soc.* **2012**, *134*, 20286-20289.

(201) Kobayashi, N.; Kamei, Y.; Shichibu, Y.; Konishi, K. Protonation-Induced Chromism of Pyridylethynyl-Appended [core+*exo*]-Type Au_8 Clusters. Resonance-Coupled Electronic Perturbation through π-Conjugated Group. *J. Am. Chem. Soc.* **2013**, *135*, 16078-16081.

(202) Wan, X. K.; Tang, Q.; Yuan, S. F.; Jiang, D. E.; Wang, Q. M. Au_{19} Nanocluster Featuring a V-Shaped Alkynyl-Gold Motif. *J. Am. Chem. Soc.* **2015**, *137*, 652-655.

(203) Smirnova, E. S.; Echavarren, A. M. A Hexanuclear Gold Cluster Supported by Three-Center-Two-Electron Bonds and Aurophilic Interactions. *Angew. Chem. Int. Ed.* **2013**, *52*, 9023-9026.

(204) Nolan, S. P. The Development and Catalytic Uses of *N*-Heterocyclic Carbene Gold Complexes. *Acc. Chem. Res.* **2011**, *44*, 91-100.

(205) Ranganath, K. V. S.; Kloesges, J.; Schäfer, A. H.; Glorius, F. Asymmetric Nanocatalysis: *N*-Heterocyclic Carbenes as Chiral Modifiers of Fe$_3$O$_4$/Pd Nanoparticles. *Angew. Chem. Int. Ed.* **2010**, *49*, 7786-7789.

(206) Ranganath, K. V. S.; Schäfer, A. H.; Glorius, F. Comparison of Superparamagnetic Fe$_3$O$_4$-Supported *N*-Heterocyclic Carbene-Based Catalysts for Enantioselective Allylation. *ChemCatChem* **2011**, *3*, 1889-1891.

(207) Dreaden, E. C.; Alkilany, A. M.; Huang, X.; Murphy, C. J.; El-Sayed, M. A. The Golden Age: Gold Nanoparticles for Biomedicine. *Chem. Soc. Rev.* **2012**, *41*, 2740-2779.

(208) Dykman, L.; Khlebtsov, N. Gold Nanoparticles in Biomedical Applications: Recent Advances and Perspectives. *Chem. Soc. Rev.* **2012**, *41*, 2256-2282.

(209) Fratoddi, I.; Venditti, I.; Cametti, C.; Russo, M. V. Gold Nanoparticles and Gold Nanoparticle-Conjugates for Delivery of Therapeutic Molecules. Progress and Challenges. *J. Mater. Chem. B* **2014**, *2*, 4204-4220.

(210) Chardon, E.; Puleo, G. L.; Dahm, G.; Guichard, G.; Bellemin-Laponnaz, S. Direct Functionalisation of Group 10 *N*-Heterocyclic Carbene Complexes for Diversity Enhancement. *Chem. Commun.* **2011**, *47*, 5864-5866.

(211) Melaiye, A.; Sun, Z.; Hindi, K.; Milsted, A.; Ely, D.; Reneker, D. H.; Tessier, C. A.; Youngs, W. J. Silver(I)−Imidazole Cyclophane Gem-Diol Complexes Encapsulated by Electrospun Tecophilic Nanofibers: Formation of Nanosilver Particles and Antimicrobial Activity. *J. Am. Chem. Soc.* **2005**, *127*, 2285-2291.

(212) Lee, C. K.; Vasam, C. S.; Huang, T. W.; Wang, H. M. J.; Yang, R. Y.; Lee, C. S.; Lin, I. J. B. Silver(I) *N*-Heterocyclic Carbenes with Long *n*-Alkyl Chains. *Organometallics* **2006**, *25*, 3768-3775.

(213) Choi, J.; Kang, N.; Yang, H. Y.; Kim, H. J.; Son, S. U. Colloidal Synthesis of Cubic-Phase Copper Selenide Nanodiscs and Their Optoelectronic Properties. *Chem. Mater.* **2010**, *22*, 3586-3588.

(214) Lin, I. J. B.; Vasam, C. S. Preparation and Application of *N*-Heterocyclic Carbene Complexes of Ag(I). *Coordin. Chem. Rev.* **2007**, *251*, 642-670.

(215) Xiu, Z.-m.; Zhang, Q.-b.; Puppala, H. L.; Colvin, V. L.; Alvarez, P. J. J. Negligible Particle-Specific Antibacterial Activity of Silver Nanoparticles. *Nano Lett.* **2012**, *12*, 4271-4275.

(216) Planellas, M.; Pleixats, R.; Shafir, A. Palladium Nanoparticles in Suzuki Cross-Couplings: Tapping into the Potential of Tris-Imidazolium Salts for Nanoparticle Stabilization. *Adv. Synth. Catal.* **2012**, *354*, 651-662.

(217) Dyson, P. J. Arene Hydrogenation by Homogeneous Catalysts: Fact or Fiction? *Dalton Trans.* **2003**, 2964-2974.

(218) Bayram, E.; Linehan, J. C.; Fulton, J. L.; Roberts, J. A. S.; Szymczak, N. K.; Smurthwaite, T. D.; Özkar, S.; Balasubramanian, M.; Finke, R. G. Is It Homogeneous or Heterogeneous Catalysis Derived from [RhCp*Cl$_2$]$_2$? *In Operando* XAFS, Kinetic, and Crucial Kinetic Poisoning Evidence for Subnanometer Rh$_4$ Cluster-Based Benzene Hydrogenation Catalysis. *J. Am. Chem. Soc.* **2011**, *133*, 18889-18902.

(219) Sonnenberg, J. F.; Morris, R. H. Distinguishing Homogeneous from Nanoparticle Asymmetric Iron Catalysis. *Catal. Sci. Technol.* **2014**, *4*, 3426-3438.

(220) Soulé, J.-F.; Miyamura, H.; Kobayashi, S. Copolymer-Incarcerated Nickel Nanoparticles with *N*-Heterocyclic Carbene Precursors as Active Cross-Linking Agents for Corriu–Kumada–Tamao Reaction. *J. Am. Chem. Soc.* **2013**, *135*, 10602-10605.

(221) Aslanov, L.; Zakharov, V.; Zakharov, M.; Kamyshny, A.; Magdassi, S.; Yatsenko, A. Stabilization of Silicon Nanoparticles by Carbenes. *Russ. J. Coord. Chem.* **2010**, *36*, 330-332.

(222) Liu, C. Y.; Holman, Z. C.; Kortshagen, U. R. Hybrid Solar Cells from P3HT and Silicon Nanocrystals. *Nano Lett.* **2009**, *9*, 449-452.

(223) Pavesi, L.; Turan, R. *Silicon Nanocrystals: Fundamentals, Synthesis and Applications*; John Wiley & Sons, 2010.

(224) Heath, J. R. A Liquid-Solution-Phase Synthesis of Crystalline Silicon. *Science* **1992**, *258*, 1131-1133.

(225) Mayeri, D.; Phillips, B. L.; Augustine, M. P.; Kauzlarich, S. M. Nmr Study of the Synthesis of Alkyl-Terminated Silicon Nanoparticles from the Reaction of $Sicl_4$ with the Zintl Salt, NaSi. *Chem. Mater.* **2001**, *13*, 765-770.

(226) Baldwin, R. K.; Pettigrew, K. A.; Ratai, E.; Augustine, M. P.; Kauzlarich, S. M. Solution Reduction Synthesis of Surface Stabilized Silicon Nanoparticles. *Chem. Commun.* **2002**, 1822-1823.

(227) Pettigrew, K. A.; Liu, Q.; Power, P. P.; Kauzlarich, S. M. Solution Synthesis of Alkyl- and Alkyl/Alkoxy-Capped Silicon Nanoparticles Via Oxidation of Mg_2Si. *Chem. Mater.* **2003**, *15*, 4005-4011.

(228) Zou, J.; Baldwin, R. K.; Pettigrew, K. A.; Kauzlarich, S. M. Solution Synthesis of Ultrastable Luminescent Siloxane-Coated Silicon Nanoparticles. *Nano Lett.* **2004**, *4*, 1181-1186.

(229) Warner, J. H.; Hoshino, A.; Yamamoto, K.; Tilley, R. D. Water-Soluble Photoluminescent Silicon Quantum Dots. *Angew. Chem. Int. Ed.* **2005**, *44*, 4550-4554.

(230) Veinot, J. G. C. Synthesis, Surface Functionalization, and Properties of Freestanding Silicon Nanocrystals. *Chem. Commun.* **2006**, 4160-4168.

(231) Bell, J. P.; Cloud, J. E.; Cheng, J. F.; Ngo, C.; Kodambaka, S.; Sellinger, A.; Williams, S. K. R.; Yang, Y. A. *N*-Bromosuccinimide-Based Bromination and Subsequent Functionalization of Hydrogen-Terminated Silicon Quantum Dots. *RSC Adv.* **2014**, *4*, 51105-51110.

(232) Cheng, X. Y.; Lowe, S. B.; Ciampi, S.; Magenau, A.; Gaus, K.; Reece, P. J.; Gooding, J. J. Versatile "Click Chemistry" Approach to Functionalizing Silicon Quantum Dots: Applications toward Fluorescent Cellular Imaging. *Langmuir* **2014**, *30*, 5209-5216.

(233) Dasog, M.; De los Reyes, G. B.; Titova, L. V.; Hegmann, F. A.; Veinot, J. G. C. Size *vs* Surface: Tuning the Photoluminescence of Freestanding Silicon Nanocrystals across the Visible Spectrum Via Surface Groups. *ACS Nano* **2014**, *8*, 9636-9648.

(234) White, M. A.; Johnson, J. A.; Koberstein, J. T.; Turro, N. J. Toward the Syntheses of Universal Ligands for Metal Oxide Surfaces: Controlling Surface Functionality through Click Chemistry. *J. Am. Chem. Soc.* **2006**, *128*, 11356-11357.

(235) Zhukhovitskiy, A. V.; Mavros, M. G.; Van Voorhis, T.; Johnson, J. A. Addressable Carbene Anchors for Gold Surfaces. *J. Am. Chem. Soc.* **2013**, *135*, 7418-7421.

(236) Nuzzo, R. G.; Allara, D. L. Adsorption of Bifunctional Organic Disulfides on Gold Surfaces. *J. Am. Chem. Soc.* **1983**, *105*, 4481-4483.

(237) Nuzzo, R. G.; Zegarski, B. R.; Dubois, L. H. Fundamental-Studies of the Chemisorption of Organosulfur Compounds on Au(111). Implications for Molecular Self-Assembly on Gold Surfaces. *J. Am. Chem. Soc.* **1987**, *109*, 733-740.

(238) Love, J. C.; Estroff, L. A.; Kriebel, J. K.; Nuzzo, R. G.; Whitesides, G. M. Self-Assembled Monolayers of Thiolates on Metals as a Form of Nanotechnology. *Chem. Rev.* **2005**, *105*, 1103-1169.

(239) Brust, M.; Walker, M.; Bethell, D.; Schiffrin, D. J.; Whyman, R. Synthesis of Thiol-Derivatized Gold Nanoparticles in a 2-Phase Liquid-Liquid System. *J. Chem. Soc., Chem. Commun.* **1994**, 801-802.

(240) Brust, M.; Fink, J.; Bethell, D.; Schiffrin, D. J.; Kiely, C. Synthesis and Reactions of Functionalized Gold Nanoparticles. *J. Chem. Soc., Chem. Commun.* **1995**, 1655-1656.

(241) Zheng, N.; Fan, J.; Stucky, G. D. One-Step One-Phase Synthesis of Monodisperse Noble-Metallic Nanoparticles and Their Colloidal Crystals. *J. Am. Chem. Soc.* **2006**, *128*, 6550-6551.

(242) Angelici, R. J.; Lazar, M. Isocyanide Ligands Adsorbed on Metal Surfaces: Applications in Catalysis, Nanochemistry, and Molecular Electronics. *Inorg. Chem.* **2008**, *47*, 9155-9165.

(243) Angelici, R. J. Organometallic Chemistry and Catalysis on Gold Metal Surfaces. *J. Organomet. Chem.* **2008**, *693*, 847-856.

(244) Zhou, Y.; Trewyn, B. G.; Angelici, R. J.; Woo, L. K. Catalytic Reactions of Carbene Precursors on Bulk Gold Metal. *J. Am. Chem. Soc.* **2009**, *131*, 11734-11743.

(245) Weidner, T.; Baio, J. E.; Mundstock, A.; Grosse, C.; Karthäeuser, S.; Bruhn, C.; Siemeling, U. NHC-Based Self-Assembled Monolayers on Solid Gold Substrates. *Aust. J. Chem.* **2011**, *64*, 1177-1179.

(246) Liu, Y. F.; Lindner, P. E.; Lemal, D. M. Thermodynamics of a Diaminocarbene-Tetraaminoethylene Equilibrium. *J. Am. Chem. Soc.* **1999**, *121*, 10626-10627.

(247) Hahn, F. E.; Wittenbecher, L.; Le Van, D.; Fröhlich, R. Evidence for an Equilibrium between an *N*-Heterocyclic Carbene and Its Dimer in Solution. *Angew. Chem. Int. Ed.* **2000**, *39*, 541-544.

(248) Chen, Y. T.; Jordan, F. Reactivity of the Thiazolium C2 Ylide in Aprotic-Solvents: Novel Experimental-Evidence for Addition Rather Than Insertion Reactivity. *J. Org. Chem.* **1991**, *56*, 5029-5038.

(249) Alder, R. W.; Blake, M. E.; Chaker, L.; Harvey, J. N.; Paolini, F.; Schütz, J. When and How Do Diaminocarbenes Dimerize? *Angew. Chem. Int. Ed.* **2004**, *43*, 5896-5911.

(250) Alder, R. W.; Chaker, L.; Paolini, F. P. V. Bis(Diethylamino)Carbene and the Mechanism of Dimerisation for Simple Diaminocarbenes. *Chem. Commun.* **2004**, *0*, 2172-2173.

(251) Wanzlick, H. W.; Schikora, E. Ein Neuer Zugang Zur Carben-Chemie. *Angew. Chem. Int. Ed.* **1960**, *72*, 494-494.

(252) Wanzlick, H. W. Aspects of Nucleophilic Carbene Chemistry. *Angew. Chem. Int. Ed.* **1962**, *1*, 75-80.

(253) Çetinkaya, B.; Dixneuf, P.; Lappert, M. F. Carbene Complexes. Part VIII. Chromium(0), Iron(0), Rhodium(I), Iridium(I), Nickel(Ii), Palladium(Ii), Platinum(Ii), and Gold(I)

Mono-Carbene and Oligo-Carbene Species from Electron-Rich Olefins. *J. Chem. Soc., Dalton Trans.* **1974**, 1827-1833.

(254) Lappert, M. F. The Coordination Chemistry of Electron-Rich Alkenes (Enetetramines). *J. Organomet. Chem.* **1988**, *358*, 185-214.

(255) Wanzlick, H. W.; Schikora, E. Ein Nucleophiles Carben. *Chem. Ber.* **1961**, *94*, 2389-2393.

(256) Denk, M. K.; Rodezno, J. M.; Gupta, S.; Lough, A. J. Synthesis and Reactivity of Subvalent Compounds: Part 11. Oxidation, Hydrogenation and Hydrolysis of Stable Diamino Carbenes. *J. Organomet. Chem.* **2001**, *617–618*, 242-253.

(257) Hu, X. L.; Castro-Rodriguez, I.; Olsen, K.; Meyer, K. Group 11 Metal Complexes of *N*-Heterocyclic Carbene Ligands: Nature of the Metal-Carbene Bond. *Organometallics* **2004**, *23*, 755-764.

(258) Nemcsok, D.; Wichmann, K.; Frenking, G. The Significance of p Interactions in Group 11 Complexes with *N*-Heterocyclic Carbenes. *Organometallics* **2004**, *23*, 3640-3646.

(259) Weck, M.; Jackiw, J. J.; Rossi, R. R.; Weiss, P. S.; Grubbs, R. H. Ring-Opening Metathesis Polymerization from Surfaces. *J. Am. Chem. Soc.* **1999**, *121*, 4088-4089.

(260) Khramov, D. M.; Bielawski, C. W. Triazene Formation Via Reaction of Imidazol-2-Ylidenes with Azides. *Chem. Commun.* **2005**, 4958-4960.

(261) For Au, the basis set was LANL2DZ + effective core potential, and for all other atoms it was 6-31G*.

(262) Martin, D.; Canac, Y.; Lavallo, V.; Bertrand, G. Comparative Reactivity of Different Types of Stable Cyclic and Acyclic Mono- and Diamino Carbenes with Simple Organic Substrates. *J. Am. Chem. Soc.* **2014**, *136*, 5023-5030.

(263) Lavallo, V.; Mafhouz, J.; Canac, Y.; Donnadieu, B.; Schoeller, W. W.; Bertrand, G. Synthesis, Reactivity, and Ligand Properties of a Stable Alkyl Carbene. *J. Am. Chem. Soc.* **2004**, *126*, 8670-8671.

(264) Jerabek, P.; Roesky, H. W.; Bertrand, G.; Frenking, G. Coinage Metals Binding as Main Group Elements: Structure and Bonding of the Carbene Complexes [TM(cAAC)$_2$] and [TM(cAAC)$_2$]$^+$ (TM = Cu, Ag, Au). *J. Am. Chem. Soc.* **2014**, *136*, 17123-17135.

(265) Molina, L. M.; Hammer, B. Theoretical Study of Thiol-Induced Reconstructions on the Au(111) Surface. *Chem. Phys. Lett.* **2002**, *360*, 264-271.

(266) Maksymovych, P.; Sorescu, D. C.; Yates, J. T. Gold-Adatom-Mediated Bonding in Self-Assembled Short-Chain Alkanethiolate Species on the Au(111) Surface. *Phys. Rev. Lett.* **2006**, *97*.

(267) Jiang, D. E.; Tiago, M. L.; Luo, W. D.; Dai, S. The "Staple" Motif: A Key to Stability of Thiolate-Protected Gold Nanoclusters. *J. Am. Chem. Soc.* **2008**, *130*, 2777-2779.

(268) Maksymovych, P.; Yates, J. T. Au Adatoms in Self-Assembly of Benzenethiol on the Au(111) Surface. *J. Am. Chem. Soc.* **2008**, *130*, 7518-7519.

(269) Voznyy, O.; Dubowski, J. J.; Yates, J. T.; Maksymovych, P. The Role of Gold Adatoms and Stereochemistry in Self-Assembly of Methylthiolate on Au(111). *J. Am. Chem. Soc.* **2009**, *131*, 12989-12993.

(270) Chaudhuri, A.; Lerotholi, T. J.; Jackson, D. C.; Woodruff, D. P.; Dhanak, V. Local Methylthiolate Adsorption Geometry on Au(111) from Photoemission Core-Level Shifts. *Phys. Rev. Lett.* **2009**, *102*, 126101.

(271) Voznyy, O.; Dubowski, J. J. c(4 x 2) Structures of Alkanethiol Monolayers on Au (111) Compatible with the Constraint of Dense Packing. *Langmuir* **2009**, *25*, 7353-7358.

(272) Gronbeck, H.; Odelius, M. Photoemission Core-Level Shifts Reveal the Thiolate-Au(111) Interface. *Phys. Rev. B* **2010**, *82*.

(273) Maksymovych, P.; Sorescu, D. C.; Voznyy, O.; Yates, J. T. Hybridization of Phenylthiolate- and Methylthiolate-Adatom Species at Low Coverage on the Au(111) Surface. *J. Am. Chem. Soc.* **2013**, *135*, 4922-4925.

(274) Saini, G.; Nasini, A. G. *Atti Accad. Sci. Torino* **1955-1956**, *90*, 586.

(275) Nasini, A. G.; Trossarelli, L.; Saini, G. Reactions of Diazoalkanes Upon Metallic Surfaces: Polymer Formation and a Stereoregulating Action of Gold. *Makromol. Chem.* **1961**, *44-6*, 550-569.

(276) Jellema, E.; Jongerius, A. L.; Reek, J. N. H.; de Bruin, B. C1 Polymerisation and Related C-C Bond Forming 'Carbene Insertion' Reactions. *Chem. Soc. Rev.* **2010**, *39*, 1706-1723.

(277) Seshadri, K.; Atre, S. V.; Tao, Y.-T.; Lee, M.-T.; Allara, D. L. Synthesis of Crystalline, Nanometer-Scale, $-(CH_2)_x-$ Clusters and Films on Gold Surfaces. *J. Am. Chem. Soc.* **1997**, *119*, 4698-4711.

(278) Seshadri, K.; Wilson, A. M.; Guiseppi-Elie, A.; Allara, D. L. Toward Controlled Area Electrode Assemblies: Selective Blocking of Gold Electrode Defects with Polymethylene Nanocrystals. *Langmuir* **1999**, *15*, 742-749.

(279) Guo, W. F.; Jennings, G. K. Use of Underpotentially Deposited Metals on Gold to Affect the Surface-Catalyzed Formation of Polymethylene Films. *Langmuir* **2002**, *18*, 3123-3126.

(280) Tao, Y.-T.; Pandian, K.; Lee, W.-C. Microfabrication of Interdigitated Polyaniline/Polymethylene Patterns on a Gold Surface. *Langmuir* **1998**, *14*, 6158-6166.

(281) Lee, W.-C.; Pandian, K.; Tao, Y.-T. Patterning Ultrathin Polymethylene Films: Applications as a Resist in Electrochemical Growth of Conducting Patterns. *Mol. Cryst. Liq. Cryst. Sci. Technol., Sect. A* **1999**, *337*, 13-18.

(282) Hu, W.-S.; Lin, Y.-F.; Tao, Y.-T.; Hsu, Y.-J.; Wei, D.-H. Highly Oriented Growth of *p*-Sexiphenyl Molecular Nanocrystals on Rubbed Polymethylene Surface. *Macromolecules* **2005**, *38*, 9617-9624.

(283) Hu, W.-S.; Weng, S.-Z.; Tao, Y.-T.; Liu, H.-J.; Lee, H.-Y.; Fan, L.-J.; Yang, Y.-W. Oriented Growth of Crystalline Pentacene Films with Preferred *a-b* in-Plane Alignment on a Rubbed Crystalline Polymethylene Surface. *Langmuir* **2007**, *23*, 12901-12909.

(284) Bai, D.; Jennings, G. K. Surface-Catalyzed Growth of Polymethylene-Rich Copolymer Films on Gold. *J. Am. Chem. Soc.* **2005**, *127*, 3048-3056.

(285) Bai, D.; Habersberger, B. M.; Jennings, G. K. pH-Responsive Copolymer Films by Surface-Catalyzed Growth. *J. Am. Chem. Soc.* **2005**, *127*, 16486-16493.

(286) Bai, D.; Habersberger, B. M.; Jennings, G. K. ACS symposium series, 2007; p. 95-106.

(287) Bai, D.; Elliott, S. M.; Jennings, G. K. pH-Responsive Membrane Skins by Surface-Catalyzed Polymerization. *Chem. Mater.* **2006**, *18*, 5167-5169.

(288) Banks, R. L.; Bailey, G. C. Olefin Disproportionation. A New Catalytic Process. *Ind. Eng. Chem. Prod. Res. Dev.* **1964**, *3*, 170-173.

(289) Bradshaw, C. P. C.; Howman, E. J.; Turner, L. Olefin Dismutation: Reactions of Olefins on Cobalt Oxide-Molybdenum Oxide-Alumina. *J. Catal.* **1967**, *7*, 269-276.

(290) Zahidi, E. M.; Oudghiri-Hassani, H.; McBreen, P. H. Formation of Thermally Stable Alkylidene Layers on a Catalytically Active Surface. *Nature* **2001**, *409*, 1023-1026.

(291) Siaj, M.; Oudghiri Hassani, H.; Zahidi, E.; McBreen, P. H. Cyclobutanone, Cyclobutylidene and Oxo Species on β-Mo_2C. *Surf. Sci.* **2005**, *579*, 1-10.

(292) Gao, F.; Wang, Y.; Tysoe, W. T. Formation and Decomposition of C_3 Metallacycles from Ethylene and Methylene on Moal Alloy Thin Films. *J. Am. Chem. Soc.* **2006**, *128*, 7091-7096.

(293) Siaj, M.; McBreen, P. H. Creating, Varying, and Growing Single-Site Molecular Contacts. *Science* **2005**, *309*, 588-590.

(294) Siaj, M.; Dubuc, N.; McBreen, P. H. Olefin Metathesis Activity of Double Bond Contacts to a Conducting Solid: Alkylidenes on β-Mo$_2$C. *J. Phys. Chem. C* **2009**, *113*, 12331-12339.

(295) Siaj, M.; Temprano, I.; Dubuc, N.; McBreen, P. H. Preparation and Olefin-Metathesis Activity of Cyclopentylidene-Oxo Initiator Sites on a Molybdenum Carbide Surface. *J. Organomet. Chem.* **2006**, *691*, 5497-5504.

(296) Temprano, I.; Goubert, G.; Behan, G.; Zhang, H.; McBreen, P. H. Spectroscopic and Structural Characterization of the Formation of Olefin Metathesis Initiating Sites on Unsupported β-Mo$_2$C. *Catal. Sci. Tech.* **2011**, *1*, 1449-1455.

(297) Oudghiri-Hassani, H.; Zahidi, E.; Siaj, M.; Wang, J.; McBreen, P. H. Passivation of Metal Carbide Surfaces: Relevance to Carbon Nanotube–Metal Interconnections. *Appl. Surf. Sci.* **2003**, *212–213*, 4-9.

(298) Oudghiri-Hassani, H.; Siaj, M.; McBreen, P. H. Origins of the High Thermal Stability of Alkylidene Groups on the Surface of β-Mo$_2$C. *J. Phys. Chem. C* **2007**, *111*, 5954-5962.

(299) Siaj, M.; Reed, C.; Oyama, S. T.; Scott, S. L.; McBreen, P. H. Dissociation of Acetaldehyde on β-Mo$_2$C to Yield Ethylidene and Oxo Surface Groups: A Possible Pathway for Active Site Formation in Heterogeneous Olefin Metathesis. *J. Am. Chem. Soc.* **2004**, *126*, 9514-9515.

(300) Gunia, M.; Jakob, P.; Sander, W.; Wöll, C. Photoinduced Reactions of a Carbene Precursor with Chemisorbed CO on a Metal Surface: Diphenyldiazomethane on CO-Covered Ru(0001). *J. Phys. Chem. B* **2004**, *108*, 14025-14031.

(301) Tulevski, G. S.; Myers, M. B.; Hybertsen, M. S.; Steigerwald, M. L.; Nuckolls, C. Formation of Catalytic Metal-Molecule Contacts. *Science* **2005**, *309*, 591-594.

(302) Ren, F.; Feldman, A. K.; Carnes, M.; Steigerwald, M.; Nuckolls, C. Polymer Growth by Functionalized Ruthenium Nanoparticles. *Macromolecules* **2007**, *40*, 8151-8155.

(303) Calderon, N.; Chen, H. Y.; Scott, K. W. Olefin Metathesis – a Novel Reaction for Skeletal Transformations of Unsaturated Hydrocarbons. *Tetrahedron Lett.* **1967**, 3327-3329.

(304) Number of active sites per particle = [Polymer]$_{final}$/[Ru Particles] at ~quantitative conversion = ([Monomer]$_o$/DP)/[Ru Particles]; [Monomer]$_o$ = (0.5 g/94.15 g•mol^{-1})/0.015 L = 0.354 M; DP = 200.103 g•mol^{-1}/94.15 g•mol^{-1} = 2124. Therefore, the number of active sites per particle = (0.354 M/2124)/(7•10^{-8}) = 2380 ~ 2400 when rounded to two significant figures.

(305) Chen, W.; Davies, J. R.; Ghosh, D.; Tong, M. C.; Konopelski, J. P.; Chen, S. Carbene-Functionalized Ruthenium Nanoparticles. *Chem. Mater.* **2006**, *18*, 5253-5259.

(306) Chen, S. W.; Huang, K.; Stearns, J. A. Alkanethiolate-Protected Palladium Nanoparticles. *Chem. Mater.* **2000**, *12*, 540-547.

(307) Zamborini, F. P.; Gross, S. M.; Murray, R. W. Synthesis, Characterization, Reactivity, and Electrochemistry of Palladium Monolayer Protected Clusters. *Langmuir* **2001**, *17*, 481-488.

(308) Chen, S. W.; Sommers, J. M. Alkanethiolate-Protected Copper Nanoparticles: Spectroscopy, Electrochemistry, and Solid-State Morphological Evolution. *J. Phys. Chem. B* **2001**, *105*, 8816-8820.

(309) Kim, Y. G.; Garcia-Martinez, J. C.; Crooks, R. M. Electrochemical Properties of Monolayer-Protected Au and Pd Nanoparticles Extracted from within Dendrimer Templates. *Langmuir* **2005**, *21*, 5485-5491.

(310) Tong, M. C.; Chen, W.; Sun, J.; Ghosh, D.; Chen, S. W. Dithiocarbamate-Capped Silver Nanoparticles. *J. Phys. Chem. B* **2006**, *110*, 19238-19242.

(311) Chen, W.; Chen, S.; Ding, F.; Wang, H.; Brown, L. E.; Konopelski, J. P. Nanoparticle-Mediated Intervalence Transfer. *J. Am. Chem. Soc.* **2008**, *130*, 12156-12162.

(312) Chen, W.; Brown, L. E.; Konopelski, J. P.; Chen, S. Intervalence Transfer of Ferrocene Moieties Adsorbed on Electrode Surfaces by a Conjugated Linkage. *Chem. Phys. Lett.* **2009**, *471*, 283-285.

(313) Chen, W.; Zuckerman, N. B.; Lewis, J. W.; Konopelski, J. P.; Chen, S. Pyrene-Functionalized Ruthenium Nanoparticles: Novel Fluorescence Characteristics from Intraparticle Extended Conjugation. *J. Phys. Chem. C* **2009**, *113*, 16988-16995.

(314) Kang, X.; Chen, W.; Zuckerman, N. B.; Konopelski, J. P.; Chen, S. Intraparticle Charge Delocalization of Carbene-Functionalized Ruthenium Nanoparticles Manipulated by Selective Ion Binding. *Langmuir* **2011**, *27*, 12636-12641.

(315) Kang, X.; Li, X.; Hewitt, W. M.; Zuckerman, N. B.; Konopelski, J. P.; Chen, S. Manipulation of Intraparticle Charge Delocalization by Selective Complexation of Transition-Metal Ions with Histidine Moieties. *Anal. Chem.* **2012**, *84*, 2025-2030.

(316) Chen, W.; Zuckerman, N. B.; Konopelski, J. P.; Chen, S. Pyrene-Functionalized Ruthenium Nanoparticles as Effective Chemosensors for Nitroaromatic Derivatives. *Anal. Chem.* **2009**, *82*, 461-465.

(317) Chen, W.; Pradhan, S.; Chen, S. Photoluminescence and Conductivity Studies of Anthracene-Functionalized Ruthenium Nanoparticles. *Nanoscale* **2011**, *3*, 2294-2300.

(318) Kang, X.; Zuckerman, N. B.; Konopelski, J. P.; Chen, S. Alkyne-Functionalized Ruthenium Nanoparticles: Ruthenium–Vinylidene Bonds at the Metal–Ligand Interface. *J. Am. Chem. Soc.* **2012**, *134*, 1412-1415.

(319) Liu, W.; Sharp, I. D.; Tilley, T. D. Multifunctional Silicon Surfaces: Reaction of Dichlorocarbene Generated from Seyferth Reagent with Hydrogen-Terminated Silicon (111) Surfaces. *Langmuir* **2013**, *30*, 172-178.

(320) Geuter, J. G. A. Ueber Die Zersetzung Des Chloroforms Durch Alkoholische Kalilösung. *Justus Liebigs Ann. Chem.* **1862**, *123*, 121-122.

(321) Ballestri, M.; Chatgilialoglu, C.; Clark, K. B.; Griller, D.; Giese, B.; Kopping, B. Tris(Trimethylsilyl)Silane as a Radical-Based Reducing Agent in Synthesis. *J. Org. Chem.* **1991**, *56*, 678-683.

CHAPTER 2. Addressable Carbene Anchors for Gold Surfaces

2.1 Introduction

Since its discovery in 1983,[1] the chemisorption of thiols on gold surfaces has enabled countless technological advances in the fields of electronics,[2] sensing,[3] microfabrication,[4] and nanotechnology.[5] Despite this broad utility, S-Au monolayers have limitations. For example, the relatively weak S-Au bond (~45 kcal/mol)[6] can lead to monolayer desorption at moderate temperatures (~100–150 °C).[6,7] Furthermore, S-Au monolayers often have ill-defined binding geometries.[8] Finally, S-Au bonds typically have low conductance, which could limit their use in molecular electronics applications.[9]

Other anchor groups have been explored for binding to gold surfaces. Though some of these, such as alkyl[10,11] and dithiocarbamate[9], display increased conductance or improved binding strength, there is still need for a general, synthetically-versatile complement to Au-S monolayer formation.

We were drawn to N-heterocyclic carbenes (NHCs)[12] as a potentially useful class of reagents for binding to inorganic surfaces (Figure 1). NHCs offer a combination of exceptional σ-donating and moderate π-backbonding ability,[13] which has made them ligands of choice for late transition metals like Ru(II)[14,15] and Au(I)[16]. We envisioned that these same characteristics could lead to strong, partially conjugated surface bonds. Furthermore, the synthetic flexibility of NHCs could facilitate their general use for surface functionalization.
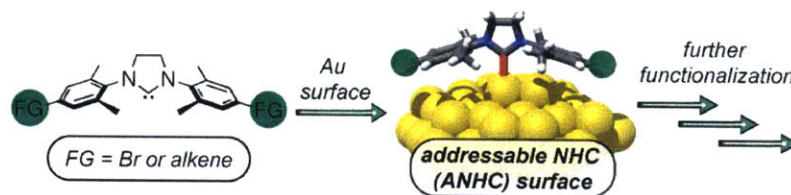
Figure 1. Functionalization of gold with ANHCs.

To date, one published work[17] explored the use of NHCs for coating planar gold surfaces; three reports[18-20] entertained gold nanoparticle stabilization with NHCs. While these studies are encouraging, they provide no details for such parameters as bond strength, rate of adsorption, layer density, or electronic structure. Moreover, the exclusively N,N-dialkyl NHCs described rendered the surfaces inert towards further functionalization.

2.2 Results and Discussion
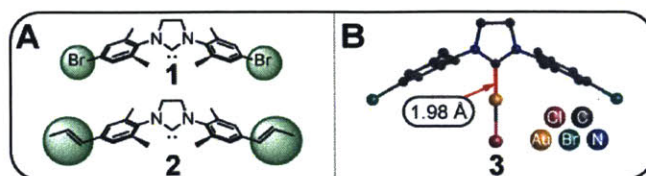
Figure 2. A. ANHC structures. **B.** Crystal structure of complex **3**.

To study NHC-gold surface binding and facilitate NHC monolayer functionalization, we prepared (see Experimental) two "addressable NHCs" (ANHCs) that possess aryl-bromide[21] (**1**, Figure 2A) and β-methylstyrene (**2**, Figure 2A) functional groups. Both ANHCs form mono- and bis-Au(I) complexes (e.g., **3**, Figure 2B) upon exposure to (Ph₃P)AuCl in THF (see Experimental). The crystal structure of **3** features a C-Au bond length of 1.98 Å, which is consistent with reported values for IMes- and SIMes-Au(I) complexes (2.00 and 1.98 Å, respectively).[22] Of note, this bond length is much shorter than the Au-S bond length (2.2-2.6 Å) observed in crystal structures of thiolate-stabilized gold nanoparticles.[23]

Quartz crystal microbalance with dissipation (QCM-D) was used to study binding of **1** and commercially-available IMes to gold surfaces. For all QCM-D experiments, a THF solution of free carbene was flown over a gold-coated sensor; binding was characterized via changes in frequency (F) and dissipation (D) of the sensor. The carbene solutions were prepared as follows (see Experimental for details):
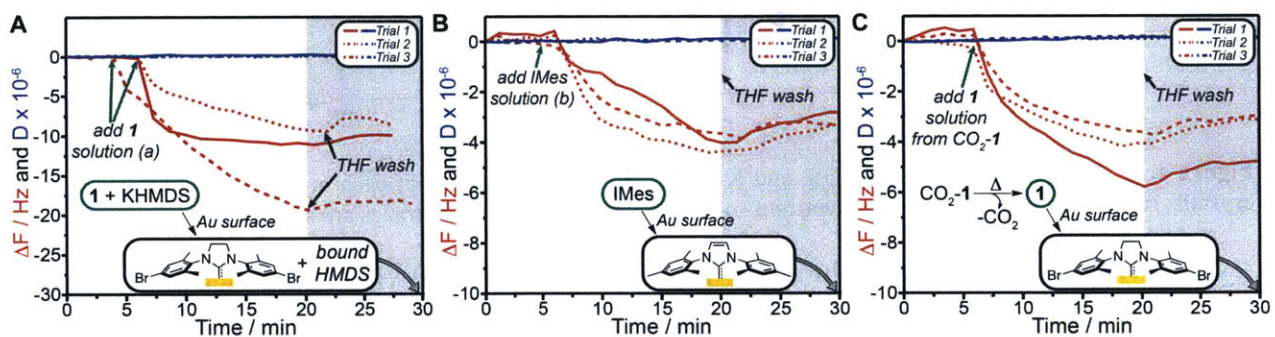
Figure 3. QCM-D analyses of binding of carbene solutions to gold surfaces. **A.** Solution (a): ANHC **1** generated via exposure of **IS1** to KHMDS in THF. **B.** Solution (b): Commercially available NHC IMes in THF. **C.** THF solution of ANHC **1** generated via decarboxylation of CO₂-**1** (no KHMDS present). The measured areal mass densities (AMDs) for each sample are 210 ± 80, 56 ± 6, and 63 ± 14 ng/cm² respectively.

(a) For **1** and **2**: A THF suspension of imidazolium salt ANHC precursor (**IS1** or **IS2**, see Experimental) was exposed to potassium hexamethyldisilazide (KHMDS, 1.0 equiv) under N₂. The resulting solution was filtered through a 0.25 μm syringe filter.

(b) For IMes: IMes was dissolved in THF under N₂. The solution was filtered through a 0.25 μm filter.

85

Both carbene solutions showed a rapid frequency change upon introduction to the QCM-D sensor; saturation was approached within 15 min (Figures 3A and 3B). As expected for rigid monolayers,[24] the surfaces were characterized by small ratios of $\Delta D : \Delta F$ ($\ll$ 4 e-7 Hz^{-1}). The areal mass density (AMD) of bound species was estimated using the Sauerbrey method.[24,25] Average AMD values for **1** and IMes taken from three measurements were 210 ± 80 ng/cm^2 and 56 ± 6 ng/cm^2, respectively.

Control experiments with HMDS amine or amide in the absence of carbene showed little binding of the former, but significant binding of the latter (Figure 4). Thus, we hypothesized that binding of residual HMDS amide led to the larger AMD, and increased deviation, for **1** compared to IMes.
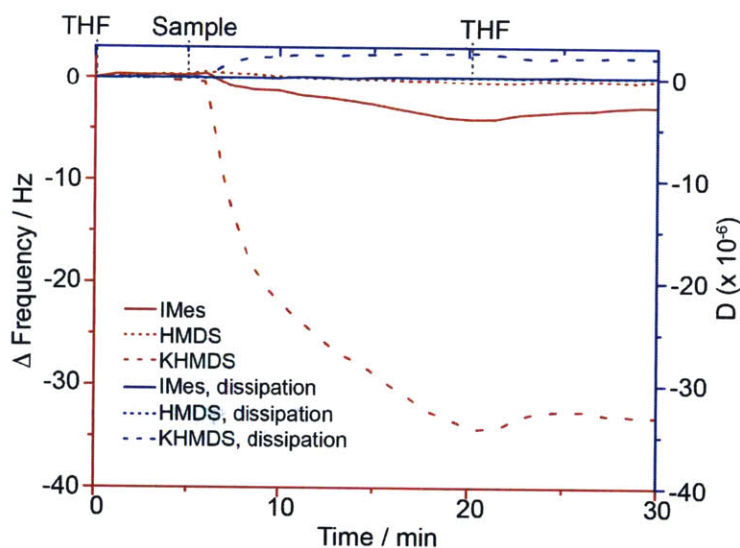
Figure 4. QCM-D gravimetry of HMDS, and KHMDS (0.21 mM solutions of each in THF) on gold-coated quartz crystals; representative 7th frequency overtone and corresponding dissipation traces are shown.

To test this hypothesis, a solution of **1** in THF was prepared via thermal decarboxylation of an independently synthesized CO_2-**1** adduct (see Experimental). The average AMD value fore this solution of **1** without HMDS was 63 ± 14 ng/cm^2 (Figure 3C), which agrees well with the value for IMes.

Based on the dimensions of **1** obtained via crystallography (Figure 2B), we estimate the maximum possible AMD for a monolayer of **1** on a perfectly flat surface to be 85 ng/cm^2. This limit would be higher for a rough surface. Given the steric bulk of **1** and IMes, the measured AMDs (~63 and ~56 ng/cm^2, respectively) are reasonable.
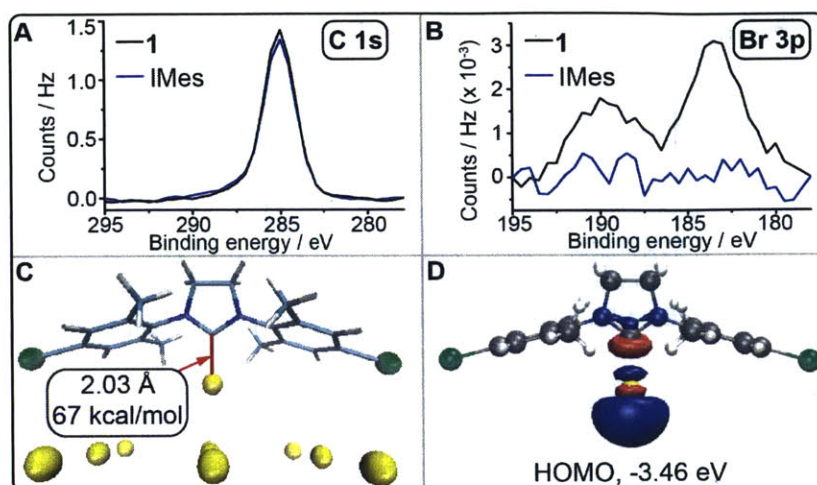
Figure 5. A.–B. C 1s (A) and Br 3p (B) regions of the XPS spectra for **1** and IMes bound to planar gold surfaces. **C.** DFT model of **1** bound to a gold surface. **D.** HOMO of the **1**-Au(0) complex.

Monolayers of **1** and IMes prepared via immersion of gold-coated silicon wafers in solutions (a) or (b), respectively, were characterized by narrow-scan X-ray photoelectron spectroscopy (XPS). The spectra were normalized to the transmission-corrected area of the carbon peaks (Figure 5A). The surface exposed to **1** showed a significant Br signal (Figure 5B). The measured Br/N ratio of 0.16 : 1 corresponds to a mixed monolayer with 21% **1** and 79% HMDS by mass (Table 1). Surfaces treated with IMes showed no detectable Br (Figure 5B), though similar content of nitrogen and N 1s binding energy (Figure 6, Table 1).

Table 1. XPS analysis of NHC binding and brush polymer growth

Sample	C1s normalized area[a] (e-3)	N1s normalized area[a] (e -3)	Br3p normalized area[a] (e-3)	F1s normalized area[a] (e-3)	Br / F : N ratio
1	27.4	1.04	0.17		0.16 (Br)
IMes	27.4	1.15			
Brush-polymer (QCM-D)[b]	27.4[c]	1.75[c]		4.05[c]	2.32 (F)
Polymerization control (no **Ru**, QCM-D)	27.4	2.65		0.61	0.23 (F)
Polymerization control (**1** instead of **2**, QCM-D)	27.4[d]	0.92[d]	Not detected	1.90[d]	2.06 (F)

[a]Area was normalized by the raw area of the C1s peak and also by the elements' corresponding RSF values.
[b]Ru 3p 3/2 region was analyzed by XPS as described above (linear baseline from 465.885 to 458.92 eV; corrected RSF = 185.820), revealing a normalized peak area of 0.0455 e -3.
[c]The C1s, N1s, and F1s absolute peak areas (before normalization) are 369.3, 37.5, and 175, respectively.
[d]The C1s, N1s, and F1s absolute peak areas (before normalization) are 421.6, 22.6, 93.6 respectively.
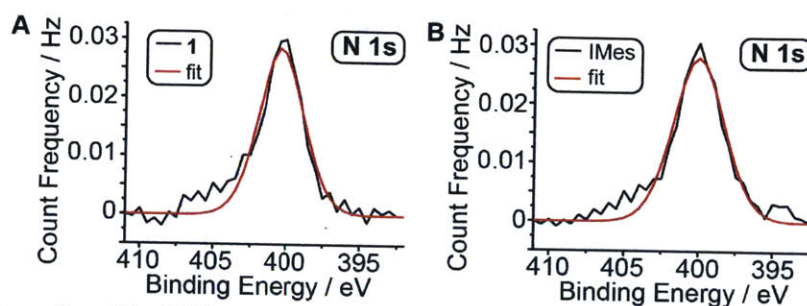
Figure 6. A.–B. N 1s region of the XPS spectra for **1** (A) and IMes (B) bound to planar gold surfaces

In order to gain further insight into the nature of the NHC-Au surface interaction, density functional theory (DFT) was used to model the binding of **1** to a charge neutral gold adatom above a fixed gold lattice. The calculated structure (Figure 5C) possesses a C-Au bond length of 2.03 Å, which agrees well with that of the crystal structure for **3**. Furthermore, the calculated homolytic Au-C bond dissociation energy (BDE) was found to be 67 kcal/mol, which is more than 20 kcal/mol larger than a typical Au-S bond. Calculations performed using either a single gold atom or gold clusters produced similar **1**-Au sigma-bonding orbitals, which suggests that the bonding is highly localized to a single gold atom.

We next studied the electronic structure of the **1-Au** bond via DFT using the B3LYP functional; the basis set was LANL2DZ + effective core potential for gold, and 6-31g* for all other atoms. For clarity, we present results (Figures 5D and 7) from the simplest (one gold atom) model. The electron density in the HOMO (Figure 5D) is delocalized over the gold atom *and* the carbene carbon; this delocalization extends to the nitrogen atoms in the HOMO. These results suggest that ANHCs could form conductive surface linkages.

HOMO - 1	LUMO	LUMO + 1
-6.39 eV	-0.88 eV	-0.80 eV

Figure 7. HOMO-1 and LUMO, and LUMO+1 orbitals of the **1**-Au(0) complex.

Next we sought to demonstrate chemical modification of an ANHC-gold surface. Attempts to perform various metal-catalyzed cross coupling reactions on **1**-Au surfaces were met with difficulty due to non-specific adsorption. Thus, we focused on modification of the olefins of **2**-Au monolayers. We envisioned that treatment of **2**-Au surfaces with 3rd generation Grubbs

catalyst[26] (***Ru***, Figure 8A) would generate surface-bound initiators for ring-opening metathesis polymerization (ROMP).[27,28]
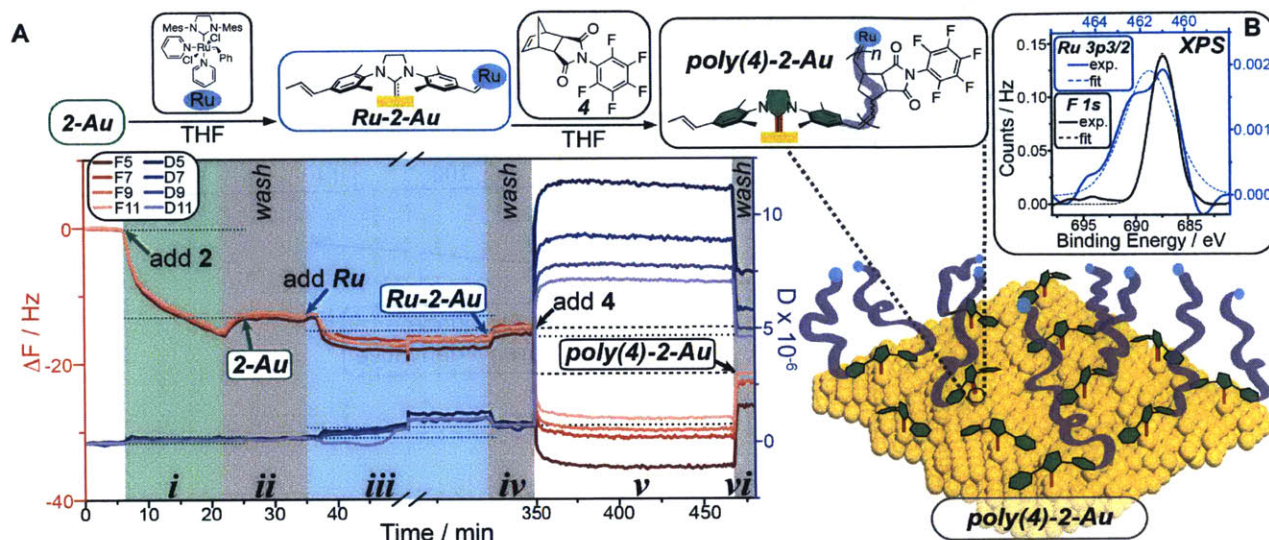
Figure 8. **A.** Scheme for ROMP from **2-Au** surfaces and QCM-D data for the surface functionalization process. Red and blue curves correspond to various frequency (*Fj*, inset legend) and dissipation (*Dj*, inset legend) overtones, respectively. **B.** The F 1s and Ru 3p 3/2 regions of the XPS spectrum of **poly(4)-2-Au**.

A series of model experiments using an isolated bis-**2**-Au complex demonstrated that cross-metathesis between ***Ru*** and **2** was efficient in solution (Figures 9–10, Table 2). Encouraged by these results, we performed the sequence of reactions depicted in Figure 8A on a gold-coated QCM-D sensor; relevant steps are labeled *i-vi*. First, exposure of the sensor to a 0.21 mM solution of **2** (prepared via method (a)) for 15 min (region *i*) followed by a wash with fresh THF (region *ii*) resulted in an AMD of 230 ng/cm^2. If we assume that **2** binds to the surface with equal affinity to IMes then ~61 ng/cm^2 of this AMD value corresponds to **2**.
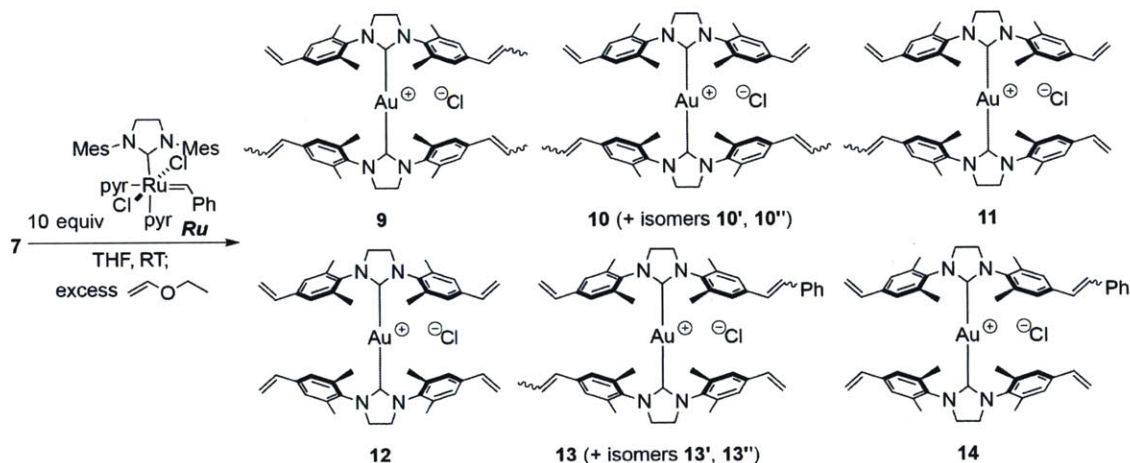
Figure 9. Products produced from cross-metathesis of **7** with ***Ru*** quenched with ethyl vinyl ether.

89

Table 2. Normalized abundances of most abundant m/z peaks corresponding to **7** and cross-metathesis products from Figure 9

Time (h)	Relative [7]	Relative [9]	Relative [10] + [10'] + [10'']	Relative [11]	Relative [12]	Relative [13] + [13'] + [13'']	Relative [14]
0	100	0	0	0	0	0	0
1	37	74	21	2.5	0	0	0
2	8	94	63	10	0	0	0
4	0	38	85	38	7	0	0
20	0	5	15	80	100	14	68
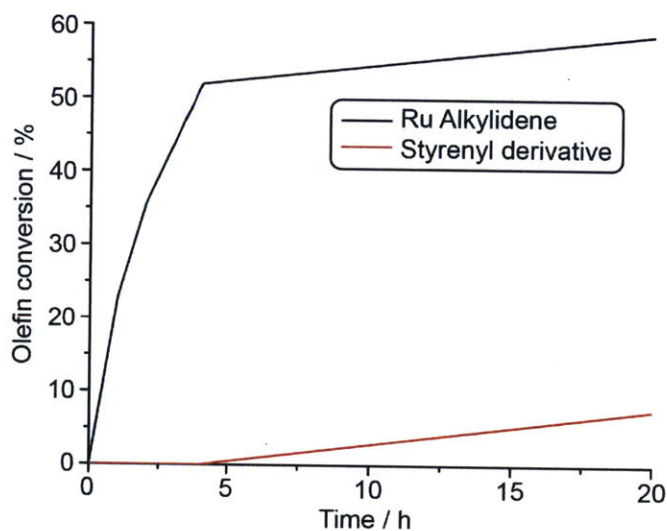
Figure 10. Conversion of olefins to Ru alkylidenes or styrenyl derivatives.

The surface was then exposed to a 5.80 mM solution of **Ru** in THF for 5 h (region ***iii***). Another THF wash was performed (region ***iv***). At this stage, the surface consisted of putative Ru-benzylidene complexes bound via the **2-Au** linkage (**Ru-2-Au** surface). The **2-Au** to **Ru-2-Au** process coincided with a ~2.6 Hz frequency change, and a significant change in dissipation (from ~0.2 e-6 to ~0.7 e-6). The Voigt model[29,30] was used to calculate an AMD of 60 ng/cm^2 of bound **Ru** (see Experimental for details). This AMD combined with the estimated AMD of **2** (61 ng/cm^2) corresponds to ~39% olefin conversion, which is consistent with the percentage of cross metathesis observed in solution studies (Figure 10).

Subsequent exposure of the surface to pentafluorophenyl *exo*-norbornene derivative **4** (0.121 M in THF) for 2 hours (region ***v***) resulted in drastically altered frequency and dissipation values along with an observed dispersion in $\frac{1}{j}\Delta f$ for different overtones j (Figure 7A). These results are consistent with growth of a soft polymer brush from the surface (**poly(4)-2-Au**).[24] The ΔAMD from polymerization was 1520 ng/cm^2, which, if polymer solvation is neglected, translates to an average degree of polymerization (DP) of 35.
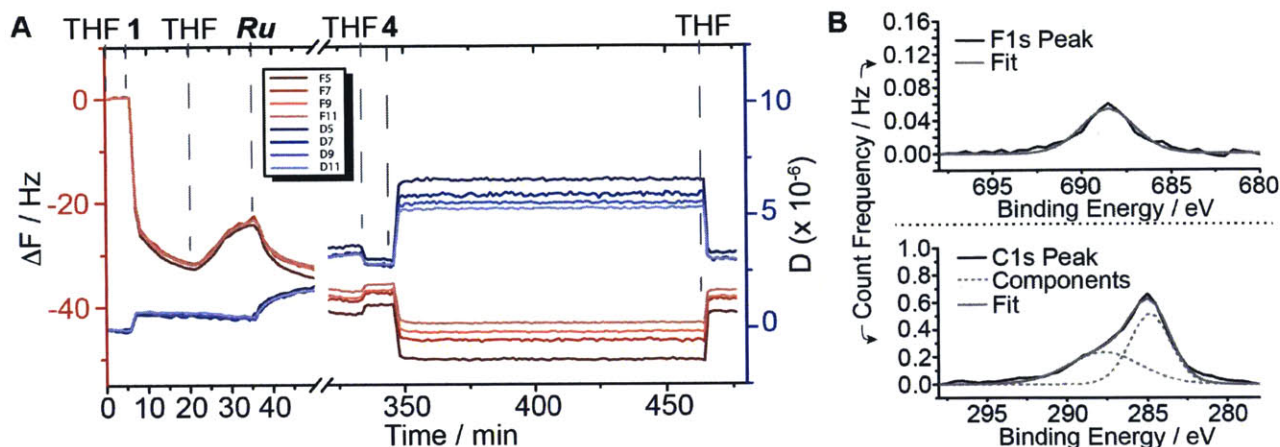
Figure 11. **A.** QCM-D gravimetry control (frequency and dissipation overtones 5, 7, 9, and 11 – see inset) of brush polymer formation in which **1** was used in place of **2**. **B.** XPS of the F1s and C1s regions of the resulting sensor surface.

No polymerization was observed when the same sequence of events was carried out using **1** rather than **2** (Figure 11), which confirms the role of the olefinic groups of **2**. Finally, exposure of a **2-Au** surface to monomer **4** in the absence of **Ru** gave no change in dissipation and a ΔAMD of ~53 ng/cm^2 from non-specific adsorption (Figure 12); no polymerization occurred.
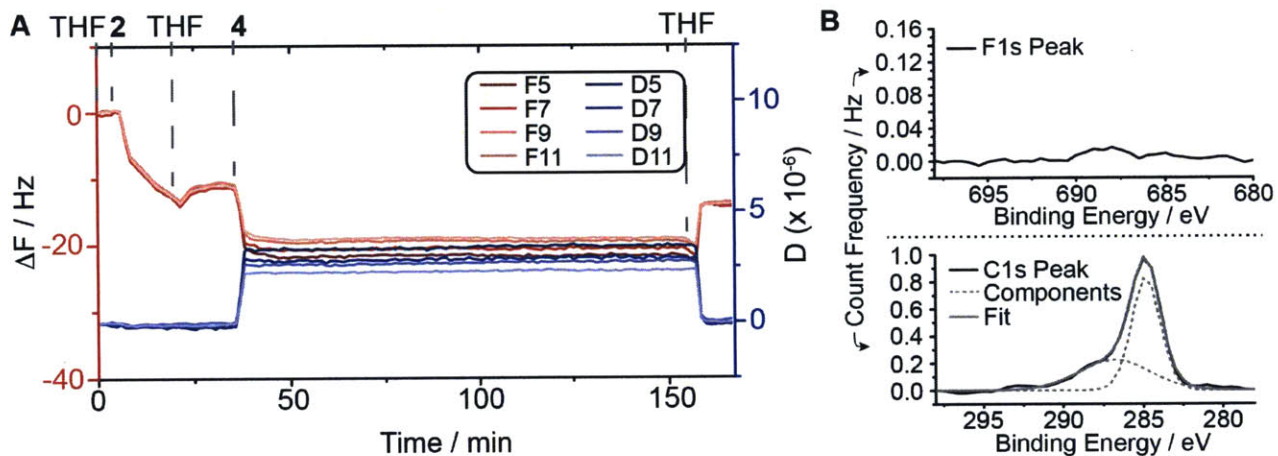
Figure 12. **A.** QCM-D gravimetry control (frequency and dissipation overtones 5, 7, 9, and 11 – see inset) of brush polymer formation in which catalyst **Ru** was not added. **B.** XPS of the F1s and C1s regions of the resulting sensor surface.

XPS analysis was performed on the same surfaces used for QCM-D experiments (Figures 8B, 11B, and 12B; Table 1). As expected, the **poly(4)-2-Au** surface exhibited high fluorine content along with Ru (Figure 8B). Control samples with **1** or no **Ru** showed much lower fluorine signal from adsorbed **4**. The Ru/F ratio for **poly(4)-2-Au** (see Experimental) was used to calculate an average brush DP of 18 (assuming 1 Ru per polymer chain and 5 F atoms per

polymer repeat unit). The difference in DP compared to QCM-D is likely due to polymer solvation.[31]

Tapping mode atomic force microscopy (AFM) of these surfaces revealed a marked difference in roughness. **Poly(4)-2-Au** had a roughness (RMS) of 5.6 nm (Figure 13A). In contrast, the roughness of control sensors was 1.4 nm (no **Ru**, Figure 13B) and 2.0 nm (**1-Au** monolayer, Figure 14), which matches that reported for bare sensors (3 nm).[32] The elongated features present only in the AFM image of **poly(4)-2-Au** (Figure 13A) resemble those reported for other poly-norbornene grafted surfaces.[27]
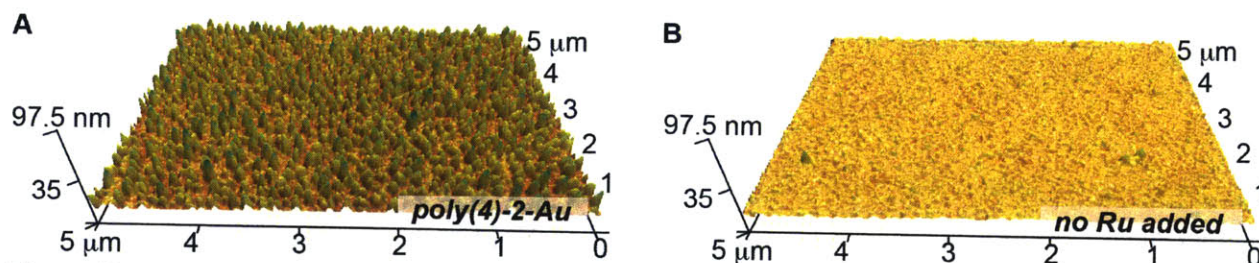
Figure 13. A.–B. AFM characterization of (A) **poly(4)-2-Au** surface and (B) control surface with no **Ru** catalyst added.
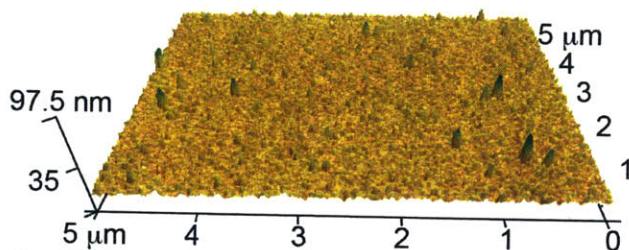
Figure 14. AFM characterization of sensor from QCM-D polymerization control in which **1** was used in place of **2**.

2.3 Conclusions

In this report we have described the first examples of gold surface functionalization with addressable NHCs (ANHCs). We describe details of the ANHC-surface binding interaction, and demonstrate the growth of novel polymer brushes from robust ANHC monolayers. We expect that these results will spark interest in the use of ANHCs and other stable carbenes as general surface anchors.

2.4 Experimental

Materials and Methods

All reagents, solvents, and gold-coated silicon wafers were purchased from Sigma-Aldrich® or VWR and used as supplied unless otherwise noted. Ruthenium catalyst **Ru**[26] (see Figure 9 for structure) and N-(pentafluorophenyl)-cis-5-norbornene-exo-dicarboximide[33] (**4**, see Figure 8 for

structure) were prepared according to literature procedures. Degassed tetrahydrofuran (THF) was passed through a solvent purification column prior to use in air-sensitive experiments.[34] Industrial grade CO_2 gas was purchased from Airgas USA, LLC, and passed through a short column of Drierite® absorbent (purchased from VWR) during use.

Liquid chromatography–mass spectrometry (LC/MS) and preparative HPLC were performed on an Agilent 1260 LC system equipped with a Zorbax SB-C18 rapid resolution HT column and an Advanced Materials Technology HALO® C18 high performance column. Solvent gradients consisted of mixtures of nano-pure water with 0.1% acetic acid (AcOH) and HPLC-grade acetonitrile. Mass spectra were obtained using an Agilent 6130 single quadrupole mass spectrometer.

^{1}H nuclear magnetic resonance (^{1}H-NMR) and ^{13}C nuclear magnetic resonance (^{13}C-NMR) spectra were recorded on two Bruker AVANCE-400 NMR spectrometers. Chemical shifts are expressed in parts per million (ppm), and splitting patterns are designated as s (singlet), d (doublet), t (triplet), q (quartet), m (multiplet), and br (broad); AB designates a system of protons whose coupling constant is comparable to their chemical shift difference. Coupling constants J are reported in Hertz (Hz). MestReNova LITE v5.2.5-4119 software (Mestrelab Research S.L.) was used to analyze the NMR spectra. Spectra were referenced to solvent peaks as reported in literature.[35] Water present in the NMR solvent was observed in ^{1}H NMR spectra at 3.3–3.4 ppm (in DMSO-d^6).

High-resolution mass spectrometry (HRMS) was obtained using a Bruker Daltonics APEXIV 4.7 Tesla Fourier Transform Ion Cyclotron Resonance Mass Spectrometer (FT-ICR-MS).

X-ray photoelectron spectroscopy (XPS) was carried out at the MIT Center for Materials Science and Engineering on a Physical Electronics Versaprobe II X-ray Photoelectron Spectrometer. For non-conductive samples (*e.g.* quartz crystals), argon ion charge neutralization was employed. The step size used in all narrow-scan experiments was 0.50 eV, and a pass energy of 117.4 was chosen. XPS data processing was carried out using CasaXPS software written by Neal Fairley. All spectra were calibrated by setting the carbon peak at 285.0 eV. All narrow-scan spectra were smoothed using the 5-point quadratic Savitzky-Golay algorithm[36] and baseline-corrected using a linear baseline shape. The spectra were then normalized by the area of the corresponding carbon peak and by the elements' corrected relative sensitivity factors specific to the XPS instrument for the chosen pass energy (C1s = 36.557; N1s = 58.185; Br3p = 186.857;

F1s = 116.964). The following boundaries were used for baseline correction: C1s: 298 – 278 eV; N1s: 410.906 – 392.997 eV; Br3p: 195 – 178 eV; F1s: 698 – 680 eV. The calculated areas were automatically corrected for instrumental influences in CasaXPS by dividing by the product of the transmission coefficient and the mean free path (116.4 in all collected spectra). The samples studied by XPS were prepared by immersion of gold-coated silicon wafers in THF solutions of carbenes (described below) for 24 h in the glove box (N_2), followed by washing with THF, dichloromethane (DCM), methanol (MeOH), and hexane.

Quartz crystal microbalance with dissipation monitoring (QCM-D) gravimetry was performed in a four-hand AtmosBag polyethylene glovebag purchased from Sigma-Aldrich® using the Q-Sense E1 instrument, Q-Sense flow module 401, and optically polished (RMS roughness ~ 3 nm) gold-coated AT-cut quartz crystal sensors with the fundamental frequency of 4.95 MHz (Q-Sense, Gothenburg, Sweden); the corresponding constant $C = 17.5$ ng/(Hz · cm^2) (rounded to the nearest 0.5). Liquid was drawn through the system using a peristaltic pump (REGLO Digital/Ismatec® SA, IDEX Health & Science, Glattbrugg, Switzerland). Highly chemical-resistant Kalrez® sealing gasket and O-ring were used in all experiments, and non-teflon tubing was replaced with GORE® Style 100CR highly resistant pump tubing together with a Perifit-PEEK fitting for this tubing. An actual temperature of 23.6 °C (set temperature of 23.7 °C) and true flow rate of 0.332 mL/min (nominal pump rate of 0.0144 mL/min) were used in all experiments; flow was paused only to switch solutions and to allow for 2-5 h exposure of sensors to solution of monomer **4** or catalyst ***Ru***. At the start of each measurement, stable baselines for both F and D were achieved; at the end of each measurement, the system was rinsed with THF (40 mL) and methanol (40 mL) (with the exception of IMes, **1** generated from CO_2-**1**, HMDS, and KHMDS which were not washed with methanol) at a nominal pump flow rate of ~0.62-0.66 mL/min (true rate ~14-15 mL/min). After rinsing with pure solvent, the sensors were dried under a flow of nitrogen gas and stored in ambient. Before each experiment, the sensors were cleaned as recommended by QSense by 10 min UV/ozone treatment, followed by immersion into a 5:1:1 mixture of nano-pure water, 25% $NH_4OH_{(aq)}$, and 30% $H_2O_{2(aq)}$ at 75 °C for 5 min and 10 min UV/ozone treatment. Frequency shift and dissipation were measured and recorded at multiple harmonics (fundamental frequency, 3rd, 5th, 7th, 9th, 11th, and 13th overtone) with the QSoft 401 software (Q-sense, Gothenburg, Sweden) in real-time throughout the adhesion process; the software automatically normalized each curve by the overtone number

and plotted them as such. For non-dissipative samples, the areal mass density change was determined using the Sauerbrey model: $\Delta m = -C \cdot j^{-1} \cdot \Delta F$, where j is the overtone number, m is areal mass density (also referred to as AMD), F is sensor frequency, and C is the constant defined above (17.5 ng/(Hz $\cdot$ cm^2)).[25] Data analyses for cases where Sauerbrey model was not applicable were done with QTools (Q-sense, Gothenburg, Sweden) using Voigt viscoelastic modeling.[29,30] The constraints applied in the modeling were as follows: only overtones 3, 5, 7, 9, and 11 were used in the analysis; the Voigt viscoelastic model was applied to the entire duration of the experiment, with the output being areal mass density for layer 1 (L1); fluid density = 1016 kg/m^3, fluid viscosity = 0.00046 kg/m·s, and L1 density = 1000 kg/m^3; 0.0001 < L1 viscosity (kg/ m·s) < 0.01, 0.0001 < L1 shear (Pa) < 1 e9, and 0.0001 < L1 mass (ng/cm^2) < 1 e5.

Atomic force microscopy (AFM) was carried out in tapping mode on an MFP-3D AFM instrument (Asylum Research, Santa Barbara, CA) using a silicon probe with a resonant frequency of 300 kHz (F$_o$) and a nominal spring constant of 40 N/m, designed for tapping mode (AppNano; MikroMasch). The following parameters were used in the measurements: scan rate: 0.75 Hz; resolution: 512 points/line, 512 lines/raster; scan angle: 0°; the measurements were carried out in ambient conditions. The data was analyzed using the Igor Pro 6.22A| MFP3D 101010-1403 combined software.

Elemental analysis was carried out by Atlantic Microlab, Inc. (Norcross, GA).

Computational Details

All density functional theory computations were done using the *Q-Chem* software package.[37] The bond dissociation enthalpy (BDE) was calculated for a variety of NHC-gold complexes. In each case, a gas-phase geometry optimization was performed using the B3LYP exchange-correlation functional and the LANL2DZ basis set and effective core potential for gold and the 6-31g* basis set for every other atom (implemented in Q-Chem as "LACVP"). Following the geometry optimization, three single-point energy calculations were performed at the relaxed geometry: One of the entire NHC-gold complex, one of just the NHC molecule, and one of just the gold atoms. The BDE was calculated as: BDE = E$_{complex}$ − (E$_{NHC}$ + E$_{Au}$).

For the "expanded" model gold system presented in Figure 5C, all gold-gold distances were set to 4.08 Å, the lattice parameter for bulk gold,[38] and all gold atoms were subsequently fixed in place for the duration of the calculation. The geometry optimization was then performed

allowing the NHC molecule to relax in the field of the fixed gold atoms. Since not all atoms were allowed to relax in this simulation, several other calculations were performed on model gold systems to confirm the calculated BDE. A four-atom gold cluster was chosen as the primary model as it is the smallest cluster of gold atoms that can model binding to the each the atop, bridge, and hollow sites realized on a gold surface. According to the Blyholder model,[39] the energetics of the binding of substrates to surfaces should quantitatively captured by studying the binding of substrates to small clusters. This has also been put into practice recently for the study of the binding of thiolate headgroups to gold.[40]

The globally-optimized geometry of a four-atom gold cluster was obtained from the Cambridge Cluster Database.[41] The geometry of the four gold atoms was allowed to relax; then, all gold atoms were fixed while the geometry of the NHC was allowed to relax. For this system, the NHC-gold bond length was determined to be 2.01 Å, and the BDE 66 kcal/mol. Next, the gold atom in contact with the NHC molecule was allowed to relax while the other three gold atoms remained fixed. For this system, the NHC-gold bond length was determined to be 2.01 Å, and the BDE 66 kcal/mol. Next, all constraints were removed and the geometry of the NHC-gold system was allowed to relax to a global minimum. The gold cluster reorganized to a planar geometry, and the NHC-gold bond length stretched slightly to 2.04 Å. The BDE also increased slightly to 68 kcal/mol. Bond length and BDE values reported in the main text represent a compromise among all of the structures studied computationally.

Cartesian coordinates of optimized 10-gold surface

Au	4.071020	-4.088494	0.426976
Au	4.079867	-0.008504	0.426866
Au	4.088714	4.071486	0.426896
Au	0.008723	4.080333	0.426715
Au	-4.071267	4.089180	0.426605
Au	-4.080114	0.009189	0.426780
Au	-4.088960	-4.070801	0.427097
Au	-0.008970	-4.079648	0.426795
Au	-0.000123	0.000343	0.426891
Au	0.034192	0.001844	-2.183613
C	-0.781275	-0.003152	-6.450312
C	0.766034	0.001201	-6.468403
H	-1.215491	0.882182	-6.924448
H	1.183195	0.889118	-6.952426
C	0.016941	0.000770	-4.217244

N	-1.092540	-0.001746	-4.987542
N	1.109738	0.002511	-5.011347
C	2.477637	0.004018	-4.556304
C	3.128147	1.237491	-4.346854
C	3.129424	-1.228055	-4.342384
C	4.471185	1.223575	-3.937231
C	4.472380	-1.211520	-3.932780
C	5.116923	0.006686	-3.740698
H	4.990591	2.158205	-3.764448
H	4.993161	-2.144944	-3.757811
C	-2.452699	-0.003817	-4.510888
C	-3.106224	-1.237201	-4.299557
C	-3.107230	1.228081	-4.293449
C	-4.444076	-1.222270	-3.873307
C	-4.445081	1.210120	-3.867742
C	-5.087407	-0.006842	-3.666844
H	-4.960041	-2.158155	-3.695166
H	-4.961965	2.144700	-3.685608
C	2.403366	-2.545580	-4.485815
H	1.833248	-2.608274	-5.419302
H	3.107297	-3.381417	-4.464672
H	1.695410	-2.685642	-3.658879
C	2.400832	2.554038	-4.494937
H	3.104011	3.390711	-4.478521
H	1.828915	2.612455	-5.427668
H	1.694369	2.697078	-3.667226
C	-2.419179	2.563360	-4.471012
H	-2.296715	3.061598	-3.501510
H	-1.426268	2.461095	-4.912397
H	-3.014101	3.229496	-5.105908
C	-2.418854	-2.571892	-4.484558
H	-3.008401	-3.229747	-5.133140
H	-1.420761	-2.468280	-4.913705
H	-2.308699	-3.080557	-3.519171
Br	7.009486	0.008655	-3.150841
Br	-6.974400	-0.008461	-3.058937
H	-1.210270	-0.892795	-6.921185
H	1.188033	-0.884656	-6.951909

Cartesian coordinates of constrained 4-gold cluster

Au	-0.214674	0.260190	0.164193
Au	1.952370	-1.569387	0.439977
Au	-0.692503	-2.380188	1.123154
Au	0.008816	-1.960977	-1.606661
C	-0.386519	2.258639	-0.025738
N	-1.556830	2.922405	-0.158730

N	0.637123	3.143182	-0.052102
C	-1.365935	4.395378	-0.326358
C	0.168514	4.556539	-0.190702
C	-2.859020	2.302072	-0.136991
C	-3.443739	1.884640	-1.351319
C	-4.712420	1.285344	-1.309894
C	-5.352227	1.113282	-0.086169
C	-4.770330	1.508854	1.113485
C	-3.502007	2.110339	1.103304
H	-5.179216	0.947405	-2.226794
H	-5.278901	1.342729	2.054978
C	2.033748	2.794295	0.028484
C	2.662558	2.758660	1.291330
C	2.729259	2.480421	-1.157546
C	4.089287	2.142768	-1.066358
C	4.709182	2.119108	0.178041
C	4.023164	2.417600	1.351893
H	4.640807	1.888579	-1.962714
H	4.526906	2.375898	2.310047
C	-2.712643	2.016929	-2.667949
H	-3.334593	1.658115	-3.492259
H	-1.789596	1.424294	-2.662768
H	-2.435535	3.055147	-2.887476
C	-2.833860	2.476369	2.407970
H	-2.398796	3.481744	2.385086
H	-2.022386	1.772192	2.632003
H	-3.547286	2.434535	3.235032
C	1.894060	3.021518	2.566223
H	1.136034	2.245890	2.731143
H	1.374639	3.986648	2.545910
H	2.565026	3.022489	3.429466
C	2.034824	2.434275	-2.498095
H	2.763446	2.422559	-3.313029
H	1.366273	3.288364	-2.650126
H	1.428072	1.522692	-2.578892
Br	-7.146188	0.267348	-0.051485
Br	6.629259	1.630560	0.282284
H	-1.920972	4.936985	0.444820
H	-1.737258	4.712435	-1.305952
H	0.625355	5.019201	-1.070243
H	0.456288	5.136005	0.692150

Cartesian coordinates of optimized 4-gold cluster

Au	0.832528	2.209328	-1.290145
Au	-0.450823	2.696969	1.030592
Au	2.148694	2.070252	-3.530255

98

Au	-0.401777	0.133680	0.280741
C	-0.575090	-1.892652	0.166961
N	-1.737073	-2.579253	0.076621
N	0.454781	-2.766928	0.198379
C	-1.533646	-4.061870	0.059383
C	0.004480	-4.192987	0.122557
C	1.856572	-2.427355	0.233675
C	2.510089	-2.338357	1.480535
C	3.883429	-2.049736	1.494178
C	4.558850	-1.863620	0.291470
C	3.913870	-1.940571	-0.937960
C	2.538384	-2.221529	-0.983358
C	1.820610	-2.249430	-2.312637
Br	6.503812	-1.476339	0.335437
H	4.458284	-1.777169	-1.859411
C	1.762920	-2.511677	2.783254
H	4.408342	-1.968065	2.438212
H	1.235724	-3.472108	2.831828
H	1.015374	-1.719797	2.916436
H	2.452411	-2.466908	3.630541
H	2.536634	-2.294976	-3.136872
H	1.224877	-1.337679	-2.447318
H	1.144284	-3.106846	-2.403888
C	-3.058536	-2.008379	0.004192
C	-3.630369	-1.767029	-1.262705
C	-4.944006	-1.273995	-1.319042
C	-5.638731	-1.030038	-0.138424
C	-5.067918	-1.245280	1.111859
C	-3.757626	-1.741684	1.199606
C	-3.116640	-1.942829	2.553428
Br	-7.499136	-0.350294	-0.240428
H	-5.624358	-1.031645	2.015941
H	-5.405290	-1.080071	-2.279731
C	-2.853826	-1.988857	-2.540943
H	-1.992953	-1.312131	-2.599499
H	-3.486001	-1.799821	-3.412359
H	-2.470719	-3.013022	-2.625306
H	-3.838655	-1.756494	3.352771
H	-2.275131	-1.253348	2.693016
H	-2.730084	-2.960634	2.682896
H	-1.960102	-4.489578	-0.852368
H	-2.036111	-4.515961	0.918789
H	0.426640	-4.669556	-0.766976
H	0.349651	-4.740862	1.003813

Crystallographic Information

Low-temperature diffraction data (φ- and ω-scans) were collected on a Bruker-AXS X8 Kappa Duo diffractometer coupled to a Smart Apex2 CCD detector with Cu K_α radiation (λ = 1.54178 Å) from an $I\mu S$ micro-source. The diffractometer was purchased with the help of funding from the National Science Foundation (NSF) under Grant Number CHE-0946721. The structure was solved by direct methods using SHELXS[42] and refined against F^2 on all data by full-matrix least squares with SHELXL-97[43] following established refinement strategies[44].

Details of Calculations

<u>Calculation used to determine the degree of polymerization (DP) of the brush polymer in Table 1</u>

DP = [normalized area(F)/5]/[normalized Area(Ru)] = [4.05 e-3)/5]/[0.0455 e-3] = 18.

<u>Model study on the formation of Ru alkylidenes from bis-NHC complex 7 and 3rd generation Grubbs catalyst *Ru*</u>

The values in Table 2 were multiplied by the appropriate factors to get the total abundance of the isotope series for each species (the factors were in the range of 1.619 – 1.734). The resulting values were normalized by dividing each one by the sum of the values in the corresponding row (*i.e.*, for each time point). Because we know the number of propenyl groups, vinyl groups and styrenyl groups in the starting material and each of the products, and because the vinyl groups are indicative of Ru alkylidenes present before quenching with ethyl vinyl ether, we were able to calculate percentage of olefins converted to Ru alkylidenes and ones converted to styrenyl substituents (Figure 10).

<u>Calculation used to determine the conversion of olefins to ruthenium alkylidenes in QCM-D experiments</u>

% Conversion of olefins to Ru alkylidenes = 100% * (nmol catalyst bound)/(2 * nmol 2 bound to surface) = 100% * [mass density of catalyst bound / (MW catalyst – MW methylstyrene – 2 * MW pyridine)] / [2 * mass density of NHC bound / MW 2] = 100% * [60 ng/cm^2 / (726.74 – 118.177 – 2 * 79.1 g/mol)]/[2 * 61 ng/cm^2 / 358.45 g/mol] = 39 %

Synthetic Procedures and Characterization

Synthesis of imidazolium salts IS1 and IS2
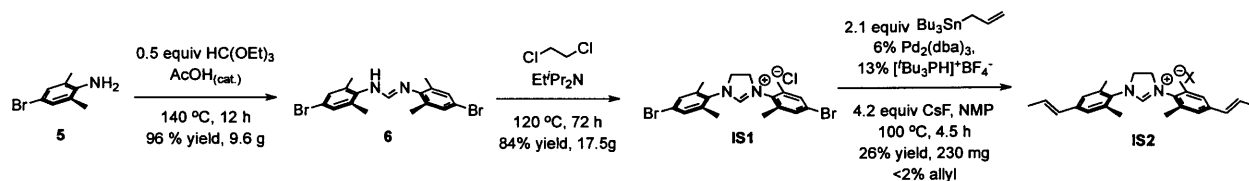
***N,N'*-bis(4-bromo-2,6-dimethylphenyl)formimidamide 6.** Prepared according to the general procedure of Grubbs *et al.*[45] in 96% yield (9.6 g) as a light-brown solid; in CDCl$_3$ at 25 °C, **6** exists as two isomers in ~1:1 ratio (peaks listed together). ^{1}H NMR (400 MHz, CDCl$_3$): δ 7.39-7.20 (br, 2H), 7.22 (s, 2H), 7.21 (s, 1H), 7.17 (br, 4H), 7.14 (s, 1H), 5.47 (d, J = 12 Hz, 1H), 2.22 (s, 12H), 2.21 ppm (s, 12H). ^{13}C NMR (100 MHz, CDCl$_3$): δ 146.55, 144.12, 136.16, 135.27, 131.65, 131.16, 130.98 (br), 130.80, 119.95, 115.95, 18.68, 18.61, 17.86 ppm. LCMS: calcd. for C$_{17}$H$_{18}$Br$_2$N$_2$ [M + H]$^+$, 411.0; found, 411.0.

1,3-bis(4-bromo-2,6-dimethylphenyl)-4,5-dihydro-1*H*-imidazol-3-ium chloride IS1. Prepared according to the general procedure of Grubbs *et al.*[45] (72 h) in 84% yield (17.5 g) as a beige powdery solid. ^{1}H NMR (400 MHz, DMSO-d^6): δ 9.27 (s, 1H), 7.55 (s, 4H), 4.50 (s, 4H), 2.40 ppm (s, 12H). ^{13}C NMR (100 MHz, DMSO-d^6): δ 169.40, 138.58, 131.39, 122.89, 50.79, 17.13 ppm. TOF HRMS: calcd. for C$_{19}$H$_{21}$Br$_2$N$_2$Cl [M - Cl]$^+$, 437.0046; found, 437.0031.

1,3-bis(2,6-dimethyl-4-((*E*)-prop-1-en-1-yl)phenyl)-4,5-dihydro-1*H*-imidazol-3-ium salt (mixture of counterions) IS2. To a dry 7-mL vial with stir bar were added **IS1** (946 mg, 2.00 mmol), Pd$_2$(dba)$_3$ (110 mg, 0.12 mmol) and ^{t}Bu$_3$PH$^+$BF$_4^-$ (76 mg, 0.13 mmol), and the mixture was brought into the glove box with a nitrogen atmosphere. To the vial were added first CsF (1.28 g, 8.40 mmol), then allyltri-*n*-butylstannane (1.30 mL, 4.20 mmol; freeze-pump-thawed), and then *N*-methyl-2-pyrrolidone (2.0 mL). The vial was capped, the contents of the vial were briefly mixed and the vial was heated in a sand bath to 100 °C with stirring outside the glove box for 4.5 h. The contents of the vial were transferred to a 10-mL syringe and filtered through a PTFE syringe filter (0.25 μm pore size) into stirring diethyl ether (125 mL, -20 °C). The vial was rinsed with dichloromethane (DCM, 2 x 1 mL), and the washings were filtered into diethyl ether, as well. Precipitate was collected by filtration *in vacuo* over a nylon membrane filter, washing

with diethyl ether (2 x 25 mL, -20 °C). Collected white solid was re-dissolved in DCM (2 mL) and precipitated by adding diethyl ether (2 mL); the product was filtered *in vacuo*, and this precipitation / filtration protocol was repeated twice. The product was further purified by column chromatography on the Biotage® Isolera Prime™ Flash Purification System using a 50 g SNAP Ultra Flash Cartridge (3% methanol (MeOH) in DCM for 12 column volumes (CV), 3 → 5% MeOH over 4 CV, 5 → 10% MeOH over 4 CV, and maintained at 10% methanol for 4 CV; TLC R_f in 5% methanol in DCM = 0.17), affording **IS2** as a beige solid (230 mg, 26% yield). ^{1}H NMR (400 MHz, CDCl$_3$): δ 9.01 (s, 1H), 7.04 (s, 4H), 6.28 (AB d, J = 16.0 Hz, 2H), 6.25 (AB dq, J_1 = 15.6 Hz, J_2 = 4.8, 2H), 4.59 (s, 4H), 2.38 (s, 12H), 1.87 ppm (d, J = 4.8 Hz, 6H). ^{13}C NMR (100 MHz, CDCl$_3$): δ 159.17, 140.05, 135.49, 131.08, 129.71, 128.50, 126.71 ppm. TOF HRMS: calcd. for C$_{25}$H$_{31}$N$_2$Cl [M - Cl]$^+$, 359.2482; found, 359.2476. Elemental analysis calc. 76.0% C, 7.9% H, 7.1% N, 9.0 %Cl; found 67.8% C, 7.1% H, 6.3%N, 1.0% Cl, suggesting a mixture of counterions for **IS2** (*e.g.*, Br⁻).

Synthesis of NHC-Au(I) complexes 3, 7, and 8
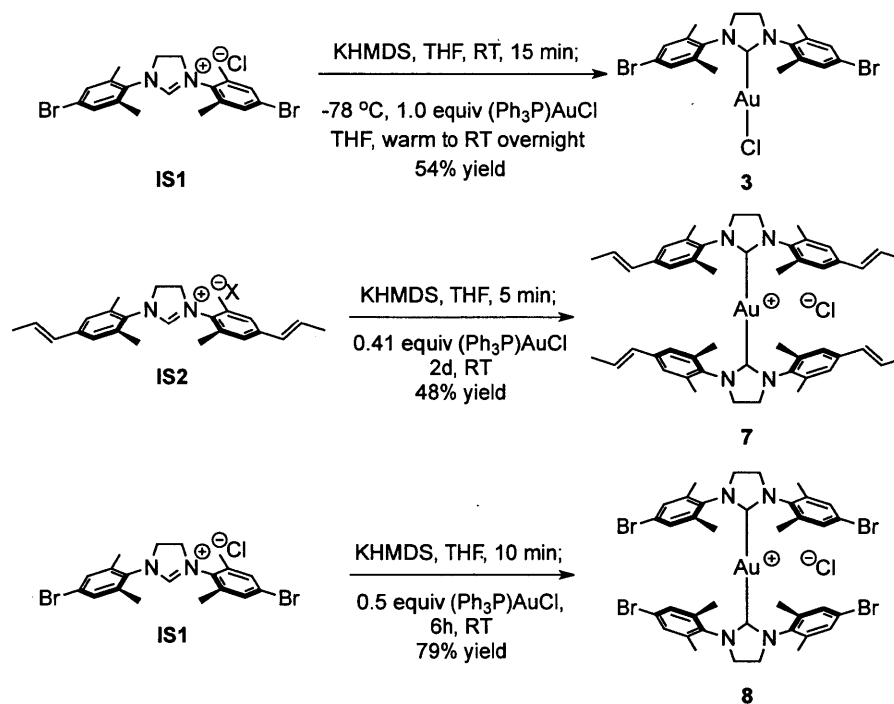
(1,3-bis(4-bromo-2,6-dimethylphenyl)-4,5-dihydro-1*H*-imidazol-3-ium-2-yl)chloroaurate(I) 3. To a 25-mL 3-necked flask containing **IS1** (95.5 mg, 0.202 mmol) and a stir bar under nitrogen were added THF (5 mL, anhydrous) and then 1.0 M KHMDS in THF (0.202 mL) via syringe. The mixture (**IS1** is insoluble in THF) was stirred for 15 min, during

which the dispersion became clearer and formation of tiny colorless microcrystalline solid was noted. The resulting mixture was added dropwise via syringe to a 50-mL 2-necked flask with a stirring solution of (Ph$_3$P)AuCl (100 mg, 0.202 mmol) in THF (5.0 mL, anhydrous) under nitrogen at -78 °C. The reaction mixture was stirred for 1 hr at -78 °C and was then allowed to warm up to room temperature overnight. The reaction mixture was then filtered first *in vacuo* over a nylon membrane filter, washing with THF (3 x 5 mL); the filtrate was concentrated by rotary evaporation, re-dissolved in DCM (2 mL), filtered through a cotton plug, and mixed with hexanes (10 mL). After 3 hrs, the precipitate was filtered *in vacuo* over a nylon membrane filter and dried *in vacuo*, affording **3** (73 mg, 54 % yield) as a gray solid. For X-ray crystallography, an 11 mg sample was dissolved in DCM (2 mL) and crystallized over 2 days by slow diffusion of hexane at room temperature. ^{1}H NMR (400 MHz, CDCl$_3$): δ 7.31 (s, 4H), 3.99 (s, 4H), 2.32 (s, 12H). ^{13}C NMR (100 MHz, CDCl$_3$): δ 138.06, 136.16, 132.24, 50.67, 18.05 ppm (carbene carbon signal not detected). LCMS: calcd. for C$_{19}$H$_{20}$AuBr$_2$N$_2$Cl [M − Cl + MeCN]$^+$, 674.0; found, 674.0.

Bis(1,3-bis(2,6-dimethyl-4-((*E*)-prop-1-en-1-yl)phenyl)-4,5-dihydro-1*H*-imidazol-3-ium-2-yl)aurate(I) chloride 7. A 7-mL vial containing **IS2** (79.0 mg, 0.200 mmol) and a stir bar, as well as a 3-mL vial with (Ph$_3$P)AuCl (49.5 mg, 0.100 mmol) were taken inside the glove box with nitrogen atmosphere. To both vials was added anhydrous THF (1.5 mL to the former and 1.0 mL to the latter). To the vial with a stirring mixture of **IS2** in THF was added 1.0 M KHMDS in THF (0.20 mL), and after 5 min, to the resulting solution was added the solution of (Ph$_3$P)AuCl dropwise. The vial was washed with 0.1 mL THF and this was also added to the reaction mixture. After 1 d, added an additional portion of NHC **2** (formed from 16.2 mg of **IS2**, 0.3 mL THF, and 0.041 mL of 1.0 M KHMDS in THF in the glove box). After one more day, the reaction was filtered through a PTFE syringe filter (0.25 μm pore size) into hexanes (15 mL). The precipitate was collected by filtration *in vacuo* over a nylon membrane, washing with hexanes (3 x 5 mL), and then dried *in vacuo*, affording **7** as a beige powdery solid (45.6 mg, 48 % yield). ^{1}H NMR (400 MHz, CDCl$_3$): δ 6.90 (s, 8H), 6.39 (AB d, J = 16.4 Hz, 2H), 6.32 (AB dq, J = 16.0 Hz, 2H), 3.92 (s, 8H), 1.97 (d, J = 5.2 Hz, 12H), and 1.84 (s, 24 H). ^{13}C NMR (100 MHz, CDCl$_3$): δ 206.27, 138.22, 135.81, 135.01, 130.24, 127.28, 126.13, 51.45, 18.76, 17.57 ppm. TOF HRMS: calcd. for C$_{50}$H$_{60}$AuN$_4$Cl [M - Cl]$^+$, 913.4478; found, 913.4470.

Bis(1,3-bis(4-bromo-2,6-dimethylphenyl)-4,5-dihydro-1H-imidazol-3-ium-2-yl)aurate(I) chloride 8. Under positive pressure of nitrogen, to a 50-mL 2-neck flask vial equipped with a stir bar was added **IS1** (0.9447 g, 2.00 mmol), and a Merlic-type solid addition adapter containing (Ph$_3$P)AuCl (0.495 g, 1.00 mmol) was attached; the set up was evacuated and re-filled with nitrogen thee times. To the flask was added anhydrous THF (25 mL) and then, while stirring, 1.0 M KHMDS in THF (2.0 mL); after 10 min, the solid-addition adapter was inverted, adding (Ph$_3$P)AuCl to the reaction mixture. Immediate formation of white precipitate was observed. After 6 hrs, the reaction mixture was opened to air, filtered *in vacuo* over a nylon membrane, washing with THF (3 x 8 mL), and then re-dissolved in minimal dichloromethane and filtered again. The filtrate was concentrated by rotary evaporation and dried *in vacuo*, affording **8** as an off-white solid (0.875 g, 79 % yield). ^{1}H NMR (400 MHz, DMSO-d^6): δ 7.35 (s, 8H), 3.98 (s, 8H), and1.93 ppm (s, 24H). ^{13}C NMR (100 MHz, DMSO-d^6): δ 204.61, 138.42, 135.80, 131.00, 121.74, 50.68, 16.69 ppm. TOF HRMS: calcd. for C$_{38}$H$_{40}$AuBr$_4$N$_4$Cl [M - Cl]$^+$, 1068.9622; found, 1068.9640.

Synthesis of CO$_2$-1 adduct and its decarboxylation
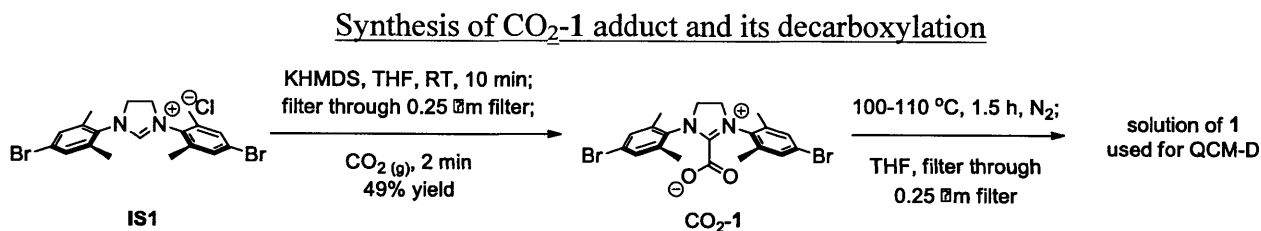
1,3-Bis(4-bromo-2,6-dimethylphenyl)-4,5-dihydro-1H-imidazol-3-ium-2-carboxylate

CO$_2$-1. A 7-mL vial containing **IS1** (236 mg, 0.500 mmol) and a stir bar was taken inside the glove box with nitrogen atmosphere. To the vial was added anhydrous THF (3.5 mL) and to the stirring suspension was added 1.0 M KHMDS in THF (0.50 mL). After 10 min, the reaction mixture was filtered through a 0.25 μm PTFE syringe filter into a 2-5 mL Biotage® microwave vial, and the vial was capped and removed from the glove box. Through the solution was then bubbled CO$_2$ gas, with white precipitate forming instantly. After 2 min, the reaction mixture was filtered over a medium-porosity frit, washing with THF (5 mL). Drying *in vacuo* afforded CO$_2$-1 adduct as a powdery white solid (117 mg, 49% yield). ^{1}H NMR (400 MHz, DMSO-d^6): δ 7.45 (s, 4H), 4.31 (s, 4H), and 2.40 ppm (s, 12H). ^{13}C NMR (100 MHz, DMSO-d^6): δ 164.06, 153.56,

139.37, 133.03, 131.09, 122.63, 49.23, 16.83 ppm. LCMS: calcd. for $C_{20}H_{20}Br_2N_2O_2$ [M - CO_2 + H]$^+$, 437.0; found, 437.0.

Preparation of carbene solutions

Solutions of **1** and **2** used in QCM-D were prepared by addition of one equivalent of KHMDS in THF to a suspension of the corresponding imidazolium salt in THF. The resulting mixture was filtered through a 0.25 μm PTFE syringe filter and diluted to 0.21 mM concentration of carbene. Solutions of IMes used in QCM-D were prepared by dissolving IMes in THF, filtering the resulting solution through a 0.25 μm PTFE syringe filter, and diluting to 0.21 mM concentration of IMes.

Solutions of **1** and IMes used in preparing samples solely for XPS characterization were prepared as above, except without filtration and at a concentration of 10. mM.

Preparation of solution of **1** from CO_2-**1** was done as follows: decarboxylation was carried out over the course of 1.5 h at 100–110 °C under a continuous flow of N_2 on 4.27 mg of sample, followed by addition of 1 mL THF, filtration, and 42-fold dilution.

2.5 Spectra
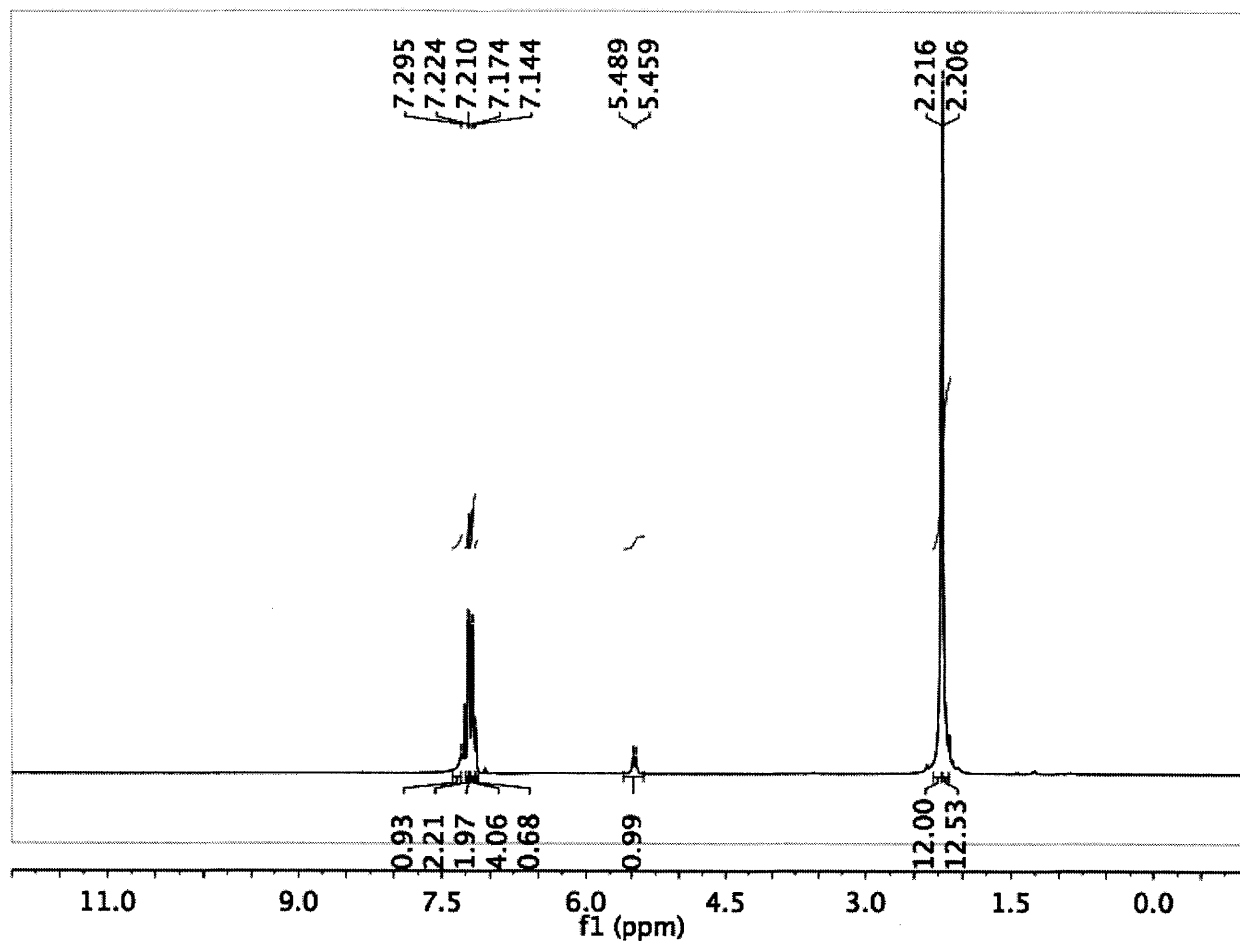
Figure 15. ^{1}H NMR spectrum of **6** in CDCl$_3$.
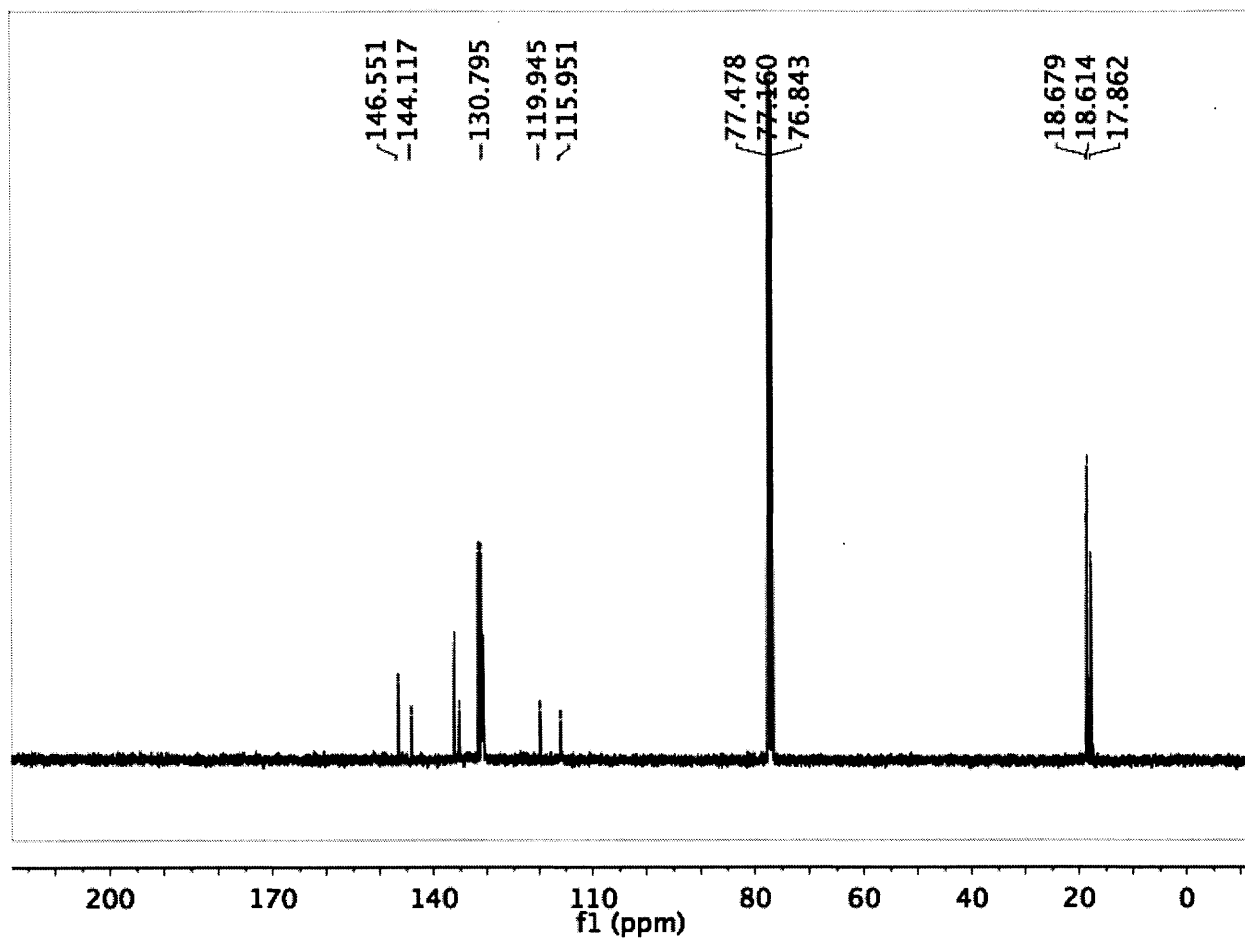
Figure 16. ^{13}C NMR spectrum of **6** in CDCl$_3$.
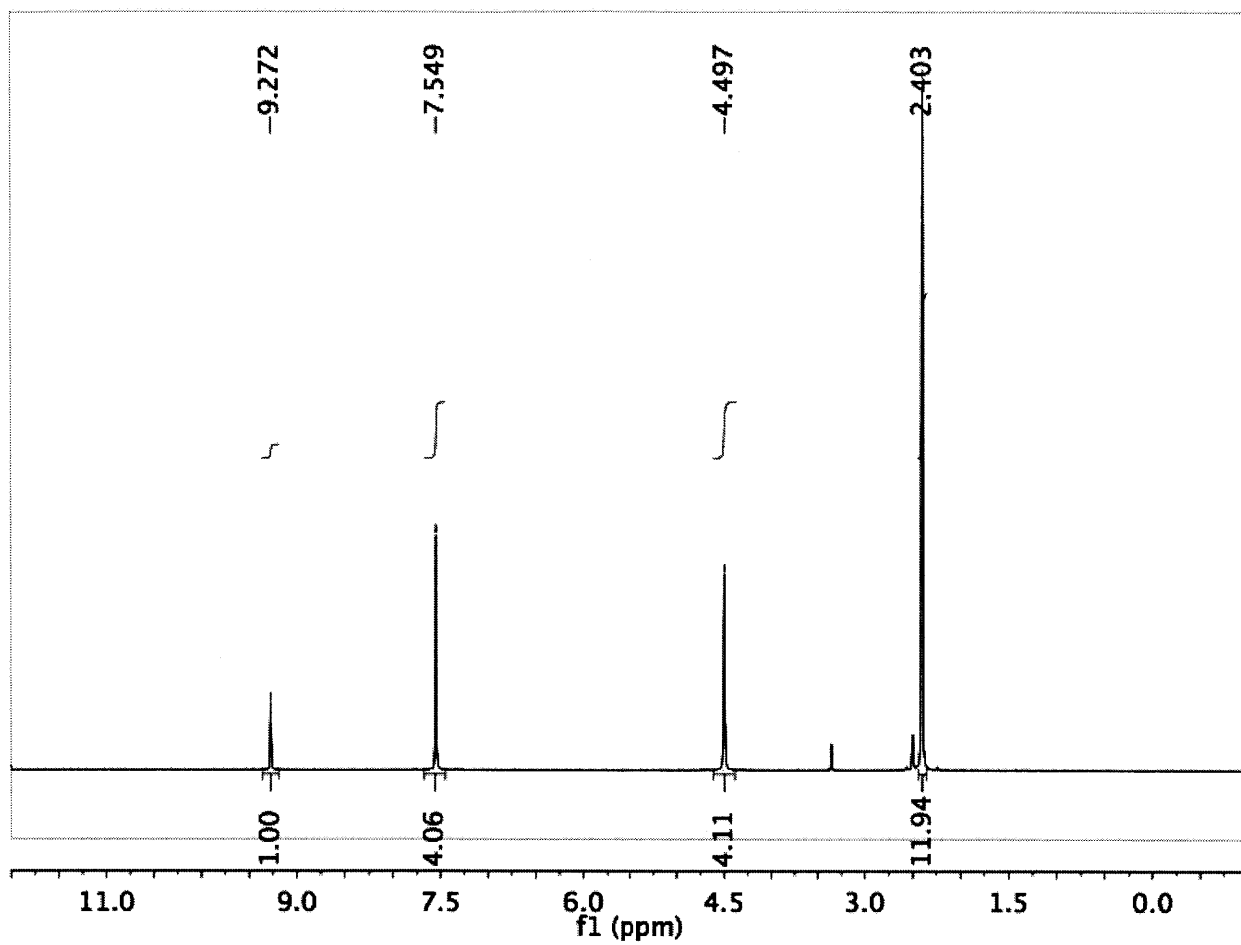
Figure 17. ^{1}H NMR spectrum of **IS1** in DMSO-d^6.

9.272

7.549

4.497

2.403

1.00

4.06

4.11

11.94

11.0   9.0   7.5   6.0   4.5   3.0   1.5   0.0
              f1 (ppm)

108
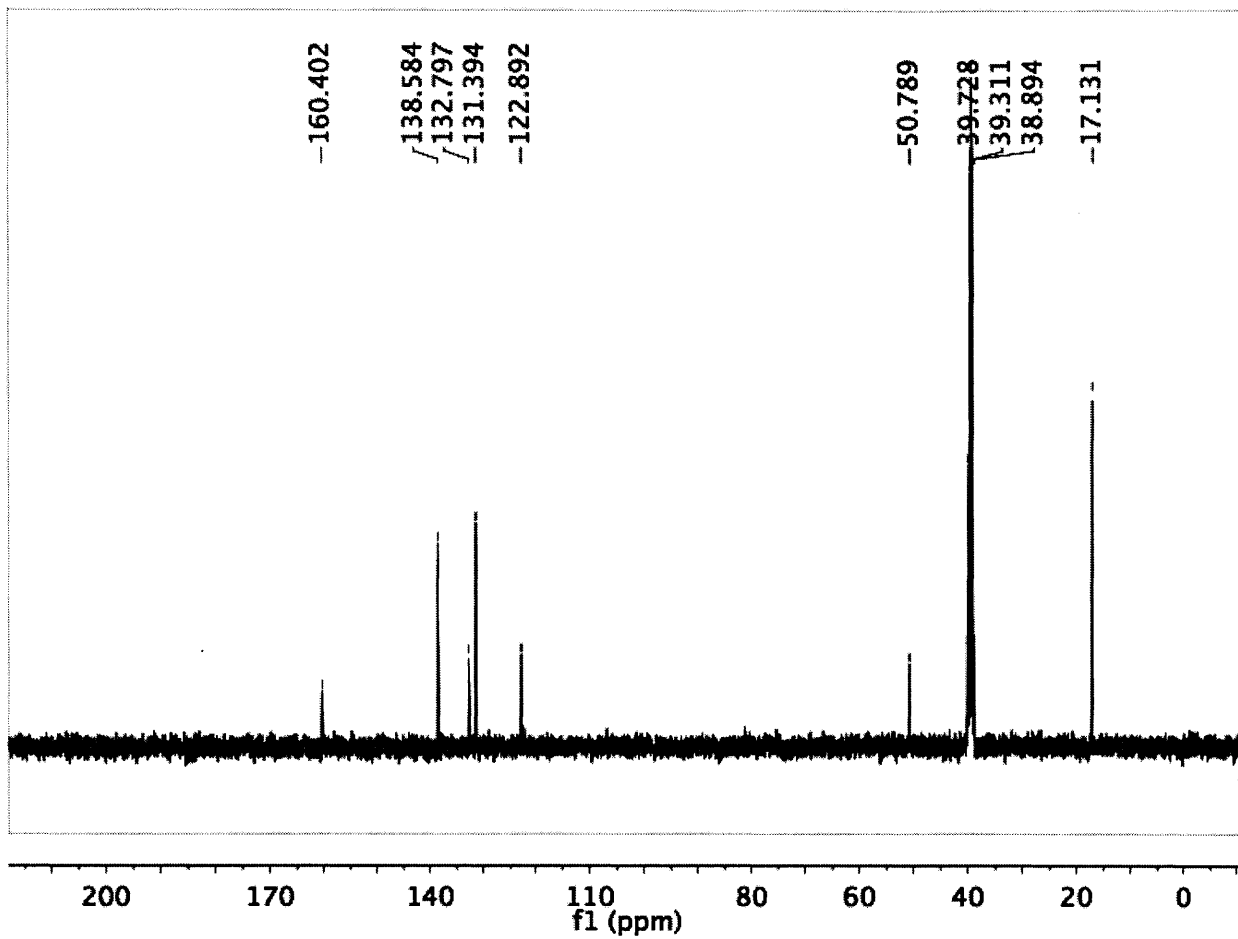
Figure 18. ^{13}C NMR spectrum of **IS1** in DMSO-d^6.
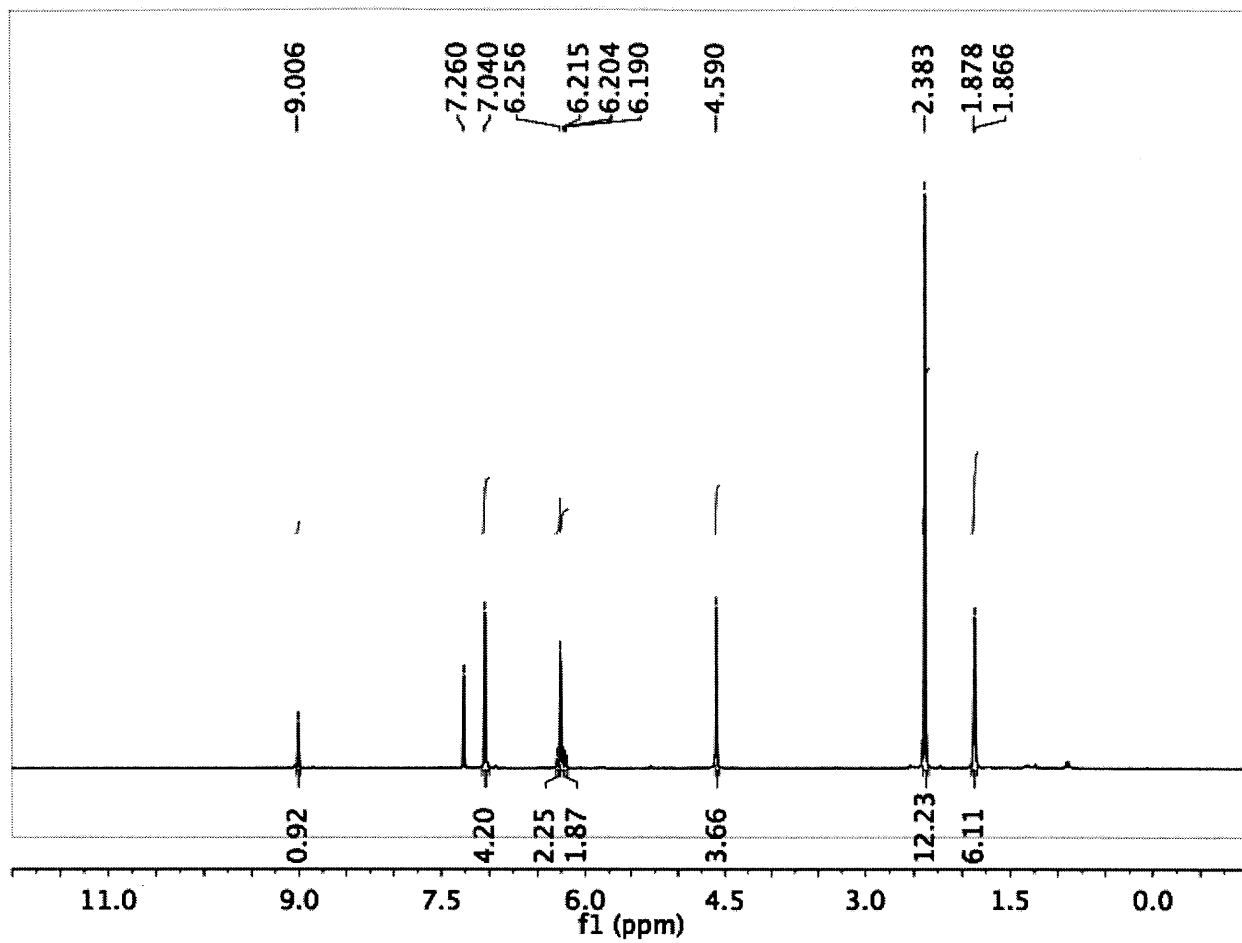
Figure 19. ^{1}H NMR spectrum of **IS2** in CDCl$_3$.
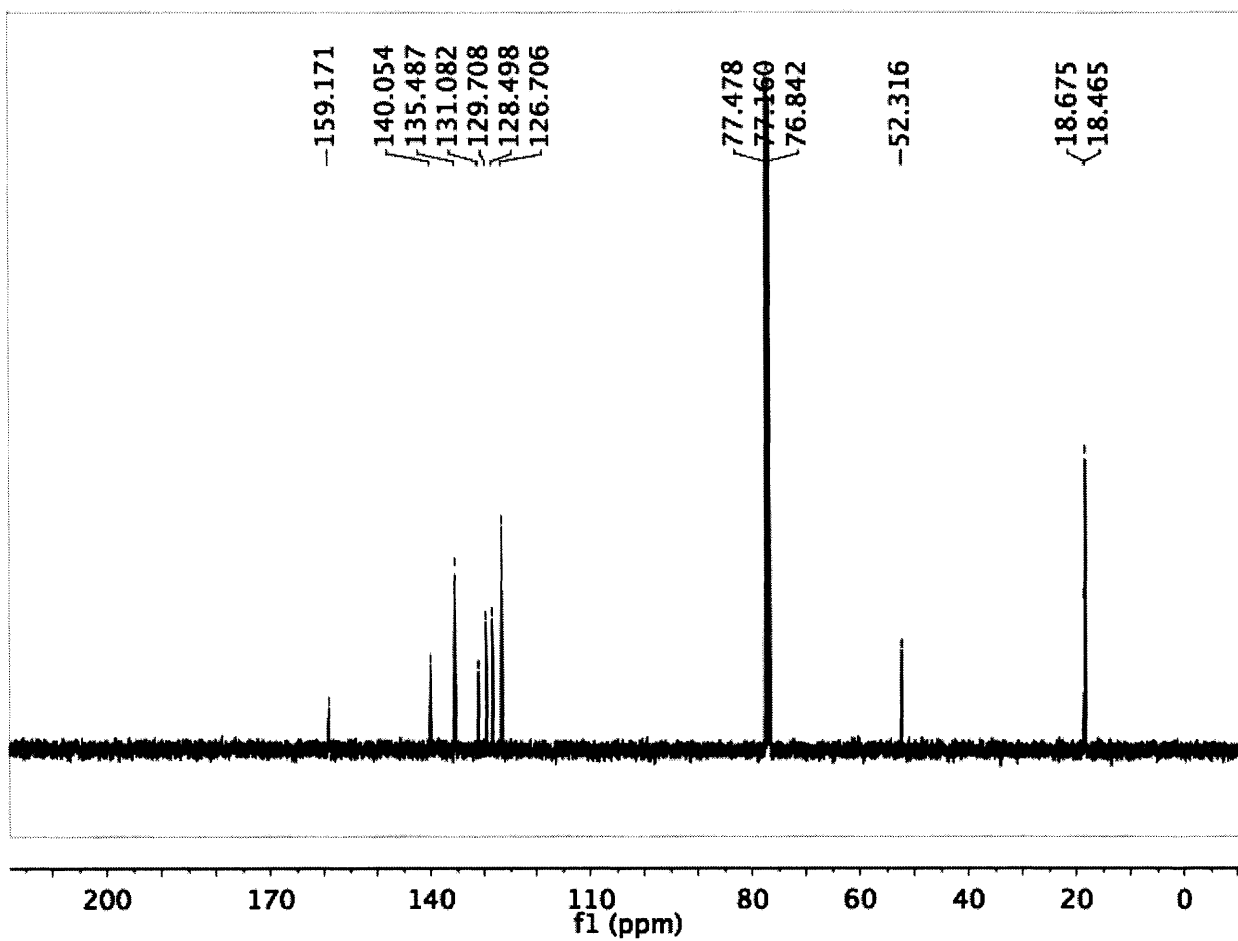
Figure 20. ^{13}C NMR spectrum of **IS2** in CDCl$_3$.
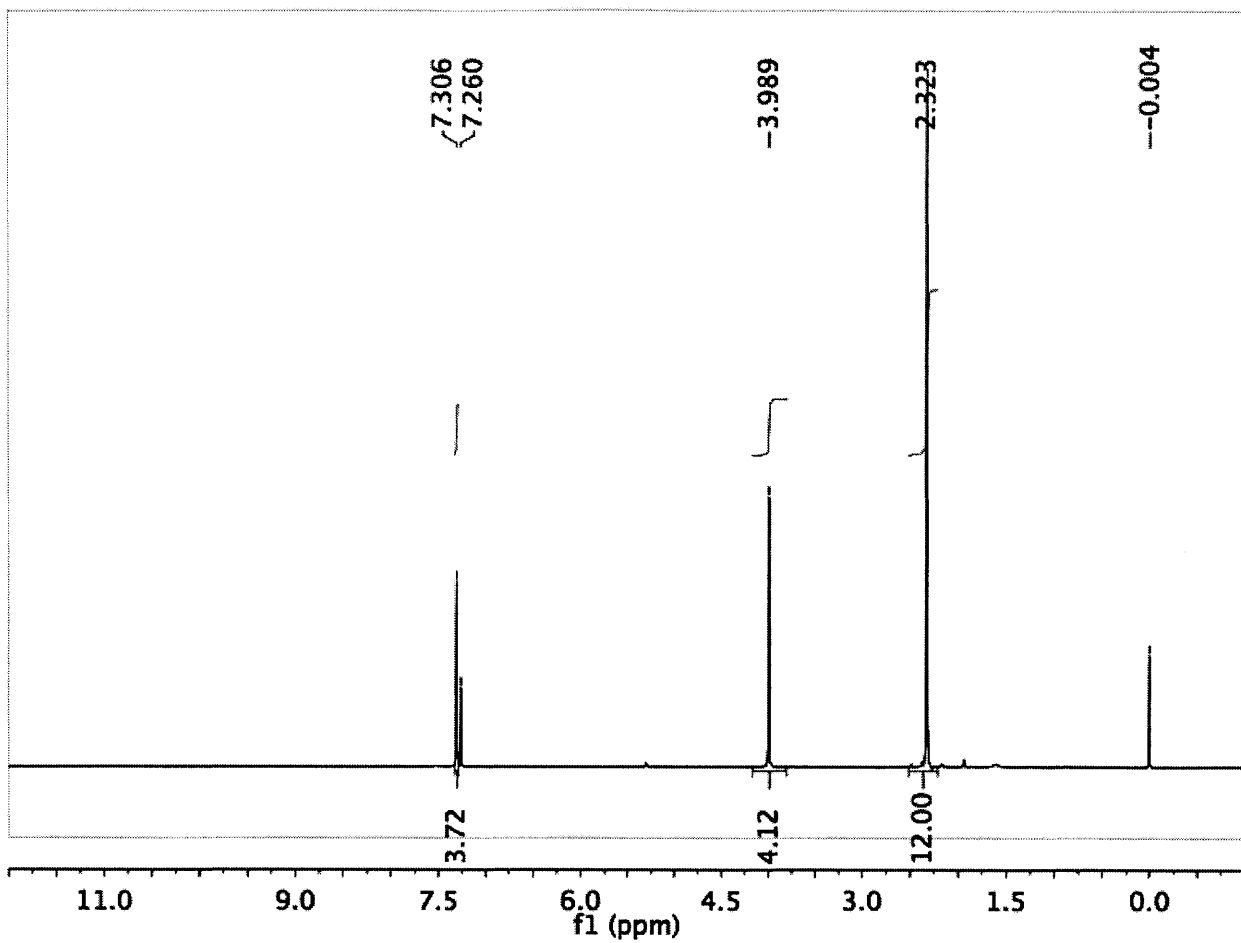
Figure 21. ^{1}H NMR spectrum of **3** in CDCl$_3$ (TMS peak is seen at 0.00ppm).
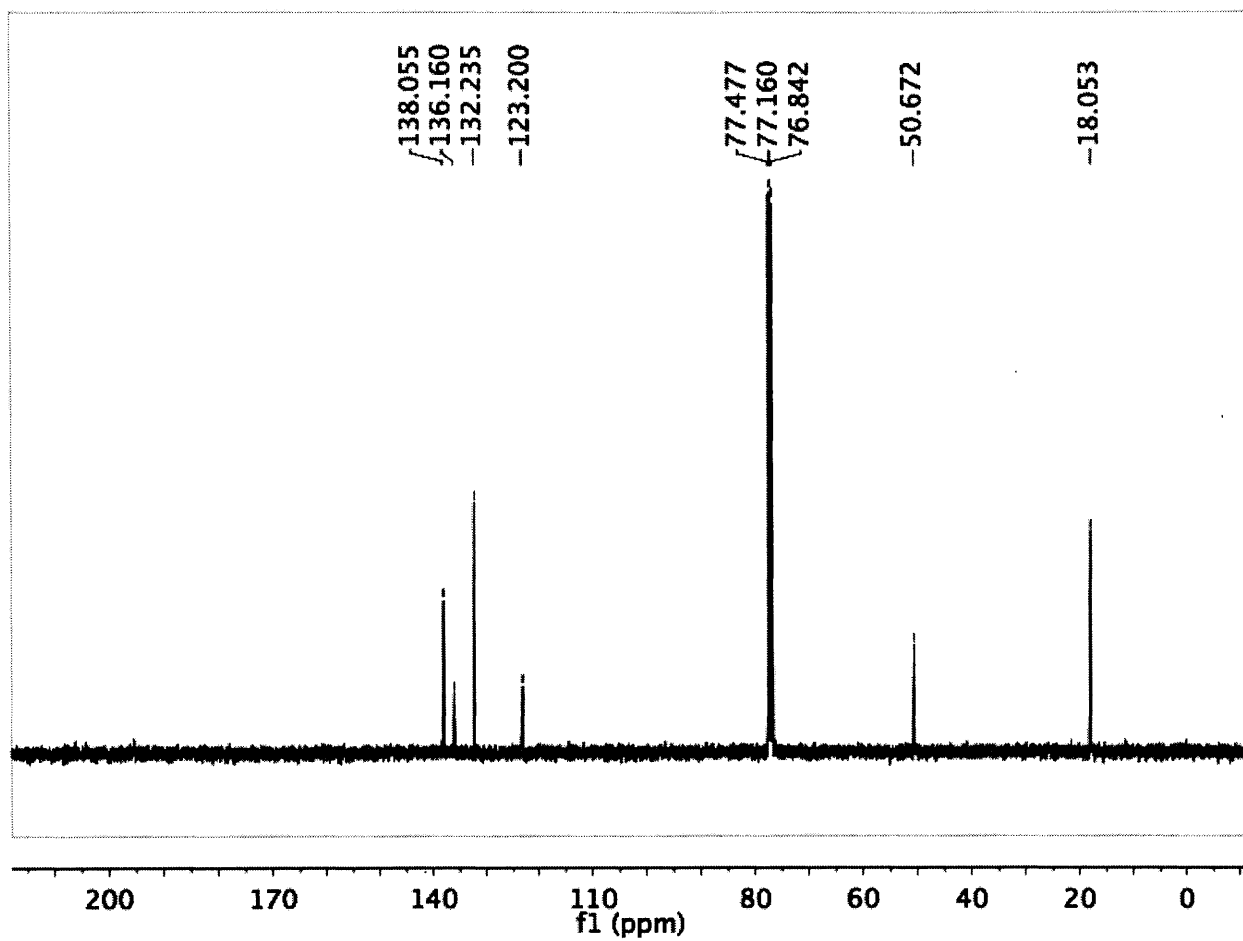
Figure 22. ^{13}C NMR spectrum of **3** in CDCl$_3$.

Peak labels: 138.055, 136.160, 132.235, 123.200, 77.477, 77.160, 76.842, 50.672, 18.053
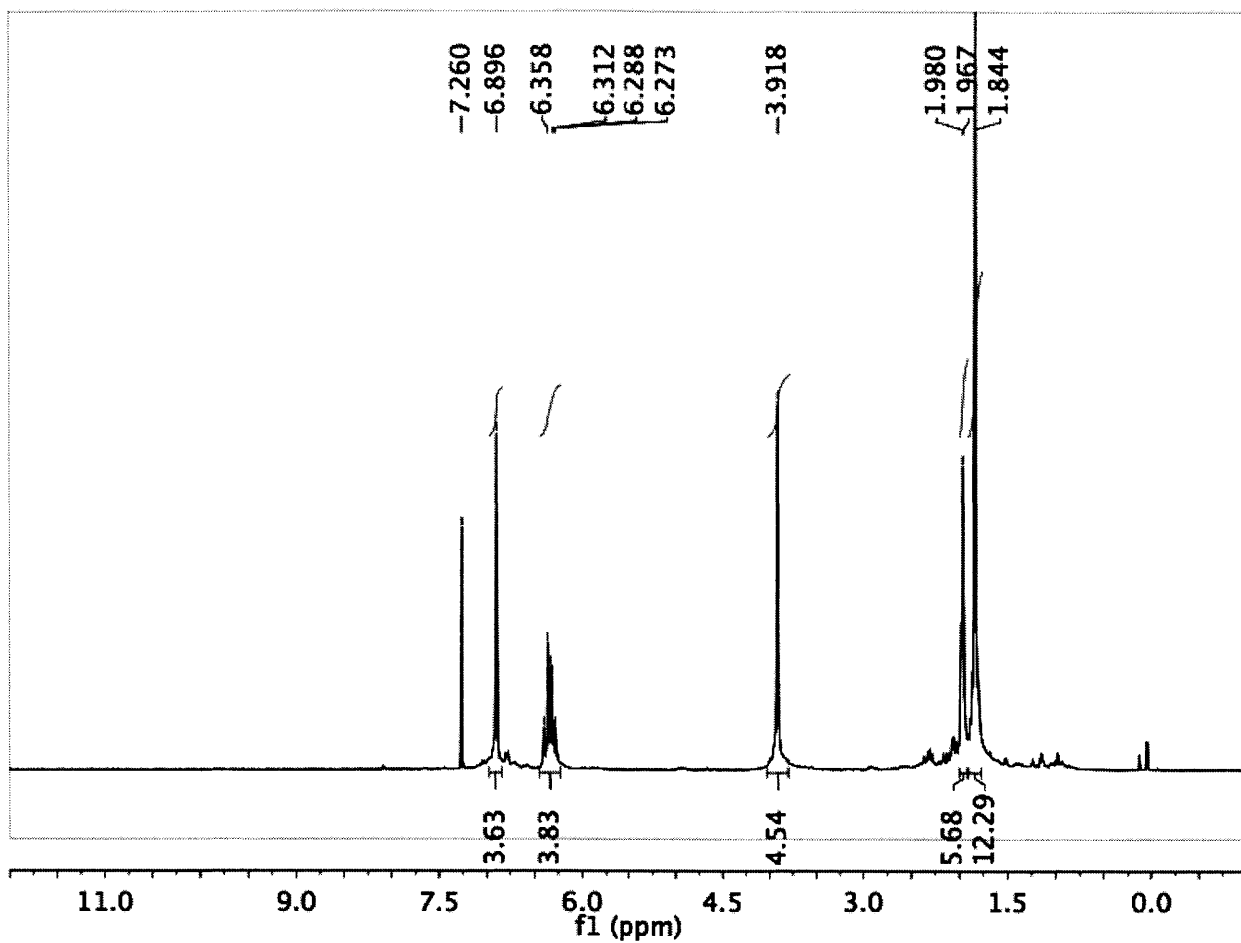
Figure 23. ^{1}H NMR spectrum of **7** in CDCl$_3$.

114
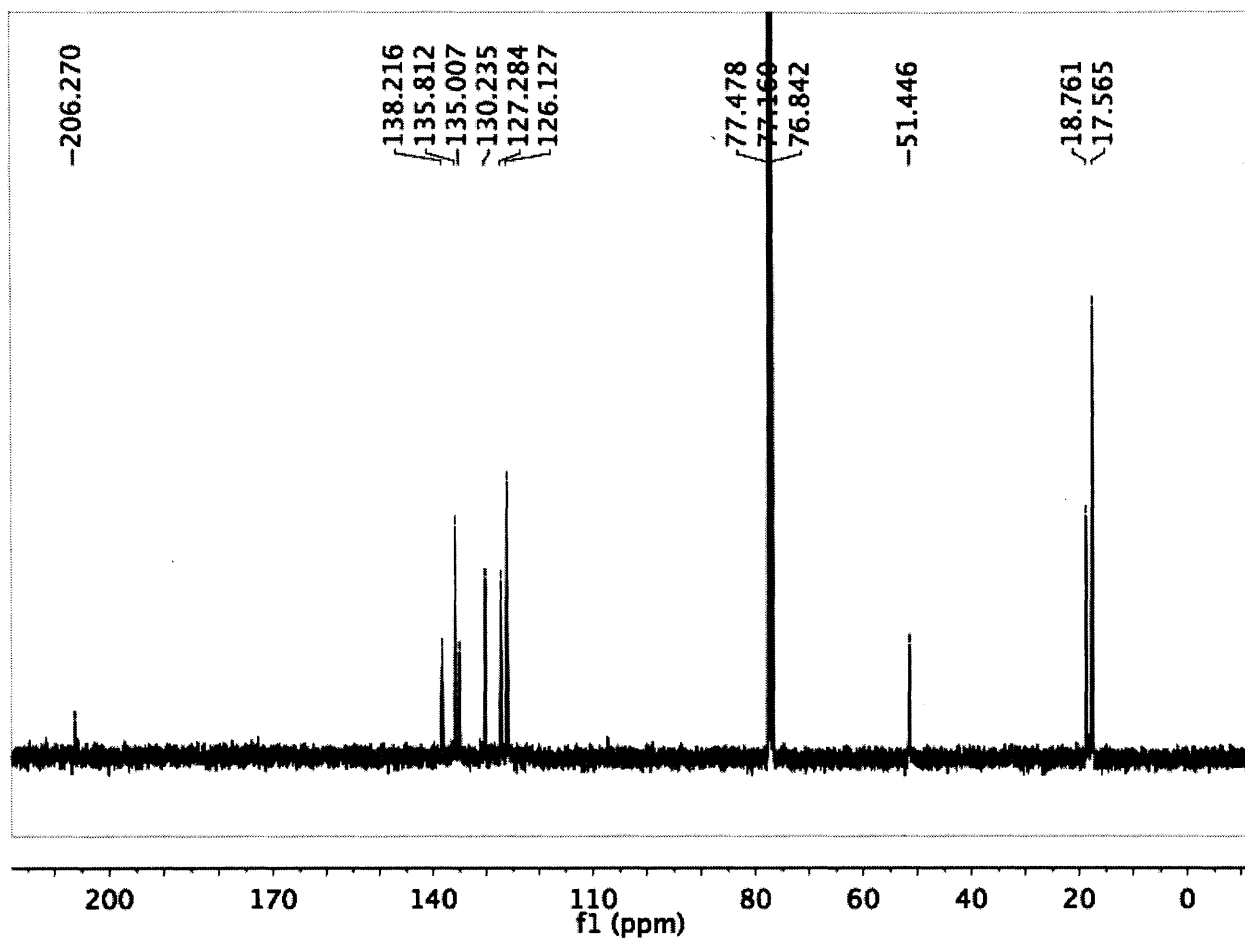
Figure 24. ^{13}C NMR spectrum of **7** in CDCl$_3$.

115
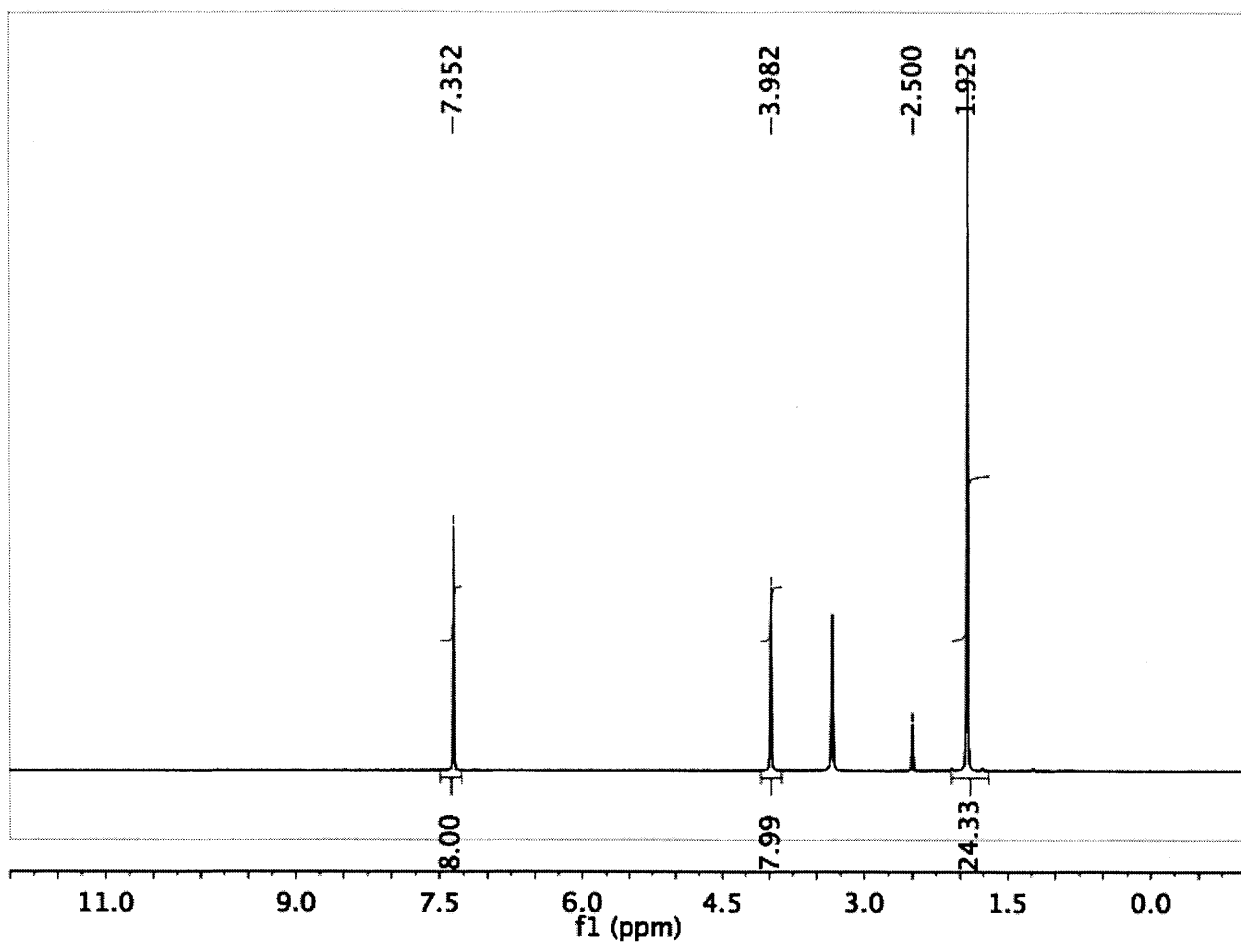
Figure 25. ^{1}H NMR spectrum of **8** in DMSO-d^6.
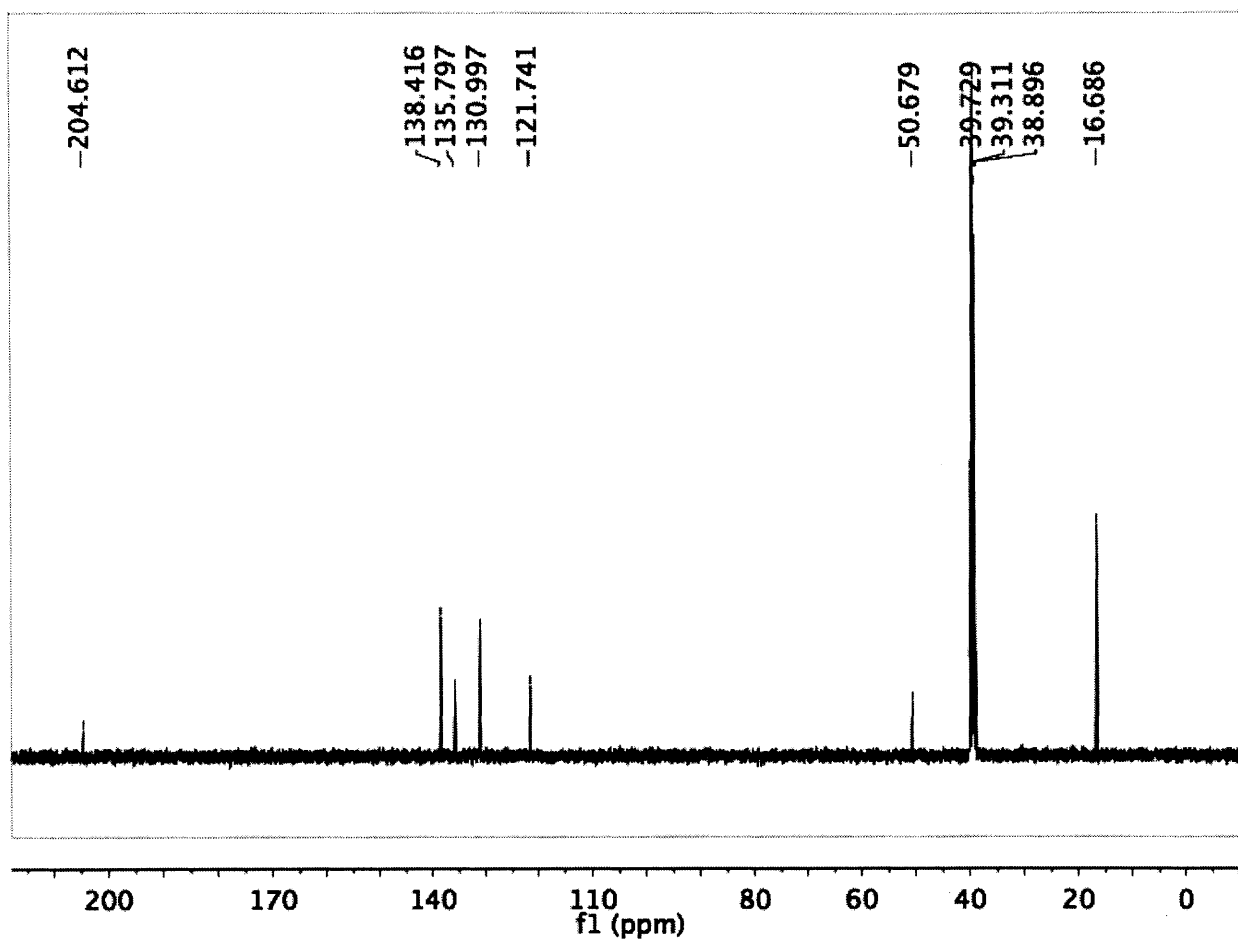
Figure 26. ¹³C NMR spectrum of **8** in DMSO-*d⁶*.
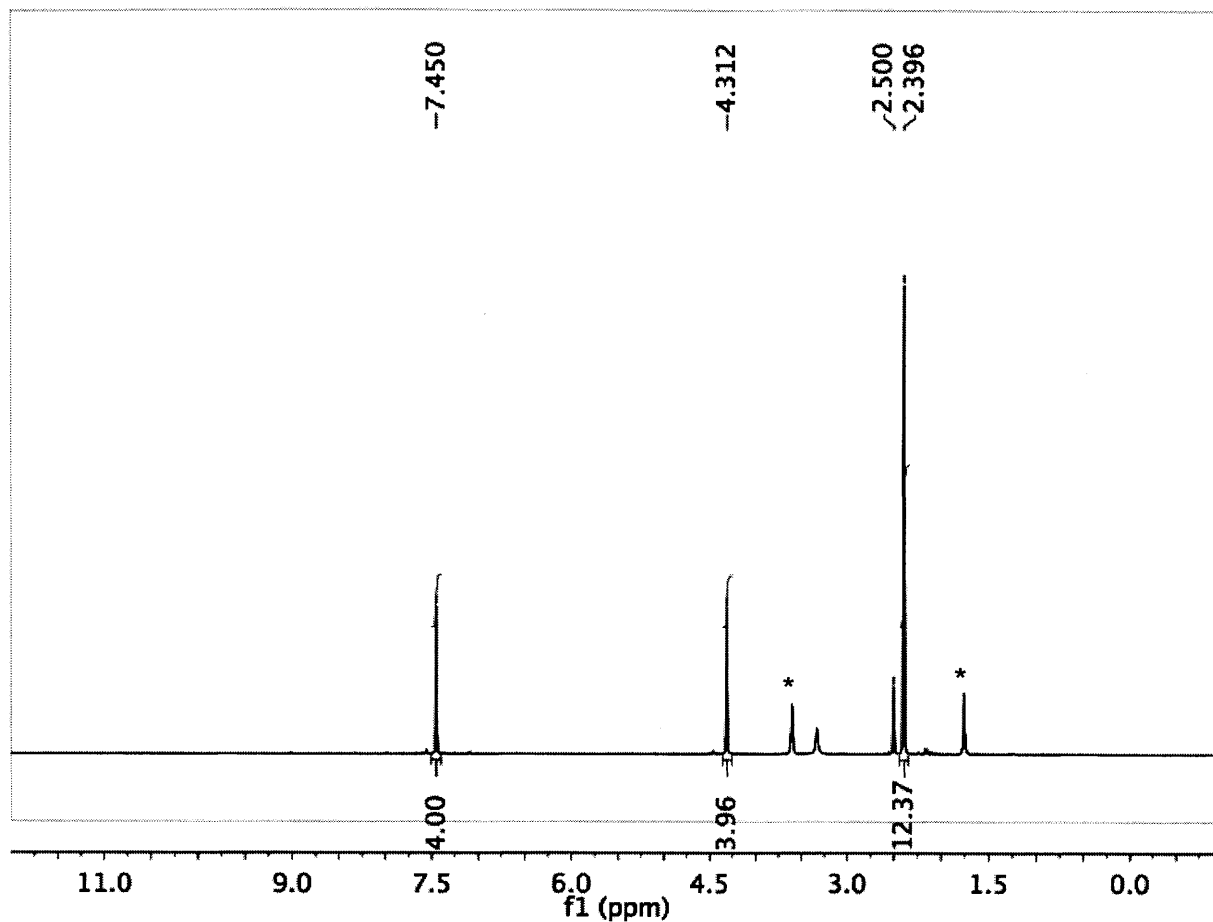
Figure 27. ^{1}H NMR spectrum of CO_2-**1** in DMSO-d^6; * = THF

118
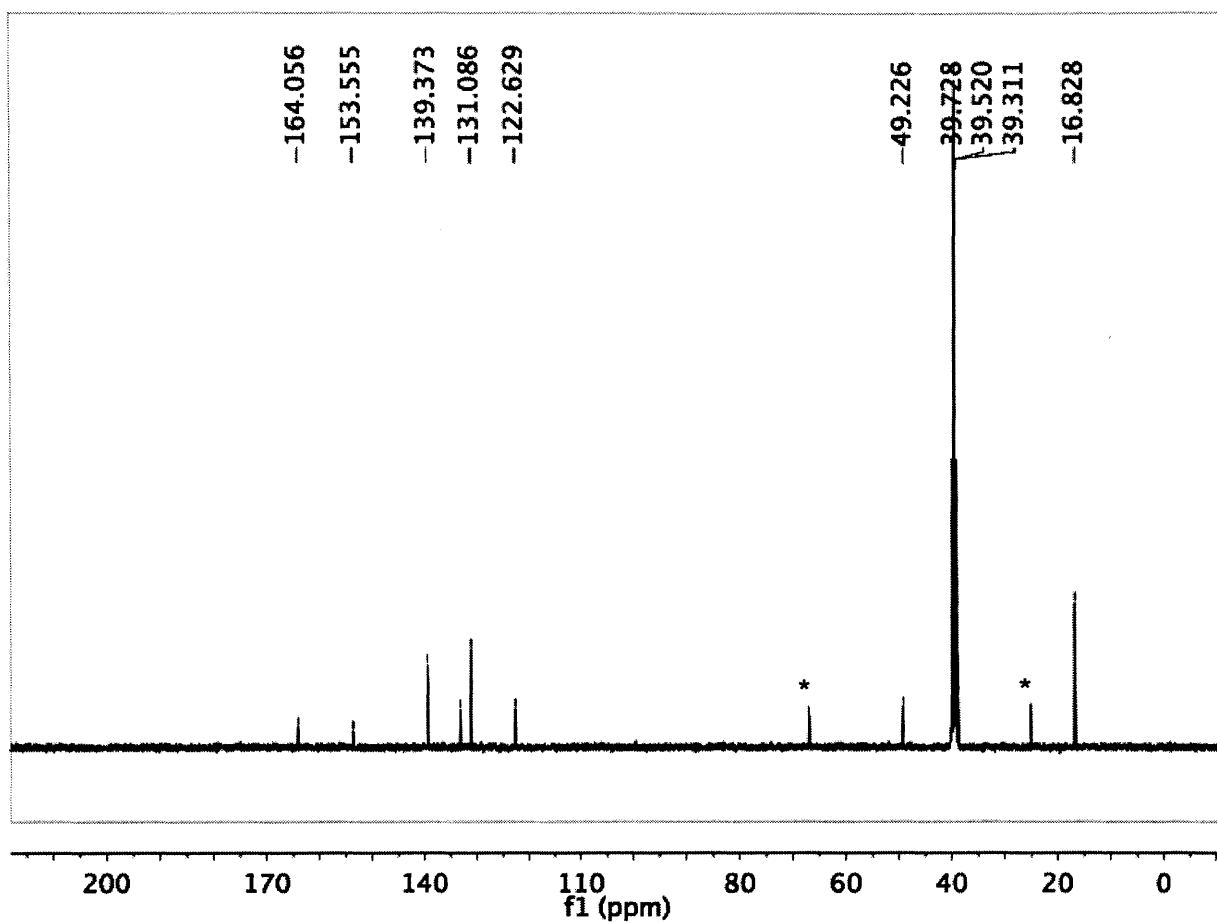
Figure 28. ^{13}C NMR spectrum of CO_2-1 in DMSO-d^6; * = THF

Peak labels (left to right): 164.056, 153.555, 139.373, 131.086, 122.629, 49.226, 39.728, 39.520, 39.311, 16.828

f1 (ppm)

119

2.6 References

(1)   Nuzzo, R. G.; Allara, D. L. Adsorption of Bifunctional Organic Disulfides on Gold Surfaces. *J. Am. Chem. Soc.* **1983**, *105*, 4481-4483.

(2)   DiBenedetto, S. A.; Facchetti, A.; Ratner, M. A.; Marks, T. J. Molecular Self-Assembled Monolayers and Multilayers for Organic and Unconventional Inorganic Thin-Film Transistor Applications. *Adv. Mater.* **2009**, *21*, 1407-1433.

(3)   Ranieri, A.; Monari, S.; Sola, M.; Borsari, M.; Battistuzzi, G.; Ringhieri, P.; Nastri, F.; Pavone, V.; Lombardi, A. Redox and Electrocatalytic Properties of Mimochrome VI, a Synthetic Heme Peptide Adsorbed on Gold. *Langmuir* **2010**, *26*, 17831-17835.

(4)   Koh, S. Strategies for Controlled Placement of Nanoscale Building Blocks. *Nanoscale Res. Lett.* **2007**, *2*, 519-545.

(5)   Love, J. C.; Estroff, L. A.; Kriebel, J. K.; Nuzzo, R. G.; Whitesides, G. M. Self-Assembled Monolayers of Thiolates on Metals as a Form of Nanotechnology. *Chem. Rev.* **2005**, *105*, 1103-1170.

(6)   Nuzzo, R. G.; Zegarski, B. R.; Dubois, L. H. Fundamental Studies of the Chemisorption of Organosulfur Compounds on Gold(111). Implications for Molecular Self-Assembly on Gold Surfaces. *J. Am. Chem. Soc.* **1987**, *109*, 733-740.

(7)   Cometto, F. P.; Patrito, E. M.; Paredes Olivera, P.; Zampieri, G.; Ascolani, H. Electrochemical, High-Resolution Photoemission Spectroscopy and vdW-DFT Study of the Thermal Stability of Benzenethiol and Benzeneselenol Monolayers on Au(111). *Langmuir* **2012**, *28*, 13624-13635.

(8)   Pensa, E.; Cortés, E.; Corthey, G.; Carro, P.; Vericat, C.; Fonticelli, M. H.; Benítez, G.; Rubert, A. A.; Salvarezza, R. C. The Chemistry of the Sulfur–Gold Interface: In Search of a Unified Model. *Acc. Chem. Res.* **2012**, *45*, 1183-1192.

(9)   von Wrochem, F.; Gao, D.; Scholz, F.; Nothofer, H.-G.; Nelles, G.; Wessels, J. M. Efficient Electronic Coupling and Improved Stability with Dithiocarbamate-Based Molecular Junctions. *Nat. Nanotechnol.* **2010**, *5*, 618-624.

(10)   Cheng, Z. L.; Skouta, R.; Vazquez, H.; Widawsky, J. R.; Schneebeli, S.; Chen, W.; Hybertsen, M. S.; Breslow, R.; Venkataraman, L. *In Situ* Formation of Highly Conducting Covalent Au-C Contacts for Single-Molecule Junctions. *Nat. Nanotechnol.* **2011**, *6*, 353-357.

(11)   Chen, W.; Widawsky, J. R.; Vázquez, H.; Schneebeli, S. T.; Hybertsen, M. S.; Breslow, R.; Venkataraman, L. Highly Conducting π-Conjugated Molecular Junctions Covalently Bonded to Gold Electrodes. *J. Am. Chem. Soc.* **2011**, *133*, 17160-17163.

(12)   Kirmse, W. The Beginnings of *N*-Heterocyclic Carbenes. *Angew. Chem. Int. Ed.* **2010**, *49*, 8798-8801.

(13)   Jacobsen, H.; Correa, A.; Poater, A.; Costabile, C.; Cavallo, L. Understanding the M(NHC) (NHC = *N*-Heterocyclic Carbene) Bond. *Coord. Chem. Rev.* **2009**, *253*, 687-703.

(14)   Huang, J.; Stevens, E. D.; Nolan, S. P.; Petersen, J. Olefin Metathesis-Active Ruthenium Complexes Bearing a Nucleophilic Carbene Ligand. *J. Am. Chem. Soc.* **1999**, *121*, 2674-2678.

(15)   Scholl, M.; Trnka, T. M.; Morgan, J. P.; Grubbs, R. H. Increased Ring Closing Metathesis Activity of Ruthenium-Based Olefin Metathesis Catalysts Coordinated with Imidazolin-2-Ylidene Ligands. *Tetrahedron Lett.* **1999**, *40*, 2247-2250.

(16) Nolan, S. P. The Development and Catalytic Uses of *N*-Heterocyclic Carbene Gold Complexes. *Acc. Chem. Res.* **2011**, *44*, 91-100.

(17) Weidner, T.; Baio, J. E.; Mundstock, A.; Grosse, C.; Karthaeuser, S.; Bruhn, C.; Siemeling, U. NHC-Based Self-Assembled Monolayers on Solid Gold Substrates. *Aust. J. Chem.* **2011**, *64*, 1177-1179.

(18) Serpell, C. J.; Cookson, J.; Thompson, A. L.; Brown, C. M.; Beer, P. D. Haloaurate and Halopalladate Imidazolium Salts: Structures, Properties, and Use as Precursors for Catalytic Metal Nanoparticles. *Dalton Trans.* **2013**, *42*, 1385-1393.

(19) Vignolle, J.; Tilley, T. D. *N*-Heterocyclic Carbene-Stabilized Gold Nanoparticles and Their Assembly into 3d Superlattices. *Chem. Commun.* **2009**, 7230-7232.

(20) Hurst, E. C.; Wilson, K.; Fairlamb, I. J. S.; Chechik, V. *N*-Heterocyclic Carbene Coated Metal Nanoparticles. *New J. Chem.* **2009**, *33*, 1837-1840.

(21) Süßner, M.; Plenio, H. p-Face Donor Properties of *N*-Heterocyclic Carbenes. *Chem. Commun.* **2005**, 5417-5419.

(22) de Frémont, P.; Scott, N. M.; Stevens, E. D.; Nolan, S. P. Synthesis and Structural Characterization of *N*-Heterocyclic Carbene Gold(I) Complexes. *Organometallics* **2005**, *24*, 2411-2418.

(23) Jadzinsky, P. D.; Calero, G.; Ackerson, C. J.; Bushnell, D. A.; Kornberg, R. D. Structure of a Thiol Monolayer-Protected Gold Nanoparticle at 1.1 Å Resolution. *Science* **2007**, *318*, 430-433.

(24) Reviakine, I.; Johannsmann, D.; Richter, R. P. Hearing What You Cannot See and Visualizing What You Hear: Interpreting Quartz Crystal Microbalance Data from Solvated Interfaces. *Anal. Chem.* **2011**, *83*, 8838-8848.

(25) Sauerbrey, G. Z. Verwendung Von Schwingquarzen Zur Wägung Dünner Schichten Und Zur Mikrowägung. *Physik* **1959**, *155*, 206-222.

(26) Love, J. A.; Morgan, J. P.; Trnka, T. M.; Grubbs, R. H. A Practical and Highly Active Ruthenium-Based Catalyst That Effects the Cross Metathesis of Acrylonitrile. *Angew. Chem. Int. Ed.* **2002**, *41*, 4035-4037.

(27) Kong, B.; Lee, J. K.; Choi, I. S. Surface-Initiated, Ring-Opening Metathesis Polymerization: Formation of Diblock Copolymer Brushes and Solvent-Dependent Morphological Changes. *Langmuir* **2007**, *23*, 6761-6765.

(28) Weck, M.; Jackiw, J. J.; Rossi, R. R.; Weiss, P. S.; Grubbs, R. H. Ring-Opening Metathesis Polymerization from Surfaces. *J. Am. Chem. Soc.* **1999**, *121*, 4088-4089.

(29) Johannsmann, D. Viscoelastic, Mechanical, and Dielectric Measurements on Complex Samples with the Quartz Crystal Microbalance. *Phys. Chem. Chem. Phys.* **2008**, *10*, 4516-4534.

(30) Voinova, M. V.; Rodahl, M.; Jonson, M.; Kasemo, B. Viscoelastic Acoustic Response of Layered Polymer Films at Fluid-Solid Interfaces: Continuum Mechanics Approach. *Phys. Scr.* **1999**, *59*, 391-396.

(31) Müller, M. T.; Yan, X.; Lee, S.; Perry, S. S.; Spencer, N. D. Lubrication Properties of a Brushlike Copolymer as a Function of the Amount of Solvent Absorbed within the Brush. *Macromolecules* **2005**, *38*, 5706-5713.

(32) Reported by QSense® on www.q-sense.com/sensors-and-coatings-1.

(33) Blackmore, P. M.; Feast, W. J. Stereoregular Fluoropolymers: 6. The Ring-Opening Polymerization of N-Pentafluorophenylbicyclo[2.2.1]Hept-5-Ene-2,3-Dicarboximide. *J. Fluorine Chem.* **1988**, *40*, 331-347.

(34)   Pangborn, A. B.; Giardello, M. A.; Grubbs, R. H.; Rosen, R. K.; Timmers, F. J. Safe and Convenient Procedure for Solvent Purification. *Organometallics* **1996**, 15, 1518-1520.

(35)   Fulmer, G. R.; Miller, A. J. M.; Sherden, N. H.; Gottlieb, H. E.; Nudelman, A.; Stoltz, B. M.; Bercaw, J. E.; Goldberg, K. I. NMR Chemical Shifts of Trace Impurities: Common Laboratory Solvents, Organics, and Gases in Deuterated Solvents Relevant to the Organometallic Chemist. *Organometallics* **2010**, *29*, 2176-2179.

(36)   Savitzky, A.; Golay, M. J. E. Smoothing and Differentiation of Data by Simplified Least Squares Procedures. *Anal. Chem.*, **1964**, *36*, 1627-1639.

(37)   Shao, Y.; Fusti-Molnar, L.; Jung, Y.; Kussmann, J.; Ochsenfeld, C.; Brown, S. T.; Gilbert, A. T. B.; Slipchenko, L. V.; Levchenko, S. V.; O'Neill, D. P.; DiStasio Jr., R. A.; Lochan, R. C.; Wang, T.; Beran, G. J. O.; Besley, N. A.; Herbert, J. M.; Lin, C. Y.; Van Voorhis, T.; Chien, S. H.; Sodt, A.; Steele, R. P.; Rassolov, V. A.; Maslen, P. E.; Korambath, P. P.; Adamson, R. D.; Austin, B.; Baker, J.; Byrd, E. F. C.; Daschel, H.; Doerksen, R. J.; Dreuw, A.; Dunietz, B. D.; Dutoi, A. D.; Furlani, T. R.; Gwaltney, S. R.; Heyden, A.; Hirata, S.; Hsu, C.-P.; Kedziora, G.; Khaliullin, R. Z.; Klunzinger, P.; Lee, A. M.; Lee, M. S.; Liang, W. Z.; Lotan, I.; Nair, N.; Peters, B.; Proynov, E. I.; Pieniazek, P. A.; Rhee, Y. M.; Ritchie, J.; Rosta, E.; Sherrill, C. D.; Simmonett, A. C.; Subotnik, J. E; Woodcock III, H. L.; Zhang, W.; Bell, A. T.; Chakraborty, A. K.; Chipman, D. M.; Keil, F. J.; Warshel, A.; Hehre, W. J.; Schaefer III, H. F.; Kong, J.; Krylov, A. I.; Gill, P. M. W.; Head-Gordon, M. Advances in Methods and Algorithms in a Modern Quantum Chemistry Program Package. *Phys. Chem. Chem. Phys.* **2006**, *8*, 3172-3191.

(38)   King, H. W. Crystal Structures and Lattice Parameters of Allotropes of the Elements. In *CRC Handbook of Chemistry and Physics*; 93rd ed.; Haynes, W. M., Ed.; CRC Press/Taylor and Francis: Boca Raton, FL, 2005.

(39)   Blyholder, G. CNDO Model of Carbon Monoxide Chemisorbed on Nickel. *J. Phys. Chem.* **1975**, *79*, 756-761.

(40)   Goel, S.; Velizhanin, K. A.; Piryatinski, A.; Tretiak, S.; Ivanov, S. A. DFT Study of Ligand Binding to Small Gold Clusters. *J. Phys. Chem Lett.* **2010**, *1*, 927-931.

(41)   Doye, J. P. K.; Wales, D. J. Global Minima for Transition Metal Clusters Described by Sutton–Chen Potentials. *New J. Chem.* **1998**, *22*, 733-744.

(42)   Sheldrick, G. M. Phase Annealing in SHELX-90: Direct Methods for Larger Structures. *Acta Crystallogr. Sect. A* **1990**, *A46*, 467-473.

(43)   Sheldrick, G. M. A Short History of SHELX. *Acta Crystallogr. Sect. A* **2008**, *A64*, 112-122.

(44)   Müller, P. Practical Suggestions for Better Crystal Structures. *Crystallogr. Rev.* **2009**, *15*, 57-83.

(45)   Kuhn, K. M.; Grubbs, R. H. A Facile Preparation of Imidazolinium Chlorides. *Org. Lett.* **2008**, *10*, 2075-2077.

CHAPTER 3. Reactions of Persistent Carbenes with Hydrogen-Terminated Silicon Surfaces

3.1 Introduction
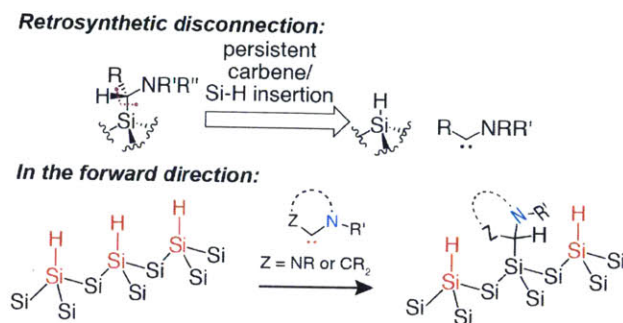
Figure 1. The proposed approach toward silicon surface modification.

The properties of materials are often dictated in large part by their surface functionality.[1-5] Currently, the methods available for controlled surface modification are not as well developed as solution synthetic methodologies. Furthermore, surface functionalization methods are generally limited in their substrate scope: surface anchors that bind strongly to metals are rarely suitable for nonmetals or metal oxides and visa versa. Given these limitations, there is continued need for surface anchors that are more universal in scope and that facilitate precise control over surface functionality.

One of the most demanding surfaces in this regard is that of silicon, on which the present-day semiconductor industry is largely founded. Silicon surfaces – and in particular, their defects – play an active role in charge recombination, a generally undesirable process that leads to reduced device performance.[6] Although this challenge has been partially addressed through organic and/or inorganic surface passivation routes (i.e., via formation of Si-C bonds[7-13] or Si-H/heteroatom bonds,[14,15] respectively), the continued evolution of silicon-based technologies will require new methods for the precise and controlled introduction of surface functionality.

Although traditional silicon passivation routes have enabled the incorporation of useful functional groups into surface-grafted monolayers, these functional groups are generally separated from the surface via long insulating alkane spacers.[16,17] In many applications, a preferred design would utilize a short, perhaps one-carbon, spacer between the surface and the functionality; it would provide a thermally and hydrolytically-stable surface anchor while at the same time permit through-bond/-space electronic coupling between the functional group and the surface.

Recent reports demonstrated that amines are highly versatile functional groups for modulating the properties of surfaces, including silicon.[18,19] However, covalent attachment of

amines to silicon via a one-carbon spacer is presently not feasible using conventional hydrosilylation[10,11] of imines, and no reports exist of nucleophilic alkylation of silicon surfaces with thermally unstable N,N-disubstituted aminomethyllithium reagents.[20] Application of retrosynthetic analysis to this surface-modification challenge revealed a simple disconnection (Figure 1), which in the forward sense amounts to amino-carbene insertion into the Si-H bonds of a H-terminated silicon surface (H-Si). Both the carbene and the surface are readily accessible reagents.

Carbene insertion presents an intriguing mechanistic approach to H-Si functionalization. To our knowledge, the only two existing examples involve highly reactive, non-persistent carbenes. First, Tilley and coworkers reported on the treatment of H-Si(111) (H-terminated silicon (111)) with dichlorocarbene.[21] Though very promising, this method could be limited by the use and generation of Hg-containing species, as well as the concomitant uncontrolled chlorination and bromination of the silicon surface.[21] Second, Ghadiri and coworkers reported on Rh-catalyzed carbenoid insertion on H-terminated porous silicon surfaces.[22] This approach enables the use of a wide-range of carbene precursors (diazo compounds), but hinges on the use of transition metal catalysis, which may or may not be feasible in certain applications.[22] Furthermore, lack of precedence for α-amino-α-diazo compounds or α-aminomethylmercury reagents renders the above methods incapable of installing amines with one-carbon spacers. Although another study purported to use persistent diaminocarbenes to stabilize Si nanoparticle (SiNP) surfaces,[23] to our knowledge the insertion reactivity of persistent carbenes in the context of H-terminated silicon surfaces has not been explored. As discussed above, persistent aminocarbene – e.g., N-heterocyclic carbene (NHC) – insertion would provide a natural entry into the desired amine-functionalized silicon surfaces (Figure 1).

Interest in the insertion reactivity of persistent carbenes has surged in the last 15 years; controlled bond insertion is a promising strategy to cleave H-H, C-H, and heteroatom-H bonds that are difficult to cleave by homo- and heterolysis. Particularly intriguing to us was the discovery by Bertrand and coworkers that persistent singlet NHCs readily undergo insertion into the Si-H bonds of phenylsilane, diphenylsilane, and triethoxysilane.[24] Soon after, Radius and coworkers described an insertion/ring-expansion cascade in NHC-silane systems,[25] and Bielawski and coworkers extended the silane insertion reactivity to diamidocarbenes (DACs).[26]

Inspired by these reports, and given our vision of persistent carbenes as potentially universal surface anchors,[27] we set out to explore them in the context of H-**Si** modification.

3.2 Results and Discussion

1. Model compound studies
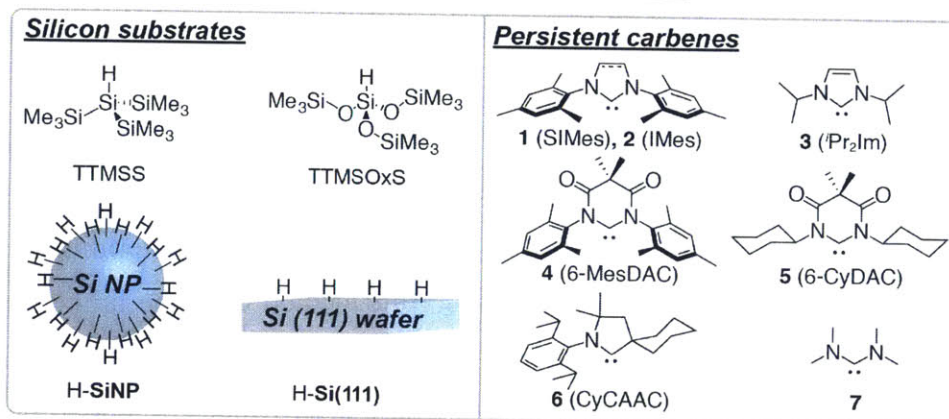
Figure 2. Silicon substrates and carbenes employed in this study.

The exploration of new reactions on surfaces can be critically informed by analogous homogeneous reactions with model compounds whose structures map well onto surface fragments. From such studies, one can gain valuable insights about relative reaction kinetics and thermodynamics, potential side reactions, and structural features of the product(s) that could extrapolate to surfaces; such information would be challenging to extract from direct surface studies. The model compound strategy also allows for a rapid screening of reactants and conditions to identify the optimal one(s) to be adapted to surfaces. For H-**Si** surfaces, we supposed that tris(trimethylsilyl)silane (TTMSS, Figure 2) would be an expedient model compound, because the electronic and steric environment of the Si-H bond in TTMSS closely approximates that of the H-**Si(111)** surface.[28] Additionally, TTMSS is an inexpensive, stable, and commercially available compound. Finally, the oxidized analogue of TTMSS, TTMSOxS (Figure 2), is expected to be a good model of backbond-oxidized silicon surface regions.

During initial screens, carbene **2** (IMes, 55 mM) was found to be unreactive toward TTMSS even after 48 h at 80 °C in benzene-d^6. Under the same conditions, carbene **1** (SIMes) underwent partial cycloelimination[29] with no evidence of insertion. We initially hypothesized that the steric bulk surrounding the Si-H bond in TTMSS inhibits the insertion of NHCs with bulky N-substituents. However, exposure of less sterically encumbered carbene **3** (^{i}Pr$_2$Im, 35 mM) to TTMSS in benzene-d^6 at 80 °C for 6 d afforded no insertion products within the limit of

detection of ^{1}H nuclear magnetic resonance (NMR) spectroscopy. Although, in the context of silane insertion, the saturated analogue of **3** (^{i}Pr$_2$ImH$_2$) is expected to be more reactive than **3** on the grounds of analogous observations for DippH$_2$ (= SIPr) vs Dipp (= IPr),[24,25] the propensity of ^{i}PrImH$_2$ to dimerize led us to exclude it from this initial carbene screen.[30] (Note that specialized conditions have enabled the preparation of ^{i}PrImH$_2$ in a way that precludes rapid dimerization, and may enable the use of this carbene in future surface functionalization studies.[31]) In any event, though the steric bulk of the tested NHCs may have been prohibitive in this system, we hypothesized that the nucleo- and/or electrophilicity of these diamino-NHCs was also insufficient to enable Si-H insertion.

To address this hypothesis, we turned to more electrophilic (and somewhat less electron-donating,[32,33] albeit comparably basic[34]) diamidocarbenes (DACs).[32,33,35] Initial studies with N,N'-dimesityl DAC (**4**, MesDAC)[32] provided little evidence of carbene insertion into the Si-H bond of TTMSS: ^{1}H NMR spectroscopy indicated that no insertion took place at 23 °C, and even after 22 h at 80 °C, only ~5% of TTMSS was converted to an unidentified new species with a higher frequency (more downfield) TMS methyl resonance. Meanwhile, the concomitant extensive (~77%) decomposition of **4** via intramolecular benzylic C-H insertion[36] rendered further investigation of this compound imprudent.

Given that the large steric bulk of **4** was a potential obstacle for the Si-H insertion, we sought to prepare a DAC with reduced steric bulk surrounding the carbene site. While to our knowledge all reported examples of DACs have large N-aryl substituents, we wondered if we could replace them with smaller N-alkyl ones. Specifically, given the conformational freedom of cyclohexyl groups, we anticipated that they might provide the ideal combination of sufficient steric bulk to inhibit DAC dimerization with the flexibility needed for DAC insertion into the Si-H bond of TTMSS. Intramolecular C-H insertion by the carbene was also expected to be minimal due to the absence of accessible activated C-H bonds.

N,N-dicyclohexyl DAC (**5**) was successfully prepared following analogous conditions to the method utilized by Hudnall and Bielawski[33] for the synthesis of aryl DACs (e.g., **4**). NaHMDS was employed as the base to generate the free carbene. The latter displayed no sign of degradation in C$_6$D$_6$ solution at 0.16 M concentration during the course of at least 3 h at 23 °C,

127
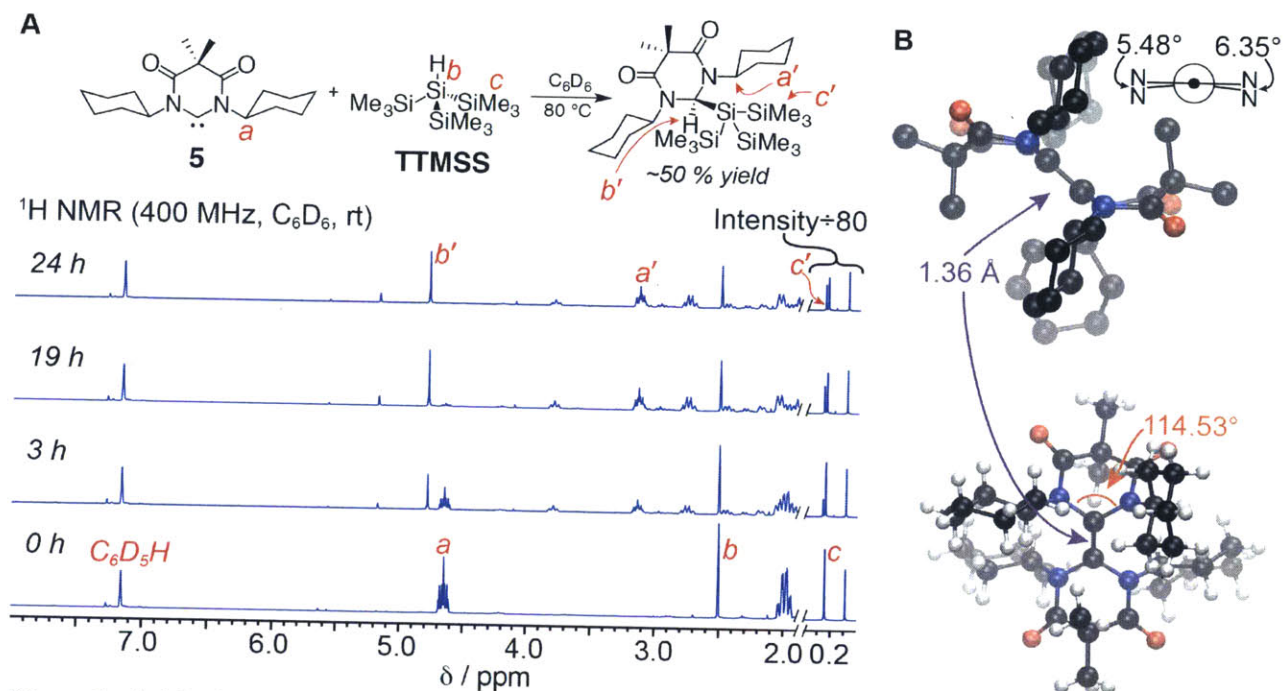
Figure 3. A. Monitoring insertion of **5** into the Si-H bond of TTMSS by ¹H NMR. **B.** X-ray crystal structure of the dimer of **5** ((**5**)₂), shown from two perspectives (hydrogen atoms not shown in the upper structure for clarity). Hydrogen atoms are in white, carbon – in black, nitrogen – in blue, and oxygen – in red.

and exhibited a characteristic carbene carbon ¹³C NMR resonance at 269.5 ppm (see Experimental).

After exposure of a 0.164 M solution of **5** in C_6D_6 to TTMSS at 23 °C, no reaction was noted by ¹H NMR during the course of 3 h. However, elevation of the temperature to 80 °C led to simultaneous consumption of the carbene and TTMSS and the appearance of new resonances corresponding to the insertion product (Figure 3A). The transformation was complete in 24 h, and the identity of the insertion product was unequivocally established through Fourier transform ion cyclotron resonance mass spectrometry (FTICR-MS) and a combination of 2-D NMR techniques (gCOSY, HSQC, gHMBC, and NOESY), in addition to 1-D NMR characterization (see Experimental). Attempts to crystallize this product failed. Although this first observation of extensive carbene insertion into the Si-H bond of TTMSS was exciting, the product was formed in only ~50% yield (by NMR) and the remainder of the carbene was consumed by side reactions. One such side reaction was identified as the formal insertion of **5** into the N-H bond of HMDS (see Experimental for details), which was generated during deprotonation of **5**•HOTf with NaHMDS. Examples of persistent carbene (including DAC) insertions into N-H bonds are well-known,[37-42] so our observation of this reactivity for **5** was not surprising. Another side reaction was the dimerization of **5** to yield a tetraamidoolefin, which was rather insoluble in C_6D_6 and

readily crystallized (Figure 3B) or precipitated out of solution. The double bond character of the bond linking the two units of **5** in **(5)$_2$** was apparent from its length of 1.36 Å[43] as well as the near co-planarity of the four nitrogen atoms attached to the olefin. Reduction of the reaction temperature to 60 °C did not alleviate the observed side processes. In particular, during preliminary H-**Si(111)** insertion experiments, we found that deposition of the poorly soluble dimer on silicon surfaces was a major complication, which compelled us to continue our search for better-suited persistent carbenes.

Although **5** was not ideally suited for H-**Si** surface functionalization via insertion, its reasonable success in the context of TTMSS insertion confirmed the benefit of elevated carbene electrophilicity in combination with steric flexibility. Informed by the insightful studies from Bertrand and coworkers[41] into H-H insertion by cyclic alkyl-amino carbenes (CAACs)s and later Bielawski and Moerdyk[36] into intermolecular 'non-acidic' C-H insertion by DACs, we speculated that insertion of carbenes into weakly-polarized Si-H bonds would require that the carbene first nucleophilically polarize the Si-H and activate it for insertion. Thus, we wondered if persistent carbenes with both elevated electro- *and* nucleophilicity would more rapidly insert into the Si-H bond of TTMSS.

CAACs[44-47] are known to be more nucleophilic and more electrophilic than typical cyclic diaminocarbenes.[41,48] Among the known variants, **6**[47] was chosen for its flexible steric bulk. Exposure of **6** (0.046 M in C$_6$D$_6$, ~85% purity by ^{1}H NMR,) to 1.13 equivalents of TTMSS at 23 °C resulted in 95% conversion to the Si-H insertion product in 3 d as indicated by ^{1}H NMR spectroscopy (Figure 4A); during the first 44 h (86% conversion), the reaction followed 2nd order kinetics ($k_2^{23°C} = 2.0$ M^{-1}·h^{-1}, see Experimental). The structure of the product was first confirmed by a combination 1-D and 2-D NMR spectroscopy and FTICR-MS (Figures 4A, 4B, and Experimental). An NOE interaction was observed for the trimethylsilyl protons *e'* and the methine proton *c''* (Figure 4B). The broadening of the TMS methyl resonance (Figure 4A) also suggested relatively slow, millisecond-timescale rotation of the tris(trimethylsilyl) group about the new Si-C bond. The identity of the product was verified by X-ray crystallography (Figure 4C), (crystals were grown in an NMR tube by slow DCM-*d^2* evaporation in air at 23 °C.) The Si-C$_{carbene}$ bond length was 1.98 Å, the Si-C$_{carbene}$-H bond angle was 104.9°, and the three Si-Si-
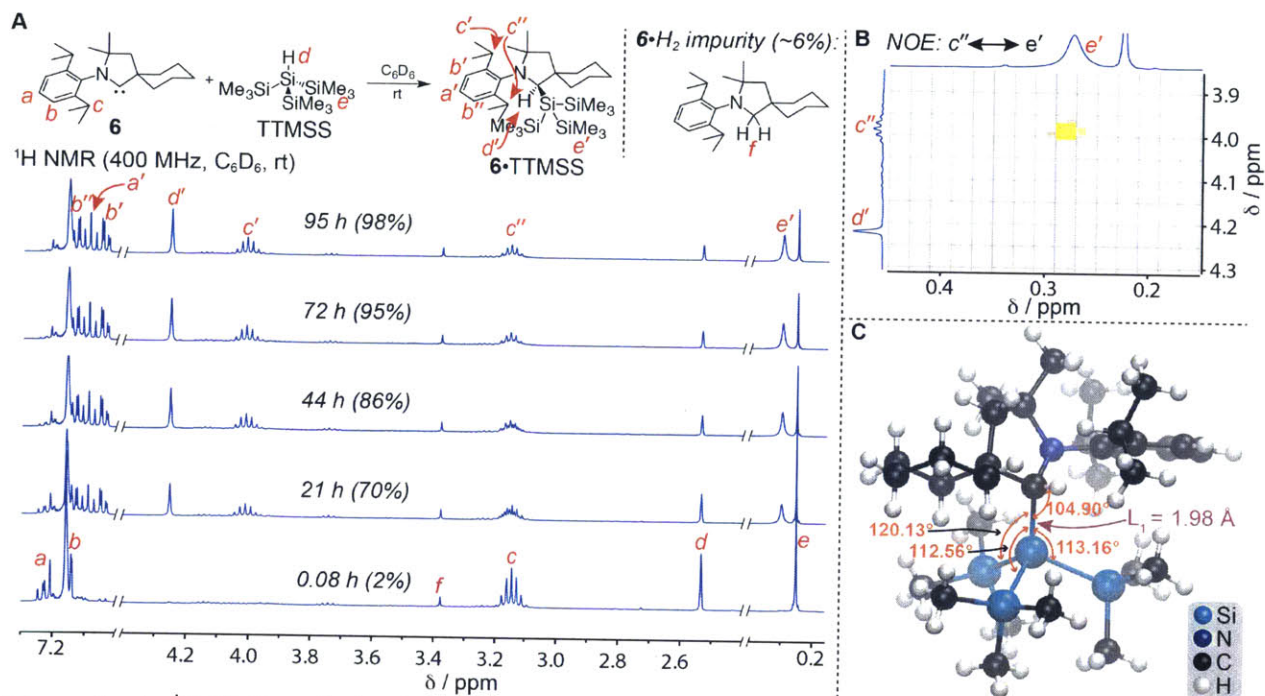
Figure 4. A. ^{1}H NMR analysis of the insertion reaction between **6** and TTMSS. **B.** Excerpt of the NOESY spectrum of the insertion product, showing an interaction between protons c'' and e'. **C.** X-ray crystal structure of **6·TTMSS**.

$C_{carbene}$ bond angles were 112.56°, 113.16°, and 120.13°; these structural parameters are analyzed in the Section IV.

The results from the model study with **6** confirmed our hypothesis that elevated carbene nucleo- and electrophilicity were critical for rapid TTMSS Si-H insertion. We also tested the insertion of **5** and **6** into the Si-H bond of TTMSOxS, and found that under identical reaction conditions as those used for TTMSS the insertion of **5** did not proceed while that of **6** proceeded much more rapidly (Figures 5A–B); the reaction was essentially complete after 5 h. This difference in reactivity, which could stem from nucleophilic vs. electrophilic polarization of the Si-H bond by these carbenes, could potentially allow for the development of site-selective functionalization of silicon surfaces.

Although **6** showed promise for Si-H insertion reactions on surfaces, we sought a carbene that could insert even more rapidly into the Si-H bond of TTMSS. Having surveyed the carbene literature, we recognized acyclic diaminocarbene (ADAC) **7**[31,49,50] as a promising candidate due to its reportedly increased nucleo- and electrophilicity compared to **6**[48] and its considerably smaller steric bulk. Although as a free carbene **7** decomposes with a half-life of a few hours at 0°C in THF, it can be considerably stabilized towards decomposition by coordination to Li(I)
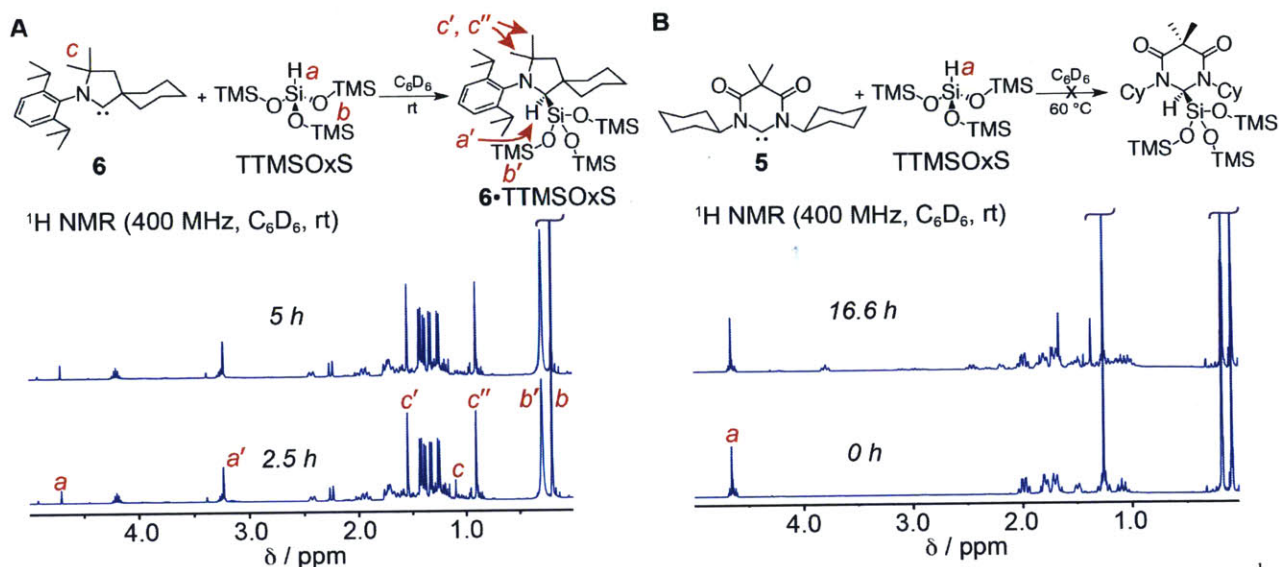
Figure 5. A.–B. Comparison of the insertion reactivity of **6** (A) and **5** (B) toward TTMSOxS, monitored by ^{1}H NMR spectroscopy.

species.[31,49,50] For instance, Alder and coworkers found that the use of a non-coordinating solvent (e.g., toluene-d^8) and a lithium base (e.g., lithium diisopropylamide (LDA) or lithium 2,2,6,6,-tetramethylpiperidine) or the addition of exogenous LiOTf could extend the half-life of **7** to many days at room temperature.[49] Guided by these precedents, we generated **7** by treatment of a suspension of **7•**HCl in toluene-d^8 at -78 °C with pre-cooled solution of LDA in toluene-d^8 (concentration of **7•**HCl in toluene-d^8 is 0.15 M).

The insolubility of **7•**HCl led to relatively long reaction times (>10 min) even upon warming to 23 °C, which led to the simultaneous generation of **7**, its dimer ((**7**)$_2$),[31] and small quantities of unidentified side-products, as detected by ^{1}H NMR. Depending on whether more or less LDA was used, **7** was accompanied by less or more dimer, respectively. To illustrate this behavior, when only 1.04 equivalents of LDA were used, deprotonation was complete after 100 min, and the ratio **7**:(**7**)$_2$ was 2:1; **7** and (**7**)$_2$ combined constituted 50% of the **7•**HCl conversion (Figure 6A). In contrast, when 2.5 equivalents of LDA were used, ~40 min was sufficient to complete the deprotonation, and the ratio of **7**:(**7**)$_2$ was 8.9:1 (Figure 6A). The ^{1}H NMR resonance corresponding to **7** shifted upfield from 2.80 ppm to 2.62 ppm in the presence of excess LDA, confirming a substantial impact of **7•**Li^{+} coordination in the latter case. Addition of 1 equivalent of TTMSS (relative to **7•**HCl) to each of the solutions of **7** led to the consumption of the carbene via Si-H insertion (rapid relative to carbene dimerization), but at noticeably different rates: within **8 min**, the reaction was already complete when 1.04 equivalents of LDA were used, but

131
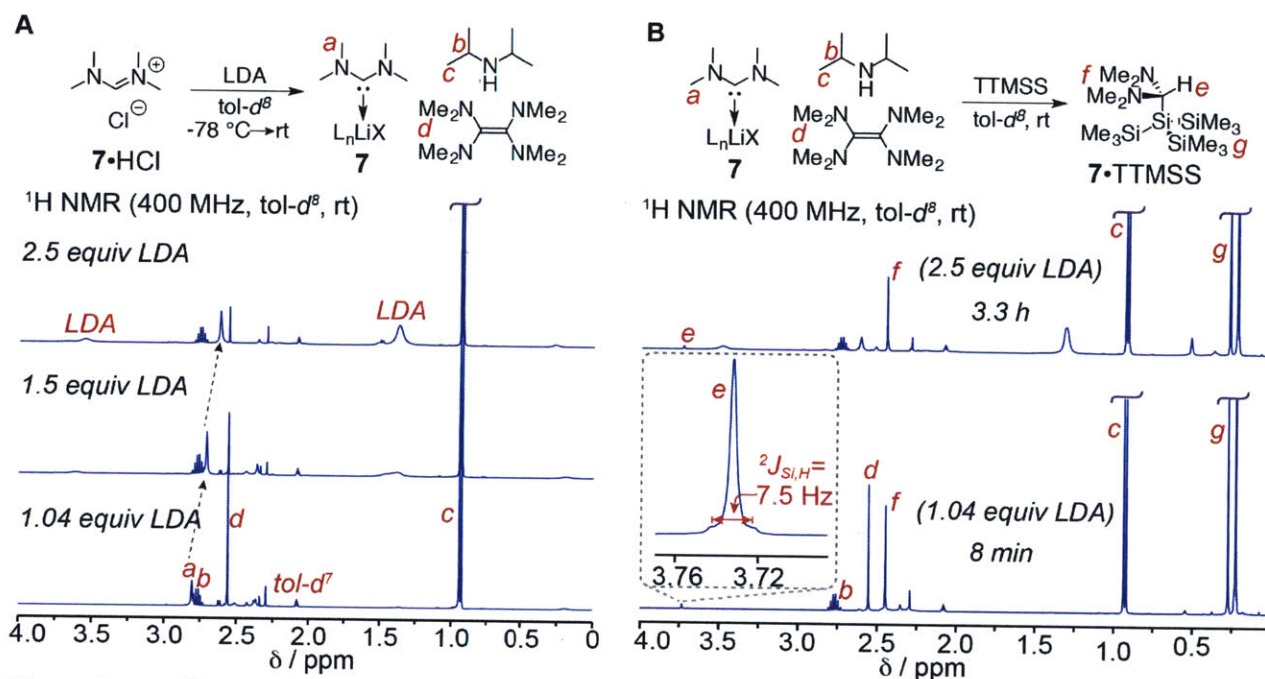
Figure 6. A. Effect of LDA equivalents on the formation of **7** from **7•HCl**, judged by ^{1}H NMR spectroscopy. **B.** ^{1}H NMR analysis of the reaction of **7** (generated using 1.04 or 2.5 equiv LDA) with TTMSS to form **7•TTMSS**. Inset zooms in on the aminal methine proton *e* of **7•TTMSS**.

when 2.5 equivalents of LDA were used, 17.2 h was necessary to reach 89% conversion (Figure 6B). The insertion product has a methine proton with a characteristic singlet resonance at 3.73 ppm with satellite peaks arising due to the ^{29}Si-^{1}H coupling with $^2J_{Si,H} = 7.5$ Hz, and its structure was verified by 1D and 2D NMR and FTICR-MS (Figure 6B, Experimental).

In the context of Si-surface functionalization (*vide infra*), we elected to use the conditions under which **7** was more reactive (1.04 equivalents of LDA) because we sought rapid surface functionalization. As noted above, dimerization also proceeds under these conditions, but 26.5% of **7** remained after 4.5 h at 23 °C, so this background process was not expected to impact H-**Si** functionalization.

2. Si NP studies

We next proceeded to explore carbene Si-H insertion in the context of Si NPs. H-**SiNPs** were prepared via the well-established sol-gel/hydrofluoric acid-etch method[51-54] (see Experimental). H-**SiNPs** are known to be difficult to disperse in organic solvents,[55] and accordingly, only aggregates of particles could be observed by transmission electron microscopy (TEM) (Figure 7A). Attenuated total reflectance (ATR)-FTIR spectroscopy indicated that the produced H-**SiNPs** contained a mixture of surface silicon mono-, di-, and tri-hydride functional groups

characterized by Si-H stretching resonances at 2081, 2098, and 2132 cm^{-1}, respectively (Figure 8A).[6,56] Additionally, ATR-FTIR detected a small Si-O stretch resonance centered at 1070 cm^{-1} (see Experimental), consistent with the X-ray photoelectron spectroscopy (XPS) results (*vide infra*).

H-**SiNPs** were treated with **6** or **7** under similar reaction conditions as the model silanes (see Experimental); in both cases a reaction was evident from the gradual color change of the liquid phase from light yellow to dark brown. The two sets of isolated NPs (**6•SiNP** and **7•SiNPs**, see Experimental) possessed notable differences in color and dispersibility: **6•SiNPs** changed from tan to dark brown upon drying *in vacuo*, while the **7•SiNPs** remained tan; furthermore, the latter were hardly re-dispersible in toluene-d^8, while the former were essentially completely re-dispersible in C$_6$D$_6$; the colloidal dispersion was stable on the timescale of hours, although precipitation was observed after ~2d.
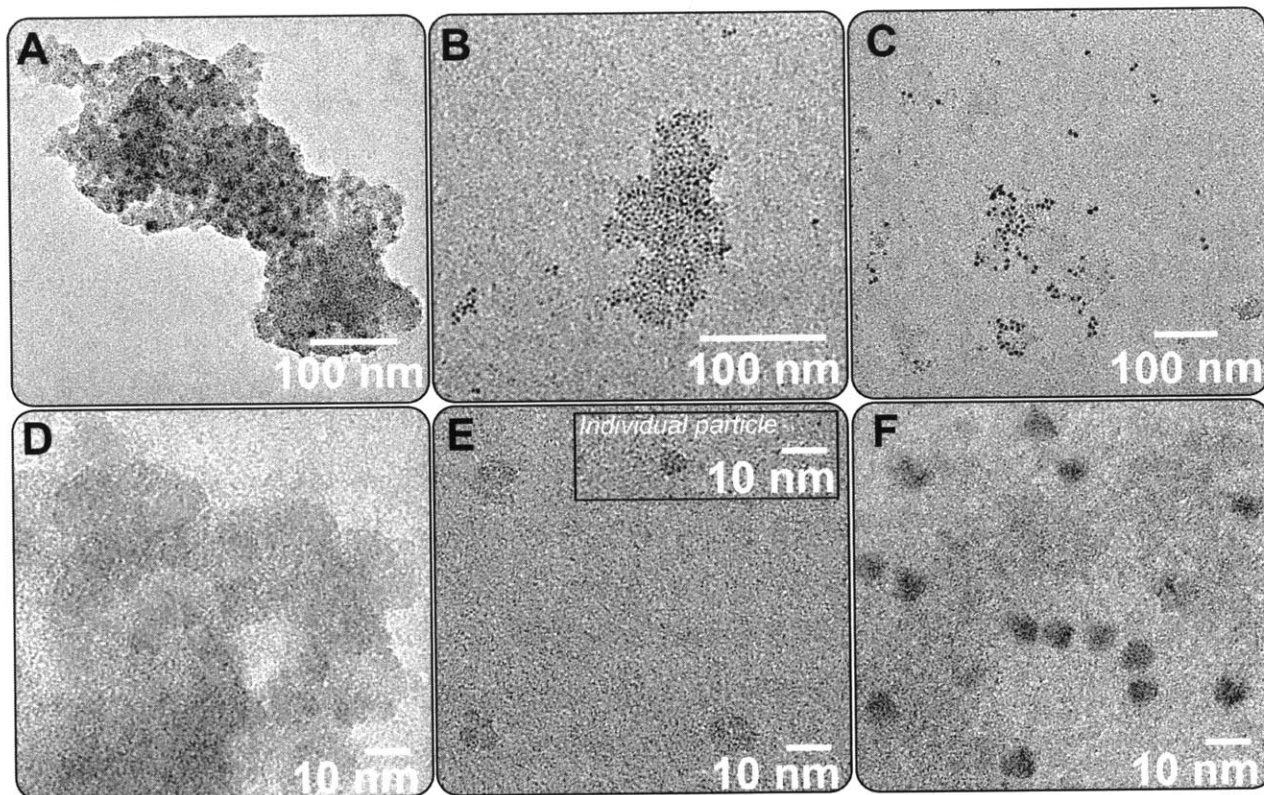
Figure 7. A.–F. TEM micrographs of H-**SiNPs** (A, D: zoomed in), **6•SiNPs** (B, E: zoomed in), and **7•SiNPs** (C, F: zoomed in). Inset in (E) illustrates an example of isolated **6•SiNPs** found on the TEM grid.

TEM of the dispersible fractions of both sets of NPs revealed more subtle differences between them (Figures 7B–C, 7E–F): perhaps due to a thicker organic coating, **6•SiNPs** displayed lower contrast with the carbon film background compared to **7•SiNPs** (Figures 7E-F);

133

furthermore, while **7•SiNPs** were generally either isolated or paired (Figures 7C, 7F), **6•SiNPs** were observed isolated (Figure 7E, inset), in clusters of 3–4 overlapping NPs (Figure 7E), and in arrays of tens–hundreds of NPs (Figure 7B). Lastly, although both sets of NPs displayed a mixture of circular and triangular shapes, the two sets of particles exhibited differences in diameter distributions: 2.7 ± 0.5 nm for **6•SiNPs** vs 6.4 ± 1.7 nm for **7•SiNP** (each determined from measurement of 250 particles; see Experimental). Similar NP size-selection due to the carbene steric bulk/curvature has been observed in previous studies of NHC-modified metal nanoparticles.[57,58]
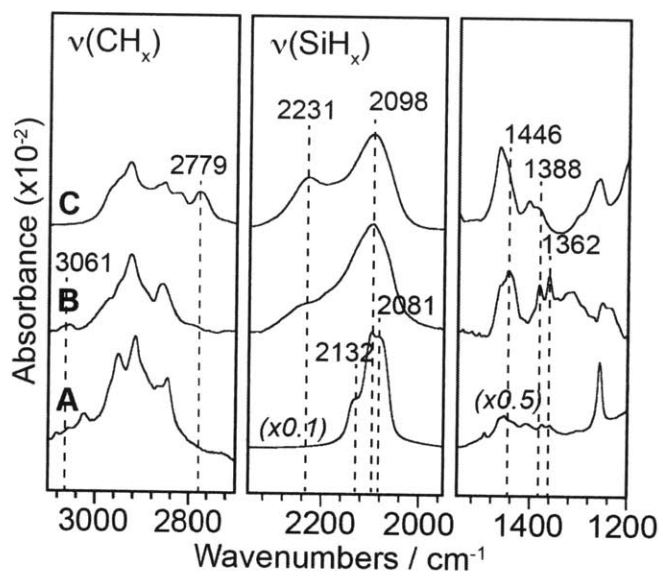
Figure 8. **A.–C.** ATR-FTIR spectra of H-**SiNPs** (A), **6•SiNPs** (B), and **7•SiNPs** (C). All absorbance values are relative to air.

ATR-FTIR (Figure 8) provided further evidence for the reactions of **6** and **7** with H-**SiNPs**. The relative intensities and frequencies of the specific CH_x stretching peaks in **6•SiNP** and **7•SiNP** are consistent with the attachment of **6** and **7** to SiNP surface sites. Two particularly notable differences in the CH_x regions between **6•SiNPs** and **7•SiNP** are (1) the resonance at ~3061 cm^{-1} present only in the spectrum of the former and (2) the resonance at ~2779 cm^{-1} present only in the spectrum of the latter. These have been assigned to the aromatic and aminal C-H stretches respectively (*vide infra*). Additionally, carbene-specific spectral differences could also be observed in the region between 1550 and 1200 cm^{-1} (Figure 8): a pair of sharp resonances at 1362 and 1388 cm^{-1} and a broader resonance centered at 1446 cm^{-1} were present only in the spectrum of **6•SiNPs**; similar features shifted to higher frequencies were noted for **7•SiNPs**, but not H-**SiNPs**. Additionally, it is important to note that some surface oxidation –

134
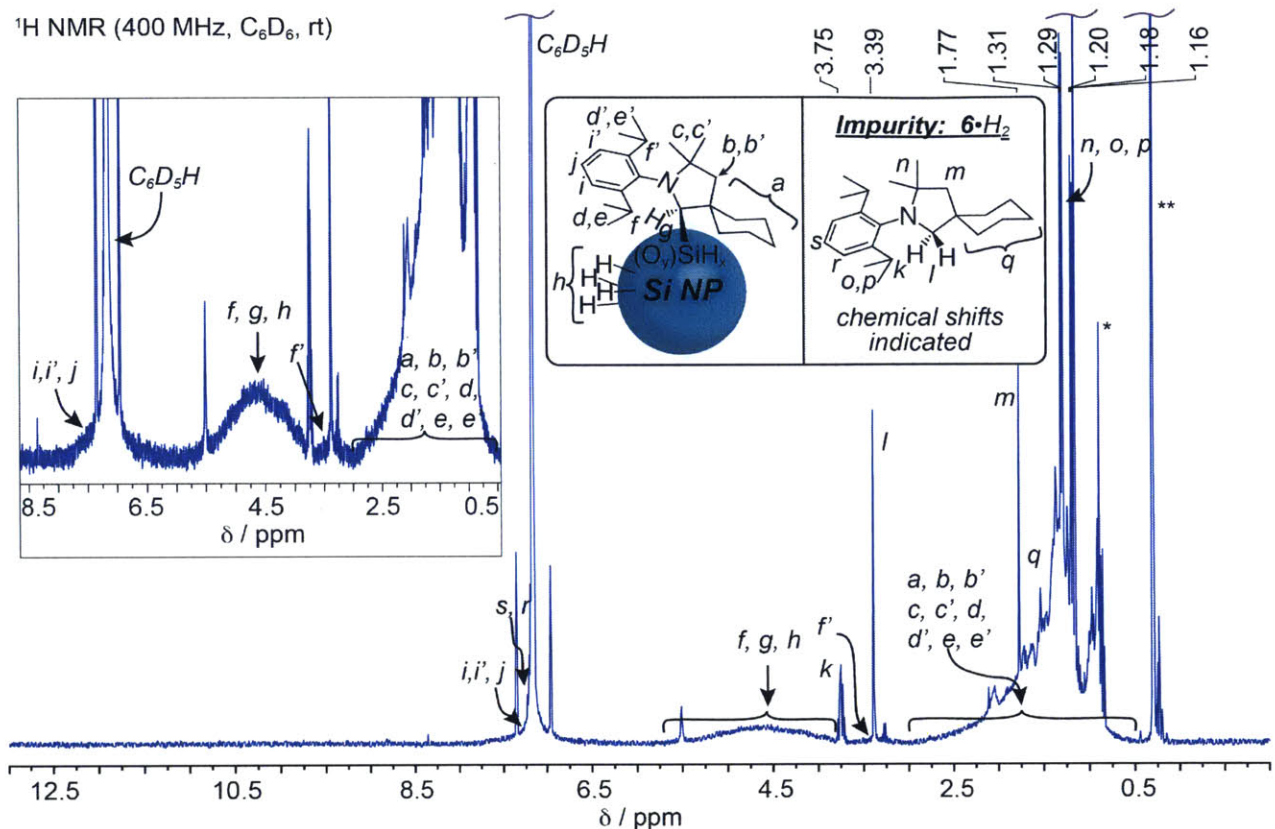
Figure 9. Solution ^{1}H NMR (400 MHz, C$_6$D$_6$, rt) spectrum of the re-dispersed **6•SiNPs**. Chemical shifts are indicated for the visible peaks corresponding to the trace **6•H$_2$**. Inset on the left zooms in on the broad resonances of **6•SiNPs**. *Hexanes resonances. **Silicone grease resonance.

more pronounced in the case of **7•SiNPs** – was evident from the appearance of a high-frequency shoulder at ~2231 cm^{-1} in the spectra of both **6•SiNPs** and **7•SiNPs** (Figures 8B–8C) and the concomitant growth of a Si-O stretching resonance (centered at 1030–1070 cm^{-1}, see Experimental). The source of and different sensitivity to oxidation are intriguing questions that will be addressed in a subsequent investigation.

^{1}H NMR spectroscopy of the isolated **6•SiNPs** re-dispersed in C$_6$D$_6$ revealed broad resonances in the ranges of 7.8–6.5 ppm, 5.8–3.6 ppm, 3.7–3.0, and 3.0–0.5 ppm (Figure 9), corresponding to **6•SiNPs**, as well as a set of sharp resonances corresponding to the dihydrogen adduct of **6** (**6•H$_2$**) formed in ~6% yield during the treatment of **6•HCl** with LDA (see Experimental). The broad nature of the peaks corresponding to **6•SiNP** is consistent with slowed tumbling of rigid ligands attached to NPs.[59] Based on the ^{1}H NMR spectrum of **6•TTMSS** (Figure 4A), the 3.0–0.5 ppm range was assigned to the cyclohexyl, methyl, and methylene protons present in the bound **6**, and the 3.7–3.0 range was assigned to one of the methine protons of the bound **6** (*f'* in Figure 9). Methine protons *f* and *g*, expected to be more downfield (see

Figure 4a), were assigned to the broad feature in the range 5.8–3.6 ppm; however, given the relative areas of f' (0.06), f and g were only expected to contribute 0.12 to this feature's total area (1.00); the remainder of the area was assigned to clustered silicon monohydrides (h in Figure 9), based on prior magic-angle spinning (MAS) NMR assignments of similar features[60,61] (Notably, no prior reports of solution ^{1}H NMR of fully or partially H-terminated SiNPs could be found). These areas allowed us to make a rough (due to peak overlap and breadth) estimate that 6–7% of the Si-H sites of H-**SiNPs** have been functionalized with **6**. Lastly, the aromatic protons of bound **6** were assigned to the broad peak between 7.8 and 6.5 ppm, which overlapped with the C_6D_5H resonance and a set of sharp resonances from **6**•H_2. These data, in conjunction with the XPS spectroscopy discussed in detail below, were consistent with carbene insertion-functionalization of H-**SiNPs**.
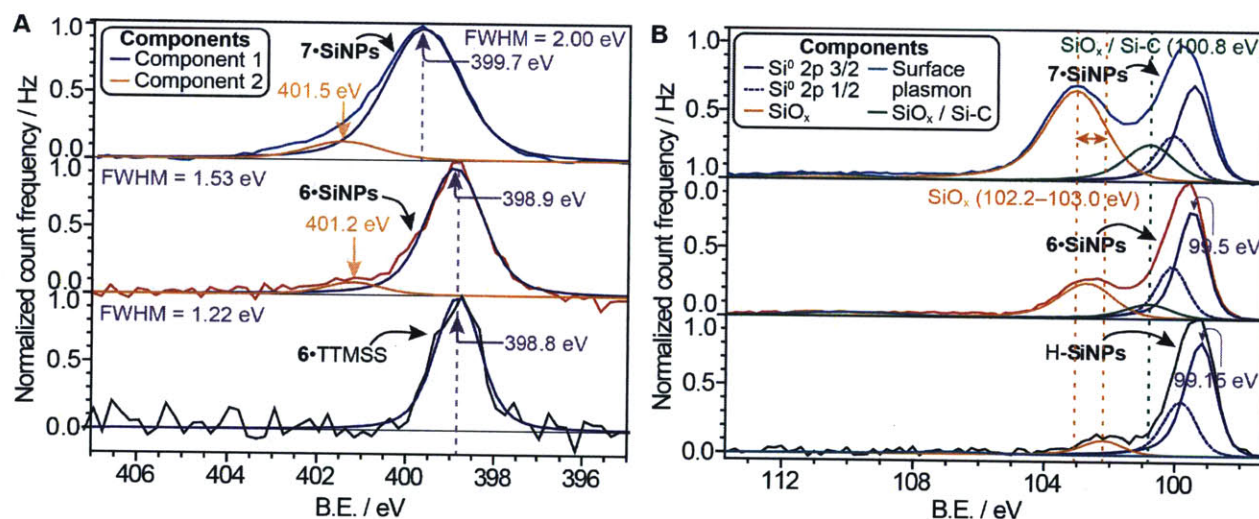
Figure 10. A. Comparison of the XPS N 1s regions of **6•TTMSS**, **6•SiNPs**, and **7•SiNPs**. **B.** Comparison of the XPS Si 2p regions of H-**SiNPs**, **6•SiNPs**, and **7•SiNPs**.

Analysis of the N1s region of the XPS data for the functionalized NPs, **6•TTMSS**, and protonated carbene precursors offered additional insight into the chemical identity and environment of the bound carbene species (Figure 10A). **6•TTMSS** and **6•SiNP** both displayed a prominent peak with the B.E. of 398.8–398.9 eV (Figure 10A), which was 3.0 eV below the B.E. observed for **6•HCl** (see Experimental). These data provide strong evidence for the insertion of **6** at the H-**SiNP** surface. Similarly, inspection of the XPS N 1s region of **7•SiNPs** (Figure 10A; note: **7•TTMSS** was too volatile to be analyzed via ultra-high vacuum XPS) revealed a peak with a B.E. of 399.7 eV, ~0.8 eV higher than for **6•SiNPs** and consistent with the expected aliphatic

amines in the monolayer.[18] Absence of a peak at 400.9 eV (N 1s B.E. of **7•HCl**, see Experimental) rules out the presence of the protonated **7** in the **7•SiNPs** sample.

Another salient feature of the N 1s regions for the surfaces, in contrast with **6•TTMSS**, is the 1.3–1.6 times greater full-width half maximum (FWHM) for the former (Figure 10A), which is consistent with the binding of **6** and **7** to not only the monohydride, but also the di- and tri-hydride as well as oxidized surface sites. Lastly the presence of minor (~9–12% area) N 1s peak components at higher B.E. for both **6•SiNPs** and **7•SiNPs** (Figure 10A) was ascribed to decomposition during extended Al Kα X-ray irradiation – XPS of **6•TTMSS** for a similar duration resulted in the formation of a new component (~5% area) at 400.7 eV (Figure 11).
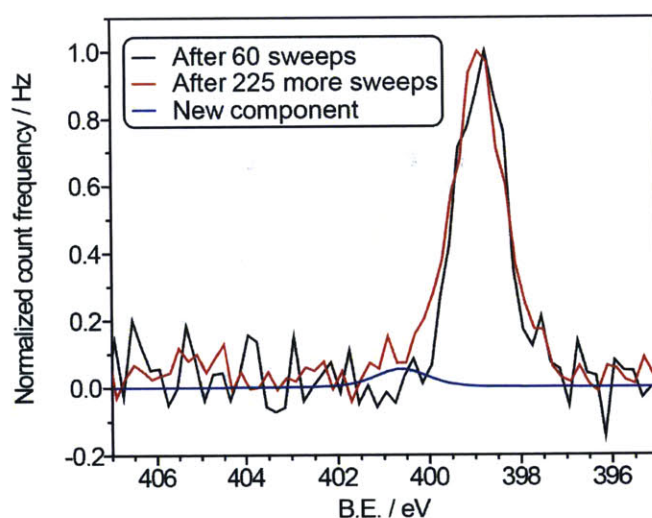
Figure 11. XPS N1s region of 6•TTMSS after 60 sweeps and after 225 more sweeps (same spot). The appearance of a new component (in blue, ~5% area) is observed.

The silicon region of the XPS spectrum was consistent with the ATR-IR results (*vide supra*) in that compared to H-**SiNPs**, **6•SiNPs** experienced a moderate increase in the silicon suboxide $(SiO_x)^{6,56,62,63}$ component, (from 10% in H-**SiNPs** to 25% in isolated **6•SiNPs**), with an increase in its B.E. to 102.7 eV (Figure 10B); **7•SiNP** exhibited a SiO_x peak at 103.0 eV, which constituted 44% of the observed Si 2p signal. Note that the assignment of the higher-B.E. Si 2p peaks to silicon *sub*oxides was supported by comparison to those observed for the H-**SiNP** precursors: 103.4 eV for $(HSiO_{1.5})_n$ and 103.8 eV for SiNPs embedded in a SiO_2 matrix (Figure 12). As mentioned above, the observed oxidation could occur during the course of functionalization or it could be the result of increased SiNP air-sensitivity after carbene functionalization; future studies will seek to further understand this oxidation process with the

ultimate goal of controlling it. However, based on the presented spectroscopic evidence, the oxidation is not detrimental to surface functionalization via carbene insertion.
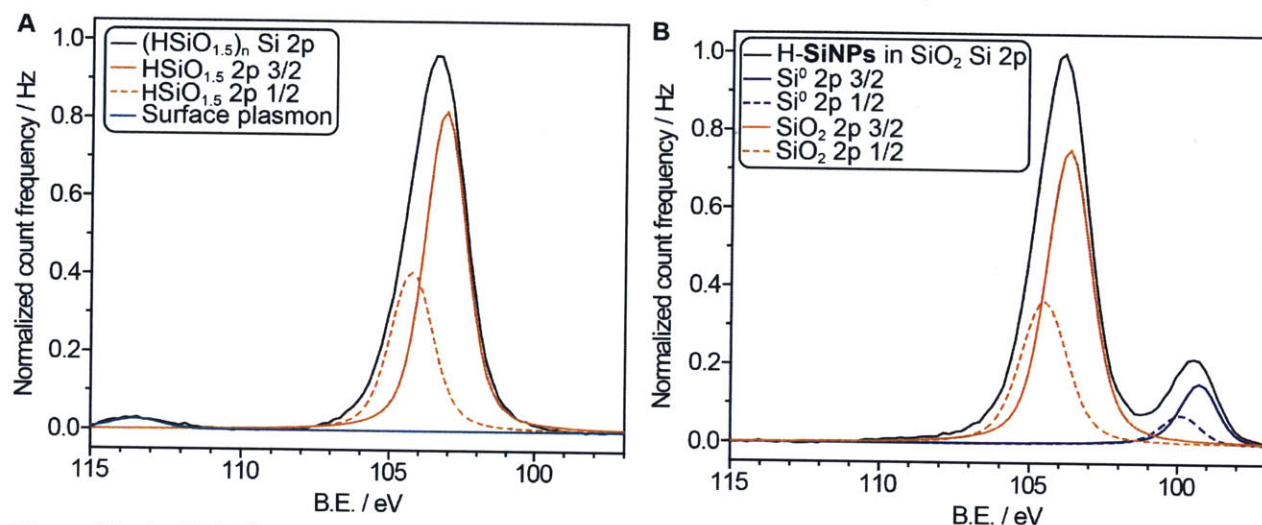
Figure 12. **A.** XPS Si 2p region of $(HSiO_{1.5})_n$. **B.** XPS Si 2p region of the SiNPs embedded in SiO_2, obtained after thermally annealing $(HSiO_{1.5})_n$ (see Experimental).

The Si 2p regions had low-intensity and broad but detectable features ~11 eV higher in B.E. than the Si^0 2p 3/2 peak (see inset in Figure 10B), which were assigned to surface plasmon energy loss.[64] Lastly, in the carbene-treated SiNP samples, improved fits for the Si 2p region were obtained when a component at 100.8 eV (Figure 10B, green trace) was incorporated. This component had greater intensity for **7·SiNPs** compared to **6·SiNPs** and was proposed to correspond to carbene-bound silicon atoms (Si-C) and low-oxidation state SiO_x.[62] This disparity in the oxidation state of the carbene-functionalized silicon surfaces and the nature of the carbenes likely contribute to the observed differences in SiNP color, dispersibility, and diameter.

3. Si wafer studies

Advancing to planar surfaces, we chose to focus on hydrogen-terminated Si(111) wafers (H-**Si(111)**); hydrogen-termination is typically more well-defined for these types of surfaces compared to Si(100).[6,65] An ideal H-**Si (111)** surface features a regular 2-D array of Si-H bonds positioned normally to the surface at atop silicon sites separated from each other by single tetravalent silicon atoms. XPS analysis of these wafers and sub-monolayer silicon oxide quantification following the method introduced by Lewis and Haber[66] confirmed that the content of the oxidized atop silicon sites was generally low (0-9% with an average of ~5% for all of the tested batches of etched wafers; see Scheme 1 in the Experimental).

138

Freshly etched wafers were exposed to a 0.048 M solution of **6** in C_6D_6 at 23 °C, as in the model studies. The insertion process for wafers was monitored by XPS. Based on the relative nitrogen content and substrate-overlayer model analysis (see Experimental), the coverage of Si(111) atop sites by **6** (Φ_6) was found to have reached 12±1% after a 10-minute exposure and saturated at 21±3% after three days (Figure 13A). This saturation coverage implies that 21±3% of the surface Si-H bonds reacted with **6**, and it is consistent with the maximal coverage of Si(111) atop sites (~20%) expected from computed structures of **6** bound to atomically rough surface models (*vide infra*).

In the case of **7**, the wafers were rinsed for ~20 sec with MilliQ™ water prior to analysis to remove physisorbed lithium-, chlorine-, and nitrogen-containing species, as confirmed by XPS. For the 20-min and 4-h treatment times, virtually identical Φ_7 was seen: 9±1% (Figure 13A). This relatively low coverage compared to the expected maximum ≥25% (based on computed surface, *vide infra*) is hypothesized to result from competitive physisorption of the species described above, as well as competitive dimerization of **7**.

Similarly to **6·TTMSS** and **6·SiNP**, the N 1s region of **6·Si(111)** XPS data exhibited a peak at the B.E. of 398.8 eV, consistent with the insertion of **6** at the H-**Si(111)** surface (Figure
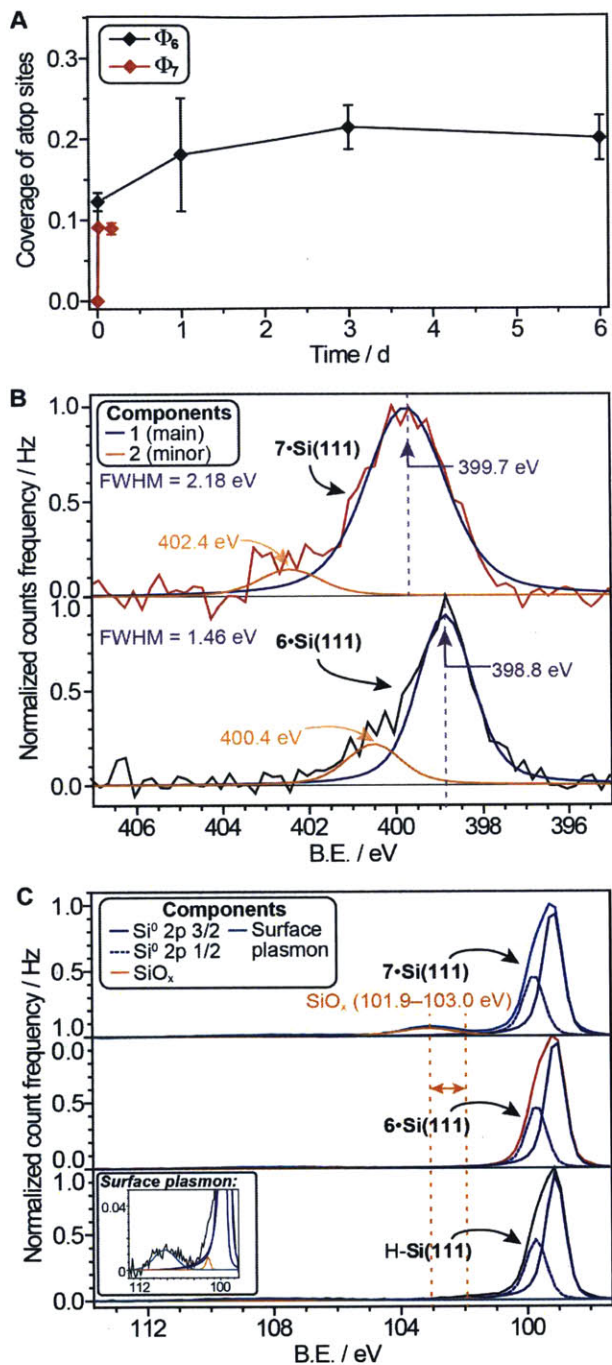
Figure 13. A. Carbene coverage of **Si(111)** by carbenes **6** and **7** from XPS. For all timepoints, averages were determined from ≥4 values, except the 10-min timepoint for **6** and 20-min timepoint for **7** (2 values for each). Error bars represent standard deviations. B. N 1s regions for **6·Si(111)** and **7·Si(111)**. C. Si 2p regions for H-**Si(111)**, **6·Si(111)** and **7·Si(111)**.

13B). Likewise, the N 1s region for **7•Si(111)** had a peak at 399.7 eV, which is identical to the value observed for **7•SiNPs**. The FWHM values observed for Si wafers were also approximately the same as those for SiNPs, which suggested that the carbenes were binding to different surface sites (*vide infra*). The additional component (~20% of the peak area, Figure 13B) at 400.4 eV in the N 1s region of **6•Si(111)** could arise, as in the case of **6•SiNPs**, through X-ray-induced decomposition. Aqueous wash, did not eliminate this component or significantly alter Φ_N (~5% change), but instead resulted in additional silicon surface oxidation (see Scheme 2 in the Experimental), with concomitant shift of the N 1s peak by +0.2–0.3 eV and increase in FWHM by ~64% (see Scheme 2 in the Experimental), which supported the proposed origin of the high-B.E. component and the elevated FWHM. The N 1s region of the **7•Si(111)** (rinsed with H_2O), also exhibited a minor peak component at 402.4 eV (Figure 13B), which is nearly identical to what has been previously noted for polyethyleneimine-ethoxylated (PEIE) (sub-)monolayers deposited from pH = 7 solutions or rinsed with H_2O (pH = 7).[18] The component at 402.4 eV was assigned, by analogy with PEIE, to the protonated (or H-bonded to H_2O) amine groups.[18] Finally, analysis of the Si 2p region (Figure 13C) revealed that **7•Si(111)**, like **7•SiNPs,** experienced substantial (72% SiO_x) surface oxidation, while treatment with **6** had virtually no effect on the state of oxidation of the **Si(111)** wafers,. Collectively, the XPS data are qualitatively consistent with the data obtained for SiNPs; they strongly support the expected structure of the monolayers derived from carbene insertion into surface Si-H bonds.

Transmission FTIR spectroscopy of H-**Si(111)** wafers treated with **6** and **7** (Figure 14) also indicated structural correspondence between the planar surfaces, SiNPs, and the model compounds in this study. IR spectra were acquired for two separate samples reacted with each carbene; while there were small differences between samples in the total amount of surface functionalization, the resulting spectra were qualitatively the same. It is important to note at the outset that the spectrum of the initial H-**Si(111)** surface in Figure 14A demonstrates that our surface had significant atomic roughness[67,68] compared to the ideal monohydride-terminated Si(111) surface. The sharp peak at the center of the SiH stretching band (2083 cm⁻¹) arises from monohydride terraces, while the prominent shoulders at ~2067 and ~2094 cm⁻¹ correspond to coupled step monohydride (M) defects (symmetric and asymmetric vibrations, respectively). The higher-frequency tail extending out to ~2150 cm⁻¹ is likely due to dihydride (D) and trihydride (Tr) defects.[67,68] We were unable to definitively rule out higher-frequency peaks

corresponding to minority (SiO)₃SiH species due to the presence of an N_2O resonance in the same region from a small amount of impurity in the spectrometer purge gas; however, no significant Si-O stretching peaks were detected on the untreated H-**Si(111)** wafers.
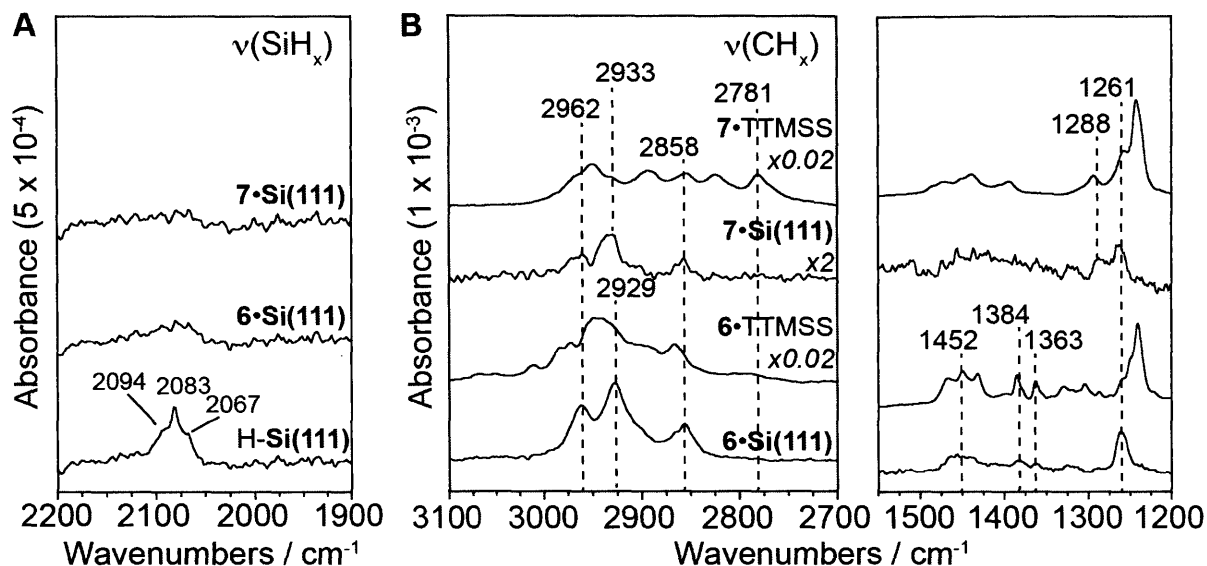
Figure 14. A.–C. Transmission FTIR spectra of (A) the Si-H stretch region of untreated and carbene-treated H-**Si(111)** wafers, ratioed to a fully oxidized (SiH$_x$-free) Si(111) surface, and (B) the 3500–2500 and 1650–1250 cm^{-1} regions of the carbene-treated H-**S(111)** wafers, ratioed to the untreated surface, compared to the corresponding TTMSS-carbene adducts.

Integration of the Si-H stretching signal from carbene-treated H-**Si(111)** wafers gave an estimated 36% conversion of the Si-H bonds upon reaction with **6** and 70% conversion upon reaction with **7**. As is evident in Figure 14A, the initially sharp $v(SiH_x)$ bands broaden considerably after reaction with the carbenes, which renders integration of this peak – and therefore the calculated Si-H conversion – sensitive to small variations in baseline; these values should therefore be considered as rough estimates. Additionally, some surface oxidation was observed for both **6•Si(111)** and **7•**Si(111), which likely accounts for some of the decrease in surface SiH$_x$ species by replacement with surface SiOH or (SiO)₃SiH species.[69] The extent of surface oxidation, estimated by integration of the Si-O stretching bands in the two samples of each reaction type at ~1000–1150 cm^{-1} (see Experimental) and comparison with the intensity of the SiO_2 phonon signal from a chemical oxide, ranged from 28-33% of a full oxide layer after reaction with **7** and from 5-24% of a full layer after reaction with **6**. These values are qualitatively consistent with the extent of oxidation determined by XPS.

The spectra in Figure 14B illustrate the changes in vibrational modes upon treatment of H-**Si(111)** with **6** and **7** and draw a comparison with the TTMSS adducts of both carbenes. Thus,

141

spectra of both **6•Si(111)** and **6•TTMSS** display a band between 1415 and 1490 cm^{-1} (centered at ~1452 cm^{-1}), as well as the peaks at 1384 and 1363 cm^{-1}, which, guided by density functional theory (DFT) computations (see Experimental) and literature,[70] have been assigned as follows: 1415–1490 cm^{-1} – to CH$_3$ and CH$_2$ asymmetric deformation vibrations, and 1363 and 1384 cm^{-1} – to CH(CH$_3$)$_2$ or C(CH$_3$)$_2$ fragment symmetric deformation vibrations. On the other hand, **7•Si(111)** and **7•TTMSS** both display a resonance at ~1288 cm^{-1}, assigned to a "wagging" vibration mode spanning multiple C-H and C-N bonds in **7** (Figure 14B). These features map well onto those observed for the corresponding SiNP samples (Figure 8).

The C-H stretch regions of the IR spectra of **6•TTMSS** and **7•TTMSS** were also quite similar to those of **6•SiNPs** and **7•SiNPs**, respectively. Namely, the spectrum of **7•TTMSS** displayed a resonance at 2781 cm^{-1} not present in the spectrum of **6•TTMSS**, while the latter alone had a low-intensity peak between 3034 and 3069 cm^{-1} corresponding to aromatic C-H stretches. DFT computation of the vibration frequencies of **7•TTMSS** indicated that, as expected,[70] the aminal C-H bond stretch has the lowest stretching frequency of the C-H bonds in the molecule – namely, 2809 cm^{-1}. Given that overestimation by, on average, 30–50 cm^{-1} is typical for DFT computations of vibrational frequencies using the PBE functional,[71,72] this value is in excellent agreement with the observed resonances at 2781 cm^{-1} (2770 cm^{-1} in SiNPs). Although these weak "marker" C-H stretch resonances were difficult to discern in the spectra of **6•Si(111)** and **7•Si(111)**, differences in relative peak intensities in the C-H stretch region for these two sets of samples are consistent with the disparity in their monolayer composition.
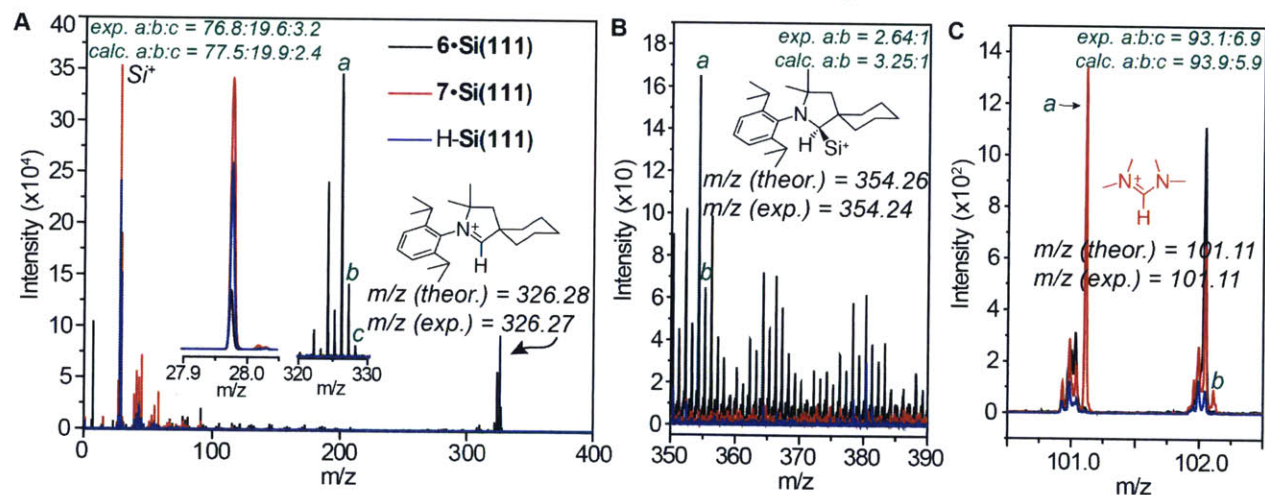
Figure 15. **A.** TOF-SIMS spectra (m/z = 0–400 Da) of H-**Si(111)** surfaces before and after functionalization with **6** and **7** (insets zoom in on Si$^+$ and 6•H$^+$ ions peaks). **B.** TOF-SIMS spectra zoomed in on the region where peaks corresponding to Si-bound **6** ions may be found. **C.** TOF-SIMS spectra zoomed in on the region where peaks corresponding to the 7•H$^+$ ions may be found.

To complement the spectroscopic data for the Si(111) wafers, time-of-flight secondary ion mass spectrometry (TOF-SIMS) was carried out on a set of wafers before and after carbene treatment. Analysis of **6•Si(111)** wafers revealed a new dominant peak at m/z = 326.27 Da (Figure 15A), which corresponds within 52 ppm (and with an identical isotope pattern) to **6•H$^+$**. A weaker signal at 354.24 was also observed, which was consistent (within 62 ppm) with **6•H(Si)$^+$** (Figure 15B). C–Si fragmentation to yield **6•H$^+$** was similarly dominant in the FTICR-MS of the **6•TTMSS** adduct (see Experimental). TOF-SIMS of **7•Si(111)** likewise revealed an ion peak that was unique to this surface among the three tested (Figure 15C): namely, the ion with m/z = 101.11, which, along with the isotope pattern, corresponded remarkably to the theoretical ones for **7•H$^+$**. In conjunction with the spectroscopic evidence above, these TOF-SIMS data strongly support the structural assignments of the carbene Si-H insertion-derived monolayers.

Lastly, the surface morphology was inspected for the Si(111) wafers before and after exposure to carbenes. As anticipated from the analysis of IR spectra (*vide supra*), nanoscopic surface roughness was observed by tapping-mode atomic force microscopy (AFM), which revealed an abundance of triangular etch pits of various lateral cross-sections (~70–160 nm) and depths (1–5 nm) (Figure 16A). Such features have been
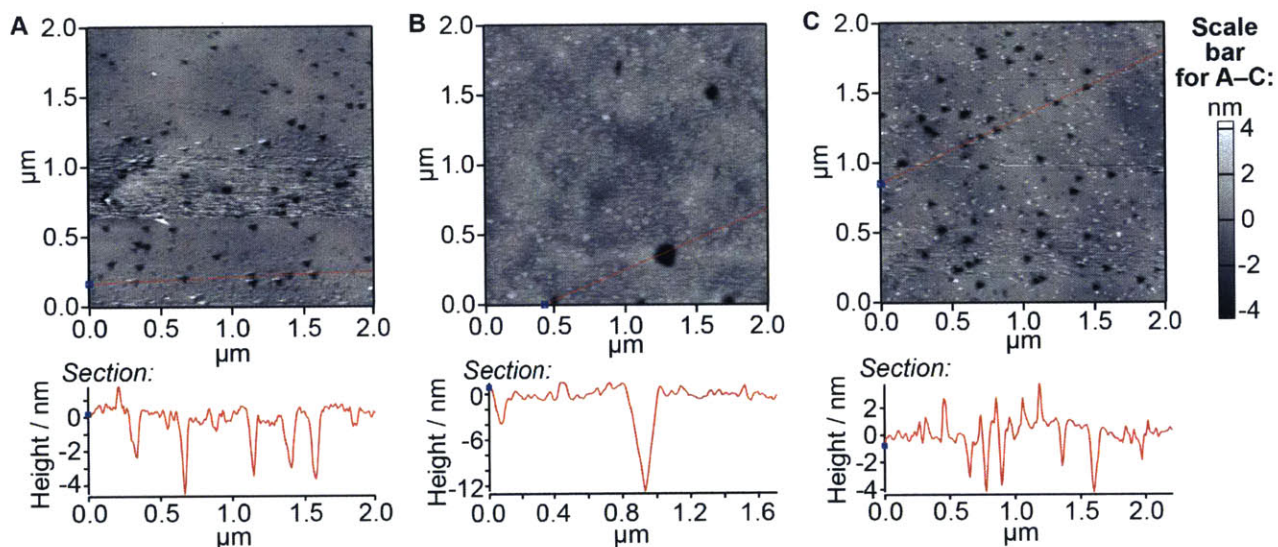
Figure 16. **A.–C.** Representative tapping-mode AFM height retraces for (A) an H-Si(111) wafer, (B) a **6•Si(111)** wafer rinsed with MilliQ™ water for ~30 s, and (C) a **7•Si(111)** wafer rinsed with MilliQ™ water for ~30 s, derived from the same batch of etched wafers. The red line in the images indicates the cross-sections, from which the height plots below the AFM images were generated.

previously been demonstrated to result from the presence of dissolved oxygen in aqueous etchants.[73,74] Inspection of the AFM height retraces for **6•Si(111)** and **7•(111)**,both briefly rinsed with water, revealed clear morphological differences between these surfaces and also in comparison with H-**Si(111)** (Figure 16B–C). Specifically, while the density and size of "triangular" pits in **7•Si(111)** was roughly the same as in H-**Si(111)**, **6•Si(111)** exhibited fewer but larger ones (e.g. the ~12 nm deep and ~200 nm wide pit in Figure 16B). On the other hand, **7•Si(111)** appeared to have a much higher density of small elevated features compared to the other two. The origin of these morphological differences could stem from a combination of surface functionalization with carbenes as well as surface oxidation, as noted earlier.

4. Computational studies

To gain more insight into the thermodynamics of insertion of **6** and **7** into the Si-H bonds of TTMSS, TTMSOxS, and H-**Si** surfaces, as well as into the geometry of the resultant monolayers, we set out to investigate these systems computationally. As a valuable point of comparison, we also included **5** and its analogous insertion products in this study. We employed density functional theory (DFT) with the PBE functional[75] and 6-311g** basis set to model the structures, similarly to previous studies of organic monolayers on Si(111).[76,77]

ΔH = -14.5 kcal/mol   ΔH = -17.5 kcal/mol   ΔH = -26.5 kcal/mol
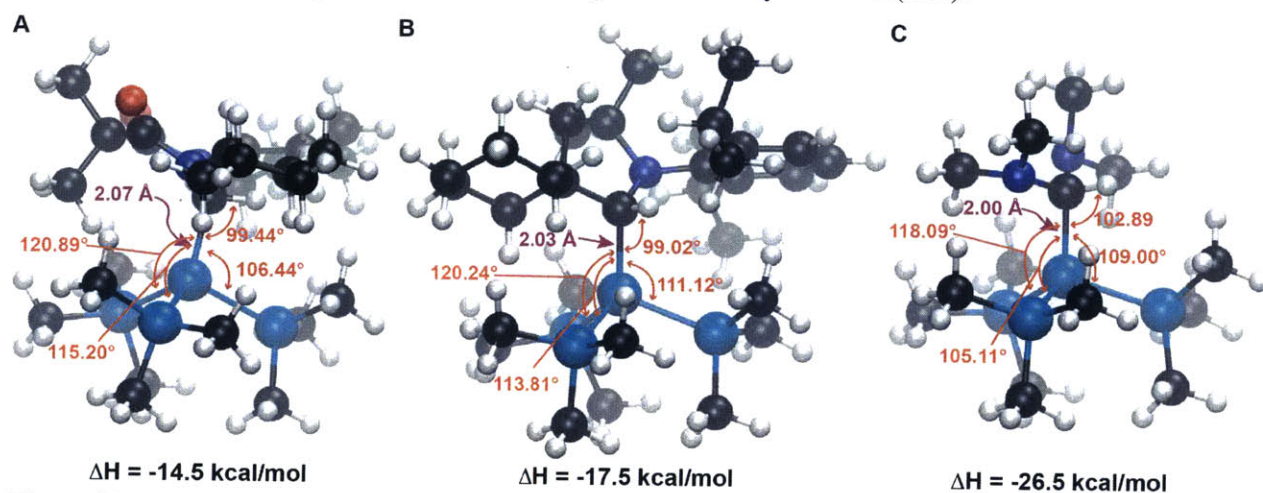
Figure 17. **A.–C.** Computed energy-minimized structures (represented as ball-and-stick models) of **5•**TTMSS (A), **6•**TTMSS (B), and **7•**TTMSS (C). Hydrogen atoms are in white, carbon – in black, nitrogen – in blue, oxygen – in red, and silicon – in cyan.

Comparing the TTMSS adducts, we find that for all three carbenes, the enthalpy change (ΔH) for the Si-H insertion is moderate in magnitude and negative (Figure 17A–C), consistent with the experimentally observed insertion reactivity. The ΔH appears to be positively correlated with the

Si-C$_{carbene}$ bond length and is greatest in magnitude for carbene **7** (-26.5 kcal/mol), for which this bond length is the shortest (2.00 Å). Notably, the C$_{carbene}$-Si bond lengths and the proximal Si-C$_{carbene}$-H bond angles for all structures both show sizable deviations from what might be expected for a Si$_{sp3}$-C$_{sp3}$ system (1.86 Å[78] and 109.5°, respectively). Furthermore, one of the three Si-Si-C$_{carbene}$ bond angles in each molecule is expanded to ~118–121°, which is due to the inclination of the Si-C$_{carbene}$ bond relative to the normal of the plane spanned by the "peripheral" Si atoms," most evident in Figure 17A.

We find a very similar pattern in the crystal structure of **6**•TTMSS (Figure 4C): the Si-Si-C$_{carbene}$ angles are equal to within 1.5°, and although the Si-C$_{carbene}$ bond length is 0.05 Å shorter (at 1.98 Å), and the Si-C$_{carbene}$-H bond angle is slightly larger (104.9°) – the difference which can be attributed to the self-interaction error inherent in DFT calculations – these results point to substantial steric interaction between the carbene- and TTMSS-derived portions of the molecules, which induces the observed structural distortions. Such distortions have previously been observed in bis(hypersilyl)methane, which has a similar steric bulk relationship between a tris(trimethylsilyl)silyl (*i.e.* hypersilyl) group and another molecular fragment attached to it.[79]
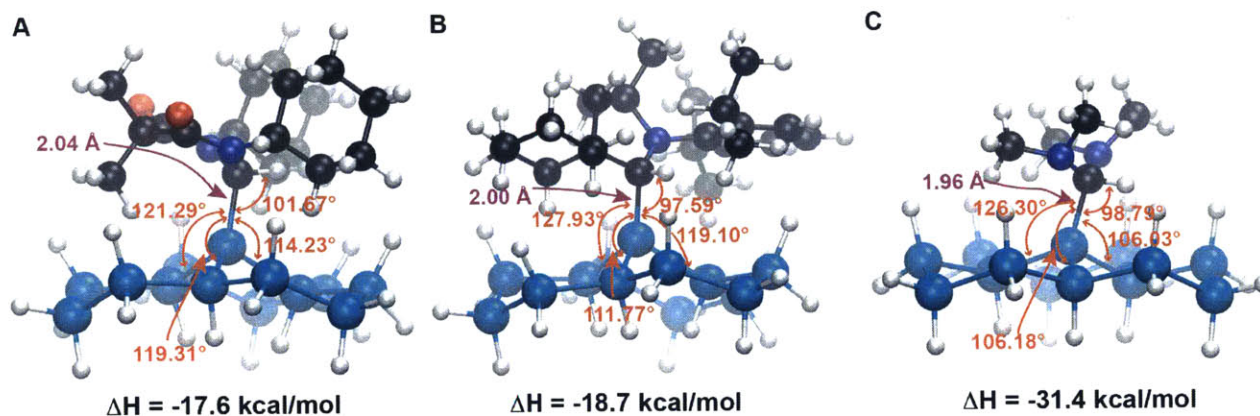
Figure 18. A.–C. Computed energy-minimized structures (represented as ball-and-stick models) of insertion products of **5** (A), **6** (B), and **7** (C) into the central Si-H bond of a 13-Si-atom, one-layer H-Si(111) surface model. Hydrogen atoms are in white, carbon – in black, nitrogen – in blue, oxygen – in red, and silicon – in cyan.

Extending these computations to surfaces, we designed a one-layer 13-Si-atom model of a H-**Si(111)** surface, for which valence of all silicon atoms was fulfilled via appended hydrogen atoms (Figures 18A–18C). This particular model was selected because it is the minimal such surface, whose size is large enough to span carbenes **5–7**, and thereby take steric effects between the carbene and the silicon surface into account. The computed ΔH values were slightly greater in magnitude for the Si$_{13}$ model (1.2–4.9 kcal/mol) than in corresponding TTMSS adducts, and

145

accordingly, the Si-C$_{carbene}$ bond lengths were slightly shorter, though the "tilt" of the Si-C$_{carbene}$ bond was still pronounced. A new feature that was not evident in the TTMSS adducts was the buckling of the silicon surface, which was absent in the case of **7**, but noticeable in the case of **5** and **6**, the more sterically demanding carbenes. This buckling presumably alleviates that steric strain that would otherwise be present.

To evaluate the likelihood that such a deformation might take place at a real, rigid silicon surface, we constructed a three-layer silicon model to test the insertion of **6**, a more sterically demanding carbene, and **7**, a less sterically encumbered one. The geometry of the three-layer model with no molecular adduct was allowed to relax; then, the bottom two layers of atoms were frozen in place, and the molecules **6** and **7** were inserted into the Si-H bond. The geometries of the top layer of the surface model plus the organic molecule were allowed to relax, with the bottom two layers held fixed at their
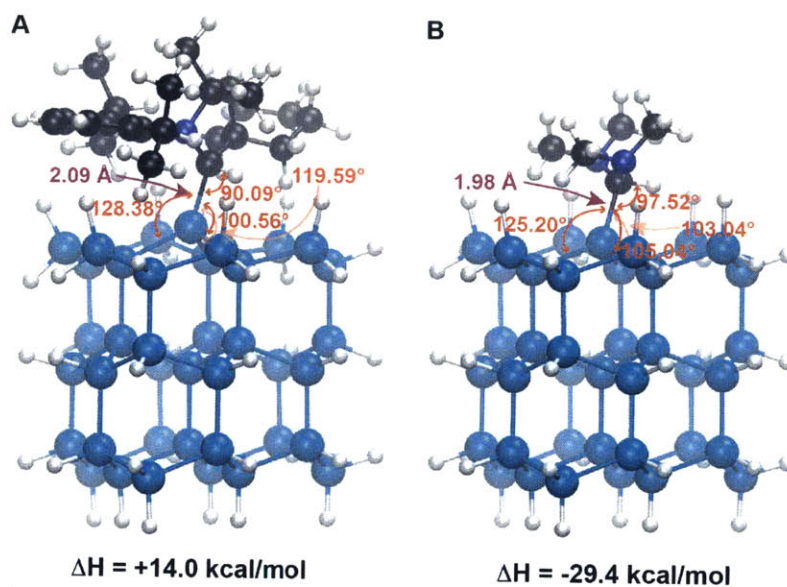
Figure 19. A.–B. Computed energy-minimized structures (represented as ball-and-stick models) of insertion products of **6** (A) and **7** (B) into the central Si-H bond of a 39-Si-atom, three-layer H-**Si(111)** surface model. Hydrogen atoms are in white, carbon – in black, nitrogen – in blue, and silicon – in cyan.

vacuum-optimized geometry (Figure 19). In this case, the computed ΔH was moderate and positive for **6**, indicating that a perfectly flat H-terminated silicon surface is unlikely to participate in insertion reactions with **6** (Figure 19A). The analogous three-layer model for **7** produced virtually identical results to the one-layer model, which validated the use of the simpler 13-Si atom model (Figure 19B).

However, as was described above, our H-**Si(111)** surfaces – and certainly the H-**SiNP** surfaces – were not flat and possessed numerous defects both at the atomic level and at the nanoscale; also, the binding of both **6** and **7** was observed for these surfaces, with all evidence suggesting that insertion, indeed, took place. Thus, we were compelled to conclude that, while **7** (and **5**) can, in principle, bind to flat regions, **6** must primarily bind to the defect sites. Defects discussed earlier – namely, D, Tr, M, and (SiO)$_3$SiH – were thus incorporated onto the one-layer surface, and the insertion of **6** and **7** was examined (Figure 20A–F).
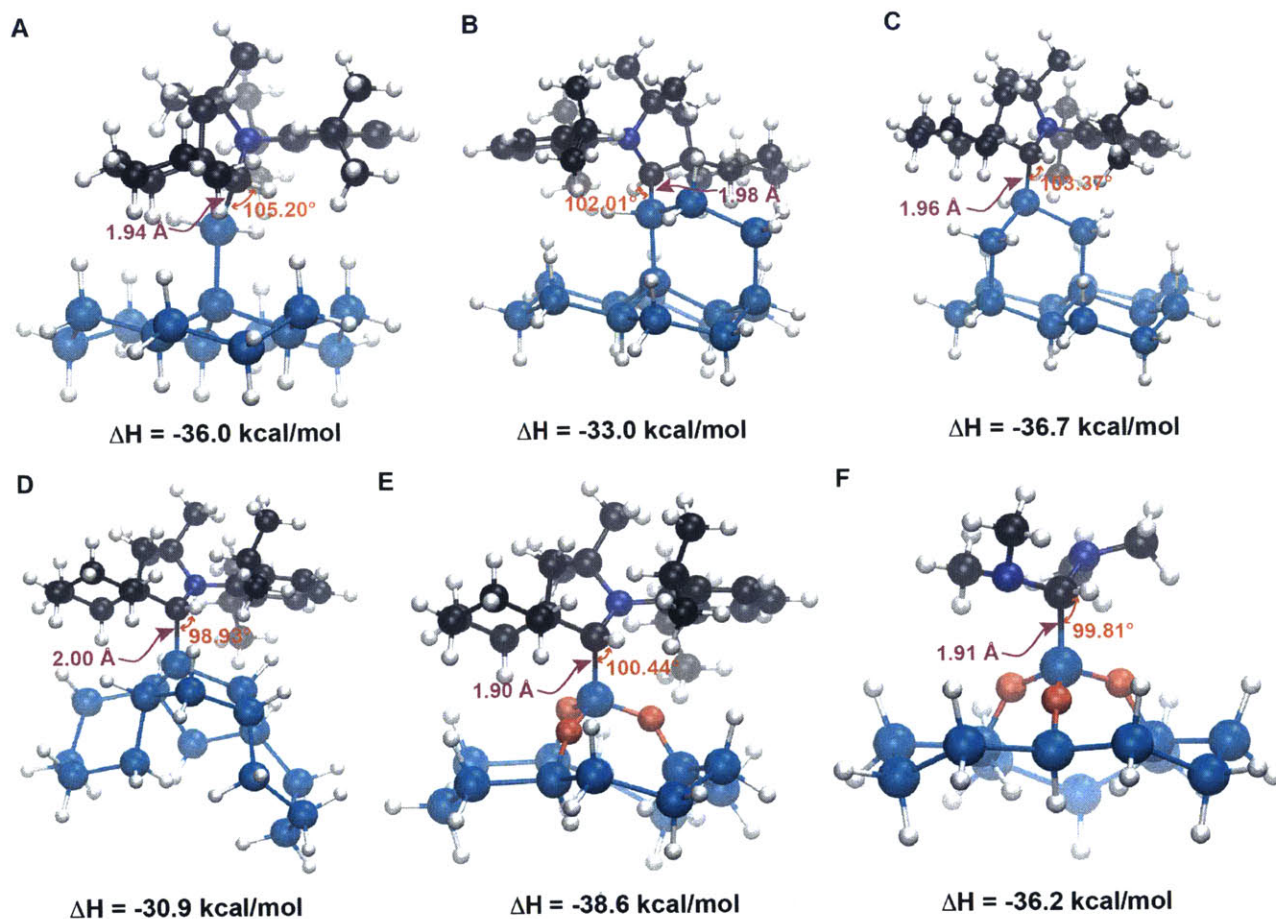
Figure 20. A.–F. Computed energy-minimized structures (represented as ball-and-stick models) of insertion products of **6** with the following surface defects: Tr (A), two sets of variants of D (B, C), M (D), and (SiO)$_3$SiH (E). The latter is also computed for carbene **7** (F). The 13-Si atom base layer was the same as used for the calculations presented in Figure 18; silicon atoms were displaced from this base layer, and additional oxygen and silicon atoms were included in the surface model, as needed to form the defects studied. Hydrogen atoms are in white, carbon – in black, nitrogen – in blue, oxygen – in red, and silicon – in cyan.

The results revealed that in all the cases that were explored, binding of **6** to the defects was highly thermodynamically favorable, and the resulting Si-C$_{carbene}$ bond length continued to decrease with increased magnitude of ΔH. The greatest magnitude of ΔH (-38.6 kcal/mol) was seen for insertion of **6** at the oxidized silicon (*i.e.*, (SiO)$_3$SiH), accompanied by the shortest Si-

$C_{carbene}$ bond length of 1.90 Å. Insertion of **7** was tested only on the latter substrate, and this process was nearly equally thermodynamically favorable. Hence, these results support the notion that **6** inserts primarily into the "more exposed" Si-H bonds of silicon surfaces, while **7** is perhaps less selective.

3.3 Conclusions

Herein, we demonstrated the use of persistent carbenes for functionalization of hydrogen-terminated silicon surfaces. Model compounds, Si NPs, and Si(111) wafers were used as substrates to investigate carbene reactivity with Si-H bonds. Through the use of a combination of characterization techniques, several valuable insights were gained that will aide the future development of carbene-derived monolayers. (1) We found that both enhanced nucleophilicity and electrophilicity (e.g., in CAACs and ADACs) as well as reduced or flexible steric bulk of the persistent carbene were necessary to achieve rapid Si-H insertion reactivity. (2) The reaction of CAAC **6** with Si(111) surfaces proceeds cleanly at rt and is complete within three days at concentrations as low as 0.048 M, having reached expected coverage of ~21±3%, while in the case of **7**, which was plagued by decomposition, saturation is observed after 20 min, with carbene coverage of 9±1%, and significant concomitant oxidation of the surface. (3) Both carbenes appear to bind to a range of surface sites (e.g., terrace Si-H and defects M, D, Tr, and oxidized surface sites); in fact, reaction with the defects is thermodynamically favored for the sterically more encumbered carbene **6**. Thus, we anticipate that **6** may be well-suited for the functionalization of hydrogen-terminated Si(100) surfaces. (4) CAAC **6**, due to its large steric bulk, leaves unreacted Si-H bonds at the surface of both Si(111) wafers and SiNPs, which could prove valuable for silicon patterning. (5) Lastly, the fact that redispersible SiNPs with unreacted Si-H functionality can be obtained by functionalization with carbene **6** indicates that CAAC-type carbenes could, with optimization, deliver stable SiNP with previously inaccessible physicochemical properties.

3.4 Experimental
Materials

Tris(trimethylsilyl)silane and tris(trimethylsiloxy)silane were purchased from Sigma-Aldrich® and VWR, respectively, subjected to three freeze-pump-thaw cycles, dried for several

hours over activated 3Å molecular sieves (from Mallinckrodt Baker) and stored in the glove box. Triethyl orthoformate was purchased from VWR. Dimethylmalonyl dichloride was purcahsed from TCI America and subjected to three freeze-pump-thaw cycles prior to use. 3-Chloro-2-methyl-1-propene was purchased from TCI America and dried over activated 3Å molecular sieves prior to use. 1,3-Bis(2,4,6-trimethylphenyl)-4,5-dihydroimidazol-2-ylidene (SIMes) and 1,3-bis(2,4,6-trimethylphenyl)imidazol-2-ylidene (IMes) were purchased from Strem Chemicals, Inc. MilliQ™ or de-ionized (de-I) water was used as indicated. CMOS-grade H_2O_2 was purchased from J. T. Baker, and ACS-grade 12M $HCl_{(aq)}$ was purchased from EMD Millipore. All deuterated solvents were purchased from Cambridge Isotope Laboratories, Inc.; if used for reactions involving air-sensitive species, they were subjected to three freeze-pump-thaw cycles, and stored over activated 3Å molecular sieves in the glove box. 2.0 M HCl in diethyl ether, redistilled anhydrous diisopropylamine, 2,6-diisopropylaniline, cyclohexanecarboxaldehyde, cyclohexylamine, acetic acid, trimethylsilyl trifluoromethylsulfonate, the 0.5 M solution of potassium hexamethyldisilazide in toluene, the 1.6 M solution of ^{n}BuLi in hexanes, trichlorosilane, chlorotrimethylsilane, and sodium hexamethyldisilazide, 48 wt.% $HF_{(aq)}$ were purchased from Sigma-Aldrich® and used as received. N,N,N',N'-tetramethylformamidinium chloride and N,N'-diisopropylimidazolium chloride were also purchased from Sigma-Aldrich®; these hygroscopic compounds were dried at 70–80 °C for 2 d under vacuum (~60–100 mTorr) prior to transferring to and storage in a nitrogen-filled glove box. All other solvents and reagents were purchased from Sigma-Aldrich® or VWR and used as received.

Si(111) wafers used for all but the FTIR studies (purchased from MTI corporation) were produced via the Czochralski process, and were characterized by n-type semiconductivity, a resistivity of 1–10 Ohm•cm, 4" diameter, 0.5 mm thickness, and polished on one side. Surface roughness for these wafers was <0.5 nm. Pieces of ~1 x 1 cm^2 dimensions were cut and cleaned and then etched to prepare H-Si(111) as follows. The silicon wafers were first cleaned with the SC-1 solution (5:1:1 of de-I water, 29% $NH_4OH_{(aq)}$, 30 wt.% $H_2O_{2(aq)}$) for 15 minutes at 75 °C.[80] The wafers were then rinsed with de-I water and etched for 30 min in 8 parts buffered oxide etch (BOE, 7:1 by volume of 40% $NH_4F_{(aq)}$ / 48% $HF_{(aq)}$) to 1 part of 29% $NH_4OH_{(aq)}$.[65] The pH value of the latter solution was generally ~7–8. **CAUTION: solutions of HF should be handled using special precautions: in addition to the standard laboratory protective gear, one should don a Tychem® QC (or analogous) apron, face shield, and multiple layers of**

gloves, which should be HF-resistant, and efficient fume hood ventilation is critical. The wafers were then quickly rinsed with de-I water (the resulting H-terminated surfaces, blow-dried using a nitrogen gun and transferred to a nitrogen-filled glove box. Etched wafers were stored in the glove box in the dark at -35 °C when not in use.

Methods

Solution nuclear magnetic resonance (NMR) spectroscopy

^{1}H, ^{13}C (^{1}H-decoupled), and ^{19}F NMR spectra were recorded on two Bruker AVANCE 400 MHz spectrometers (supported by NIH Grant # 1S10RR013886-01), and all 2D NMR (and in one case, ^{1}H NMR) was carried out on the Varian 500 MHz NMR spectrometer (supported by the NSF grant # DBI-9729592). Chemical shifts are expressed in parts per million (ppm), and splitting patterns are designated as s (singlet), d (doublet), t (triplet), sept (septet), m (multiplet), b (broad). Scalar coupling constants J are reported in Hertz (Hz). MestReNova v10.0.2-15465 software (Mestrelab Research S.L.) was used to analyze the NMR spectra. ^{1}H and ^{13}C NMR spectra were referenced to solvent peaks as reported in literature.[81] ^{19}F NMR spectra were referenced using C_6F_6 (-162.2 ppm[82]) as an external reference.

Mass spectrometry (MS)

High-resolution mass spectrometry (HRMS) was obtained using either (1) a Bruker Daltonics® APEXIV 4.7 Tesla Fourier Transform Ion Cyclotron Resonance Mass Spectrometer (FT-ICR-MS) with a direct analysis in real time (DART) or electrospray ionization (ESI) ion sources (NSF Grant #CHE-0234877). Unless state otherwise, the analysis was carried out in positive ion mode.

For time-of-flight secondary ion mass spectrometry (TOF-SIMS) characterization, samples were submitted to TASCON USA. IONTOF TOF-SIMS 5-300 instrument was used, and the analysis was carried out in positive ion mode using Bi_x^+ (primarily Bi_3^+) ions with an energy of 30 keV. Raster area was 200 x 200 μm^2 in size. The m/z ratios observed were generally accurate to 2 decimals places ± 0.02 (e.g., known fragments $C_9H_7^+$ and $C_{17}H_{11}^+$ were measured to be 115.049 (expected at 115.054) and 217.07 (expected 215.086) Da, respectively). Data was reduced prior to plotting by binning every ten data points to render the data set manageable.

Infra-red (IR) spectroscopy

Attenuated total reflectance Fourier transform IR (ATR-FTIR) spectroscopy was carried out using a Thermo Scientific Nicolet 6700 FT-IR instrument equipped with a germanium ATR crystal. A background spectrum was collected prior to spectroscopy of the samples, and 16 scans were collected in the "Ge transmission" mode and averaged for small-molecule samples, while 64 scans were done for H-SiNPs, and 512 scans were done for the functionalized nanoparticle samples. OMNIC™ software was used to analyze the IR data: unless otherwise specified, the spectra were baseline-corrected. Resonance energies are expressed in wavenumbers (cm^{-1}), and resonances are designated as s (strong), m (medium), w (weak), or b (broad).

Samples for surface FTIR analysis were cut from a 100-mm double-side polished, float-zone Si(111) wafer (Montco Silicon, N-type, resistivity > 1000 ohm•cm) and used as received (i.e. the H-terminated surface was created from the interface of the native oxide and the underlying substrate). Transmission IR spectra (1,000 scans each, 4 cm^{-1} resolution) were recorded with a room-temperature DTGS detector on a Nicolet Nexus 6700 spectrometer with the incident beam 60° from the surface normal, to afford approximately equal sensitivity to modes oriented parallel and perpendicular to the surface. Absorbance spectra were generated with a reference spectrum chosen to highlight features of interest as indicated in the figure captions; the original H-Si(111) surface was used to highlight species arising from surface functionalization, while an oxidized version of that surface (exposed for 10 minutes at 70-80°C to an SC-2 solution of 4:1:1 H_2O: 30% H_2O_2: conc. HCl to remove all SiH_x species) was used to quantify SiH_x species.

X-ray photoelectron spectroscopy (XPS)

1. *Sample preparation for XPS.* Silicon wafers and silicon nanoparticle powders were affixed to insulating double-sided tape (from 3M™). Solutions of model compounds were drop-cast onto silicon wafers in the glove box, allowed to dry, and also affixed to insulating double-sided tape. Samples were exposed to air no more than 10 min prior to being placed into the Vacuum state during XPS.

2. *XPS parameters.* X-ray photoelectron spectroscopy (XPS) was carried out at the MIT Center for Materials Science and Engineering on a Physical Electronics Versaprobe II X-ray Photoelectron Spectrometer (NSF award# DMR – 1419807). Main chamber pressure during

XPS analysis was in the range of 2 x 10^{-9} to 8 x 10^{-9} Torr. Both neutralizers ("e-neut" and "I-neut") were employed for all samples during the XPS analysis. Spot size was 200 μm in diameter, and the X-ray source had 50 W power and 15 kV potential applied to it. Monochromatized Al Kα X-ray source was used, with the corresponding photon energy of 1486.6 eV. The photon incidence angle was 90°, the take-off angle was 45° (unless stated otherwise), and the acceptance angle of the Versaprobe analyzer was 20°. For all samples, prior to collection of the narrow-region data, automatic z-alignment was performed, and two cycles of a survey scan at a pass energy of 187.85 eV were collected and averaged (data not shown). Narrow region scans were then carried out as follows: a pass energy of 46.95 eV with a step size of 0.200 eV were used; 21 cycles (4 for drop-cast model compounds) of sweeps were carried out for each region, with the number of sweeps per cycle dependent on the probed orbital: Si 2p – 1 cycle, Si 2s – 1, C 1s – 1, N 1s – 15, O 1s – 1, Cl 2p – 1, F 1s – 1, and Li 1s – 1. CasaXPS Version 2.3.17PR1.1 software was used to process and analyze the XPS data as follows. Notably, the transmission correction was virtually identical for all regions, and did not affect the computations.

3. Binding energy (B.E.) calibration for XPS spectra.

A. *Silicon wafers*. The B.E. scale was calibrated to the Si 2p 3/2 component at 99.15 eV.

B. *Silicon nanoparticles*. The XPS spectra of unfunctionalized H-**SiNPs** were calibrated to Si 2p 3/2 component at 99.15 eV, which also placed the C1s peak (adventitious oxidized hydrocarbons (oxyhydrocarbons) + tape adhesive) at 285.0 eV, as expected. This same C 1s peak shape was observed for **6·SiNPs**, and was used to calibrate the energy scale for this sample (note: a small shift to higher B.E.s was observed for the Si^0 2p peak component for these treated particles). The energy scale of **7·SiNPs** was calibrated by referencing the Si^0 2p 3/2 component to the one in **6·SiNPs** (the C 1s peak shape was different for this sample, so adventitious oxyhydrocarbons + tape adhesive could not be utilized to calibrate its B.E. scale).

C. *Model compounds*. Spectra were collected over regions were the film was thin enough for the silicon underneath to be probed as well. Thus, the B.E. scale was calibrated to the observed Si^0 2p 3/2 component at 99.15 eV.

D. *H-SiNP precursors*. The B.E. scale was calibrated to the adventitious carbon peak (285.0 eV) as in B.

4. *Baseline selection for XPS regions.* Linear baselines were chosen for all regions except Si 2p and Cl 2p regions, for which U 3 Tougaard and Tougaard baselines[83,84] were used, respectively.

5. *Lineshape selection and fitting of XPS spectra.* N 1s, C 1s, and O 1s peaks were fitted using LF(1,1,255,280) lineshapes[83] through the application of the Downhill Simplex approximation provided in the CasaXPS software[83]; standard deviation of the residual was typically between 0.5 and 3. Si 2p peaks were fitted using LF(0.85,1.2,255,280) lineshapes (GL(30) for the plasmon peak) through the application of the Downhill Simplex approximation provided in the CasaXPS software; standard deviation of the residual was generally between 0.8 and 3 (1 being an indicator of an excellent fit); the effective RSF calculated from the fit was also within ~10% of actual RSF, which also affirmed that good fits were obtained. The relationship between the Si 2p 3/2 and Si 2p ½ components was constrained to be as follows: Area of Si 2p ½ = 0.51 x Area of Si 2p 3/2; fwhm of Si 2p ½ = 1.059 x fwhm of Si 2p 3/2; position of Si 2p ½ (in eV) = 0.61554 + position of Si 2p 3/2 component (fwhm = full-width half-maximum). The components of the N 1s regions were constrained to have the same fwhm for carbene **6**; for carbene **7**, the smaller component was generally found to be ~0.79 x fwhm of the main component, and this constraint was thus applied to standardize the fitting.

6. *Calculation of surface silicon suboxide content on silicon wafers.* For this calculation, we employed the convenient procedure developed and validated by Lewis and coworkers.[13,66] Namely, the expected ratio of the component areas corresponding to the oxidized surface silicon and the non-oxidized bulk silicon for a Si(111) surface covered with a monolayer of oxidized silicon was first determined as follows (equation (0.1)[13,66]):

$$\frac{I_{Si\,surface}}{I_{Si\,bulk}} = \frac{n_{Si\,surface}}{n_{Si\,bulk} \times l_{Si} - n_{Si\,surface}}, where\ l_{Si} = \lambda_{Si} \times \sin\theta\,, \tag{0.1}$$

where $I_{Si\,surface}$ and $I_{Si\,bulk}$ are the intensities corresponding to the oxidized surface and bulk components of the Si 2p peak (the ratio of these is equivalent to the ratio of the observed peak areas), $n_{Si\,surface}$ and $n_{Si\,bulk}$ are bulk and areal densities of silicon (7.8 x 10^{14} atoms/cm^2, and 5.0 x 10^{22} atoms/cm^3, respectively[13,66]), θ is the take-off angle (45° in our case), and λ_{Si} is the inelastic mean free path of Si 2p electrons through silicon (1.6 nm[13,66,85]). Thus, the expected ratio

$\frac{I_{Si\,surface}}{I_{Si\,bulk}} = 0.16$. The observed ratios were then divided by this value to quantify the percent of oxidized atop sites on the Si(111) surface.

7. *Calculation of inelastic mean free paths.* Inelastic mean free paths (λ) of N 1s, C 1s, and Si 2p electrons through the hydrocarbon overlayer consisting of bound carbenes and adventitious oxyhydrocarbons were calculated using equation (0.2), developed by Whitesides and coworkers.[86]

$$\lambda(\text{Å}) = 9.0 + 0.022 \times (K.E.\,(eV)), \tag{0.2}$$

where K.E.(eV) is the kinetic energy (in units of eV) of the photoelectron, equal to 1486.6 eV – B.E. Values obtained from this formula (3.3 nm for N 1s, 3.5 nm for C 1s, and 4.0 nm for Si 2p photoelectrons) were virtually identical to the values obtained from a more recent, refined formula.[87]

8. *Calculation of overlayer thicknesses.* Because the inelastic mean free paths for C 1s and Si 2p electrons are approximately equal, the simplified substrate-overlayer model[88,89] could be employed to determine the overlayer thickness d_{ov} (formula (0.3)).

$$d_{ov} = \bar{\lambda} \times \sin\theta \times \ln\left(1 + \frac{I_C \times RSF_{Si} \times \rho_{Si}}{I_{Si} \times RSF_C \times \rho_C}\right), \tag{0.3}$$

where $\bar{\lambda}$ is the average inelastic mean free path (3.4 nm), θ is the take-off angle, I_C and I_{Si} are relative intensities (or areas) of the C 1s and Si 2p peaks, respectively, RSF_C and RSF_{Si} are the instrument- and pass energy-specific adjusted relative sensitivity factors for C 1s and Si 2p regions (14.563 and 19.701, respectively), and ρ_{Si} and ρ_C are silicon and carbon atom densities in bulk silicon (5×10^{22} atoms/cm^3) and the carbene/oxyhydrocarbon overlayer ($\sim 3.3 \times 10^{22}$ atoms/cm^3), respectively. Note that a value of 0.033 mol C/cm^3 (equivalent to 2.0×10^{22} atoms/cm^3) has been used in some reports[63,66]; however in our case, the carbene/oxyhydrocarbon overlayer was estimated based on XPS analysis to have a C:O ratio of $\sim$6-6.5:1, and the average carbon atom density in representative oxyhydrocarbons (namely, tridecane-1,3-diol, cyclohexanol, tridecylic acid, hexanol) – 3.3×10^{22} atoms/cm^3 – was the one we used. (Note: using the value of 2.0×10^{22} instead had only a minor effect on the calculation of carbene

coverage – *vide infra*). Typical values for d_{ov} of surfaces treated with **6** were 1.6–2.1 nm, while d_{ov} of surfaces treated with **7** were 1.1–1.5 nm.

9. *Calculation of carbene coverage of the atop sites on Si(111)*. The substrate-overlayer model[89] (formula (0.4)) was first utilized to quantify the volumetric density of nitrogen atoms in the overlayer (ρ_N in formula (0.4)):

$$\rho_N = \frac{I_N \times RSF_{Si}}{I_{Si} \times RSF_N} \times \rho_{Si} \times \frac{e^{-\frac{d_{ov}}{\lambda_{Si} \times \sin\theta}}}{1 - e^{-\frac{d_{ov}}{\lambda_N \times \sin\theta}}}, \tag{0.4}$$

where I_N is the relative intensity (area) of the N 1s peak, RSF_N is the instrument- and pass energy-specific adjusted relative sensitivity factor for the N 1s region (23.236), λ_N is 3.3 nm, as stated earlier, and d_{ov} is the overlayer thickness of the given sample. The areal coverage of nitrogen was then equal to $\rho_N \times d_{ov}$, and the coverage of atop silicon sites by nitrogen $\Phi_N = \rho_N \times d_{ov}/n_{Si\,surface}$, which in the case of carbene **6** was taken to be equal to the coverage of atop silicon sites by **6** (Φ_6), since **6** was the principal source of observed nitrogen and each molecule of **6** has one nitrogen atom; in the case of **7**, the analogous quantity Φ_7 was taken to equal $\Phi_N \times 0.5$ because each molecule of **7** has two nitrogen atoms.

Transmission electron microscopy (TEM)

Dilute (color not detectable by eye) solutions of NPs were drop-cast (one drop) on a carbon film 200-mesh copper TEM grid (CF200-CU, Electron Microscopy Sciences), and the solvent was allowed to evaporate. Microscopy was performed on the FEI Tecnai G2 Spirit TWIN TEM at the MIT Center for Materials Science and Engineering (National Science Foundation award # DMR-1419807). The data was analyzed using the ImageJ software, as shown below in Figures 21 and 22.
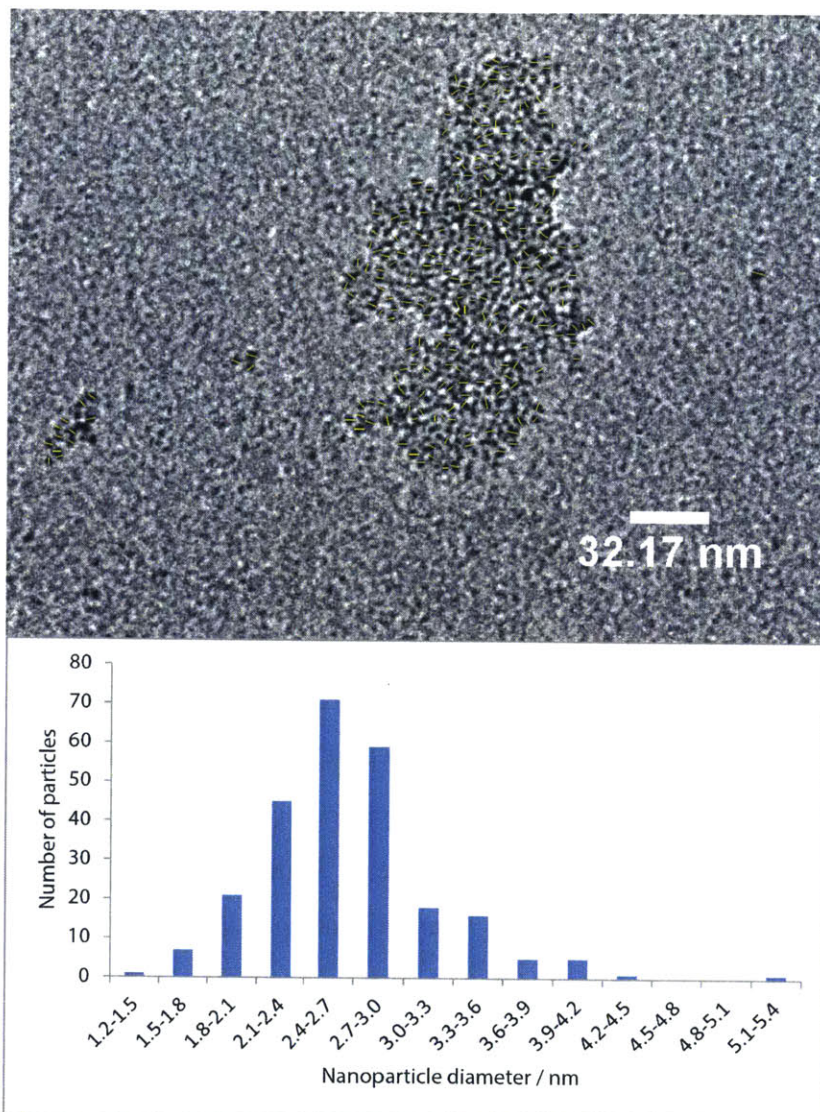
Figure. 21 TEM analysis of the **6**•SiNP diameter distribution (yellow lines mark the measured diameters). The particle sizes were binned and plotted in a histogram.
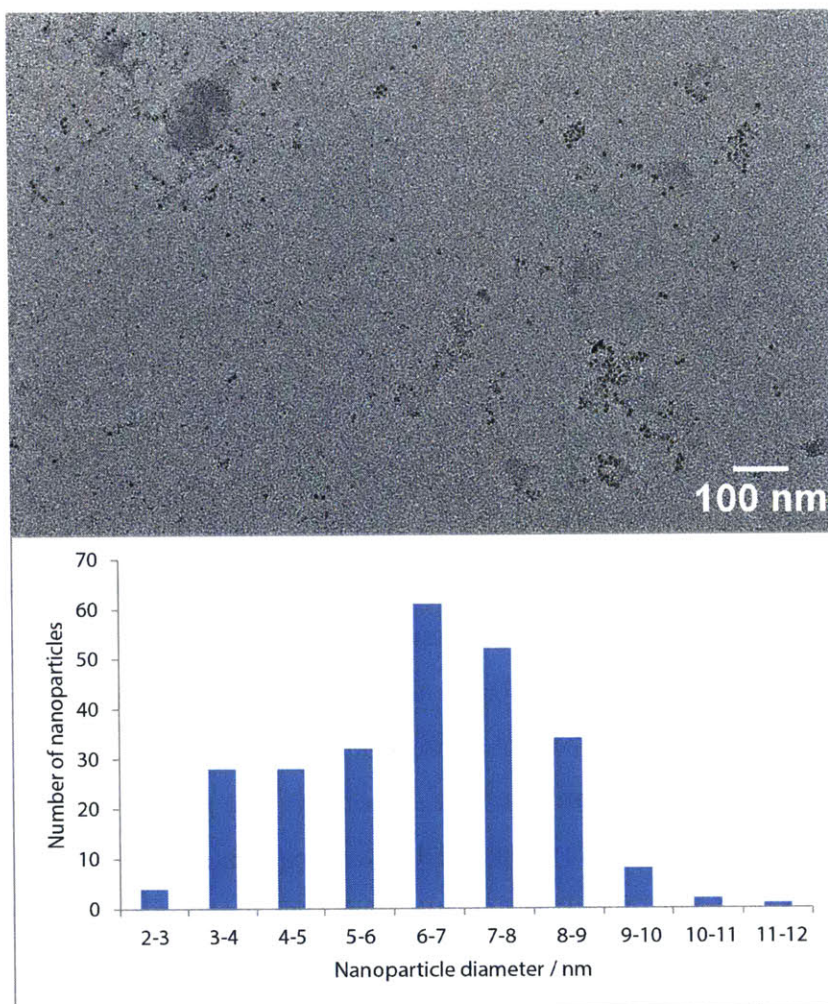
Figure 22. TEM analysis of the 7•SiNP diameter distribution (yellow lines mark the measured diameters). The particle sizes were binned and plotted in a histogram.

Atomic force microscopy (AFM)

AFM was carried out in tapping mode on an MFP-3D AFM instrument (Asylum Research, Santa Barbara, CA) using OTESPA 1-Ohm silicon probes with a cantilever that possesses a resonant frequency of 312–343 kHz (F_o) and a nominal spring constant of 12-103 N/m (Bruker). The following parameters were used in the measurements: scan size of 2 μm x 2 μm, scan rate = 0.75 Hz; scan angle = 90°, set point ~740 mV; points & lines = 256; integral gain = 5.00; the measurements were carried out in ambient conditions. The data was analyzed using the Igor Pro 6.22A| MFP3D 101010-1403 combined software.

X-ray crystallography

Low-temperature (100 K) diffraction data (φ- and ω-scans) were collected on a Bruker X8 Kappa Duo four-circle diffractometer coupled to a Smart Apex2 CCD detector, with Mo K_α radiation (λ = 0.71073 Å) from an $I\mu S$ micro-source. The diffractometer was purchased with the help of funding from the National Science Foundation (NSF) under Grant Number CHE-0946721. The structure was solved by direct methods using SHELXS[90] and refined against F^2 on all data by full-matrix least squares with SHELXL-97[91] following established refinement strategies[92].

Computations

All calculations were performed using a modified version of QChem 4.2[93] using PBE exchange and correlation[75] and the 6-311g** basis set. Initial molecular geometries were taken from the UFF-minimized structure of the molecules and molecular adducts studied.[94] Geometries were then optimized with DFT, and a frequency analysis was performed at each minimum. In the case of structures involving molecules **5** and **6**, several initial geometries related by rotation and boat-chair inversion of cyclohexyl side groups were optimized, to ensure that the DFT-optimized geometry corresponded to a global – not just a local – energy minimum. A stability analysis was performed to confirm that each optimized geometry was, in fact, a minimum—i.e., that the DFT-minimized structure contained no imaginary eigenvalues of the Hessian.

Adduct formation enthalpies computed correspond to the enthalpies of the reaction:

$$R_2C: + H\text{-}SiR'_3 \rightarrow R_2C(H)\text{-}SiR'_3$$
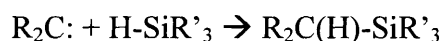
occurring in the gas phase at 0 K. The overall ΔH of this reaction was computed by taking the total DFT energy of the product at its minimum-energy geometry minus the overall DFT energies of each reactant at their minimum-energy geometries. For example, ΔH values for the formation of the carbene-TTMSS adducts were computed by subtracting the energies of optimized **5**, **6**, and **7** plus the energy of optimized TTMSS from the energies of the optimized **5•TTMSS**, **6•TTMSS**, and **7•TTMSS**, respectively.

In the case of the three-layer silicon surface models described in the main text, the bottom two layers of silicon (plus any hydrogen atoms attached to them) were frozen at the optimum

geometry of the pristine surface for all NHC-silicon adduct calculations. This was done because silicon atoms away from the surface are not expected to significantly move in the presence of a molecule bound to the surface. Three DFT calculations were then performed to compute each ΔH of insertion: (1) optimization of the three-layer surface model; (2) optimization of the molecule **6** or **7**; and (3) optimization of the molecule-surface adduct with the bottom two layers of silicon atoms held fixed at the geometry obtained after calculation (1). The ΔH values were computed by $\Delta H = (3) - [(1) + (2)]$.

The coordinates for the computed structures and relevant computed vibrational frequencies are presented in what follows below.

50
Optimized geometry of molecule **5** in .xyz format

C	0.98915	1.59881	1.40021
C	1.26299	2.56483	0.26982
C	0.08497	3.55669	0.17557
H	-0.05284	4.10579	1.13222
H	-0.85857	3.01552	-0.05586
H	0.26011	4.31020	-0.62280
C	2.56423	3.33159	0.59104
H	2.79209	4.08126	-0.19746
H	3.42150	2.62695	0.66193
H	2.47940	3.87701	1.55597
C	1.42744	1.88680	-1.07142
N	0.90223	0.24641	1.20842
N	1.32530	0.53089	-1.22986
C	1.07974	-0.35956	-0.10354
O	0.86680	2.06027	2.52870
O	1.67964	2.59318	-2.04058
C	-0.80551	-2.78506	3.82731
C	-1.00471	-1.30506	4.17101
C	0.60427	-3.01467	3.27339
H	-0.95530	-3.40414	4.73783
H	-1.55769	-3.09412	3.06831
C	0.83415	-2.14623	2.02942
H	1.35736	-2.75735	4.05077
H	0.73045	-4.08668	3.00955
C	-0.77094	-0.42355	2.93487
H	-0.29104	-1.01144	4.97246
H	-2.03677	-1.14889	4.55205
C	0.65610	-0.63847	2.36449
H	0.11098	-2.45273	1.24073
H	1.86478	-2.32898	1.65448
H	-1.52167	-0.67342	2.15279
H	-0.93654	0.62986	3.23572
H	1.41168	-0.40074	3.14835
C	1.77888	-2.18299	-3.95623
C	0.64280	-1.74071	-4.88379
C	1.56532	-1.61743	-2.54587
H	2.75110	-1.82160	-4.35801
H	1.81188	-3.29290	-3.91265
C	1.50077	-0.06346	-2.57071
H	0.61780	-2.03296	-2.13506
H	2.40651	-1.94978	-1.89937
C	0.56506	-0.21163	-4.93214
C	0.35261	0.36516	-3.52451
H	0.28894	1.46664	-3.62169

```
H     -0.61856      0.00611     -3.11801
H      1.50895      0.19491     -5.35852
H     -0.27388      0.09588     -5.59271
H     -0.32253     -2.14905     -4.51115
H      0.81750     -2.13920     -5.90628
H      2.47532      0.28861     -2.98029
```

Optimizied geometry of molecule **6** in .xyz format

C	-0.03469	-0.03715	0.31062
C	1.21054	0.26865	-0.52268
C	0.60151	0.69463	-1.87575
C	-0.75559	1.36035	-1.54857
H	0.37426	-0.23803	-2.42285
H	1.27981	1.23610	-2.57083
N	-1.12312	0.74215	-0.24421
C	2.05695	1.37555	0.17038
C	2.10545	-0.98744	-0.71174
C	2.71126	-1.47127	0.61345
H	2.93359	-0.74403	-1.41445
H	1.51717	-1.82053	-1.15542
C	3.54570	-0.35730	1.24991
H	1.89971	-1.77709	1.30963
H	3.35629	-2.35655	0.42645
C	2.67594	0.87934	1.48948
H	4.39007	-0.09281	0.57554
H	3.96867	-0.71062	2.21472
H	1.46514	2.26416	0.42747
H	2.87861	1.68613	-0.51230
H	3.29667	1.68595	1.93581
H	1.86848	0.62912	2.21230
C	-2.49079	0.38815	0.13230
C	-3.42832	1.42708	0.48756
C	-4.75278	1.09787	0.81722
C	-5.17649	-0.20791	0.85957
C	-4.29483	-1.23701	0.60965
C	-2.94246	-1.00180	0.25585
H	-4.69801	-2.23114	0.70014
H	-6.20150	-0.43094	1.12874
H	-5.46669	1.86779	1.07716
C	-3.03541	2.89115	0.63201
C	-3.83221	3.79299	-0.32839
H	-4.91773	3.77212	-0.09926
H	-3.70596	3.46804	-1.38000
H	-3.48303	4.84381	-0.24038
C	-3.22470	3.37201	2.08083
H	-4.28855	3.33977	2.39491
H	-2.86994	4.42012	2.18377
H	-2.63031	2.73735	2.77300
H	-1.96166	3.00294	0.47014
C	-2.03445	-2.25014	0.04927
C	-2.63818	-3.59574	0.51187
H	-2.92839	-3.54191	1.58329

H	-1.88464	-4.40775	0.41699
H	-3.51476	-3.88922	-0.10497
C	-1.62017	-2.43358	-1.40745
H	-0.95858	-3.31911	-1.52240
H	-1.05036	-1.57790	-1.74417
H	-2.51262	-2.56040	-2.05718
H	-1.14530	-2.15197	0.69851
C	-0.53085	2.89717	-1.53027
H	-1.47043	3.46670	-1.51419
H	-0.05668	3.21639	-2.48393
H	0.10093	3.26821	-0.71463
C	-1.78978	1.08851	-2.67153
H	-1.99295	0.01480	-2.82140
H	-1.42875	1.49547	-3.64087
H	-2.75962	1.57066	-2.43396

19
Optimized geometry of molecule 7 in .xyz format

C	0.75148	0.06339	2.53274
N	0.08907	-1.18597	2.99757
N	0.45479	1.22484	3.43286
C	1.21558	1.12339	4.69515
H	0.94533	0.22098	5.26701
H	0.97457	1.97590	5.36694
H	2.31209	1.11683	4.50530
C	0.74693	2.53955	2.84087
H	1.80873	2.60561	2.51754
H	0.54873	3.35283	3.57261
H	0.05731	2.74539	2.00066
C	-1.17587	-1.02463	3.73467
H	-1.72825	-1.98781	3.74525
H	-1.82704	-0.28864	3.21626
H	-1.01144	-0.69755	4.78045
C	1.01733	-2.13998	3.61237
H	1.88778	-2.30713	2.94233
H	0.51275	-3.11946	3.75460
H	1.38512	-1.79144	4.59584

41

Optimized geometry of TTMSS in .xyz format

Si	-0.00460	0.27845	0.34235
Si	-2.18607	0.78918	0.83476
Si	1.26401	1.80973	-0.82480
Si	0.52348	-1.92567	0.18065
H	0.47767	0.46812	1.71265
C	-2.91786	-0.49038	1.97893
H	-3.04084	-1.45267	1.45640
H	-3.92104	-0.15079	2.30814
H	-2.26377	-0.60773	2.86748
C	-3.29421	0.94934	-0.65908
H	-3.30994	-0.00577	-1.22123
H	-2.92835	1.76788	-1.31157
H	-4.32334	1.18985	-0.31639
C	-2.31446	2.36135	1.85321
H	-3.36111	2.48372	2.19822
H	-2.05091	3.26520	1.27814
H	-1.65264	2.27454	2.74002
C	0.41634	3.20134	0.11130
H	0.84876	4.21506	0.00363
H	0.34295	2.97995	1.19239
H	-0.59159	3.25322	-0.35285
C	2.28108	3.12776	-1.75114
H	1.63252	3.89419	-2.22220
H	2.95027	2.70011	-2.52207
H	2.92285	3.65135	-0.99993
C	2.87401	0.89697	-0.41377
H	2.94822	0.66326	0.66521
H	3.80986	1.41106	-0.71855
H	2.85476	-0.04527	-1.00364
C	-0.70660	-2.95828	1.12160
H	-0.35594	-4.00946	1.15034
H	-1.67999	-2.93019	0.59688
H	-0.79954	-2.57442	2.15813
C	0.61743	-2.61136	-1.55328
H	0.89200	-3.68629	-1.49058
H	1.39362	-2.07235	-2.13270
H	-0.36691	-2.51639	-2.05397
C	2.15740	-2.20819	1.04734
H	2.35840	-3.29692	1.09983
H	2.09381	-1.79888	2.07712
H	2.99311	-1.72619	0.51054

91

Optimized geometry of **5•TTMSS** in .xyz format

C	0.60821	0.75455	1.44438
C	0.56846	1.86224	0.40273
C	-0.86063	2.30936	0.18469
H	-1.30817	2.69456	1.12675
H	-1.44474	1.43159	-0.11682
H	-0.90063	3.10927	-0.58554
C	1.36558	3.08085	0.95534
H	1.36027	3.92739	0.23440
H	2.42275	2.79872	1.15584
H	0.92347	3.46316	1.90133
C	1.26457	1.40014	-0.88164
N	0.73452	-0.56789	1.08341
N	1.46368	0.06294	-1.13754
C	0.67616	-0.91234	-0.36063
O	0.67858	1.07788	2.62320
O	1.84012	2.24196	-1.56119
C	0.92152	-3.99517	3.84756
C	0.57240	-2.61274	4.39957
C	2.00649	-3.86428	2.77889
H	1.28692	-4.64424	4.67208
H	0.01494	-4.46673	3.40917
C	1.53265	-2.95678	1.63628
H	2.92636	-3.43637	3.23575
H	2.25584	-4.86960	2.37613
C	0.08266	-1.68572	3.27852
H	1.47175	-2.16767	4.88005
H	-0.21942	-2.71208	5.17321
C	1.14467	-1.54170	2.14385
H	0.66509	-3.43208	1.14421
H	2.37223	-2.89244	0.91795
H	-0.85630	-2.08405	2.87728
H	-0.16602	-0.72357	3.75993
H	2.07097	-1.13598	2.61230
C	4.29825	-2.01670	-2.82588
C	3.96946	-1.69232	-4.28619
C	3.07424	-1.77419	-1.93085
H	5.13959	-1.37294	-2.48609
H	4.61891	-3.07727	-2.74090
C	2.58504	-0.30949	-2.04135
H	2.28129	-2.47586	-2.23509
H	3.37225	-1.98989	-0.88554
C	3.51089	-0.23575	-4.40965
C	2.28752	0.03346	-3.52044

166

H	2.01229	1.09744	-3.65022
H	1.44281	-0.57793	-3.86964
H	4.34144	0.43769	-4.10254
H	3.25904	-0.01306	-5.46882
H	3.16920	-2.37060	-4.65067
H	4.86994	-1.85427	-4.91660
H	3.46716	0.29247	-1.71960
Si	-1.11919	-1.26924	-1.15919
H	1.05674	-1.91638	-0.50493
Si	-2.19585	0.20463	-2.62327
Si	-2.73952	-1.82670	0.35129
Si	-0.89790	-3.21819	-2.38814
C	-2.91921	-0.45519	1.60993
H	-3.23713	0.47250	1.09449
H	-1.96852	-0.25694	2.13092
H	-3.69657	-0.73635	2.34921
C	-2.48510	-3.50945	1.14196
H	-1.50135	-3.62936	1.61039
H	-2.57869	-4.29860	0.37515
H	-3.27590	-3.67306	1.90208
C	-4.43927	-1.96874	-0.42159
H	-4.74253	-1.00835	-0.87244
H	-4.46320	-2.75630	-1.19452
H	-5.17127	-2.22812	0.37030
C	-2.52422	-4.07117	-2.76492
H	-2.31163	-4.98872	-3.35068
H	-3.20391	-3.43692	-3.35595
H	-3.02516	-4.37831	-1.83110
C	0.08065	-4.51052	-1.45061
H	1.10565	-4.15767	-1.23453
H	0.14669	-5.42946	-2.06807
H	-0.42876	-4.75871	-0.50098
C	-0.08790	-2.99541	-4.05736
H	-0.09285	-3.96979	-4.58707
H	0.95729	-2.68582	-3.95117
H	-0.63899	-2.25260	-4.66464
C	-3.35251	-0.74316	-3.74402
H	-2.78203	-1.46714	-4.35235
H	-4.13279	-1.26018	-3.15608
H	-3.84559	-0.03211	-4.43794
C	-3.35084	1.53415	-1.95022
H	-2.84599	2.37190	-1.45333
H	-3.88643	1.98326	-2.81145
H	-4.10088	1.09749	-1.26636
C	-1.02274	1.06269	-3.78516
H	-1.60459	1.71087	-4.47179

| H | -0.48882 | 0.31090 | -4.39217 |
| H | -0.31628 | 1.69091 | -3.21027 |

100

Optimized geometry of **6·TTMSS** in .xyz format

N	5.968462	12.880613	11.871154
C	5.690073	13.211253	14.295211
C	4.274883	13.585529	14.803236
H	3.651702	13.956667	13.975333
H	3.788641	12.665254	15.165206
C	4.283637	14.617757	15.945747
H	4.634913	15.595400	15.569562
H	3.249592	14.785020	16.292216
C	5.167744	14.174953	17.121158
H	5.244418	14.984265	17.866551
H	4.684764	13.326173	17.635118
C	6.567624	13.753928	16.650001
H	7.146594	13.345513	17.495485
H	7.121261	14.645218	16.302781
C	6.512737	12.719697	15.512024
H	6.076054	11.779033	15.890026
H	7.538159	12.475433	15.184069
C	6.389957	14.424225	13.640692
H	6.068056	15.385623	14.067692
H	7.478147	14.354411	13.811262
C	6.118845	14.362049	12.126505
C	4.839128	15.149406	11.757202
H	4.713200	15.218910	10.668166
H	4.898764	16.177411	12.150464
H	3.939415	14.677092	12.169837
C	7.292326	14.999503	11.365577
H	8.258291	14.581351	11.675423
H	7.308777	16.080106	11.578776
H	7.201448	14.873893	10.278095
C	6.751929	12.247943	10.839872
C	6.234616	12.186767	9.507000
C	6.957001	11.502148	8.515473
H	6.552311	11.457345	7.500820
C	8.165270	10.868553	8.795224
H	8.696878	10.316463	8.016399
C	8.705795	10.984801	10.073986
H	9.685568	10.544673	10.281326
C	8.051812	11.698039	11.092369
C	4.948869	12.895881	9.082443
H	4.451796	13.223017	10.007003
C	3.962263	12.005023	8.305380
H	4.400367	11.622918	7.369141
H	3.070974	12.591152	8.028313
H	3.631257	11.141490	8.894903

C	5.264194	14.135987	8.217533
H	5.953758	14.834856	8.711506
H	4.337813	14.684625	7.980600
H	5.728050	13.836574	7.263217
C	8.855604	11.943319	12.375226
H	8.268509	12.616353	13.016052
C	9.157795	10.667526	13.183746
H	8.243636	10.166231	13.530157
H	9.767521	10.913172	14.068521
H	9.724743	9.940260	12.580466
C	10.186487	12.662927	12.058676
H	10.887705	11.994456	11.534977
H	10.674259	12.988142	12.991875
H	10.038203	13.546367	11.420771
C	5.708908	12.134081	13.140608
H	6.567153	11.467928	13.340771
Si	4.220986	10.751664	13.162323
Si	1.964334	11.389691	12.613678
C	1.754473	12.708207	11.260218
H	0.674043	12.843259	11.079762
H	2.218836	12.409816	10.310748
H	2.167201	13.685240	11.549315
C	0.997751	12.048455	14.120835
H	1.400363	13.005230	14.484529
H	0.985238	11.342634	14.964674
H	-0.048910	12.221865	13.817536
C	1.021854	9.853497	11.992991
H	-0.012997	10.145167	11.745515
H	0.973092	9.054311	12.747044
H	1.477221	9.435868	11.082412
Si	3.931897	9.651204	15.317282
C	3.597606	10.688512	16.884930
H	2.777496	11.410871	16.757945
H	4.479863	11.229160	17.251476
H	3.293989	9.978743	17.673992
C	5.442416	8.567776	15.743167
H	5.284226	8.081156	16.720385
H	6.364680	9.166136	15.813879
H	5.612449	7.777301	14.997529
C	2.386028	8.531583	15.273344
H	2.344863	7.835397	14.428302
H	1.467066	9.137523	15.260761
H	2.373209	7.936853	16.202945
Si	4.829553	8.785702	11.855381
C	3.839937	7.241519	12.382474
H	2.754013	7.378032	12.276470

H	4.052224	6.915331	13.410318
H	4.139237	6.422554	11.705962
C	4.540950	8.886569	9.982810
H	5.171651	9.647747	9.505831
H	3.489155	9.084982	9.727751
H	4.806708	7.907259	9.548841
C	6.657711	8.311673	12.073969
H	6.819616	7.338077	11.580101
H	6.953104	8.204094	13.127835
H	7.323210	9.043640	11.595818

60
Optimized geometry of **7•TTMSS** in .xyz format

Si	0.26885	0.24411	0.67985
Si	-2.00423	0.83094	0.47211
C	-2.39159	0.85273	-0.97678
C	-2.25798	2.19107	1.05175
C	-2.87572	-0.16256	1.18203
Si	1.63156	1.82899	-0.40892
C	1.29808	1.86480	-1.87094
C	3.08139	1.47339	-0.26054
C	1.41281	3.19891	0.16181
Si	0.64545	-1.90863	-0.20246
C	0.29344	-1.92661	-1.66038
C	-0.20031	-2.92700	0.50336
C	2.08683	-2.29788	-0.05626
C	0.75148	0.06339	2.53274
N	0.08907	-1.18597	2.99757
N	0.45479	1.22484	3.43286
H	1.85359	-0.08739	2.46530
C	1.21558	1.12339	4.69515
H	0.94533	0.22098	5.26701
H	0.97457	1.97590	5.36694
H	2.31209	1.11683	4.50530
C	0.74693	2.53955	2.84087
H	1.80873	2.60561	2.51754
H	0.54873	3.35283	3.57261
H	0.05731	2.74539	2.00066
C	-1.17587	-1.02463	3.73467
H	-1.72825	-1.98781	3.74525
H	-1.82338	-0.27059	3.24889
H	-1.00422	-0.71502	4.78474
C	0.98968	-2.16456	3.62628
H	1.84870	-2.37939	2.95585
H	0.45494	-3.12538	3.78605
H	1.37428	-1.80993	4.60146
H	2.23494	-3.27660	-0.46254
H	2.35291	-2.29790	0.98013
H	2.70071	-1.59677	-0.58209
H	3.68102	2.20457	-0.76126
H	3.25847	0.51053	-0.69234
H	3.33879	1.45143	0.77781
H	0.46581	-2.90538	-2.05687
H	0.90149	-1.21796	-2.18287
H	-0.73809	-1.66932	-1.78144
H	-1.77886	1.55737	-1.49922
H	-3.41901	1.13761	-1.06705

H	-2.25323	-0.12124	-1.39765
H	1.91901	2.58545	-2.36085
H	0.27051	2.13570	-1.99585
H	1.46684	0.89880	-2.29903
H	-0.01389	-3.89524	0.08783
H	-1.23393	-2.67914	0.38051
H	0.04365	-2.93297	1.54516
H	-2.70535	-1.13884	0.77860
H	-3.90318	0.10442	1.04805
H	-2.64022	-0.16187	2.22579
H	2.04020	3.90126	-0.34612
H	1.65423	3.19374	1.20421
H	0.38797	3.47889	0.03444
H	-1.64238	2.91122	0.55444
H	-2.02479	2.18293	2.09600
H	-3.28776	2.44922	0.91826

35
Optimized geometry of one-layer model of Si(111) surface in .xyz format

Si	-0.01032	-0.07879	-0.19982
Si	2.04643	0.29887	-0.96930
Si	-1.17930	1.81665	-0.27928
Si	-1.00513	-1.61022	-1.47612
H	1.97056	0.78818	-2.35312
Si	3.22153	-1.59441	-0.90509
Si	3.04437	1.81981	0.31906
H	-1.07702	-1.12664	-2.86209
Si	-3.06123	-1.98889	-0.70331
Si	0.16507	-3.50592	-1.40230
Si	-3.24208	1.44809	0.48136
H	-1.24026	2.29666	-1.66711
Si	-0.19117	3.34399	1.00912
H	0.05949	-0.56217	1.18624
H	4.57853	-1.34143	-1.41053
Si	2.22113	-3.12687	-2.18165
H	3.28943	-2.07936	0.48084
H	2.99633	-4.37534	-2.14503
H	2.13660	-2.63457	-3.56433
H	-0.49809	-4.51927	-2.23535
H	0.24387	-3.97857	-0.01257
H	4.40602	2.06309	-0.17842
H	3.10192	1.32255	1.70124
Si	1.87541	3.71956	0.25571
H	1.80896	4.20524	-1.13012
H	2.53020	4.72557	1.10439
H	-0.12822	2.84544	2.39058
H	-0.96528	4.59292	0.96657
H	-3.71353	-3.01009	-1.53529
Si	-4.23491	-0.09325	-0.79050
H	-2.98202	-2.45728	0.68790
H	-4.01057	2.70019	0.42896
H	-3.17028	0.96650	1.86824
H	-5.59584	-0.33644	-0.29082
H	-4.29304	0.38061	-2.18092

85

Optimized geometry of **5**•[one-layer Si(111) surface] in .xyz format

C	1.68100	-1.26514	1.51877
C	2.16013	-0.14887	0.69174
C	1.06389	0.95720	0.73860
H	0.86759	1.30459	1.77582
H	0.10374	0.56978	0.32430
H	1.34668	1.85130	0.14053
C	3.47786	0.42454	1.25954
H	3.80721	1.31204	0.67371
H	4.28388	-0.33653	1.23831
H	3.33615	0.77419	2.30603
C	2.34157	-0.50506	-0.72468
N	1.30530	-2.51261	1.04122
N	1.99719	-1.73184	-1.27513
C	1.46356	-2.88966	-0.43180
O	1.54797	-1.00736	2.71793
O	2.72337	0.41362	-1.44140
C	-1.45918	-4.81793	3.61393
C	-1.37534	-3.29281	3.68337
C	-0.08551	-5.40431	3.29053
H	-1.81844	-5.21496	4.58795
H	-2.17783	-5.11748	2.82174
C	0.44241	-4.83337	1.95399
H	0.62613	-5.15946	4.11340
H	-0.15198	-6.50614	3.25340
C	-0.79737	-2.71559	2.38332
H	-0.71453	-2.99848	4.52973
H	-2.38483	-2.86948	3.87280
C	0.60766	-3.32564	2.07999
H	-0.25679	-5.07238	1.13339
H	1.41635	-5.29130	1.81080
H	-1.47704	-2.92131	1.52730
H	-0.76472	-1.61488	2.51072
H	1.24865	-3.25422	2.99297
C	2.20727	-2.42021	-5.11056
C	0.83134	-1.90539	-5.53035
C	2.19171	-2.82214	-3.61417
H	2.96701	-1.62339	-5.27751
H	2.52249	-3.25607	-5.76166
C	1.84618	-1.63840	-2.76463
H	1.45680	-3.62201	-3.40163
H	3.21512	-3.08872	-3.37328
C	0.45218	-0.70003	-4.66342
C	0.46585	-1.06694	-3.16429
H	0.25469	-0.13870	-2.59082

175

H	-0.32817	-1.80932	-2.93839
H	1.19312	0.11250	-4.84569
H	-0.54739	-0.31852	-4.95792
H	0.07751	-2.71302	-5.41111
H	0.86193	-1.60343	-6.59979
H	2.60239	-0.91640	-3.14584
Si	3.52867	-5.56371	-2.54405
Si	2.40748	-6.06201	-4.48583
Si	2.32369	-4.75786	-0.74824
Si	0.66276	-7.42398	-4.23104
H	3.32626	-6.62716	-5.48023
H	1.61267	-5.03177	-5.12463
Si	-0.62530	-6.50615	-2.66726
H	-0.08083	-7.60411	-5.48663
H	1.14039	-8.72594	-3.74303
Si	0.80214	-6.46281	-0.98145
H	-1.68513	-7.48802	-2.37912
H	-1.20414	-5.19096	-2.97133
Si	5.49267	-4.43084	-2.61200
H	3.94772	-6.94764	-2.28888
Si	3.82513	-5.74471	0.68461
Si	5.71161	-4.69125	1.07950
Si	6.77638	-4.98290	-0.85881
H	5.28809	-2.97605	-2.55362
H	6.23792	-4.79337	-3.82245
H	8.07167	-4.29180	-0.84170
H	7.00501	-6.43056	-0.99655
Si	0.31606	-8.11983	0.43061
H	1.70302	-7.48579	-1.51317
Si	2.26350	-8.98543	1.05141
H	-0.37005	-9.16268	-0.34788
H	-0.56358	-7.78830	1.54472
Si	3.33923	-7.37457	2.15793
H	3.02587	-9.35368	-0.15836
H	2.06476	-10.20500	1.84791
H	6.47502	-5.44867	2.08701
H	5.44827	-3.32182	1.53352
H	4.39023	-6.84470	-0.10285
H	4.61373	-7.98450	2.56816
H	2.56968	-6.96184	3.33491
H	0.43395	-3.05331	-0.81265

94

Optimized geometry of **6**•[one-layer Si(111) surface] in .xyz format

N	5.96846	12.88061	11.87115
C	5.69007	13.21125	14.29521
C	4.27488	13.58553	14.80324
H	3.65170	13.95667	13.97533
H	3.78864	12.66525	15.16521
C	4.28364	14.61776	15.94575
H	4.63491	15.59540	15.56956
H	3.24959	14.78502	16.29222
C	5.16774	14.17495	17.12116
H	5.24442	14.98427	17.86655
H	4.68476	13.32617	17.63512
C	6.56762	13.75393	16.65000
H	7.14659	13.34551	17.49548
H	7.12126	14.64522	16.30278
C	6.51274	12.71970	15.51202
H	6.07605	11.77903	15.89003
H	7.53816	12.47543	15.18407
C	6.38996	14.42422	13.64069
H	6.06806	15.38562	14.06769
H	7.47815	14.35441	13.81126
C	6.11885	14.36205	12.12650
C	4.83913	15.14941	11.75720
H	4.71320	15.21891	10.66817
H	4.89876	16.17741	12.15046
H	3.93941	14.67709	12.16984
C	7.29233	14.99950	11.36558
H	8.25829	14.58135	11.67542
H	7.30878	16.08011	11.57878
H	7.20145	14.87389	10.27810
C	6.75193	12.24794	10.83987
C	6.23462	12.18677	9.50700
C	6.95700	11.50215	8.51547
H	6.55231	11.45735	7.50082
C	8.16527	10.86855	8.79522
H	8.69688	10.31646	8.01640
C	8.70580	10.98480	10.07399
H	9.68557	10.54467	10.28133
C	8.05181	11.69804	11.09237
C	4.94887	12.89588	9.08244
H	4.45180	13.22302	10.00700
C	3.96226	12.00502	8.30538
H	4.40037	11.62292	7.36914
H	3.07097	12.59115	8.02831
H	3.63126	11.14149	8.89490

C	5.26419	14.13599	8.21753
H	5.95376	14.83486	8.71151
H	4.33781	14.68463	7.98060
H	5.72805	13.83657	7.26322
C	8.85560	11.94332	12.37523
H	8.26851	12.61635	13.01605
C	9.15780	10.66753	13.18375
H	8.24364	10.16623	13.53016
H	9.76752	10.91317	14.06852
H	9.72474	9.94026	12.58047
C	10.18649	12.66293	12.05868
H	10.88771	11.99446	11.53498
H	10.67426	12.98814	12.99188
H	10.03820	13.54637	11.42077
C	5.70891	12.13408	13.14061
H	6.56715	11.46793	13.34077
Si	4.33979	10.68876	13.18376
Si	2.13257	11.01541	12.83290
Si	1.46390	11.23107	10.74042
Si	0.96690	12.26133	14.26758
H	1.53351	9.70100	13.10526
Si	4.19052	9.57967	15.15648
Si	2.96379	10.46037	16.81503
Si	6.15640	8.75977	15.83457
H	3.34725	8.40758	14.88220
Si	4.69873	8.79309	11.99069
H	3.72544	7.83808	12.53935
Si	4.09457	8.67334	9.87250
Si	6.67343	7.82775	12.28517
H	-0.42398	12.34881	13.80059
H	1.45295	13.63166	14.44869
Si	0.91344	10.99829	16.10638
Si	6.71917	7.14189	14.40730
H	5.97528	8.11358	17.14288
H	7.20191	9.78345	15.93636
H	4.23255	7.28799	9.40029
H	5.03600	9.46820	9.08005
Si	1.91117	9.23588	9.78115
H	5.64597	6.14205	14.52067
H	7.99831	6.51238	14.76121
H	7.73697	8.72164	11.83537
H	6.75225	6.61234	11.46190
H	0.25697	9.74409	15.71040
H	0.12505	11.64026	17.16900
H	3.56530	11.62686	17.38655
H	2.83495	9.48058	17.90237

H	2.03590	12.45404	10.17372
H	0.00178	11.37651	10.72180
H	1.16429	8.22779	10.54690
H	1.45244	9.22687	8.38469

54

Optimized geometry of **7**•[one-layer Si(111) surface] in .xyz format

Si	0.24358	0.23736	0.82837
Si	-1.93444	0.59842	0.36583
H	-2.03739	0.61903	-1.10000
Si	-2.56069	2.63431	1.03337
Si	-3.38022	-1.02021	0.92454
Si	1.30933	1.78172	-0.44461
H	0.93895	1.49143	-1.83693
Si	3.50627	1.52987	-0.17796
Si	0.73390	3.94433	-0.19626
Si	0.74750	-1.66610	-0.23955
H	0.45010	-1.48437	-1.66745
Si	-0.52663	-3.37025	0.44044
Si	2.92226	-2.11137	-0.02536
C	0.87284	0.11200	2.67885
N	0.57112	-1.21932	3.18662
N	0.45943	1.20160	3.59426
H	1.98092	0.12972	2.53622
C	1.07699	1.07877	4.91584
H	0.77587	0.14152	5.40054
H	0.73265	1.90910	5.55189
H	2.19157	1.11272	4.88006
C	0.72940	2.52617	3.05444
H	1.81548	2.72392	2.89089
H	0.35140	3.29131	3.75078
H	0.20973	2.66040	2.09624
C	-0.77546	-1.43738	3.68294
H	-0.98050	-2.51991	3.72731
H	-1.50216	-0.97861	2.99767
H	-0.95911	-1.01366	4.69380
C	1.59678	-1.95358	3.91179
H	2.58548	-1.73092	3.48446
H	1.41958	-3.03844	3.80137
H	1.64302	-1.73879	5.00296
H	4.21956	2.55488	-0.95253
Si	4.08061	-0.46791	-0.99240
H	3.83854	1.66047	1.24838
H	-0.14207	-4.56790	-0.32016
Si	-2.66216	-2.90019	-0.05220
H	-0.32533	-3.66509	1.85934
Si	-1.49946	4.10619	-0.29099
H	-2.29521	2.81744	2.46827
H	-3.99972	2.79845	0.78356
H	-1.90867	5.48170	0.03073
H	-1.91277	3.78387	-1.66336

H	1.36597	4.78259	-1.22426
H	1.19669	4.45910	1.09864
H	3.24193	-3.37242	-0.70973
H	3.29230	-2.23291	1.38428
H	5.52348	-0.69569	-0.82780
H	3.74213	-0.46564	-2.42253
H	-3.54382	-4.01903	0.31055
H	-2.71925	-2.68713	-1.50544
H	-4.71225	-0.68789	0.39918
H	-3.56288	-1.20317	2.36909

79

Optimized geometry of three-layer Si(111) surface model in .xyz format

Si	0.560444	-0.227327	2.074264
Si	3.767963	-2.067351	1.033247
Si	0.436635	-4.003833	1.399830
Si	3.866283	1.683972	1.669455
Si	0.634057	3.562356	2.680922
Si	-2.742151	-2.159741	2.393474
Si	-2.641433	1.656213	3.037326
Si	-0.866947	3.013690	6.256110
H	-3.316159	1.022618	6.846393
H	2.120946	4.188953	6.232023
Si	-1.816871	0.967973	6.945001
Si	1.466084	2.880917	6.579928
H	-1.456421	0.688762	8.378334
H	1.773050	2.576667	8.020429
Si	-0.984564	-0.785281	5.597240
Si	2.355680	1.156931	5.230524
H	-3.420065	-2.775763	6.198398
Si	-1.921163	-2.837510	6.299567
H	5.339456	2.316022	5.226260
Si	1.362577	-0.892026	5.868164
Si	4.689011	1.005383	5.572803
H	-1.563053	-3.062393	7.743087
H	1.668453	-1.145851	7.323535
H	4.949050	0.728350	7.028013
Si	-1.069502	-4.589709	4.970047
Si	2.254481	-2.666902	4.584390
Si	5.572863	-0.730530	4.242384
Si	1.263285	-4.687517	5.304536
Si	4.588551	-2.757435	4.939810
H	1.854859	-5.844851	4.548698
H	4.846235	-2.981128	6.404635
H	1.569533	-4.882022	6.764289
H	5.174233	-3.917924	4.184105
Si	-1.464553	-0.382966	3.296197
Si	1.867676	1.555370	2.930132
Si	-1.344841	3.402038	3.961922
Si	-1.542662	-4.176761	2.679236
Si	1.768373	-2.258748	2.285288
Si	5.075416	-0.327885	1.954626
H	-2.109124	4.695784	3.838641
H	-1.437811	4.150654	7.064125
H	-1.706088	-5.897790	5.363777
H	7.069778	-0.798688	4.403053
H	6.371526	-0.233241	1.190264

H	-2.370498	-5.317471	2.143676
H	4.683612	2.834294	2.199516
H	1.472523	4.700378	3.204661
H	1.211507	-5.291775	1.511938
H	4.520855	-3.368149	1.147859
H	-4.041986	-2.239465	3.152535
H	-3.942769	1.551216	3.790646
Si	0.155163	3.976340	0.388061
Si	-2.173370	4.093987	0.023561
Si	3.392132	2.093413	-0.624698
Si	1.052597	2.220924	-0.909845
Si	-3.135565	2.063576	0.746336
Si	4.243272	0.362342	-1.984652
Si	0.074781	0.176135	-0.230006
Si	-2.267476	0.290531	-0.547475
Si	3.291715	-1.673215	-1.263357
Si	0.950912	-1.579194	-1.553555
Si	-3.238101	-1.760722	0.101507
Si	-0.047410	-3.614337	-0.896343
Si	-2.377146	-3.489191	-1.255406
H	-3.032539	-4.799690	-0.917242
H	-2.653425	-3.186669	-2.701904
H	-4.734936	-1.676586	-0.051269
H	0.622355	-1.284486	-2.994808
H	0.539835	-4.744556	-1.701763
H	3.870673	0.614304	-3.419349
H	5.743144	0.305749	-1.893904
H	3.849604	-2.820624	-2.065455
H	0.721414	2.433363	-2.365136
H	4.016733	3.409851	-1.009211
H	-2.448447	4.292869	-1.441163
H	-2.765424	5.255877	0.772362
H	0.808441	5.276057	-0.005665
H	-2.526299	0.543731	-2.010710
H	-4.633217	2.115498	0.587635

Optimized geometry of **6**•[three-layer Si(111) surface] in .xyz format; bolded atoms were frozen for the optimization

Si	0.652766	-0.389700	2.213546
Si	3.865135	-2.203353	1.164187
Si	0.570985	-4.137693	1.517872
Si	3.918823	1.536264	1.826539
Si	0.710110	3.372572	2.854807
Si	-2.622738	-2.317068	2.538160
Si	-2.536203	1.445170	3.184328
Si	-0.860078	2.716855	6.403495
H	-3.283082	0.718604	6.078699
H	2.039548	3.947037	6.078126
Si	-1.980809	0.673172	6.829009
Si	1.490519	2.679247	6.673680
H	-2.341467	0.462639	8.265517
H	1.879849	2.668853	8.123455
Si	-0.764124	-1.097587	5.845562
Si	2.424447	0.839853	5.504239
H	-3.322391	-2.950632	5.717195
Si	-1.916488	-3.121796	6.222557
H	5.075808	2.197764	4.491987
Si	1.611391	-1.283700	6.394099
Si	4.782068	1.014105	5.369259
H	-1.983257	-3.437738	7.680327
H	5.449126	1.303986	6.673007
Si	-0.918891	-4.842858	4.949513
Si	2.388453	-2.840061	4.738737
Si	5.701422	-0.873182	4.278199
Si	1.440641	-4.963875	5.152177
Si	4.755704	-2.995040	4.752426
H	1.960078	-5.946214	4.138664
H	5.290560	-3.608430	6.013383
H	1.866057	-5.465315	6.501316
H	5.165569	-3.917644	3.638141
Si	-1.301937	-0.590089	3.506236
Si	1.939084	1.340993	3.153626
Si	-1.281814	3.208928	4.119526
Si	-1.437224	-4.351120	2.708447
Si	1.879837	-2.392595	2.441293
Si	5.192578	-0.450032	2.007004
H	-2.053141	4.499702	4.004536
H	-1.438165	3.821759	7.250046
H	-1.538012	-6.181790	5.252796
H	7.196101	-0.903769	4.473470
H	6.447891	-0.327603	1.181036

H	-2.247741	-5.471401	2.106930
H	4.730328	2.709962	2.303522
H	1.543179	4.511518	3.383114
H	1.339637	-5.431322	1.577284
H	4.622386	-3.503293	1.223077
H	-3.921415	-2.429943	3.291368
H	-3.859559	1.327643	3.891078
Si	0.222518	3.862245	0.549516
Si	-2.106012	3.979895	0.185016
Si	3.459488	1.979315	-0.463244
Si	1.119958	2.106825	-0.748394
Si	-3.068212	1.949485	0.907796
Si	4.310628	0.248245	-1.823194
Si	0.142138	0.062045	-0.068554
Si	-2.200122	0.176435	-0.386024
Si	3.359068	-1.787305	-1.101904
Si	1.018268	-1.693285	-1.392104
Si	-3.170742	-1.874815	0.262966
Si	0.019948	-3.728435	-0.734884
Si	-2.309792	-3.603285	-1.093954
H	-2.965182	-4.913785	-0.755784
H	-2.586062	-3.300765	-2.540444
H	-4.667582	-1.790685	0.110186
H	0.689708	-1.398585	-2.833354
H	0.607188	-4.858655	-1.540304
H	3.938028	0.500205	-3.257894
H	5.810498	0.191655	-1.732444
H	3.916958	-2.934715	-1.904004
H	0.788768	2.319265	-2.203684
H	4.084088	3.295755	-0.847754
H	-2.381092	4.178775	-1.279704
H	-2.698062	5.141785	0.933816
H	0.875798	5.161965	0.155796
H	-2.458942	0.429635	-1.849254
H	-4.565862	2.001405	0.749096
H	0.193302	-7.169097	7.665276
H	1.183042	-7.484765	9.926072
H	7.144132	-1.028290	8.187142
H	4.022968	-4.348591	8.649579
H	4.614116	-4.558101	10.311792
H	3.145096	-5.398669	9.778587
C	3.705217	-4.458649	9.697096
H	5.215535	-2.619470	7.969829
C	-0.402231	-6.374597	8.141401
C	0.768960	-6.540068	10.315473
C	6.253424	-0.927165	8.830190

H	6.474516	-1.526366	9.730695
H	1.400622	-5.309546	8.642417
H	-0.805488	-5.729672	7.352718
C	5.038612	-1.540839	8.104624
C	0.459227	-5.583399	9.142097
H	-1.259477	-6.858896	8.636088
H	1.489490	-6.139300	11.039643
H	-0.154883	-6.785167	10.864234
H	4.967927	-1.114437	7.087217
C	2.866311	-3.248887	10.180669
C	6.068478	0.547096	9.231365
H	4.761889	-2.219540	10.548382
H	6.851876	0.835453	9.952103
H	6.223679	1.185340	8.347337
H	3.177882	-3.790571	12.241237
C	3.736696	-1.980821	10.231530
C	3.695709	-1.305898	8.837571
N	1.800799	-2.867962	9.189937
C	2.329286	-3.527968	11.590235
C	-0.213861	-4.279411	9.577018
H	1.607861	-4.351539	11.622923
C	2.487736	-2.085503	8.115550
H	-2.022647	-5.363300	10.030713
C	0.419488	-2.991655	9.563838
C	4.679258	0.842611	9.817674
C	-1.544641	-4.380266	10.018758
C	3.538120	0.221725	8.989697
H	4.622745	0.466800	10.854775
H	3.326006	-1.301592	10.995481
H	1.843228	-2.639525	12.014227
H	3.527944	0.682437	7.987256
H	4.528454	1.933062	9.885031
C	-0.300157	-1.880503	10.107263
H	2.574227	0.474080	9.449589
C	-2.285644	-3.263327	10.398211
H	1.477745	-0.791559	10.389576
C	-1.656600	-2.021414	10.440818
C	0.408915	-0.604178	10.544568
H	-3.333601	-3.367440	10.689659
H	0.401297	-1.234787	12.659760
H	0.225810	0.530808	8.680455
C	0.197848	-0.341172	12.051251
C	0.035412	0.655376	9.758146
H	-2.205568	-1.153484	10.816921
H	0.865132	0.467054	12.392140
H	0.625576	1.518897	10.104743

```
H    -0.836482    -0.027256    12.263451
H    -1.027711     0.905355     9.887394
H     3.009866    -2.848422     7.496531
```

Optimized geometry of **7**•[three-layer Si(111) surface] in .xyz format; bolded atoms were frozen for the optimization

Si	0.583485	-0.221378	2.097354
Si	3.784044	-2.056006	1.058942
Si	0.465499	-3.992332	1.421877
Si	3.866525	1.699523	1.696680
Si	0.637676	3.566085	2.704792
Si	-2.708222	-2.157269	2.418362
Si	-2.620571	1.638584	3.057685
Si	-0.907590	3.020753	6.270461
H	-3.413989	1.064306	6.400775
H	2.010551	4.243745	6.114304
Si	-1.977159	0.995501	6.838550
Si	1.432410	2.935124	6.580182
H	-1.989540	0.768011	8.324017
H	1.779698	2.784218	8.032519
Si	-0.938673	-0.795554	5.686332
Si	2.328810	1.165303	5.290618
H	-3.478873	-2.706934	5.806032
Si	-2.034996	-2.829327	6.207937
H	5.288714	2.392439	5.100801
Si	1.430579	-0.905568	6.032715
Si	4.681940	1.088342	5.539495
H	-2.020485	-3.088737	7.689235
H	5.054330	0.900228	6.985336
Si	-1.047672	-4.593000	4.987425
Si	2.262013	-2.644943	4.645871
Si	5.572812	-0.685105	4.257937
Si	1.298089	-4.718890	5.242967
Si	4.608719	-2.732798	4.927240
H	1.804329	-5.788328	4.313498
H	4.942182	-3.011768	6.366412
H	1.681012	-5.124553	6.636203
H	5.186669	-3.854771	4.109608
Si	-1.416268	-0.392131	3.350304
Si	1.873639	1.561507	2.973323
Si	-1.350980	3.409261	3.969989
Si	-1.516103	-4.181704	2.693444
Si	1.792594	-2.247832	2.329708
Si	5.086430	-0.304932	1.966765
H	-2.124040	4.696068	3.827895
H	-1.497928	4.152579	7.071892
H	-1.684709	-5.903155	5.375362
H	7.069113	-0.738976	4.435552
H	6.384110	-0.200430	1.206072

H	-2.341060	-5.321448	2.150738
H	4.691723	2.850736	2.212905
H	1.467870	4.711964	3.224745
H	1.244978	-5.278291	1.519630
H	4.552615	-3.347828	1.170407
H	-4.011026	-2.237173	3.170496
H	-3.929218	1.530537	3.796004
Si	0.162883	3.975214	0.409211
Si	-2.165647	4.092864	0.044711
Si	3.399853	2.092284	-0.603549
Si	1.060323	2.219794	-0.888699
Si	-3.127847	2.062454	0.767491
Si	4.250993	0.361214	-1.963499
Si	0.082503	0.175014	-0.208859
Si	-2.259757	0.289404	-0.526329
Si	3.299433	-1.674336	-1.242209
Si	0.958633	-1.580316	-1.532409
Si	-3.230377	-1.761846	0.122661
Si	-0.039687	-3.615466	-0.875189
Si	-2.369427	-3.490316	-1.234259
H	-3.024817	-4.800816	-0.896089
H	-2.645697	-3.187796	-2.680749
H	-4.727217	-1.677716	-0.030119
H	0.630073	-1.285616	-2.973659
H	0.547553	-4.745686	-1.680609
H	3.878393	0.613174	-3.398199
H	5.750863	0.304624	-1.872749
H	3.857323	-2.821746	-2.044309
H	0.729133	2.432234	-2.343989
H	4.024453	3.408724	-0.988059
H	-2.440727	4.291744	-1.420009
H	-2.757697	5.254754	0.793511
H	0.816163	5.274934	0.015491
H	-2.518577	0.542604	-1.989559
H	-4.625497	2.114374	0.608791
C	2.317764	-1.175945	7.784241
N	2.247675	-2.559618	8.246797
N	2.103381	-0.036722	8.675639
H	3.362519	-1.056096	7.437464
C	0.818707	0.072745	9.346612
H	0.012807	-0.258431	8.677926
H	0.626131	1.125981	9.615421
H	0.755439	-0.526512	10.279803
C	3.208315	0.330976	9.555796
H	3.267018	-0.287088	10.477359
H	3.091526	1.383129	9.867821

H	4.164177	0.245706	9.018962
C	3.355998	-3.006981	9.086615
H	3.281160	-2.662428	10.140765
H	4.310905	-2.650108	8.672620
H	3.384168	-4.109615	9.097677
C	0.969347	-3.054391	8.730419
H	0.746369	-2.770902	9.780652
H	0.951230	-4.155898	8.672594
H	0.155976	-2.670723	8.099258

38

Optimized geometry of Si(111) surface model with T defect in .xyz format

Si	-0.008037	-0.083709	-0.189136
Si	2.181099	0.314554	-1.000600
Si	-1.252301	1.929155	-0.277511
Si	-1.064300	-1.702126	-1.557581
H	2.043157	0.802372	-2.419721
Si	3.435738	-1.686143	-1.039461
Si	3.250895	2.007405	0.251393
H	-1.103052	-1.139705	-2.955044
Si	-3.287692	-2.074458	-0.854291
Si	0.182654	-3.706813	-1.612564
Si	-3.473763	1.568813	0.438338
H	-1.291525	2.365862	-1.718895
Si	-0.194083	3.627144	0.976983
Si	0.093158	-0.855021	2.038190
H	4.824447	-1.407885	-1.544865
Si	2.373459	-3.303397	-2.389260
H	3.557120	-2.209199	0.364065
H	3.169420	-4.579035	-2.418939
H	2.294882	-2.776537	-3.794453
H	-0.510832	-4.714193	-2.487627
H	0.243747	-4.275173	-0.222829
H	4.636233	2.240076	-0.285307
H	3.385602	1.545275	1.674905
Si	1.997764	4.005410	0.190685
H	1.920988	4.477703	-1.233788
H	2.672578	5.079916	0.998066
H	-0.138978	3.198857	2.416249
H	-1.003384	4.892602	0.907612
H	-3.933414	-3.112322	-1.730222
Si	-4.527746	-0.068148	-0.893798
H	-3.262556	-2.613570	0.548202
H	-4.240720	2.861485	0.391943
H	-3.447618	1.104928	1.867286
H	-5.936857	-0.306798	-0.425396
H	-4.591228	0.431535	-2.309473
H	0.874496	-2.133234	2.116877
H	-1.286218	-1.108456	2.570758
H	0.760357	0.163660	2.914349

Optimized geometry of the adduct of molecule **6** with the above T-defect surface

Si	0.093614	-0.142901	0.339010
Si	2.063500	0.578805	-0.765870
Si	-1.528866	1.560130	0.050910
Si	-0.646203	-1.913084	-1.064361
H	1.653487	0.658190	-2.215804
Si	3.757823	-1.064717	-0.664492
Si	2.811539	2.756286	-0.239008
H	-0.675452	-1.384175	-2.475889
Si	-2.825140	-2.669175	-0.553569
Si	0.897817	-3.701433	-1.012801
Si	-3.633635	0.874107	0.872783
H	-1.683526	1.745035	-1.437827
Si	-0.783847	3.638133	0.884990
Si	0.079279	-1.079321	2.531931
H	5.023636	-0.554604	-1.297167
Si	3.014921	-3.004426	-1.786917
H	4.069143	-1.384780	0.770459
H	4.024076	-4.112884	-1.657401
H	2.895030	-2.665272	-3.246356
H	0.405384	-4.844994	-1.857202
H	1.023988	-4.202789	0.397761
H	3.934301	3.121321	-1.171455
H	3.363916	2.792978	1.156942
Si	1.068235	4.339567	-0.396431
H	0.637998	4.447109	-1.832075
H	1.559307	5.693352	0.039067
H	-0.366407	3.488478	2.320930
H	-1.883344	4.662906	0.836150
H	-3.248451	-3.674552	-1.589879
Si	-4.394813	-0.907605	-0.473990
H	-2.806915	-3.373873	0.771777
H	-4.609146	2.017782	0.816606
H	-3.511447	0.442313	2.305229
H	-5.727410	-1.419621	0.000532
H	-4.582129	-0.375542	-1.867455
H	0.924318	-2.320834	2.512352
H	-1.352302	-1.527834	2.596436
H	1.198280	-1.354096	8.433231
C	0.371485	-1.160489	7.732092
H	-0.395943	-1.931840	7.894668
H	-0.067758	-0.184723	7.981523
H	-1.517465	1.384091	8.399539
H	2.507049	-2.635514	6.679666
H	-1.065509	-4.010673	7.146658

H	-1.220457	3.039942	7.807193
H	2.911676	-0.278870	6.371173
C	-1.809050	2.123602	7.638808
C	1.599600	-2.553515	6.059456
H	0.934487	-3.384351	6.331933
H	1.573297	0.838730	6.671720
C	-1.577195	-4.451108	6.277534
C	0.908323	-1.187836	6.294479
C	1.890536	-0.019381	6.054534
H	-1.044667	-5.375278	5.999302
H	-2.591268	-4.734678	6.603684
H	-2.867473	2.374485	7.811228
H	3.525326	2.251582	5.833521
H	4.604122	-0.142507	5.075008
H	1.888101	-2.687809	5.007849
C	-1.579374	1.595588	6.207536
H	5.453981	2.035471	4.285962
H	-0.495894	1.446670	6.090984
C	3.357709	2.414190	4.752965
C	4.334053	0.180496	4.053396
C	-1.640295	-3.478035	5.082609
C	-2.263717	0.249742	5.978219
C	4.456910	1.706149	3.949134
N	-0.161253	-0.915477	5.282801
C	-1.566722	-0.934885	5.585934
C	-2.294144	-2.158361	5.477743
C	-3.648658	0.190931	6.200518
C	1.806239	0.372030	4.555013
H	3.410702	3.504276	4.594244
C	-3.672455	-2.167322	5.747162
C	-4.356214	-1.004313	6.091695
H	-0.612907	-3.241829	4.767810
H	-4.179719	1.102625	6.488280
H	1.189898	2.423355	4.965216
H	5.058642	-0.308385	3.380829
C	1.959968	1.902375	4.370227
C	2.916428	-0.307696	3.709585
H	-4.223139	-3.108454	5.667483
H	2.868812	-1.402978	3.803771
H	-1.487360	3.599080	5.325831
H	-5.432238	-1.029238	6.280684
C	-2.035097	2.653473	5.182808
C	0.346420	-0.075066	4.173351
C	-2.348696	-4.159266	3.897380
H	-1.785511	-5.051908	3.580844
H	-3.110110	2.868370	5.294322

```
H     4.371882      2.001955      2.887914
H    -3.365974     -4.489299      4.162830
H    -0.283672      0.826830      4.067049
H     1.760794      2.156259      3.312211
H    -1.872958      2.320422      4.146550
H     2.722239     -0.083732      2.642639
H    -2.428175     -3.484075      3.033638
```

42
Optimized geometry of Si(111) surface model with D defect in .xyz format

Si	-0.026404	-0.055321	-0.289426
Si	2.195459	0.354455	-1.005077
Si	-1.221821	1.984385	-0.440197
Si	-1.049443	-1.636120	-1.725503
H	2.119037	0.909032	-2.404316
Si	3.434857	-1.654696	-1.082986
Si	3.224637	1.976625	0.368976
H	-1.069749	-1.036938	-3.108487
Si	-3.275722	-2.020383	-1.027839
Si	0.199080	-3.638945	-1.815662
Si	-3.533911	1.757444	-0.010456
H	-1.074644	2.440607	-1.869237
Si	-0.242322	3.620966	0.952415
Si	0.018465	-0.923877	1.907642
H	4.842175	-1.369537	-1.529677
Si	2.404726	-3.206204	-2.531337
H	3.503627	-2.238104	0.299970
H	3.200457	-4.480402	-2.602075
H	2.356015	-2.616456	-3.912703
H	-0.477901	-4.618853	-2.733613
H	0.234248	-4.250928	-0.443467
H	4.637862	2.212080	-0.088078
H	3.282437	1.451032	1.775460
Si	2.003346	3.995144	0.333964
H	2.023575	4.540202	-1.066362
H	2.640940	5.017069	1.234603
H	-0.299276	3.138755	2.374499
H	-1.027096	4.901342	0.873530
H	-3.900059	-3.050004	-1.935063
Si	-4.503795	-0.013357	-1.233704
Si	-3.269978	-2.903408	1.163106
H	-4.219888	3.049858	-0.359136
H	-3.736747	1.517963	1.458310
H	-5.929439	-0.218198	-0.799851
H	-4.518621	0.369690	-2.687403
H	-2.597329	-4.247533	1.121477
H	-4.681835	-3.118026	1.633749
Si	-2.115629	-1.539681	2.705699
H	-1.972835	-2.270289	4.012220
H	-2.920443	-0.297651	2.961168
H	0.645224	0.073119	2.842301
H	0.895812	-2.145018	1.902964

101
Optimized geometry of adduct of molecule **6** with edge site of D-defect surface

Si	-0.02640	-0.05532	-0.28943
Si	2.19546	0.35446	-1.00508
Si	-1.22182	1.98439	-0.44020
Si	-1.04944	-1.63612	-1.72550
H	2.11904	0.90903	-2.40432
Si	3.43486	-1.65470	-1.08299
Si	3.22464	1.97663	0.36898
H	-1.06975	-1.03694	-3.10849
Si	-3.27572	-2.02038	-1.02784
Si	0.19908	-3.63895	-1.81566
Si	-3.53391	1.75744	-0.01046
H	-1.07464	2.44061	-1.86924
Si	-0.24232	3.62097	0.95242
Si	0.01846	-0.92388	1.90764
H	4.84218	-1.36954	-1.52968
Si	2.40473	-3.20620	-2.53134
H	3.50363	-2.23810	0.29997
H	3.20046	-4.48040	-2.60208
H	2.35602	-2.61646	-3.91270
H	-0.47790	-4.61885	-2.73361
H	0.23425	-4.25093	-0.44347
H	4.63786	2.21208	-0.08808
H	3.28244	1.45103	1.77546
Si	2.00335	3.99514	0.33396
H	2.02358	4.54020	-1.06636
H	2.64094	5.01707	1.23460
H	-0.29928	3.13876	2.37450
H	-1.02710	4.90134	0.87353
H	-3.90006	-3.05000	-1.93506
Si	-4.50380	-0.01336	-1.23370
Si	-3.26998	-2.90341	1.16311
H	-4.21989	3.04986	-0.35914
H	-3.73675	1.51796	1.45831
H	-5.92944	-0.21820	-0.79985
H	-4.51862	0.36969	-2.68740
H	-2.59733	-4.24753	1.12148
H	-4.68184	-3.11803	1.63375
Si	-2.11563	-1.53968	2.70570
H	-1.97283	-2.27029	4.01222
H	-2.92044	-0.29765	2.96117
H	0.64522	0.07312	2.84230
H	-2.41548	-4.48719	7.09730
C	-1.34347	-4.44942	6.79112
H	-0.99838	-6.57032	7.01842

H	-0.82209	-4.24571	7.74384
C	-0.94324	-5.80163	6.21664
H	-1.67044	-6.08378	5.42523
H	-1.56879	-2.43914	6.12128
C	-1.15705	-3.37204	5.69220
H	-1.87563	-3.85098	4.98964
H	-0.33374	-1.00953	7.64155
H	-0.62004	-0.52876	5.90835
C	0.12845	-0.59009	6.71980
C	0.45562	-5.73390	5.58791
H	0.84369	-3.30546	7.20795
H	1.19679	-5.55216	6.39576
H	0.40650	0.44653	6.98687
C	0.30342	-3.17773	4.97277
H	0.68272	-6.72920	5.15612
C	1.13580	-2.90189	6.23218
C	0.57909	-4.63730	4.46937
C	1.36357	-1.42634	6.31413
H	-0.12226	-4.86657	3.63966
H	2.17031	3.13873	7.31621
H	1.63002	1.38804	5.54657
C	0.95809	-1.93654	3.88435
H	1.93938	-1.61396	8.46083
H	2.08958	3.71703	5.00024
H	2.09561	-3.39411	6.14556
N	1.80139	-1.11980	4.93156
C	2.39406	-1.29863	7.49306
C	2.86426	2.29620	7.12425
C	2.66437	1.73631	5.66747
C	2.82964	2.93306	4.72993
H	1.59496	-4.72580	4.05515
H	2.66052	1.62253	7.96637
H	2.65690	2.62690	3.68452
H	2.78608	-0.31332	7.63622
H	1.74883	-2.48885	3.34126
H	3.29236	-1.90575	7.35997
C	3.25699	-0.76147	4.90400
H	3.89458	2.67826	7.29026
C	3.64616	0.60293	5.29976
H	3.83964	3.38699	4.82491
H	3.29537	-3.61704	4.60555
C	4.30429	-3.29443	4.79129
C	4.37756	-1.74886	4.85447
H	4.73520	-3.55766	2.66926
C	5.00969	0.94143	5.43398
C	5.10760	-3.91931	3.64374

H	4.32110	-3.65442	7.03350
H	5.31125	1.94043	5.71467
C	4.85515	-3.94283	6.11501
H	4.99199	-5.02740	3.68214
H	4.79303	-5.05103	6.08530
C	5.70631	-1.28437	5.01410
C	6.00795	0.02316	5.27168
H	6.19599	-3.71955	3.73136
H	5.92589	-3.69536	6.29504
H	6.54425	-1.96733	4.98926
H	7.04259	0.31807	5.41273

101

Optimized geometry of adduct of molecule **6** with center site of D-defect surface

Si	-0.02640	-0.05532	-0.28943
Si	2.19546	0.35446	-1.00508
Si	-1.22182	1.98439	-0.44020
Si	-1.04944	-1.63612	-1.72550
H	2.11904	0.90903	-2.40432
Si	3.43486	-1.65470	-1.08299
Si	3.22464	1.97663	0.36898
H	-1.06975	-1.03694	-3.10849
Si	-3.27572	-2.02038	-1.02784
Si	0.19908	-3.63895	-1.81566
Si	-3.53391	1.75744	-0.01046
H	-1.07464	2.44061	-1.86924
Si	-0.24232	3.62097	0.95242
Si	0.01846	-0.92388	1.90764
H	4.84218	-1.36954	-1.52968
Si	2.40473	-3.20620	-2.53134
H	3.50363	-2.23810	0.29997
H	3.20046	-4.48040	-2.60208
H	2.35602	-2.61646	-3.91270
H	-0.47790	-4.61885	-2.73361
H	0.23425	-4.25093	-0.44347
H	4.63786	2.21208	-0.08808
H	3.28244	1.45103	1.77546
Si	2.00335	3.99514	0.33396
H	2.02358	4.54020	-1.06636
H	2.64094	5.01707	1.23460
H	-0.29928	3.13876	2.37450
H	-1.02710	4.90134	0.87353
H	-3.90006	-3.05000	-1.93506
Si	-4.50380	-0.01336	-1.23370
Si	-3.26998	-2.90341	1.16311
H	-4.21989	3.04986	-0.35914
H	-3.73675	1.51796	1.45831
H	-5.92944	-0.21820	-0.79985
H	-4.51862	0.36969	-2.68740
H	-2.59733	-4.24753	1.12148
H	-4.68184	-3.11803	1.63375
Si	-2.11563	-1.53968	2.70570
H	-2.92044	-0.29765	2.96117
H	-4.43762	-5.34673	7.88303
C	-3.89701	-5.46165	6.90837
H	-3.98430	-7.61805	6.63398
H	-3.04625	-5.71190	7.54466
C	-3.92918	-6.69172	6.01679

H	-4.81131	-6.67170	5.34181
H	-4.13137	-3.33823	6.64280
C	-3.86053	-4.15512	5.97922
H	-4.69224	-4.18955	5.23997
H	-2.89108	-2.16667	8.20261
H	-3.25660	-1.50029	6.53483
C	-2.47046	-1.67221	7.29855
C	-2.60451	-6.69443	5.23102
H	-1.74268	-4.33309	7.50700
H	-1.76450	-6.81773	5.95196
H	-2.18022	-0.65890	7.61840
C	-2.44677	-4.03609	5.25843
H	-2.57948	-7.57452	4.55212
C	-1.51300	-3.94666	6.51429
C	-2.36856	-5.38541	4.42823
C	-1.26796	-2.47844	6.73724
H	-3.12787	-5.33650	3.61786
H	-1.13719	2.10874	7.39481
H	-1.46943	0.27213	5.78167
C	-1.79874	-2.75518	4.36886
H	-0.47253	-2.78581	8.76864
H	-1.43646	2.56454	5.03046
H	-0.58187	-4.47580	6.32844
N	-0.97447	-2.04892	5.37923
C	-0.12541	-2.37645	7.79266
C	-0.30342	1.40119	7.19412
C	-0.48320	0.76637	5.80114
C	-0.60295	1.87951	4.76324
H	-1.38828	-5.51072	3.93276
H	-0.34095	0.66463	8.01095
H	-0.84781	1.44258	3.77725
H	0.19582	-1.34594	7.96916
H	-1.11282	-3.29009	3.71090
H	0.77254	-2.94242	7.49659
C	0.35735	-1.59916	5.14352
H	0.65443	1.95207	7.26913
C	0.63956	-0.22650	5.42636
H	0.33281	2.47205	4.70027
H	0.30769	-4.35372	4.57563
C	1.31319	-4.01523	4.51044
C	1.44775	-2.49687	4.78094
H	1.10548	-3.84044	2.34939
C	1.95772	0.23229	5.33519
C	1.71829	-4.40137	3.08490
H	1.71949	-4.69149	6.56598
H	2.19116	1.26616	5.54387

C	2.07245	-4.88097	5.53428
H	1.52309	-5.48640	2.92289
H	1.88210	-5.95967	5.33340
C	2.74048	-1.96519	4.70454
C	2.99095	-0.62681	4.97835
H	2.79309	-4.21002	2.90130
H	3.16401	-4.70350	5.49772
H	3.57518	-2.60325	4.44583
H	4.00243	-0.25354	4.91946
H	0.55629	0.06497	2.77328
H	0.81519	-2.09901	1.88140

42

Optimized geometry of one-layer Si(111) surface model with M defect.

Si	-2.291757	0.546003	0.364310
Si	-2.631203	1.183786	-1.878056
Si	-0.292099	-0.636887	0.776771
H	-3.460505	-0.277664	0.829195
H	-2.252336	1.789314	1.209869
Si	-3.166464	-0.614959	-3.301175
H	-1.392656	1.862619	-2.391786
H	-3.749190	2.188896	-1.918190
Si	-1.165559	-3.702632	-1.818848
Si	-0.197610	-2.932738	0.203870
Si	1.705097	0.235751	-0.133644
H	-0.083241	-0.611267	2.270613
Si	0.332206	-5.414170	-2.471138
Si	3.238632	-1.412705	0.579037
H	1.629385	0.284957	-1.633868
H	2.035709	1.610380	0.372296
Si	2.476101	-4.526026	-2.006439
H	0.103656	-6.631711	-1.617765
H	0.168508	-5.809633	-3.911592
Si	2.134249	-3.448033	0.077627
H	2.475526	-4.456048	1.143575
H	-0.820130	-3.737910	1.314202
Si	5.500465	-1.158865	-0.043805
H	3.208185	-1.337389	2.085684
Si	5.882526	-0.730724	-2.329294
H	6.262253	-2.389671	0.363016
H	6.049374	-0.006341	0.751860
Si	5.473550	-2.587346	-3.720186
H	7.315253	-0.303835	-2.493397
H	5.014619	0.413755	-2.771483
Si	-1.376027	-2.129161	-3.565849
H	-3.535502	-0.065926	-4.651900
H	-4.366053	-1.341584	-2.762281
H	-2.532792	-4.266245	-1.537146
H	-0.096597	-1.354255	-3.708110
H	-1.575071	-2.894194	-4.845706
Si	3.190933	-3.177578	-3.806042
H	3.482148	-5.632912	-1.835249
H	2.360380	-1.927356	-3.869211
H	2.938931	-3.942142	-5.076855
H	6.279080	-3.760183	-3.237424
H	5.939069	-2.258430	-5.112005

101
Optimized geometry of adduct of molecule **6** with M-defect Si(111) surface model

Si	-2.29176	0.54600	0.36431
Si	-2.63120	1.18379	-1.87806
Si	-0.29210	-0.63689	0.77677
H	-3.46050	-0.27766	0.82920
H	-2.25234	1.78931	1.20987
Si	-3.16646	-0.61496	-3.30118
H	-1.39266	1.86262	-2.39179
H	-3.74919	2.18890	-1.91819
Si	-1.16556	-3.70263	-1.81885
Si	-0.19761	-2.93274	0.20387
Si	1.70510	0.23575	-0.13364
H	-0.08324	-0.61127	2.27061
Si	0.33221	-5.41417	-2.47114
Si	3.23863	-1.41271	0.57904
H	1.62939	0.28496	-1.63387
H	2.03571	1.61038	0.37230
Si	2.47610	-4.52603	-2.00644
H	0.10366	-6.63171	-1.61776
H	0.16851	-5.80963	-3.91159
Si	2.13425	-3.44803	0.07763
H	2.47553	-4.45605	1.14358
Si	5.50047	-1.15887	-0.04380
H	3.20818	-1.33739	2.08568
Si	5.88253	-0.73072	-2.32929
H	6.26225	-2.38967	0.36302
H	6.04937	-0.00634	0.75186
Si	5.47355	-2.58735	-3.72019
H	7.31525	-0.30384	-2.49340
H	5.01462	0.41375	-2.77148
Si	-1.37603	-2.12916	-3.56585
H	-3.53550	-0.06593	-4.65190
H	-4.36605	-1.34158	-2.76228
H	-2.53279	-4.26624	-1.53715
H	-0.09660	-1.35425	-3.70811
H	-1.57507	-2.89419	-4.84571
Si	3.19093	-3.17758	-3.80604
H	3.48215	-5.63291	-1.83525
H	2.36038	-1.92736	-3.86921
H	2.93893	-3.94214	-5.07686
H	6.27908	-3.76018	-3.23742
H	5.93907	-2.25843	-5.11200
H	-6.04893	-1.75127	-1.31561
H	-5.99199	-2.56936	2.62951
H	-6.50890	-2.83799	0.00366

C	-5.82995	-2.74485	-0.86780
H	-4.54170	-1.64774	2.15650
C	-4.89248	-2.46516	2.78056
H	-4.82270	-2.08095	3.80167
H	-4.18459	-2.00244	0.23182
H	-3.74114	-1.00840	5.99066
H	-7.21224	-3.76528	-2.18822
C	-4.34851	-2.80550	-0.42862
C	-6.14314	-3.83647	-1.88688
H	-5.81689	-4.44474	1.30389
H	-1.59908	-0.14721	5.14539
C	-3.35026	-2.04758	5.94300
H	-3.71641	-2.58814	-1.28359
H	-5.52214	-3.68436	-2.79782
H	-5.81844	-4.77143	3.78959
H	-4.23972	-2.68128	5.81243
H	-2.70572	-1.82890	3.86188
C	-4.18858	-3.84418	2.58975
C	-4.71551	-4.52226	1.38694
C	-1.17167	-1.17556	5.12623
C	-2.28292	-2.17253	4.81609
C	-4.70331	-4.74488	3.77146
C	-3.86180	-4.13658	0.19590
H	-2.93161	-2.30894	6.93520
C	-5.86162	-5.21376	-1.27633
H	-6.55526	-5.39073	-0.43353
H	-4.36143	-4.43260	4.75794
H	-0.39022	-1.22385	4.35091
N	-2.69278	-3.80833	2.37127
H	-4.55361	-5.60804	1.53318
H	-0.71604	-1.37872	6.11569
C	-2.26075	-3.91801	0.89965
C	-4.36573	-5.32776	-0.85738
H	-6.10572	-5.99416	-2.03283
H	-4.37245	-5.79031	3.67689
C	-1.75610	-3.61346	4.65951
H	-3.95127	-5.42934	-1.88183
C	-1.94315	-4.38901	3.45167
H	-4.17458	-6.33981	-0.44407
H	-1.85138	-4.90562	0.73013
C	-1.10838	-4.18970	5.75600
H	-0.96564	-3.62456	6.66671
H	-2.63871	-6.43938	1.68121
C	-1.54367	-5.79113	3.46964
H	-3.57242	-7.78337	3.50122
C	-1.91266	-6.83150	2.38574

C	-0.64936	-5.49481	5.71428
C	-2.65322	-8.06512	2.95410
C	-0.86657	-6.28308	4.59567
H	-2.96688	-8.73478	2.12267
H	-0.18015	-6.42302	1.12178
C	-0.68004	-7.28938	1.60143
H	-0.15825	-5.91635	6.57929
H	-0.98655	-7.99622	0.79887
H	-2.01791	-8.66121	3.63750
H	-0.54486	-7.31421	4.63634
H	0.04486	-7.79935	2.26744

38

Optimized geometry of model of Si(111) surface with an oxidation defect, $(SiO)_3SiH$

Si	-0.034958	-0.311742	1.812872
Si	2.381902	0.476523	-0.050418
Si	-1.469415	2.203549	0.553853
Si	-1.130544	-1.865621	-0.707528
Si	3.665032	-1.391412	-0.726606
Si	3.336447	2.563882	0.520985
Si	-3.492788	-1.976426	-0.744989
Si	0.269596	-3.662553	-1.344009
Si	-3.820591	1.958936	0.473201
Si	-0.393476	4.235485	1.109583
H	4.828782	-0.954580	-1.573636
Si	2.378503	-2.859333	-2.075360
H	4.207444	-2.094484	0.484034
H	3.237188	-4.045130	-2.424378
H	2.113628	-2.115693	-3.356257
H	-0.318471	-4.413883	-2.506842
H	0.412774	-4.618174	-0.195020
H	4.518428	2.864447	-0.359477
H	3.812645	2.528602	1.944320
Si	1.782439	4.321693	0.168013
H	1.583397	4.401116	-1.321283
H	2.427396	5.612741	0.595315
H	-0.352313	4.391090	2.602275
H	-1.143587	5.407939	0.539082
H	-3.972204	-2.772482	-1.927792
Si	-4.434201	0.188565	-0.982185
H	-3.984277	-2.653180	0.501816
H	-4.469063	3.199202	-0.078076
H	-4.348504	1.734494	1.860634
H	-5.932820	0.052755	-0.945788
H	-4.069021	0.648701	-2.367445
O	-0.928398	1.071128	1.678748
O	-0.711777	-1.497170	0.882638
H	-0.758997	-0.715116	-1.610904
H	-0.967647	1.834274	-0.820993
O	1.509551	-0.022955	1.302630
H	1.432015	0.759379	-1.188596
H	-0.012046	-0.746968	3.222475

Optimized geometry of **6**•(SiO)₃SiH surface model in .xyz format

N	6.252417	13.019042	11.900766
C	5.874613	13.288867	14.323536
C	4.446781	13.625878	14.837491
H	3.825762	14.036294	14.028172
H	3.964721	12.682959	15.150157
C	4.440902	14.580074	16.044269
H	4.815932	15.575658	15.745585
H	3.400456	14.736882	16.375656
C	5.293040	14.040005	17.200498
H	5.332082	14.770624	18.025624
H	4.814682	13.130347	17.608436
C	6.709178	13.688519	16.725675
H	7.288073	13.235358	17.547831
H	7.244602	14.614329	16.445164
C	6.678775	12.730037	15.525218
H	6.224338	11.771777	15.836376
H	7.708933	12.499973	15.201477
C	6.575104	14.526215	13.705287
H	6.226403	15.472708	14.144313
H	7.660173	14.466480	13.899296
C	6.341752	14.488256	12.178515
C	5.034456	15.227013	11.795868
H	4.946837	15.330882	10.705154
H	5.025172	16.241263	12.227646
H	4.145444	14.688893	12.152086
C	7.504967	15.157664	11.433954
C	6.996894	12.372281	10.855571
C	6.416144	12.269970	9.558375
C	7.113533	11.606304	8.536309
H	6.663428	11.536802	7.542066
C	8.353604	11.016063	8.767597
H	8.874164	10.486120	7.966047
C	8.928485	11.121198	10.032829
H	9.912597	10.678173	10.210699
C	8.292076	11.810551	11.077269
C	5.046706	12.853147	9.232795
H	4.628345	13.226670	10.178468
C	4.080323	11.785339	8.694976
H	4.429722	11.353103	7.743382
H	3.085178	12.223059	8.517600
H	3.976001	10.966672	9.421378
C	5.152107	14.027211	8.240386
H	5.826495	14.816143	8.607313
H	4.161845	14.478601	8.065133

H	5.542427	13.688820	7.266487
C	9.062748	11.949545	12.389539
H	8.478388	12.600390	13.056509
C	9.261499	10.591634	13.093297
H	8.306167	10.075590	13.274204
H	9.767250	10.724188	14.063466
H	9.884127	9.920957	12.479415
C	10.430394	12.632730	12.182831
H	11.106564	12.006054	11.580411
H	10.920038	12.810030	13.154155
H	10.330402	13.599671	11.667356
C	5.913623	12.260208	13.126227
H	6.731165	11.543862	13.348107
Si	4.442020	11.064692	12.964526
Si	1.433610	11.077187	12.633688
Si	0.530091	10.885750	10.456244
Si	0.244770	12.178283	14.363793
Si	3.737102	9.105456	15.495252
Si	2.485028	10.206150	17.173168
Si	5.663862	7.848098	16.051328
Si	4.421751	8.278823	11.548468
Si	3.382710	8.017046	9.443432
Si	6.339713	7.003344	12.102066
H	-1.214351	12.308402	14.023165
H	0.796137	13.561002	14.563119
Si	0.369913	10.900241	16.355380
Si	6.191268	6.278814	14.354210
H	5.442007	7.062858	17.315216
H	6.814723	8.785227	16.289488
H	3.257668	6.534591	9.208999
H	4.188204	8.588777	8.315966
Si	1.149450	8.827055	9.449307
H	7.577014	7.820566	11.870501
H	6.435398	5.762737	11.257302
H	-0.406521	9.639541	16.087874
H	-0.346437	11.634546	17.456796
H	3.253210	11.374465	17.721645
H	2.217050	9.258120	18.310318
H	0.888890	12.074648	9.614922
H	-0.970695	10.839884	10.562542
H	0.358935	7.789307	10.199797
H	0.639787	8.822387	8.032881
O	4.783821	9.900637	11.823784
H	7.466689	5.578148	14.739050
H	5.093399	5.250651	14.389969
H	7.398204	15.057868	10.343363

```
H    8.473601    14.726655    11.722332
H    7.521373    16.232265    11.674255
O    2.981929    11.758464    12.553977
O    4.253267    10.283633    14.421906
H    2.774186     8.155104    14.832766
H    1.555975     9.647506    13.107235
H    3.358995     7.828357    12.520863
```

Optimized geometry of **7**•(SiO)₃SiH surface model in .xyz format

Si	0.406982	0.116163	1.420417
Si	-2.208546	0.037663	-0.253509
Si	-3.263657	2.120646	-0.618141
Si	-3.421656	-1.962054	0.118047
Si	1.554078	1.980667	-0.753998
Si	3.898839	1.808262	-1.022482
Si	0.381450	4.014188	-1.049957
Si	1.312939	-2.264970	-0.634186
Si	0.028224	-4.200282	-0.196202
Si	3.675129	-2.308671	-0.758133
C	0.836288	-0.039985	3.271076
N	0.094136	-1.168531	3.849097
N	0.900516	1.179545	4.097089
H	1.877490	-0.407272	3.192830
C	2.239868	1.743812	4.233937
H	2.947416	0.962606	4.551036
H	2.229162	2.521591	5.014744
H	2.621503	2.208349	3.297387
C	-0.080780	2.221299	3.794567
H	0.170630	2.800383	2.878875
H	-0.134749	2.926858	4.639574
H	-1.078134	1.782445	3.662489
C	-1.297834	-0.876821	4.194120
H	-1.800314	-1.816598	4.473539
H	-1.821472	-0.456584	3.324150
H	-1.393075	-0.172168	5.047760
C	0.794490	-1.754724	4.993642
H	1.801275	-2.078568	4.686261
H	0.244257	-2.642766	5.341176
H	0.893352	-1.048829	5.845131
H	4.397243	2.786047	-2.051623
Si	4.508549	-0.347782	-1.803870
H	4.572831	2.127392	0.281584
H	0.485677	-5.347503	-1.055572
Si	-2.252796	-3.840049	-0.736312
H	0.188596	-4.603173	1.240722
Si	-1.834725	3.608072	-1.789950
H	-3.689674	2.702295	0.698874
H	-4.491998	1.959960	-1.471702
H	-2.541635	4.931110	-1.914277
H	-1.705713	3.048811	-3.180753
H	1.029178	4.856277	-2.115011
H	0.397638	4.796652	0.231873
H	4.161824	-3.466052	-1.586974

```
H     4.245800    -2.458575     0.623591
H     6.011706    -0.429418    -1.822859
H     4.048627    -0.410409    -3.235199
H    -3.024449    -5.080517    -0.372387
H    -2.311346    -3.711729    -2.234307
H    -4.745614    -1.927127    -0.595299
H    -3.693991    -2.108557     1.587360
O    -1.217100     0.271645     1.094805
O     0.973210    -1.207302     0.613242
O     1.200509     1.448717     0.809099
H    -1.356707    -0.219261    -1.472313
H     0.825361    -1.705264    -1.946764
H     0.963527     1.023947    -1.762501
```

Computed vibrational frequencies of 5•TTMSS in cm^{-1}

31.25	36.14	44.5	51.6	52.02	59.69	62.1	72.56
81.09	83.07	86.08	88.05	96.05	102.73	105.28	111.9
123.34	127.01	134.6	143.97	148.43	152.54	153.48	155.39
160.25	165.13	169.15	173.54	174.59	181.96	184.6	189.93
194.78	203.95	207.89	209.99	214.15	214.95	219.86	220.9
227.32	230.78	234	235.53	237.5	246.14	247.87	255.56
259.96	261.59	267.75	272.29	290.97	295.69	324.18	327.83
345.98	351.36	359.61	375.16	400.78	407.7	424.09	432.52
434.22	439.6	447.98	460.74	479.33	486.33	500.89	577.21
604.21	607.17	611.4	622.86	655.25	657.16	660.79	662.44
665.87	670.5	674.17	678.56	679.08	689.93	701.34	709.44
724.18	730.9	737.38	739.68	748.07	750.61	756.63	761.51
767.15	773.35	779.25	799.45	810.41	828.09	832.39	836.15
837.26	837.79	840.08	843.19	844.18	846	849.79	863.11
869.08	873.7	883.22	885.04	901.07	906.06	915.28	935.52
942.67	974.48	993.92	1005.09	1008.15	1019.34	1024.61	1042.54
1046.1	1061.19	1068.71	1081.17	1083.33	1102.07	1114.67	1124.92
1133.13	1135.74	1144.93	1152.69	1181.59	1186.59	1198.78	1210.27
1226.09	1233.03	1234.82	1235.91	1237.78	1238.15	1239.84	1244.31
1245.65	1247.59	1249.06	1250.98	1253.66	1257.71	1258.65	1284.98
1288.34	1306.45	1310.26	1314.42	1318.98	1323.35	1328.04	1328.89
1331.63	1335.75	1336.7	1338.04	1350.93	1356.87	1367.73	1375.59
1387.2	1398.79	1401.67	1403.24	1404.77	1406.35	1406.7	1409.06
1411.89	1414.14	1417.09	1418.03	1418.38	1420.36	1423.54	1423.86
1425.79	1428.87	1430.91	1431.86	1433.04	1433.57	1434.2	1434.45
1436.71	1439.35	1442.56	1442.98	1446.74	1449.68	1456.41	1456.81
1460.63	1651.05	1679.86	2941.09	2941.3	2943.57	2943.98	2950.77
2951	2953.76	2953.92	2956.68	2963.89	2964.73	2965.42	2965.97
2966.4	2967.06	2967.34	2968.54	2968.56	2969.68	2974.19	2989.4
2995.91	2997.94	2999.28	2999.35	2999.63	3002.31	3003.36	3008.46
3009.72	3014.48	3040.66	3041.43	3042.44	3042.83	3043.56	3045.72
3046.25	3046.94	3048.64	3049.89	3052.6	3054.75	3057.41	3061.04
3063.91	3065.15	3066.45	3067.22	3072.33	3074.92	3075.83	3076.45
3078.62	3079.79	3088.17					

Computed vibrational frequencies of **6·TTMSS** in cm^{-1}

32.41	38.97	47.78	55.46	57.54	67.99	70.66	82.38
84.34	87.83	94.14	98.07	100.66	107.88	113.41	116.79
119.54	127.41	132.42	135.12	142.17	145.37	147.4	153.26
155.84	156.73	164.12	167.05	171.63	175.91	179.47	180.47
195.7	196.23	198.67	206.77	209.04	211.65	216.69	221.45
221.93	222.85	226.69	230.15	231.93	237.17	240.72	242.46
247.46	249.57	256.58	263.19	266.32	270.77	280.68	285.8
287.93	295.76	302.09	307.97	314.58	327.64	347.77	367.99
379.36	394	403.13	406.31	416.88	427.52	440.13	446.43
452.44	455.62	488.23	517.51	527.53	545.74	578.53	584.38
607.34	608.25	611.69	617.97	625.1	629.72	654.33	662.69
663.22	664.54	667.89	669.23	671.75	675.31	678.41	684.5
722.03	726.5	728.67	735.63	743.75	745.37	748.62	752.73
757.26	773.15	787.3	799.12	811.56	829.35	831.16	834.18
835.18	837.01	837.5	838.92	841.61	844.3	848.29	861.54
867.76	871.92	882.59	890.84	900.84	901.8	902.4	907.64
915.01	917.33	930.7	934.81	938.38	939.05	943.92	962.39
979.18	1013.12	1025.57	1026.81	1031.81	1032.8	1047.27	1071.26
1084.53	1087.27	1090.05	1097.6	1121.9	1130.41	1133.36	1140.36
1144.08	1152.08	1161.14	1175.14	1201.27	1214.66	1223.53	1224.57
1225.15	1227.31	1228.08	1229.38	1229.87	1231.71	1239.86	1241.04
1242.33	1244.08	1245.81	1250.79	1263.29	1271.05	1278.08	1283.68
1289.79	1298.22	1304.6	1314.09	1316.3	1320.69	1328	1335.33
1338.17	1340.81	1343.48	1346.77	1360.89	1368.46	1370.34	1398.14
1399.83	1402.3	1404.38	1405.35	1407.73	1408.97	1411.49	1411.97
1413.98	1415.63	1416.74	1419.49	1419.9	1423.07	1425.25	1426.86
1428.01	1429.32	1430.43	1432.6	1435.98	1436.63	1437.42	1439.19
1441.33	1442.08	1442.54	1443.61	1446.47	1447.72	1450.77	1454.7
1457.45	1459.78	1462.83	1464.19	1469.34	1566.54	1583.52	2946.09
2951.51	2952.01	2957.02	2960.19	2960.58	2961.09	2963.54	2963.61
2964.41	2964.83	2965.37	2966.18	2966.29	2966.61	2967.64	2968.35
2968.58	2968.81	2975.87	2979.63	2985.52	2990.89	2992.99	2998.32
3009.8	3011.15	3012.45	3022.71	3023.67	3027.35	3029.51	3034.54
3037.31	3037.55	3038.77	3040.48	3041.62	3042.31	3043.07	3043.9
3044	3047.23	3050.63	3052.3	3054.32	3056.84	3057.28	3058.75
3065.1	3065.78	3073.38	3073.5	3079.43	3080.42	3081.2	3081.9
3083.8	3083.98	3086.61	3094.36	3100.1	3116.01		

Computed vibrational frequencies of 7•TTMSS in cm^{-1}

38.56	41.96	46.77	55.07	62.79	67.38	77.23	95.43
107.91	111	127.82	137.73	138.94	143.88	149.37	153.22
156.75	159.59	161.08	165.11	170.45	173.83	178.19	180.93
183.8	185.48	194.37	200.83	204.1	210.44	213.4	214.99
220.04	224.37	227.88	230.96	232.34	233.51	247.46	257.03
271.23	279.79	306.67	311.34	338.97	362.35	421.5	429.38
432.06	454.8	542.3	603.17	607.61	609.35	665.49	666.52
668.41	669.42	671.81	672.56	678.09	680.68	683.31	698.32
725.04	734.75	736.99	741.27	747.71	750.47	829.51	832.87
835.13	835.7	835.98	841.32	844.32	845.36	846.23	852.04
865.52	971.91	1019.89	1029.02	1041.26	1074.01	1082.02	1119.2
1123.37	1152.39	1204.6	1212.18	1223.84	1228.82	1229	1230.45
1234.37	1235.18	1240.58	1240.96	1243.37	1249.99	1277.63	1340.23
1377.97	1390.35	1399.69	1400.14	1402.77	1405.03	1405.88	1406.56
1408.39	1408.88	1410.33	1411.65	1412.69	1415.58	1416.57	1417.71
1419.6	1421.01	1421.97	1423.63	1424.9	1429.04	1430.7	1433.83
1436.7	1443.38	1449.12	1456.3	1462.3	1477.61	2809.38	2828.7
2840.48	2856.1	2878.6	2956.45	2959.91	2960.27	2960.78	2962.7
2963.99	2964.49	2964.87	2965.12	2968.34	2980.23	2994.16	3003.8
3036.24	3036.71	3036.91	3037.22	3037.99	3038.8	3040	3041.16
3041.59	3047.26	3049.08	3049.93	3050.39	3050.73	3052.66	3056.89
3059.01	3059.74	3060.51	3063.98	3069.86	3074.63		

Computation of Model Reaction Kinetics

<u>Kinetics of the reaction between **6** and TTMSS</u>

Initial parameters: $[TTMSS]_o = 0.052$ M, $[6]_o = 0.046$ M; $x = [6 \bullet TTMSS]$. The following 2nd order reaction differential equation can be written using these parameters:

$$\frac{dx}{dt} = k[TTMSS][6] = k(0.046M - x)(0.052 - x),$$ (0.5)

which can be converted to the integrated rate law

$$166.67 \times \ln\left(\frac{0.052M - x}{0.046M - x}\right) = kt + 20.434.$$ (0.6)

Plotting $166.67\ln\left(\frac{0.052M - x}{0.046M - x}\right)$ vs t (Figure 23), where concentrations have been determined by ^{1}H NMR, affords (to two significant figures) $k = 2.0$ M^{-1}h^{-1} and a y-intercept of 20. The fact that the latter is within ~2% of expected (20.434) confirms the validity of the fit.
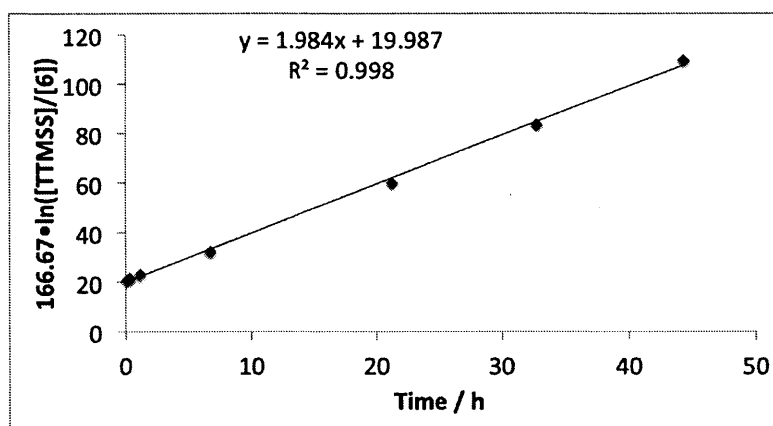
Figure 23. 2nd order rate law fit for the reaction between **6** and TTMSS.

Synthetic Procedures

All air-sensitive reactions were executed using standard Schlenk and glove box techniques. All glassware used in air-sensitive reactions was heated in a 120 °C oven for at least 4 hours or was flame-dried under dynamic vacuum prior to use.

<u>Reproduced Syntheses of Previously Reported Compounds</u>

Lithium diisopropylamide was prepared and recrystallized following the procedure from the Collum laboratory.[95] Solutions of carbene **3** (^{i}Pr$_2$Im) were prepared as reported previously,[96] except using the chloride salt as the starting material and C$_6$D$_6$ as solvent. N,N'-dimesitylformamidine was prepared following the procedure of Grubbs and Kuhn.[97] N,N'-

215

dimesityl-*N*-(trimethylsilyl)-formamidine was prepared following the procedure reported by Grubbs and Despagnet-Ayoub[98]; the ^{1}H NMR (400 MHz, C_6D_6, 25 °C) of this compound was consistent with the previous report by Gade and coworkers.[99] *N,N'*-dicyclohexylformamidine was prepared following the procedure of Ehrhart and Taylor.[100] *N,N'*-dicyclohexyl-*N*-(trimethylsilyl)-formamidine was prepared analogously to *N,N'*-dimesityl-*N*-(trimethylsilyl)-formamidine[98]; the ^{1}H and ^{13}C NMR (C_6D_6, 400 MHz, 298 K) spectra of this compound were consistent with the previously reported ones by Bertrand and coworkers.[101]

Hydrogen-terminated silicon nanoparticles H-SiNPs were prepared according to a slightly modified sol-gel procedure[51-53] as follows: (1) $HSiCl_3$ was exhaustively hydrolyzed to afford $(HSiO_{1.5})_n$ as a white solid, which was dried for 2 d *in vacuo*; (2) the dried product (3.447 g) was heated in a quartz boat inside a furnace to 1100 °C at a rate of 20 °C/min (high heating rate is critical![54]) under a flow of reducing atmosphere (4% H_2 in argon), to afford a brown solid (3.344, 97% yield) consisting of silicon nanoparticles embedded in a silica matrix; **CAUTION: silane, a toxic and explosive gas, is generated during this step, so slower heating rates which lead to build up of silane show be avoided! Furthermore, care must be taken to avoid leaks in the set-up and to ensure rapid dilution of any silane that may escape with the flowing 4% H_2 in argon.** (3) A portion (1.6 g) of the resulting solid was ground to a fine powder and subjected to 2.5 h etching in 4:1 48 wt.% $HF_{(aq)}$/ EtOH solution in a teflon beaker triply-rinsed with MilliQ™ water; **CAUTION: solutions of HF should be handled using special precautions: in addition to the standard laboratory protective gear, one should don a Tychem® QC (or analogous) apron, face shield, and multiple layers of gloves, which should be HF-resistant, and efficient fume hood ventilation is critical.** (4) Brown particles were extracted into toluene similarly to the reported procedure, and the extract of H-SiNPs was stirred with the saturated $NaHCO_{3(aq)}$ solution to quench residual HF and dilute the fluoride content; then the organic phase was centrifuged in a polypropylene centrifuge tube, the pellet was rinsed with de-I water, re-suspended in toluene, centrifuged again, and the pellet was transferred into a 20-mL scintillation vial using 4 x 2 mL anhydrous benzene. Evaporation of benzene in the dark at rt afforded H-SiNPs (103 mg, ~6% yield) as a dark brown solid, which was stored in the glove box at -35 °C.

Modified Syntheses and Characterization of Previously Reported Compounds

1,3-dimesityl-5,5-dimethyl-4,6-dioxo-3,4,5,6-tetrahydropyrimidin-1-ium trifluoromethanesulfonate 4•HOTf.[102] The chloride version of this compound has been prepared and characterized previously,[32,40] but the characterization of the trifloromethanesulfonate salt has not been reported. The latter has been prepared analogously to the procedure reported by Bielawski and Hudnall,[33] described in the following. To N,N'-dimesityl-N-(trimethylsilyl)-formamidine[98] (0.355 g, 1.01 mmol) in a 20-mL scintillation vial equipped with a PTFE-coated magnetic stir-bar in the glove box was added anhydrous toluene (1.75 mL). To this well-stirred solution was added a solution dimethylmalonyl dichloride (0.132 mL, 1.00 mmol) in toluene (5.3 mL), and this solution was allowed to stir at rt for 2 h. At this point, trimethylsilyl trifluoromethanesulfonate (0.178 mL, 0.983 mmol) was added, which resulted in immediate gelation; the gel was mixed until it transformed again into a free-flowing mixture, at which point it was concentrated to dryness *in vacuo* and triturated with hexanes. Removal of the remaining solvent *in vacuo* afforded 4•HOTf (0.389 mg, 74% yield) as a powdery faint-yellow solid. ^{1}H NMR (400 MHz, CD_2Cl_2, 25 °C): δ 9.85 (s, 1H), 7.09 (s, 4H), 2.36 (s, 6H), 2.27 (s, 12H), 1.95 ppm (s, 6H). ^{13}C NMR (100 MHz, CD_2Cl_2, 25 °C): δ 169.7, 164.6, 142.6, 135.3, 130.8, 130.0, 120.6 (q, $J^{13}_C{}^{-19}_F$ = 3.2 Hz, $\underline{C}F_3$ in OTf), 54.9, 24.8, 21.2, 18.5 ppm. ^{19}F NMR (376.4 MHz, CD_2Cl_2, 25 °C) δ -75.0 ppm (s). FT-ICR-ESI HRMS: calcd. for $(C_{24}H_{29}N_2O_2)^+(CF_3SO_3)^-$ [M − CF_3SO_3]$^+$, most abundant m/z = 377.2224; found, 377.2240; calcd. for $(C_{24}H_{29}N_2O_2)^+(CF_3SO_3)^-$ [M − $C_{24}H_{29}N_2O_2$]$^-$, most abundant m/z = 148.9526; found, 148.9524. ATR-FTIR: 3684.2–3194.5 (b), 3110.1–2963.2 (w, b), 2963.2 –2848.5 (w, b), 1803.0 (m), 1766.9 (m), 1618.3 (s), 1602.0 (m), 1484.4 (w), 1462.9 (m), 1392.6 (m), 1336.5 (s), 1252.4 (s), 1177.9 (m), 1162.6 (m), 1085.6 (w), 1026.5 (s), 981.0 (w), 938.4 (w), 881.3 (w), 852.8 (m), 764.2 (m), 669.7 (w), 635.9 cm^{-1} (s).

1,3-dimesityl-5,5-dimethyl-4,6-dioxo-3,4,5,6-tetrahydropyrimidin-2-ylidene 4 (6-MesDAC).[32,40] To a mixture of 4•HOTf (0.043 g, 0.082 mmol) and sodium hexamethyldisilazide (0.015 g, 0.082 mmol) in a 4-mL scintillation vial equipped with a PTFE-coated magnetic stir-bar in the glove box was added C_6D_6 (0.5 mL), and the reaction mixture was allowed to stir for 1.5 h at rt, after which it was filtered through a 0.23 μm PTFE syringe filter to afford a solution of 4 and hexamethyldisilazane (HMDS) in C_6D_6 (quantitative by ^{1}H NMR; 4 was not isolated). ^{1}H NMR (400 MHz, C_6D_6, 25 °C): δ 6.79 (s, 4H), 2.11 (s, shoulder at 2.12

ppm, 18H), 1.49 ppm (s, 6H). ^{13}C NMR (100 MHz, C$_6$D$_6$, 25 °C): δ 277.8, 170.2, 138.8, 137.7, 134.6, 129.6, 51.1, 24.6, 21.0, 18.3 ppm. These values are virtually identical to the previously reported ones.[40]

1-cyclohexyl-N-(2,6-diisopropylphenyl)methanimine.[45,47] This compound was prepared following the procedure for the related trivertal derivative from Bertrand and coworkers,[44] except using cyclohexylcarboxaldehyde instead of trivertal. This compound had been reported previously by Bertrand and coworkers,[45,47] but its spectroscopic characterization has not yet been reported. ^{1}H NMR (400 MHz, CDCl$_3$, 25 °C): δ 7.52 (d, J = 4.9 Hz, 1H), 7.19–7.03 (m, 3H), 2.95 (sept, J = 6.9 Hz, 2H), 2.49 (bm, 1H), 2.00 (bm, 2H), 1.86 (bm, 2H), 1.53–1.21 (6H), 1.17 ppm (d, 6.9 Hz 12H). ^{13}C NMR (100 MHz, CDCl$_3$, 25 °C): δ 171.2, 149.2, 137.6, 123.9, 122.9, 44.4, 29.5, 27.7, 26.2, 25.6, 23.6 ppm.

N-(2,6-diisopropylphenyl)-1-(1-(2-methylallyl)cyclohexyl)methanimine.[45] This compound was prepared following the procedure analogous to the related trivertal derivative from Bertrand and coworkers,[44] except using 1-cyclohexyl-N-(2,6-diisopropylphenyl)methanimine as the starting material. Notably, residual 1-cyclohexyl-N-(2,6-diisopropylphenyl)methanimine was separated and removed by sublimation at 55 °C for 2 d under Schlenk line vacuum (~60-100 mTorr), affording the product as a yellow oil in 84% yield in >95% purity, whose ^{1}H NMR (400 MHz, CDCl$_3$, 25 °C) spectrum was identical to the reported one.[45]

2-(2,6-diisopropylphenyl)-3,3-dimethyl-2-azaspiro[4.5]dec-1-en-2-ium chloride 6•HCl (CyCAAC•HCl).[45] This compound was prepared on ~1.2 g scale following the approach utilized by Bertrand and coworkers to prepare the trivertal analogue, except using N-(2,6-diisopropylphenyl)-1-(1-(2-methylallyl)cyclohexyl)methanimine as the starting material, and adding 1.13 equiv of HCl in Et$_2$O, prior to concentrating, adding toluene, and heating at 110 °C for 3 d. Additionally, the concentrated product was rinsed with 3 x 10 mL hexanes, redissolved in anhydrous DCM (3 + 2 mL), and filtered through a 0.45 µm PTFE syringe filter, and concentrated to dryness *in vacuo* to afford the product as an off-white solid in 70 % yield. The ^{13}C NMR (100 MHz, CDCl$_3$, 25 °C) spectrum was nearly identical to the reported, the only notable difference being the chemical shift of the N=CH ^{13}C resonance, which appeared at 194.3

ppm, 1.3 ppm higher in frequency (*i.e.*, downfield) relative to the reported.[45] Similarly, the ^{1}H NMR (100 MHz, CDCl$_3$, 25 °C) spectrum was nearly identical (resonances within 0.1 ppm and identical coupling constants) to the reported, with the exception of two notable differences: the N=C<u>H</u> proton resonance appeared at 11.3 ppm, or 0.6 ppm higher in frequency (*i.e.*, downfield) relative to the reported,[45] and one of the cyclohexyl methylene proton pairs (axial or equatorial) appearing at 2.59 ppm (ddd ~ td, 12.9, 12.9, 3.8 Hz, 2H) instead of as part of the multiplet in the range 1.80–1.34 ppm as reported.[45] ATR-FTIR: 3077.8 (w), 2973.1 (m), 2937.1 (m), 2858.7 (m), 2824.1 (m), 1639.8 (m), 1468.8 (m), 1446.8 (m), 1361.8 (m), 1350.1 (m), 1328.6 (w), 1268.0 (w), 1184.7 (w), 1144.5 (m), 1096.0 (w), 1056.7 (m), 956.6 (w), 933.3 (w), 811.1 (s), 768.0 cm^{-1} (w).
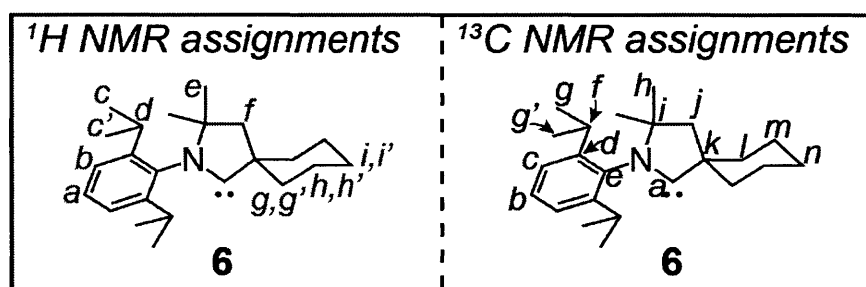
2-(2,6-diisopropylphenyl)-3,3-dimethyl-2-azaspiro[4.5]dec-2-ylidene 6 (CyCAAC).[47]

This compound was prepared as a viscous yellow oil (81% yield) following the procedure for the one used for the trivertal CAAC analogue,[44] except using 6•HCl as the starting material. Based on ^{1}H NMR integration relative to an internal standard (TTMSS at reaction time of 5 min), purity of the prepared **6** was estimated to be 85%; one of the impurities (~6%) was determined to be 6•H$_2$ by comparison of ^{1}H NMR resonances (e.g., 3.38 (s)) to reported ones.[41] This impurity likely arose due to presence of LiH in the LDA, and along with other impurities was an unreactive spectator in all subsequent transformations. ^{1}H NMR (400 MHz, C$_6$D$_6$, 25 °C): δ 7.23 (skewed dd, J = 8.5, 6.6 Hz, 1H, *a*), 7.15 (skewed dd, J = 6.6, 1.3 Hz, 2H, *b*, overlapping partially with C$_6$D$_5$H resonance), 3.15 (sept, J = 6.8 Hz, 2H, *d*), 2.28 (ddd ~ td, J = 12.5, 10.8, 4.2 Hz, 2H, *g* or *g'*), 2.06–1.94 (m, 2H, *h* or *h'*), 1.65 (m, 2H, *i* or *i'*, identified via HSQC), 1.57 (m, 2H, *i'* or *i*, identified via HSQC), 1.52 (s, 2H, *f*), 1.46 (m, 2H, *h'* or *h*, identified via HSQC), 1.40 (m, 2H, *g'* or *g*, identified via HSQC), 1.24 (d, J = 6.9 Hz, 6H, *c* or *c'*), 1.21 (d, J = 6.7 Hz, 6H, *c'* or *c*), 1.09 (s, 6H, *e*). ^{13}C NMR (100 MHz, C$_6$D$_6$, 25 °C): δ 316.1 (*a*, carbene carbon), 146.1 (*e*), 138.2 (*d*), 127.8 (*b*, overlapping with C$_6$D$_6$ triplet, chemical shift and connection to H$_{para}$

established from HSQC), 123.8 (*c*), 81.1 (*i*), 63.7 (*k*), 48.3 (*j*), 36.6 (*l*), 29.6 (*h*), 29.5 (*f*), 26.8 (*n*), 26.2 (*g* or *g'*), 23.4 (*m*), 21.9 ppm (*g'* or *g*). ^{13}C NMR (100 MHz, THF-d^8, 25 °C): δ 316.7, 146.3, 138.5, 128.1, 123.9, 81.7, 63.8, 48.8, 36.9, 29.79, 29.75, 27.2, 26.0, 23.7, 21.7 ppm. Assignments were confirmed by a combination of HSQC, gHMBC, and COSY (see Spetroscopy Data). The ^{13}C NMR characterization in THF-d^8 was similar but not identical to the reported, (particularly, the carbene carbon was reported to be at 309.4 ppm – more than 7 ppm lower in frequency).[47] This difference is likely due to coordination of t **6** to LiOTf present in in the reported carbene, and absence of such an interaction in our case.

<u>Syntheses and Characterization of New Compounds</u>

1,3-dicyclohexyl-5,5-dimethyl-4,6-dioxo-3,4,5,6-tetrahydropyrimidin-1-ium trifluoromethanesulfonate 5•HOTf. To *N,N'*-dicyclohexyl-*N*-(trimethylsilyl)-formamidine ·(0.2805 g, 1.00 mmol) in a 20-mL scintillation vial equipped with a PTFE-coated magnetic stir-bar in the glove box was added anhydrous toluene (1.75 mL). To this well-stirred solution was added a solution dimethylmalonyl dichloride (0.181 mL, 1.37 mmol) in toluene (5.3 mL), and this solution was allowed to stir at rt for 2 h. At this point, trimethylsilyl trifluoromethanesulfonate (0.181 mL, 1.00 mmol) was added, and the reaction mixture was stirred for 1h, at which point it was concentrated to dryness *in vacuo*, which afforded **5•HOTf** (0.443 g, 97% yield) as a powdery white solid. ^{1}H NMR (400 MHz, CD$_2$Cl$_2$, 25 °C): δ 8.79 (s, 1H), 4.44 (dddd ~ tt, J = 12.2, 12.2, 3.5, 3.5 Hz, 2H), 2.08 (dm, J$_{doublet}$ = 10.9 Hz, 4H), 1.96 (dm, J$_{doublet}$ = 13.8 Hz, 4H), 1.80–1.66 (m, 6H), 1.60 (s, 6H), 1.47 (dddd ~ qt, J = 13.0, 13.0, 3.2, 3.2 Hz, 4H), 1.28 ppm (dddd ~ qt, J = 13.0, 13.0, 3.6, 3.6 Hz, 2H). ^{13}C NMR (100 MHz, CD$_2$Cl$_2$, 25 °C): δ 170.7, 157.1, 120.9 (q, J^{13}$_C$-^{19}$_F$ = 3.2 Hz, $\underline{C}$F$_3$ in OTf), 61.2, 52.8, 31.2, 25.9, 25.1, 23.0 ppm. ^{19}F NMR (376.4 MHz, CD$_2$Cl$_2$, 25 °C) δ -74.8 ppm (s). FT-ICR-ESI HRMS: calcd. for (C$_{18}$H$_{29}$N$_2$O$_2$)$^+$(CF$_3$SO$_3$)$^-$ [M – CF$_3$SO$_3$]$^+$, most abundant *m/z* = 305.2224; found, 305.2227; calcd. for (C$_{18}$H$_{29}$N$_2$O$_2$)$^+$(CF$_3$SO$_3$)$^-$ [M – (C$_{18}$H$_{29}$N$_2$O$_2$)]$^-$, most abundant *m/z* = 148.9526; found, 148.9531. ATR-FTIR: 3688.2–3004.9 (b), 2936.3 (m), 2861.0 (w), 1780.3 (w), 1753.4 (m), 1633.9 (m), 1457.0 (w), 1388.0 (w), 1311.4 (m), 1268.7 (m), 1255.1 (s), 1224.0 (w), 1159.8 (m), 1030.6 (s), 998.6 (w), 637.3 cm^{-1} (s).

1,3-dicyclohexyl-5,5-dimethyl-4,6-dioxo-3,4,5,6-tetrahydropyrimidin-2-ylidene 5 (6-CyDAC). To a mixture of 5•HOTf (0.0373 g, 0.082 mmol) and sodium hexamethyldisilazide (0.015 g, 0.082 mmol) in a 4-mL scintillation vial equipped with a PTFE-coated magnetic stir-bar in the glove box was added C_6D_6 (0.5 mL), and the reaction mixture was allowed to stir for 30 min at rt, after which it was filtered through a 0.23 μm PTFE syringe filter to afford a solution of 5 and HMDS in C_6D_6 (quantitative by ^1H NMR; 5 was not isolated). ^1H NMR (400 MHz, C_6D_6, 25 °C): δ 4.66 (dddd ~ tt, J = 11.7, 11.7, 3.9, 3.9 Hz, 2H), 2.00 (ddd ~ qd, J = 12.6, 12.6, 3.6 Hz, 4H), 1.84–1.76 (dm, $J_{doublet}$ = 12.7 Hz, 4H), 1.74–1.66 (dm, $J_{doublet}$ = 13.7 Hz, 4H), 1.54–1.46 (dm, $J_{doublet}$ = 12.7 Hz, 2H), 1.26 (dddd ~ qt, J = 13.3, 13.3, 3.5, 3.5 Hz, 4H), 1.26 (s, 6H, overlaps with multiplet at 1.26 ppm), 1.08 ppm (dddd ~ qt, J = 12.7, 12.7, 3.6, 3.6 Hz, 2H). ^{13}C NMR (100 MHz, C_6D_6, 25 °C): δ 269.5, 170.9, 57.6, 49.7, 33.2, 26.1, 25.8, 23.9 ppm. FT-ICR-ESI HRMS: calcd. for $C_{18}H_{28}N_2O_2$ $[M+H]^+$, most abundant m/z = 305.2224; found, 305.2227.
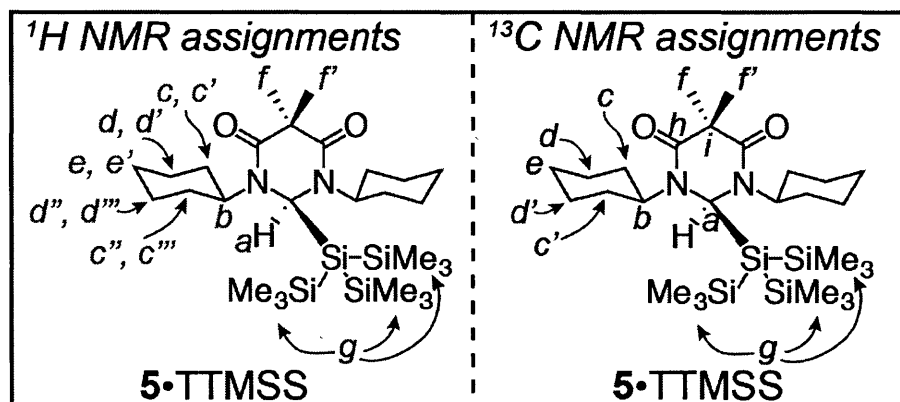
1,3-dicyclohexyl-2-(1,1,1,3,3,3-hexamethyl-2-(trimethylsilyl)trisilan-2-yl)-5,5-dimethyldihydropyrimidine-4,6(1H,5H)-dione 5•TTMSS. To the solution of 5 (0.082 mmol) in anhydrous C_6D_6 (0.5 mL) in a 4-mL vial prepared as above in the glove box was added via gas-tight syringe TTMSS (25.3 μL, 0.082 mmol), and the reaction mixture was transferred to a J. Young NMR tube, sealed, and allowed to proceed at rt (no stirring) in the dark; after 3 h, no conversion was noted by ^1H NMR, and the reaction temperature was increased to 80 °C. The reaction was monitored by ^1H NMR as shown in Figure 3, and reached >95% conversion of 5 after 24 h; in addition to the formation of 5•TTMSS as the major product (~50% yield by ^1H NMR), two side-reactions were noted: formation of 5•HMDS via insertion of 5 into the N-H bond of HMDS (analogous to known N-H insertions by persistent carbenes[37-42,103]) was indicated

by the appearance of ^{1}H NMR resonances at 5.17 ppm (s, 1H) and 0.18 ppm (two overlapping s ~ d, 18H) (see Spetroscopy Data for crude **5•TTMSS**) and mass spectrometry (m/z = 466.3342, see Spectroscopy Data); dimerization of **5** via coupling of the carbenes was confirmed by X-ray crystallography (Figure 3B); the product was characterized without isolation. ^{1}H NMR (500 MHz, C$_6$D$_6$, 25 °C): δ 4.78 (s, 1H, *a*), 3.14 (dddd ~ tt, J = 11.6, 11.6, 3.7, 3.7 Hz, 2H, *b*), 2.76 (m, 2H, *c'''*(axial)), 2.05 (bd, J = 12.8 Hz, 2H, *c"* (equatorial)), 1.90 (m, 2H, *c'* (axial)), 1.85–1.80 (m, 2H, *c* (equatorial)), 1.77 (s, 3H, *f* or *f'*), 1.66 (bm, 4H, two sets of the *d-d'''*), 1.46 (s, 3H, *f* or *f'*), 1.41 (bd, J = 11.6 Hz, 2H, *e* (equatorial)), 1.14–1.07 (m, 4H, two other sets of the *d-d'''*), 1.07–1.01 (m, 2H, *e'* (axial)), 0.26 ppm (s, 27H (observed 24H, but this is within error of integration), *g*). ^{13}C NMR (100 MHz, C$_6$D$_6$, 25 °C): δ 171.7 (*h*), 65.6 (*a*), 62.9 (*b*), 48.6 (*i*), 31.4 (*c'*), 30.4 (*c*), 26.8 (*d* or *d'*), 26.7 (*d* or *d'*), 25.8 (*e*), 23.6 (*f* or *f'*), 22.8 (*f* or *f'*), 3.1 ppm (*g*). Assignments were confirmed by a combination of HSQC, gHMBC, NOESY, and COSY (see Spetroscopy Data). Of particularly importance were the following observations:

(1) Vicinal coupling between proton *b* and the proton corresponding to the resonance at 2.76 ppm. This proton was also attached to the same carbon atom (at 31.4 ppm) as the one with resonance at 2.05 ppm.

(2) Protons with resonances at 1.90 ppm and 1.85–1.80 ppm were attached to the same carbon atom (at 30.4 ppm), but only the one at 1.85–1.80 ppm had through-space coupling to proton *a*, indicating that it was in the equatorial orientation. The magnitude of its vicinal coupling constants was smaller than that for the proton at 1.90 ppm, as expected for a proton in the equatorial orientation on a cyclohexyl ring.

(3) Protons with resonances at 1.66 ppm and 1.14–1.07 ppm couple strongly through-bond and through-space, and couple through-bond to *c'''*. Thus, they are *d"* and *d'''*.

FT-ICR-ESI HRMS: calcd. for C$_{27}$H$_{56}$N$_2$O$_2$Si$_4$ [M + H]$^+$, most abundant m/z = 553.3492; found, 553.3506.

¹H NMR assignments	¹³C NMR assignments
6•TTMSS	6•TTMSS
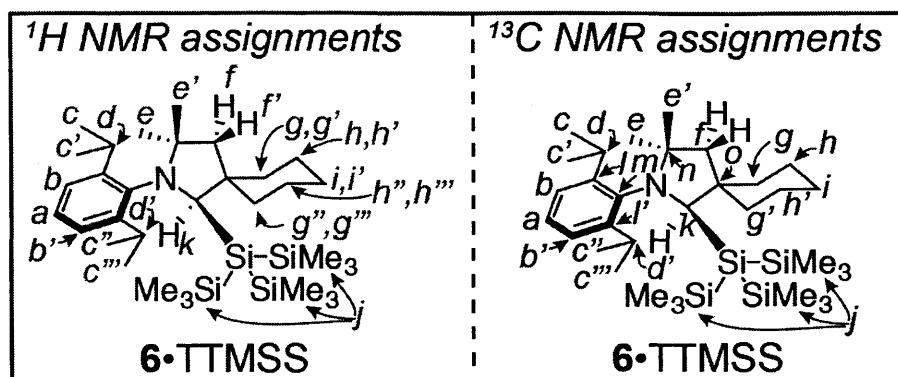
2-(2,6-diisopropylphenyl)-1-(1,1,1,3,3,3-hexamethyl-2-(trimethylsilyl)-trisilan-2-yl)-3,3-dimethyl-2-azaspiro[4.5]decane 6•TTMSS. To the solution of **6** (9.0 mg, 85% pure, 0.023 mmol) in anhydrous C_6D_6 (0.5 mL) in a 4-mL vial in the glove box was added via gas-tight syringe TTMSS (8.0 μL, 0.026 mmol), and the reaction mixture was transferred to a J. Young NMR tube, sealed, and allowed to proceed at rt (no stirring necessary) in the dark. The reaction was monitored by ¹H NMR as shown in Figure 4, and reached ~95% conversion of **6** to **6•TTMSS** after 3 d, with no evidence of side reactions; the product was characterized without isolation, except for X-ray crystallography, the product was concentrated, redissolved in CD_2Cl_2, and crystallized in an NMR tube by slow evaporation of CD_2Cl_2 at rt. ¹H NMR (400 MHz, C_6D_6, 25 °C): δ 7.14 (dd, J = 7.5, 2.1 Hz, 1H, *b'*), 7.09 (dd ~ t, J = 7.5, 7.5 Hz, 1H, *a*), 7.04 (dd, J = 7.5, 2.1 Hz, 1H, *b*), 4.25 (s, 1H, *k*), 4.01 (sept, J = 6.8 Hz, 1H, *d'*), 3.15 (sept, J = 6.7 Hz, 1H, *d*), 2.30 (d, J = 12.9 Hz, 1H, *f'*), 2.26–2.17 (m, 1H, *g"* (equatorial)), 1.96–1.84 (m, 2H, *g'''* (axial) and *g* or *g'*), 1.79 (d, J = 13.1 Hz, 1H, f), 1.73–1.66 (bm, 2H, *h* or *h'* and *i* or *i'*), 1.60–1.53 (s overlapping with m, 5H, *e'*, *h"*, *h'''*, and *i* or *i'*), 1.46 (d, J = 6.8 Hz, 3H, *c'''*), 1.45–1.43 (d overlapping with m, $J_{doublet}$ = 6.7 Hz, 4H, *c'* and *g* or *g'*), 1.43–1.40 (m, 1H, *h* or *h'*), 1.20 (d, J = 6.8 Hz, 3H, *c"*), 1.09 (d, J = 6.7 Hz, 3H, *c*), 0.91 (s, 3H, *e*), 0.30 ppm (bs, 27H, *j*). ¹³C NMR (100 MHz, C_6D_6, 25 °C): δ 150.0 (*l'*), 148.6 (*l*), 146.4 (*m*), 126.7 (*b*), 126.2 (*a*), 125.2 (*b'*), 74.6 (*k*), 64.5 (*n*), 53.2 (*f*), 46.8 (*o*), 38.7 (*g*), 37.0 (*g'*), 33.0 (*e'*), 29.7 (*e*), 29.4 (*d*), 27.6 (*c"*), 27.0 (*d'*), 26.2 (*c*), 26.0 (*c'''*), 24.9 (*c'*), 24.5 (*h* or *h'*), 24.1 (*h* or *h'*), 22.9 (*i*), 5.3 ppm (*j*). Assignments were confirmed by a combination of HSQC, gHMBC, NOESY, and COSY (see Spetroscopy Data). Of particularly importance were the following observations:

(1)   Through-space ¹H-¹H interactions between *k* and *d*, *d* and *c*, *d* and *c'*, and *k* and *c'* but not *k* and *c, as well as* an interaction between *c'''* and *j* established the "front" vs

"back" positioning relative to the face of the pyrrolidine ring, as well as the upper and lower positioning relative to the phenyl ring.

(2)   Through space ^{1}H-^{1}H interactions between d and f, establishing the identity of f

(3)   Through space ^{1}H-^{1}H interactions between d and e established the identity of e.

(4)   Through space ^{1}H-^{1}H interactions between g''' and j, establishing the axial orientation of g'''; the through space ^{1}H-^{1}H interactions between g'' and e' confirmed the equatorial orientation of g''.

(5)   The attachment to the same carbon (i, 22.9 ppm) of protons that were consequently assigned to be i and i'.

(6)   gHMBC cross-peaks with proton "f" helped to identify g and g'.

(7)   Given the remaining carbons h, h', and i, and the protons attached to them, as determined from HSQC, their through-bond and through-space interactions were next compared to assign the remaining resonances (e.g., carbon g' expected cross-peak with protons h'' or h''' allowed assignment of the latter).

FT-ICR-ESI HRMS: calcd. for $C_{32}H_{63}NSi_4$ [M - (TMS)$_3$Si]$^+$, most abundant m/z = 326.2842; found, 326.2822. ATR-FTIR: 3100.0–3036.7 (w), 3010.6 (w), 2971.7 (w), 2941.2 (m), 2866.5 (m), 1467.2 (m), 1449.5 (m), 1431.2 (m), 1384.9 (m), 1362.8 (m), 1328.9 (w), 1304.2 (w), 1240.8 (s), 1163.3 (m), 1148.5 (m), 1025.5 (m), 862.2 (m), 831.1 (s), 764.5 (m), 750.9 (m), 681.0 cm^{-1} (m).

Note: For analysis by ATR-FTIR and XPS, a portion of the product was purified by column chromatography over silica gel with pentane as the eluent (streaks, R$_f$ = 0–0.54; streak was faint under UV light – phosphomolybdic acid stain visualized it better), and crystallized by slow evaporation of benzene at rt, which afforded 6•TTMSS in 92 mol% purity, the remainder being 6•H$_2$.

2-(2,6-diisopropylphenyl)-1-(1,1,1,5,5,5-hexamethyl-3-((trimethylsilyl)oxy)trisiloxan-3-yl)-3,3-dimethyl-2-azaspiro[4.5]decane 6•TTMSOxS. To the solution of **6** (9.0 mg, 85% pure, 0.023 mmol) in anhydrous C$_6$D$_6$ (0.5 mL) in a 4-mL vial in the glove box was added via gas-tight syringe TTMSOxS (9.6 μL, 0.028 mmol), and the reaction mixture was transferred to a J. Young NMR tube, sealed, and allowed to proceed at rt (no stirring necessary) in the dark. The reaction was monitored by ^{1}H NMR as shown in Figure 5, and reached essentially quantitative

conversion of **6** to **6•TTMSOxS** already after 5 h, with no evidence of side reactions; partial characterization was done for **6•TTMSOxS** without isolation. ^{1}H NMR (400 MHz, C$_6$D$_6$, 25 °C): δ 7.18–7.13 (m, 2H, overlapping with C$_6$D$_5$H), 7.03 (m (second order coupling), 1H), 4.20 (sept, J = 7.0 Hz, 1H), 3.25 (sept, J = 6.7 Hz, 1H), 3.23 (s, 1H), 2.43 (bd, J = 13.3 Hz, 1H), 2.25 (d, J = 12.6 Hz, 1H), 1.95 (m, 2H), 1.55 (s, 3H), 1.43 (d, J = 6.8 Hz, 3H), 1.39 (d, J = 6.7 Hz, 3H), 1.33 (d, J = 6.9 Hz, 3H), 1.26 (d, J = 6.7 Hz, 3H), 0.30 (bs, 18H (observed 16H)), -0.11 ppm (bs, 9H (observed 8.5H)); the remaining proton resonances overlapped between 1.93 and 0.83 ppm and were not specifically assigned. ^{13}C NMR (100 MHz, C$_6$D$_6$, 25 °C): δ 151.6, 149.0, 144.0, 126.3, 124.9, 68.1, 64.3, 52.5, 45.5, 42.2, 35.4, 32.9, 29.0, 28.8, 27.2, 26.4, 26.3, 25.7, 25.3, 24.7, 23.5, 3.0, 2.4 ppm (note: two resonances (one aromatic, one aliphatic carbon) were not resolved). FT-ICR-ESI HRMS: calcd. for C$_{32}$H$_{63}$NO$_3$Si$_4$ [M]$^+$, most abundant m/z = 621.3880; found, 621.3866.
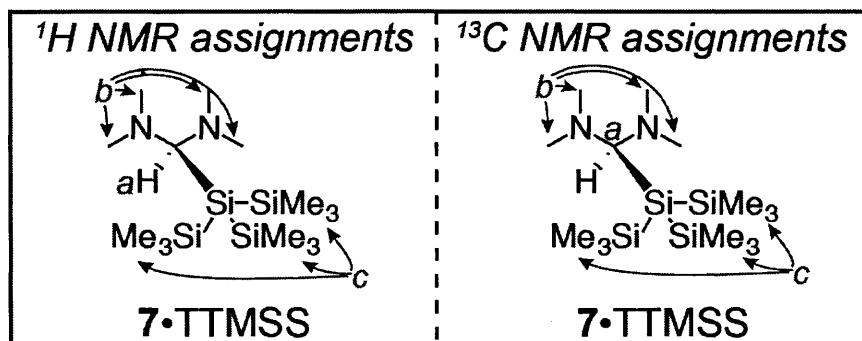
1-(1,1,1,3,3,3-hexamethyl-2-(trimethylsilyl)trisilan-2-yl)-*N,N,N',N'*-tetramethylmethanediamine **7•TTMSS**. Preparation of **7**[49,50]: to the mixture of **7•HCl** (22.6 mg, 0.165 mmol) and toluene-d^8 (0.5 mL) in a 4-mL vial equipped with a stir bar at -78 °C in the glove box was added a solution of LDA (18.6 mg, 0.174 mmol) in anhydrous toluene-d^8 (0.5 mL) cooled to -78 °C; the vial containing LDA was rinsed with 0.1 mL cooled toluene-d^8 and this rinsing was added to the vial with **7•HCl**. The reaction was brought to room temperature and allowed to stir for 1.7 h; at this point, 0.88 mL of the reaction mixture was filtered through a 0.23 μm PTFE syringe filter into a J. Young NMR tube. Addition of TTMSS (38.4 μL, 0.124 mmol) led to complete conversion of **7** to **7•TTMSS** in ≤8 min. The product was characterized without isolation. ^{1}H NMR (400 MHz, C$_6$D$_6$, 25 °C): δ 3.73 (s, 1H, *a*; satellite peaks: J(^{29}Si-^{1}H) = 7.9 Hz), 2.56 (s, 12H, *b*), 0.27 ppm (bs, 27H, *c*). ^{13}C NMR (100 MHz, C$_6$D$_6$, 25 °C): δ 82.4 (*a*), 41.2

(*b*), 2.2 ppm (*c*). FT-ICR-DART HRMS: calcd. for $C_{14}H_{40}N_2Si_4$ [M − Me$_2$N]$^+$, most abundant m/z = 304.1763; found, 304.1751. Assignments were confirmed by a combination of HSQC, gHMBC, NOESY, and COSY (see Spetroscopy Data). Of particularly importance was the observation of an NOE between protons *a* and *c*, and the HSQC cross-peaks between the protons a and b with the corresponding carbons. ATR-FTIR: 2949.8 (w), 2893.7 (w), 2854.4 (w), 2824.7 (w), 2781.1 (w), 1468.6 (w), 1438.9 (w), 1394.7 (w), 1242.7 (m), 1009.0 (m), 829.6 (s), 747.7 (w), 723.3 (w), 683.8 (m), 624.3 cm^{-1} (m).

Note: For analysis by ATR-FTIR, a portion of the product was partially purified by sublimation at 60 °C for 3 h, affording a soft white solid with residual TTMSS. The spectrum of 7•TTMSS was obtained as a weighted difference between the spectrum of this sublimed product and that of pure TTMSS (where the weighting was applied to eliminate the residual Si-H stretch resonance from TMSS at 2049.9 cm^{-1}).

Functionalization of H-SiNPs and H-Si(111)

6•SiNPs. To H-SiNPs (10.0 mg) in a 4-mL vial equipped with a stir bar in the glove box was added a solution of **6** (18.2 mg, ~85% pure **6**, 0.048 mmol) in 1.0 mL C$_6$D$_6$. The reaction mixture was sealed and stirred at rt in the dark; the solution color changed from very faint yellow to progressively darker brown during the course of this transformation. After 3 days, the reaction mixture was filtered through a 0.23 μm PTFE syringe filter to afford a clear brown solution and ~2.5 mg of insoluble brown solid (collected from the filter membrane). The solution was concentrated to ~0.5 mL *in vacuo* on the Schlenk line, transferred to a centrifuge tube with the aide of 0.2 mL C$_6$D$_6$, and 10 mL of anhydrous hexanes were added to it. Yellow precipitate formed and was isolated by centrifugation (3000 rpm, 5 min) and decantation of the yellow supernatant. The centrifugation/decanation cycle was repeated two more times (the last supernatant was nearly colorless), and the isolated pellet was dried *in vacuo* on the Schlenk line for 6 h to afford a brown solid (2.1 mg).

7•SiNPs. To H-SiNPs (10.0 mg) in a 4-mL vial equipped with a stir bar in the glove box was added a solution of **7** in 1.1 mL toluene-d^8 prepared exactly as in the synthesis of 7•TTMSS. The reaction mixture was sealed and stirred at rt in the dark; the solution color changed from very faint yellow to progressively darker brown during the course of this transformation. After 5.3 h,

the reaction mixture was filtered through a 0.23 μm PTFE syringe filter to afford a clear brown solution and ~2.5 mg of insoluble brown solid (collected from the filter membrane). The solution was concentrated to ~0.5 mL *in vacuo* on the Schlenk line, transferred to a centrifuge tube with the aide of 0.2 mL C_6D_6, and 10 mL of anhydrous hexanes were added to it. Yellow precipitate formed and was isolated by centrifugation (3000 rpm, 5 min) and decantation of the faint yellow supernatant. The centrifugation/decanation cycle was repeated once more (this last batch of supernatant was nearly colorless), and the isolated pellet was dried *in vacuo* on the Schlenk line overnight to afford a tan solid (2.3 mg).

6•Si(111). In the glove box, a pair of H-**Si(111)** wafers was placed polished side up into 20-mL glass vial, and a solution of **6** (18.2 mg, ~85% pure **6**, 0.048 mmol) in 1.0 mL C_6D_6 was added to cover the wafers. The vial was sealed and the reaction was allowed to proceed in the dark for the requisite amount of time (3 days, except when conversion was monitored by XPS), at which point the wafers were removed with clean steel tweezers and rinsed via syringe with benzene (5 mL) prior to analysis.

7•Si(111). In the glove box, a pair of H-**Si(111)** wafers was placed polished side up into 20-mL glass vial, and a solution of **7** in 1.1 mL toluene-d^8 (prepared as before) was added to cover the wafers. The vial was sealed and the reaction was allowed to proceed in the dark for the requisite amount of time (4 h, except when conversion was monitored by XPS), at which point the wafers were removed with clean steel tweezers and rinsed via syringe with toluene (5 mL). The wafers were then removed from the glove box, rinsed for ~20 sec with MilliQ™ water (residual water wicked off on the edge with a Kim-Wipe), and brought back into the glove box for storage.

Scheme 1. XPS Si 2p analysis of a representative set of H-**Si(111)** wafers.
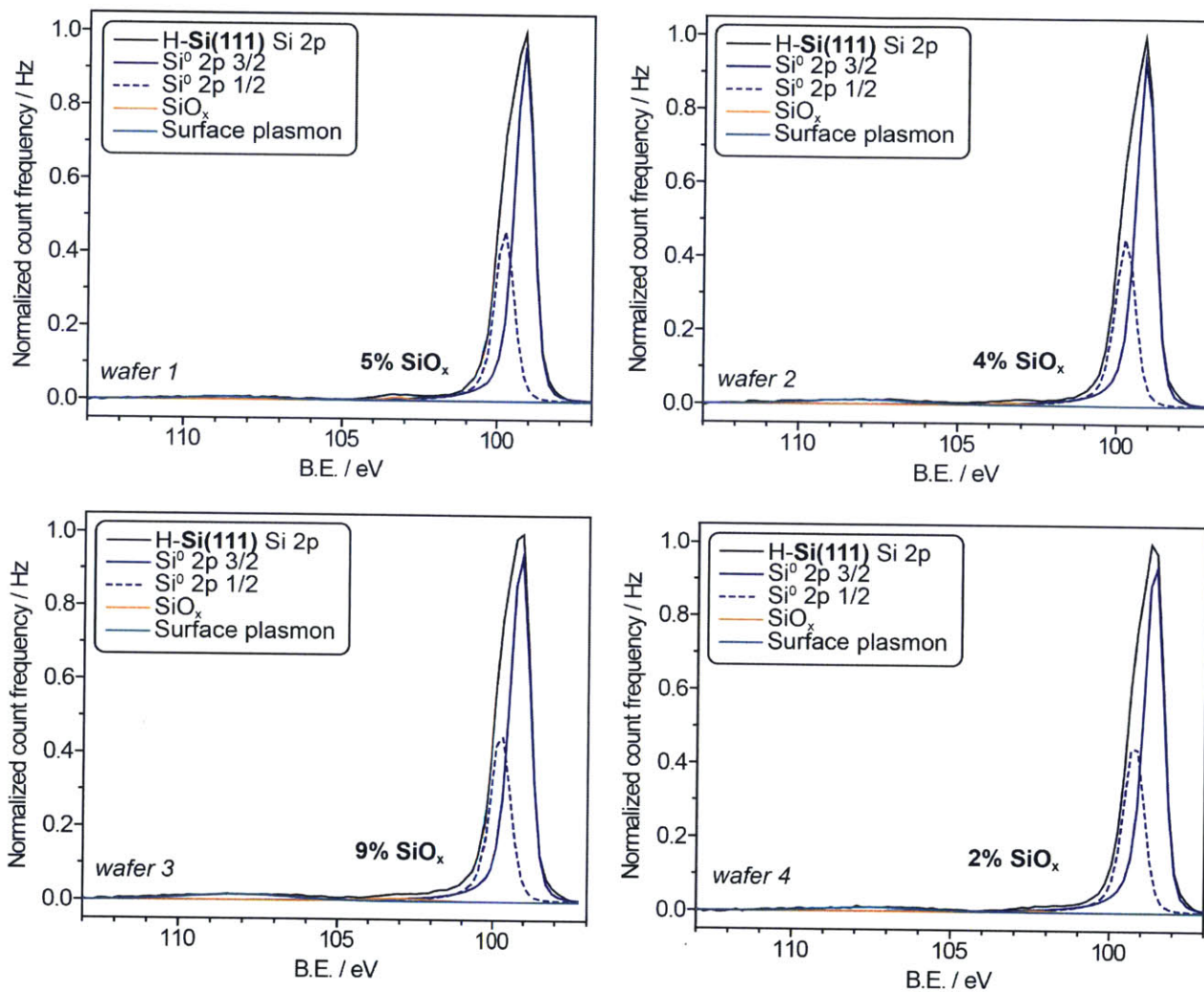
Scheme 2. XPS Si 2p and N1s analysis of a **6·Si(111)** wafer before a ~20 second rinse with MilliQ™ H_2O and after (two spots were tested on the same wafer). Increase in SiO_x content after the rinse was apparent. Additionally, the rinse led to an increase in the FWHM of component 1 in the N 1s region with virtually no change in the overall peak area.

Si 2p region

Components
— Si^0 2p 3/2 — Surface plasmon
---- Si^0 2p 1/2
— SiO_x

After H_2O, spot #2

9% SiO_x

Components
— Si^0 2p 3/2 — Surface plasmon
---- Si^0 2p 1/2
— SiO_x

After H_2O, spot #1

27% SiO_x

Components
— Si^0 2p 3/2 — Surface plasmon
---- Si^0 2p 1/2
— SiO_x

Before H_2O

0% SiO_x

Normalized count frequency / Hz

B.E. / eV

N 1s region

Components
— 1 (main)
— 2 (minor)

0.3 eV

After H_2O, spot #2

FWHM = 2.59 eV;
N1s area relative to
Si 2p = 0.019

Components
— 1 (main)
— 2 (minor)

After H_2O, spot #1

FWHM = 2.48 eV;
N 1s area relative to
Si 2p = 0.020

Components
— 1 (main)
— 2 (minor)

Before H_2O

FWHM = 1.55 eV;
N1s area relative to
Si 2p = 0.021

Count frequency normalized by transmission-corrected Si 2p area / Hz

B.E. / eV

229

3.5 Spectra

Figure 24. ^{1}H NMR (400 MHz, CD$_2$Cl$_2$, 25 °C) spectrum of **4**•HOTf.
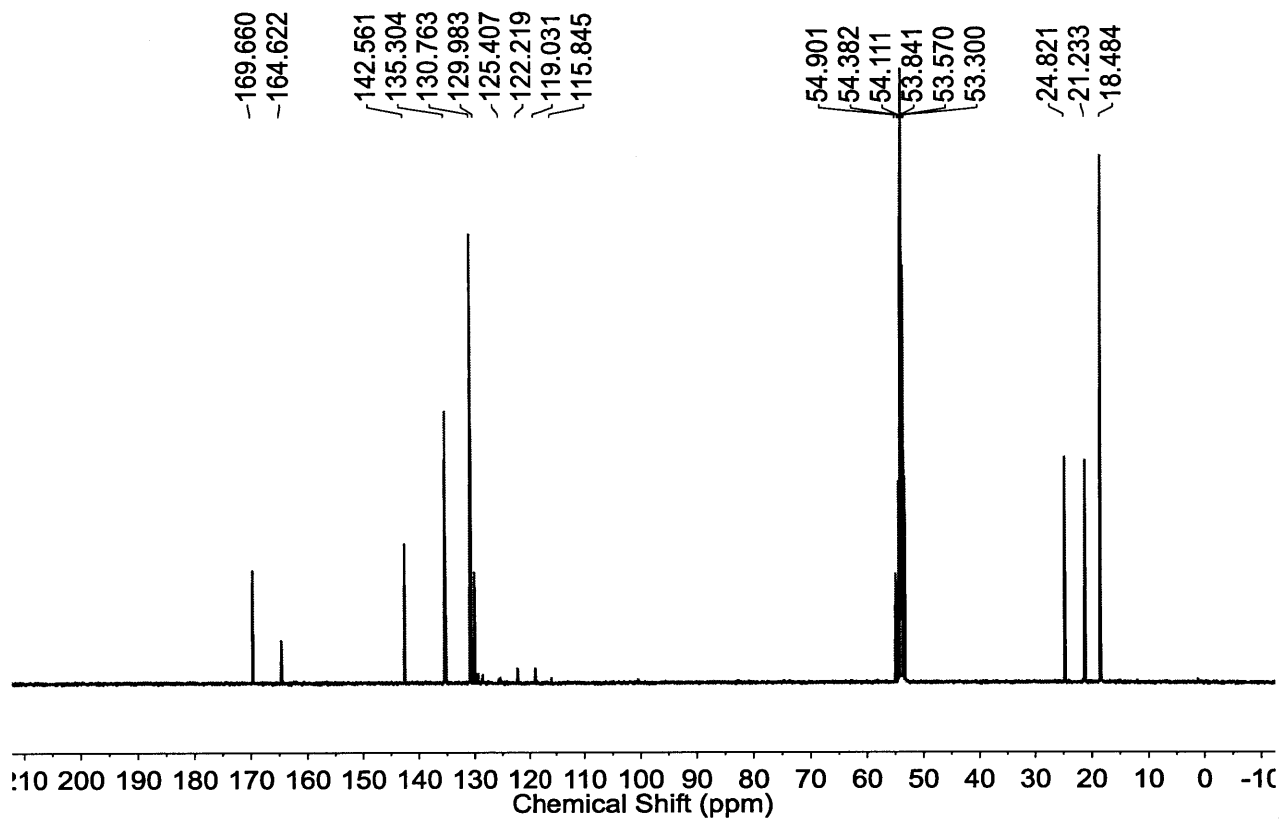
Figure 25. ^{13}C NMR (100 MHz, CD_2Cl_2, 25 °C) spectrum of **4·HOTf**.
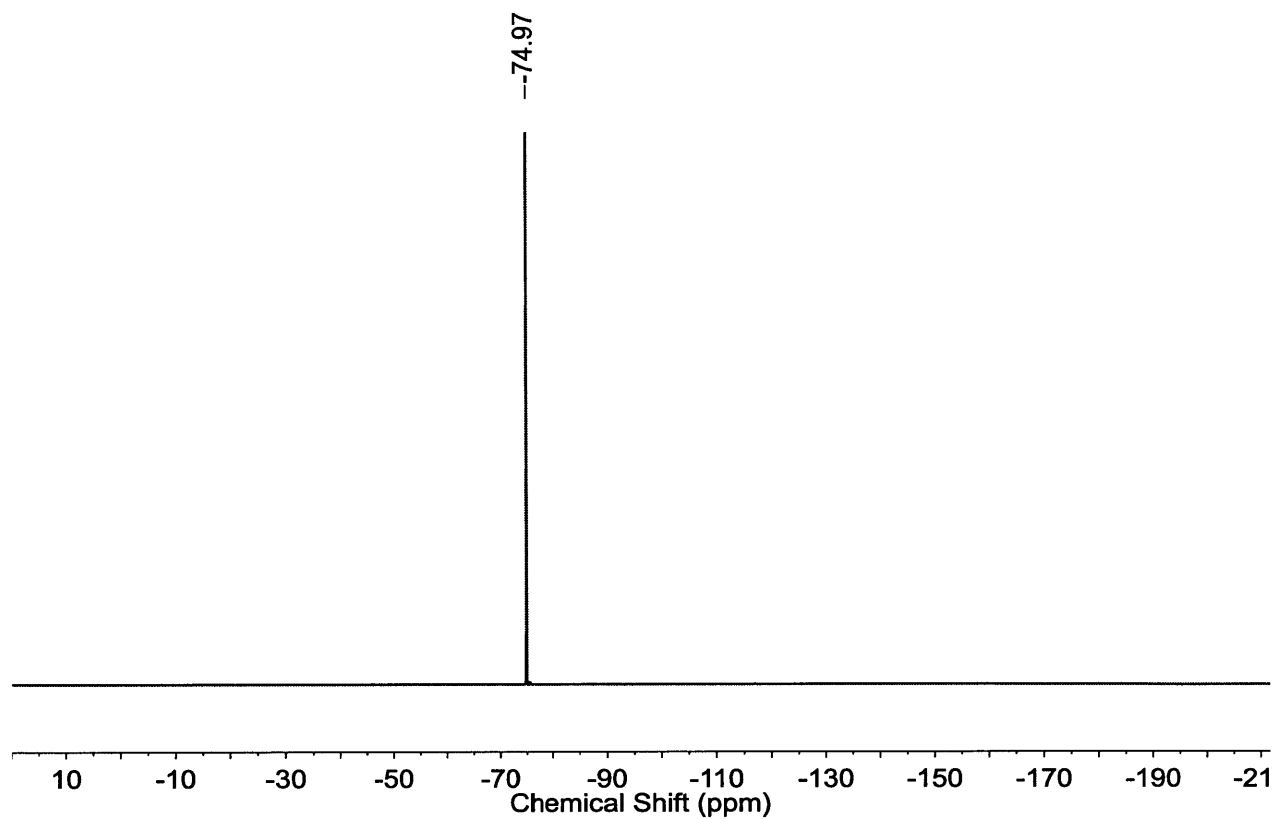
Figure 26. ^{19}F NMR (376.4 MHz, CD_2Cl_2, 25 °C) spectrum of **4•HOTf**.
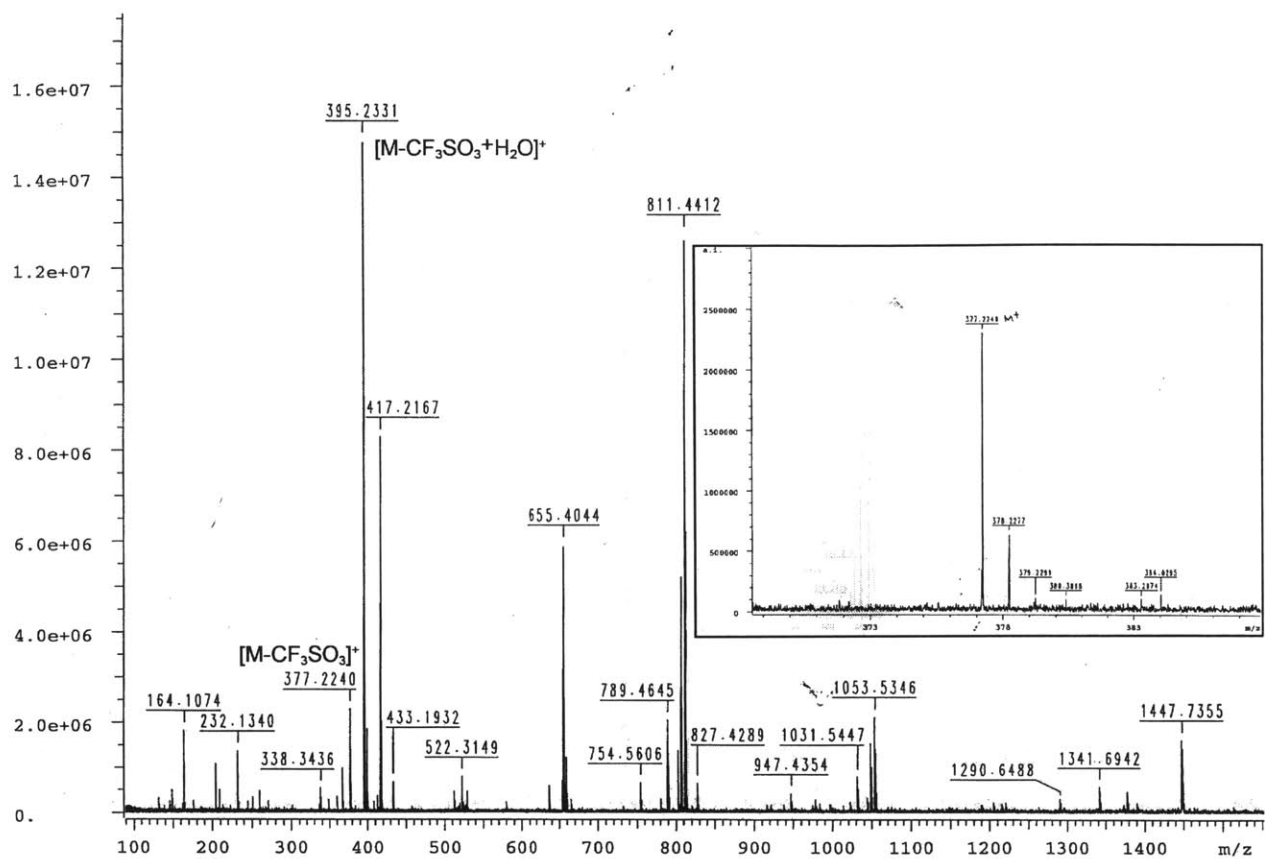
Figure 27. FT-ICR-ESI HRMS of **4•HOTf**. Inset depicts the isotope pattern of the [M-CF₃SO₃]⁺ ion.
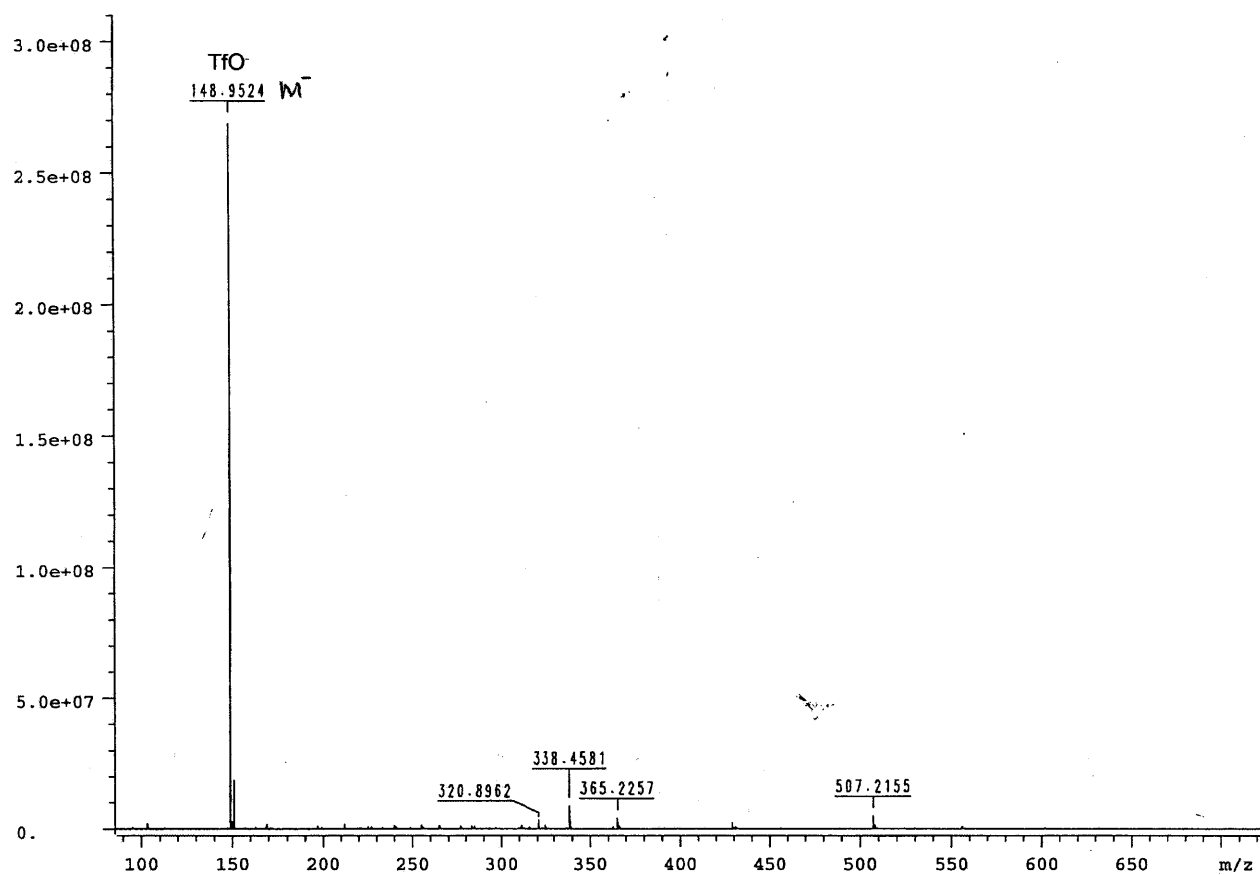
Figure 28. FT-ICR-ESI HRMS (negative ion mode) of **4•HOTf**.
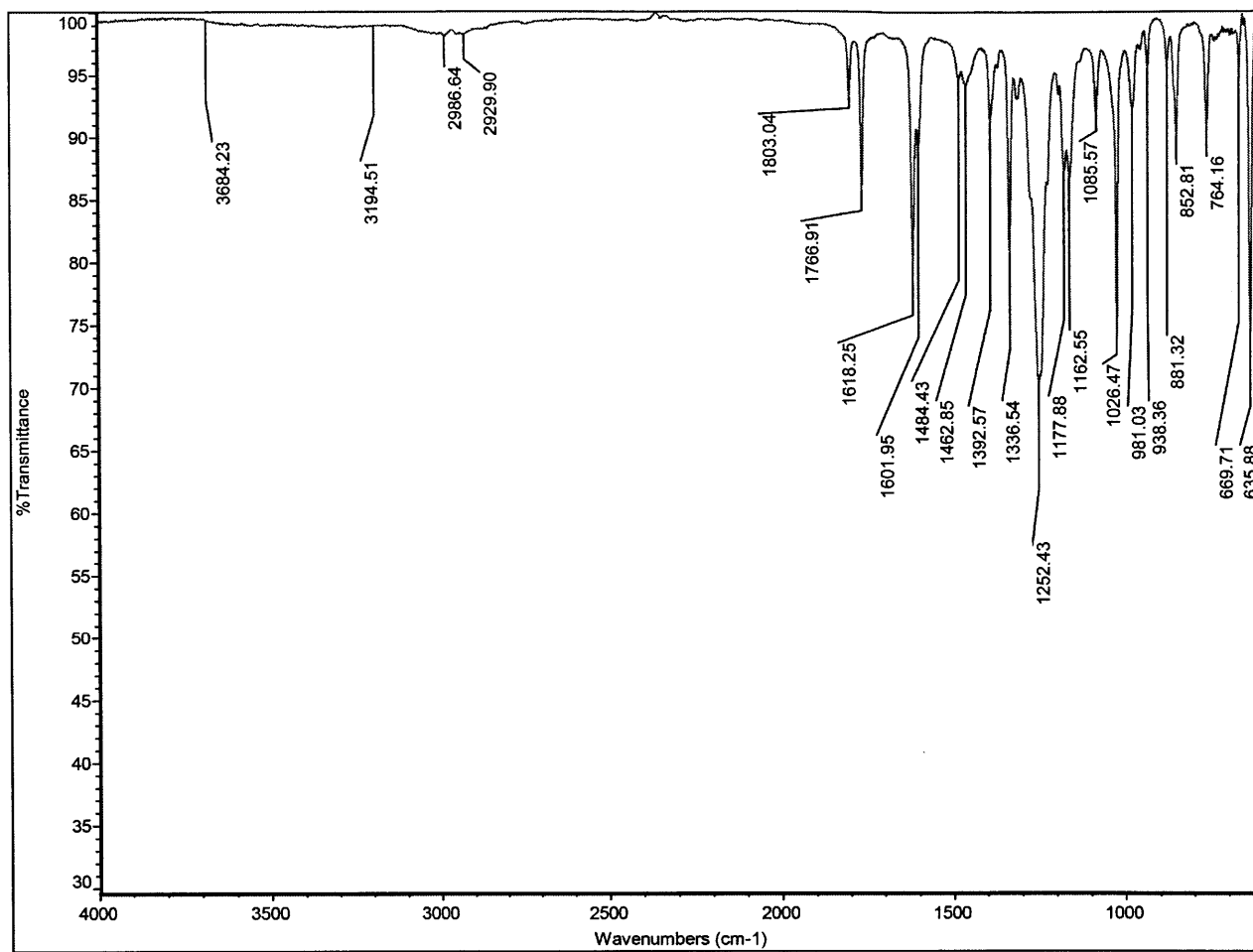
Figure 29. ATR-FTIR spectrum of 4•HOTf.
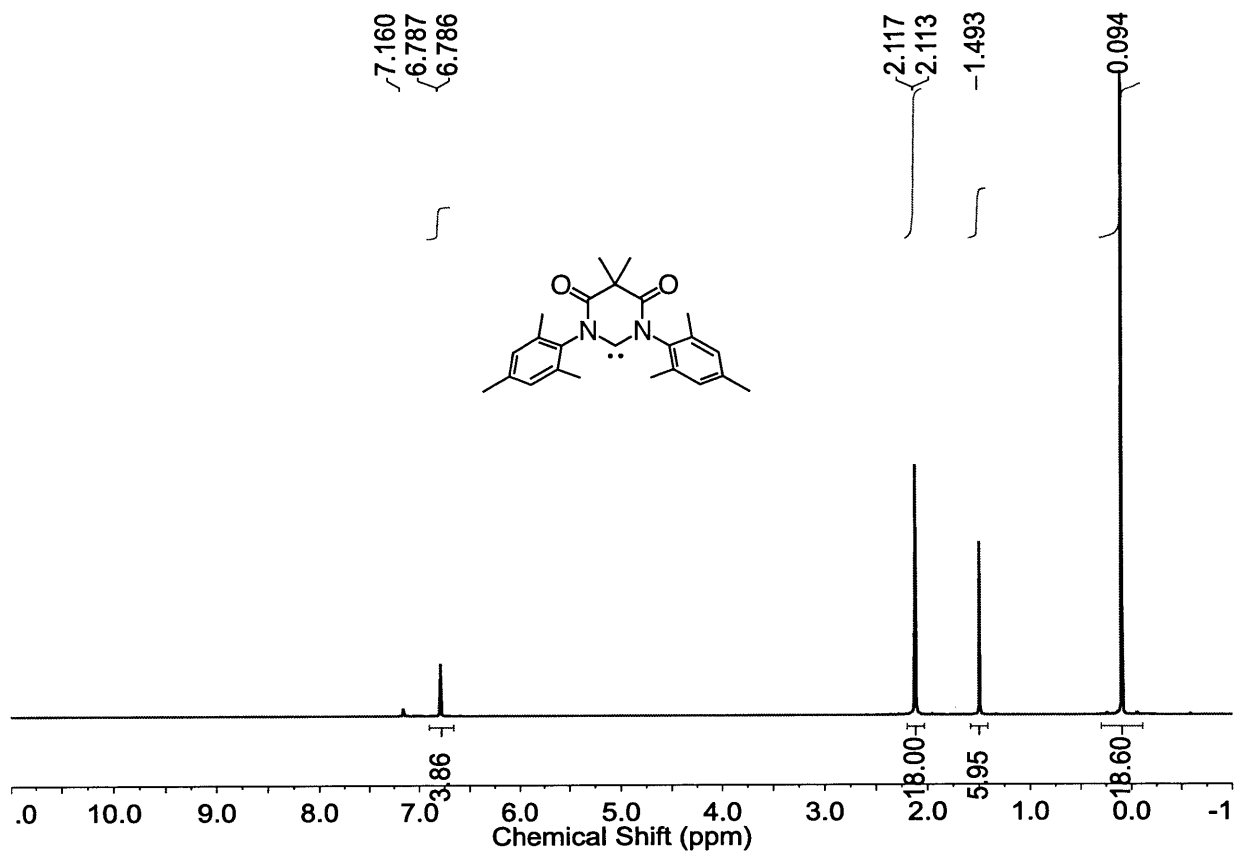
Figure 30. ^{1}H NMR (400 MHz, C_6D_6, 25 °C) spectrum of **4**.

236
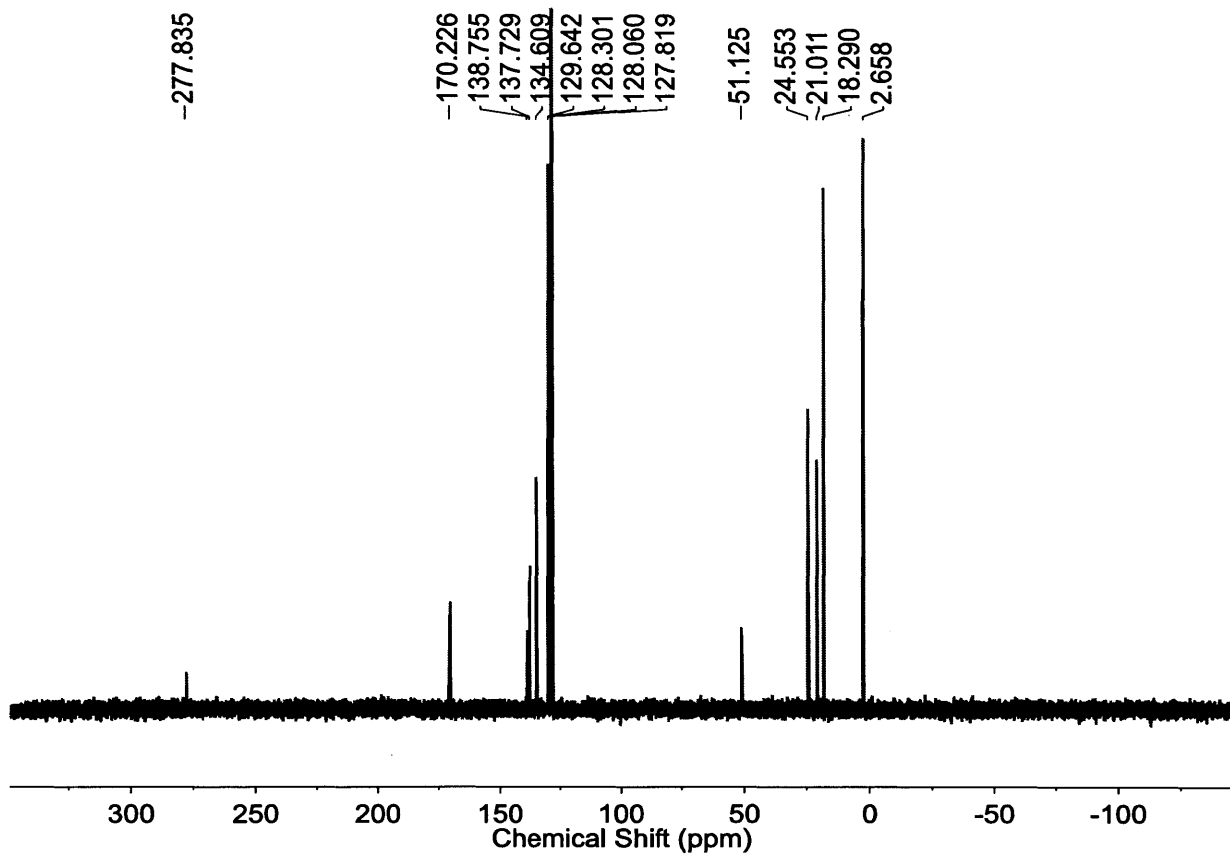
Figure 31. ^{13}C NMR (100 MHz, C_6D_6, 25 °C) spectrum of 4.

237
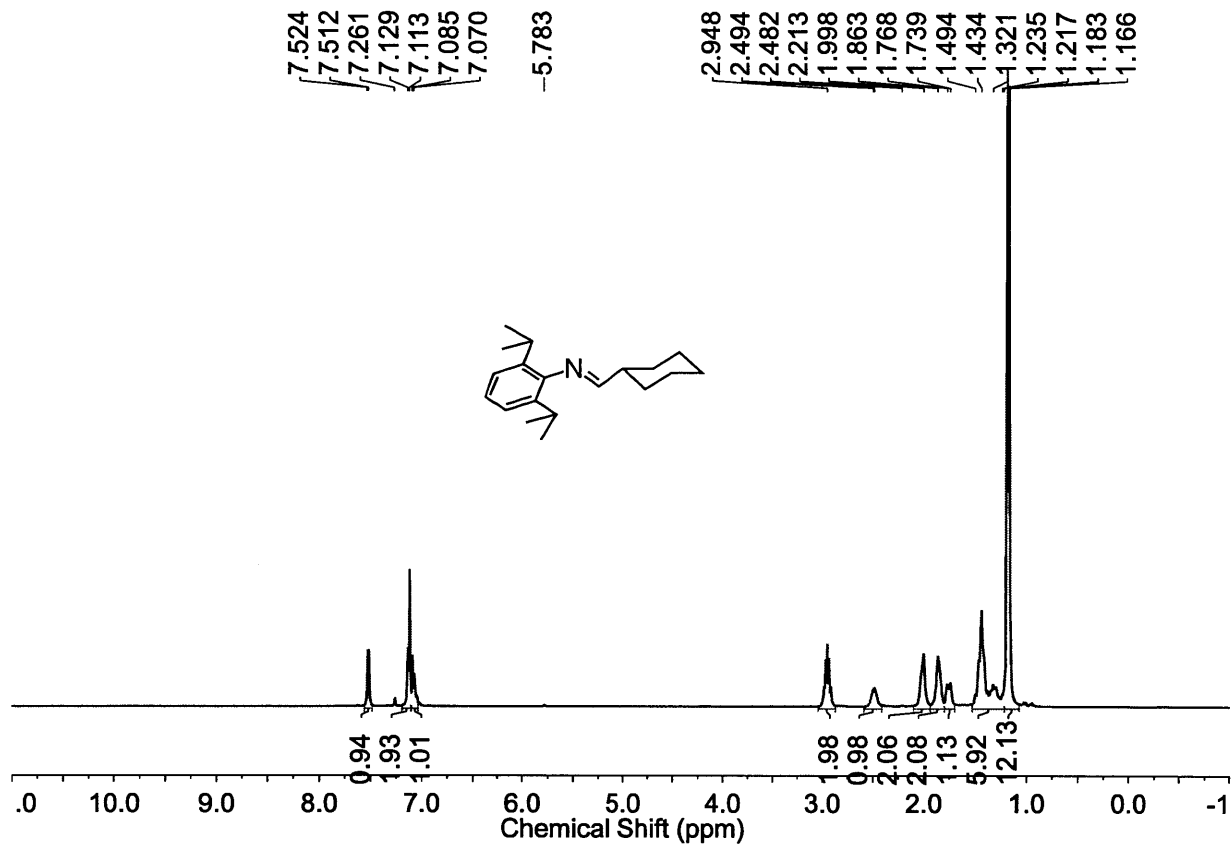
Figure 32. ^{1}H NMR (400 MHz, CDCl$_3$, 25 °C) spectrum of 1-cyclohexyl-*N*-(2,6-diisopropylphenyl)methanimine.
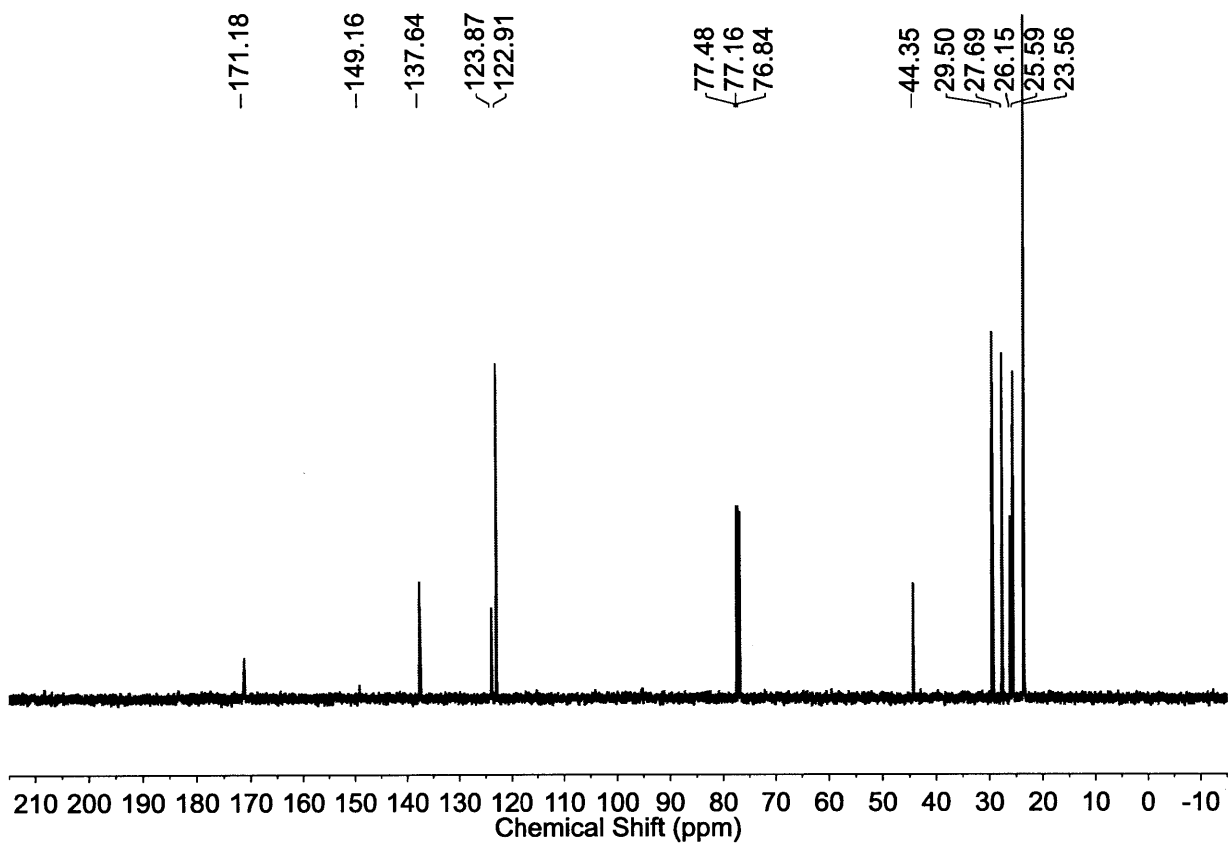
Figure 33. ^{13}C NMR (100 MHz, CDCl$_3$, 25 °C) spectrum of 1-cyclohexyl-*N*-(2,6-diisopropylphenyl)methanimine.

239
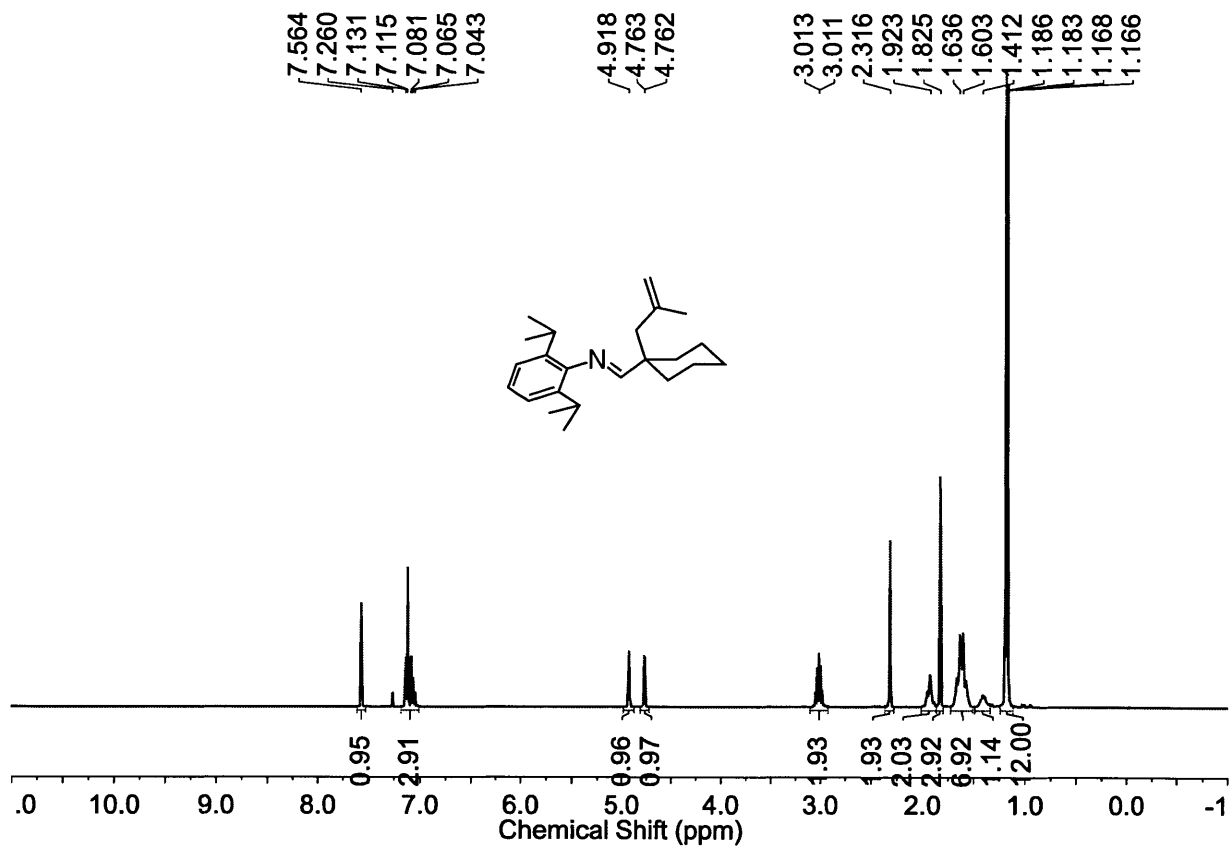
Figure 34. ¹H NMR (400 MHz, CDCl₃, 25 °C) spectrum of *N*-(2,6-diisopropylphenyl)-1-(1-(2-methylallyl)cyclohexyl)methanimine .
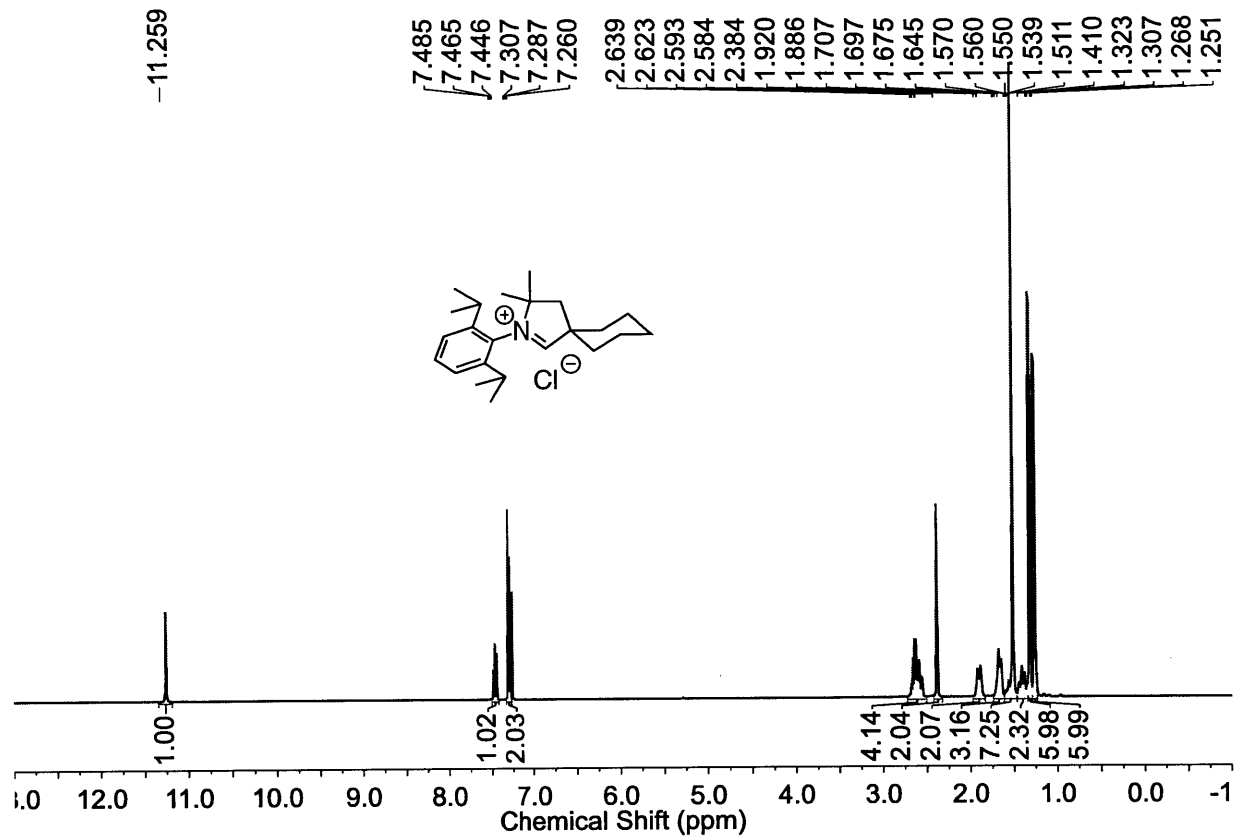
Figure 35. ^{1}H NMR (400 MHz, CDCl$_3$, 25 °C) spectrum of **6•HCl**.
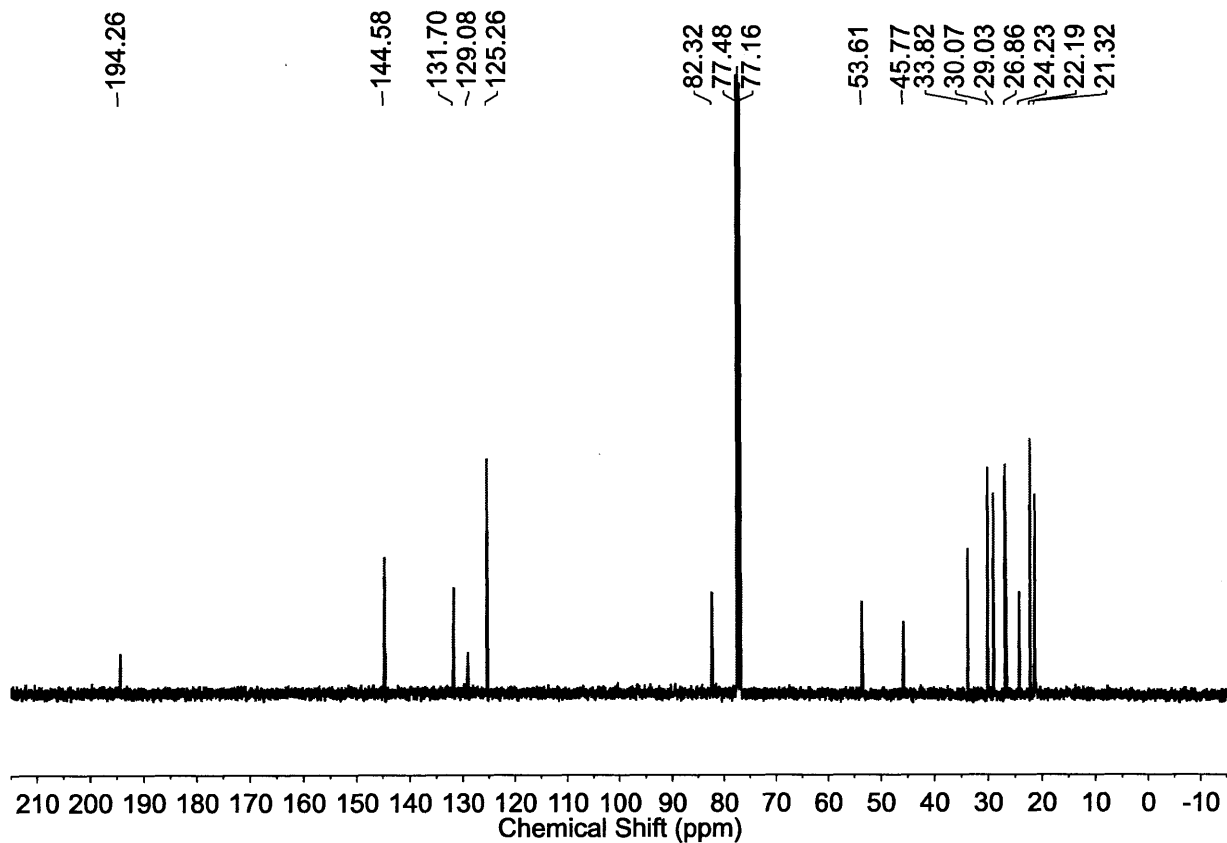
Figure 36. ^{13}C NMR (100 MHz, CDCl$_3$, 25 °C) spectrum of **6·HCl**.

242
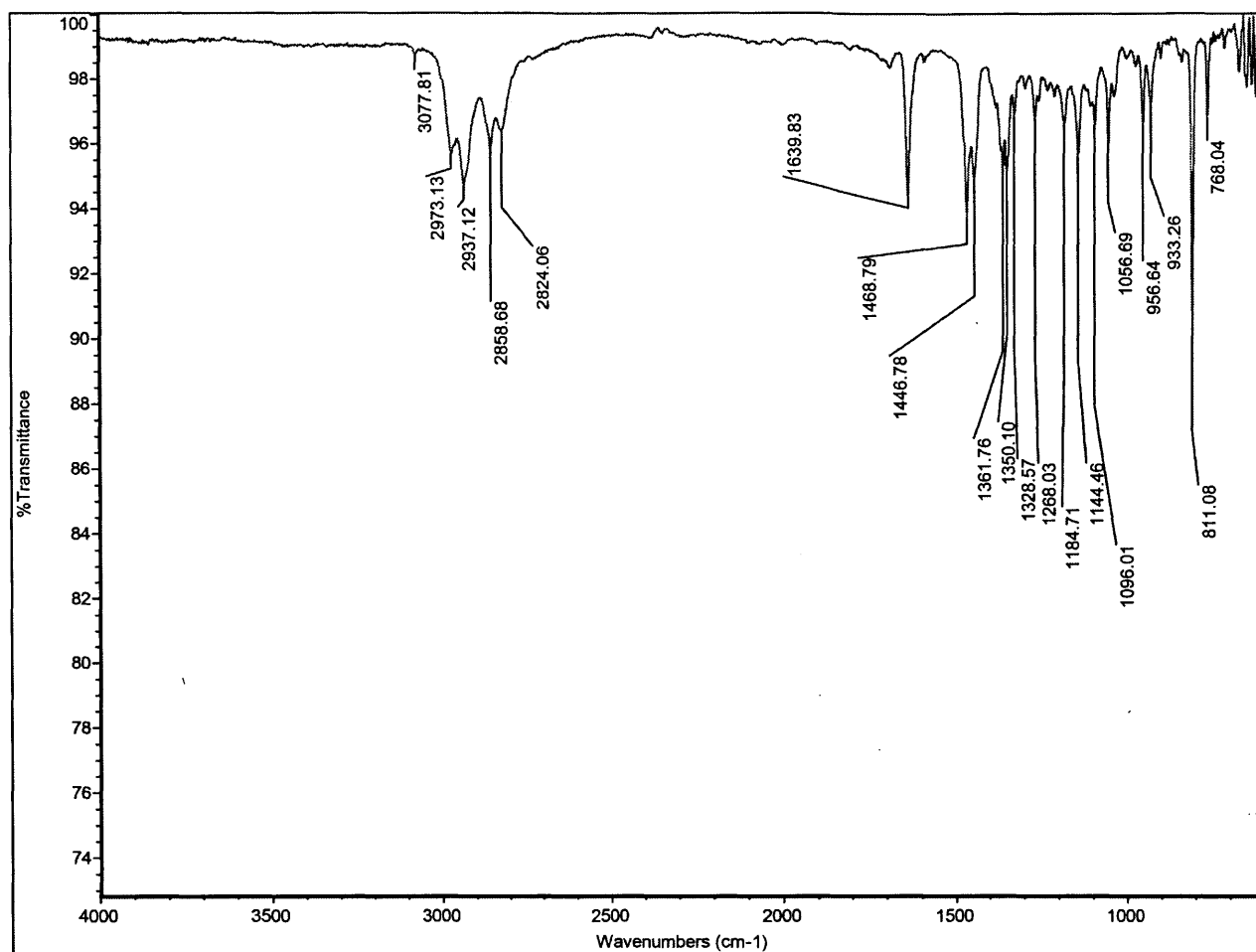
Figure 37. ATR-FTIR spectrum of 6•HCl.
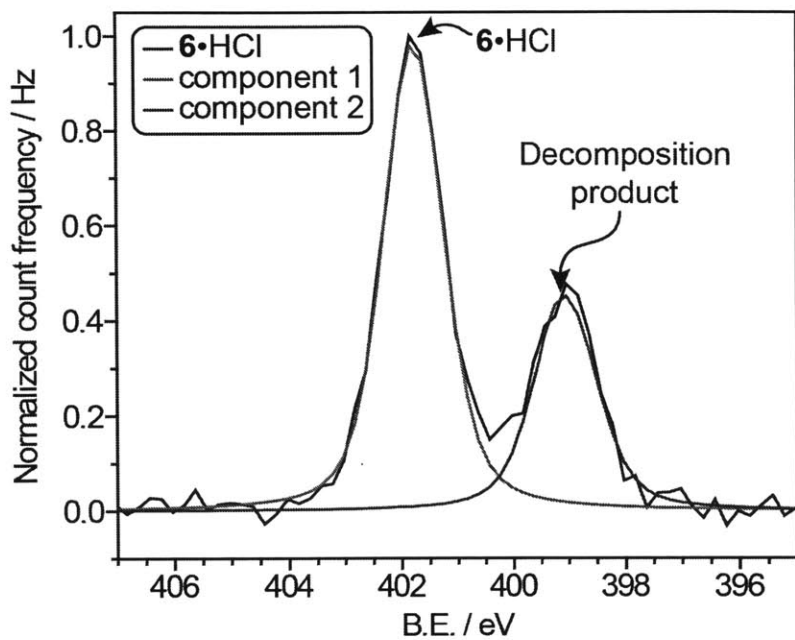
Figure 38. XPS N1s region of **6**•HCl; decomposition due to X-ray irradiation led to the appearance of another peak, as indicated in the figure.
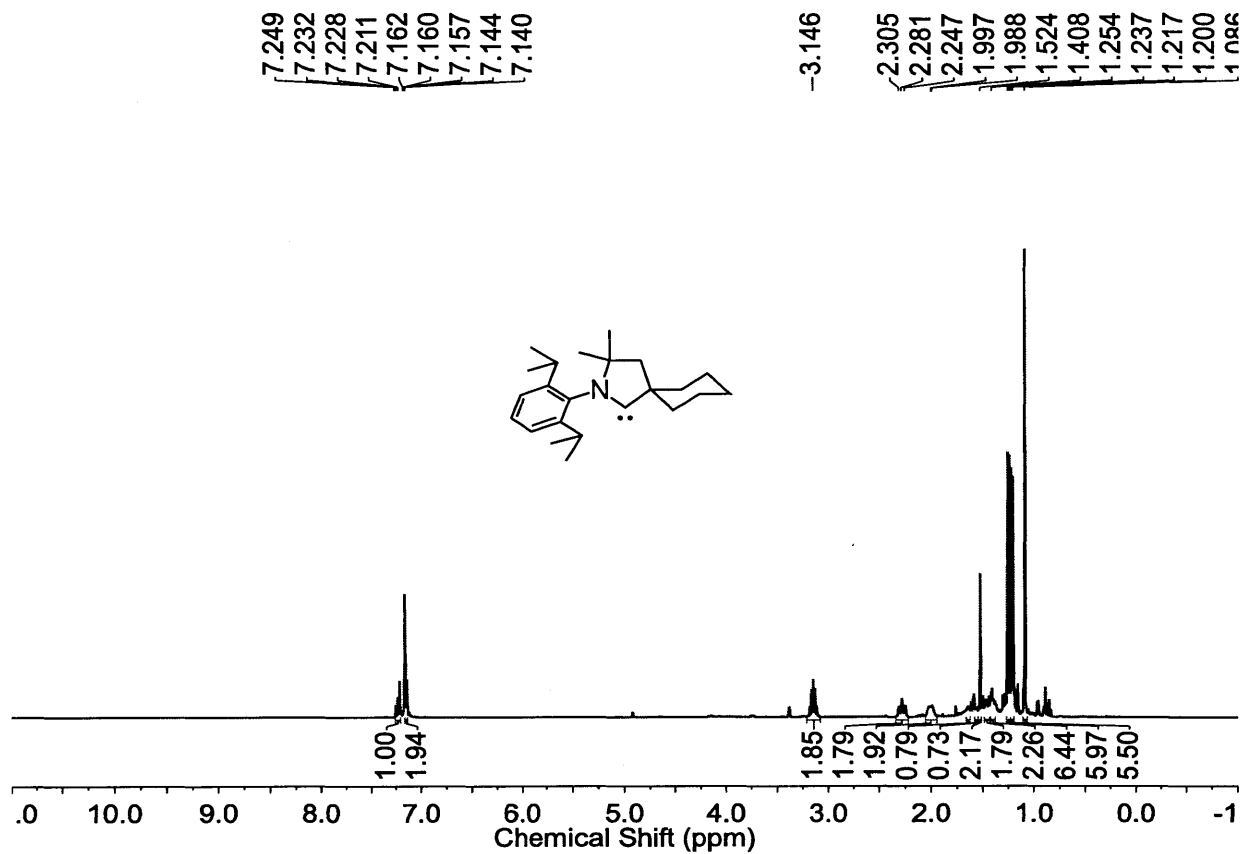
Figure 39. ^{1}H NMR (400 MHz, C_6D_6, 25 °C) spectrum of **6**.
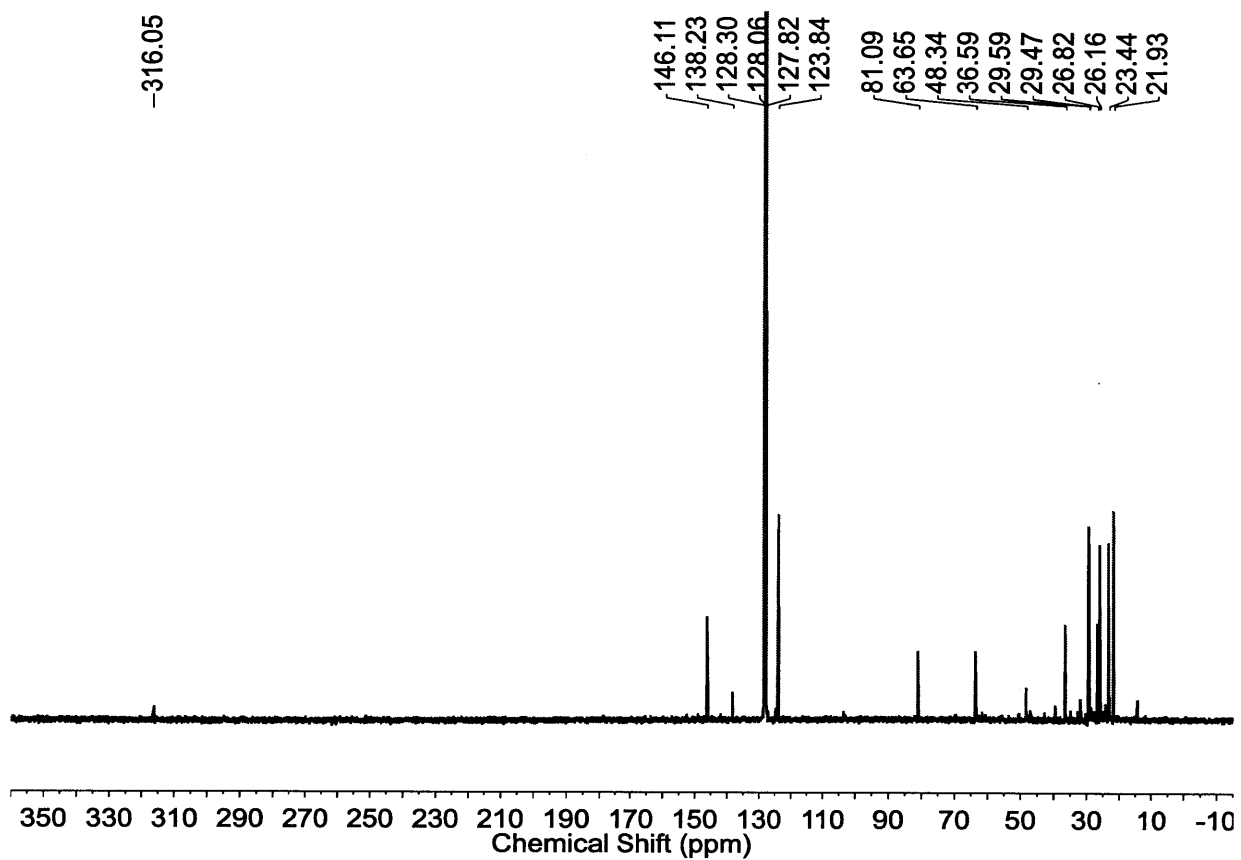
Figure 40. ^{13}C NMR (100 MHz, C_6D_6, 25 °C) spectrum of **6**.
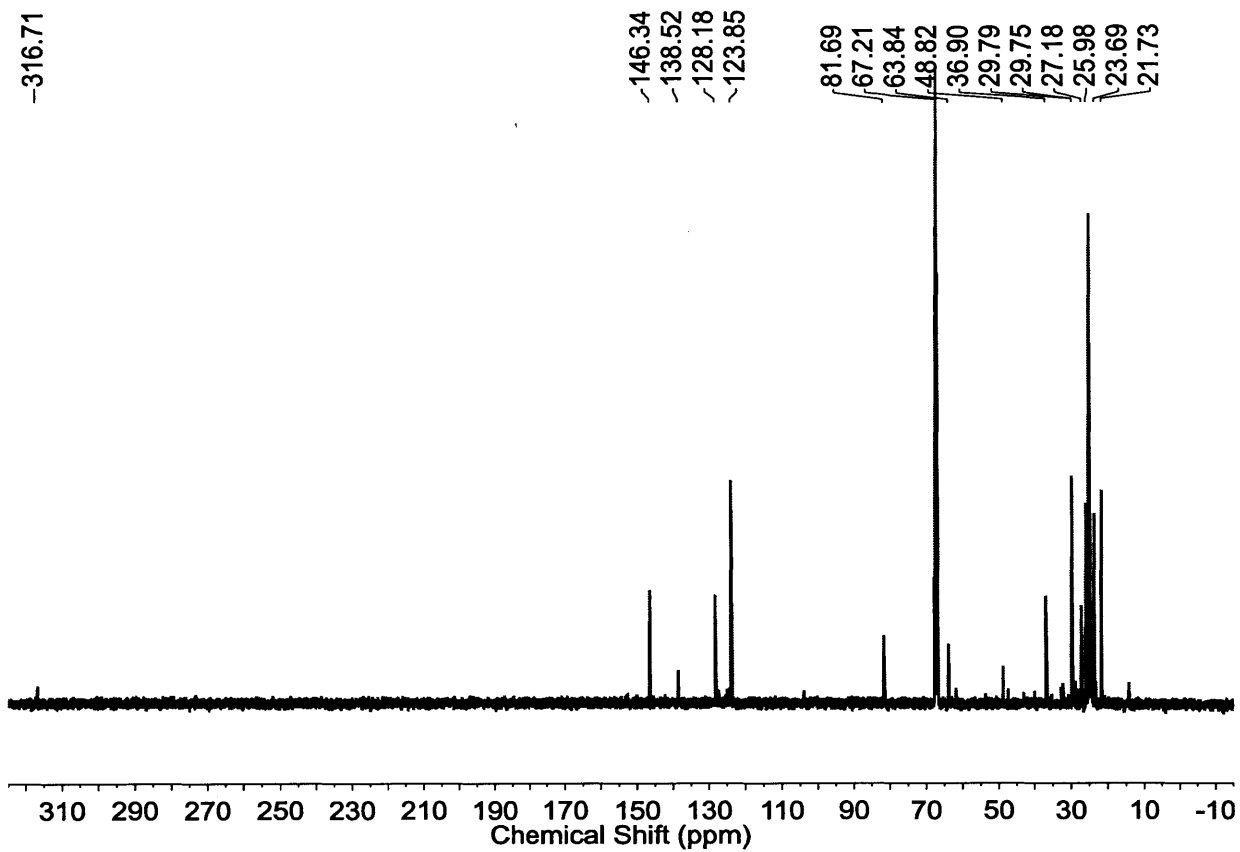
Figure 41. ^{13}C NMR (100 MHz, THF-d^8, 25 °C) spectrum of **6**.

316.71
146.34
138.52
128.18
123.85
81.69
67.21
63.84
48.82
36.90
29.79
29.75
27.18
25.98
23.69
21.73

310 290 270 250 230 210 190 170 150 130 110 90 70 50 30 10 -10
Chemical Shift (ppm)

247
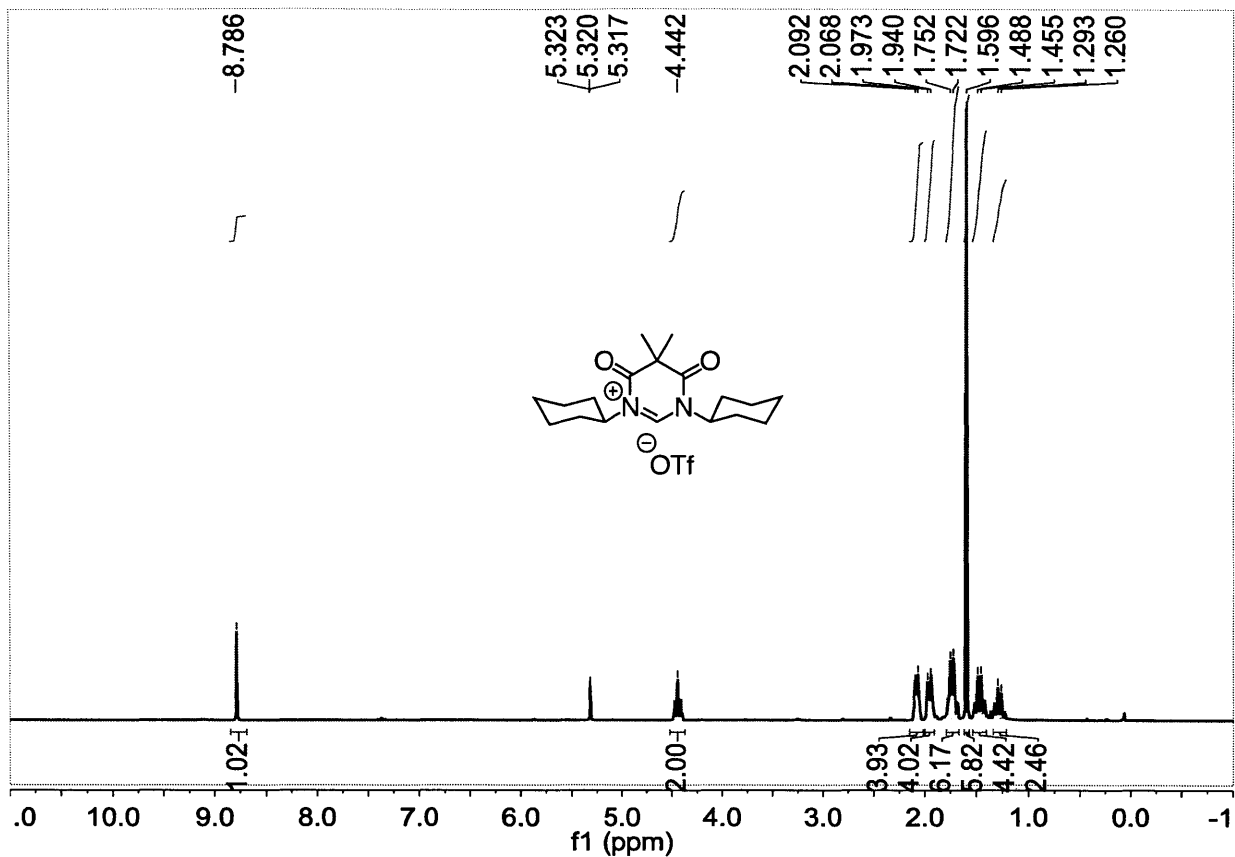
Figure 42. ^{1}H NMR (400 MHz, CD$_2$Cl$_2$, 25 °C) spectrum of **5•HOTf**.

248
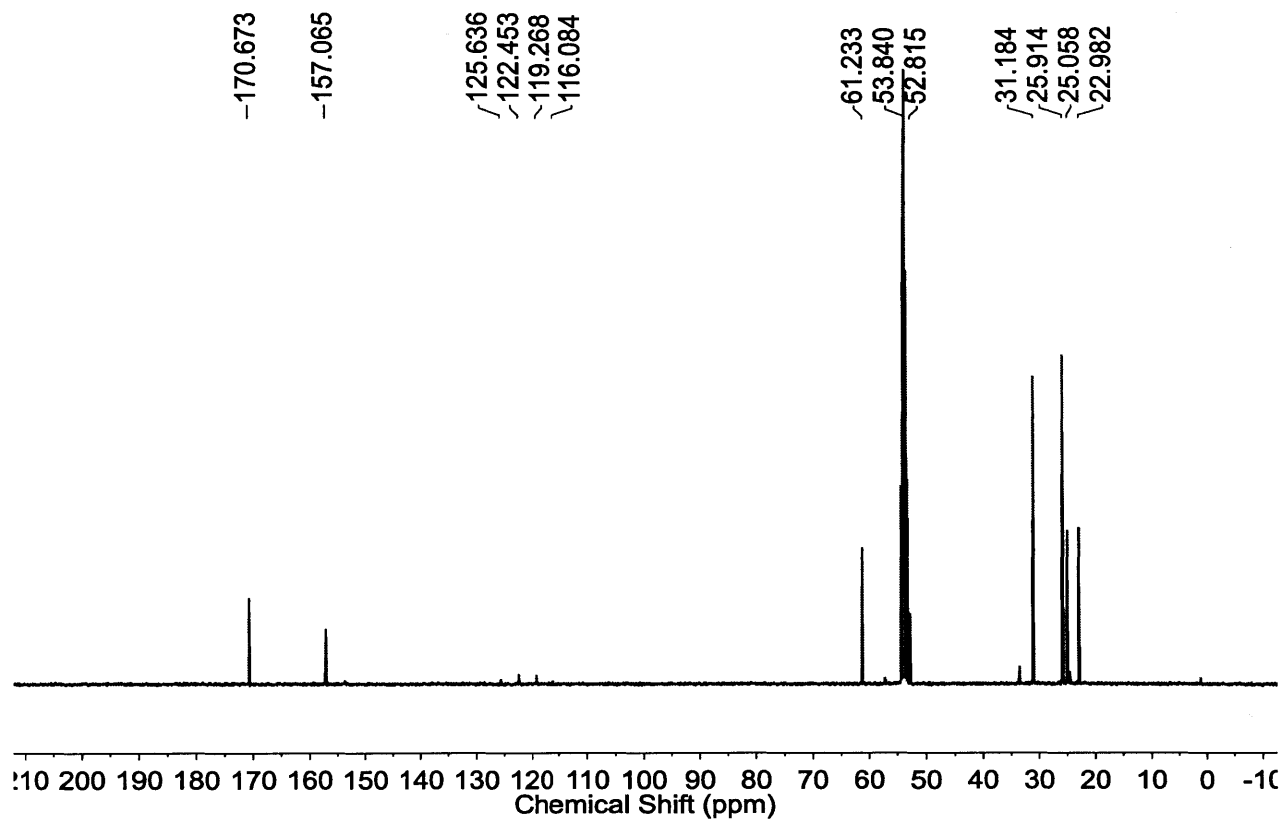
Figure 43. ^{13}C NMR (100 MHz, CD_2Cl_2, 25 °C) spectrum of **5•HOTf**.

Peak labels: 170.673, 157.065, 125.636, 122.453, 119.268, 116.084, 61.233, 53.840, 52.815, 31.184, 25.914, 25.058, 22.982

Chemical Shift (ppm)

--74.78

10   -10   -30   -50   -70   -90   -110   -130   -150   -170   -190   -21
                              Chemical Shift (ppm)
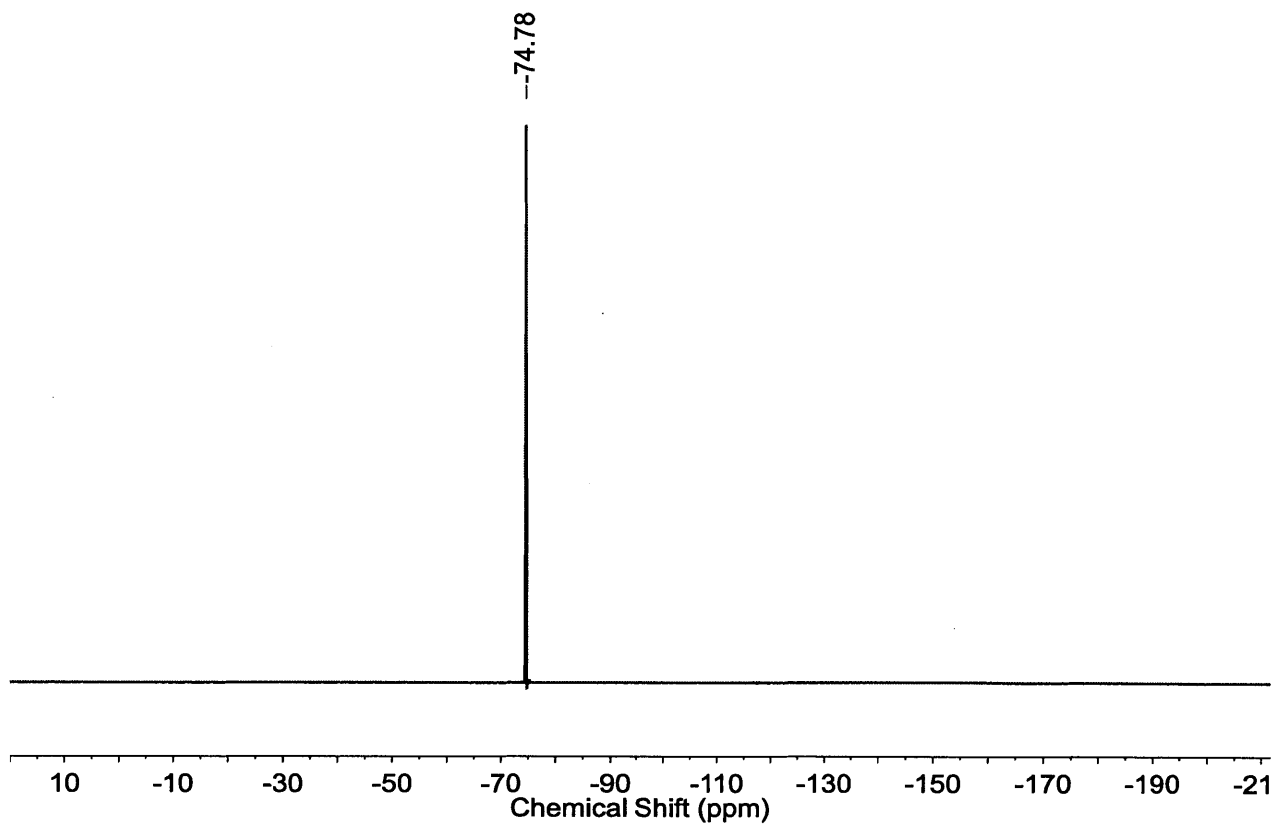
Figure 44. ^{1}H NMR (376.4 MHz, CD$_2$Cl$_2$, 25 °C) spectrum of **5•HOTf**.
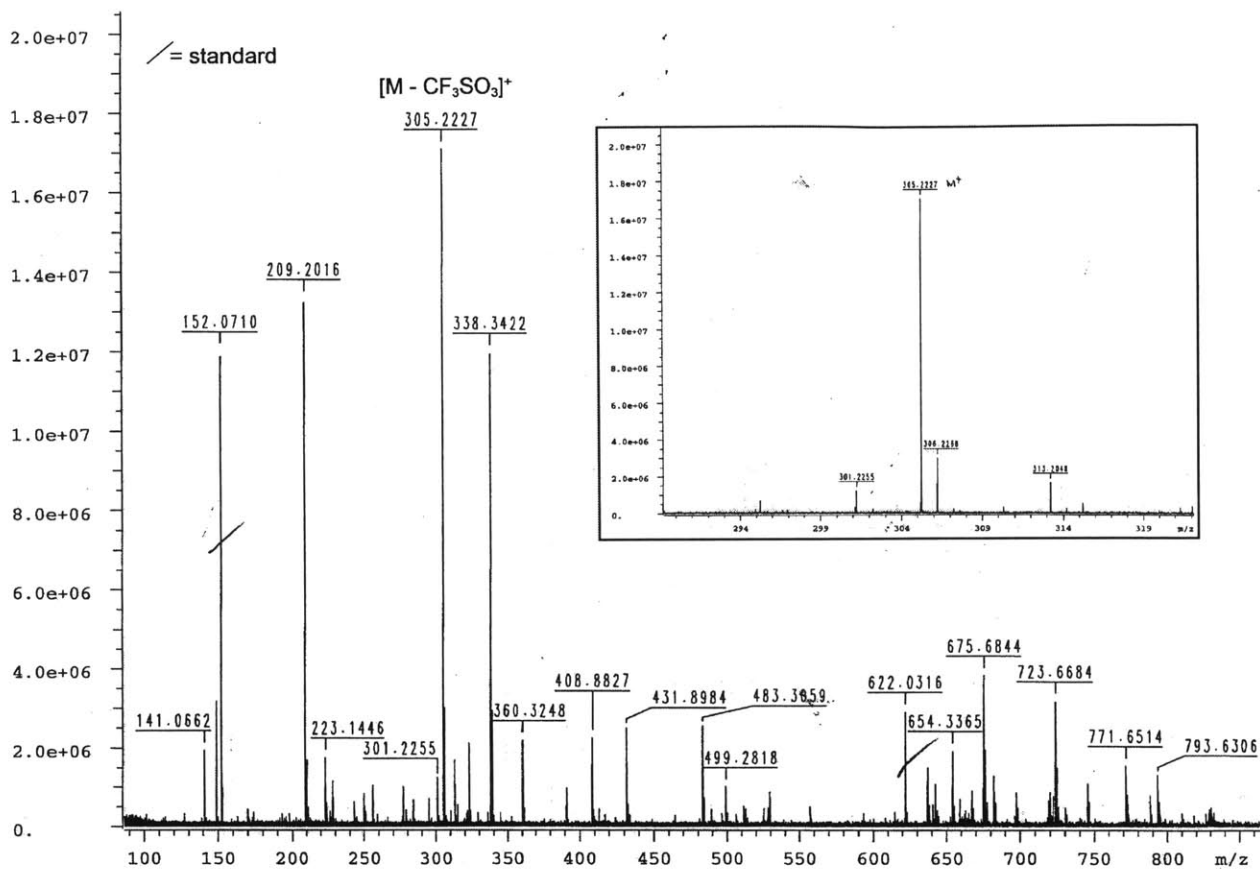
Figure 45. FT-ICR-ESI HRMS of **5·HOTf**. Inset depicts the isotope pattern of the [M-CF$_3$SO$_3$]$^+$ ion.
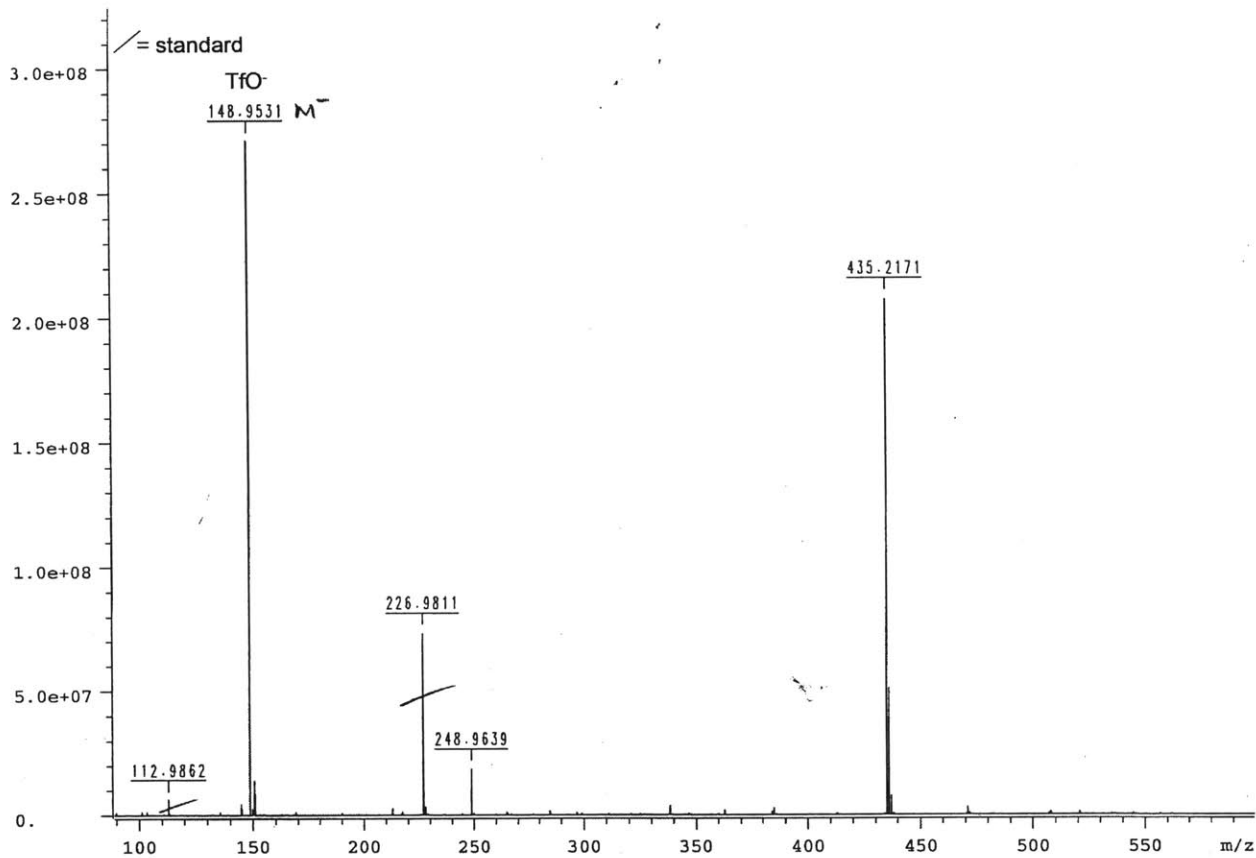
Figure 46. FT-ICR-ESI HRMS (negative ion mode) of **5**·HOTf.
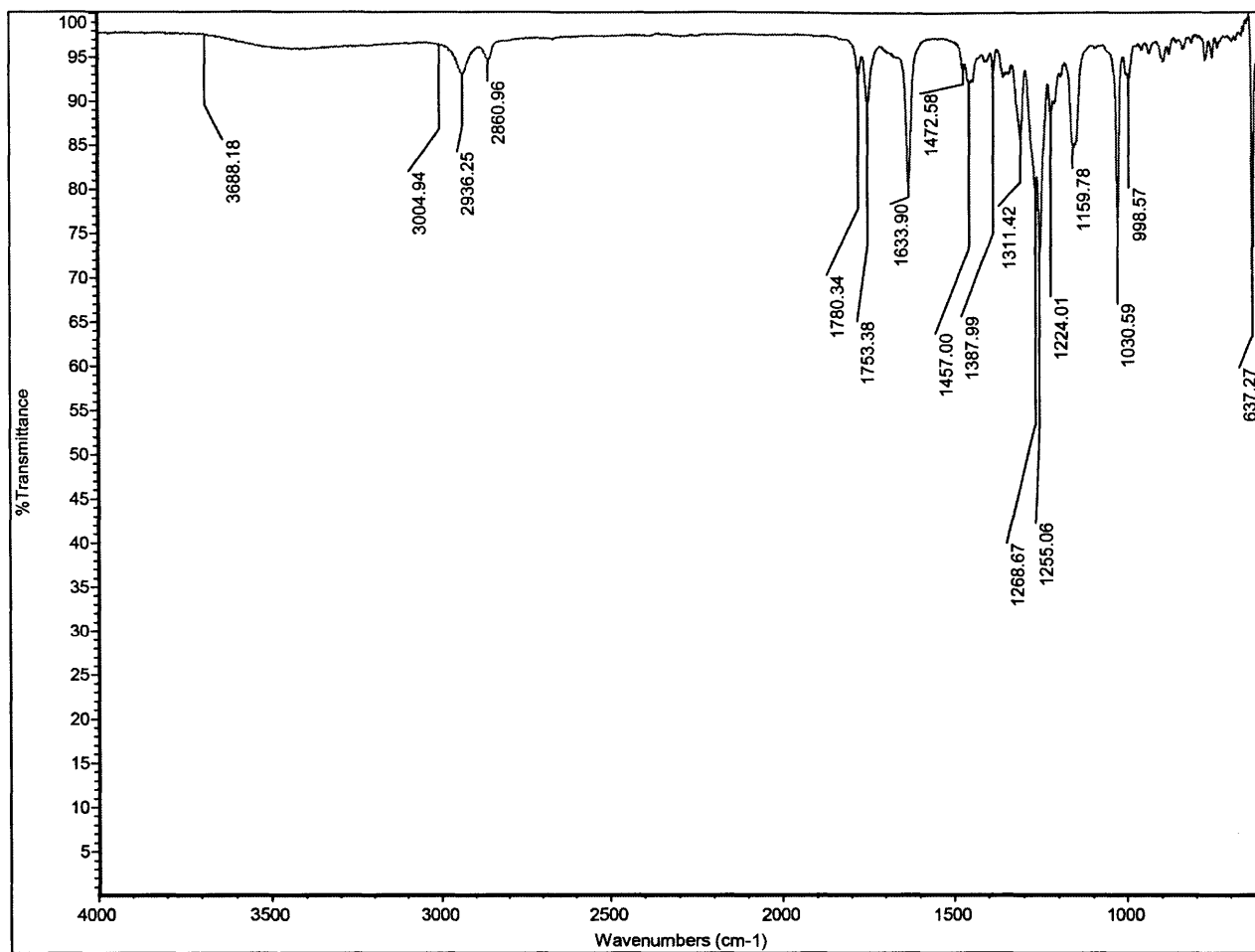
Figure 47. ATR-FTIR spectrum of 5•HOTf.
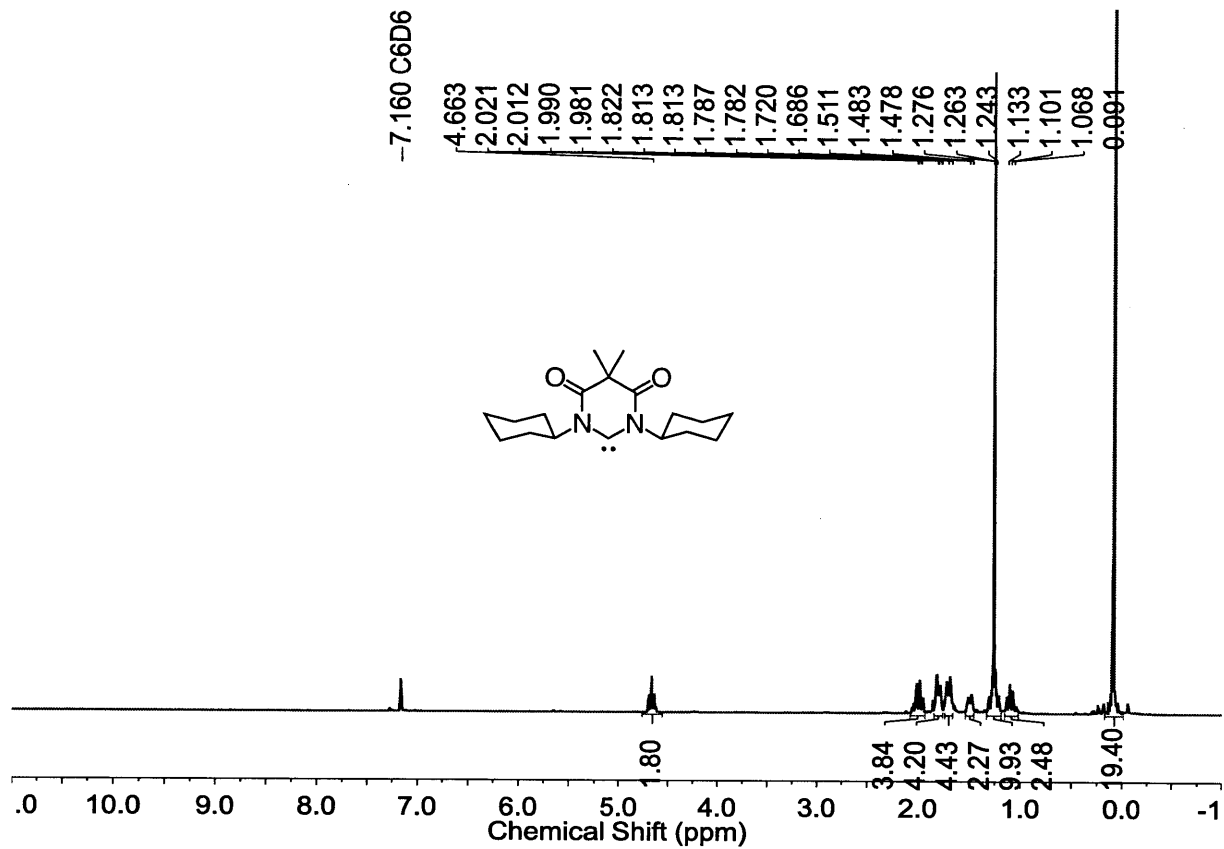
Figure 48. ^{1}H NMR (400 MHz, C_6D_6, 25 °C) spectrum of **5**.
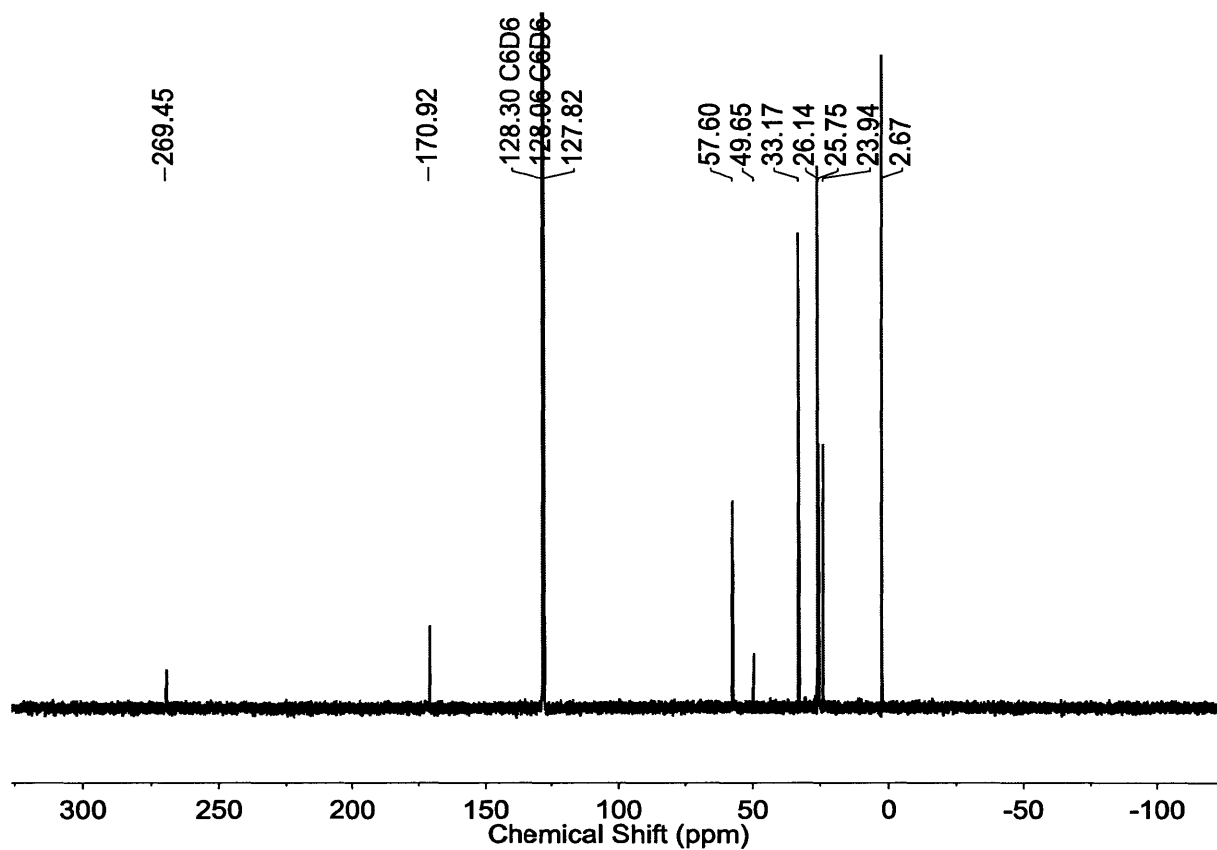
Figure 49. ^{13}C NMR (100 MHz, C_6D_6, 25 °C) spectrum of **5**.

255
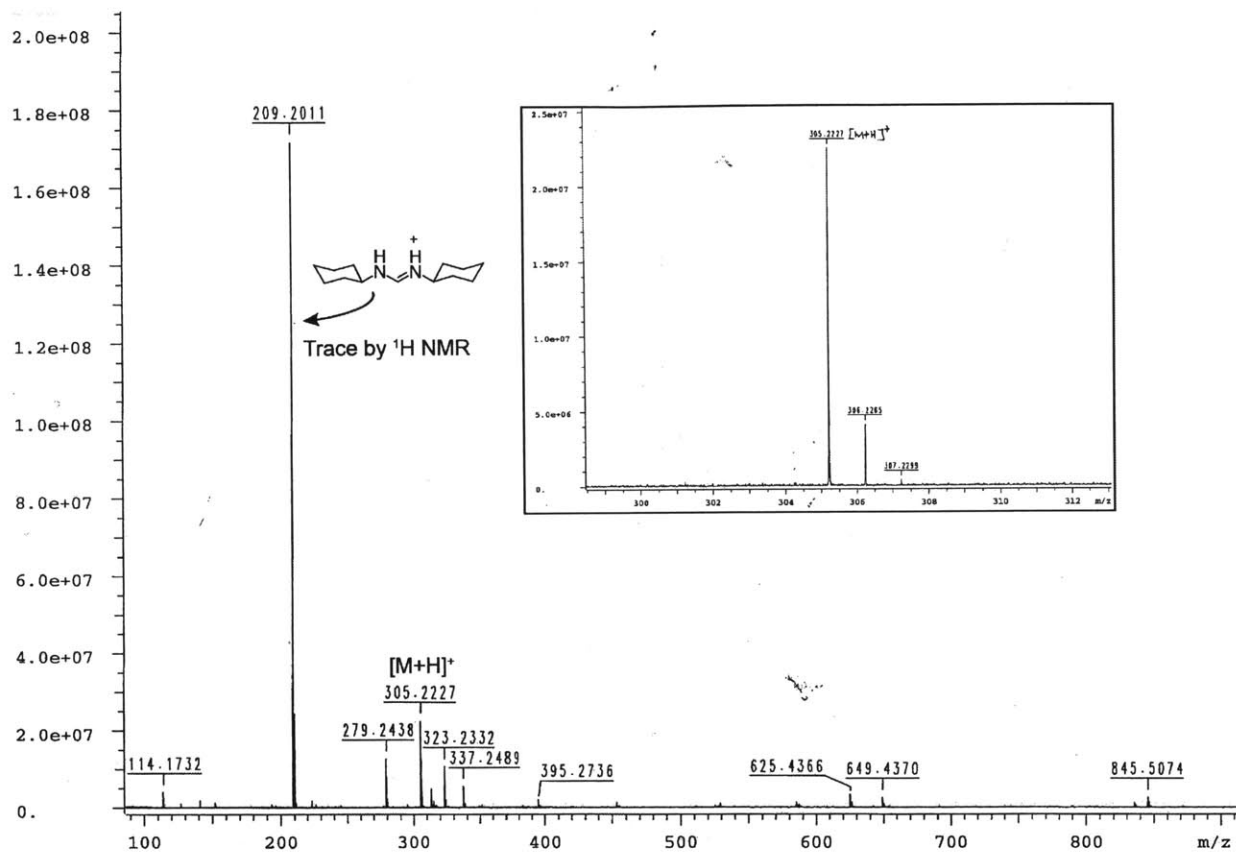
Figure 50. FT-ICR-ESI HRMS of as prepared **5**. Inset depicts the isotope pattern of the [M+H]⁺ ion.

Figure 51. ^{1}H NMR (500 MHz, C_6D_6, 25 °C) spectrum of crude **5•TTMSS**. Integration and chemical shifts are shown for peaks corresponding to **5•TTMSS** and C_6D_6.

257
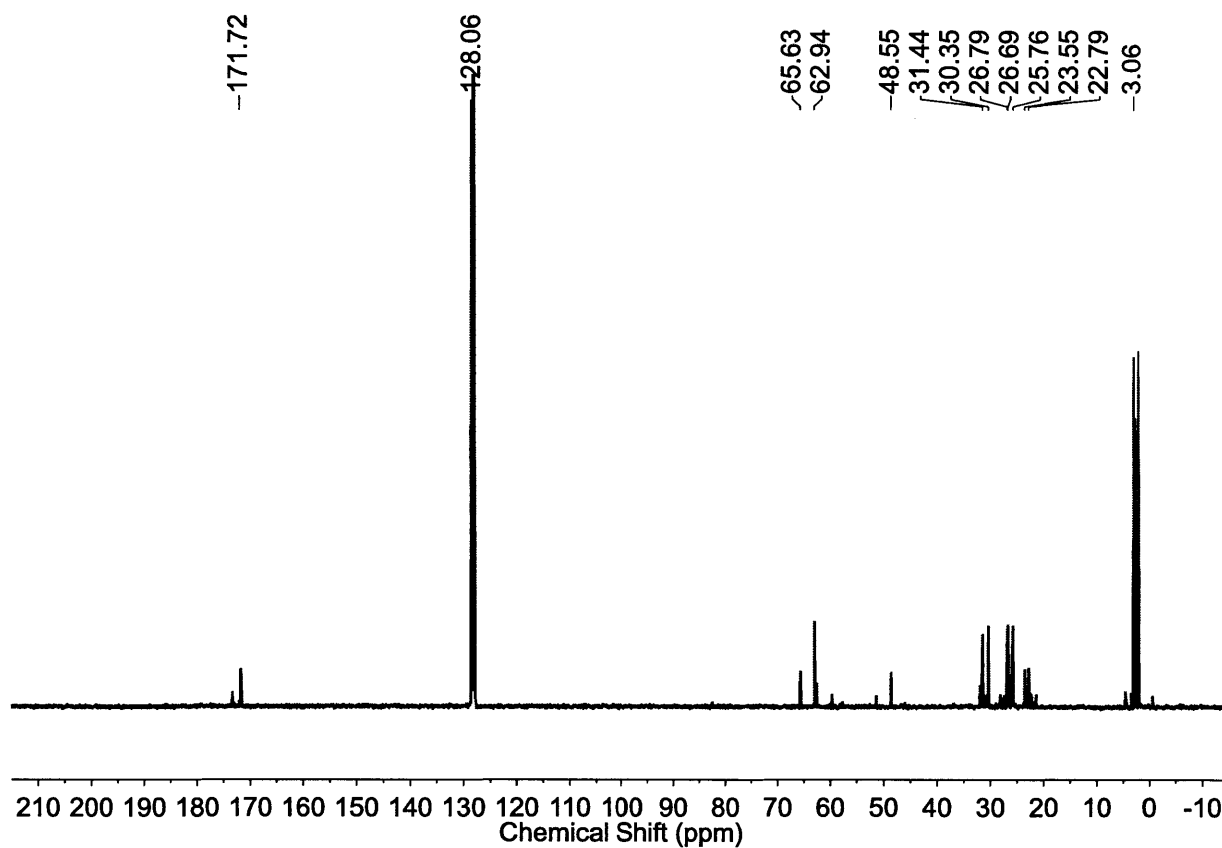
Figure 52. ^{13}C NMR (100 MHz, C_6D_6, 25 °C) spectrum of crude **5•TTMSS**. Chemical shifts are shown for peaks corresponding to **5•TTMSS** and C_6D_6.
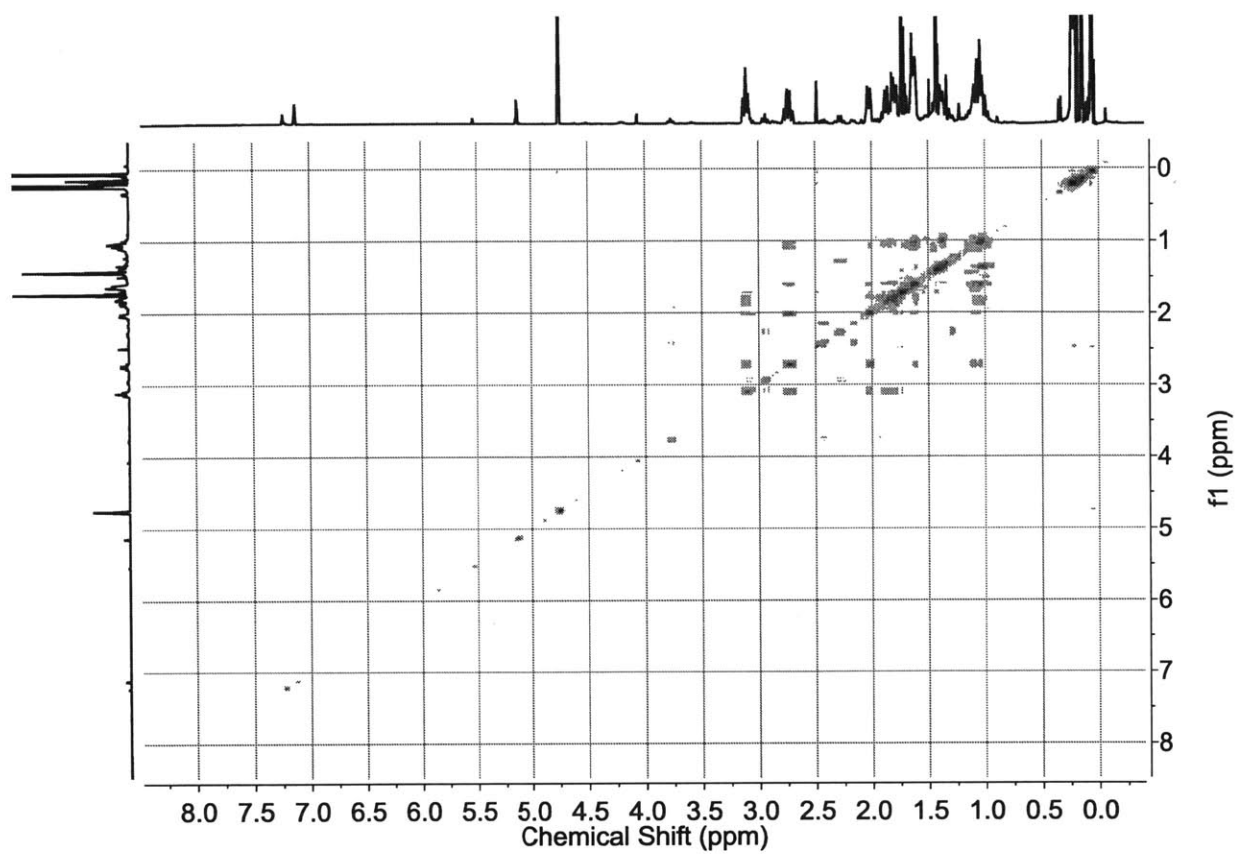
Figure 53. COSY (500 MHz (^{1}H), C_6D_6, 25 °C) spectrum of crude **5**•TTMSS.
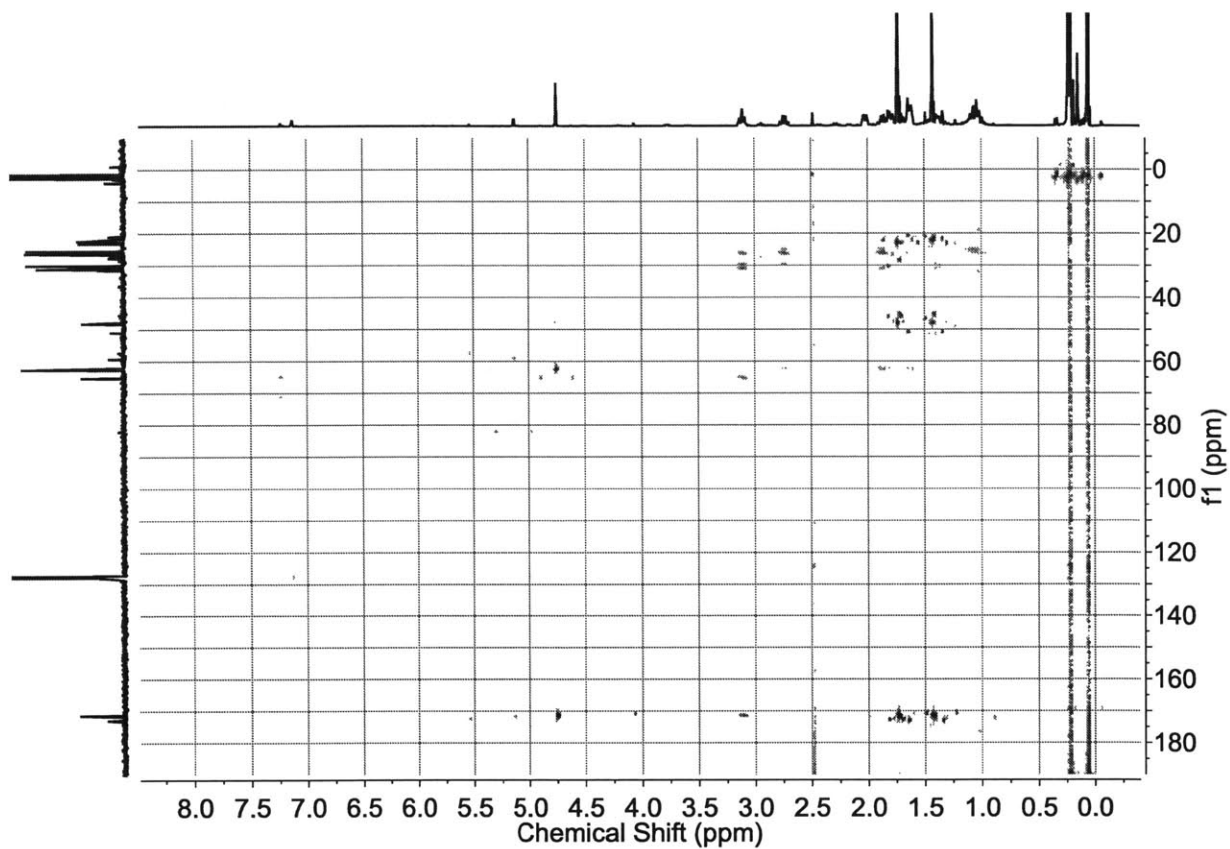
Figure 54. gHMBC (500 MHz (^{1}H), C$_6$D$_6$, 25 °C) spectrum of crude **5•**TTMSS.
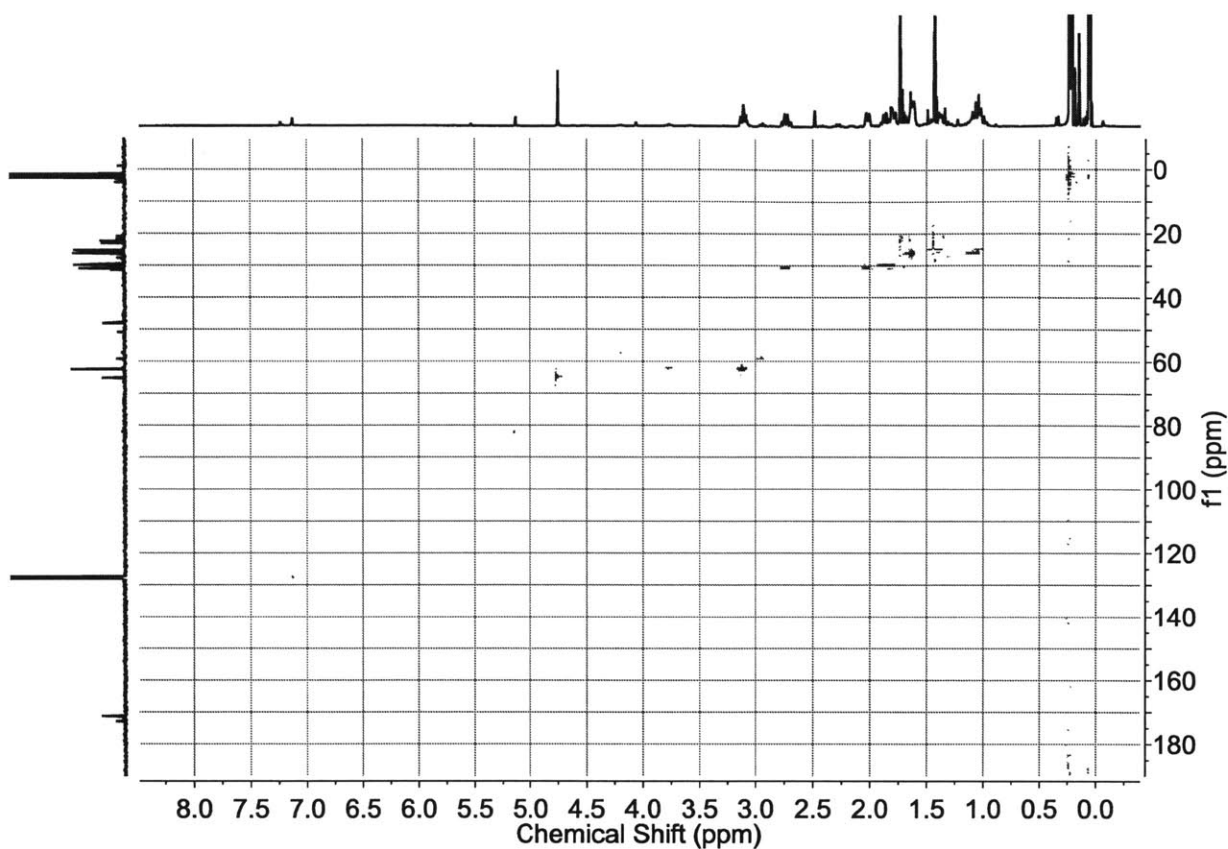
Figure 55. HSQC (500 MHz (^{1}H), C_6D_6, 25 °C) spectrum of crude **5·**TTMSS.
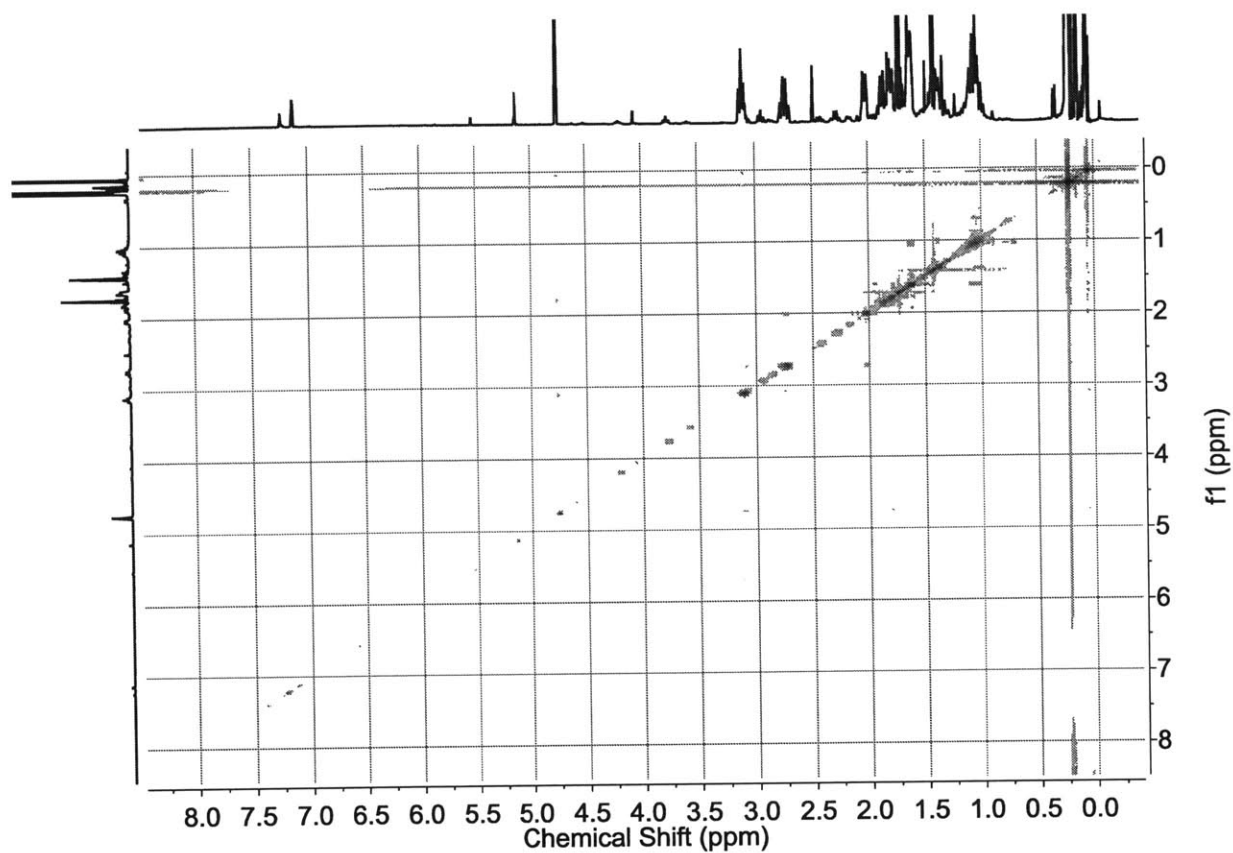
Figure 56. NOESY (500 MHz (^{1}H), C_6D_6, 25 °C) spectrum of crude **5•**TTMSS.
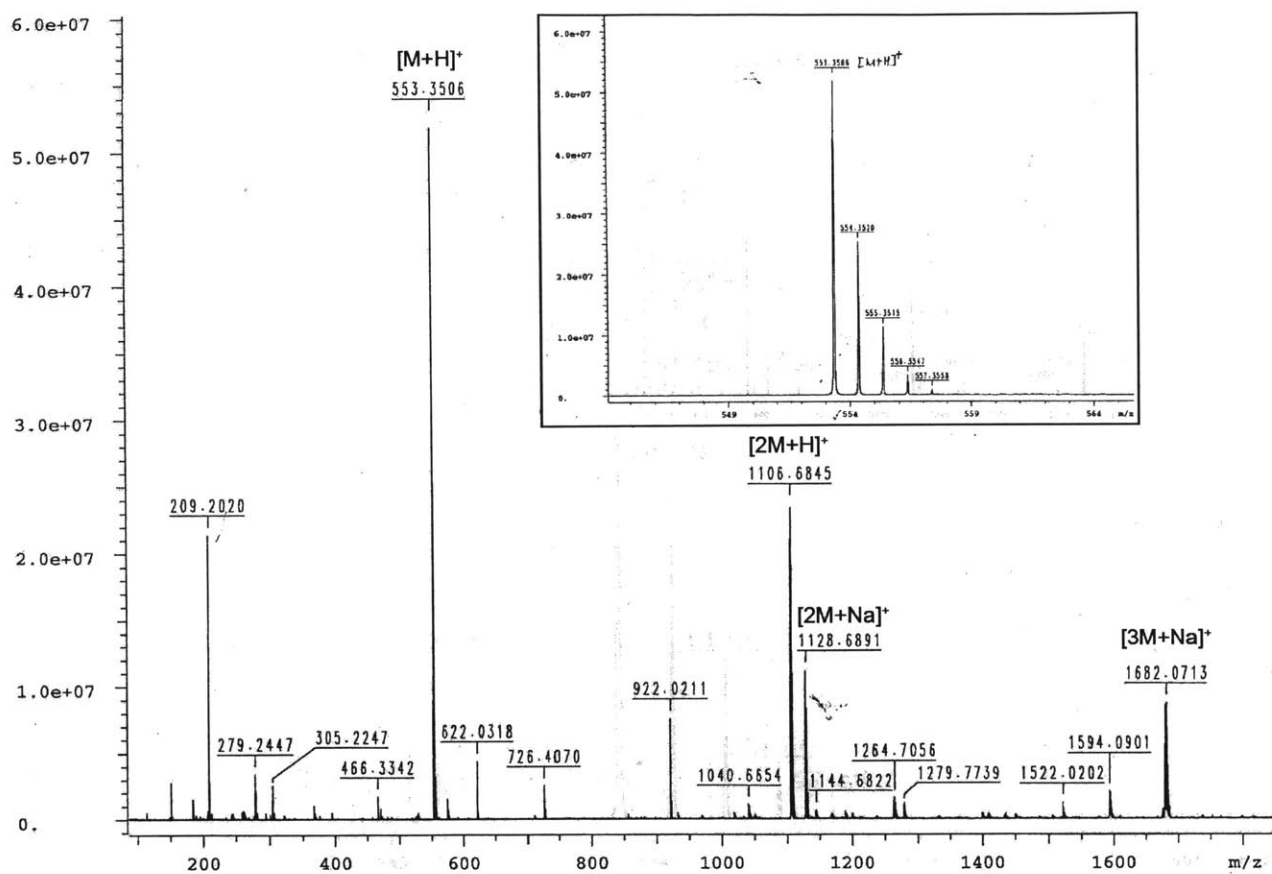
Figure 57. FT-ICR-ESI HRMS of crude **5**•TTMSS. Inset depicts the isotope pattern of the [M+H]$^+$ ion.

7.157
7.130
7.125
7.090
7.053
7.047
4.253
4.012
3.154
2.321
2.289
2.237
2.233
2.204
2.198
2.196
1.896
1.887
1.804
1.801
1.771
1.766
1.570
1.468
1.455
1.451
1.438
1.210
1.193
1.129
1.112
0.912
0.300

.38
.28
.08

.00
.16

.21

.06
.07
2.32
.37
2.55
6.35
3.58
4.04
0.99
4.43
3.12
3.15

10.0 9.0 8.0 7.0 6.0 5.0 4.0 3.0 2.0 1.0 0.0 -1
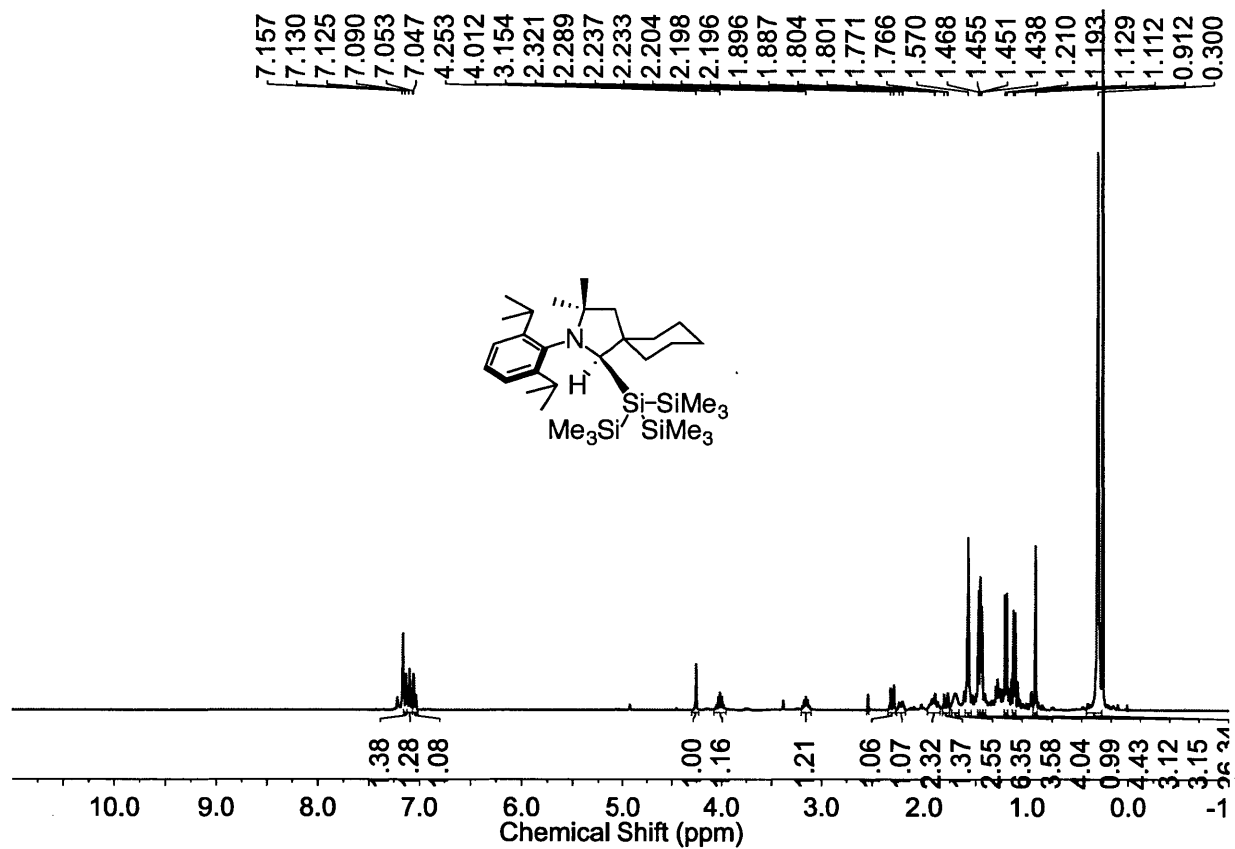
Chemical Shift (ppm)

Figure 58. ^1H NMR (400 MHz, C_6D_6, 25 °C) spectrum of crude **6·TTMSS**. Integration and chemical shifts are shown for peaks corresponding to **6·TTMSS** and C_6D_6.
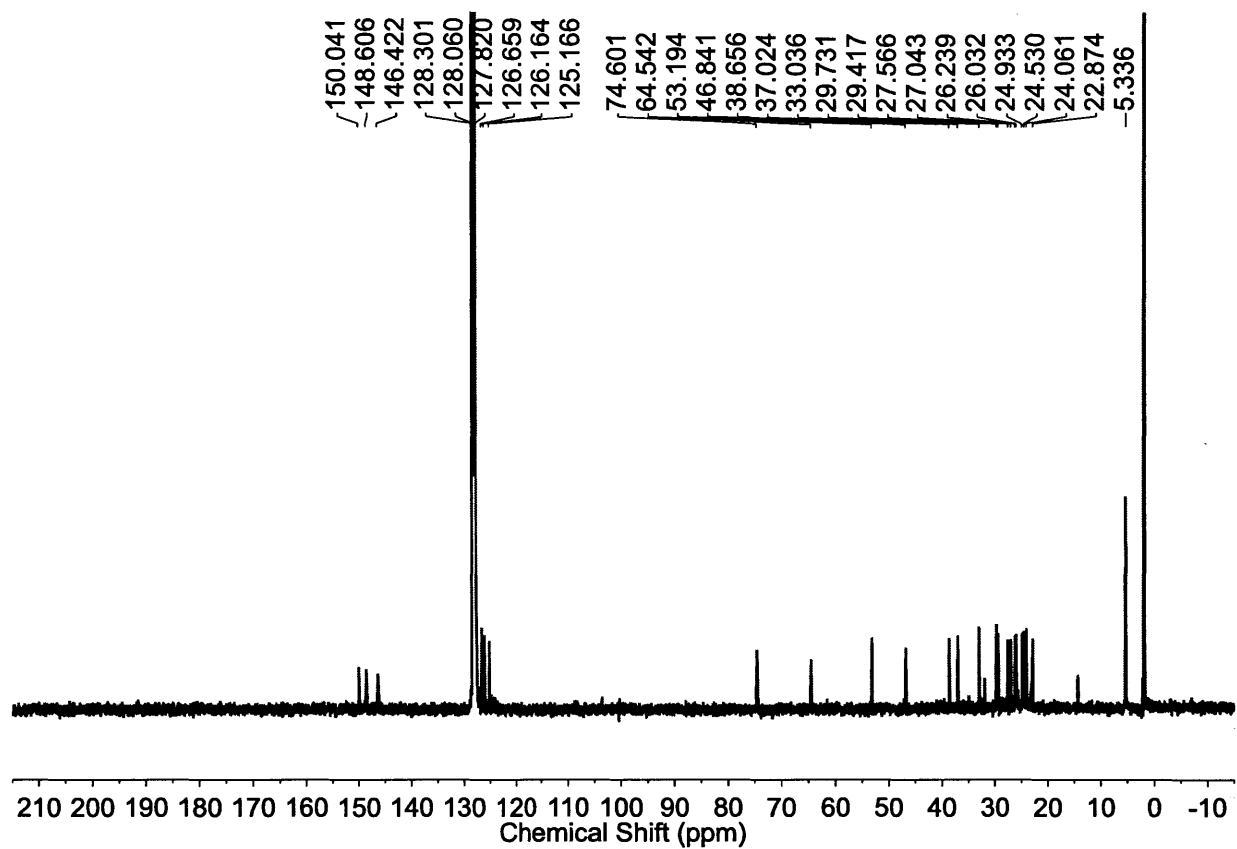
Figure 59. ^{13}C NMR (100 MHz, C$_6$D$_6$, 25 °C) spectrum of crude **6•TTMSS**. Chemical shifts are shown for peaks corresponding to **6•TTMSS** and C$_6$D$_6$.
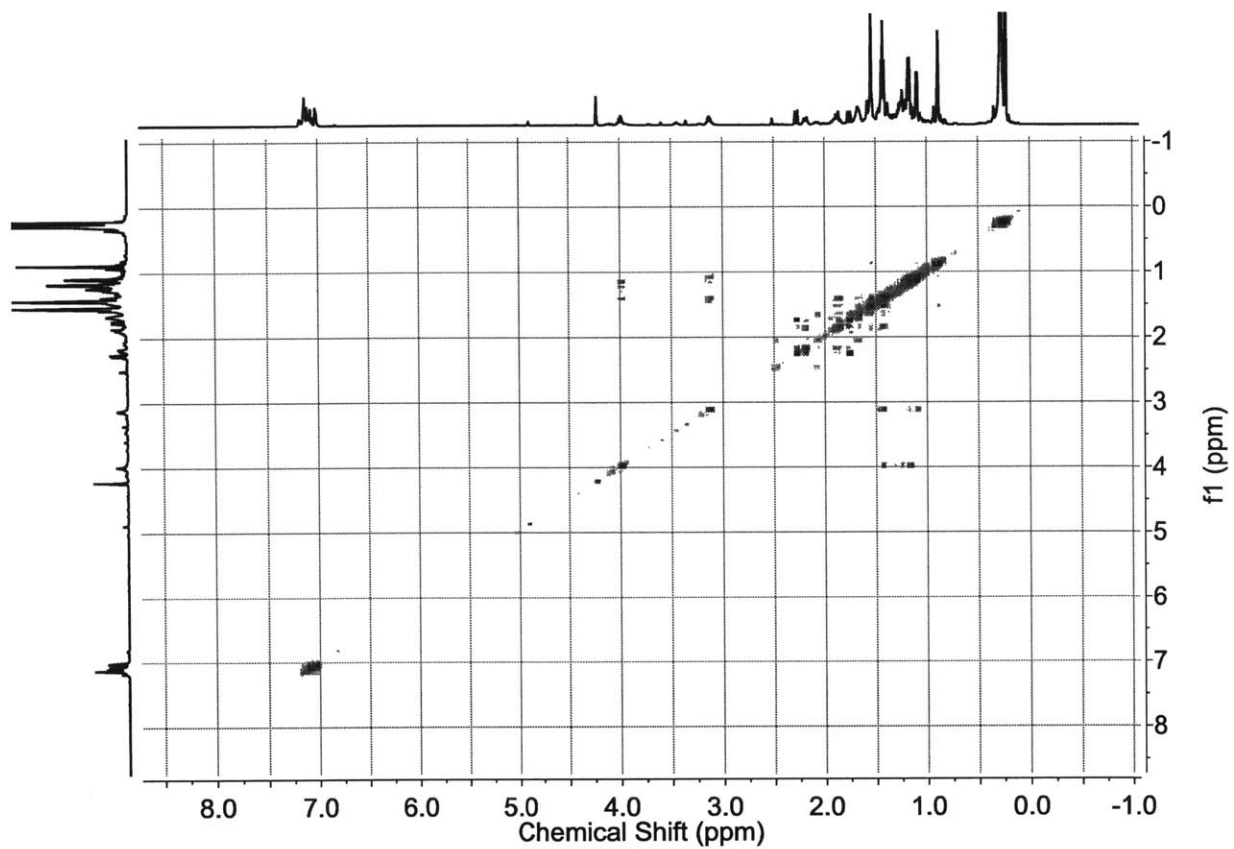
Figure 60. COSY (500 MHz (^{1}H), C$_6$D$_6$, 25 °C) spectrum of crude **6•TTMSS**.
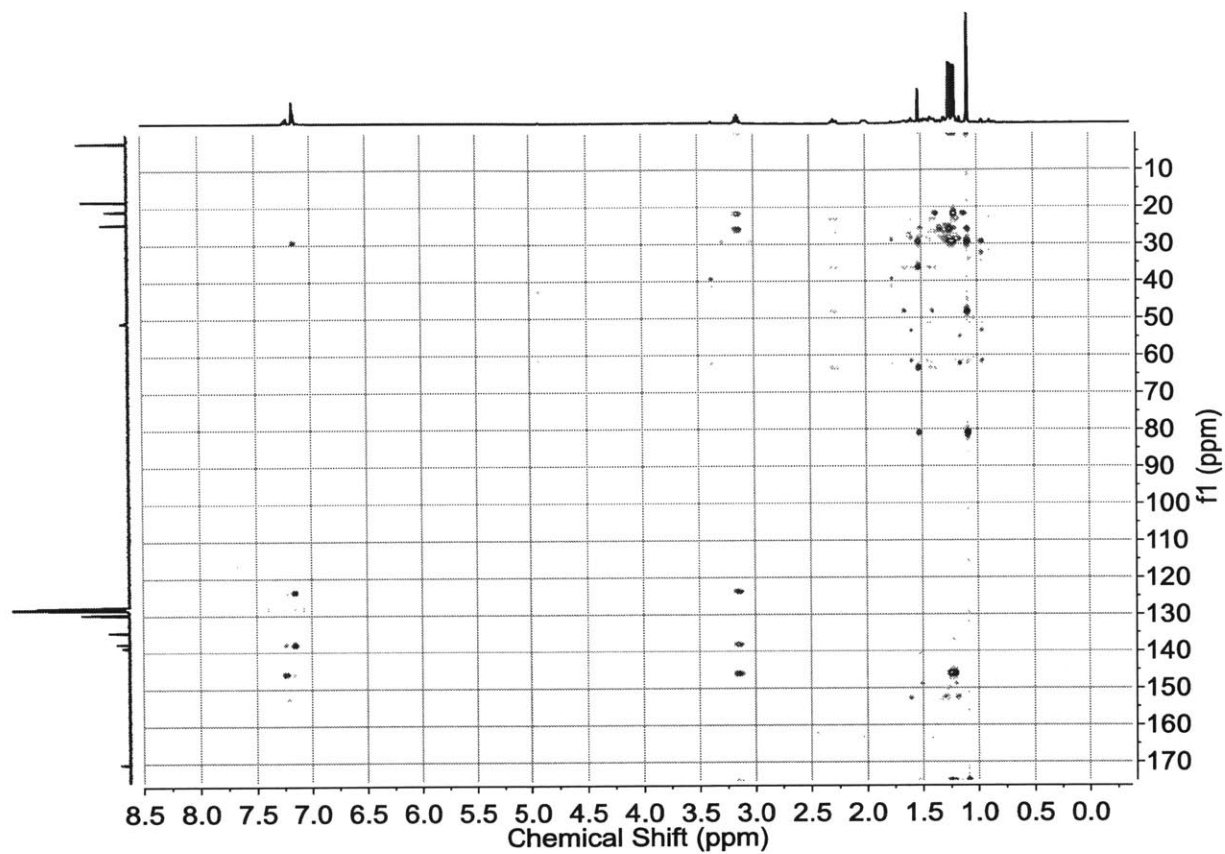
Figure 61. gHMBC (500 MHz (^{1}H), C$_6$D$_6$, 25 °C) spectrum of crude **6**•TTMSS.
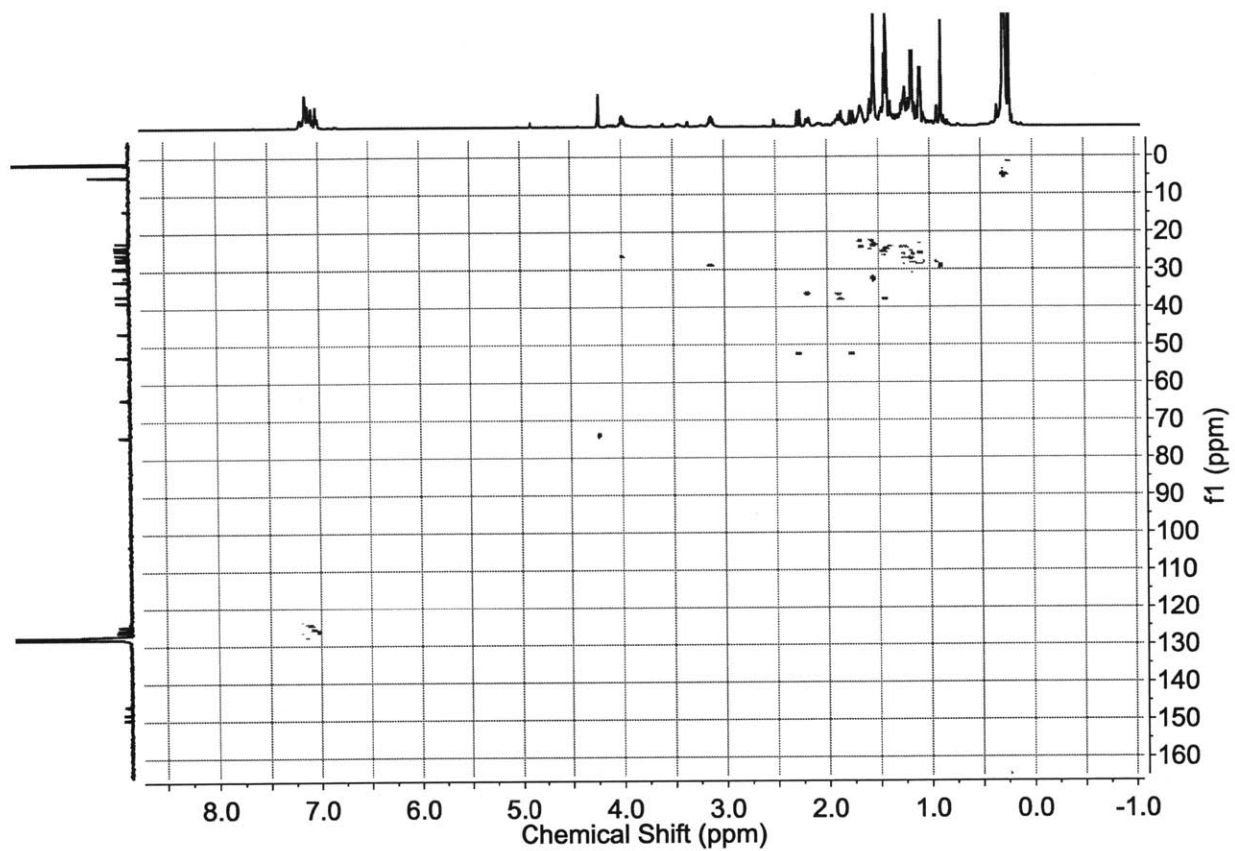
Figure 62. HSQC (500 MHz (^{1}H), C_6D_6, 25 °C) spectrum of crude **6·TTMSS**.
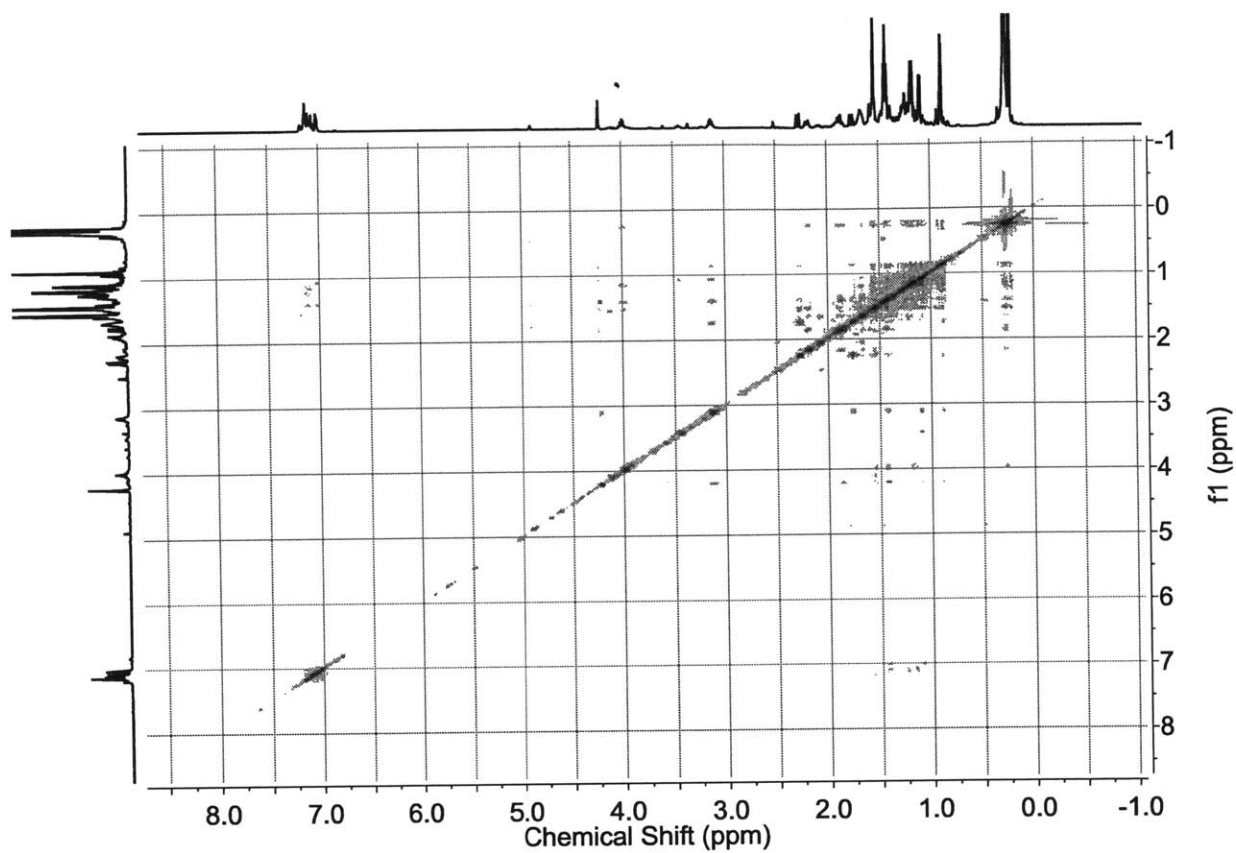
Figure 63. NOESY (500 MHz (^{1}H), C_6D_6, 25 °C) spectrum of crude **6**•TTMSS.
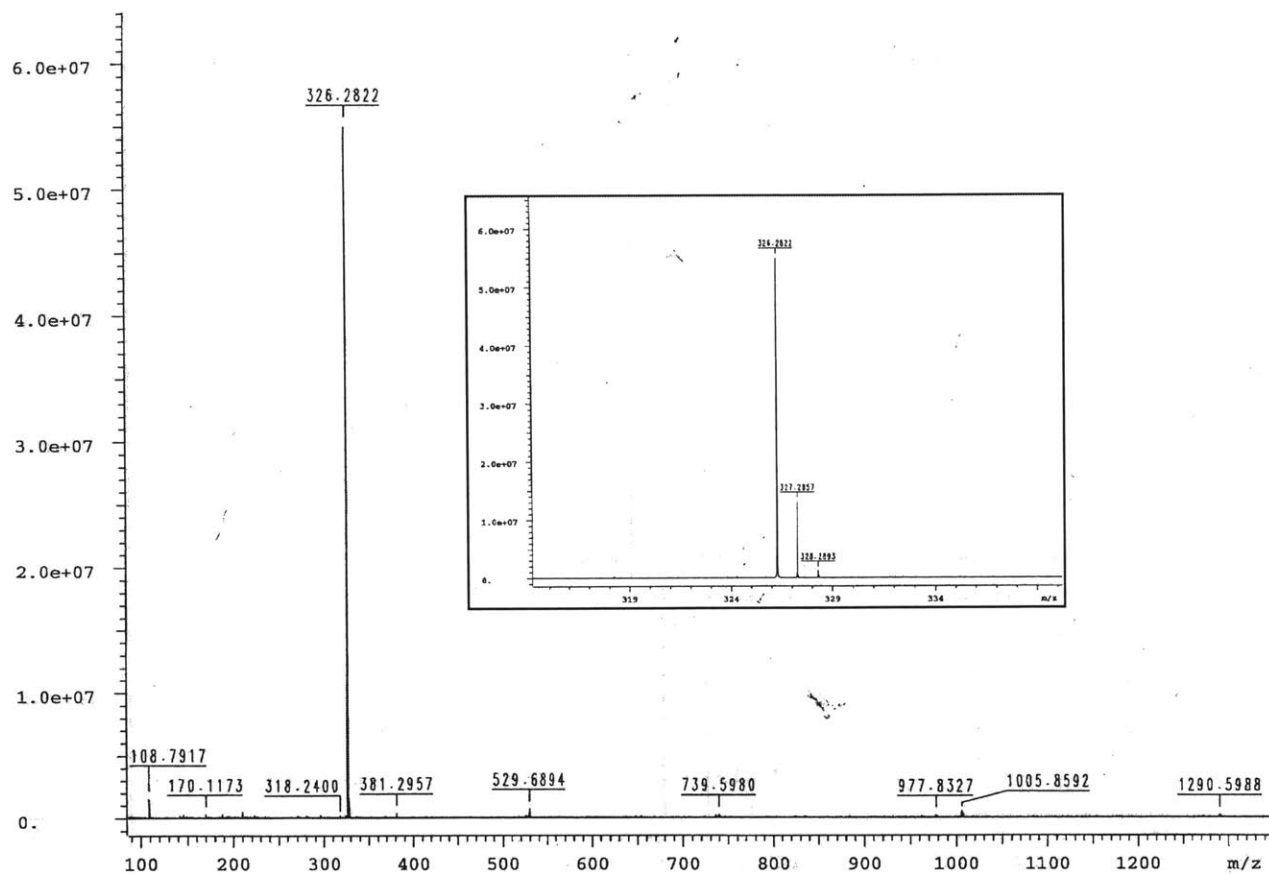
Figure 64. FT-ICR-ESI HRMS of crude **6**•TTMSS. Inset depicts the isotope pattern of the $[M-(Me_3Si)_3Si]^+$ ion.
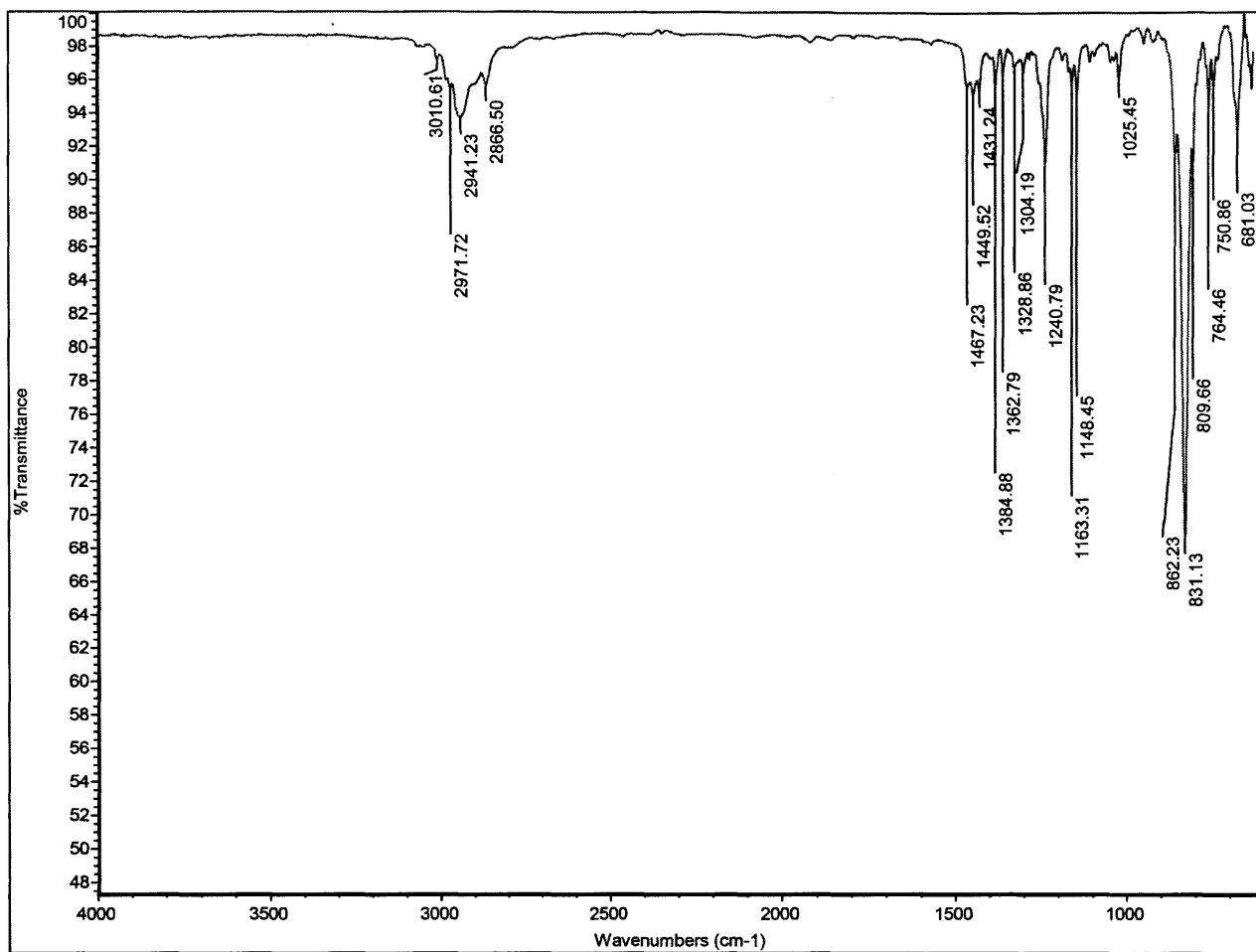
Figure 65. ATR-FTIR spectrum of **6•TTMSS**.

Figure 66. ^{1}H NMR (400 MHz, C_6D_6, 25 °C) spectrum of crude **6•TTMSOxS**. Integration and chemical shifts are shown for peaks corresponding to **6•TTMSOxS** and C_6D_6.

272
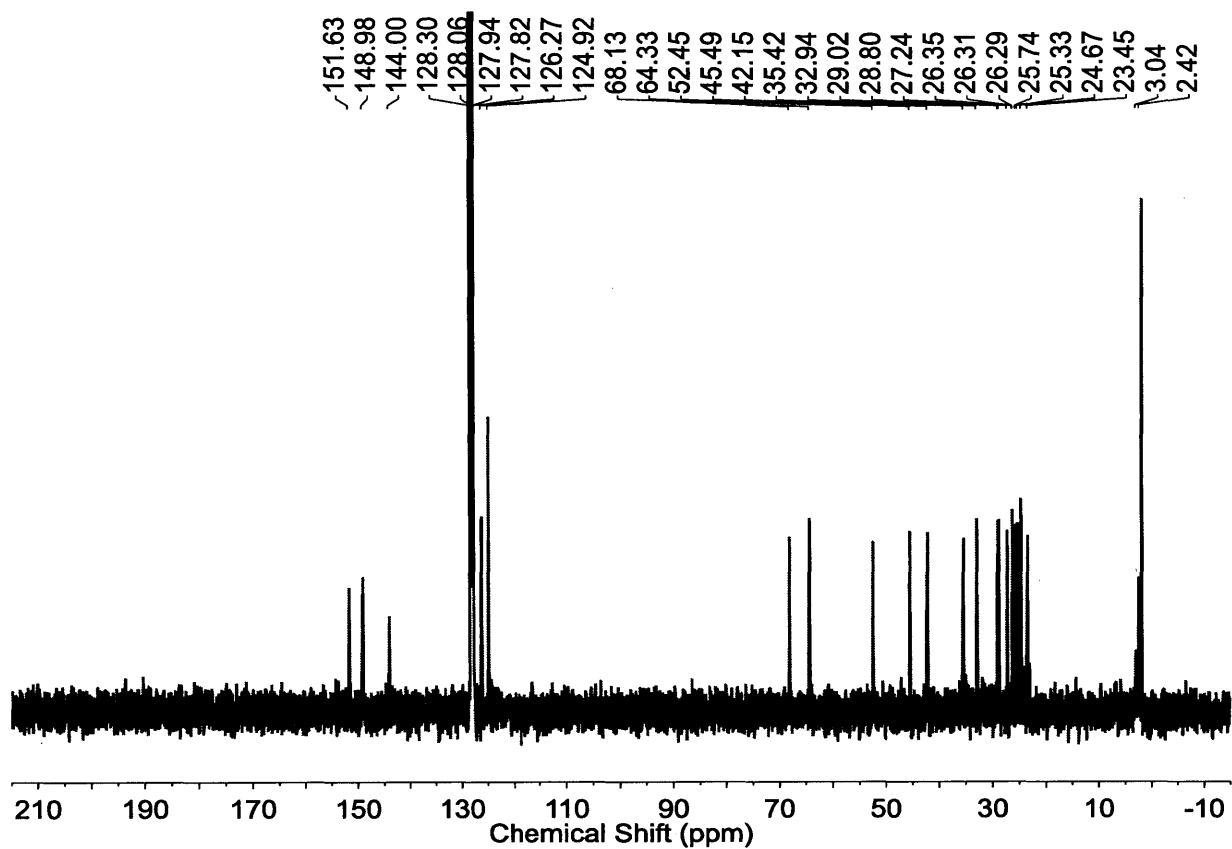
Figure 67. ^{13}C (100 MHz, C$_6$D$_6$, 25 °C) spectrum of crude 6•TTMSOxS. Chemical shifts are shown for peaks corresponding to 6•TTMSOxS and C$_6$D$_6$.
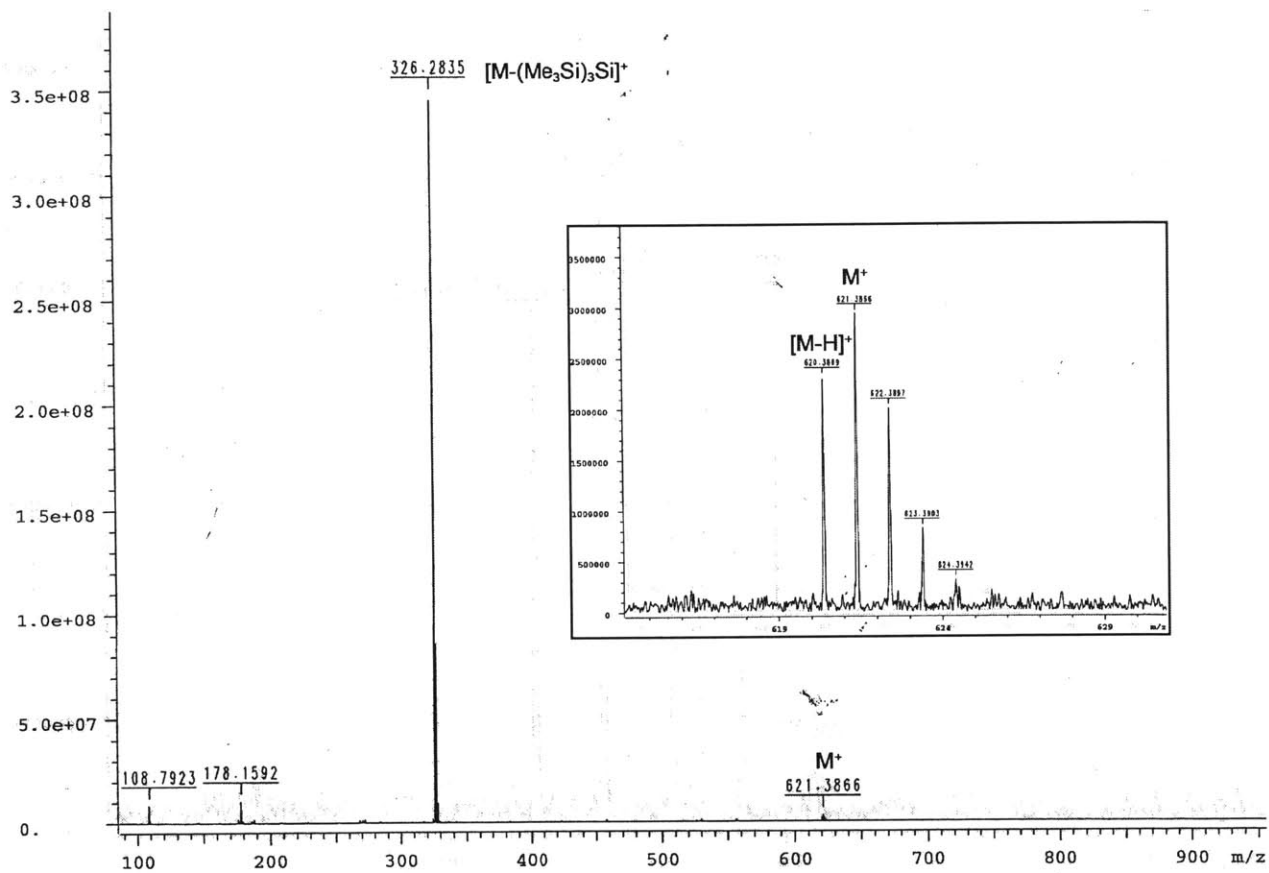
Figure 68. FT-ICR-ESI HRMS of crude **6**•TTMSOxS. Inset depicts the isotope pattern of the M⁺ ion.
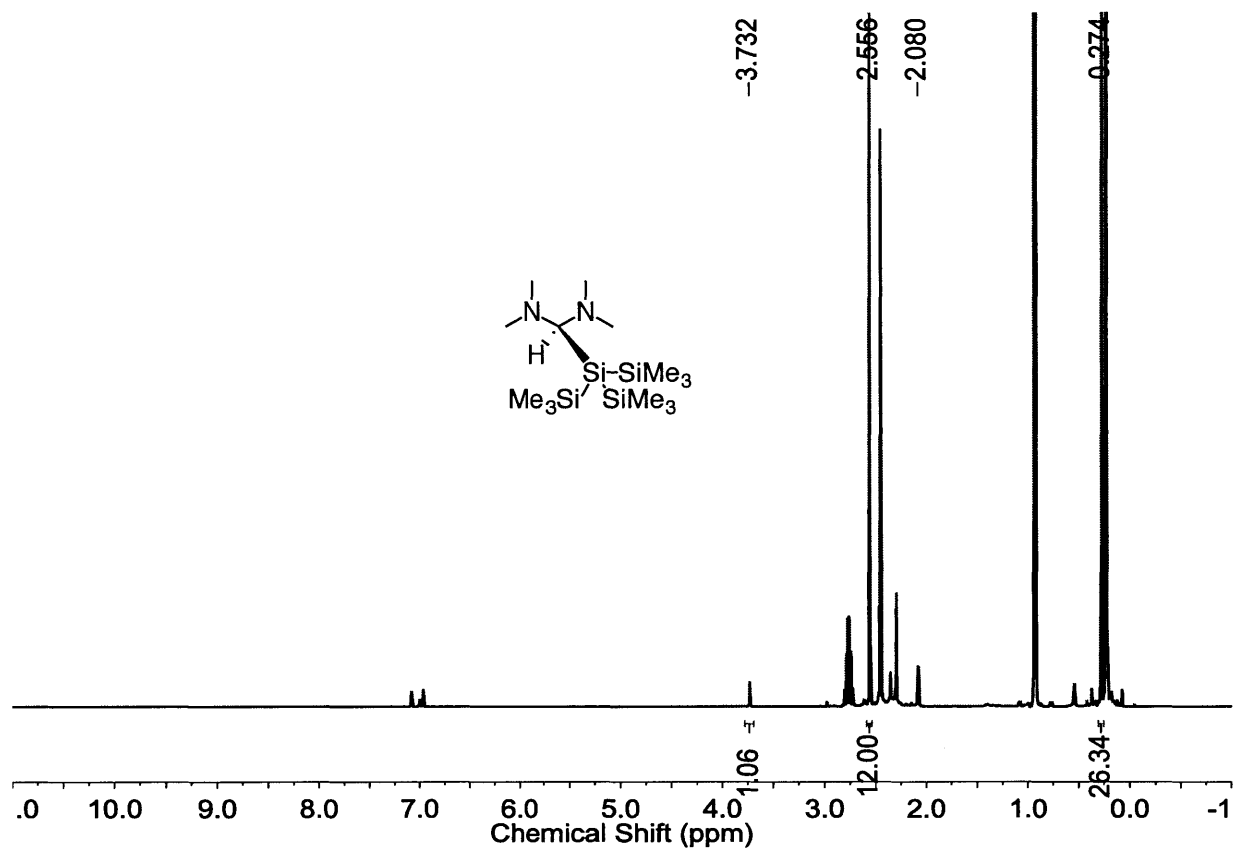
Figure 69. ¹H NMR (400 MHz, tol-d^8, 25 °C) spectrum of crude 7•TTMSS. Integration and chemical shifts are shown for peaks corresponding to 7•TTMSS and the methyl group of tol-d^8.
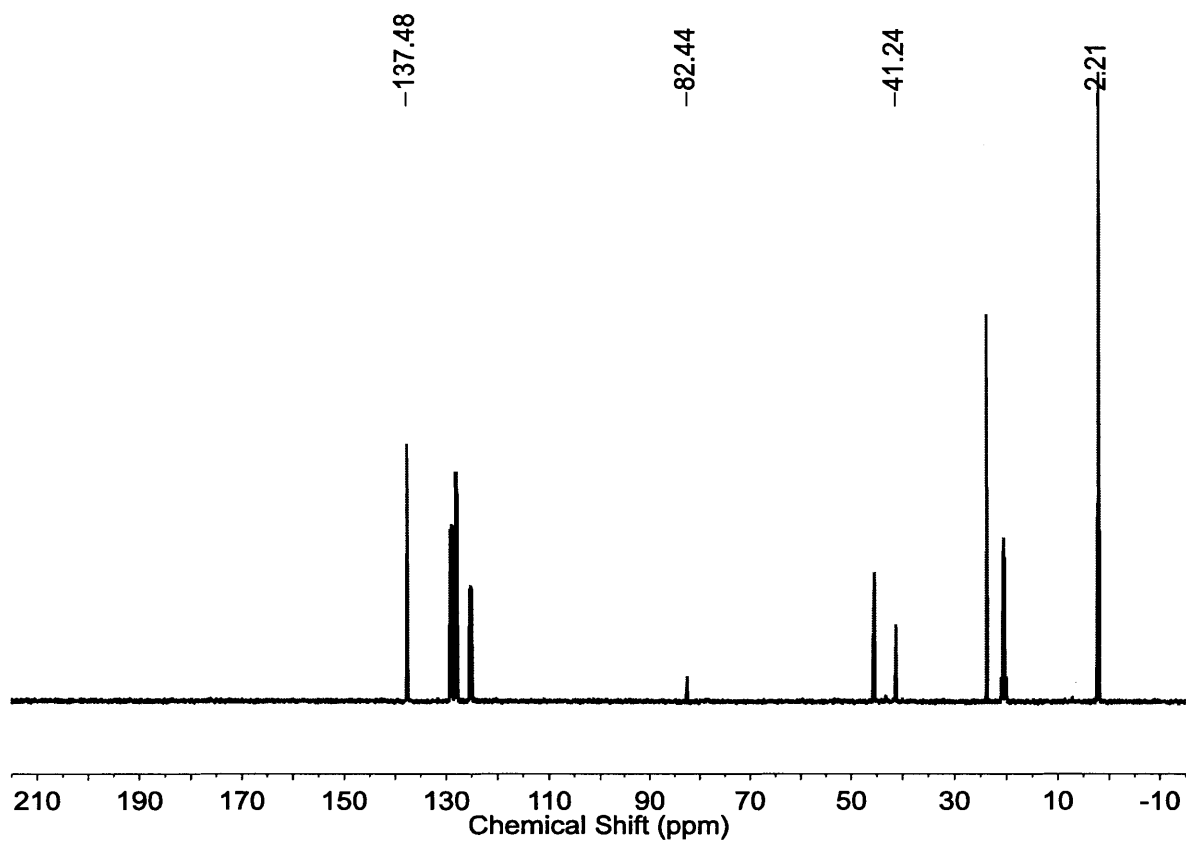
Figure 70. ^{13}C NMR (100 MHz, tol-d^8, 25 °C) spectrum of crude 7•TTMSS. Chemical shifts are shown for peaks corresponding to 7•TTMSS and the *ipso*-carbon resonance of tol-d^8.
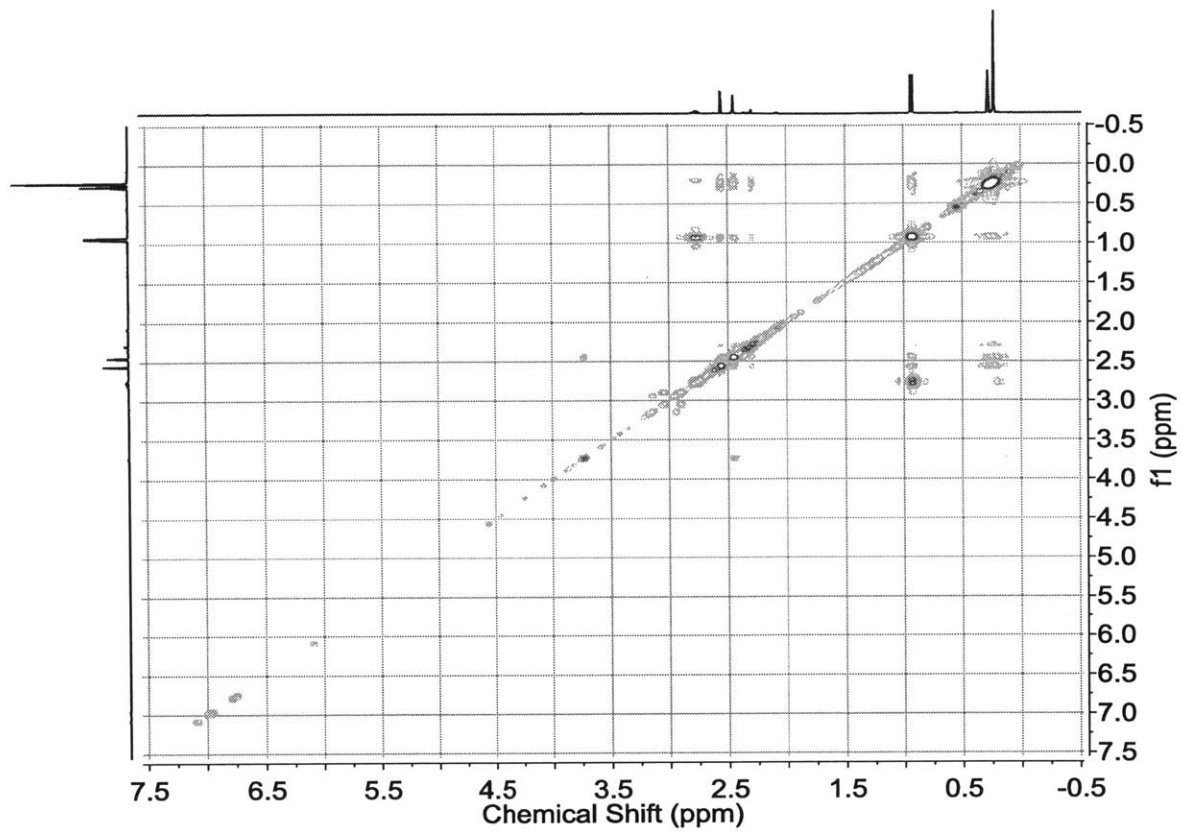
Figure 71. COSY (500 MHz (^{1}H), tol-d^8, 25 °C) spectrum of crude **7**•TTMSS.
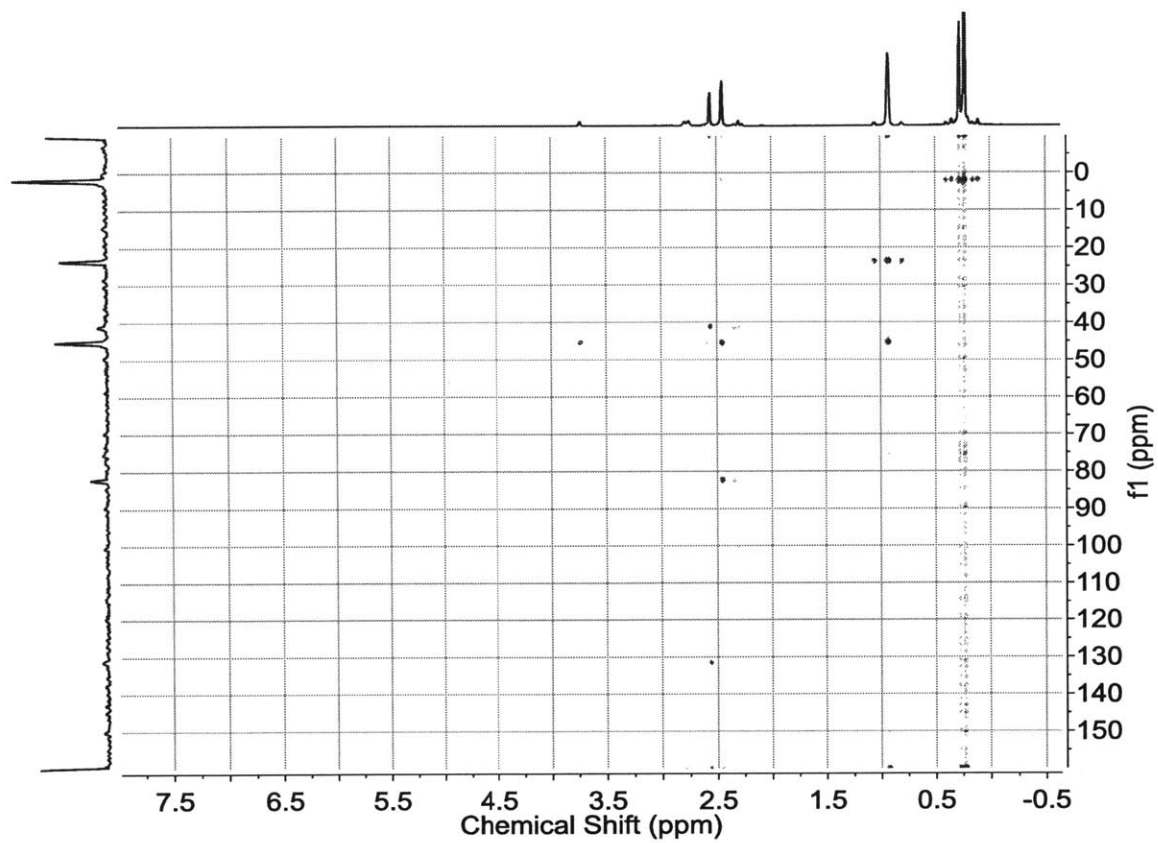
Figure 72. gHMBC (500 MHz (^{1}H), tol-d^8, 25 °C) spectrum of crude **7**•TTMSS.
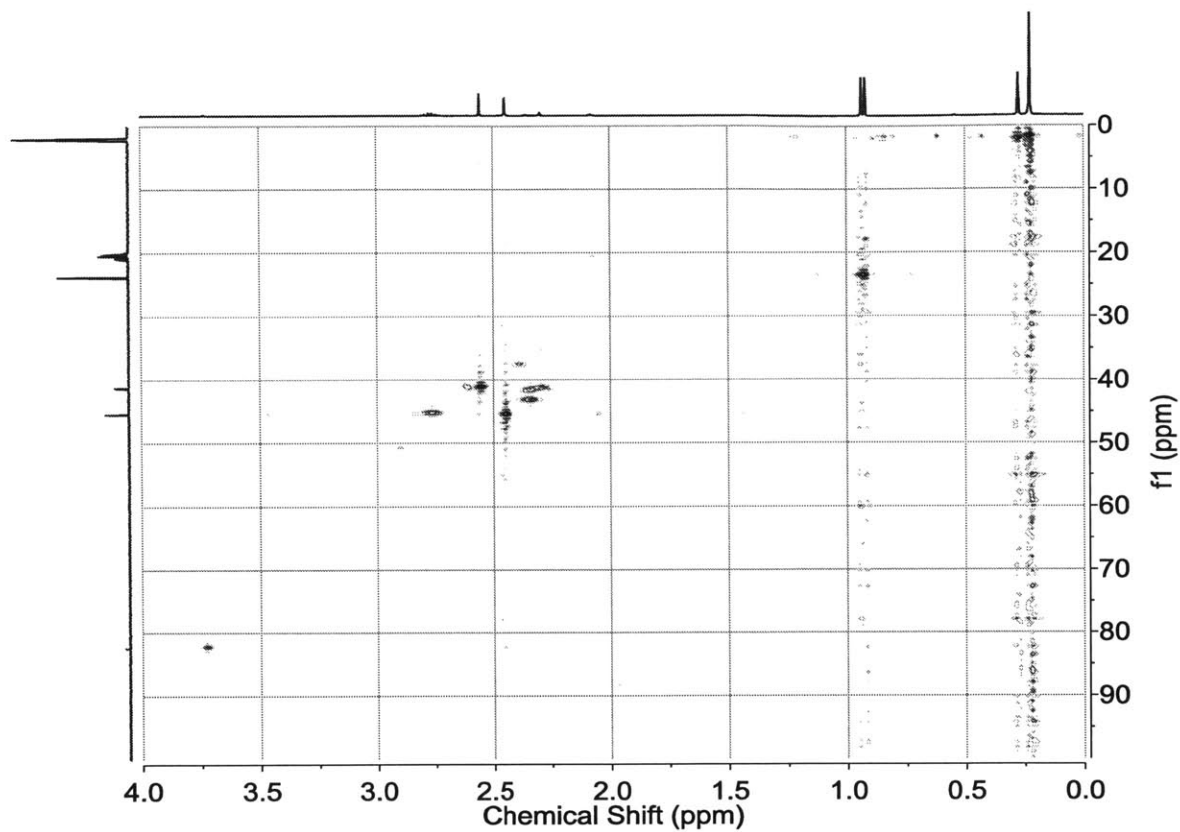
Figure 73. HSQC (500 MHz (^{1}H), tol-d^8, 25 °C) spectrum of crude **7**•TTMSS.

279
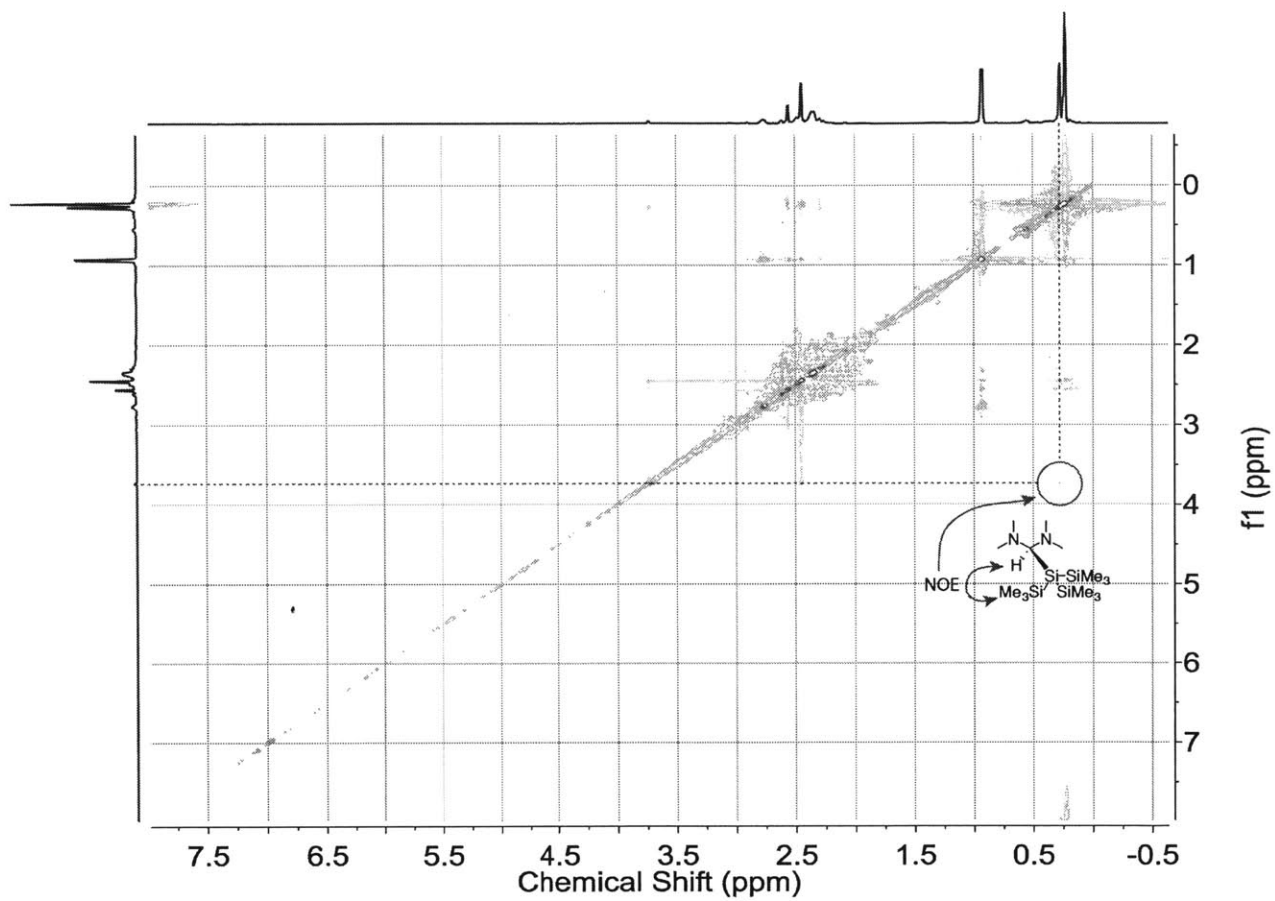
Figure 74. NOESY (500 MHz (^{1}H), tol-d^8, 25 °C) spectrum of crude **7**·TTMSS, with the NOE between the aminal and TMS protons indicated with the red circle and dotten lines.
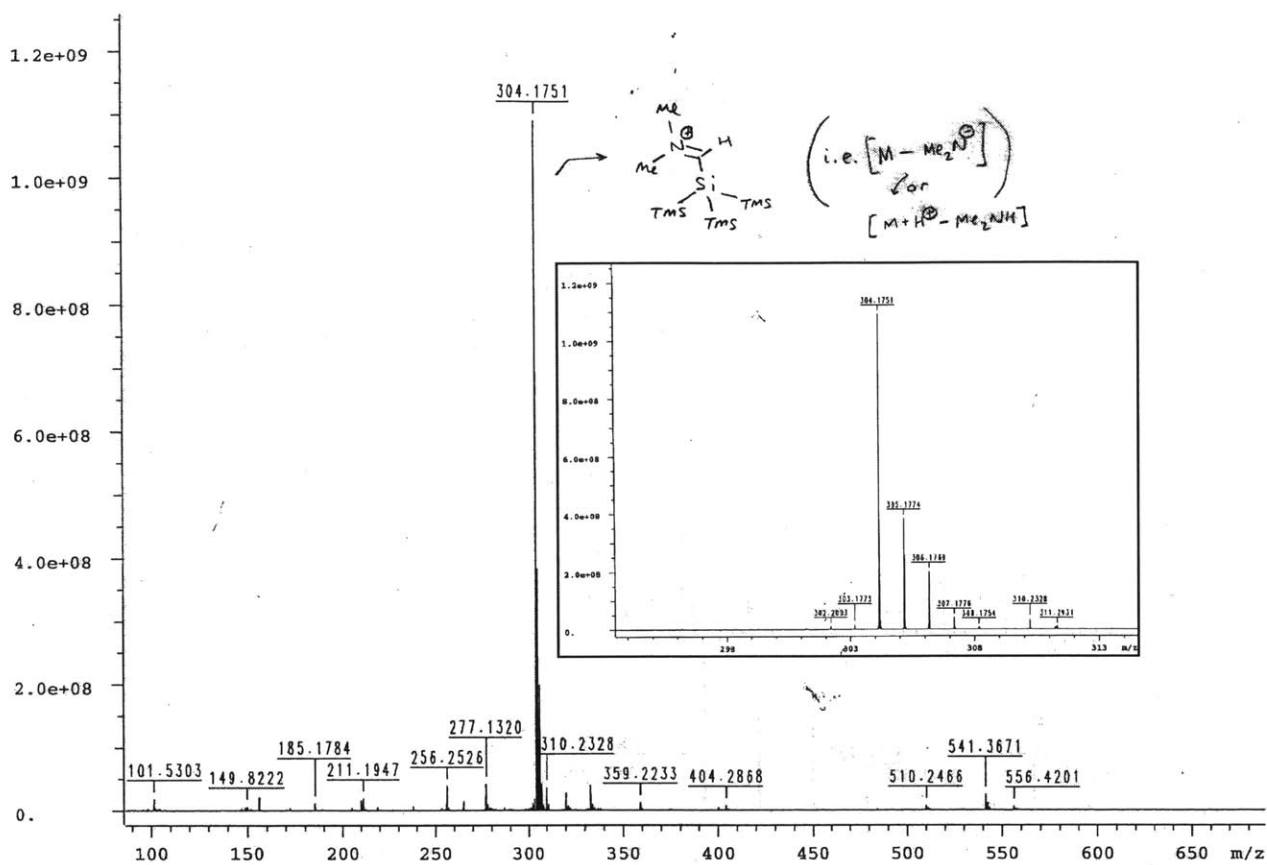
Figure 75. FT-ICR-DART HRMS of crude **7·TTMSS**. Inset depicts the isotope pattern of the [M-Me$_2$N]$^+$ ion.
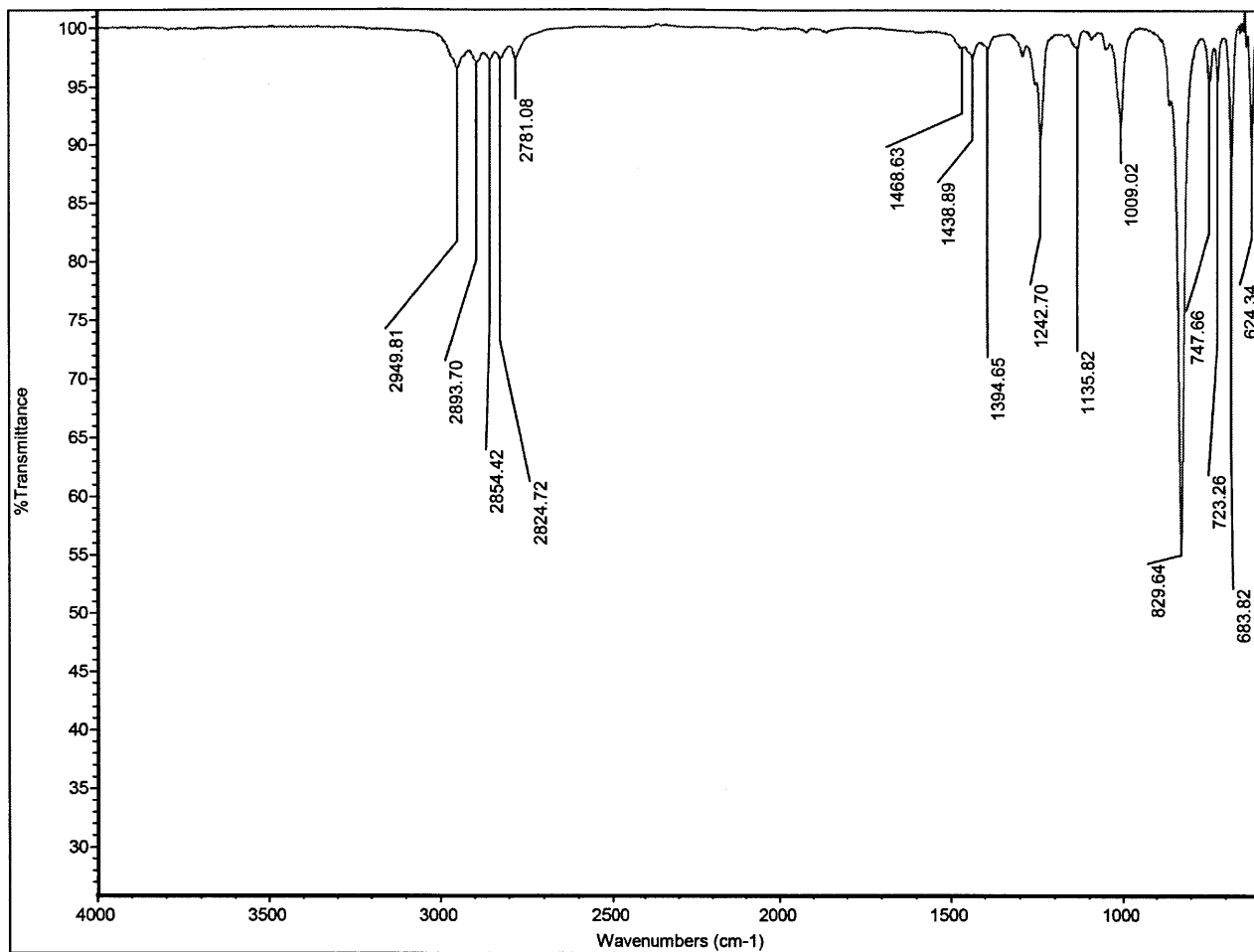
Figure 76. ATR-FTIR spectrum of 7•TTMSS, obtained as a weighted difference between the spectrum of this sublimed product and TTMSS (where the weighting was applied to eliminate the residual Si-H stretch resonance at 2051.2 cm^{-1}).
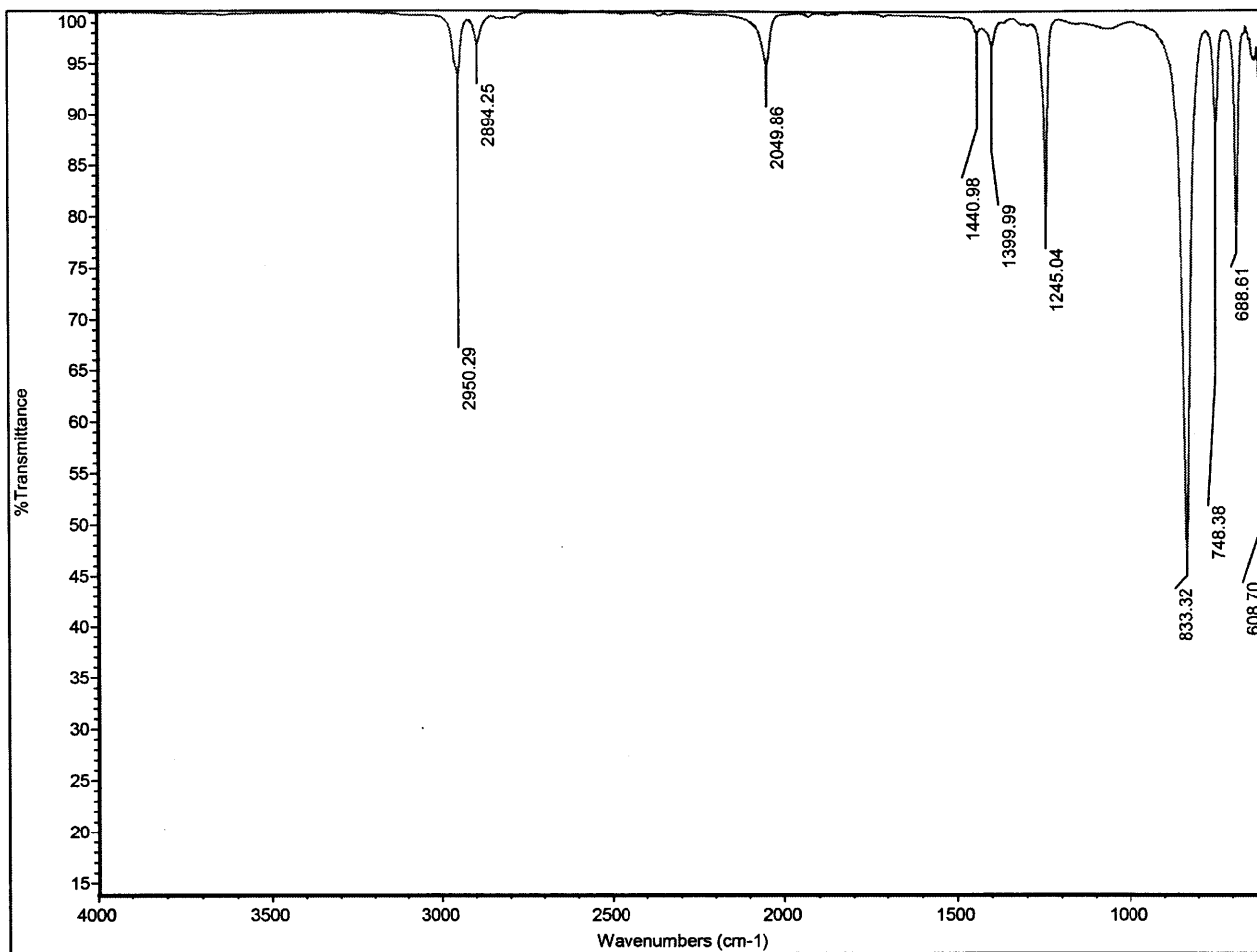
Figure 77. ATR-FTIR spectrum of TTMSS.
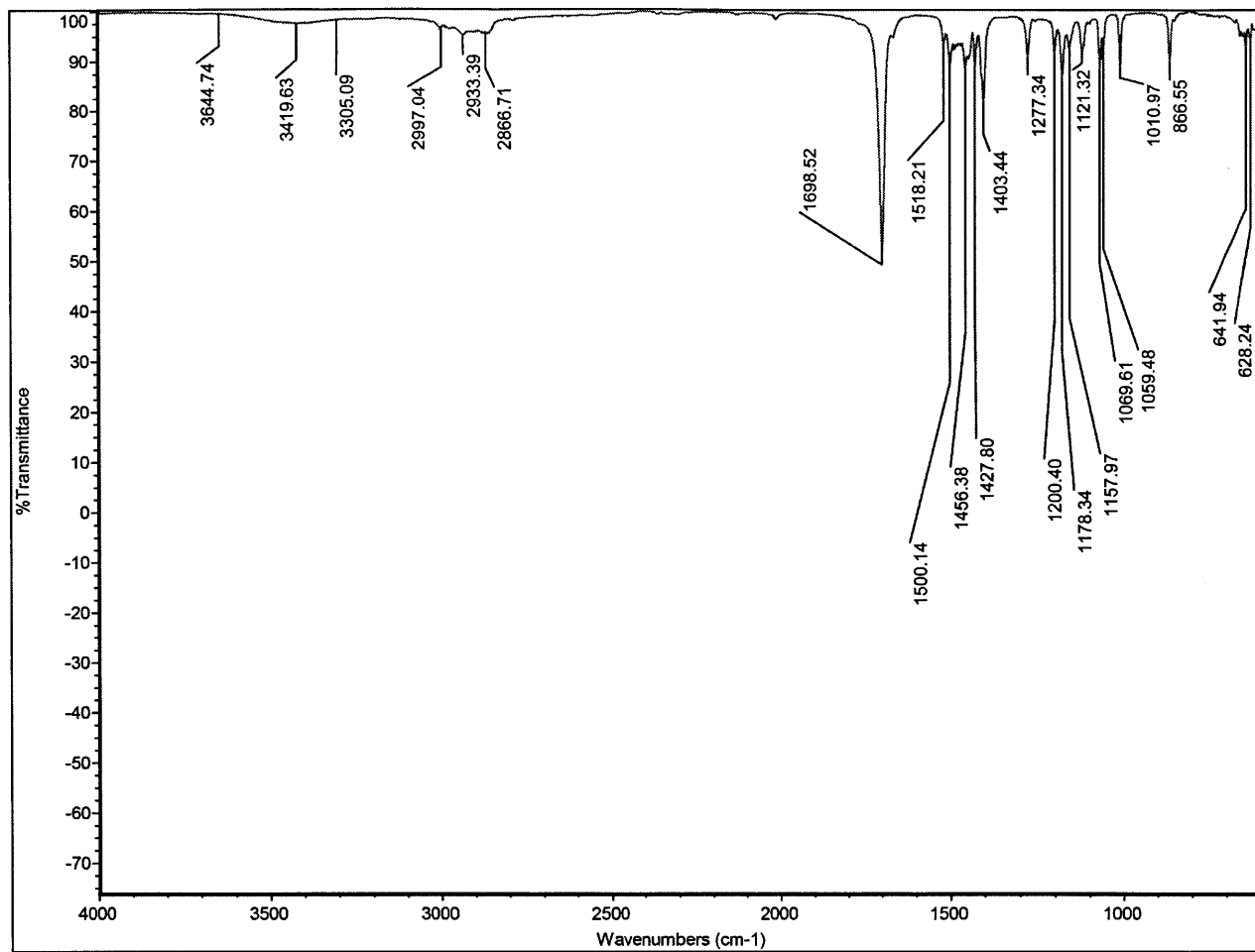
Figure 78. ATR-FTIR spectrum of 7•HCl.
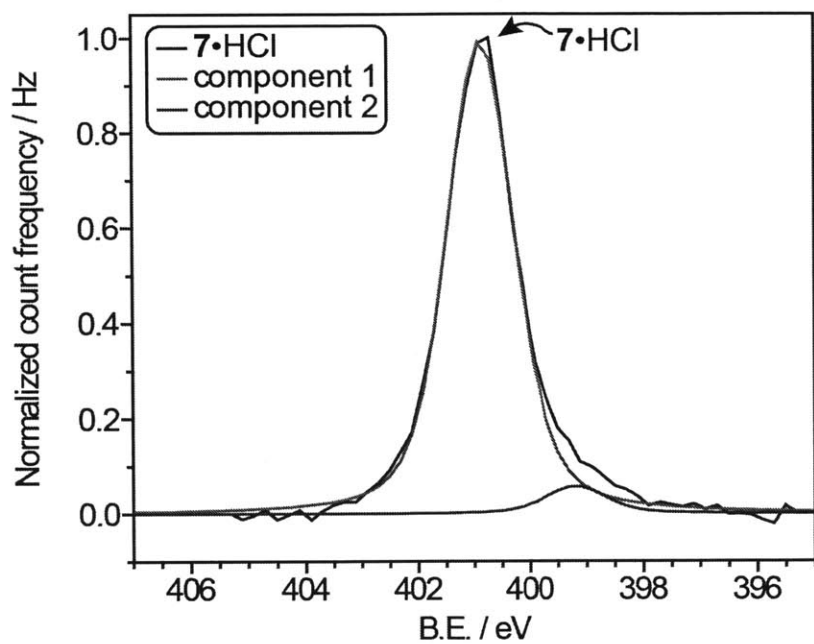
Figure 79. XPS N1s region of 7•HCl; decomposition due to X-ray irradiation led to the appearance of another peak, as indicated in the figure.
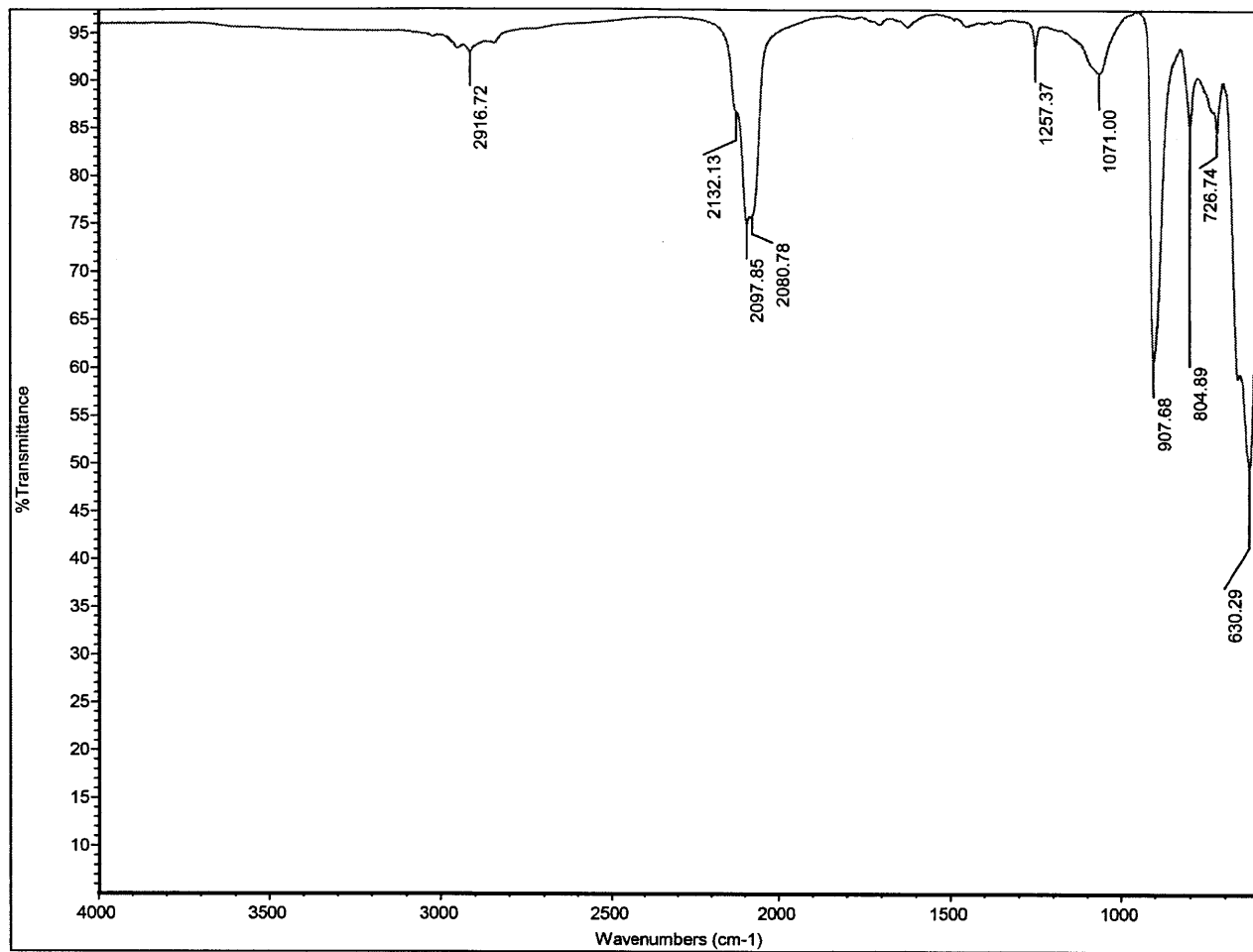
Figure 80. ATR-FTIR spectrum of H-SiNPs.

286
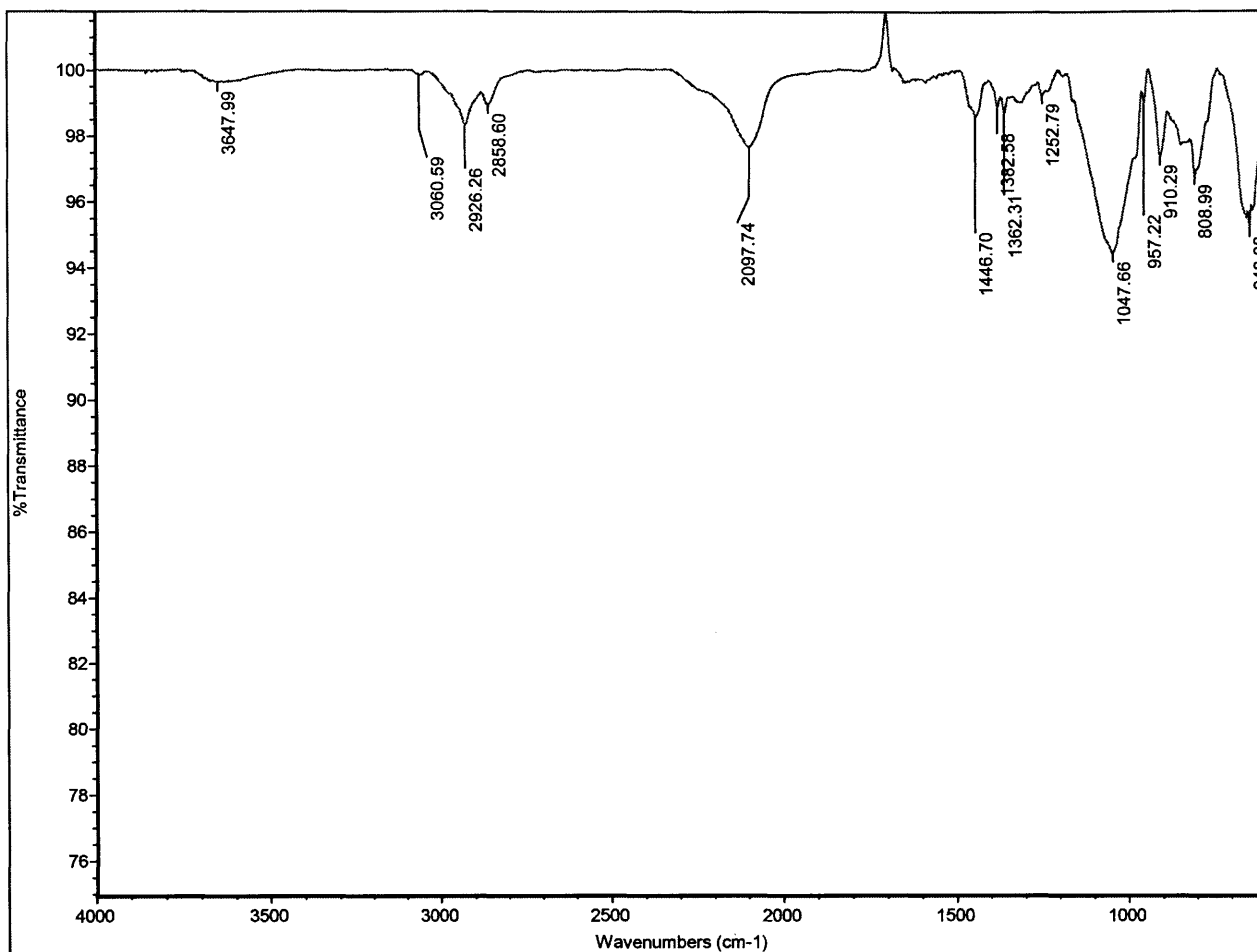
Figure 81. ATR-FTIR spectrum of **6•SiNPs**.
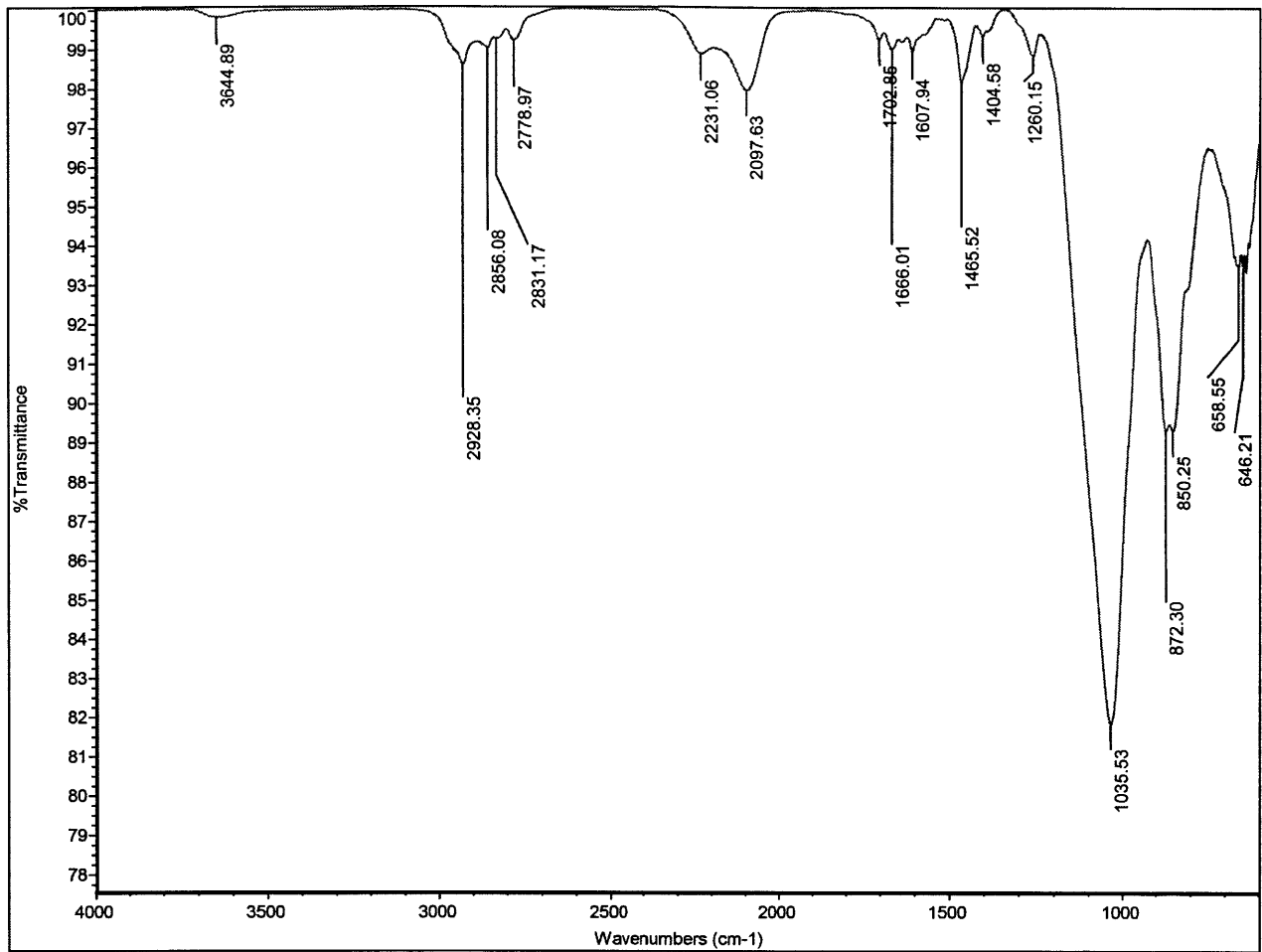
Figure 82. ATR-FTIR spectrum of 7•SiNPs.
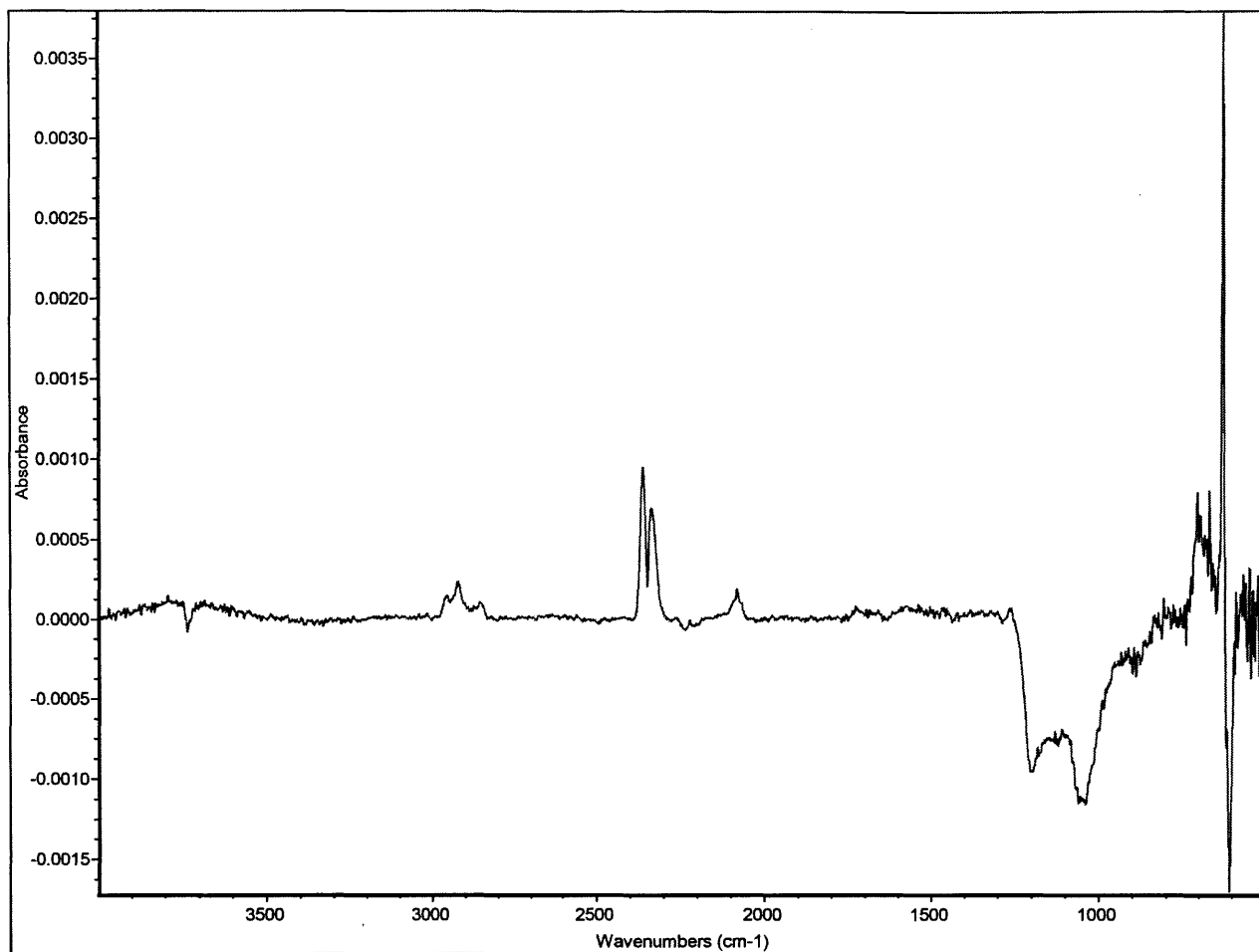
Figure 83. FTIR spectrum of the H-Si(111) ratioed to the spectrum of a fully oxidized silicon surface.
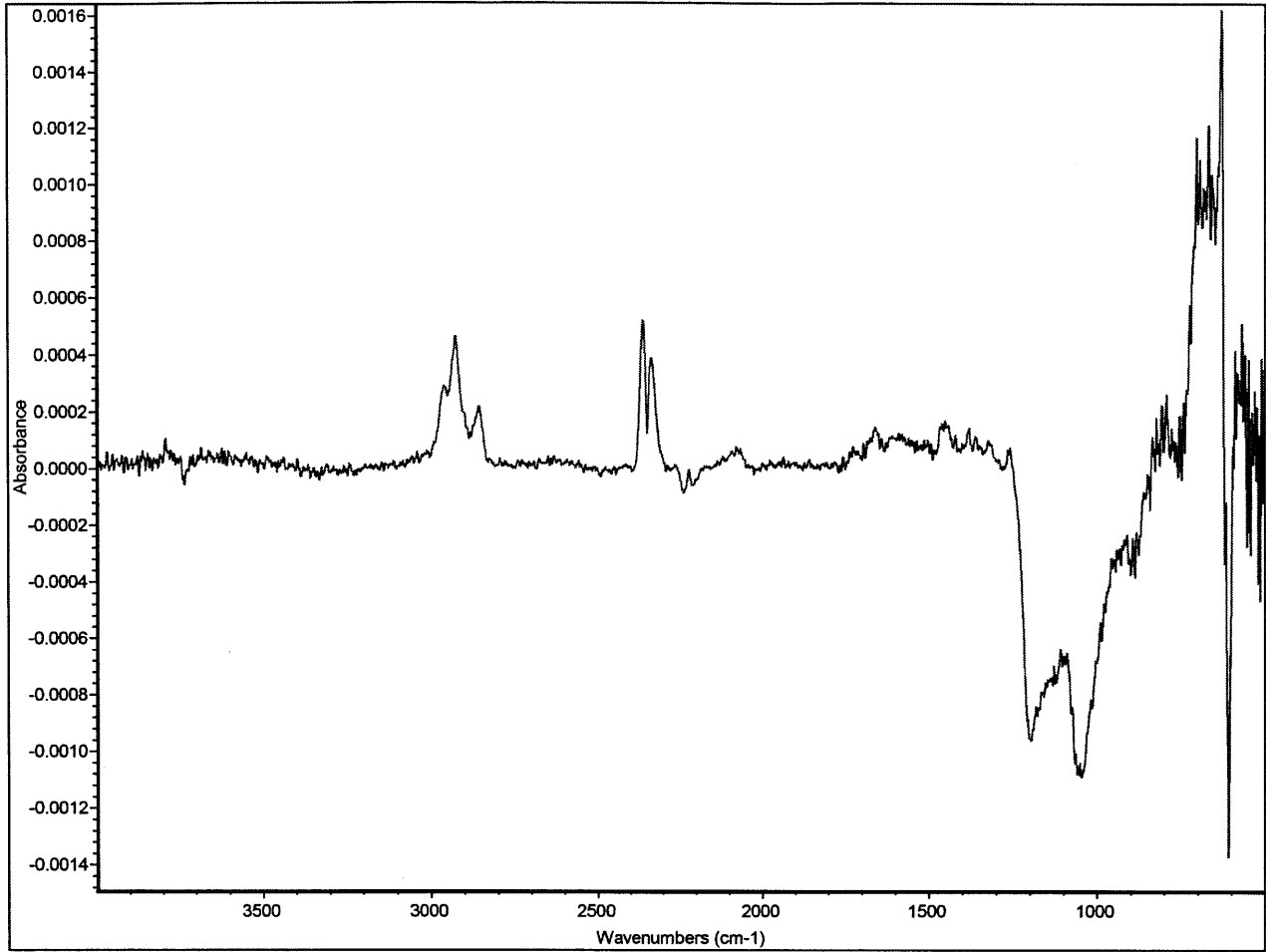
Figure 84. FTIR spectrum of the first **6•Si(111)** wafer ratioed to the spectrum of a fully oxidized silicon surface.
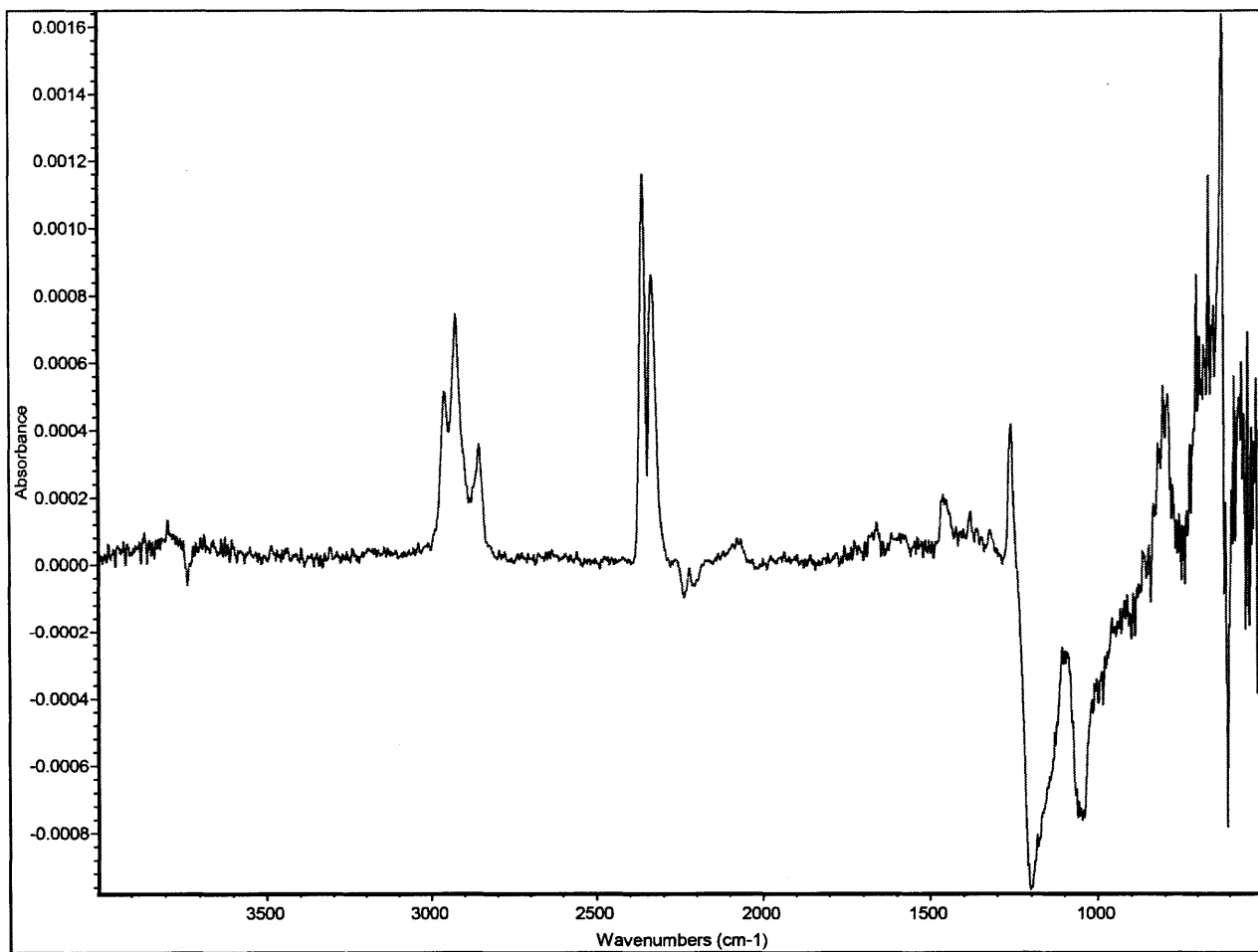
Figure 85. FTIR spectrum of the second **6•Si(111)** wafer ratioed to the spectrum of a fully oxidized silicon surface.
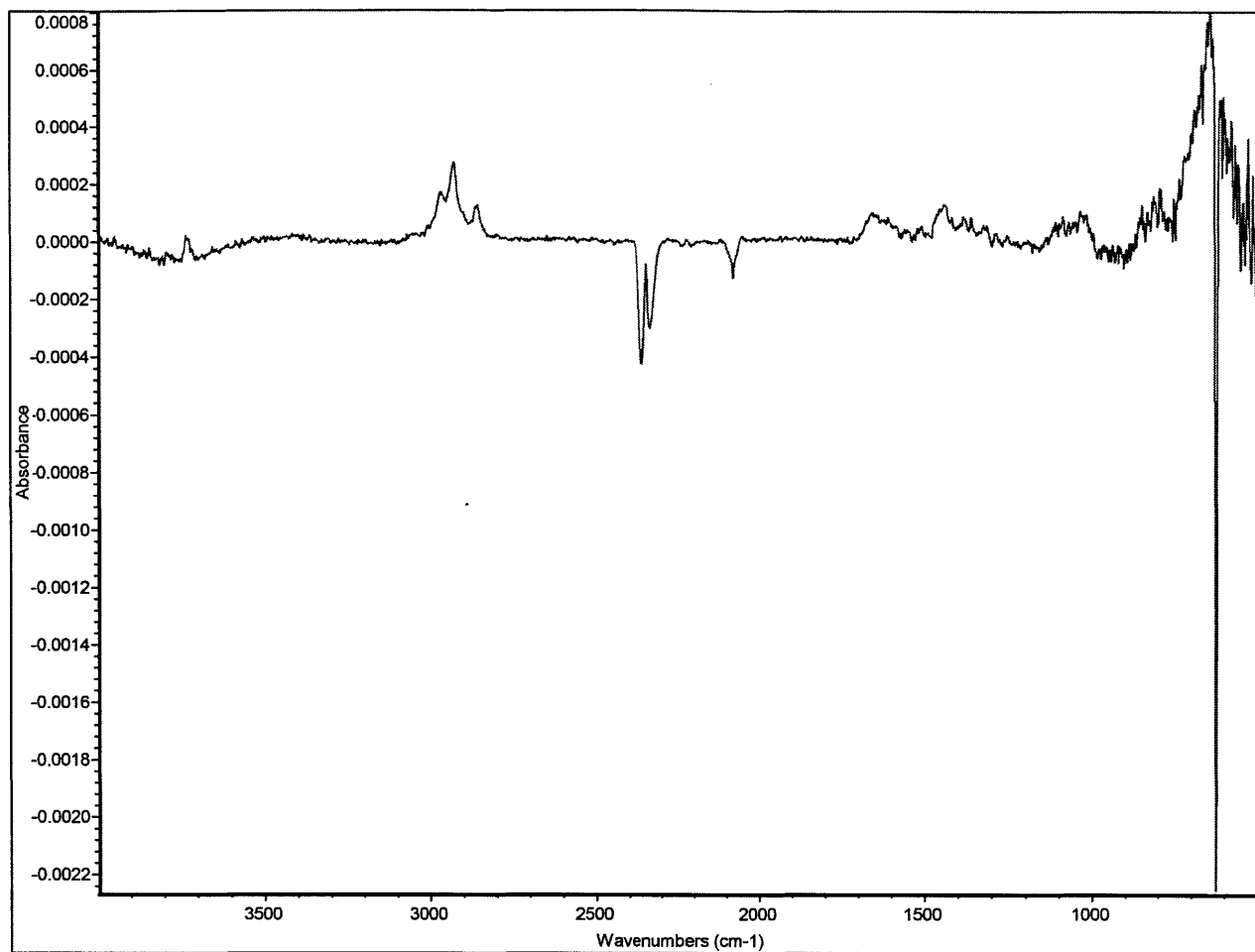
Figure 86. FTIR spectrum of the first **6•Si(111)** wafer ratioed to the spectrum of the H-Si(111) wafer.
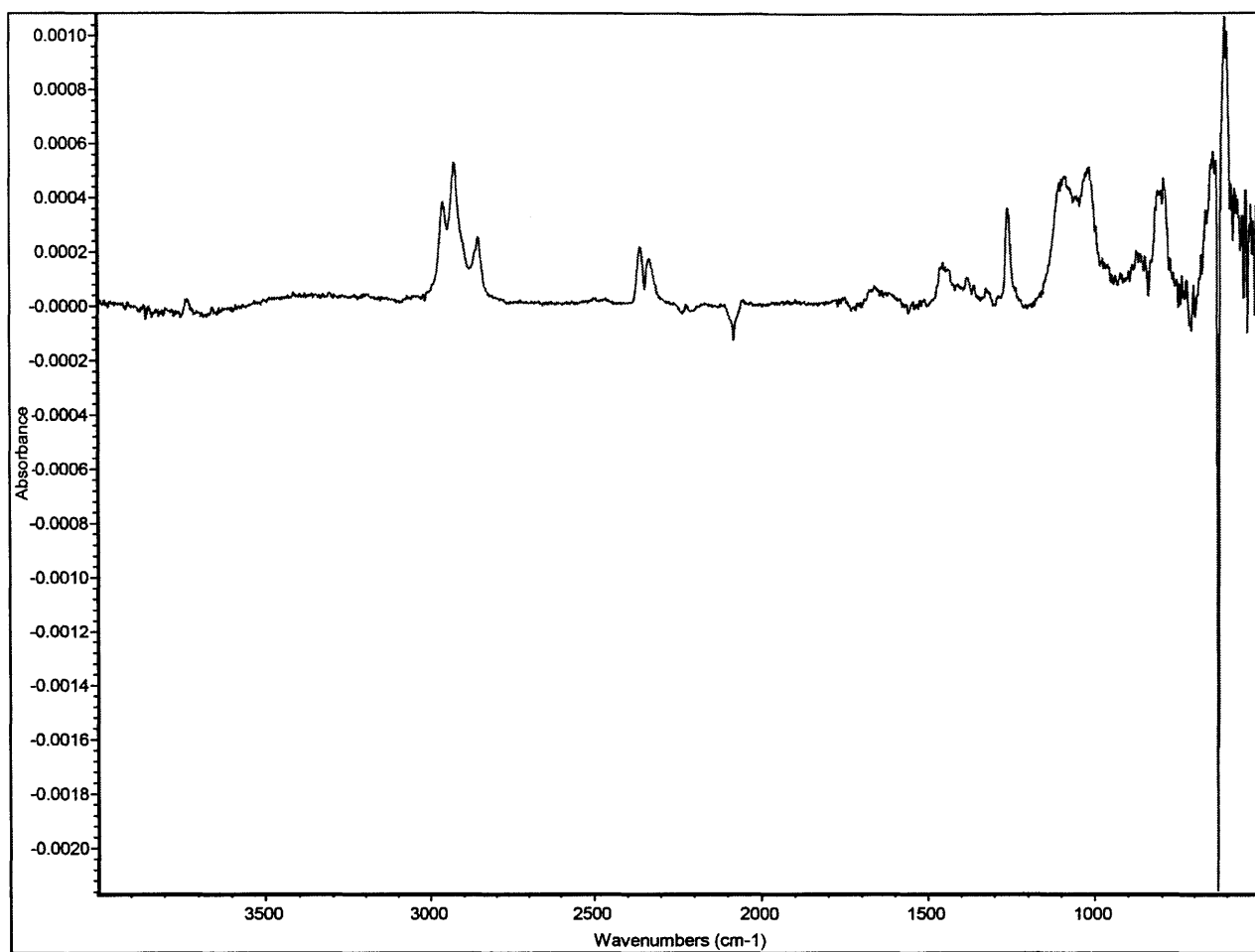
Figure 87. FTIR spectrum of the second **6•Si(111)** wafer ratioed to the spectrum of the H-**Si(111)** wafer.
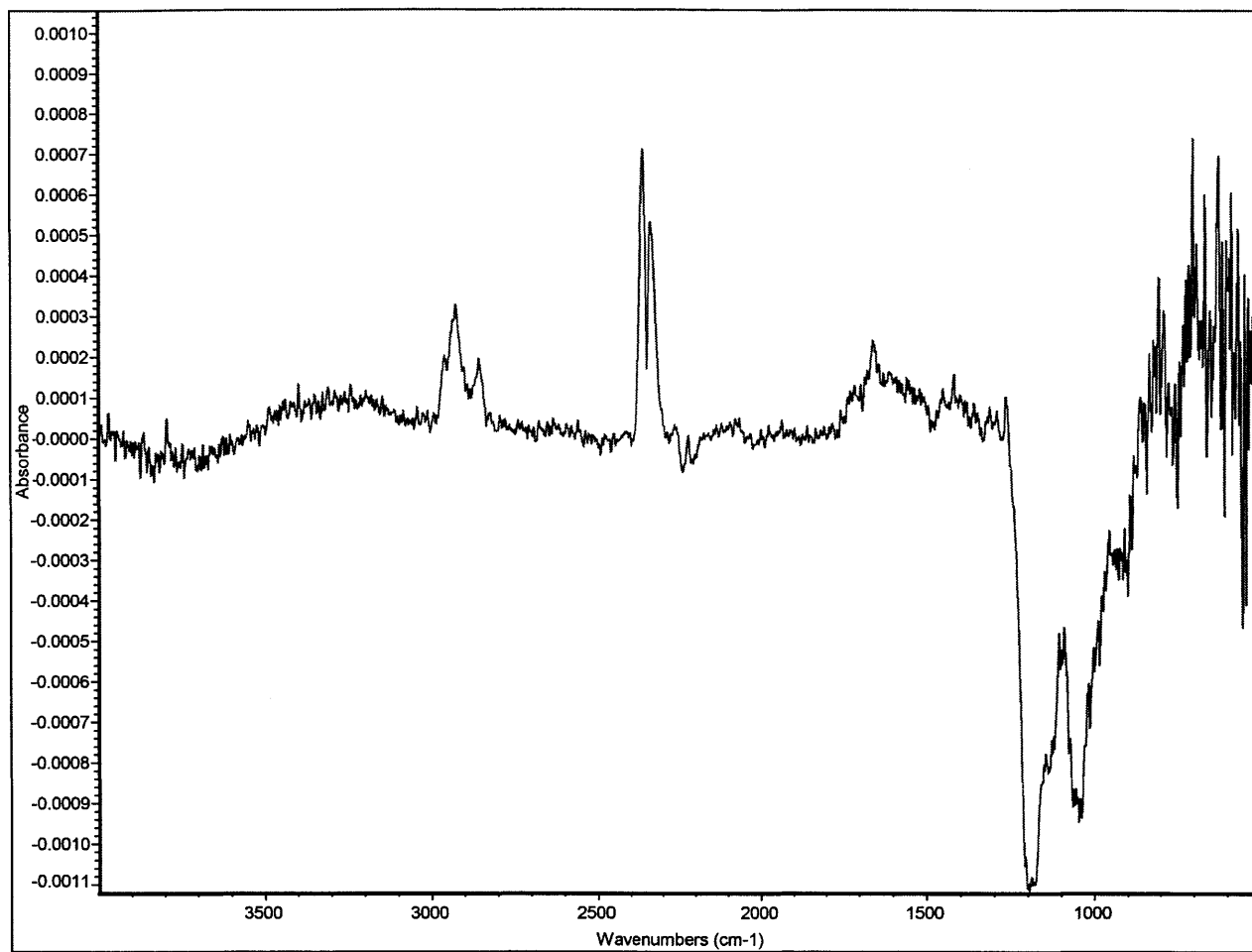
Figure 88. FTIR spectrum of the first **7•Si(111)** wafer ratioed to the spectrum of a fully oxidized silicon surface.
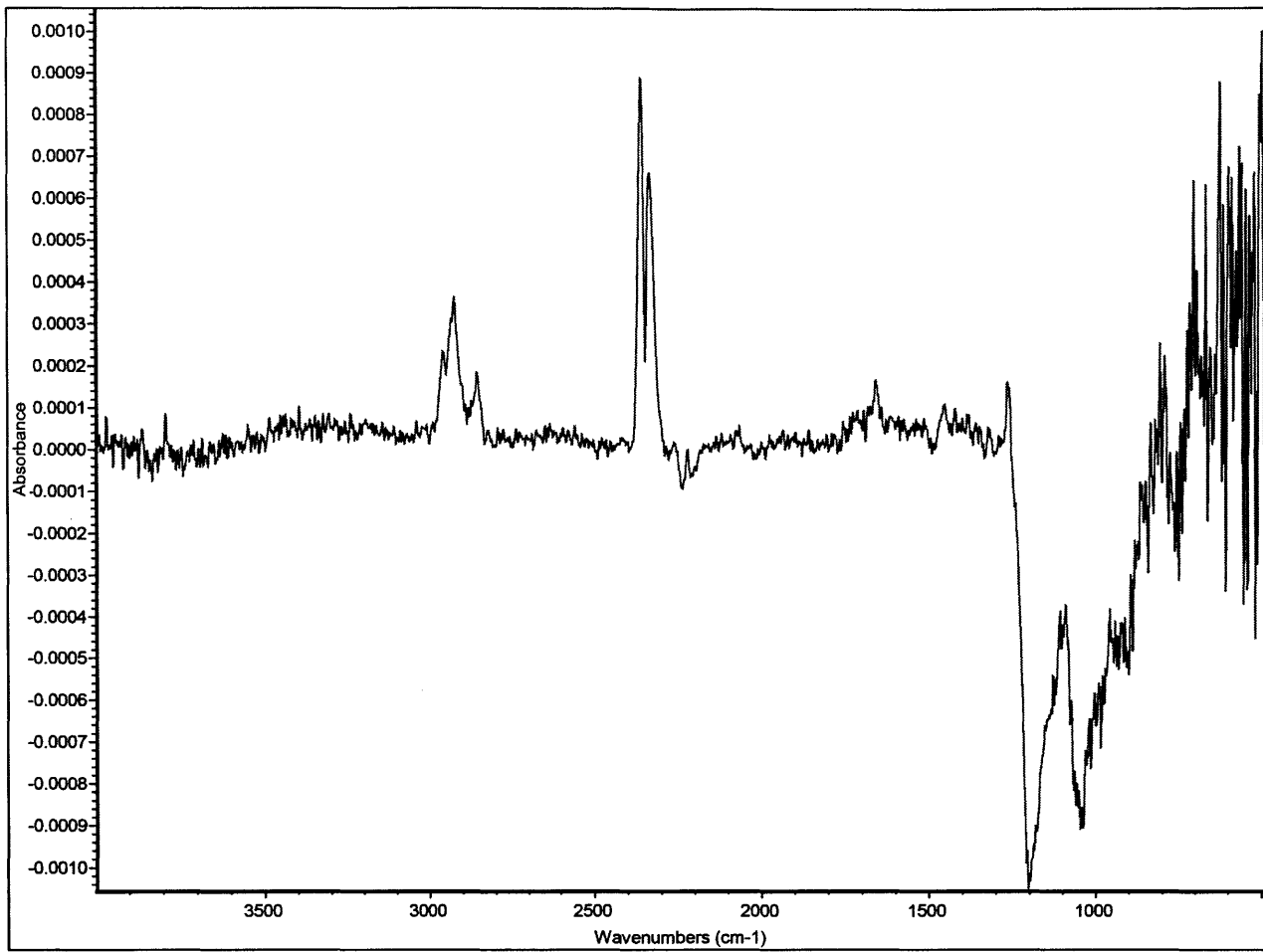
Figure 89. FTIR spectrum of the second **7·Si(111)** wafer ratioed to the spectrum of a fully oxidized silicon surface.
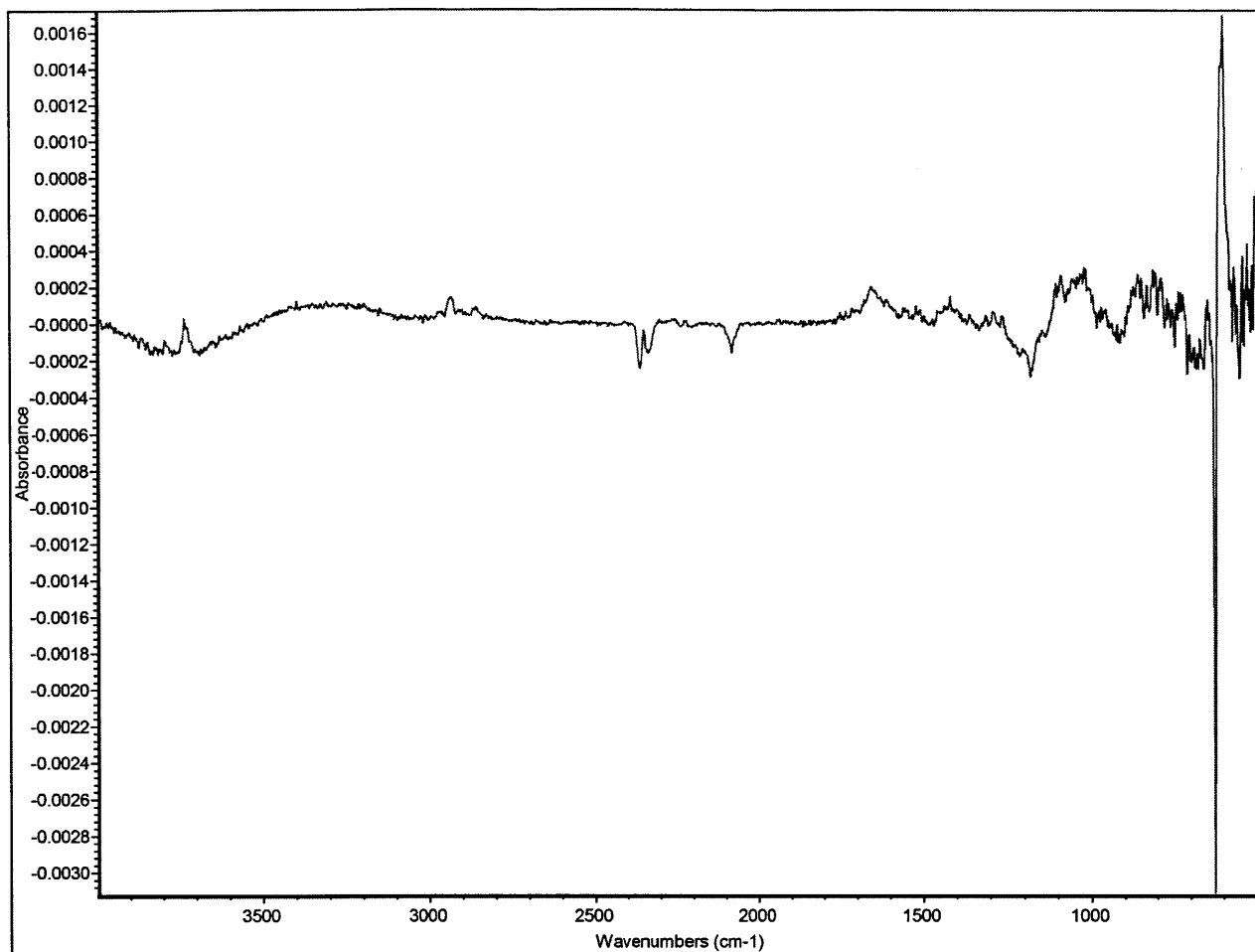
Figure 90. FTIR spectrum of the first 7•Si(111) wafer ratioed to the spectrum of the H-Si(111) wafer.
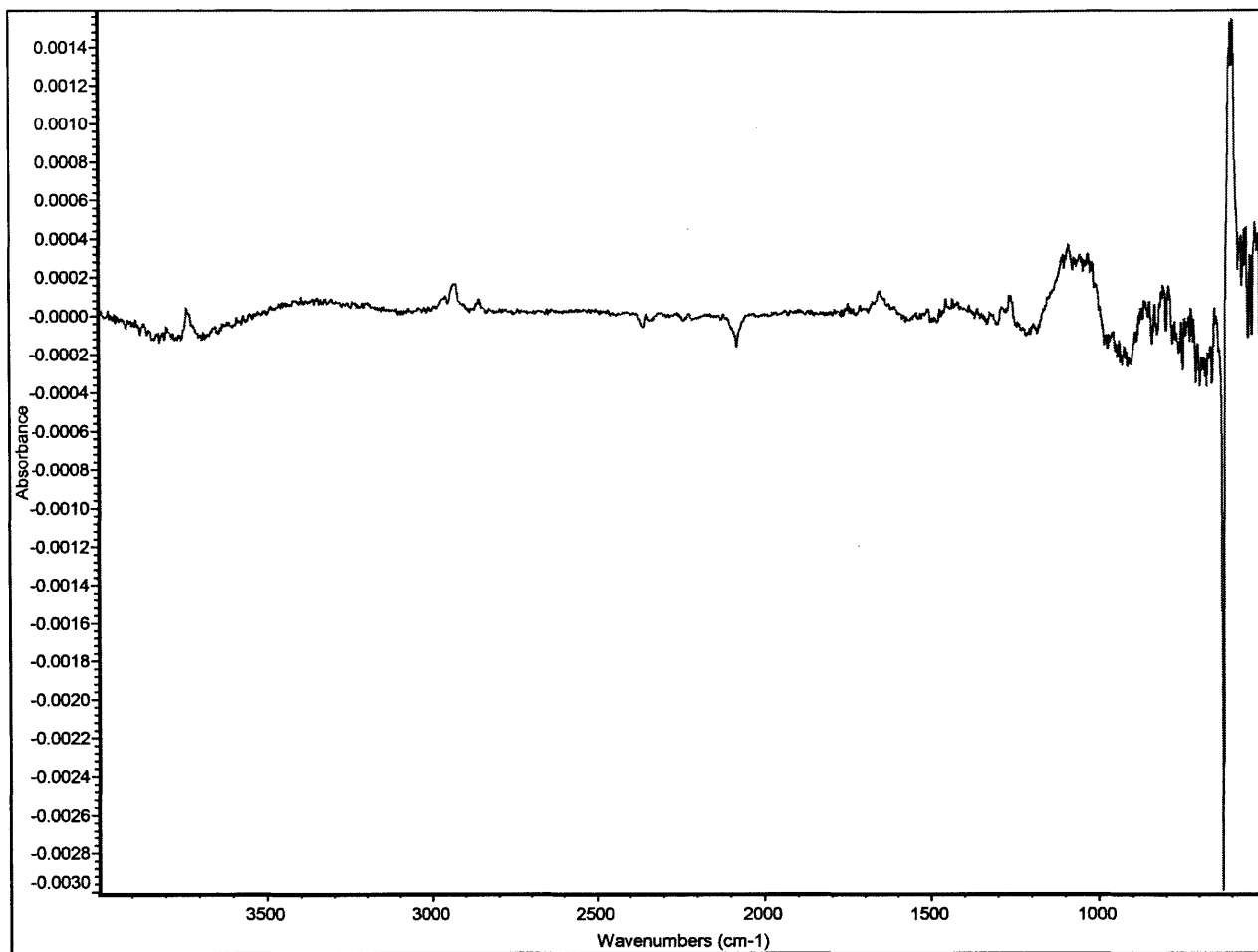
Figure 91. FTIR spectrum of the second 7•Si(111) wafer, ratioed to the spectrum of the H-Si(111) wafer.

3.6 References

(1)   *Functional Surfaces in Biology: Little Structures with Big Effects*; Gorb, S. N., ed.; Springer: Netherlands, 2009; Vol. 1.

(2)   Brillson, L. J. *Surfaces and Interfaces of Electronic Materials*; Wiley-VCH: Weinheim, 2010.

(3)   Bhushan, B. *Principles and Applications of Tribology*; 2nd ed.; John Wiley & Sons, Ltd: New York, 2013.

(4)   Birdi, K. S. *Surface Chemistry Essentials*; CRC Press: Boca Raton, 2013.

(5)   Balani, K.; Verma, V.; Agarwal, A.; Narayan, R. *Biosurfaces: A Materials Science and Engineering Perspective*; John Wiley & Sons, Inc.: Hoboken, NJ, 2015.

(6)   Higashi, G. S.; Chabal, Y. J. In *Handbook of Semiconductor Wafer Cleaning Technology*; Kern, W., Ed.; Noyes Publication: New Jersey, 1993, p. 433-496.

(7)   Ferre, R.; Martín, I.; Vetter, M.; Garín, M.; Alcubilla, R. Effect of Amorphous Silicon Carbide Layer Thickness on the Passivation Quality of Crystalline Silicon Surface. *Appl. Phys. Lett.* **2005**, *87*, 2109-2111.

(8)   Hofmann, M.; Janz, S.; Schmidt, C.; Kambor, S.; Suwito, D.; Kohn, N.; Rentsch, J.; Preu, R.; Glunz, S. W. Recent Developments in Rear-Surface Passivation at Fraunhofer ISE. *Sol. Energy Mater. Sol. Cells* **2009**, *93*, 1074-1078.

(9)   Kaminski, P. M.; Abbas, A.; Bass, K.; Claudio, G. Passivation of Silicon Wafers by Silicon Carbide (SiC_x) Thin Film Grown by Sputtering. *Energy Procedia* **2011**, *10*, 71-75.

(10)   Linford, M. R.; Chidsey, C. E. D. Alkyl Monolayers Covalently Bonded to Silicon Surfaces *J. Am. Chem. Soc.* **1993**, *115*, 12631-12632.

(11)   Linford, M. R.; Fenter, P.; Eisenberger, P. M.; Chidsey, C. E. D. Alkyl Monolayers on Silicon Prepared from 1-Alkenes and Hydrogen-Terminated Silicon. *J. Am. Chem. Soc.* **1995**, *117*, 3145-3155.

(12)   Bansal, A.; Li, X.; Lauermann, I.; Lewis, N. S.; Yi, S. I.; Weinberg, W. H. Alkylation of Si Surfaces Using a Two-Step Halogenation/Grignard Route. *J. Am. Chem. Soc.* **1996**, *118*, 7225-7226.

(13)   Webb, L. J.; Lewis, N. S. Comparison of the Electrical Properties and Chemical Stability of Crystalline Silicon(111) Surfaces Alkylated Using Grignard Reagents or Olefins with Lewis Acid Catalysts. *J. Phys. Chem. B* **2003**, *107*, 5404-5412.

(14)   Aberle, A. G. Surface Passivation of Crystalline Silicon Solar Cells: A Review. *Prog. Photovolt. Res. Appl.* **2000**, *8*, 473-487.

(15)   Green, M. L.; Gusev, E. P.; Degraeve, R.; Garfunkel, E. L. Ultrathin (<4 nm) SiO_2 and Si–O–N Gate Dielectric Layers for Silicon Microelectronics: Understanding the Processing, Structure, and Physical and Electrical Limits. *J. Appl. Phys.* **2001**, *90*, 2057-2121.

(16)   DeBenedetti, W. J. I.; Chabal, Y. J. Functionalization of Oxide-Free Silicon Surfaces. *J. Vac. Sci. Technol., A* **2013**, *31*, 050826.

(17)   Sieval, A. B.; Linke, R.; Heij, G.; Meijer, G.; Zuilhof, H.; Sudhölter, E. J. R. Amino-Terminated Organic Monolayers on Hydrogen-Terminated Silicon Surfaces. *Langmuir* **2001**, *17*, 7554-7559.

(18)   Zhou, Y.; Fuentes-Hernandez, C.; Shim, J.; Meyer, J.; Giordano, A. J.; Li, H.; Winget, P.; Papadopoulos, T.; Cheun, H.; Kim, J.; Fenoll, M.; Dindar, A.; Haske, W.; Najafabadi, E.; Khan, T. M.; Sojoudi, H.; Barlow, S.; Graham, S.; Brédas, J.-L.; Marder, S. R.; Kahn, A.;

Kippelen, B. A Universal Method to Produce Low–Work Function Electrodes for Organic Electronics. *Science* **2012**, *336*, 327-332.

(19)   Malyar, I. V.; Gorin, D. A.; Stetsyura, S. V.; Santer, S. Effect of a Nanodimensional Polyethylenimine Layer on Current–Voltage Characteristics of Hybrid Structures Based on Single-Crystal Silicon. *J. Electron. Mater.* **2012**, *41*, 3427-3435.

(20)   Ahlbrecht, H. In *Encyclopedia of Reagents for Organic Synthesis*; John Wiley & Sons, Ltd: 2001.

(21)   Liu, W.; Sharp, I. D.; Tilley, T. D. Multifunctional Silicon Surfaces: Reaction of Dichlorocarbene Generated from Seyferth Reagent with Hydrogen-Terminated Silicon (111) Surfaces. *Langmuir* **2013**, *30*, 172-178.

(22)   Saghatelian, A.; Buriak, J.; Lin, V. S. Y.; Reza Ghadiri, M. Transition Metal Mediated Surface Modification of Porous Silicon. *Tetrahedron* **2001**, *57*, 5131-5136.

(23)   Aslanov, L.; Zakharov, V.; Zakharov, M.; Kamyshny, A.; Magdassi, S.; Yatsenko, A. Stabilization of Silicon Nanoparticles by Carbenes. *Russ. J. Coord. Chem.* **2010**, *36*, 330-332.

(24)   Frey, G. D.; Masuda, J. D.; Donnadieu, B.; Bertrand, G. Activation of Si–H, B–H, and P–H Bonds at a Single Nonmetal Center. *Angew. Chem. Int. Ed.* **2010**, *49*, 9444-9447.

(25)   Schmidt, D.; Berthel, J. H. J.; Pietsch, S.; Radius, U. C–N Bond Cleavage and Ring Expansion of N-Heterocyclic Carbenes Using Hydrosilanes. *Angew. Chem. Int. Ed.* **2012**, *51*, 8881-8885.

(26)   Lastovickova, D. N.; Moerdyk, J. P.; Kelley, A. R.; Bielawski, C. W. Assessing the Reactivity of the *N,N'*-Diamidocarbenes toward Compounds Containing Early *p*-Block Elements. *J. Phys. Org. Chem.* **2015**, *28*, 75-78.

(27)   Zhukhovitskiy, A. V.; MacLeod, M. J.; Johnson, J. A. Carbene Ligands in Surface Chemistry: From Stabilization of Discrete Elemental Allotropes to Modification of Nanoscale and Bulk Substrates. *Chem. Rev.* **2015**, *115*, 11503-11532.

(28)   Chatgilialoglu, C.; Lalevée, J. Recent Applications of the $(TMS)_3SiH$ Radical-Based Reagent. *Molecules* **2012**, *17*, 527-555.

(29)   Zhukhovitskiy, A. V.; Geng, J.; Johnson, J. A. Cycloelimination of Imidazolidin-2-Ylidene N-Heterocyclic Carbenes: Mechanism and Insights into the Synthesis of Stable "NHC-CDI" Amidinates. *Chem. Eur. J.* **2015**, *21*, 5685-5688.

(30)   Denk, M. K.; Thadani, A.; Hatano, K.; Lough, A. J. Steric Stabilization of Nucleophilic Carbenes. *Angew. Chem. Int. Ed.* **1997**, *36*, 2607-2609.

(31)   Alder, R. W.; Blake, M. E.; Chaker, L.; Harvey, J. N.; Paolini, F.; Schütz, J. When and How Do Diaminocarbenes Dimerize? *Angew. Chem. Int. Ed.* **2004**, *43*, 5896-5911.

(32)   César, V.; Lugan, N.; Lavigne, G. Reprogramming of a Malonic *N*-Heterocyclic Carbene: A Simple Backbone Modification with Dramatic Consequences on the Ligand's Donor Properties. *Eur. J. Inorg. Chem.* **2010**, *2010*, 361-365.

(33)   Hudnall, T. W.; Bielawski, C. W. An *N,N'*-Diamidocarbene: Studies in C–H Insertion, Reversible Carbonylation, and Transition-Metal Coordination Chemistry. *J. Am. Chem. Soc.* **2009**, *131*, 16039-16041.

(34)   Chen, M.; Moerdyk, J. P.; Blake, G. A.; Bielawski, C. W.; Lee, J. K. Assessing the Proton Affinities of *N,N'*-Diamidocarbenes. *J. Org. Chem.* **2013**.

(35)   César, V.; Lugan, N.; Lavigne, G. A Stable Anionic *N*-Heterocyclic Carbene and Its Zwitterionic Complexes. *J. Am. Chem. Soc.* **2008**, *130*, 11286-11287.

(36)   Moerdyk, J. P.; Bielawski, C. W. *N,N'*-Diamidocarbenes Facilitate Selective C–H Insertions and Transfer Hydrogenation. *Chem. Eur. J.* **2013**, *19*, 14773-14776.

(37)   Moerdyk, J. P.; Bielawski, C. W. Reductive Generation of Stable, Five-Membered *N,N'*-Diamidocarbenes. *Chem. Commun. (Cambridge, U. K.)* **2014**, *50*, 4551-4553.

(38)   Moerdyk, J. P.; Blake, G. A.; Chase, D. T.; Bielawski, C. W. Elucidation of Carbene Ambiphilicity Leading to the Discovery of Reversible Ammonia Activation. *J. Am. Chem. Soc.* **2013**, *135*, 18798-18801.

(39)   Martin, D.; Lassauque, N.; Donnadieu, B.; Bertrand, G. A Cyclic Diaminocarbene with a Pyramidalized Nitrogen Atom: A Stable N-Heterocyclic Carbene with Enhanced Electrophilicity. *Angew. Chem. Int. Ed.* **2012**, *51*, 6172-6175.

(40)   Hudnall, T. W.; Moerdyk, J. P.; Bielawski, C. W. Ammonia N-H Activation by a *N,N'*-Diamidocarbene. *Chemical Communications (Cambridge, United Kingdom)* **2010**, *46*, 4288-4290.

(41)   Frey, G. D.; Lavallo, V.; Donnadieu, B.; Schoeller, W. W.; Bertrand, G. Facile Splitting of Hydrogen and Ammonia by Nucleophilic Activation at a Single Carbon Center. *Science* **2007**, *316*, 439-441.

(42)   Lloyd-Jones, G. C.; Alder, R. W.; Owen-Smith, G. J. J. Intermolecular Insertion of an *N,N*-Heterocyclic Carbene into a Nonacidic C–H Bond: Kinetics, Mechanism and Catalysis by (K-HMDS)$_2$ (HMDS=Hexamethyldisilazide). *Chem. Eur. J.* **2006**, *12*, 5361-5375.

(43)   Allen, F. H.; Kennard, O.; Watson, D. G.; Brammer, L.; Orpen, A. G.; Taylor, R. Tables of Bond Lengths Determined by X-Ray and Neutron Diffraction. Part 1. Bond Lengths in Organic Compounds. *J. Chem. Soc. Perk. Trans. 2* **1987**, S1-S19.

(44)   Zeng, X.; Frey, G. D.; Kinjo, R.; Donnadieu, B.; Bertrand, G. Synthesis of a Simplified Version of Stable Bulky and Rigid Cyclic (Alkyl)(Amino)Carbenes, and Catalytic Activity of the Ensuing Gold(I) Complex in the Three-Component Preparation of 1,2-Dihydroquinoline Derivatives. *J. Am. Chem. Soc.* **2009**, *131*, 8690-8696.

(45)   Jazzar, R.; Dewhurst, R. D.; Bourg, J.-B.; Donnadieu, B.; Canac, Y.; Bertrand, G. Intramolecular "Hydroiminiumation" of Alkenes: Application to the Synthesis of Conjugate Acids of Cyclic Alkyl Amino Carbenes (CAACs). *Angew. Chem. Int. Ed.* **2007**, *46*, 2899-2902.

(46)   Jazzar, R.; Bourg, J.-B.; Dewhurst, R. D.; Donnadieu, B.; Bertrand, G. Intramolecular "Hydroiminiumation and -Amidiniumation" of Alkenes: A Convenient, Flexible, and Scalable Route to Cyclic Iminium and Imidazolinium Salts. *J. Org. Chem.* **2007**, *72*, 3492-3499.

(47)   Lavallo, V.; Canac, Y.; Präsang, C.; Donnadieu, B.; Bertrand, G. Stable Cyclic (Alkyl)(Amino)Carbenes as Rigid or Flexible, Bulky, Electron-Rich Ligands for Transition-Metal Catalysts: A Quaternary Carbon Atom Makes the Difference. *Angew. Chem. Int. Ed.* **2005**, *44*, 5705-5709.

(48)   Martin, D.; Canac, Y.; Lavallo, V.; Bertrand, G. Comparative Reactivity of Different Types of Stable Cyclic and Acyclic Mono- and Diamino Carbenes with Simple Organic Substrates. *J. Am. Chem. Soc.* **2014**, *136*, 5023-5030.

(49)   W. Alder, R.; E. Blake, M.; Bortolotti, C.; Bufali, S.; P. Butts, C.; Linehan, E.; M. Oliva, J.; Guy Orpen, A.; J. Quayle, M. Complexation of Stable Carbenes with Alkali Metals. *Chem. Commun.* **1999**, 241-242.

(50) Alder, R. W.; Blake, M. E.; Oliva, J. M. Diaminocarbenes; Calculation of Barriers to Rotation About Ccarbene−N Bonds, Barriers to Dimerization, Proton Affinities, and ^{13}C NMR Shifts. *J. Phys. Chem. A* **1999**, *103*, 11200-11211.

(51) Bell, J. P.; Cloud, J. E.; Cheng, J.; Ngo, C.; Kodambaka, S.; Sellinger, A.; Ratanathanawongs Williams, S. K.; Yang, Y. N-Bromosuccinimide-Based Bromination and Subsequent Functionalization of Hydrogen-Terminated Silicon Quantum Dots. *RSC Advances* **2014**, *4*, 51105-51110.

(52) Mastronardi, M. L.; Maier-Flaig, F.; Faulkner, D.; Henderson, E. J.; Kübel, C.; Lemmer, U.; Ozin, G. A. Size-Dependent Absolute Quantum Yields for Size-Separated Colloidally-Stable Silicon Nanocrystals. *Nano Lett.* **2011**, *12*, 337-342.

(53) Veinot, J. G. C. Synthesis, Surface Functionalization, and Properties of Freestanding Silicon Nanocrystals. *Chem. Commun.* **2006**, 4160-4168.

(54) Hessel, C. M.; Henderson, E. J.; Veinot, J. G. Hydrogen Silsesquioxane: A Molecular Precursor for Nanocrystalline $Si-SiO_2$ Composites and Freestanding Hydride-Surface-Terminated Silicon Nanoparticles. *Chem. Mater.* **2006**, *18*, 6139-6146.

(55) Dasog, M.; Yang, Z.; Regli, S.; Atkins, T. M.; Faramus, A.; Singh, M. P.; Muthuswamy, E.; Kauzlarich, S. M.; Tilley, R. D.; Veinot, J. G. C. Chemical Insight into the Origin of Red and Blue Photoluminescence Arising from Freestanding Silicon Nanocrystals. *ACS Nano* **2013**, *7*, 2676-2685.

(56) Niwano, M.; Kageyama, J. i.; Kurita, K.; Kinashi, K.; Takahashi, I.; Miyamoto, N. Infrared Spectroscopy Study of Initial Stages of Oxidation of Hydrogen-Terminated Si Surfaces Stored in Air. *J. Appl. Phys.* **1994**, *76*, 2157-2163.

(57) Vignolle, J.; Tilley, T. D. N-Heterocyclic Carbene-Stabilized Gold Nanoparticles and Their Assembly into 3D Superlattices. *Chem. Commun.* **2009**, 7230-7232.

(58) Ling, X.; Roland, S.; Pileni, M.-P. Supracrystals of N-Heterocyclic Carbene-Coated Au Nanocrystals. *Chem. Mater.* **2014**, *27*, 414-423.

(59) Copéret, C.; Chaudret, B. *Surface and Interfacial Organometallic Chemistry and Catalysis*; Springer Verlag: Germany, 2005.

(60) Neiner, D.; Kauzlarich, S. M. Hydrogen-Capped Silicon Nanoparticles as a Potential Hydrogen Storage Material: Synthesis, Characterization, and Hydrogen Release. *Chem. Mater.* **2010**, *22*, 487-493.

(61) Onischuk, A. A.; Strunin, V. P.; Samoilova, R. I.; Nosov, A. V.; Ushakova, M. A.; Panfilov, V. N. Chemical Composition and Bond Structure of Aerosol Particles of Amorphous Hydrogenated Silicon Forming from Thermal Decomposition of Silane. *J. Aerosol Sci.* **1997**, *28*, 1425-1441.

(62) Yang, Z.; Gonzalez, C. M.; Purkait, T. K.; Iqbal, M.; Meldrum, A.; Veinot, J. G. C. Radical Initiated Hydrosilylation on Silicon Nanocrystal Surfaces: An Evaluation of Functional Group Tolerance and Mechanistic Study. *Langmuir* **2015**, *31*, 10540-10548.

(63) Tufts, B. J.; Kumar, A.; Bansal, A.; Lewis, N. S. X-Ray Photoelectron Spectroscopic Studies of Interfacial Chemistry at N-Type Silicon/Liquid Junctions. *J. Phys. Chem.* **1992**, *96*, 4581-4592.

(64) Erickson, N. E.; Lieberman, A. G.; Madey, T. E.; Yates, J. T., Jr. In *Semiconductor Measurement Technology: Progress Report, January 1 to June 30, 1976*; Bullis, W. M., Ed.; US Dept. of Commerce, National Bureau of Standards: Washington, D. C., 1976; Vol. 400, p. 28.

(65)   Higashi, G. S.; Chabal, Y. J.; Trucks, G. W.; Raghavachari, K. Ideal Hydrogen Termination of the Si (111) Surface. *Appl. Phys. Lett.* **1990**, *56*, 656-658.

(66)   Haber, J. A.; Lewis, N. S. Infrared and X-Ray Photoelectron Spectroscopic Studies of the Reactions of Hydrogen-Terminated Crystalline Si(111) and Si(100) Surfaces with Br_2, I_2, and Ferrocenium in Alcohol Solvents. *J. Phys. Chem. B* **2002**, *106*, 3639-3656.

(67)   Garcia, S. P.; Bao, H.; Hines, M. A. Understanding the pH Dependence of Silicon Etching: The Importance of Dissolved Oxygen in Buffered HF Etchants. *Surf. Sci.* **2003**, *541*, 252-261.

(68)   Jakob, P.; Chabal, Y. J.; Kuhnke, K.; Christman, S. B. Monohydride Structures on Chemically Prepared Silicon Surfaces. *Surf. Sci.* **1994**, *302*, 49-56.

(69)   Kulkarni, M.; Green, S. K.; Shea, C.; Queeney, K. Role of Etching in Aqueous Oxidation of Hydrogen-Terminated Si (100). *J. Phys. Chem. C* **2009**, *113*, 10206-10214.

(70)   Pretsch, E.; Bühlmann, P.; Badertscher, M. *Structure Determination of Organic Compounds: Tables of Spectral Data*; Springer-Verlag: Berlin, 2009.

(71)   Alecu, I. M.; Zheng, J.; Zhao, Y.; Truhlar, D. G. Computational Thermochemistry: Scale Factor Databases and Scale Factors for Vibrational Frequencies Obtained from Electronic Model Chemistries. *J. Chem. Theory Comput.* **2010**, *6*, 2872-2887.

(72)   Jimenez-Hoyos, C. A.; Janesko, B. G.; Scuseria, G. E. Evaluation of Range-Separated Hybrid Density Functionals for the Prediction of Vibrational Frequencies, Infrared Intensities, and Raman Activities. *Phys. Chem. Chem. Phys.* **2008**, *10*, 6621-6629.

(73)   Chao, Y.; Siller, L.; Krishnamurthy, S.; Coxon, P. R.; Bangert, U.; Gass, M.; Kjeldgaard, L.; Patole, S. N.; Lie, L. H.; O'Farrell, N.; Alsop, T. A.; Houlton, A.; Horrocks, B. R. Evaporation and Deposition of Alkyl-Capped Silicon Nanocrystals in Ultrahigh Vacuum. *Nat. Nanotechnol.* **2007**, *2*, 486-489.

(74)   Wade, C. P.; Chidsey, C. E. D. Etch-Pit Initiation by Dissolved Oxygen on Terraces of H-Si(111). *Appl. Phys. Lett.* **1997**, *71*, 1679-1681.

(75)   Perdew, J. P.; Burke, K.; Ernzerhof, M. Generalized Gradient Approximation Made Simple. *Phys. Rev. Lett.* **1996**, *77*, 3865-3868.

(76)   Kanai, Y.; Selloni, A. Competing Mechanisms in the Optically Activated Functionalization of the Hydrogen-Terminated Si(111) Surface. *J. Am. Chem. Soc.* **2006**, *128*, 3892-3893.

(77)   Takeuchi, N.; Kanai, Y.; Selloni, A. Surface Reaction of Alkynes and Alkenes with H-Si(111): A Density Functional Theory Study. *J. Am. Chem. Soc.* **2004**, *126*, 15890-15896.

(78)   *CRC Handbook of Chemistry and Physics*; 95th ed.; Haynes, W. M., Ed.; CRC press, 2014.

(79)   Gross, T.; Oehme, H.; Kempe, R. Geminal Bis(Hypersilyl) Compounds: The Synthesis and Structure of Bis[Tris(Trimethylsilyl)Silyl]Methane. *Organometallics* **1999**, *18*, 1815-1817.

(80)   Berkman, D. C.; Deal, D.; Grant, D. C.; Peterson, C. In *Handbook of Semiconductor Wafer Cleaning Technology*; Kern, W., Ed.; Noyes Publication: Park Ridge, NJ, 1993, p. 111-196.

(81)   Fulmer, G. R.; Miller, A. J. M.; Sherden, N. H.; Gottlieb, H. E.; Nudelman, A.; Stoltz, B. M.; Bercaw, J. E.; Goldberg, K. I. Nmr Chemical Shifts of Trace Impurities: Common Laboratory Solvents, Organics, and Gases in Deuterated Solvents Relevant to the Organometallic Chemist. *Organometallics* **2010**, *29*, 2176-2179.

(82) Dolbier, W. R. *Guide to Fluorine NMR for Organic Chemists*; John Wiley & Sons, Inc.: Hoboken, NJ, 2009.

(83) Fairley, N. *CasaXPS Manual 2.3. 15, Rev. 1.3, Orange Book*; CasaXPS Software Ltd., 2009.

(84) Cheng, Y.; Wang, M.; Borghs, G.; Chen, H. Gold Nanoparticle Dimers for Plasmon Sensing. *Langmuir* **2011**, *27*, 7884-7891.

(85) Hochella, M.; Carim, A. A Reassessment of Electron Escape Depths in Silicon and Thermally Grown Silicon Dioxide Thin Films. *Surf. Sci.* **1988**, *197*, L260-L268.

(86) Laibinis, P. E.; Bain, C. D.; Whitesides, G. M. Attenuation of Photoelectrons in Monolayers of *N*-Alkanethiols Adsorbed on Copper, Silver, and Gold. *J. Phys. Chem.* **1991**, *95*, 7017-7021.

(87) Walton, J.; Alexander, M.; Fairley, N.; Roach, P.; Shard, A. Film Thickness Measurement and Contamination Layer Correction for Quantitative XPS. *Surf. Interface Anal.* **2016**.

(88) Pomykal, K. E.; Fajardo, A. M.; Lewis, N. S. Stability of N-Si/CH_3OH Contacts as a Function of the Reorganization Energy of the Electron Donor. *J. Phys. Chem.* **1995**, *99*, 8302-8310.

(89) Seah, M. P.; Briggs, D. *Practical Surface Analysis: Auger and X-Ray Photoelectron Spectroscopy*; 2nd ed.; Wiley: New York, 1990; Vol. 1.

(90) Sheldrick, G. M. Phase Annealing in SHELX-90: Direct Methods for Larger Structures. *Acta Crystallogr. Sect. A* **1990**, *46*, 467-473.

(91) Sheldrick, G. M. A Short History of SHELX. *Acta Crystallogr. Sect. A* **2008**, *64*, 112-122.

(92) Müller, P. Practical Suggestions for Better Crystal Structures. *Crystallogr. Rev.* **2009**, *15*, 57-83.

(93) Shao, Y.; Gan, Z.; Epifanovsky, E.; Gilbert, A. T. B.; Wormit, M.; Kussmann, J.; Lange, A. W.; Behn, A.; Deng, J.; Feng, X.; Ghosh, D.; Goldey, M.; Horn, P. R.; Jacobson, L. D.; Kaliman, I.; Khaliullin, R. Z.; Kuś, T.; Landau, A.; Liu, J.; Proynov, E. I.; Rhee, Y. M.; Richard, R. M.; Rohrdanz, M. A.; Steele, R. P.; Sundstrom, E. J.; Woodcock, H. L.; Zimmerman, P. M.; Zuev, D.; Albrecht, B.; Alguire, E.; Austin, B.; Beran, G. J. O.; Bernard, Y. A.; Berquist, E.; Brandhorst, K.; Bravaya, K. B.; Brown, S. T.; Casanova, D.; Chang, C.-M.; Chen, Y.; Chien, S. H.; Closser, K. D.; Crittenden, D. L.; Diedenhofen, M.; DiStasio, R. A.; Do, H.; Dutoi, A. D.; Edgar, R. G.; Fatehi, S.; Fusti-Molnar, L.; Ghysels, A.; Golubeva-Zadorozhnaya, A.; Gomes, J.; Hanson-Heine, M. W. D.; Harbach, P. H. P.; Hauser, A. W.; Hohenstein, E. G.; Holden, Z. C.; Jagau, T.-C.; Ji, H.; Kaduk, B.; Khistyaev, K.; Kim, J.; Kim, J.; King, R. A.; Klunzinger, P.; Kosenkov, D.; Kowalczyk, T.; Krauter, C. M.; Lao, K. U.; Laurent, A. D.; Lawler, K. V.; Levchenko, S. V.; Lin, C. Y.; Liu, F.; Livshits, E.; Lochan, R. C.; Luenser, A.; Manohar, P.; Manzer, S. F.; Mao, S.-P.; Mardirossian, N.; Marenich, A. V.; Maurer, S. A.; Mayhall, N. J.; Neuscamman, E.; Oana, C. M.; Olivares-Amaya, R.; O'Neill, D. P.; Parkhill, J. A.; Perrine, T. M.; Peverati, R.; Prociuk, A.; Rehn, D. R.; Rosta, E.; Russ, N. J.; Sharada, S. M.; Sharma, S.; Small, D. W.; Sodt, A. Advances in Molecular Quantum Chemistry Contained in the Q-Chem 4 Program Package. *Mol. Phys.* **2015**, *113*, 184-215.

(94) Rappe, A. K.; Casewit, C. J.; Colwell, K. S.; Goddard, W. A.; Skiff, W. M. Uff, a Full Periodic Table Force Field for Molecular Mechanics and Molecular Dynamics Simulations. *J. Am. Chem. Soc.* **1992**, *114*, 10024-10035.

(95) Brondani, D.; Zapp, E.; Vieira, I. C.; Dupont, J.; Scheeren, C. W. Gold Nanoparticles in an Ionic Liquid Phase Supported in a Biopolymeric Matrix Applied in the Development of a Rosmarinic Acid Biosensor. *Analyst (Cambridge, U. K.)* **2011**, *136*, 2495-2505.

(96) Van Ausdall, B. R.; Glass, J. L.; Wiggins, K. M.; Aarif, A. M.; Louie, J. A Systematic Investigation of Factors Influencing the Decarboxylation of Imidazolium Carboxylates. *J. Org. Chem.* **2009**, *74*, 7935-7942.

(97) Kuhn, K. M.; Grubbs, R. H. A Facile Preparation of Imidazolinium Chlorides. *Org. Lett.* **2008**, *10*, 2075-2077.

(98) Despagnet-Ayoub, E.; Grubbs, R. H. A Stable Four-Membered *N*-Heterocyclic Carbene. *J. Am. Chem. Soc.* **2004**, *126*, 10198-10199.

(99) Roth, T.; Vasilenko, V.; Benson, C. G. M.; Wadepohl, H.; Wright, D. S.; Gade, L. H. Extending N-Heterocyclic Carbene Ligands into the Third Dimension: A New Type of Hybrid Phosphazane/NHC. System *Chem. Sci.* **2015**, *6*, 2506-2510.

(100) Taylor, E. C.; Ehrhart, W. A. A Convenient Synthesis of *N,N'*-Disubstituted Formamidines and Acetamidines. *J. Org. Chem.* **1963**, *28*, 1108-1112.

(101) Sun, W.-Y.; Yoshizawa, M.; Kusukawa, T.; Fujita, M. Multicomponent Metal–Ligand Self-Assembly. *Curr. Opin. Chem. Biol.* **2002**, *6*, 757-764.

(102) Verlinden, K.; Buhl, H.; Frank, W.; Ganter, C. Determining the Ligand Properties of *N*-Heterocyclic Carbenes from ^{77}Se NMR Parameters. *Eur. J. Inorg. Chem.* **2015**, *2015*, 2416-2425.

(103) Lopez-Gomez, M. J.; Martin, D.; Bertrand, G. Anti-Bredt *N*-Heterocyclic Carbene: An Efficient Ligand for the Gold(I)-Catalyzed Hydroamination of Terminal Alkynes with Parent Hydrazine. *Chem. Commun.* **2013**, *49*, 4483-4485.

CHAPTER 4. Cycloelimination of Imidazolidin-2-Ylidene *N*-Heterocyclic Carbenes: Mechanism and Insights into the Synthesis of Stable "NHC-CDI" Amidinates

4.1 Introduction

Since Arduengo's isolation of the first crystalline N-heterocyclic carbene (NHC) in 1991,[1] the unique properties of these species have led to their pervasive use in main group and organometallic chemistry, catalysis, medicinal chemistry, and materials science.[2,3] Among the various classes of NHCs, the 1,3-bis(aryl) imidazolidin-2-ylidenes (e.g., **1a-1d**, Scheme 1) are perhaps the most famous and widely used due in large part to the success of the 1,3-bis(2,4,6-trimethylphenyl)-2-imidazolidinylidene (**1d**), known as "SIMes", as a key ancillary ligand in the Grubbs 2nd-generation and Grubbs-Hoveyda olefin metathesis catalysts.[4-7] SIMes and its derivatives are widely applied as ligands in other areas of transition metal catalysis,[8-12] as stabilizers for main group,[13] d-block,[14-16] and f-block[17]

Scheme 1. Structures of NHCs and NHC-CDI adducts described in this study.

species, as organocatalysts,[9,18-22] and as anchors for the formation of stable NHC monolayers and heterogeneous catalysts.[23-25] As a testament to the general importance of this class of NHCs, SIMes and 1,3-bis(2,6-di-i-propylphenyl)imidazolidin-2-ylidene (DippH₂) are two of only a handful of persistent carbenes that are commercially available from large chemical suppliers. Thus, the discovery of new reactivity and decomposition pathways of these NHCs will have broad impact.

4.2 Results and Discussion

We report here the discovery that NHCs of the SIMes family can be converted nearly quantitatively to novel NHC-carbodiimide (NHC-CDI) amidinate adducts simply upon heating (Scheme 1). For example, heating NHC **1a** to 110 °C for 31 hours in toluene-d^8 (or for ~2 d at 100 °C in 1,2-dichlorobenzene-d^4) provides tetra-bromo NHC-CDI **2a** in >97% conversion. Analogous bis(chloro) (**1b**) and bis(fluoro) (**1c**) derivatives and SIMes (**1d**) all provide NHC-CDI adducts – **2b**, **2c**, and **2d**, respectively – under similar conditions. Notably, the "protected" carbene **1a-CO₂** (Scheme 1) and the 1a-diphenylphosphine adduct also generate **2a** upon heating for extended times.

306

Given the lack of precedent for such a transformation despite broad interest in NHC reactivity, we sought to study the mechanism of NHC-CDI formation in detail. We propose a two-step process that consists of a concerted [3+2]-cycloelimination of the 1,3-bis(aryl) imidazolidin-2-ylidene NHC to generate ethylene and a 1,3-bis(aryl) CDI, followed by trapping of this CDI with a second NHC. Mechanistic analogues for both of these steps are known for related systems. Regarding the key cycloelimination, Bertrand and co-workers reported a concerted [3+2]-cycloelimination reaction of *P*-heterocyclic carbenes that proceeded via 1st-order kinetics to provide acetonitrile and 1,3-diphosphaallene (DPA) derivatives.[26] Cycloelimination of N_2 or CO_2 to generate carbodiimides has also been observed in transiently generated tetrazolylidenes and oxadiazolinonylidenes, respectively.[27-29] Relatively unstable *N,O*-heterocyclic carbenes are known to undergo [3+2]-cycloelimination to generate ethylene and isocyanates; in these cases NHC-(isocyanate)$_2$ adducts have been observed.[30-32] The Corey-Winter reaction, whereby alkenes are synthesized via expulsion of CO_2 or CS_2, is proposed to proceed through highly unstable *O,O*- or *S,S*-heterocyclic carbenes, respectively.[33-35]
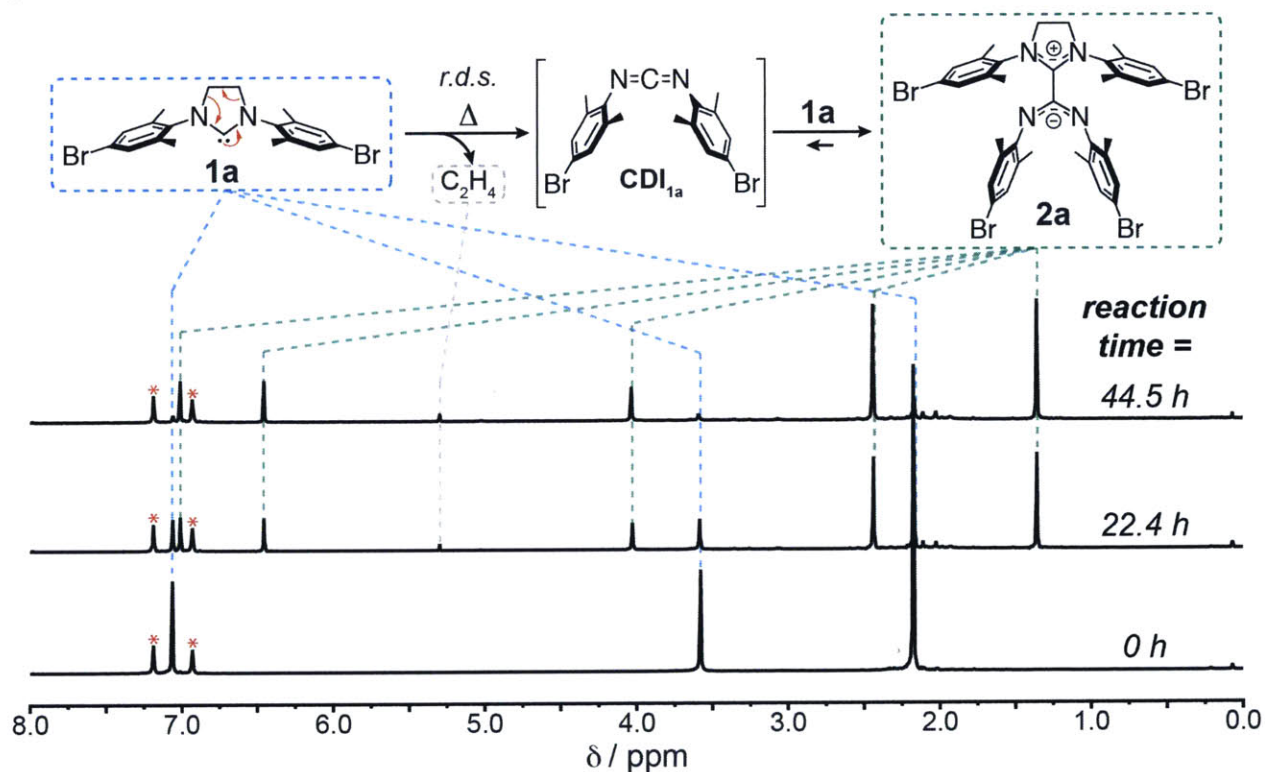
Figure 1. Proposed mechanism for the transformation of **1a** into **2a** and ethylene. Conversion with time in *o*-dichlorobenzene-*d⁴* at 100 ± 5 °C monitored via ^{1}H NMR (400 MHz).

Furthermore, cycloeliminations of tetrazole, pentazole, thiotriazole, and 1,2,4-triazole derivatives have been noted as well.[36,37] In support of the second step of our proposed mechanism: the addition of a NHC to a CDI, Kuhn and coworkers reported such a reaction to produce what is, to our knowledge, the only other example of a NHC-CDI complex (*vide infra*).[38] The tandem thermal transformation of 1,2,4-triazol-5-ylidene observed by Korotkikh and Cowley *et al.* is also consistent with the proposed reaction sequence.[39]

Our experimental data support this mechanism. ^{1}H NMR analysis of the reaction of **1a** (Figure 1) revealed the nearly quantitative formation of **2a** and ethylene. Free CDI was not observed, which suggests that the cycloelimination step is rate-limiting. The rate constants for the cycloelimination process obtained for a series of reactions conducted at various $[\mathbf{1a}]_0$ values were virtually identical ($7.4 \pm 0.7*10^{-6}$ s^{-1} at 100 ± 5°C, $\tau_{1/2} = 26$ h), which suggests an overall reaction order of one (Figure 2A). Eyring analysis (Figure 2B) provided activation parameters $\Delta S^{\neq}$ and $\Delta H^{\neq}$ of +2.62 cal/mol*K and +31.9 kcal/mol, respectively. These values are consistent with a rate-limiting cycloelimination mechanism wherein **1a** transitions to ethylene and CDI via concerted cleavage of two C-C σ bonds and formation of one C=C π bond and two N=C bonds in the transition state.[40-43]
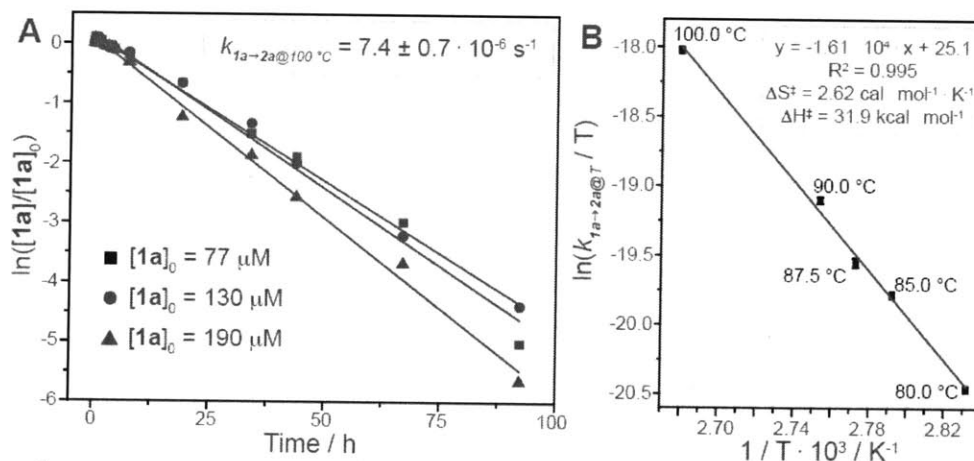
Figure 2. A. 1st-order kinetics of the consumption of **1a** at different initial concentrations in toluene-d^8 at 100 ± 5 °C. B. Eyring plot for consumption of **1a** at various temperatures.

Additional evidence for the proposed mechanism came from density functional (DFT) geometry optimization performed on NHCs **1a-d** (Figure 3 and Table 1). Examination of the ground state HOMO, LUMO, and LUMO + 1 (Figure 3) orbitals (calculated in a vacuum) revealed two key features: (1) the largest orbital coefficient of the HOMO is on the NHC carbene carbon, and (2) in both the HOMO and LUMO + 1 there are orbitals present on the NHC CH₂-

CH$_2$ backbone with the correct geometry and relative symmetry to form the π bond of the eliminated ethylene.

HOMO of **1a**: **-5.80 eV**   LUMO of **1a**   LUMO+1 of **1a**
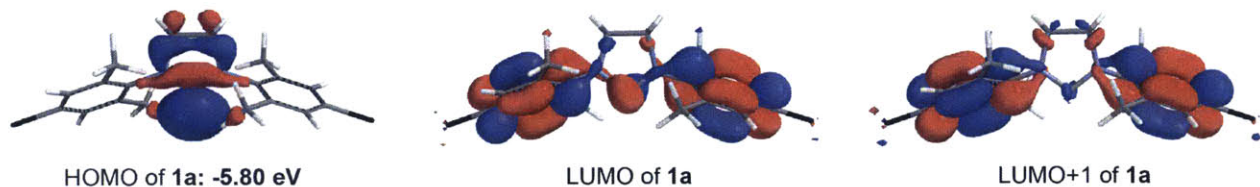
Figure 3. The HOMO, LUMO and LUMO+1 of **1a**.

Table 1. Dependence of observed reaction rate on DFT-calculated orbital energies, solvent, temperature, and *para*-substituent on the NHC aryl rings

NHC	Solvent	HOMO (eV)	LUMO, LUMO+1 (eV)	Temperature (K)*	$k_{obs} = 2 \cdot k_{1a \to CDI1a}$ (h^{-1})
1a	toluene-d^8	-5.8[a]	-0.5, -0.4[a]	373.15	0.0517
1a	pyridine-d^5	-5.8[a]	-0.5, -0.4[a]	373.15	0.0282
1a	ODCB-d^4			373.15	0.0485
1a	toluene-d^8	-5.8[b]	-0.5, -0.4[b]	373.15**	0.0400***
1a	toluene-d^8			383.15**	0.109
1a	toluene-d^8	-5.8[c]	-0.5, -0.4[c]	383.15	0.121
1b	toluene-d^8	-5.8[c]	-0.5, -0.4[c]	383.15	0.174
1c	toluene-d^8	-5.6[c]	-0.1, -0.1[c]	383.15	0.132
SIMes	toluene-d^8	-5.6[c]	-0.4, -0.3[c]	383.15	0.163

(a) DFT, B3LYP, 6-31G*, carried out using SM8 model for the corresponding *non-deuterated* solvents; (b) DFT, B3LYP, 6-31G**, carried out using SM8 model for toluene; (c) DFT, B3LYP, 6-31G**, vacuum.

*Reactions were carried out in a sand bath; temperature variation of ± 5 K throughout the sand bath

** Carried out in an oil bath, temperature variation was ± 2 K

***Average of three runs

Thus, we expect the proposed thermal [3+2]-cycloelimination, which involves six electrons, to be an orbital symmetry-allowed process.[44] Finally, the transition state geometry for the cycloelimination was modeled using DFT after an initial optimization via a semi-empirical PM3 model (Figure 4). The NHC N-C=N angle of **1a** increased from 105.58° in the ground state to 125.00° in the transition state; the N-C backbone bond lengths increased from 1.490 Å to 2.029 Å, respectively. The computed $\Delta H^{\neq}$ was 29.8 kcal/mol, which agreed well with our Eyring analysis.[45]

Figure 4. Calculated TS structure of **1a** undergoing concerted [3+2] cycloelimination.

Single crystal X-ray structures of NHC-CDI amidinates **2a** and **2d** are provided in Figure 5; analogous structures of **2b** and **2c** are provided in the Experimental. All four compounds share structural similarities: the central NHC-CDI C-C bond lengths range from 1.50 to 1.51 Å, the NHC and amidinate C-N bond lengths are 1.32–1.33 Å,

Figure 5. Crystal structure of **2a** (disorder is seen in the left N-substituent), R(F) = 0.0289, $R_w(F^2)$ = 0.0711; color legend: purple = Br, dark gray = C, light gray = H, blue = N; crystal structure of **2d**, R(F) = 0.0460, $R_w(F^2)$ = 0.1367.

the amidinate N-C=N bond angles are 139.61–140.02°, and the NHC N-C=N bond angles are 110.96–111.26°. These values agree within 2% with the values computed using DFT with B3LYP functional, a 6-31G** basis set and the symmetry constraint (Figure 6). Interestingly, the dihedral angle between the NHC and amidinate (Newman projections provided for **2a** and **2d** in Figures 5) exhibits more variation: 63.32° for **2b**, 65.51° for **2a**, 67.02° for **2c**, and 85.18° for **2d**. Though it is tempting to suggest that this large difference between halogenated adducts **2a–c** and **2d** arises from interactions between the NHC and amidinate aryl substituents, subsequent studies with other NHC and CDI components (see Experimental) show no discernable trend.

Figure 6. Structures of **2a**, **2b**, **2c**, and **2d** computed using DFT with the B3LYP functional and 6-31G** basis set; color legend for lines representing atoms: black = C, gray = H, blue = N, black = Br, green = Cl, yellow = F.

To our knowledge, despite extensive precedent for the formation of related NHC-betaine adducts,[46] there is only one reported example of an isolable un-protonated NHC-CDI adduct (the transient existence of unstable NHC-CDI intermediates has been proposed in other cases[39,47,48]): Kuhn *et al.* described the synthesis of a NHC-CDI via direct addition of the

unsaturated 1,3-dimethyl-4,5-dimethylimidazol-2-ylidene NHC to diisopropylcarbodiimide (Scheme 2A).[38] Notably, while the central NHC-CDI C-C bond length in Kuhn's adduct was 1.516 Å – nearly identical to the corresponding bond lengths in our adducts – the N-C=N angle of the amidinate component in Kuhn's adduct was nearly 10° smaller than those described here (130.4° vs. 139.61–140.02°). This dramatic difference likely stems from the larger steric bulk of the four aryl substituents in our adducts compared to that of the ^{i}Pr groups in the NHC and amidinate components of Kuhn's adduct.

These unique structural features imbue our NHC-CDI adducts with novel properties. Most notably, adducts **2a**–**2d** are bench-stable zwitterions under ambient conditions for months. Furthermore, they are stable in solution in the presence of moisture for at least 3 d (Figure 7). In contrast, upon exposure to moisture, Kuhn's adduct was sufficiently basic to deprotonate water; the protonated adduct decomposed over the course of 12 h. Along with their unprecedented stability, our NHC-CDI adducts exhibit absorbance in the visible region and violet-indigo fluorescence (389–422 nm) (Figures 8–10); the UV-vis spectrum of **2a**

Figure 7. ^{1}H NMR spectra of **2d** indicating stability of this adduct in the presence of moisture in MeCN-d^3 during the course of three days. *Residual solvent peak.

(Figures 8–9) in DCM and THF shows a series of transitions above 250 nm, with non-zero absorbance that extends to >450 nm. These optical properties arise from conjugation in the

amidinate and NHC components, which is apparent in the DFT-computed HOMO and LUMO of **2a** (see Figure 11 in the Experimental).

Single crystal X-ray structures of these complexes (see Experimental) provide NHC-CDI C-C bond length that range from 1.498 to 1.502 Å. Thus, though we expected the more electron-rich NHCs IMes and Dipp[49] to lead to NHC-CDI adducts with decreased NHC-amidinate C-C bond lengths relative to SIMes this was not the case. In

Scheme 2. An NHC-CDI adduct reported by Kuhn *et al.* and the NHC- di-*p*-tolyl-CDI adducts prepared in this work.

a) *Kuhn et al.:*

b) *this work:*

3a, Ar = mesityl (SIMes), 89% yield
3b, Ar = mesityl (IMes), 83% yield
3c, Ar = 2,6-diisopropylphenyl (Dipp), 90% yield

fact, this central C-C bond length seems to be remarkably insensitive to the steric bulk and electronics of the NHC. Variation in the amidinate N-C=N bond angles is more substantial, and appears to be correlated with the steric bulk of the NHC: 138.37° for IMes, 139.02° for SIMes, and 141.57° for Dipp.

Figure 8. A. UV-vis absorbance of **2a** at different concentrations in DCM. **B.** Computation of the extinction coefficient of **2a** for the absorbance at 294 nm using Beer's Law.

Our attempts to form NHC-CDI adducts from SIMes and 1,3-dialkyl carbodiimides (diisopropylcarbodiimide (DIC), dicyclohexylcarbodiimide (DCC), and di-tert-butylcarbodiimide (DTC)) did not give rise to stable amidinates (See Figures 12–14 in the Experimental). In the reaction of DTC with SIMes in toluene-*d*[8], no adduct formation

was observed at 25 °C. In the cases of DCC and DIC, we observed equilibria favouring the formation of the adduct, but shifted dramatically to the dissociated SIMes and carbodiimide ($K_c = 170$ M^{-1} for DCC and $K_c = 550$ M^{-1} for DIC at 25 °C) compared to *N,N*-diarylcarbodiimies ($K_c \gg 550$ M^{-1}). These results suggest that aryl substituents in the carbodiimide portion of the NHC-CDI provide increased stability likely via delocalization of the amidinate negative charge and the greater electronegativity of sp^2- *vs* sp^3-hybridized carbon.

Figure 9. UV-vis spectroscopic characterization of **2a**, **2b**, **2c**, and **2d** in THF. *Absorbance of THF was not normalized.

4.3 Conclusions

To summarize, we have discovered that [3+2]-cycloelimination reactions of NHCs of the SIMes family are remarkably facile and lead to the formation of novel, bench-stable NHC-CDI amidinates. Remarkably, despite numerous reported examples of thermally unveiled NHCs of the SIMes class,[5,50] this reactivity has not, to our knowledge, been reported. The reaction appears to proceed in

Figure 10. Fluorimetry characterization of **2a** ($\lambda_{exc} = 330$ nm), **2b** ($\lambda_{exc} = 330$ nm), **2c** ($\lambda_{exc} = 320$ nm), and **2d** ($\lambda_{exc} = 330$ nm) in THF. B-spline was used to connect the data points.

any solvent where the NHC is itself soluble and stable. Such thermally allowed cycloeliminations, as well as their photo-allowed analogues, may yet prove to take place in other types of heterocyclic carbenes (e.g., cyclic alkyl amino carbenes, CAACs) to afford new classes of zwitterionic carbene adducts. Furthermore, the identification of key structural features that lead to stable NHC-CDI adducts will guide the application of these novel structures in various settings. Current efforts in our laboratory are aimed towards the use of NHC-CDI adducts as

Lewis basic ligands in their own right, as well as on the application of this cycloelimination chemistry in new applications of NHCs.

4.4 Experimental

Materials and Methods

1,3-Bis(2,4,6-trimethylphenyl)-4,5-dihydroimidazol-2-ylidene (SIMes, 10% hydrolyzed as quantified by ^{1}H nuclear magnetic resonance (NMR); used as received without further purification), 1,3-bis(2,4,6-trimethylphenyl)imidazol-2-ylidene (IMes), 1,3-bis(2,6-diisopropylphenyl)-imidazol-2-ylidene (Dipp), 1,3-di-*p*-tolylcarbodiimide, 1M solution of potassium hexamethyldisilazide (KHMDS) in tetrahydrofuran (THF), and non-deuterated solvents were purchased from Sigma-Aldrich®. All deuterated solvents were purchased from Cambridge Isotope Laboratories, Inc. All other reagents and solvents were purchased from VWR® or Sigma-Aldrich®. All purchased reagents and solvents were used as supplied unless otherwise noted. Solvents not in Sure/Seal™ containers were degassed (unless supplied in ampules under inert atmosphere) via three freeze-pump-thaw cycles and dried over 3Å molecular sieves (from Mallinckrodt Baker) prior to use in air-sensitive experiments (*i.e.*, ones involving the use of N-heterocyclic carbenes). All air-sensitive reactions were executed in a nitrogen-atmosphere glove box or using standard Schlenk techniques using glassware dried for at least 6 h at 120 °C.

Liquid chromatography–mass spectrometry (LC/MS) were performed on an Agilent 1260 LC system equipped with an Advanced Materials Technology HALO® C18 high performance column. Solvent gradients consisted of mixtures of MilliQ™ water with 0.1% acetic acid (AcOH) and HPLC-grade acetonitrile. Mass spectra were obtained using an Agilent 6130 single quadrupole mass spectrometer.

^{1}H, ^{13}C, and ^{19}F NMR spectra were recorded on two Bruker AVANCE-400 NMR spectrometers. Chemical shifts are expressed in parts per million (ppm), and splitting patterns are designated as s (singlet), d (doublet), t (triplet), sept (septet), m (multiplet). Coupling constants J are reported in Hertz (Hz). MestReNova LITE v5.2.5-4119 software (Mestrelab Research S.L.) was used to analyze the NMR spectra. ^{1}H and ^{13}C NMR spectra were referenced to solvent peaks as reported in literature.[51] The residual solvent resonances of ODCB-d^4 were referenced to

7.19 and 6.93 ppm. ^{19}F NMR spectra were referenced using an external reference of neat $CFCl_3$ (δ = 0.00).

High-resolution mass spectrometry (HRMS) was obtained using a Bruker Daltonics APEXIV 4.7 Tesla Fourier Transform Ion Cyclotron Resonance Mass Spectrometer (FT-ICR-MS).

Ultraviolet-visible (UV-vis) spectroscopy was carried out using a Varian Cary® 50 Scan UV-Vis Spectrophotometer. The spectra were collected in dual beam mode at 600 nm/min from 800 to 200 nm, using 100% T baseline correction based on a sample of neat solvent (HPLC grade) in a quartz cuvette used for the subsequent measurements. The spectra were analyzed using the Cary WinUV software.

Fourier-transform infra-red attenuated total reflectance (FTIR-ATR) spectroscopy was carried out using a Thermo Scientific Nicolet 6700 FT-IR equipped with a germanium ATR crystal. A background spectrum was collected prior to spectroscopy of the samples, and 64 scans were collected and averaged for both background and samples. OMNIC™ software was used to analyze the IR data: no corrections were applied to the spectra shown below. Resonance energies are expressed in wavenumbers (cm^{-1}), and resonances are designated as s (strong), m (medium), w (weak), or br (broad).

Fluorimetry was carried out using Fluorolog®-3 spectrofluorometer from Jobin Yvon Horiba using the DataMax for Windows™ driving software. The following parameters were used during the fluorimetry: (1) integration time = 0.25 s; (2) increment = 1 nm; (3) excitation wavelength: variable; (4) Detector HV S = 950 V and R = 0 V; bandpass slits: excitation1 = 3.000 nm; emission1 = 5.000 nm. The data was analyzed using OMNIC™ software and plotted in OriginPro 8.5.

Melting point analysis was carried out using Mel-Temp® II from Laboratory Device, Inc., USA.

Computational Details

All computations were done using Spartan 10 (version 1.1.0). Geometry optimizations were performed using density functional theory (DFT) with the B3LYP exchange-correlation functional and 6-31G** basis set. The symmetry constraint was implemented in each case. For transition state optimizations, the following approach was implemented. Following the initial, DFT-optimized ground state (GS) geometry, the bond lengths between the NHC nitrogen atoms

and the NHC backbone carbon atoms were constrained to be progressively larger values (Δ(bond length) = 0.1 Å), until ethylene and CDI formed: progressively moving the two fragments apart approximates the proposed reaction coordinate. At each step, the GS geometry of the structure was optimized using the semi-empirical PM3 model to approximate points along the reaction coordinate-energy profile for the cycloelimination process. Once an energy maximum was reached, the corresponding geometry was used as a guess for the transition state (TS) geometry optimization using first PM3 and then DFT with a B3LYP functional and 6-31G** basis set. The vibrational frequencies were then calculated using DFT with a B3LYP functional and 6-31G** basis set, revealing a single imaginary frequency of $483.07i$ cm^{-1}. The $\Delta H^{\#}$ was evaluated by subtracting the total energy (as defined in Spartan) of the starting NHC from the TS energy. Orbital energies in a solvent were calculated using the SM8 model for the selected solvent.

Cartesian coordinates of DFT-optimized ground state geometry of 1a

N	-1.075765	0.074201	-0.948160
C	-0.000053	0.000326	-0.129578
N	1.075679	-0.069648	-0.948379
C	0.763529	0.077316	-2.398050
C	-0.763394	-0.065793	-2.398506
H	1.261479	-0.687865	-2.998395
H	1.094040	1.060391	-2.756165
H	-1.093964	-1.047075	-2.761450
H	-1.261125	0.702354	-2.995216
C	2.424703	-0.032955	-0.474489
C	5.049868	0.035417	0.413306
C	2.902950	1.117671	0.186020
C	3.256550	-1.148597	-0.684169
C	4.581863	-1.099733	-0.235351
C	4.228235	1.135923	0.632803
H	5.233347	-1.954289	-0.380762
H	4.611917	2.010352	1.146787
C	-2.424753	0.035148	-0.474404
C	-5.049669	-0.037600	0.413849
C	-2.902128	-1.117868	0.182554
C	-3.257431	1.150879	-0.680472
C	-4.582572	1.099815	-0.231450
C	-4.227309	-1.138347	0.629544
H	-5.234619	1.954387	-0.374124
H	-4.610415	-2.014693	1.140685
Br	-6.867099	-0.082024	1.036865
C	-2.749956	2.406627	-1.347836

H	-1.707683	2.599607	-1.081306
H	-3.349114	3.271105	-1.050901
H	-2.804150	2.337285	-2.441485
C	-2.012592	-2.313874	0.421876
H	-1.135661	-2.028583	1.009484
H	-1.643731	-2.734456	-0.521213
H	-2.556635	-3.101348	0.948900
C	2.747987	-2.402005	-1.355087
H	3.346723	-3.267756	-1.061012
H	2.801699	-2.329471	-2.448558
H	1.705711	-2.595131	-1.088663
C	2.013990	2.313267	0.429551
H	2.556425	3.096049	0.965148
H	1.133705	2.024668	1.010413
H	1.650962	2.741712	-0.512336
Br	6.867567	0.076942	1.035810

Cartesian coordinates of DFT-optimized transition state geometry of **1a**

N	-1.092625	0.360009	-0.712061
C	0.000449	0.029916	-0.144195
N	1.090171	-0.231658	-0.751792
C	0.681215	0.030365	-2.719848
C	-0.689355	0.325996	-2.700770
H	1.004499	-0.956457	-3.027643
H	1.397013	0.825406	-2.903868
H	-1.406023	-0.442721	-2.972265
H	-1.013324	1.341708	-2.891369
C	2.430719	-0.140977	-0.328715
C	5.107329	0.007456	0.399339
C	2.909982	1.009485	0.340301
C	3.297192	-1.213160	-0.631222
C	4.642443	-1.123882	-0.260620
C	4.257877	1.065548	0.706238
H	5.317509	-1.943557	-0.479988
H	4.639009	1.938253	1.225130
C	-2.430816	0.202931	-0.301301
C	-5.105896	-0.066410	0.399861
C	-2.891783	-1.019928	0.240863
C	-3.315021	1.287101	-0.488610
C	-4.659170	1.136470	-0.133912
C	-4.238707	-1.136394	0.595414
H	-5.347673	1.963495	-0.266746
H	-4.605447	-2.065479	1.017652
Br	-6.951298	-0.250059	0.884149
C	-2.836607	2.605048	-1.046662
H	-1.844933	2.858883	-0.664218

H	-3.529921	3.409505	-0.787741
H	-2.764682	2.577095	-2.140392
C	-1.962653	-2.188807	0.448322
H	-1.139580	-1.927031	1.121968
H	-1.506775	-2.510493	-0.494776
H	-2.500133	-3.039640	0.873994
C	2.798141	-2.455510	-1.327626
H	3.483057	-3.291790	-1.165296
H	2.718594	-2.305693	-2.410790
H	1.806057	-2.738613	-0.967170
C	1.997444	2.162905	0.670935
H	2.550076	2.963259	1.168974
H	1.180056	1.846708	1.328170
H	1.533299	2.577637	-0.230698
Br	6.953864	0.104692	0.904630

Cartesian coordinates of DFT-optimized ground state geometry of **2a**

N	1.063904	-0.284359	3.165469
C	0.000000	0.000000	2.406859
N	-1.063904	0.284359	3.165469
C	-0.748007	0.183623	4.606675
C	0.748007	-0.183623	4.606675
H	-1.374287	-0.583826	5.071128
H	-0.951422	1.136615	5.102297
H	0.951422	-1.136615	5.102297
H	1.374287	0.583826	5.071128
C	-2.374484	0.698241	2.738113
C	-4.911760	1.521462	2.051124
C	-2.633246	2.075295	2.621893
C	-3.370712	-0.274645	2.542237
C	-4.652456	0.161265	2.189466
C	-3.924120	2.477580	2.262891
H	-5.439078	-0.565146	2.019591
H	-4.148996	3.531796	2.150731
C	2.374484	-0.698241	2.738113
C	4.911760	-1.521462	2.051124
C	2.633246	-2.075295	2.621893
C	3.370712	0.274645	2.542237
C	4.652456	-0.161265	2.189466
C	3.924120	-2.477580	2.262891
H	5.439078	0.565146	2.019591
H	4.148996	-3.531796	2.150731
Br	6.674199	-2.091641	1.558091
C	3.074766	1.746578	2.677336
H	2.265232	2.021817	1.992742
H	3.959689	2.341248	2.441288

H	2.764334	2.005956	3.696898
C	1.560137	-3.104323	2.883131
H	0.627359	-2.836327	2.381997
H	1.354946	-3.204150	3.956609
H	1.871177	-4.086491	2.521280
C	-3.074766	-1.746578	2.677336
H	-3.959689	-2.341248	2.441288
H	-2.764334	-2.005956	3.696898
H	-2.265232	-2.021817	1.992742
C	-1.560137	3.104323	2.883131
H	-1.871177	4.086491	2.521280
H	-0.627359	2.836327	2.381997
H	-1.354946	3.204150	3.956609
Br	-6.674199	2.091641	1.558091
C	0.000000	0.000000	0.878593
N	-0.642036	-1.070029	0.459097
C	-1.005811	-1.421583	-0.849153
C	-1.828741	-2.334818	-3.372269
C	-1.834911	-0.614234	-1.670002
C	-0.669200	-2.729311	-1.293727
C	-1.068712	-3.165960	-2.558568
C	-2.225356	-1.080893	-2.930778
H	-0.792746	-4.159120	-2.896577
H	-2.853600	-0.456382	-3.557160
N	0.642036	1.070029	0.459097
C	1.005811	1.421583	-0.849153
C	1.828741	2.334818	-3.372269
C	0.669200	2.729311	-1.293727
C	1.834911	0.614234	-1.670002
C	2.225356	1.080893	-2.930778
C	1.068712	3.165960	-2.558568
H	2.853600	0.456382	-3.557160
H	0.792746	4.159120	-2.896577
C	2.356427	-0.722639	-1.208303
H	2.573576	-0.713298	-0.138267
H	3.275032	-0.980570	-1.742601
H	1.630915	-1.519044	-1.392776
C	-0.096306	3.673271	-0.400636
H	0.458159	3.870141	0.524246
H	-1.067112	3.264302	-0.104104
H	-0.269005	4.629103	-0.903469
C	0.096306	-3.673271	-0.400636
H	-0.458159	-3.870141	0.524246
H	1.067112	-3.264302	-0.104104
H	0.269005	-4.629103	-0.903469
C	-2.356427	0.722639	-1.208303

H	-2.573576	0.713298	-0.138267
H	-3.275032	0.980570	-1.742601
H	-1.630915	1.519044	-1.392776
Br	-2.374524	-2.947451	-5.113647
Br	2.374524	2.947451	-5.113647

Cartesian coordinates of DFT-optimized ground state geometry of 2b

N	1.100979	-0.027162	2.806072
C	0.000000	0.000000	2.048459
N	-1.100979	0.027162	2.806072
C	-0.770469	0.025856	4.247141
C	0.770469	-0.025856	4.247141
H	-1.225393	-0.841779	4.733296
H	-1.162836	0.929136	4.722663
H	1.162836	-0.929136	4.722663
H	1.225393	0.841779	4.733296
C	-2.474113	0.111881	2.382659
C	-5.148972	0.291189	1.742957
C	-3.054571	1.384859	2.242101
C	-3.213723	-1.073808	2.225033
C	-4.567555	-0.964037	1.894248
C	-4.411021	1.459039	1.910897
H	-5.163267	-1.858127	1.750894
H	-4.888031	2.424578	1.783692
C	2.474113	-0.111881	2.382659
C	5.148972	-0.291189	1.742957
C	3.054571	-1.384859	2.242101
C	3.213723	1.073808	2.225033
C	4.567555	0.964037	1.894248
C	4.411021	-1.459039	1.910897
H	5.163267	1.858127	1.750894
H	4.888031	-2.424578	1.783692
C	2.572969	2.430037	2.372819
H	1.734994	2.512823	1.672787
H	3.294430	3.222366	2.162068
H	2.191516	2.595050	3.387872
C	2.248840	-2.646497	2.438404
H	1.311566	-2.607024	1.878559
H	2.006072	-2.809608	3.495978
H	2.811882	-3.518418	2.098603
C	-2.572969	-2.430037	2.372819
H	-3.294430	-3.222366	2.162068
H	-2.191516	-2.595050	3.387872
H	-1.734994	-2.512823	1.672787
C	-2.248840	2.646497	2.438404
H	-2.811882	3.518418	2.098603

H	-1.311566	2.607024	1.878559
H	-2.006072	2.809608	3.495978
C	0.000000	0.000000	0.522138
N	-0.473918	-1.155067	0.101008
C	-0.806407	-1.547025	-1.202881
C	-1.535031	-2.541375	-3.726143
C	-1.748820	-0.851754	-2.005686
C	-0.313946	-2.799614	-1.659521
C	-0.667798	-3.273301	-2.924442
C	-2.086813	-1.353157	-3.266846
H	-0.273097	-4.220600	-3.276556
H	-2.798905	-0.815276	-3.883811
N	0.473918	1.155067	0.101008
C	0.806407	1.547025	-1.202881
C	1.535031	2.541375	-3.726143
C	0.313946	2.799614	-1.659521
C	1.748820	0.851754	-2.005686
C	2.086813	1.353157	-3.266846
C	0.667798	3.273301	-2.924442
H	2.798905	0.815276	-3.883811
H	0.273097	4.220600	-3.276556
C	2.453195	-0.381236	-1.503547
H	2.782705	-0.247131	-0.469738
H	3.331812	-0.600742	-2.116407
H	1.803135	-1.258009	-1.529444
C	-0.570110	3.650426	-0.781114
H	-0.070651	3.885502	0.165983
H	-1.507191	3.146517	-0.524191
H	-0.817580	4.592336	-1.278720
C	0.570110	-3.650426	-0.781114
H	0.070651	-3.885502	0.165983
H	1.507191	-3.146517	-0.524191
H	0.817580	-4.592336	-1.278720
C	-2.453195	0.381236	-1.503547
H	-2.782705	0.247131	-0.469738
H	-3.331812	0.600742	-2.116407
H	-1.803135	1.258009	-1.529444
Cl	-1.973678	-3.153320	-5.324362
Cl	6.853311	-0.403115	1.334996
Cl	1.973678	3.153320	-5.324362
Cl	-6.853311	0.403115	1.334996

Cartesian coordinates of DFT-optimized ground state geometry of **2c**

N	1.101267	-0.024802	2.583443
C	0.000000	0.000000	1.825402
N	-1.101267	0.024802	2.583443

C	-0.770526	0.022504	4.023990
C	0.770526	-0.022504	4.023990
H	-1.221741	-0.848014	4.508760
H	-1.166845	0.923034	4.501616
H	1.166845	-0.923034	4.501616
H	1.221741	0.848014	4.508760
C	-2.473398	0.105878	2.157272
C	-5.129123	0.277810	1.490340
C	-3.057265	1.378615	2.018020
C	-3.207487	-1.083144	1.987113
C	-4.557468	-0.977736	1.642028
C	-4.409529	1.450365	1.672027
H	-5.162496	-1.863305	1.482768
H	-4.904034	2.406370	1.539156
C	2.473398	-0.105878	2.157272
C	5.129123	-0.277810	1.490340
C	3.057265	-1.378615	2.018020
C	3.207487	1.083144	1.987113
C	4.557468	0.977736	1.642028
C	4.409529	-1.450365	1.672027
H	5.162496	1.863305	1.482768
H	4.904034	-2.406370	1.539156
C	2.559446	2.435964	2.132618
H	1.722831	2.512806	1.429747
H	3.277370	3.232206	1.924306
H	2.172732	2.598697	3.146055
C	2.255368	-2.640193	2.228058
H	1.314668	-2.604729	1.673738
H	2.019462	-2.796453	3.288280
H	2.817516	-3.513555	1.890449
C	-2.559446	-2.435964	2.132618
H	-3.277370	-3.232206	1.924306
H	-2.172732	-2.598697	3.146055
H	-1.722831	-2.512806	1.429747
C	-2.255368	2.640193	2.228058
H	-2.817516	3.513555	1.890449
H	-1.314668	2.604729	1.673738
H	-2.019462	2.796453	3.288280
C	0.000000	0.000000	0.298555
N	-0.447919	-1.166394	-0.120998
C	-0.765903	-1.560429	-1.431420
C	-1.461679	-2.555648	-3.952524
C	-1.727144	-0.886736	-2.230724
C	-0.237836	-2.796135	-1.895025
C	-0.575805	-3.272415	-3.164431
C	-2.051031	-1.389897	-3.495472

H	-0.163412	-4.205213	-3.535771
H	-2.778425	-0.882181	-4.120960
N	0.447919	1.166394	-0.120998
C	0.765903	1.560429	-1.431420
C	1.461679	2.555648	-3.952524
C	0.237836	2.796135	-1.895025
C	1.727144	0.886736	-2.230724
C	2.051031	1.389897	-3.495472
C	0.575805	3.272415	-3.164431
H	2.778425	0.882181	-4.120960
H	0.163412	4.205213	-3.535771
C	2.459667	-0.328487	-1.726244
H	2.705270	-0.223729	-0.666923
H	3.390042	-0.476642	-2.282243
H	1.859921	-1.234665	-1.837697
C	-0.666211	3.627249	-1.018307
H	-0.172605	3.873432	-0.071115
H	-1.591579	3.102176	-0.760788
H	-0.934759	4.562942	-1.516950
C	0.666211	-3.627249	-1.018307
H	0.172605	-3.873432	-0.071115
H	1.591579	-3.102176	-0.760788
H	0.934759	-4.562942	-1.516950
C	-2.459667	0.328487	-1.726244
H	-2.705270	0.223729	-0.666923
H	-3.390042	0.476642	-2.282243
H	-1.859921	1.234665	-1.837697
F	-1.785682	-3.025333	-5.183299
F	1.785682	3.025333	-5.183299
F	-6.431200	0.361644	1.157140
F	6.431200	-0.361644	1.157140

Cartesian coordinates of DFT-optimized ground state geometry of 2d

N	1.099163	-2.611259	-0.030989
C	-0.001730	-1.853170	-0.004769
N	-1.103551	-2.610031	0.018036
C	-0.773715	-4.049870	0.013509
C	0.767524	-4.050711	-0.032453
H	-1.225848	-4.533498	-0.857328
H	-1.169761	-4.528376	0.913868
H	1.163093	-4.526011	-0.934711
H	1.218926	-4.538475	0.836468
C	-2.476595	-2.184002	0.104516
C	-5.180275	-1.505782	0.290395
C	-3.057983	-2.044334	1.376120
C	-3.218475	-2.018010	-1.077428

C	-4.568040	-1.675727	-0.955240
C	-4.410874	-1.700284	1.441340
H	-5.151365	-1.529971	-1.860928
H	-4.872781	-1.575944	2.417698
C	2.472936	-2.186821	-0.113427
C	5.178419	-1.512785	-0.291275
C	3.056750	-2.042196	-1.382986
C	3.213247	-2.027760	1.070734
C	4.563456	-1.687596	0.952619
C	4.410750	-1.700110	-1.444147
H	5.145383	-1.547169	1.860091
H	4.874403	-1.571733	-2.419111
C	2.571303	-2.181811	2.426031
H	1.733175	-1.482074	2.513026
H	3.293092	-1.974467	3.219590
H	2.188075	-3.197006	2.588891
C	2.254316	-2.242816	-2.646066
H	1.319657	-1.677840	-2.613085
H	2.005169	-3.299785	-2.806305
H	2.822304	-1.910021	-3.517959
C	-2.579346	-2.166894	-2.434640
H	-3.302228	-1.954565	-3.225885
H	-2.198192	-3.181984	-2.602955
H	-1.740062	-1.468310	-2.519953
C	-2.253271	-2.252334	2.636533
H	-2.819814	-1.925041	3.511447
H	-1.318955	-1.686703	2.605135
H	-2.003397	-3.310148	2.790025
C	-0.000805	-0.327178	-0.001889
N	-0.453508	0.096532	-1.165026
C	-0.775381	1.405364	-1.554733
C	-1.478091	3.982119	-2.549010
C	-1.729472	2.207179	-0.875291
C	-0.261046	1.874525	-2.792295
C	-0.604133	3.148402	-3.249919
C	-2.043388	3.473183	-1.378145
H	-0.179755	3.492817	-4.191411
H	-2.768925	4.076328	-0.834798
N	0.452469	0.091502	1.162847
C	0.776467	1.398251	1.557568
C	1.483710	3.970013	2.561454
C	0.262586	1.863828	2.796475
C	1.732159	2.200982	0.881087
C	2.048322	3.464360	1.388656
C	0.607806	3.135584	3.258767
H	2.775154	4.068176	0.847790

H	0.183550	3.477494	4.201196
C	2.466488	1.690033	-0.330879
H	2.822747	0.668104	-0.172334
H	3.331366	2.323043	-0.552192
H	1.829592	1.678566	-1.217708
C	-0.630497	0.987258	3.640167
H	-0.135901	0.039303	3.882994
H	-1.564018	0.728375	3.129661
H	-0.886653	1.488149	4.578780
C	0.630175	0.999308	-3.639330
H	0.134777	0.052039	-3.883086
H	1.564497	0.739092	-3.130959
H	0.884987	1.502005	-4.577339
C	-2.464358	1.693359	0.335115
H	-2.818723	0.671104	0.174772
H	-3.330461	2.324733	0.556371
H	-1.828342	1.681846	1.222596
C	6.627753	-1.099910	-0.385039
H	7.215772	-1.511126	0.440763
H	6.724984	-0.008339	-0.341963
H	7.079114	-1.431233	-1.324612
C	-6.628373	-1.090285	0.390635
H	-6.719219	0.002571	0.412531
H	-7.093437	-1.473590	1.303609
H	-7.207971	-1.448071	-0.465145
C	1.807517	5.360028	3.055212
H	2.845727	5.633480	2.838008
H	1.657521	5.446820	4.136290
H	1.170583	6.116893	2.578540
C	-1.797797	5.374915	-3.037444
H	-1.135477	6.124127	-2.583770
H	-2.824684	5.663580	-2.788968
H	-1.680292	5.456582	-4.123027

HOMO: -4.85 eV   LUMO: -1.25 eV
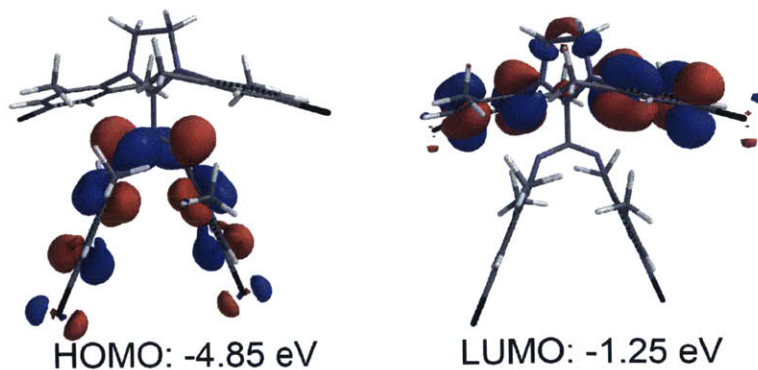
Figure 11. DFT-computed HOMO and LUMO orbitals of **2a**.

Crystallographic Information

Low-temperature (100 K) diffraction data (φ- and ω-scans) were collected on a Bruker X8 Kappa Duo four-circle diffractometer coupled to a Smart Apex2 CCD detector or a Siemens Platform three-circle diffractometer coupled to a Bruker-AXS Smart Apex CCD detector, with Mo K_α radiation ($\lambda = 0.71073$ Å) from an $I\mu S$ micro-source. The diffractometers were purchased with the help of funding from the National Science Foundation (NSF) under Grant Number CHE-0946721. The structure was solved by direct methods using SHELXS[52] and refined against F^2 on all data by full-matrix least squares with SHELXL-97[53] following established refinement strategies[54]. X-ray crystallographic structures of 2b (A), 2c (B), 3a (C), 3b (D), and 3c (E)
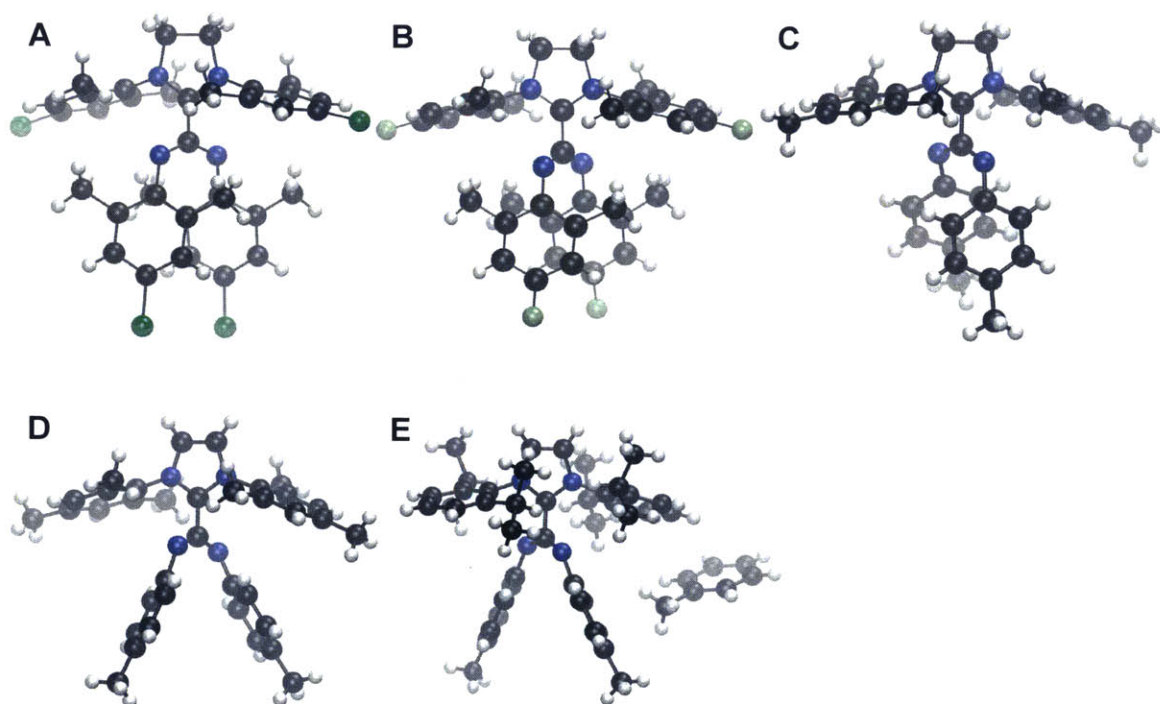
Color legend for spheres representing atoms: black = C, gray = H, blue = N, green = Cl, lime-green = F. Structure in E is co-crystallized with toluene.

Synthetic Procedures and Characterization

Synthesis of Previously Reported Compounds

Imidazolium salt **1a·HCl** was prepared as reported previously.[24] Previously reported imidazolium salts **1b·HCl** and **1c·HCl** were prepared analogously to **1a·HCl**, using the route

which had been developed by Kuhn and Grubbs.[55-57] $1a^-CO_2$ adduct was prepared as reported previously.[24]

Synthesis and Characterization of N-Heterocyclic Carbenes

1,3-bis(4-bromo-2,6-dimethylphenyl)-4,5-dihydroimidazol-2-ylidene **1a**. To 4.73 g (10.0 mmol) of imidazolium salt **1a·HCl** in a 40-mL scintillation vial in the glove box was added 10 mL anhydrous THF followed by 10. mL of 1.0 M KHMDS solution in THF (10. mmol, 1.0 equiv). The vial was closed and the mixture was agitated for 5-10 min until all of the **1a·HCl** had gone into solution, with concomitant formation of suspended fine KCl particulates. The reaction mixture was filtered through a 0.45 μm PTFE syringe filter (NOTE: these syringe filters are easily clogged; four filters had to be used to accomplish complete filtration). The solution was concentrated to dryness on the Schlenk line. The resulting crystalline solid was crushed to a powder in the glove box and triturated with anhydrous hexanes (3 x 8mL), decanting the rinsings each time. To the remaining solid was added anhydrous THF (13 mL), and the resulting mixture was re-filtered through a 0.45 μm PTFE syringe filter to remove residual KCl. The filtrate was again concentrated to dryness on the Schlenk line; the resulting solid was crushed to a powder in the glove box and triturated with hexanes (8 mL). Vacuum filtration to afforded **1a** as a beige powder (1.30 g, 29.8% yield). ^{1}H NMR (400 MHz, toluene-d^8): δ 7.07 (s, 4H), 3.09 (s, 4H), 2.00 (s, 12H). ^{13}C NMR (100 MHz, toluene-d^8): δ 244.45, 140.82, 138.79, 131.53, 120.75, 50.38, 17.87 ppm.

1,3-bis(4-chloro-2,6-dimethylphenyl)-4,5-dihydroimidazol-2-ylidene **1b**. To 383.7 mg (1.000 mmol) of imidazoium salt **1b·HCl** in a 20-mL scintillation vial in the glove box was added 4 mL anhydrous toluene followed by 1.00 mL of 1.0 M KHMDS solution in THF (1.0 mmol, 1.0 equiv). The vial was closed and the mixture was agitated for 5-10 min until all of the **1b·HCl** had gone into solution, with concomitant formation of suspended fine KCl particulates. The reaction mixture was filtered through a 0.45 μm PTFE syringe filter. The solution was concentrated to dryness on the Schlenk line. The resulting white crystalline solid was triturated in the glove box with anhydrous hexanes (3 x 2mL) while carrying out vacuum filtration over a medium-porosity frit. Drying under vacuum afforded **1b** as a white crystalline solid (267 mg,

76.9% yield). ^{1}H NMR (400 MHz, toluene-d^8): δ 6.92 (s, 4H), 3.10 (s, 4H), 2.02 (s, 12H). ^{13}C NMR (100 MHz, toluene-d^8): δ 244.66, 140.36, 138.45, 132.49, 128.56, 50.45, 17.96 ppm.

1,3-bis(4-fluoro-2,6-dimethylphenyl)-4,5-dihydroimidazol-2-ylidene **1c** was prepared following the identical protocol as for **1b**, except reduced in scale by ½ and using **1c·HCl** in place of **1b·HCl** as the starting material. **1b** was isolated as a white crystalline solid (119 mg, 75.7% yield). ^{1}H NMR (400 MHz, toluene-d^8): δ 6.62 (d, $^2J_{1H-19F}$ = 9.0 Hz, 4H), 3.13 (s, 4H), 2.07 (s, 12H). ^{13}C NMR (100 MHz, toluene-d^8): δ 245.00, 161.48 (d, $^1J_{13C-19F}$ = 244 Hz), 138.83 (d, $^3J_{13C-19F}$ = 8.70 Hz), 137.87 (d, $^4J_{13C-19F}$ = 2.87 Hz), 115.01 (d, $^2J_{13C-19F}$ = 21.8 Hz), 50.62, 18.19 (d, $^4J_{13C-19F}$ = 1.52 Hz). ^{19}F NMR (376.5 MHz, toluene-d^8): δ -116.22 (t, $^2J_{19F-1H}$ = 9.0 Hz) ppm.

<u>Synthesis and Characterization of Novel Compounds</u>

1,3-bis(4-bromo-2,6-dimethylphenyl)-4,5-dihydroimidazolium-2-(*N,N'*-bis(4-bromo-2,6-dimethylphenyl)amidinate) 2a. To **1a** (14 mg, 0.032 mmol) in a J. Young NMR tube was added 0.50 mL anhydrous toluene-d^8. The reaction mixture was heated at 110 °C in an oil bath for 31 hours, during the course of which time the solution became dark yellow, and crystallization of product was observed. The reaction mixture was concentrated *in vacuo* affording **2a** as a crystalline yellow solid (13 mg, 96% yield, 93% purity by ^{1}H NMR*). ^{1}H NMR (400 MHz, CD$_2$Cl$_2$): δ 7.31 (s, 4H), 6.42 (s, 4H), 4.28 (s, 4H), 2.62 (s, 12 H), 1.35 (s, 12H). ^{13}C NMR (100 MHz, CD$_2$Cl$_2$): δ 165.47, 147.64, 139.93, 137.82, 134.26, 132.14, 130.91, 128.74, 123.80, 111.07, 49.55, 19.09, 18.56 ppm. FT-ICR-ESI HRMS: calcd. for C$_{36}$H$_{36}$Br$_4$N$_4$ [M + H]$^+$, most abundant m/z = 844.9721; found, 844.9713. FT-IR-ATR: 3037.4 (w), 2966.3 (w), 2910.7 (w), 1576.8 (m), 1544.7 (s), 1528.9 (s), 1464.2 (m, br), 1321.0 (s), 1290.4 (m), 1030.4 (w), 1000.2 (w), 871.3 (m), 856.0 (s), 838.0 (m), 743.1 (m), 693.7 (m) cm^{-1}. Dec. pt. 256 °C (indicated by color change to dark orange/brown and confirmed by LC-MS), followed by melting at 258 °C accompanied by evolution of gas.

1,3-bis(4-chloro-2,6-dimethylphenyl)-4,5-dihydroimidazolium-2-(*N,N'*-bis(4-chloro-2,6-dimethylphenyl)amidinate) 2b was prepared following the identical protocol as for **2a**, except using **1b** (34 mg 0.098 mmol) as the starting material. Product was obtained as a crystalline

yellow solid (31 mg, 95% yield, 94% purity by ^{1}H NMR*). ^{1}H NMR (400 MHz, CD$_2$Cl$_2$): δ 7.15 (s, 4H), 6.28 (s, 4H), 4.28 (s, 4H), 2.63 (s, 12 H), 1.36 (s, 12H). ^{13}C NMR (100 MHz, CD$_2$Cl$_2$): δ 165.56, 147.21, 139.72, 138.04, 135.53, 133.76, 130.44, 129.14, 125.84, 123.21, 49.60, 19.17, 18.68 ppm. FT-ICR-ESI HRMS: calcd. for C$_{36}$H$_{36}$Cl$_4$N$_4$ [M + H]$^+$, most abundant m/z = 667.1754; found, 667.1768. FT-IR-ATR: 3046.9 (w), 2914.1 (w), 1584.2 (m), 1546.3 (s), 1530.0(s), 1466.8 (m, br), 1322.1 (m), 1292.7 (m), 1024.8 (w), 1000.4 (w), 877.6 (m), 854.1 (s), 838.9 (m), 744.1 (w), 699.9 (w) cm^{-1}. Dec. pt. 250 °C (indicated by color change to dark orange/brown), followed by melting at 255 °C accompanied by evolution of gas.

1,3-bis(4-fluoro-2,6-dimethylphenyl)-4,5-dihydroimidazolium-2-(N,N'-bis(4-fluoro-2,6-dimethylphenyl)amidinate) 2c was prepared following the identical protocol as for **2a**, except using **1c** (30 mg 0.095 mmol) as the starting material. Product was obtained as a crystalline yellow solid (30 mg, ~100% yield, 67% purity*). ^{1}H NMR (400 MHz, CD$_2$Cl$_2$): δ 6.87 (d, $^2J_{1H\text{-}19F}$ = 9.0 Hz, 4H), 6.01 (d, $^2J_{1H\text{-}19F}$ = 9.6 Hz, 4H), 4.27 (s, 4H), 2.67 (s, 12 H), 1.37 (s, 12H). ^{13}C NMR (100 MHz, CD$_2$Cl$_2$): δ 165.77, 163.08 (d, $^1J_{13C\text{-}19F}$ = 248 Hz), 156.69 (d, $^1J_{13C\text{-}19F}$ = 234 Hz), 144.73 (d, $^4J_{13C\text{-}19F}$ = 2.24 Hz), 140.52 (d, $^3J_{13C\text{-}19F}$ = 9.42 Hz), 138.71, 131.29 (d, $^4J_{13C\text{-}19F}$ = 2.83 Hz), 130.02 (d, $^3J_{13C\text{-}19F}$ = 7.57 Hz), 115.78 (d, $^2J_{13C\text{-}19F}$ = 22.5 Hz), 112.10 (d, $^2J_{13C\text{-}19F}$ = 20.9 Hz), 49.62, 19.46 (d, $^4J_{13C\text{-}19F}$ = 1.48 Hz), 19.01 (d, $^4J_{13C\text{-}19F}$ = 1.21 Hz). ^{19}F NMR (376.5 MHz, CD$_2$Cl$_2$): δ -113.20 (t, $^2J_{19F\text{-}1H}$ = 9.0 Hz), -128.87 (t, $^2J_{19F\text{-}1H}$ = 9.6 Hz) ppm. FT-ICR-ESI HRMS: calcd. for C$_{36}$H$_{36}$F$_4$N$_4$ [M + H]$^+$, most abundant m/z = 601.2949; found, 601.2924. FT-IR-ATR: 3056.4 (w), 2947.3 (w), 2909.5 (w), 1548.8 (m, br), 1478.5 (m, br), 1287.1 (s), 1129.7 (m), 1118.7 (m), 1022.7 (m, br), 854.0 (s), 740.0 (w), 698.3 (w) cm^{-1}. Dec. pt. 252 °C (indicated by color change to dark orange/brown), followed by melting at 257-258 °C accompanied by evolution of gas.

1,3-bis(2,4,6-trimethylphenyl)-4,5-dihydroimidazolium-2-(N,N'-bis(2,4,6-trimethylphenyl)amidinate) 2d was prepared following the identical protocol as for **2a**, except using SIMes (30 mg, 90% pure, 0.088 mmol) as the starting material. Product was obtained as a mixture of waxy and crystalline yellow solid (28 mg, 98% yield, 76% purity*). ^{1}H NMR (400 MHz, CD$_2$Cl$_2$): δ 6.93 (s, 4H), 6.07 (s, 4H), 4.23 (s, 4H), 2.63 (s, 12 H), 2.28 (s, 6H), 1.90 (s,

6H), 1.34 (s, 12H). ^{13}C NMR (100 MHz, CD$_2$Cl$_2$): δ 165.67, 146.49, 139.78, 138.09, 137.39, 133.02, 129.68, 128.61, 126.91, 126.83, 49.55, 21.14, 20.40, 19.23, 18.61 ppm. FT-ICR-ESI HRMS: calcd. for C$_{36}$H$_{36}$Cl$_4$N$_4$ [M + H]$^+$, most abundant m/z = 585.3952; found, 585.3932. FT-IR-ATR: 3023.2 (w, shoulder), 2914.1 (w), 1543.5 (s), 1480.2 (m, br), 1322.0 (m, br), 1280.5 (m), 1034.0 (w, br), 848.0 (m), 709.9 (w) cm^{-1}. Dec. pt. 211-215 °C (indicated by color change to dark orange/brown) with concomitant melting and evolution of gas.

1,3-bis(2,4,6-trimethylphenyl)-4,5-dihydroimidazolium-2-(N,N'-di-p-tolylamidinate) 3a.
In the glove box, to SIMes (15 mg, 90% pure, 0.044 mmol) and 1,3-di-p-tolylcarbodiimide (11.1 mg, 0.0500 mmol) in a 1-dram vial was added anhydrous toluene-d^8 (0.37 mL). The mixture was agitated for 1-2 min, transferred to a J. Young NMR tube for NMR analysis, revealing quantitative conversion of SIMes to **3a**. The sample was transferred to a 20-mL vial with the assistance of anhydrous toluene (3 x 1 mL) and concentrated *in vacuo*. The crude product was then rinsed with anhydrous hexanes (1.5 mL + 1.0 mL), cooling the vial to -30 °C before removing the rinses via syringe. The remainder was dried *in vacuo* to afford **3a** as a crystalline yellow solid (20.7 mg, 89% yield). ^{1}H NMR (400 MHz, CD$_2$Cl$_2$): δ 6.96 (d, J = 0.5 Hz, 4H), 6.40 (md, J$_{doublet}$ = 8.5 Hz, 4H), 5.75 (ddd, J =8.2, 2.5, 2.4 Hz, 4H), 4.24 (s, 4H), 2.53 (s, 12 H), 2.32 (s, 6H), 1.98 (s, 6H). ^{13}C NMR (100 MHz, CD$_2$Cl$_2$): δ 165.46, 149.39, 142.66, 139.62, 137.20, 132.64, 129.42, 127.74, 126.26, 121.11, 49.62, 21.26, 20.65, 18.17 ppm. FT-ICR-ESI HRMS: calcd. for C$_{36}$H$_{40}$N$_4$ [M + H]$^+$, most abundant m/z = 529.3326; found, 529.3318.

1,3-bis(2,4,6-trimethylphenyl)imidazolium-2-(N,N'-di-p-tolylamidinate) 3b. In the glove box, to IMes (15 mg, 0.049 mmol) and 1,3-di-p-tolylcarbodiimide (11.1 mg, 0.0500 mmol) in a 1-dram vial was added anhydrous toluene-d^8 (0.37 mL). The mixture was agitated for 1-2 min, transferred to a J. Young NMR tube for NMR analysis, revealing quantitative conversion of IMes to **3b**. The sample was transferred to a 20-mL vial with the assistance of anhydrous toluene (3 x 1 mL) and concentrated *in vacuo*. The crude product was then rinsed with anhydrous hexanes (1.5 mL + 1.0 mL), cooling the vial to -30 °C before removing the rinses via syringe. The remainder was dissolved in DCM (2 mL), transferred to a 1-dram vial and concentrated *in vacuo* to afford **3b** as a crystalline yellow solid (21.5 mg, 83% yield). ^{1}H NMR (400 MHz, CD$_2$Cl$_2$): δ 7.10 (s, 2H), 7.02 (d, J = 0.5 Hz, 4H), 6.40 (md, J$_{doublet}$ = 8.4 Hz, 4H), 5.84 (ddd, J =8.2, 2.5, 2.5

Hz, 4H), 2.36 (s, 6 H), 2.29 (s, 12H), 2.00 (s, 6H). ^{13}C NMR (100 MHz, CD$_2$Cl$_2$): δ 149.76, 149.34, 142.22, 140.33, 136.19, 133.00, 129.14, 127.74, 126.22, 121.09, 120.52, 21.32, 20.65, 18.06 ppm. FT-ICR-ESI HRMS: calcd. for C$_{36}$H$_{40}$N$_4$ [M + H]$^+$, most abundant m/z = 527.3169; found, 527.3173.

1,3-bis(2,6-diisopropylphenyl)imidazolium-2-(*N,N'*-di-*p*-tolylamidinate) 3c In the glove box, to IMes (19 mg, 0.049 mmol) and 1,3-di-*p*-tolylcarbodiimide (11.1 mg, 0.0500 mmol) in a 1-dram vial was added anhydrous toluene-d^8 (0.37 mL). The mixture was agitated for 1-2 min, transferred to a J. Young NMR tube for NMR analysis, revealing quantitative conversion of Dipp to **3c**. The sample was transferred to a 20-mL vial with the assistance of anhydrous toluene (3 x 1 mL) and concentrated *in vacuo*. The crude product was then rinsed with anhydrous hexanes (1.5 mL), cooling the vial to -30 °C before removing the rinse via syringe. The remainder was dissolved in DCM (2 mL), transferred to a 1-dram vial and concentrated *in vacuo* to afford **3c** as a lemon-yellow powdery solid (26.8 mg, 90% yield). ^{1}H NMR (400 MHz, CD$_2$Cl$_2$): δ 7.45 (t, J = 7.6 Hz, 2H), 7.28 (d, J = 7.6 Hz, 4H), 7.16 (s, 2H), 6.34 (md, J = 8.5 Hz, 4H), 5.77 (ddd, J = 8.1, 2.6, 2.5 Hz, 4H), 2.88 (sept, J = 6.9 Hz, 4 H), 1.96 (s, 6H), 1.30 (d, J = 6.8 Hz, 12H), 1.20 (d, J = 6.9 Hz, 12H). ^{13}C NMR (100 MHz, CD$_2$Cl$_2$): δ 150.61, 149.59, 146.15, 141.31, 133.20, 130.51, 127.40, 125.84, 124.10, 121.76, 120.82, 29.70, 25.22, 23.15, 20.64 ppm. FT-ICR-ESI HRMS: calcd. for C$_{42}$H$_{50}$N$_4$ [M + H]$^+$, most abundant m/z = 611.4108; found, 611.4119.

*Integration of impurity resonances and the corresponding resonances for the NHC (both normalized against one of the toluene-d^7 peaks) – e.g., in the aromatic region (6-8 ppm) – was used to quantify the impurity present in the NHC-CDI adduct at the conclusion of the reaction. All characterization was carried out after rinsing NHC-CDI crystals with toluene (3 x 1 mL) and hexane (2 x 2 mL) (or just hexane (2 x 2 mL) in the case of **2d**). Purity in each case was confirmed by ^{1}H NMR to be >95% (*vide infra*).

4.5 Spectra
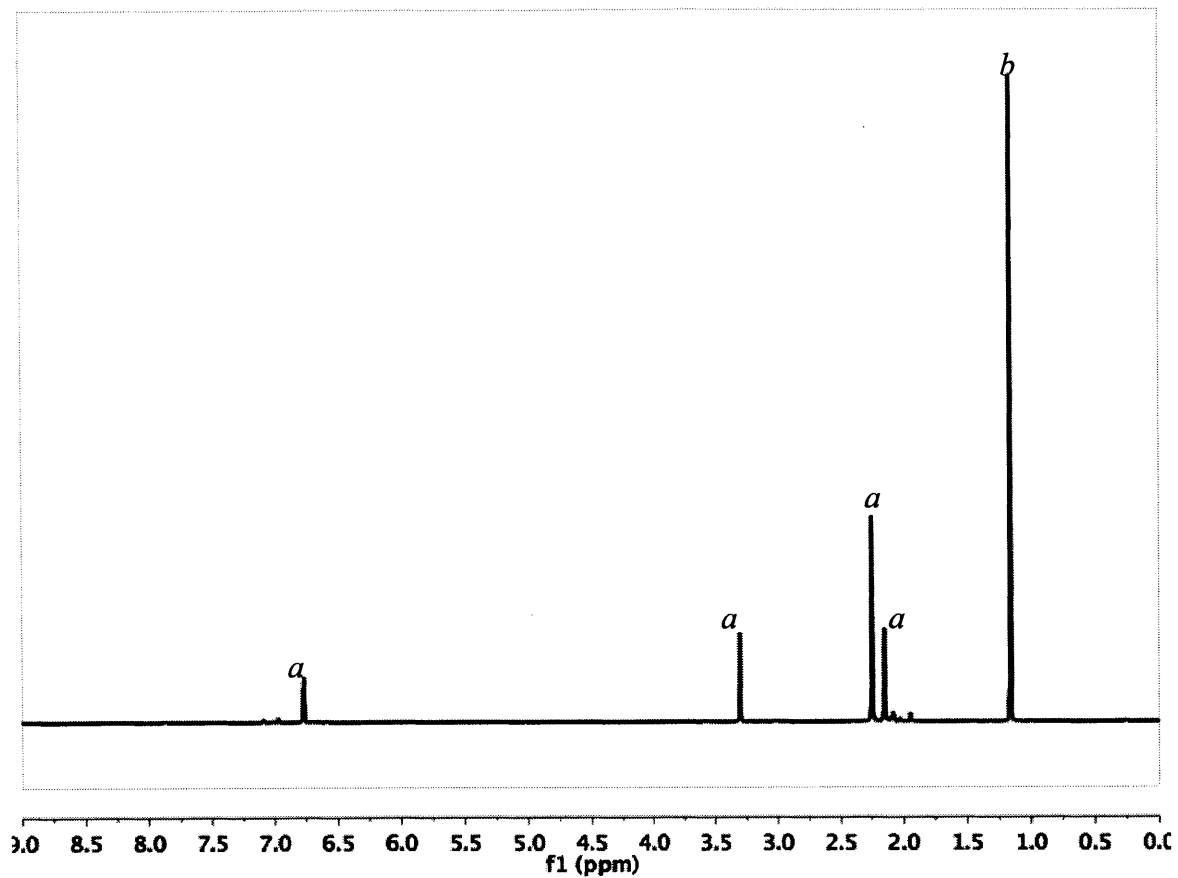
Figure 12. ^{1}H NMR of SIMes (0.091 M) + DTC (0.11 M) in toluene-d^8 at. 25 °C. Resonances (a) assigned to free SIMes. Resonance (b) was assigned to the (CH$_3$)$_3$CN protons of the free DTC. No adduct formation was observed.
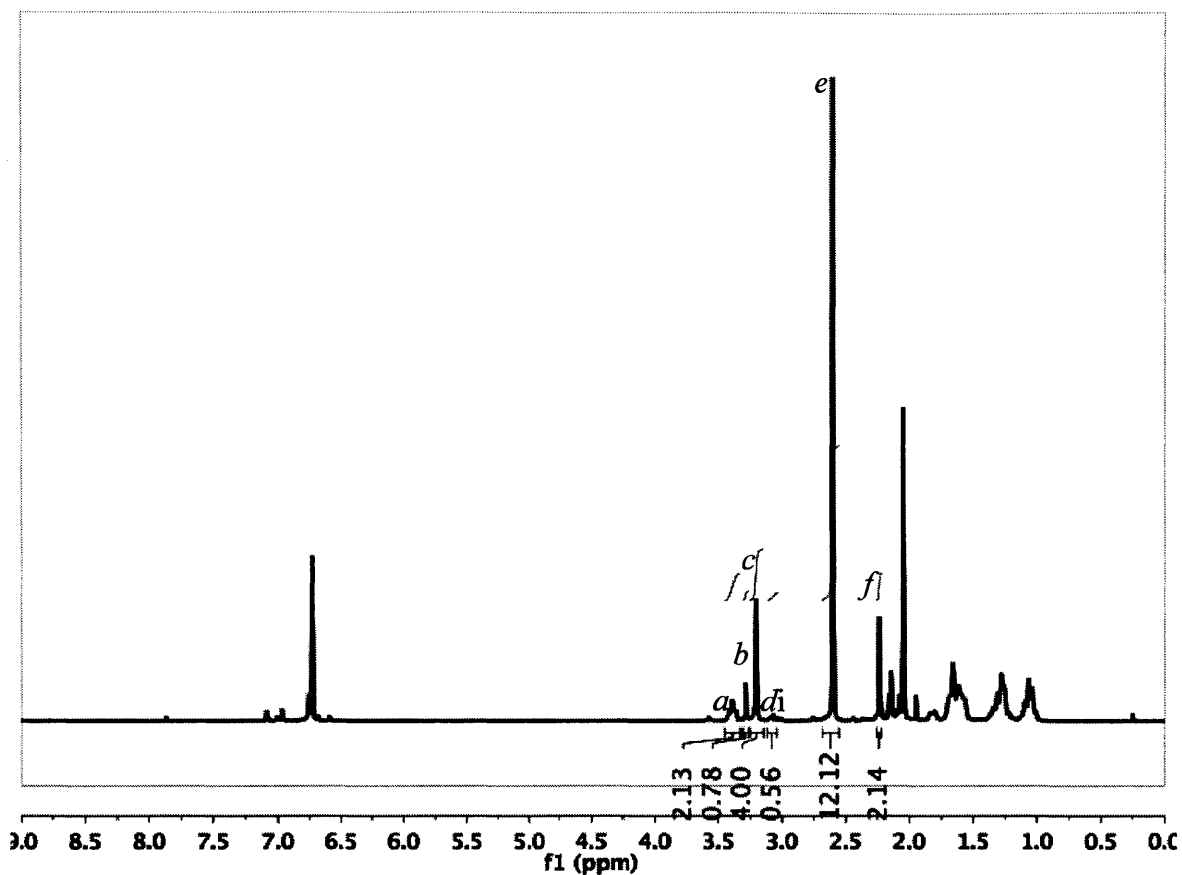
Figure 13. ^{1}H NMR of SIMes (0.13 M) + DCC (0.14 M) in toluene-d^8 at. 25 °C. The following resonances were assigned and used for calculations of the K_c:(a) the –CHN protons of the DCC portion of SIMes-DCC adduct, (b) the imidazol-2-ylidene backbone CH_2-CH_2 protons of free SIMes, (c) the imidazolinium backbone CH_2-CH_2 protons, (d) the –CHN protons of free DCC, (e) the 2,6-CH_3 protons of the SIMes portion of the SIMes-DCC adduct, and (f) the 2,6-CH_3 protons of free SIMes.

333
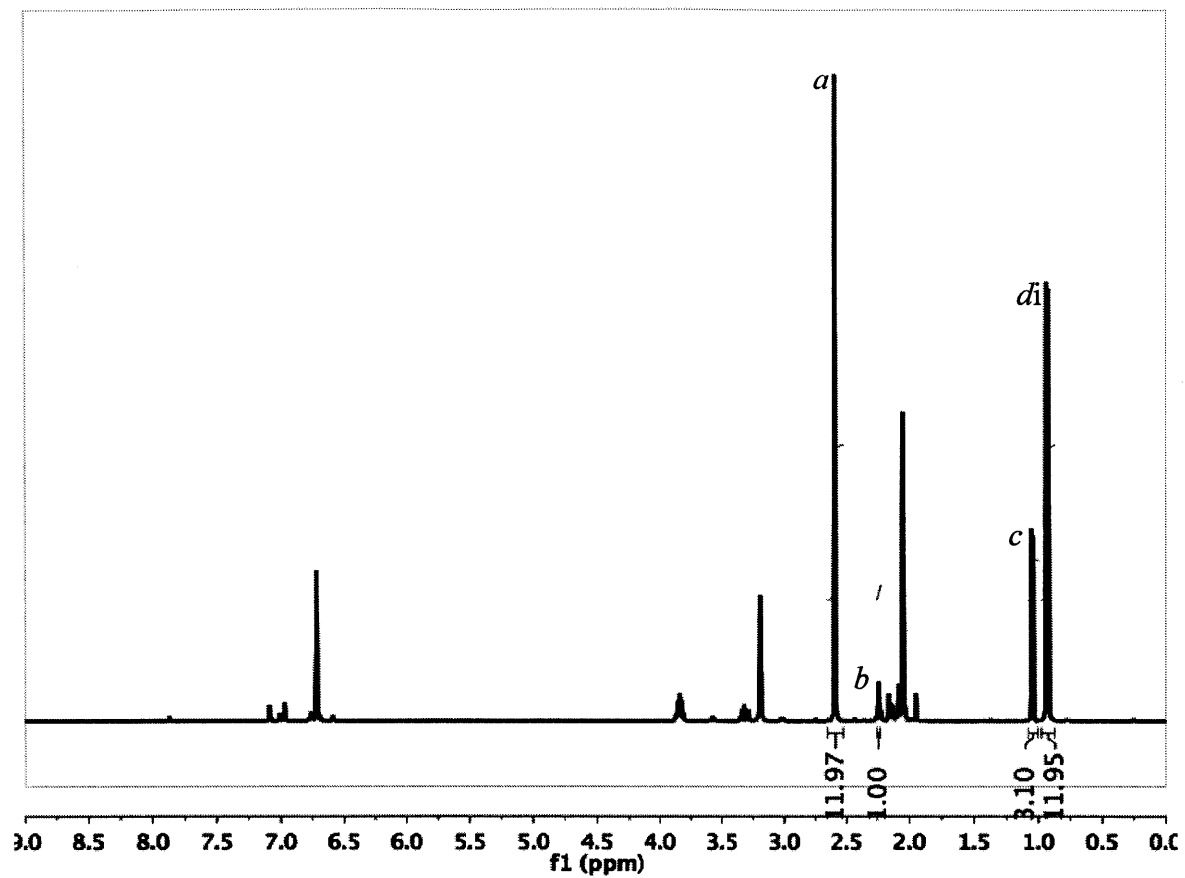
Figure 14. ^{1}H NMR of SIMes (0.091 M) + DIC (0.11 M) in toluene-d^8 at. 25 °C. The following resonances were assigned and used for calculations of the K_c:(*a*) the *2,6*-CH$_3$ protons of the SIMes portion of the SIMes-DIC adduct, (*b*) the *2,6*-CH$_3$ protons of free SIMes, (*c*) the (CH$_3$)$_2$CHN protons of free DIC, and (*d*) the (CH$_3$)$_2$CHN protons of the DIC portion of the SIMes-DIC adduct.
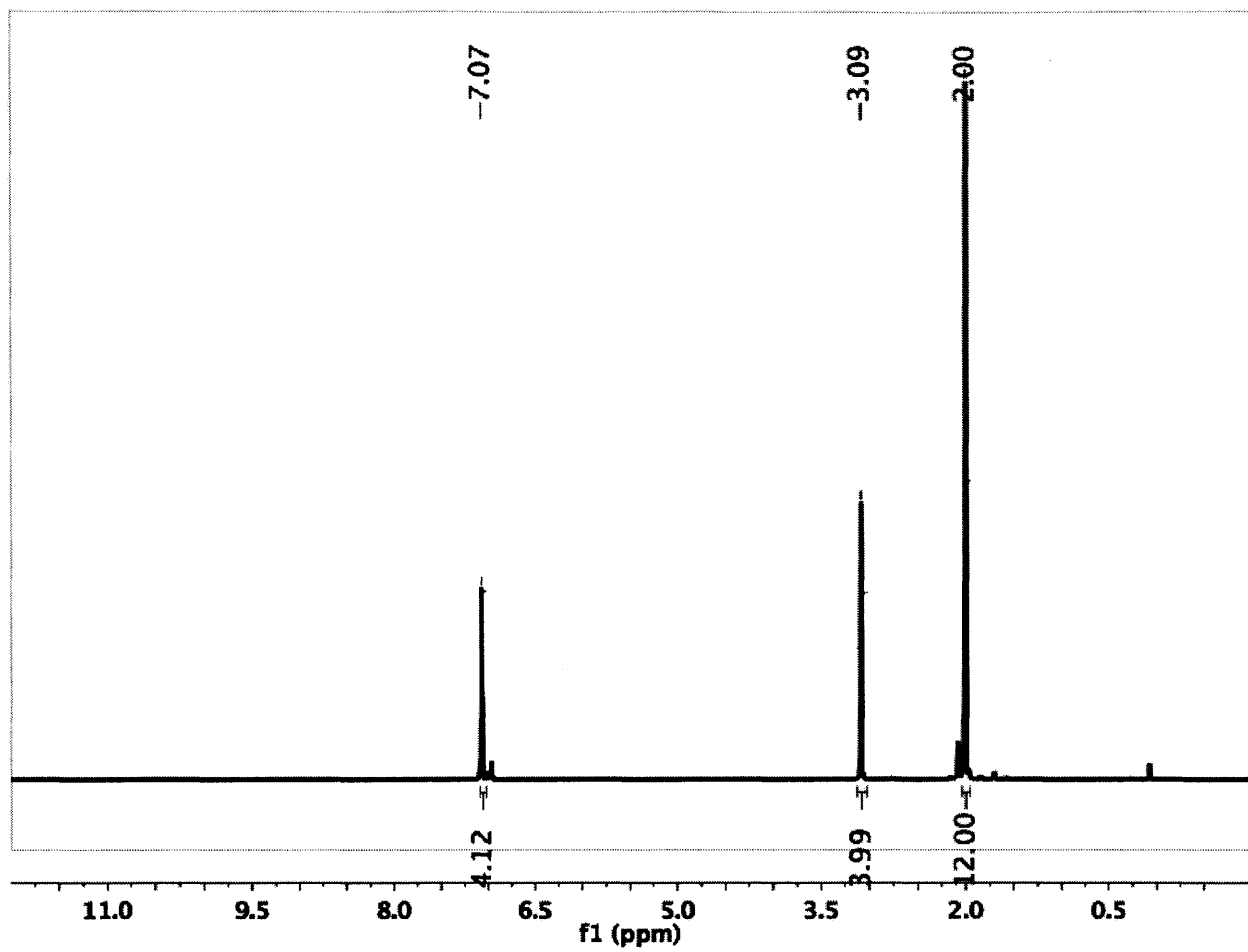
Figure 15. ^{1}H NMR of **1a** in toluene-d^8.
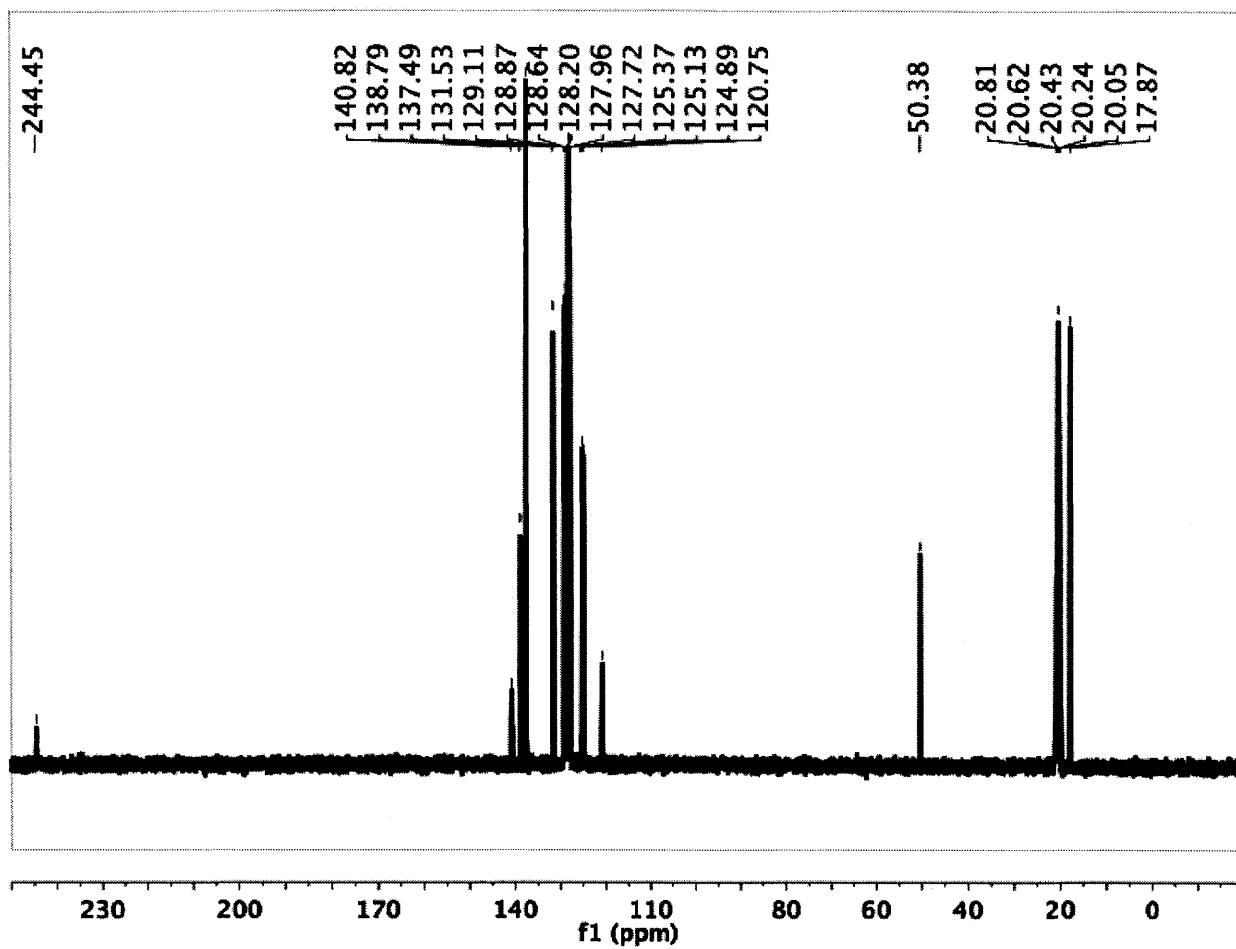
Figure 16. ^{13}C NMR of **1a** in toluene-d^8.

Peak labels (ppm): 244.45, 140.82, 138.79, 137.49, 131.53, 129.11, 128.87, 128.64, 128.20, 127.96, 127.72, 125.37, 125.13, 124.89, 120.75, 50.38, 20.81, 20.62, 20.43, 20.24, 20.05, 17.87
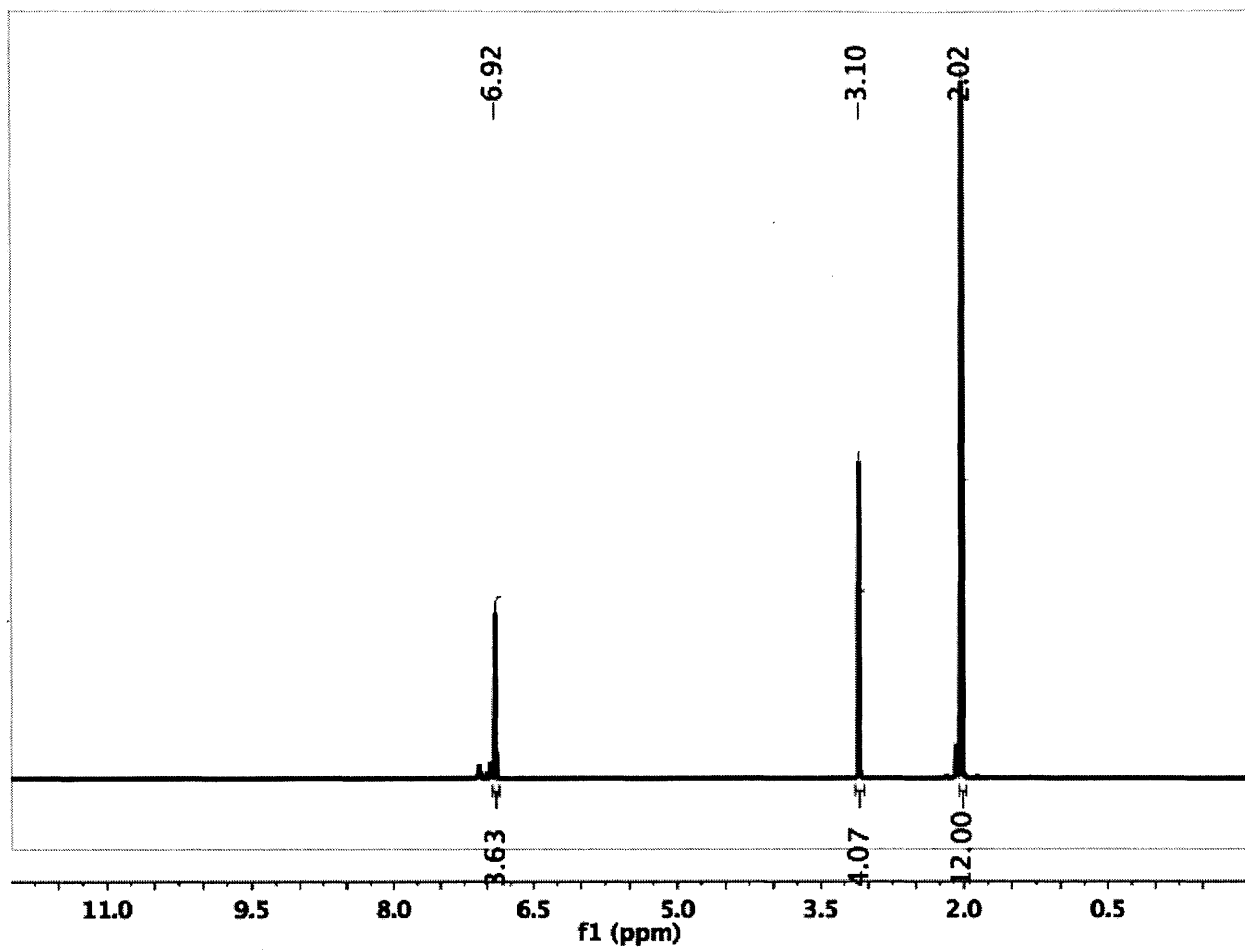
Figure 17. ^{1}H NMR of **1b** in toluene-d^8.
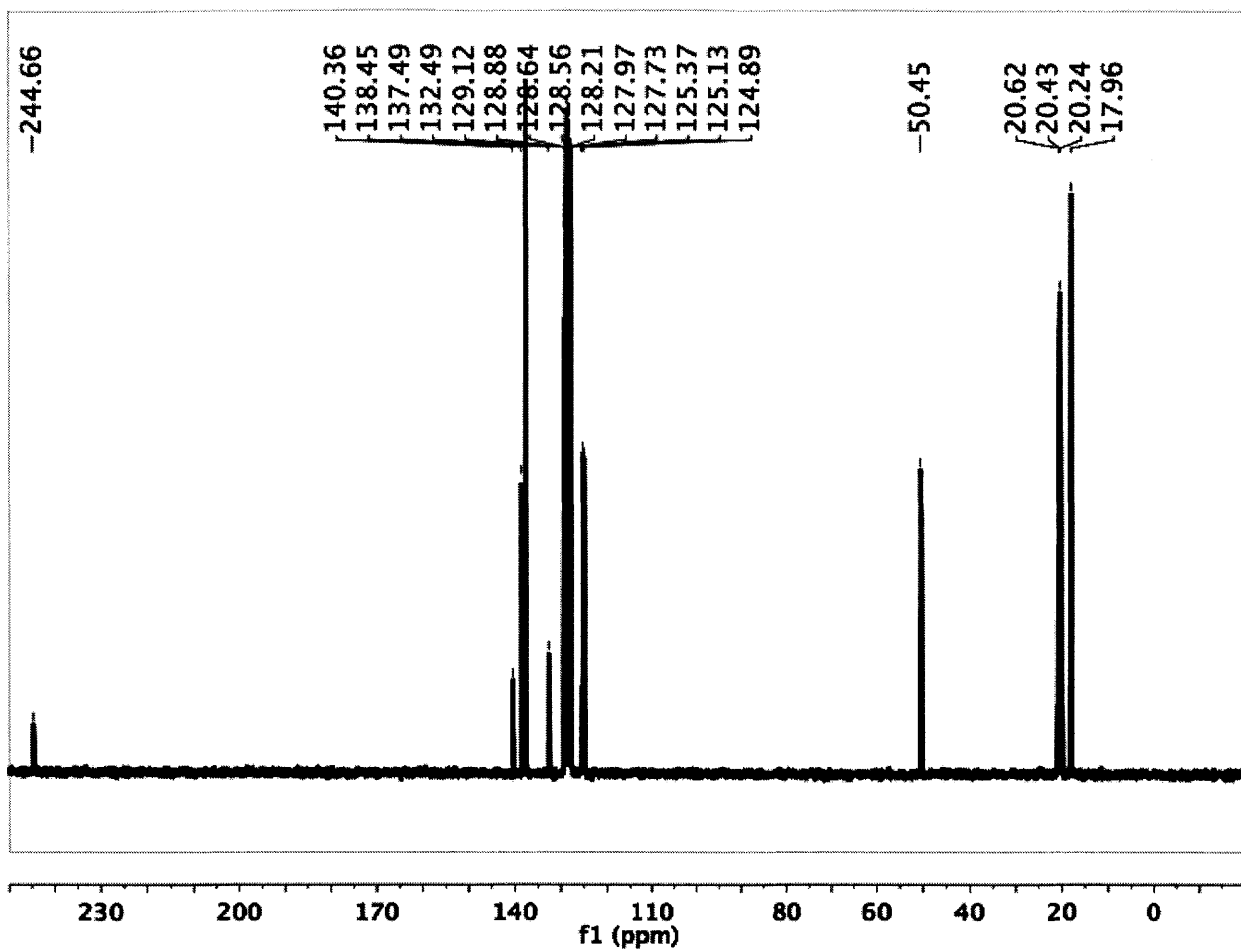
Figure 18. ^{13}C NMR of **1b** in toluene-d^8.
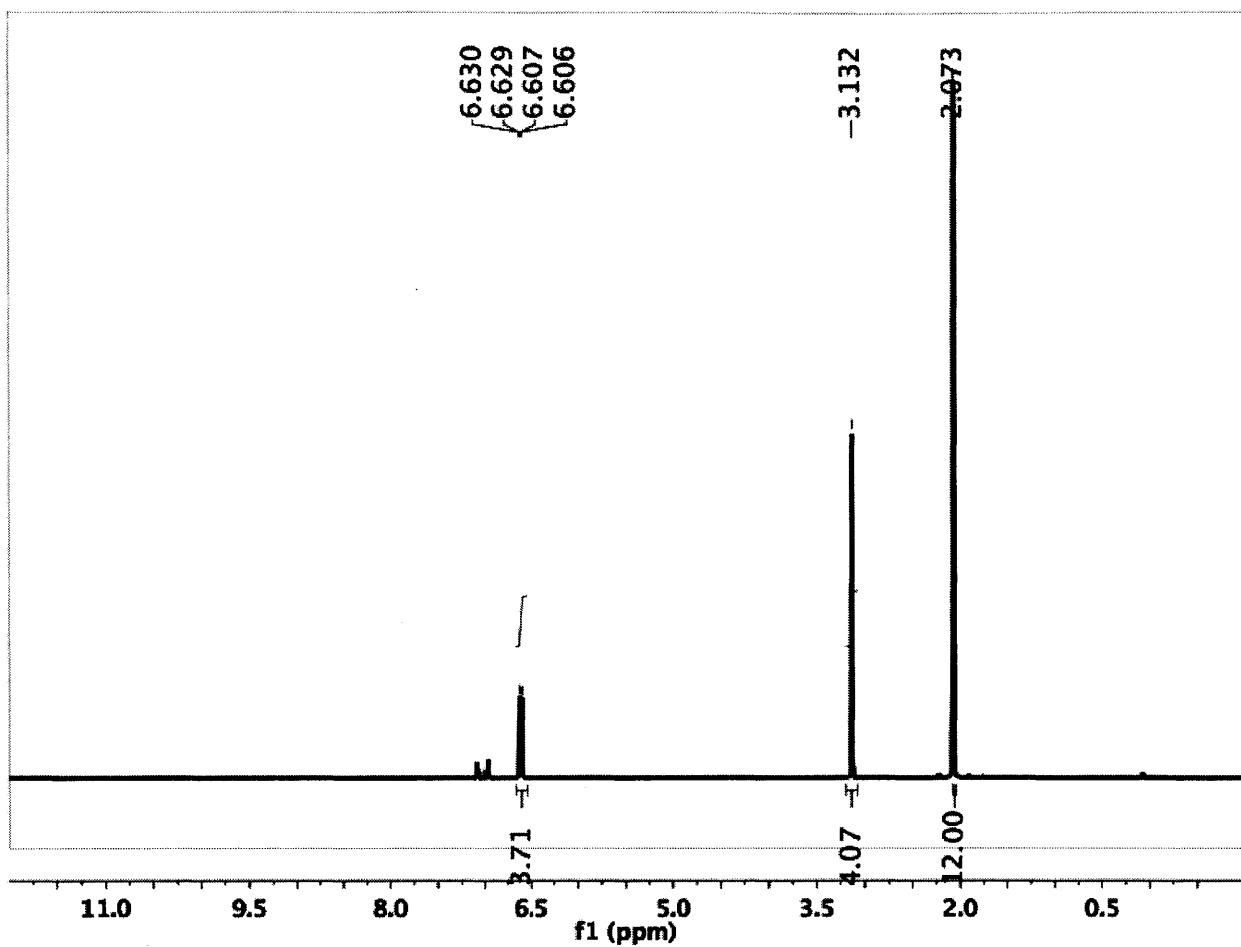
Figure 19. ^{1}H NMR of **1c** in toluene-d^8.
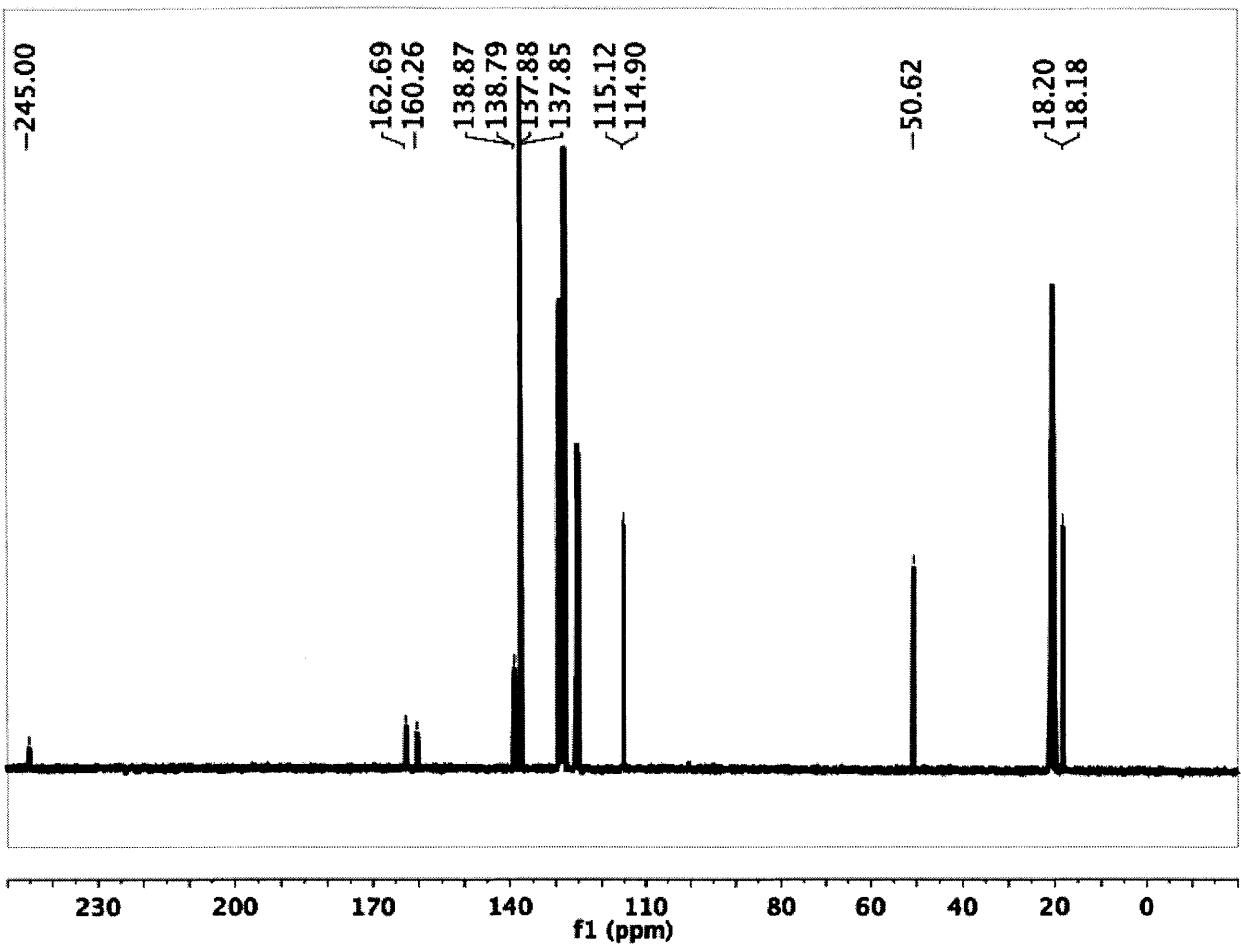
Figure 20. ^{13}C NMR of **1c** in toluene-d^8.
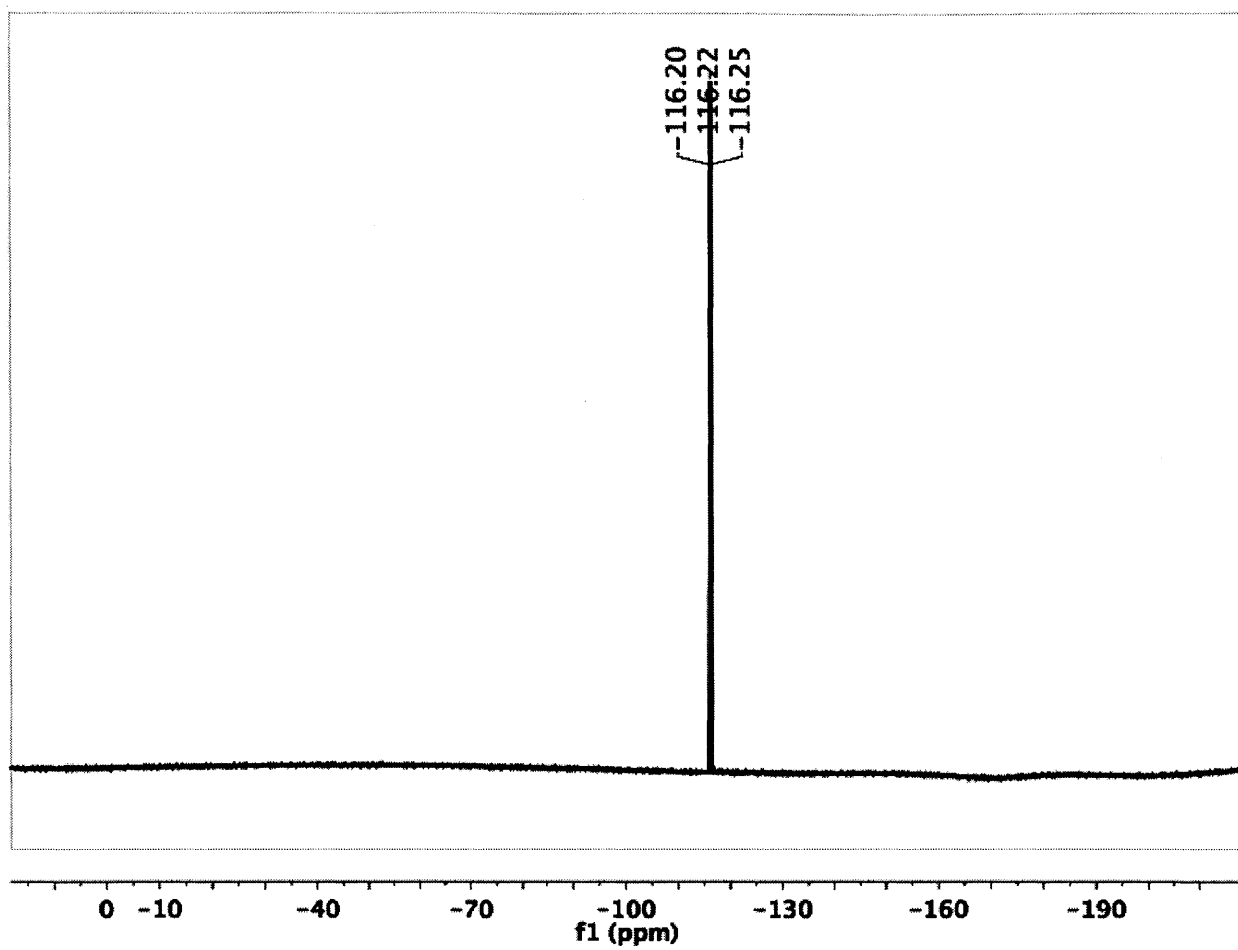
Figure 21. ^{19}F NMR of **1c** in toluene-d^8.
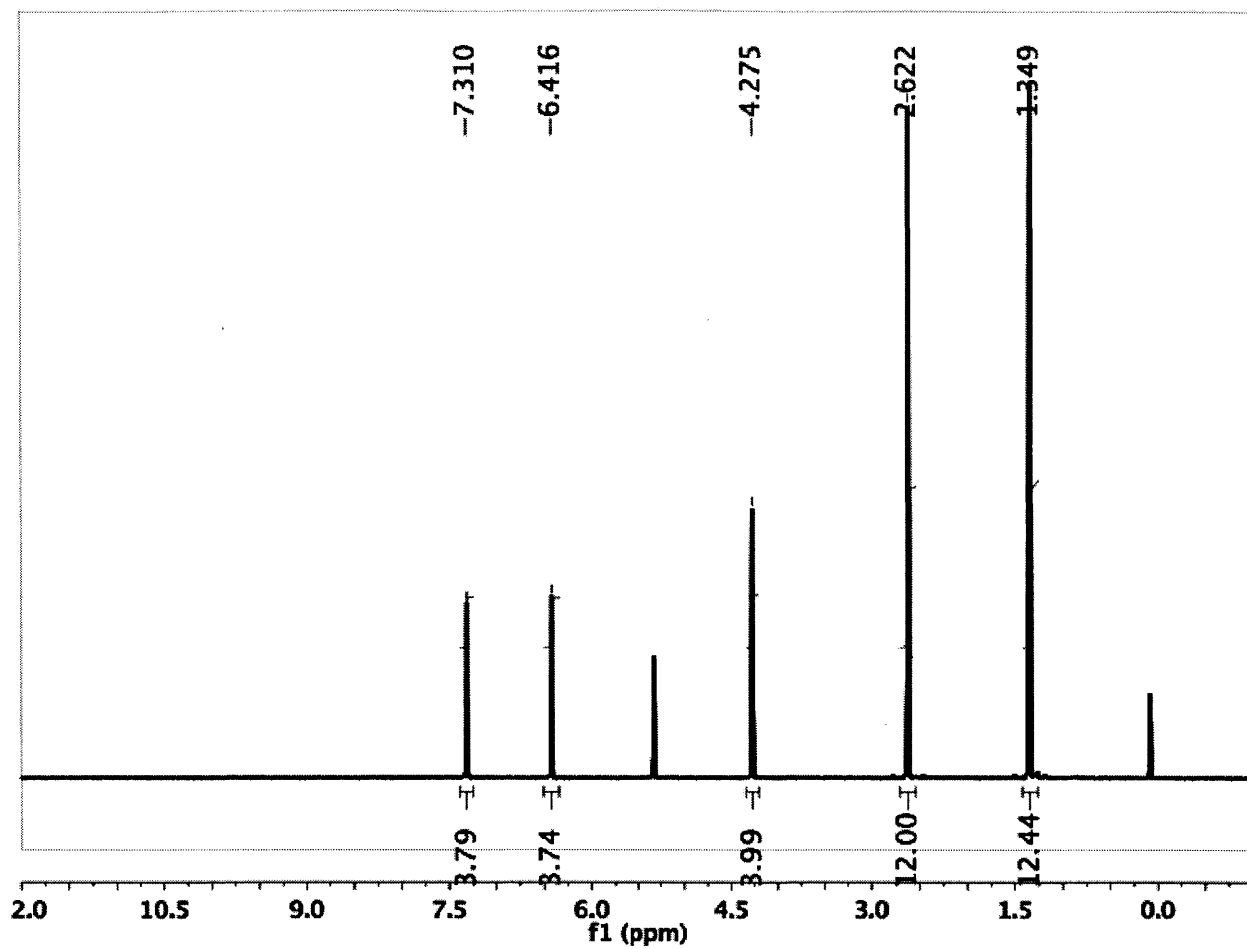
Figure 22. ^{1}H NMR of **2a** in DCM-d^2.
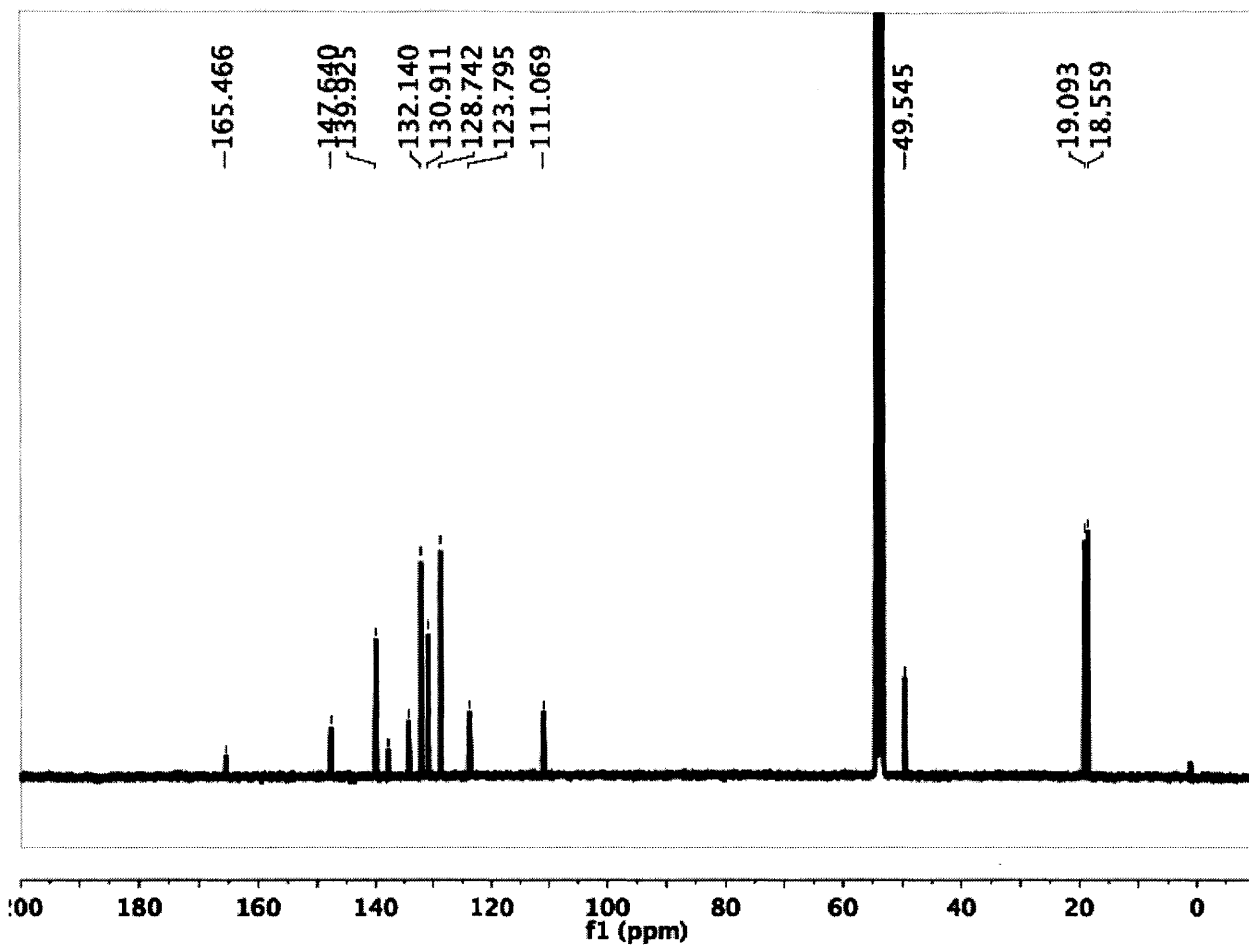
Figure 23. ^{13}C NMR of **2a** in DCM-d^2.
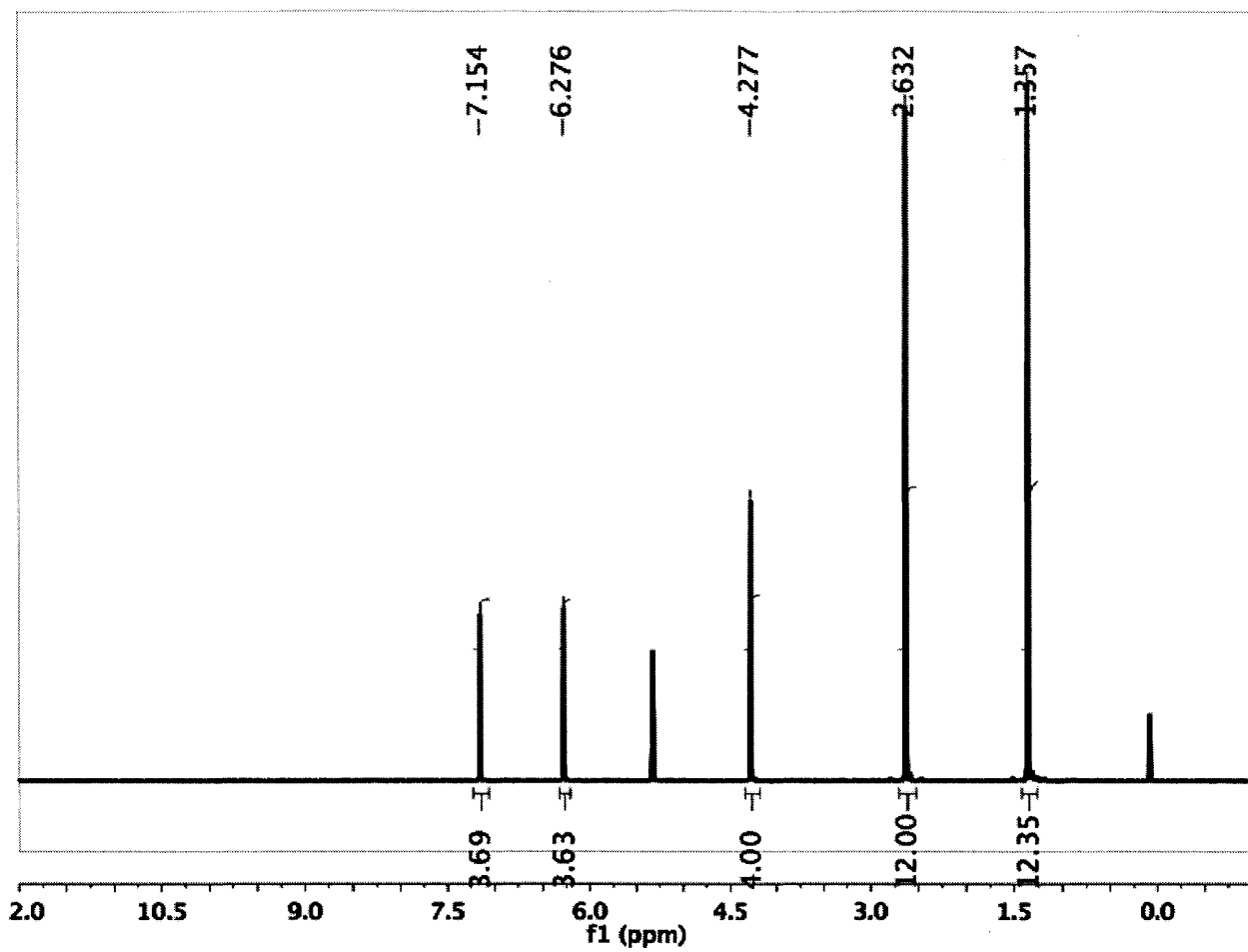
Figure 24. ^{1}H NMR of **2b** in DCM-d^2.

344
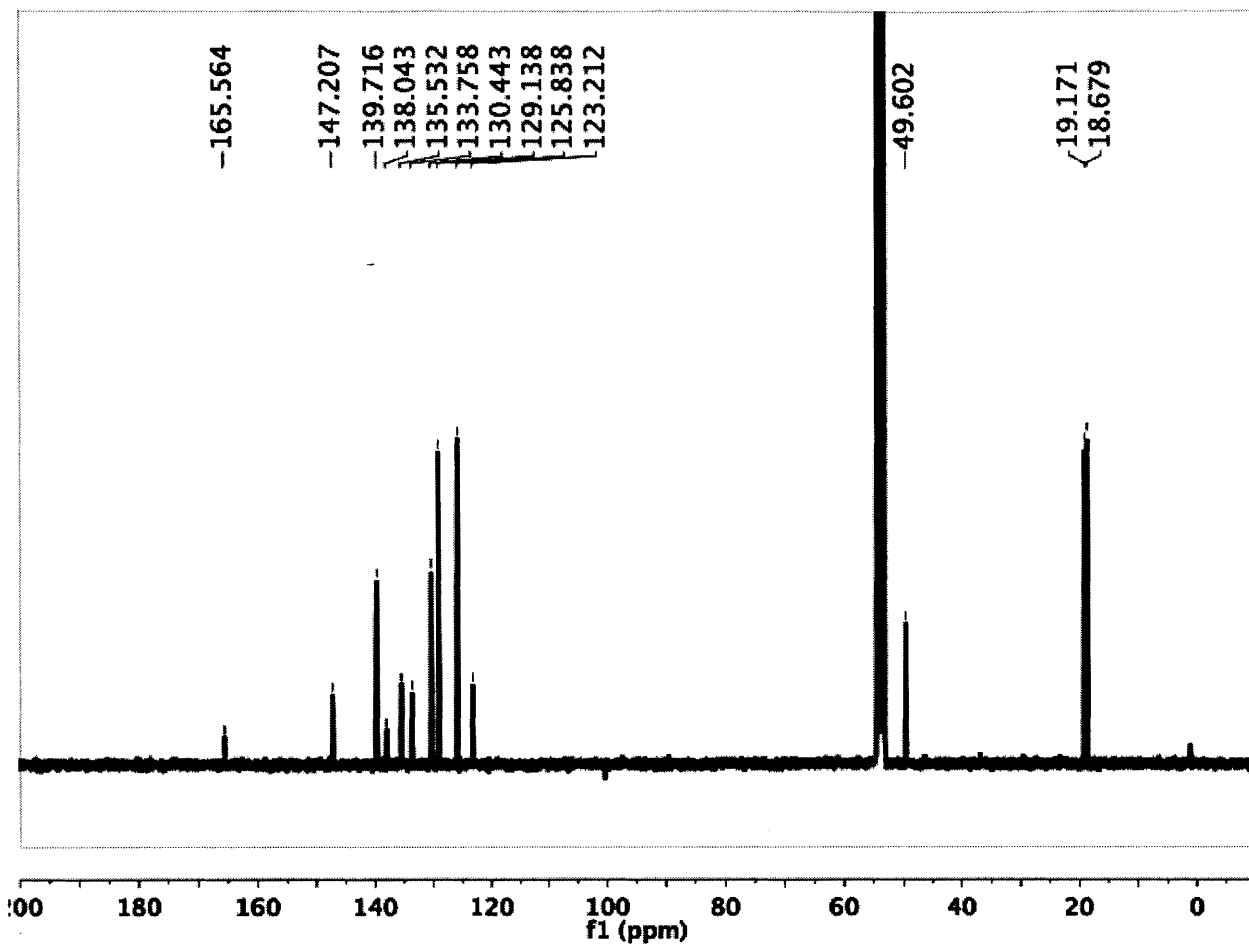
Figure 25. ^{13}C NMR of **2b** in DCM-d^2.
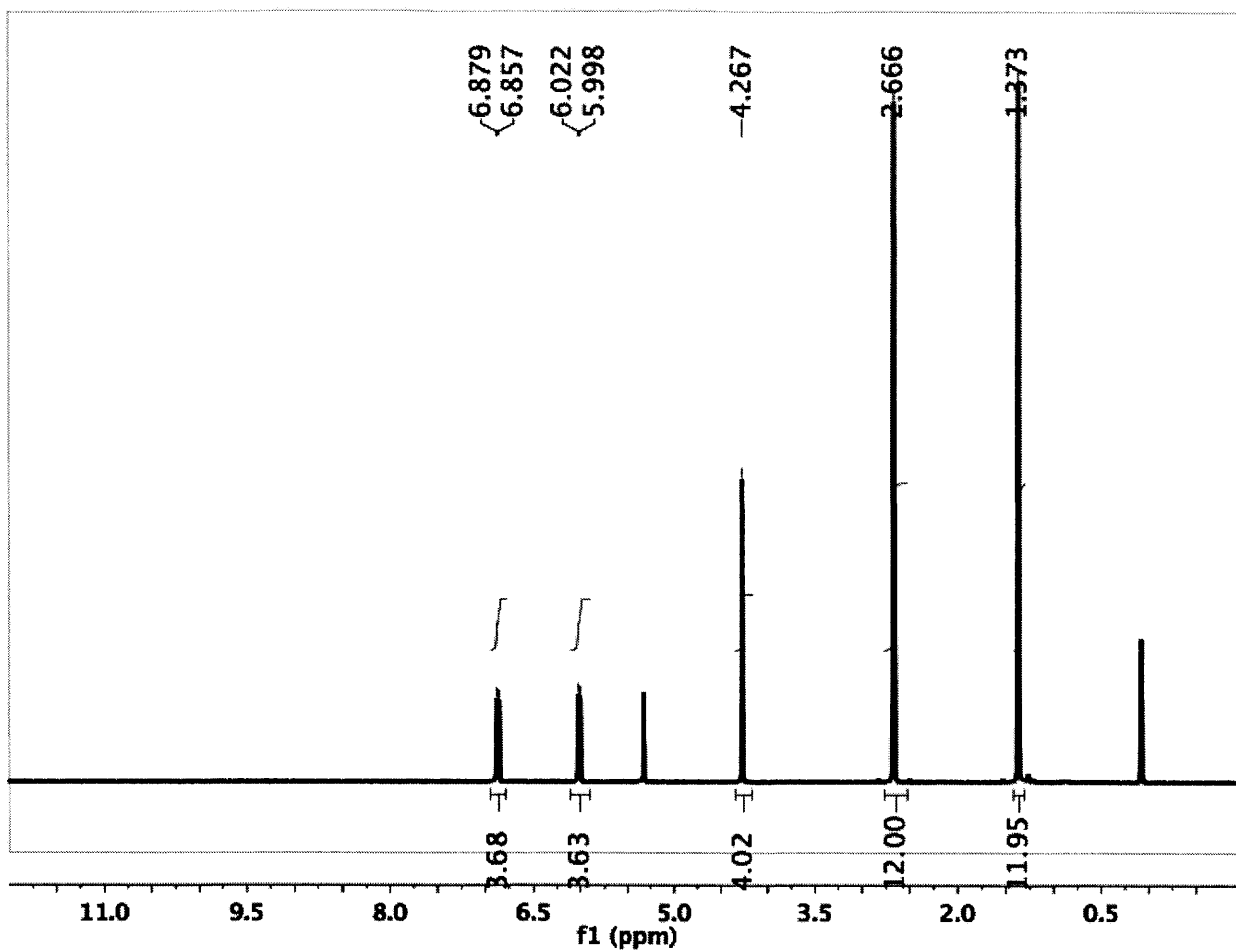
Figure 26. ^{1}H NMR of **2c** in DCM-d^2.
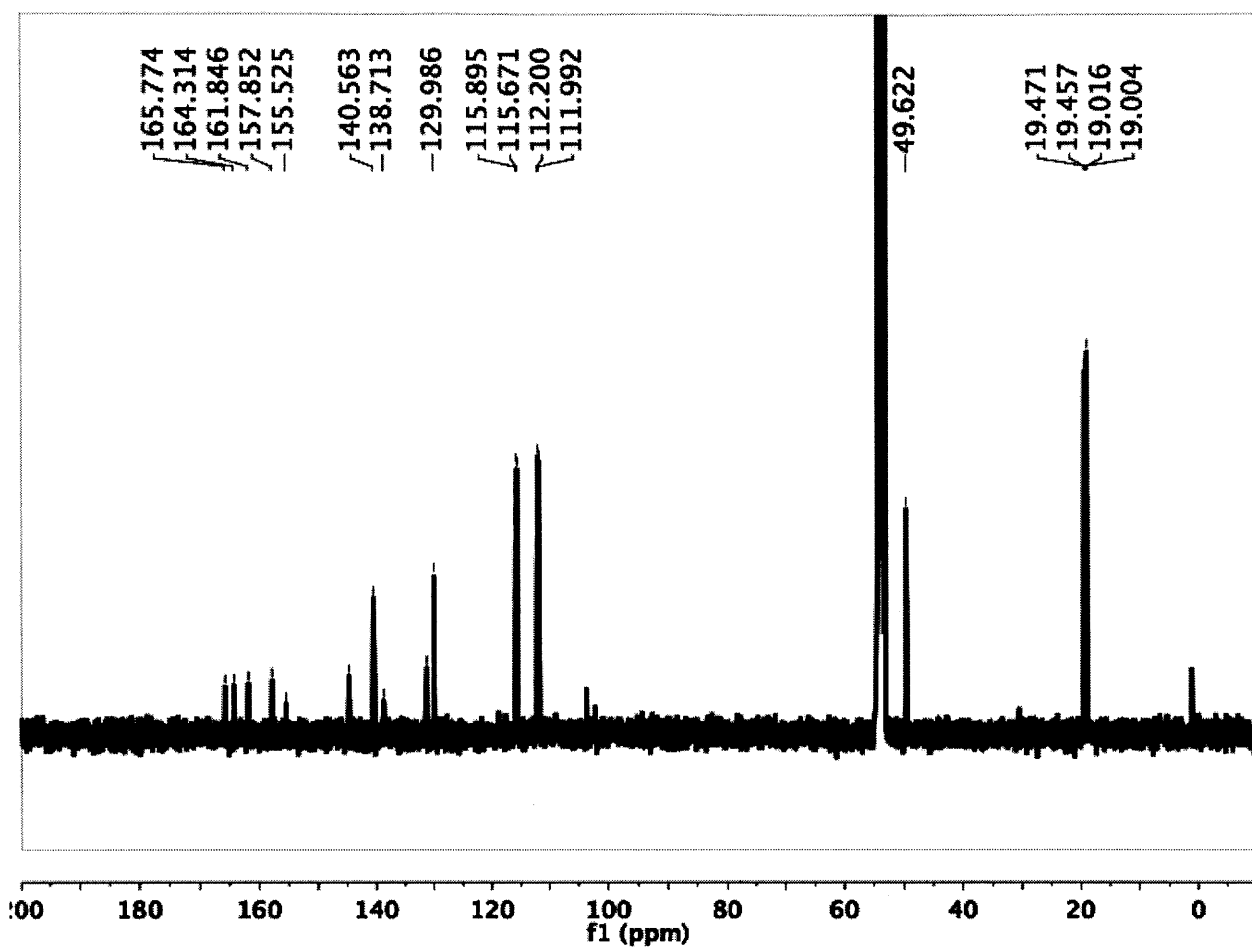
Figure 27. ^{13}C NMR of **2c** in DCM-d^2.
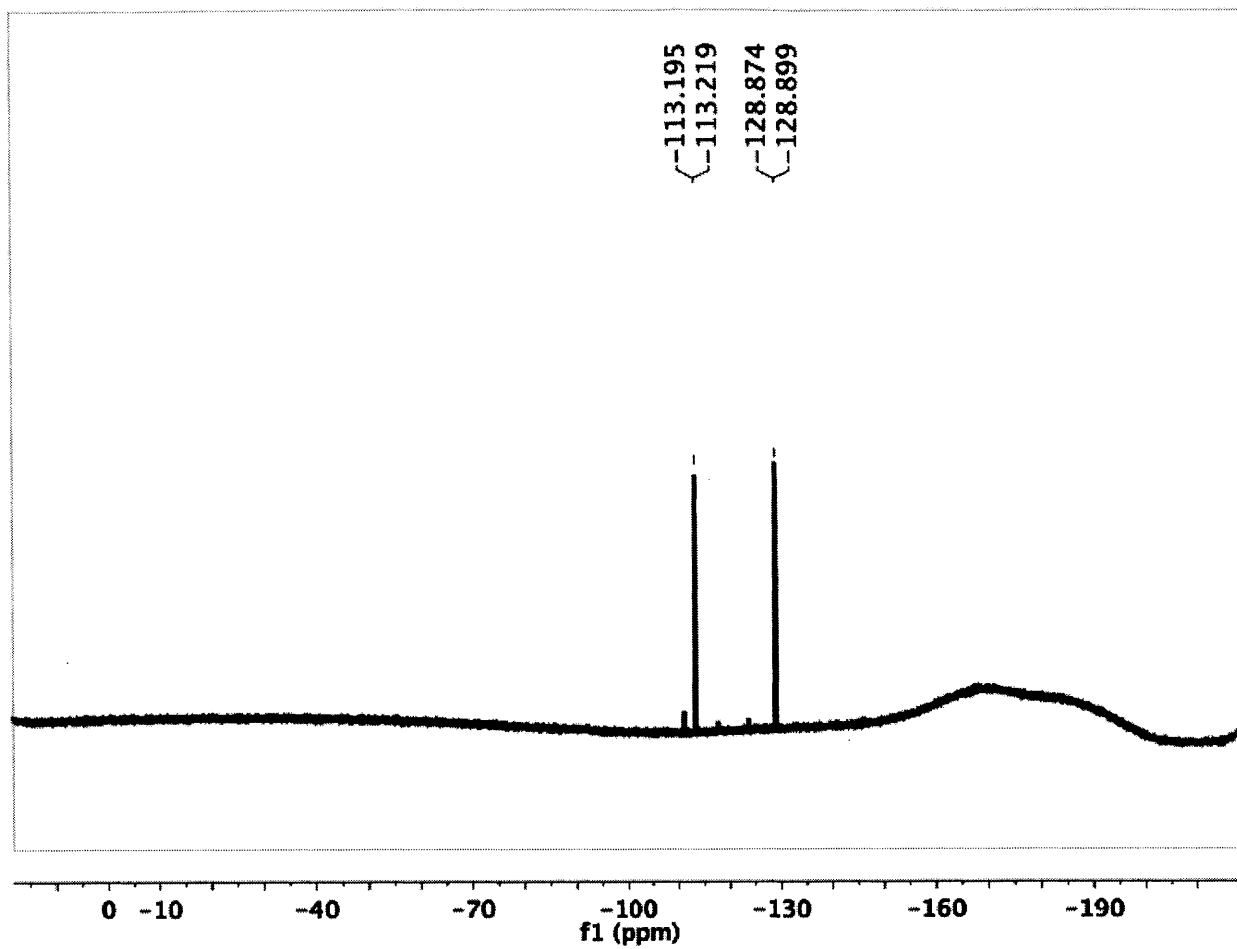
Figure 28. ^{19}F NMR of **2c** in DCM-d^2.
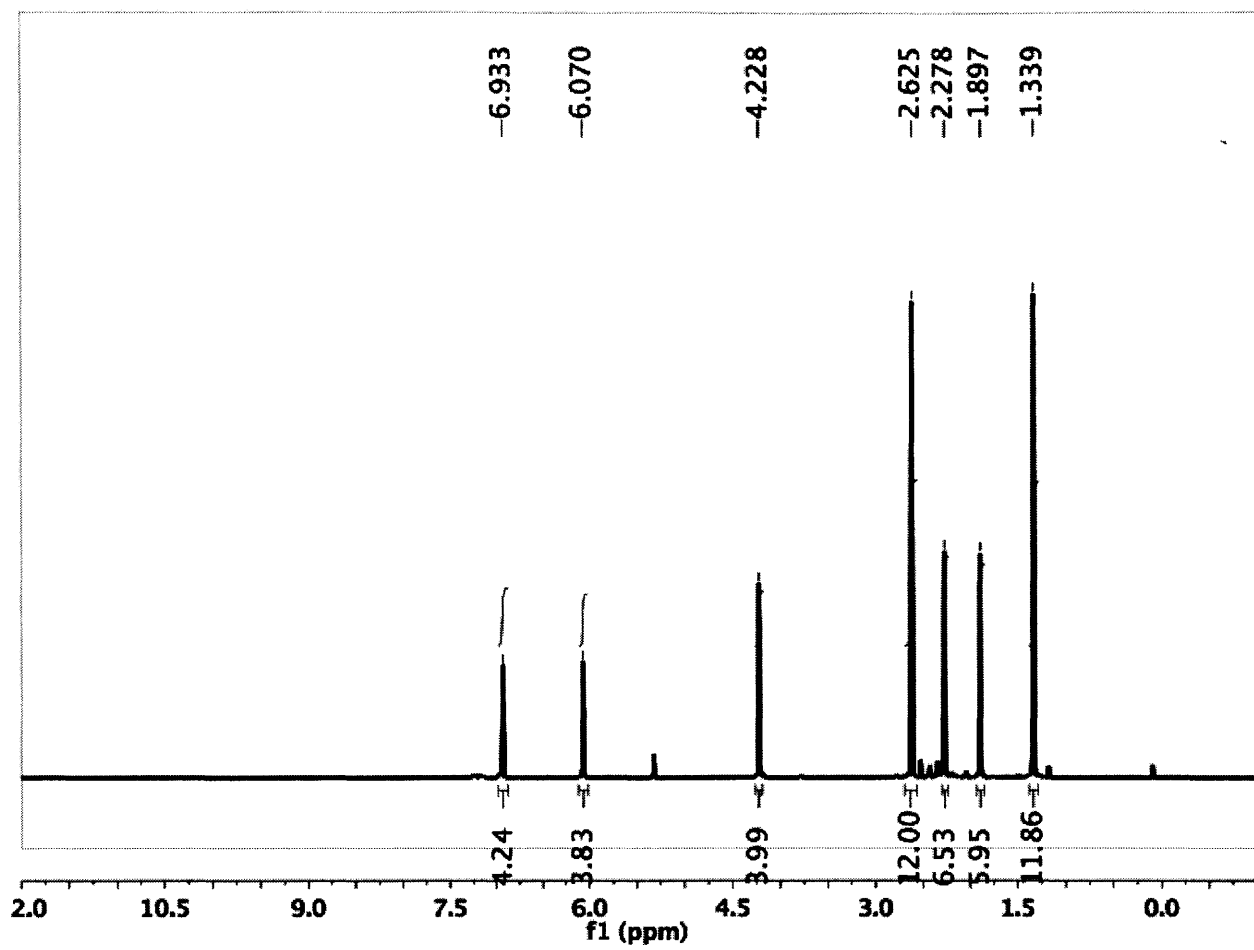
Figure 29. ^{1}H NMR of **2d** in DCM-d^2.

349
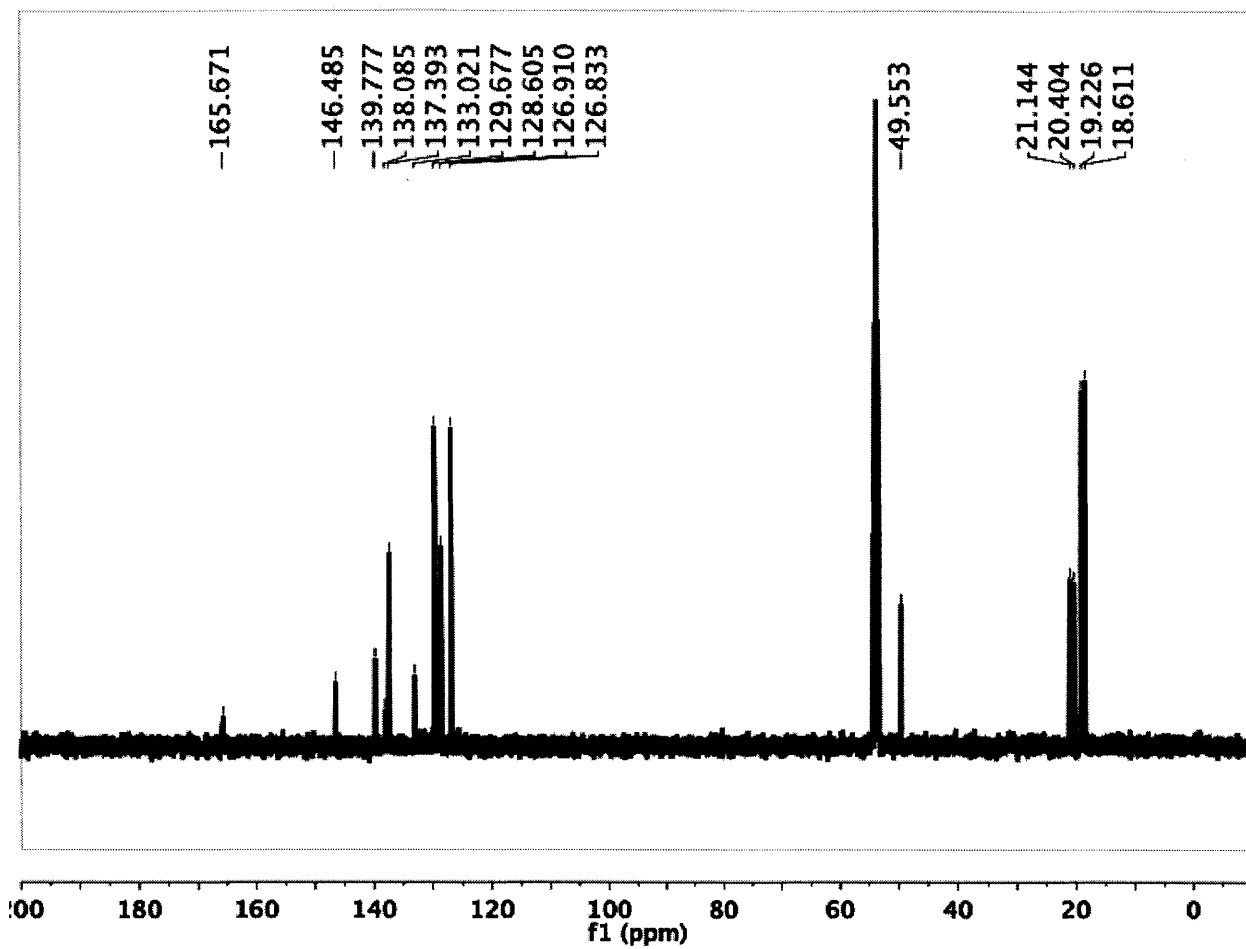
Figure 30. ^{13}C NMR of **2d** in DCM-d^2.
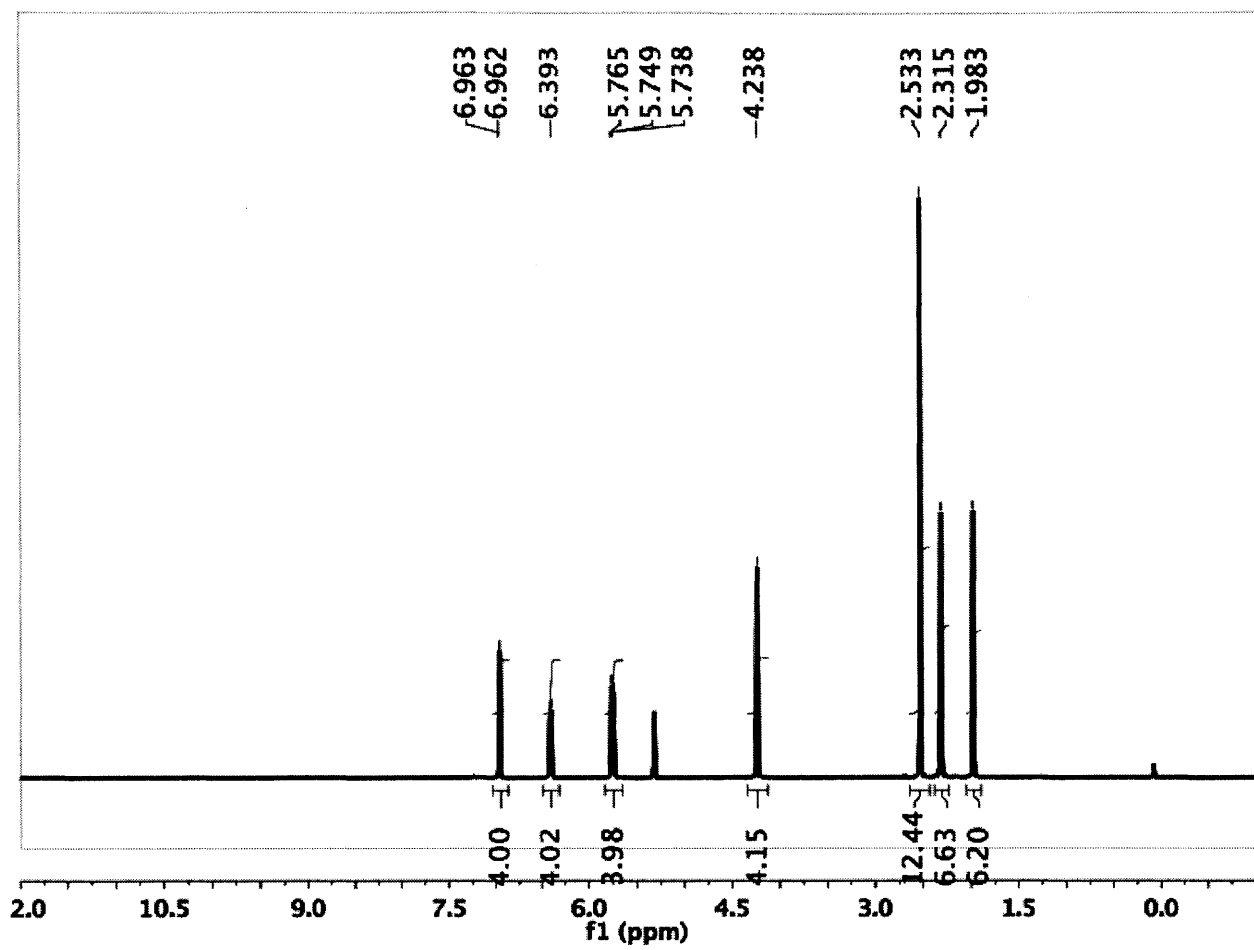
Figure 31. ^{1}H NMR of **3a** in DCM-d^2

351
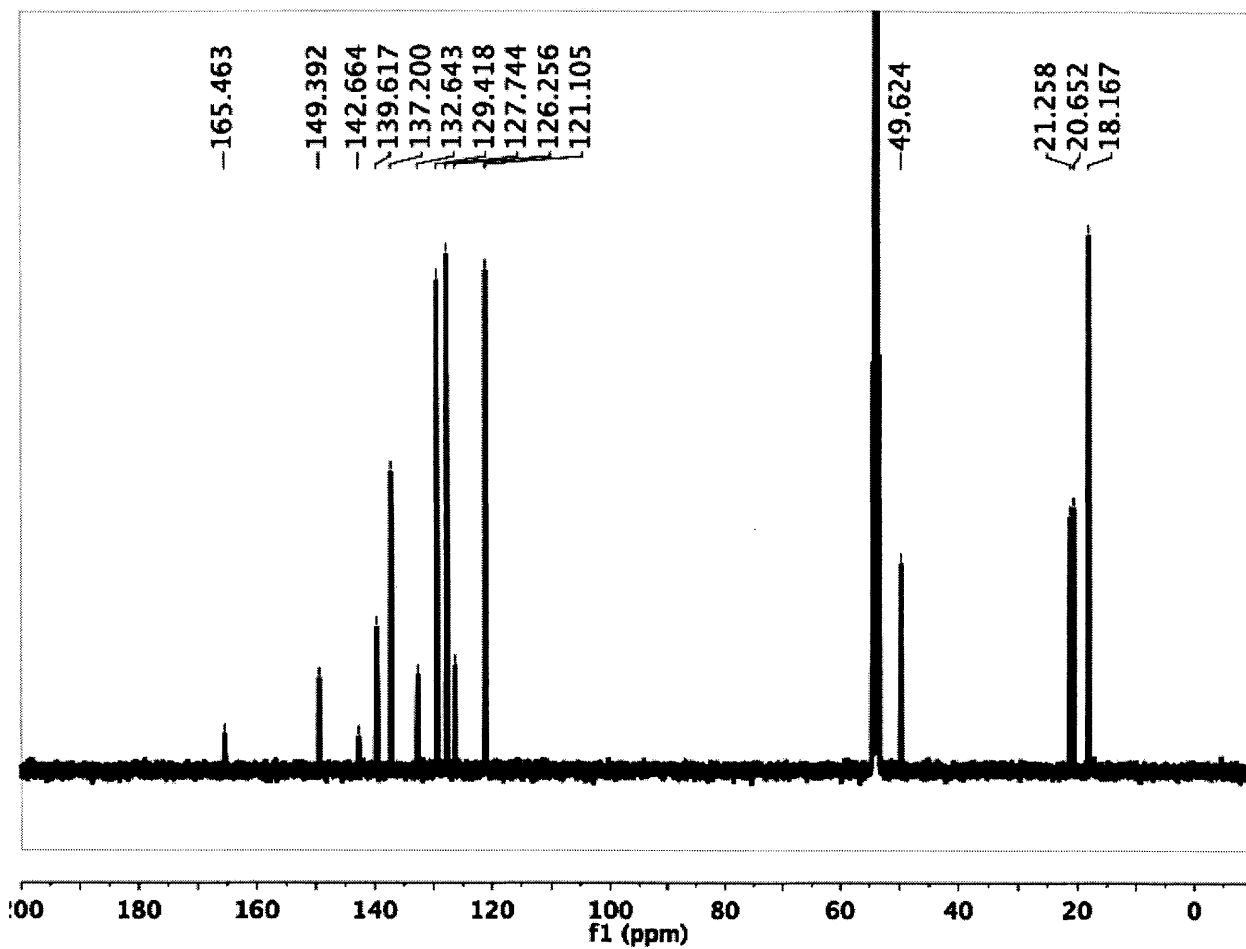
Figure 32. ^{13}C NMR of **3a** in DCM-d^2.
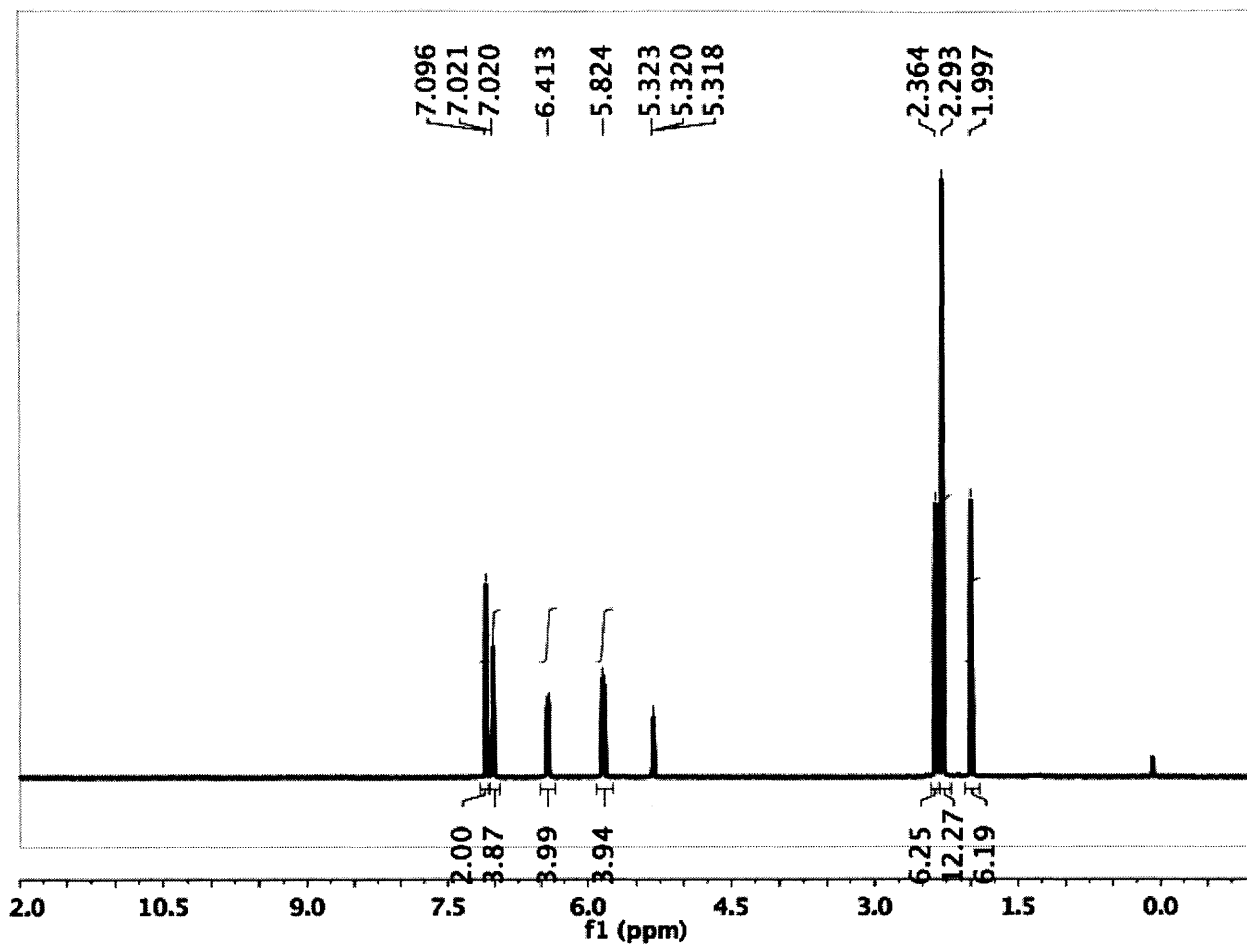
Figure 33. ^{1}H NMR of **3b** in DCM-d^2.
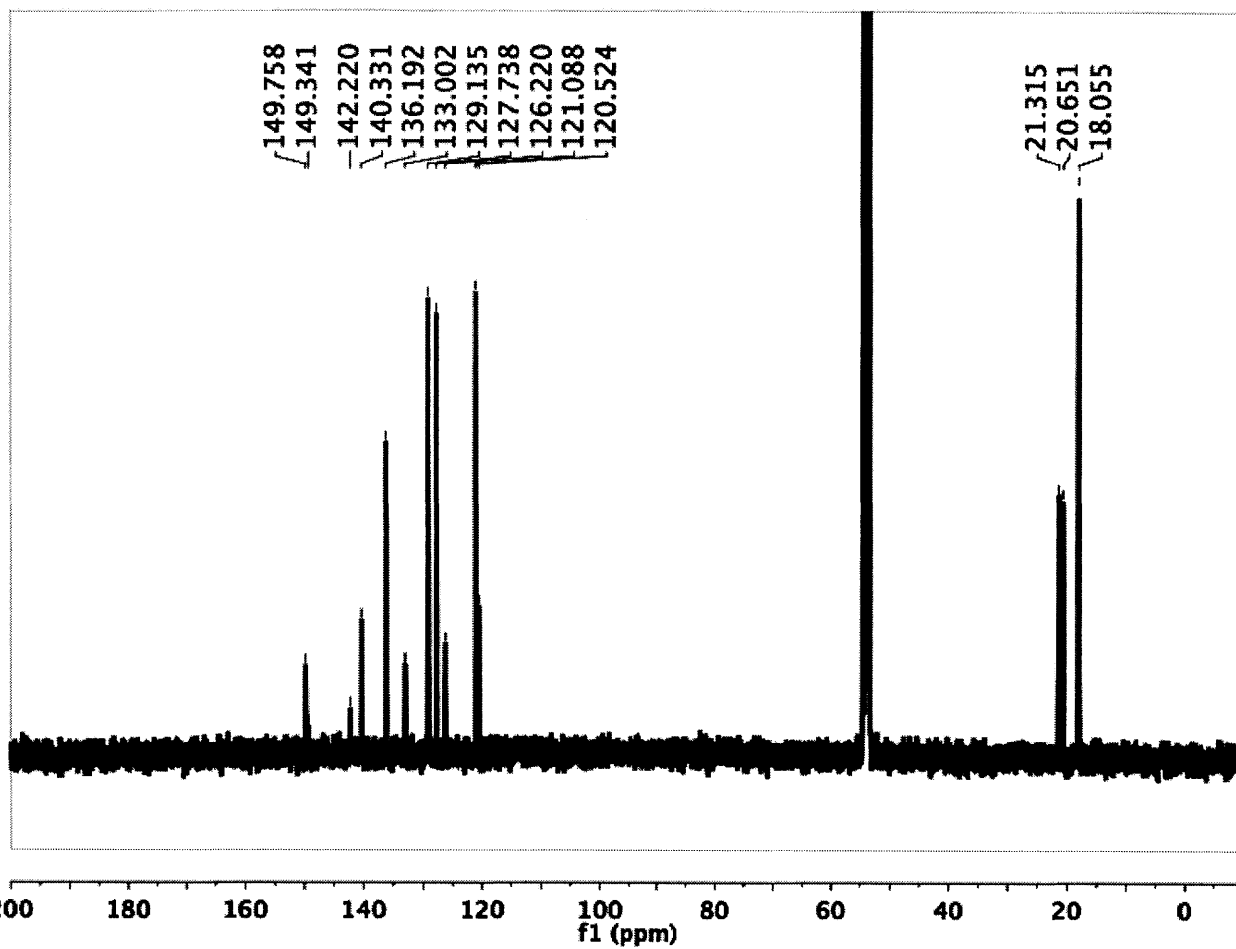
Figure 34. ^{13}C NMR of **3b** in DCM-d^2.
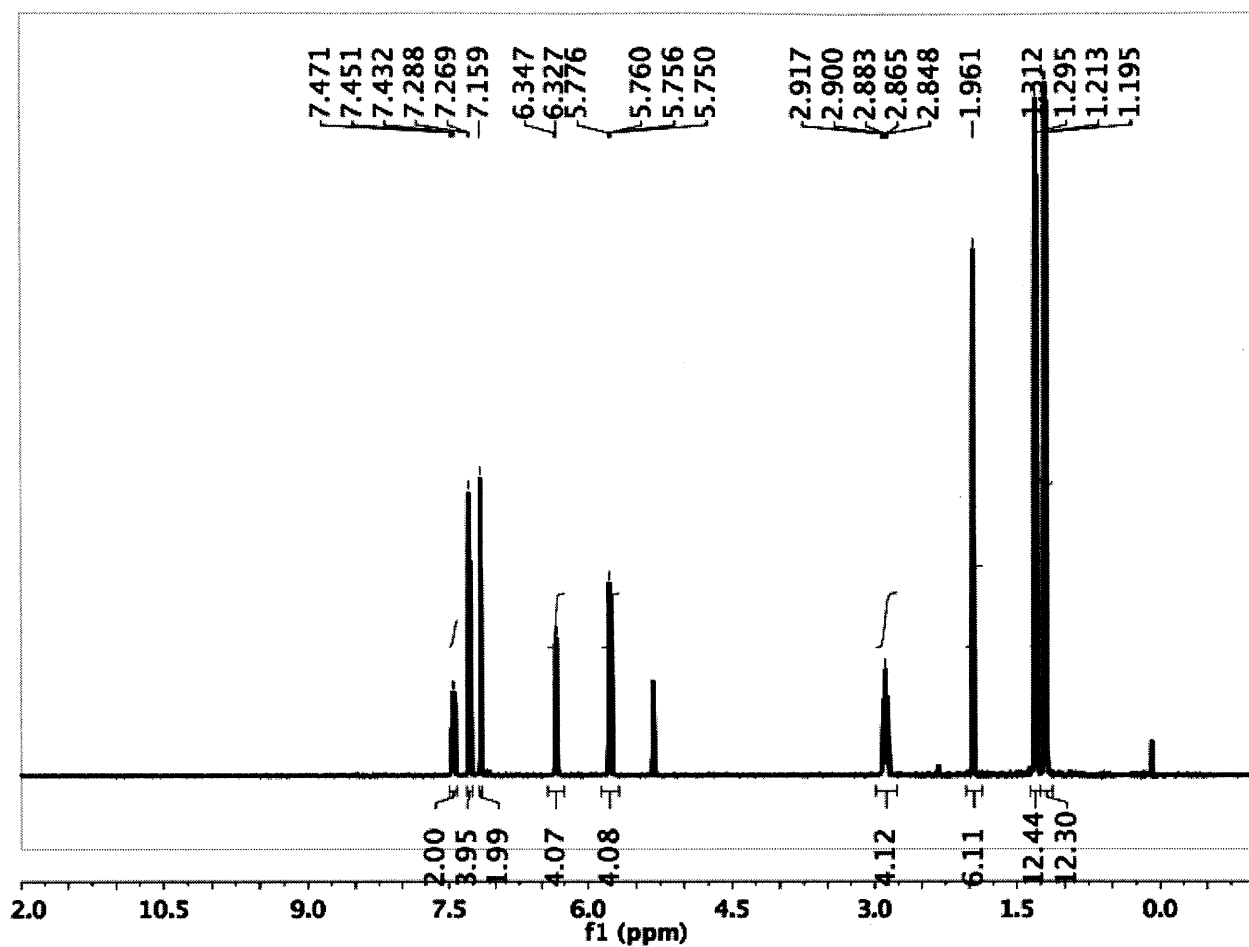
Figure 35. ^{1}H NMR of **3c** in DCM-d^2.
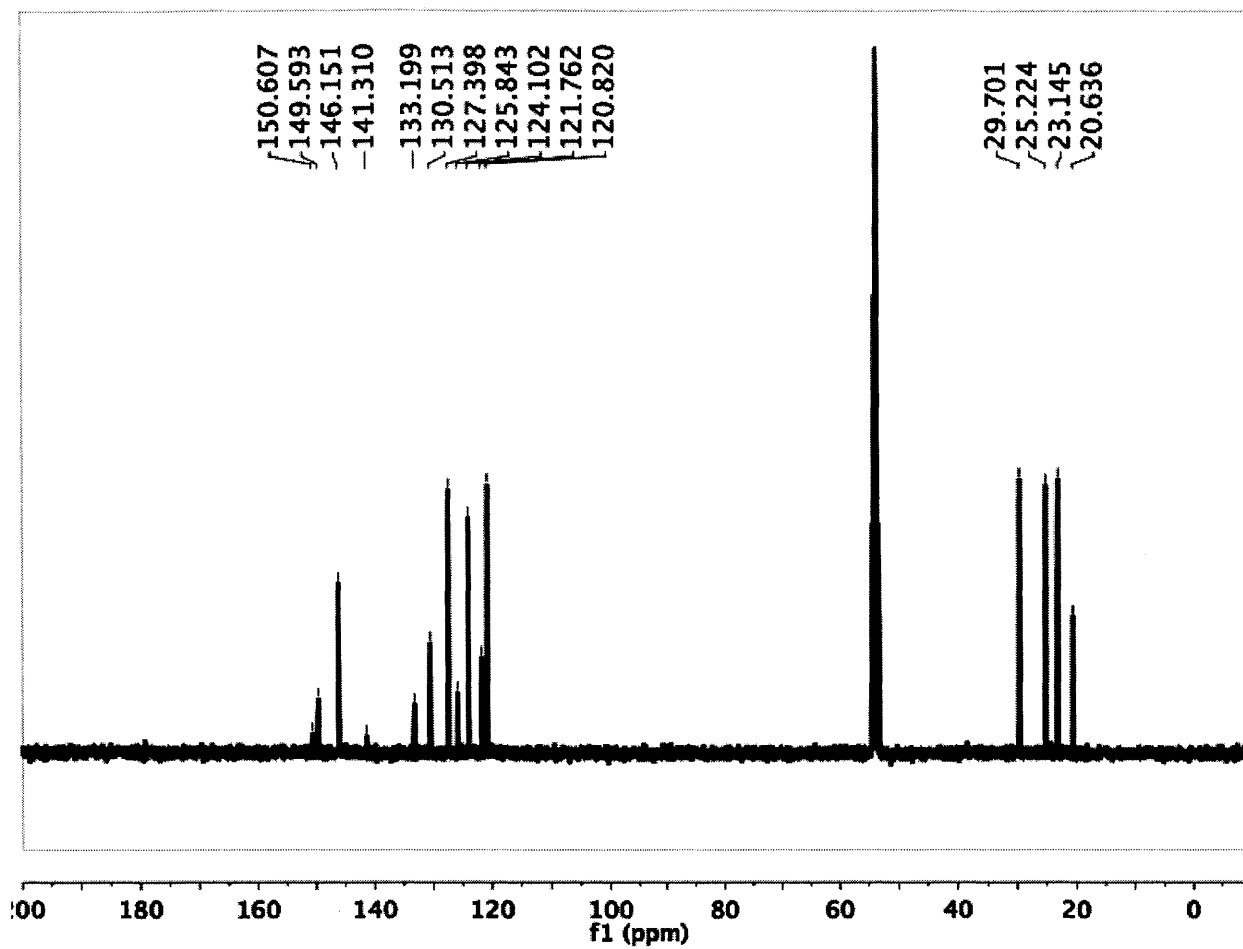
Figure 36. ^{13}C NMR of **3c** in DCM-d^2.

150.607
149.593
146.151
141.310
133.199
130.513
127.398
125.843
124.102
121.762
120.820

29.701
25.224
23.145
20.636
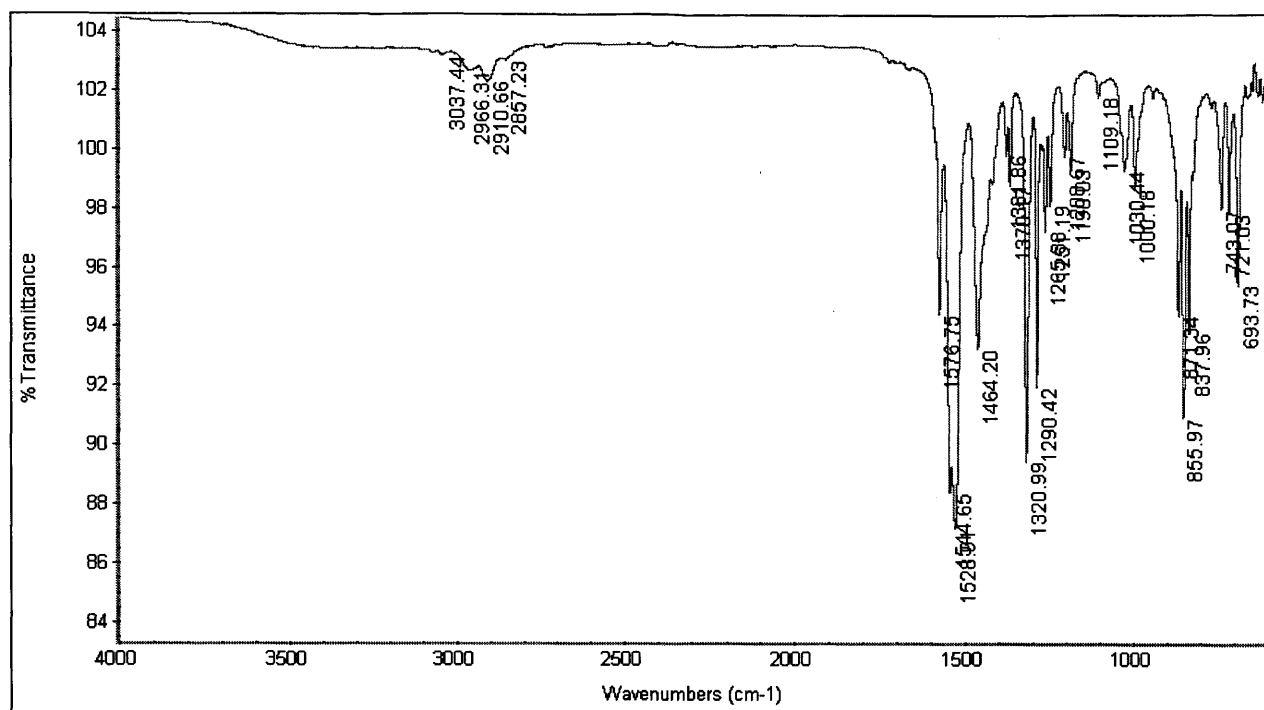
Figure 37. FT-IR-ATR of **2a**.

357
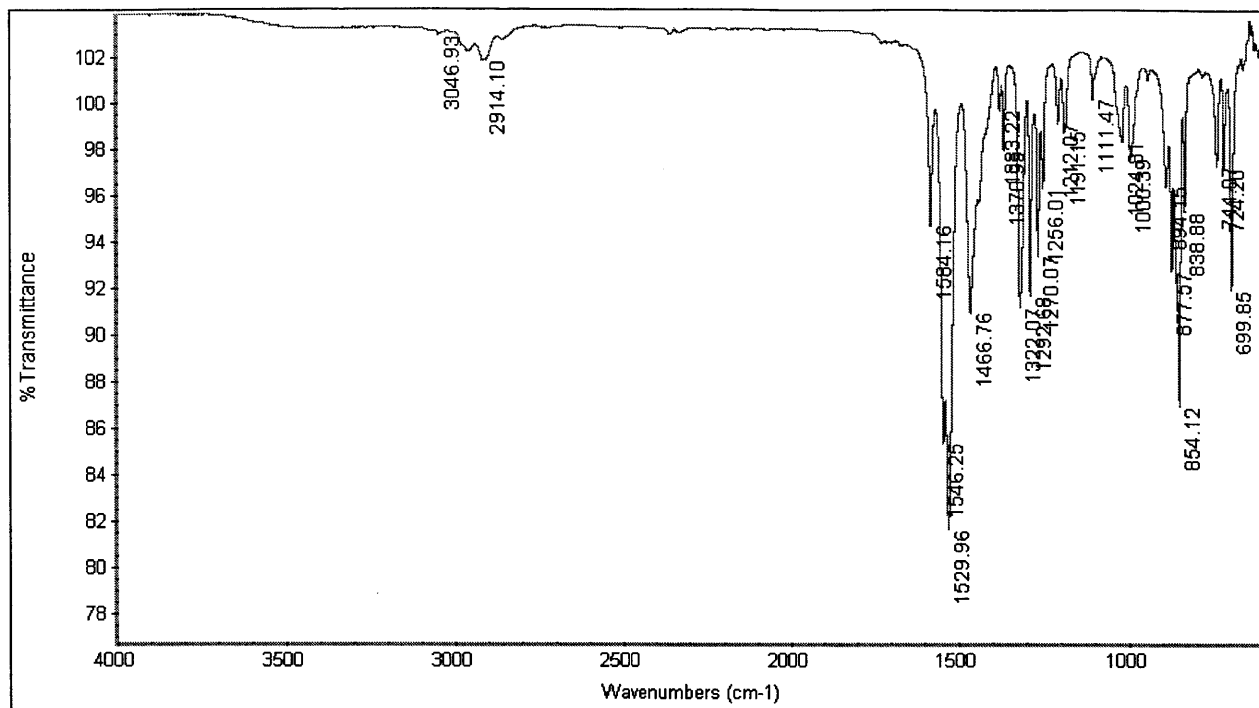
Figure 38. FT-IR-ATR of **2b**.
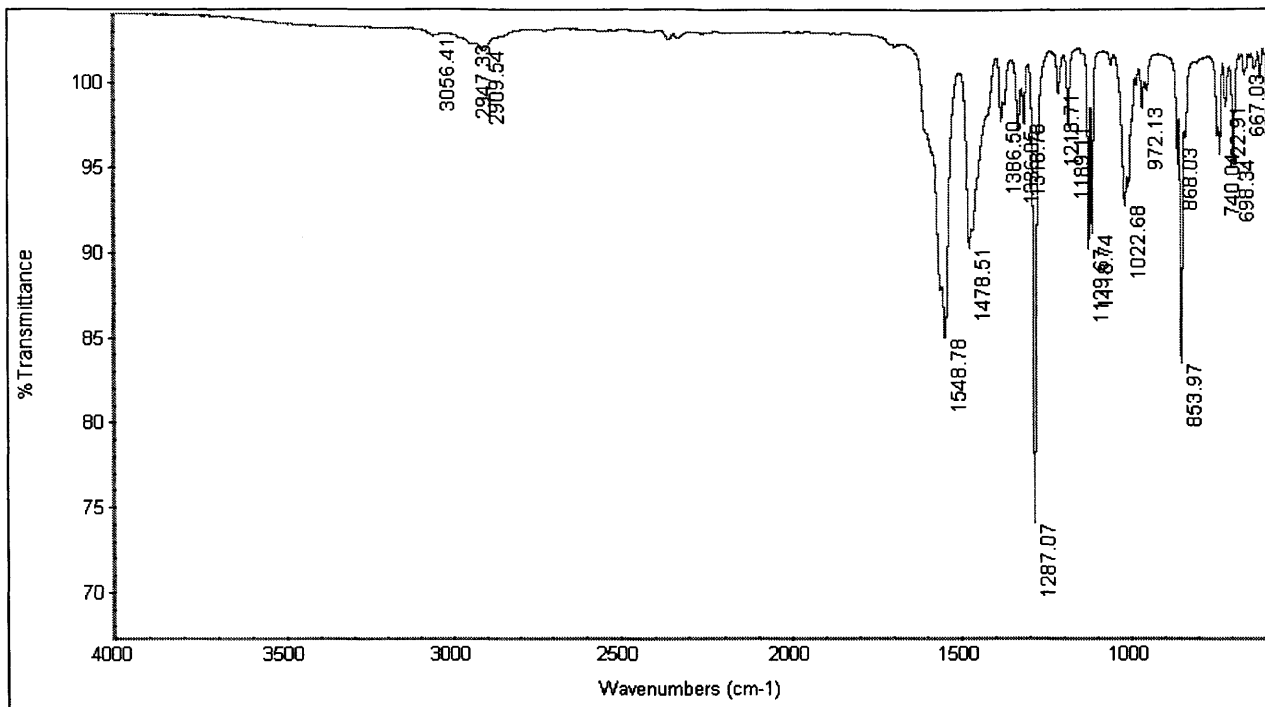
Figure 39. FT-IR-ATR of **2c**.
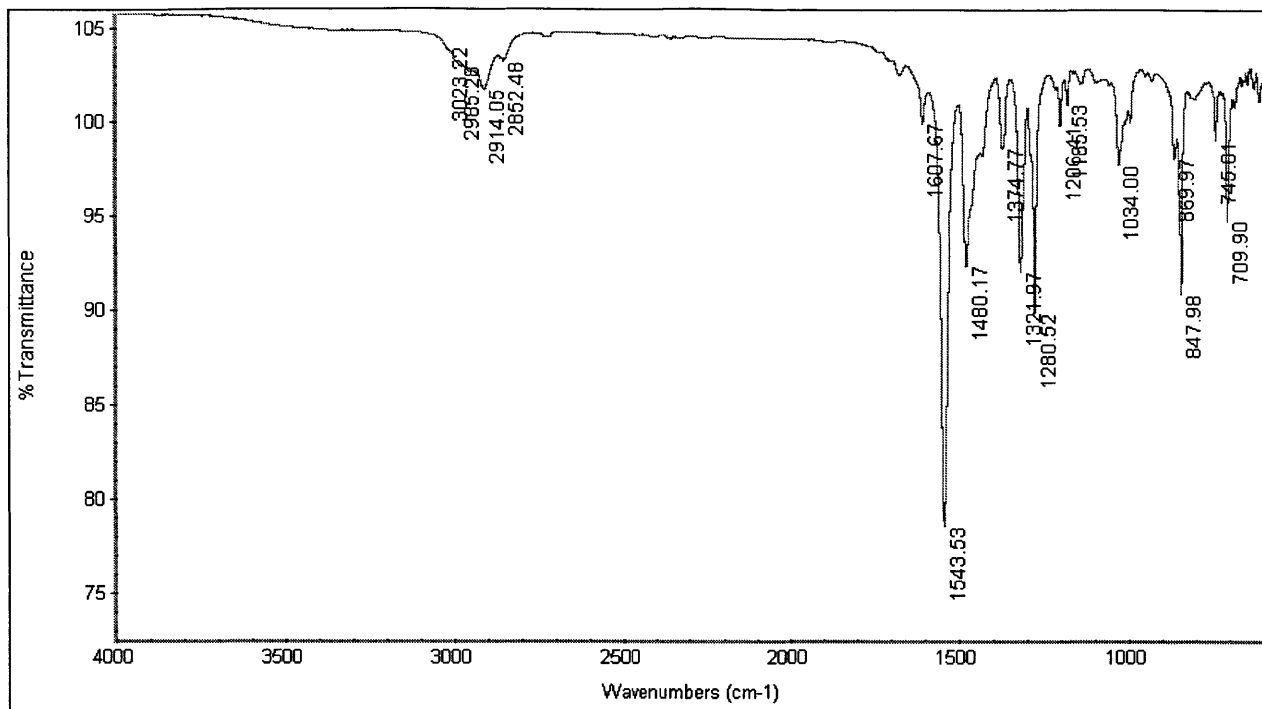
Figure 40. FT-IR-ATR of **2d**.

4.6 References

(1)   Arduengo, A. J.; Harlow, R. L.; Kline, M. A Stable Crystalline Carbene. *J. Am. Chem. Soc.* **1991**, *113*, 361-363.

(2)   Kirmse, W. The Beginnings of N-Heterocyclic Carbenes. *Angew. Chem. Int. Ed.* **2010**, *49*, 8798-8801.

(3)   Hopkinson, M. N.; Richter, C.; Schedler, M.; Glorius, F. An Overview of *N*-Heterocyclic Carbenes. *Nature* **2014**, *510*, 485-496.

(4)   Huang, J.; Stevens, E. D.; Nolan, S. P.; Petersen, J. L. Olefin Metathesis-Active Ruthenium Complexes Bearing a Nucleophilic Carbene Ligand. *J. Am. Chem. Soc.* **1999**, *121*, 2674-2678.

(5)   Scholl, M.; Ding, S.; Lee, C. W.; Grubbs, R. H. Synthesis and Activity of a New Generation of Ruthenium-Based Olefin Metathesis Catalysts Coordinated with 1,3-Dimesityl-4,5-Dihydroimidazol-2-Ylidene Ligands. *Org. Lett.* **1999**, *1*, 953-956.

(6)   Kingsbury, J. S.; Harrity, J. P. A.; Bonitatebus, P. J.; Hoveyda, A. H. A Recyclable Ru-Based Metathesis Catalyst. *J. Am. Chem. Soc.* **1999**, *121*, 791-799.

(7)   Gessler, S.; Randl, S.; Blechert, S. Synthesis and Metathesis Reactions of a Phosphine-Free Dihydroimidazole Carbene Ruthenium Complex. *Tetrahedron Lett.* **2000**, *41*, 9973-9976.

(8)   Herrmann, W. A. *N*-Heterocyclic Carbenes: A New Concept in Organometallic Catalysis. *Angew. Chem. Int. Ed.* **2002**, *41*, 1290-1309.

(9)   Nolan, S. P. *N-Heterocyclic Carbenes in Synthesis*; John Wiley & Sons, 2006.

(10)   Tekavec, T.; Louie, J. In *N-Heterocyclic Carbenes in Transition Metal Catalysis*; Glorius, F., Ed.; Springer Berlin Heidelberg: 2007; Vol. 21, p. 159-192.

(11)   Díez-González, S.; Marion, N.; Nolan, S. P. *N*-Heterocyclic Carbenes in Late Transition Metal Catalysis. *Chem. Rev.* **2009**, *109*, 3612-3676.

(12)   Nolan, S. P. The Development and Catalytic Uses of *N*-Heterocyclic Carbene Gold Complexes. *Acc. Chem. Res.* **2011**, *44*, 91-100.

(13)   Dyker, C. A.; Bertrand, G. Soluble Allotropes of Main-Group Elements. *Science* **2008**, *321*, 1050-1051.

(14)   Crudden, C. M.; Allen, D. P. Stability and Reactivity of *N*-Heterocyclic Carbene Complexes. *Coord. Chem. Rev.* **2004**, *248*, 2247-2273.

(15)   Hahn, F. E.; Jahnke, M. C. Heterocyclic Carbenes: Synthesis and Coordination Chemistry. *Angew. Chem. Int. Ed.* **2008**, *47*, 3122-3172.

(16)   Lin, J. C. Y.; Huang, R. T. W.; Lee, C. S.; Bhattacharyya, A.; Hwang, W. S.; Lin, I. J. B. Coinage Metal−*N*-Heterocyclic Carbene Complexes. *Chem. Rev.* **2009**, *109*, 3561-3598.

(17)   Arnold, P. L.; Casely, I. J. *F*-Block *N*-Heterocyclic Carbene Complexes. *Chem. Rev.* **2009**, *109*, 3599-3611.

(18)   Duong, H. A.; Cross, M. J.; Louie, J. *N*-Heterocyclic Carbenes as Highly Efficient Catalysts for the Cyclotrimerization of Isocyanates. *Org. Lett.* **2004**, *6*, 4679-4681.

(19)   Csihony, S.; Culkin, D. A.; Sentman, A. C.; Dove, A. P.; Waymouth, R. M.; Hedrick, J. L. Single-Component Catalyst/Initiators for the Organocatalytic Ring-Opening Polymerization of Lactide. *J. Am. Chem. Soc.* **2005**, *127*, 9079-9084.

(20)   Enders, D.; Niemeier, O.; Henseler, A. Organocatalysis by *N*-Heterocyclic Carbenes. *Chem. Rev.* **2007**, *107*, 5606-5655.

(21)   Jeong, W.; Hedrick, J. L.; Waymouth, R. M. Organic Spirocyclic Initiators for the Ring-Expansion Polymerization of β-Lactones. *J. Am. Chem. Soc.* **2007**, *129*, 8414-8415.

(22) Kamber, N. E.; Jeong, W.; Waymouth, R. M.; Pratt, R. C.; Lohmeijer, B. G. G.; Hedrick, J. L. Organocatalytic Ring-Opening Polymerization. *Chem. Rev.* **2007**, *107*, 5813-5840.

(23) Ranganath, K. V. S.; Kloesges, J.; Schäfer, A. H.; Glorius, F. Asymmetric Nanocatalysis: *N*-Heterocyclic Carbenes as Chiral Modifiers of Fe_3O_4/Pd Nanoparticles. *Angew. Chem. Int. Ed.* **2010**, *49*, 7786-7789.

(24) Zhukhovitskiy, A. V.; Mavros, M. G.; Van Voorhis, T.; Johnson, J. A. Addressable Carbene Anchors for Gold Surfaces. *J. Am. Chem. Soc.* **2013**, *135*, 7418-7421.

(25) Crudden, C. M.; Horton, J. H.; Ebralidze, I. I.; Zenkina, O. V.; McLean, A. B.; Drevniok, B.; She, Z.; Kraatz, H.-B.; Mosey, N. J.; Seki, T.; Keske, E. C.; Leake, J. D.; Rousina-Webb, A.; Wu, G. Ultra Stable Self-Assembled Monolayers of *N*-Heterocyclic Carbenes on Gold. *Nature Chem.* **2014**, *6*, 409-414.

(26) Masuda, J. D.; Martin, D.; Lyon-Saunier, C.; Baceiredo, A.; Gornitzka, H.; Donnadieu, B.; Bertrand, G. Stable *P*-Heterocyclic Carbenes: Scope and Limitations. *Chem. Asian J.* **2007**, *2*, 178-187.

(27) Rochat, A. C.; Olofson, R. A. Base-Induced C-H/C-D Exchange in Tetrazoles and Tetrazolium Cations. *Tetrahedron Lett.* **1969**, *10*, 3377-3380.

(28) Olofson, R. A.; Lotts, K. D. Base-Induced Fragmentations of 1,2,4-Oxadiazolin-5-Ones and Their N-Alkyl Salts. *Tetrahedron Lett.* **1979**, *20*, 3131-3134.

(29) Smith, P. A. S.; Leon, E. The Thermal Breakdown of Diaryltetrazoles. *J. Am. Chem. Soc.* **1958**, *80*, 4647-4654.

(30) Couture, P.; Terlouw, J. K.; Warkentin, J. 2-Alkoxy-2-Amino-Δ3-1,3,4-Oxadiazolines as Novel Sources of Alkoxyaminocarbenes. *J. Am. Chem. Soc.* **1996**, *118*, 4214-4215.

(31) Couture, P.; Warkentin, J. Spiro-Fused 2-Alkoxy-2-Amino-Δ3-1,3,4-Oxadiazolines. Synthesis and Thermolysis to Corresponding Aminooxycarbenes. *Can. J. Chem.* **1997**, *75*, 1264-1280.

(32) Couture, P.; Warkentin, J. Chemistry of Cyclic Aminooxycarbenes. *Can. J. Chem.* **1997**, *75*, 1281-1294.

(33) Corey, E. J.; Winter, R. A. E. A New, Stereospecific Olefin Synthesis from 1,2-Diols. *J. Am. Chem. Soc.* **1963**, *85*, 2677-2678.

(34) Lemal, D. M.; Banitt, E. H. Bis-(Alkylthio)-Carbenes. *Tetrahedron Lett.* **1964**, *5*, 245-251.

(35) Horton, D.; Tindall, C. G. Synthesis and Reactions of Unsaturated Sugars. XI. Evidence for a Carbenoid Intermediate in the Corey-Winter Alkene Synthesis. *J. Org. Chem.* **1970**, *35*, 3558-3559.

(36) Olofson, R. A.; Pepe, J. P. *N*-Cyanamidopyrroles and *N*-Cyanamidoimines from 4-Amino-1,2,4-Triazole. *Tetrahedron Lett.* **1979**, *20*, 3129-3130.

(37) Huisgen, R. Thermische Stabilität Und Aromatischer Charakter: Ringöffnungen Der Azole. *Angew. Chem.* **1960**, *72*, 359-372.

(38) Kuhn, N.; Steimann, M.; Weyers, G.; Henkel, G. 1,3-Diisopropyl-4,5-Dimethylimidazolium-2-*N,N'*-Diisopropylamidinat, Ein Neuartiges Betain. *Z. Naturforsch., B: Chem. Sci.* **1999**, *54*, 434-440.

(39) Korotkikh, N. I.; Glinyanaya, N. V.; Cowley, A. H.; Moore, J. A.; Knishevitsky, A. V.; Pekhtereva, T. M.; Shvaika, O. P. Tandem Transformations of 1,2,4-Triazol-5-Ylidenes into 5-Amidino-1,2,4-Triazoles. *Arkivoc* **2007**, 156-172.

(40) Grummitt, O.; Ardis, A. E.; Fick, J. Thermal Dissociation of Methyldihydrothiophene-1-Dioxides. *J. Am. Chem. Soc.* **1950**, *72*, 5167-5170.

(41) Baldwin, J. E. Cycloadditions: X. Kinetics of the Thermal Decarbonylation of Dicyclopentadiene-1.8-Dione. *Can. J. Chem.* **1966**, *44*, 2051-2056.

(42) Turro, N. J.; Chow, M.-F.; Rigaudy, J. Mechanism of Thermolysis of Endoperoxides of Aromatic Compounds. Activation Parameters, Magnetic Field, and Magnetic Isotope Effects. *J. Am. Chem. Soc.* **1981**, *103*, 7218-7224.

(43) Yang, N. C. C.; Chen, M. J.; Chen, P. Chemistry of Benzene-Anthracene Cyclodimers. *J. Am. Chem. Soc.* **1984**, *106*, 7310-7315.

(44) Hoffmann, R.; Woodward, R. B. Orbital Symmetry Control of Chemical Reactions. *Science* **1970**, *167*, 825-831.

(45) Zheng, J.; Zhao, Y.; Truhlar, D. G. Representative Benchmark Suites for Barrier Heights of Diverse Reaction Types and Assessment of Electronic Structure Methods for Thermochemical Kinetics. *J. Chem. Theory Comput.* **2006**, *3*, 569-582.

(46) Delaude, L. Betaine Adducts of *N*-Heterocyclic Carbenes: Synthesis, Properties, and Reactivity. *Eur. J. Inorg. Chem.* **2009**, *2009*, 1681-1699.

(47) Takamizawa, A.; Hirai, K.; Matsumoto, S. Addition Reactions of Thiazolium Ylids with Arylisothiocyanates and Di-*p*-Tolylcarbodiimide. Novel Zwitter-Ionic Compounds Stabilized by Nitrogen and Sulfur. *Tetrahedron Lett.* **1968**, *9*, 4027-4030.

(48) Takamizawa, A.; Matsumoto, S.; Makino, I. Synthese of 4-Aryliminoparabanic Acids and 2-Arylimino-2,3-Dihydro-1,4-Thiazine Derivatives Via 2-*N,N'*-Diarylamidinothiazolium Salts. *Chem. Pharm. Bull.* **1974**, *22*, 311-315.

(49) Dröge, T.; Glorius, F. The Measure of All Rings—*N*-Heterocyclic Carbenes. *Angew. Chem. Int. Ed.* **2010**, *49*, 6940-6952.

(50) Naumann, S.; Buchmeiser, M. R. Liberation of *N*-Heterocyclic Carbenes (NHCs) from Thermally Labile Progenitors: Protected NHCs as Versatile Tools in Organo- and Polymerization Catalysis. *Cat. Sci. Technol.* **2014**, *4*, 2466-2479.

(51) Fulmer, G. R.; Miller, A. J. M.; Sherden, N. H.; Gottlieb, H. E.; Nudelman, A.; Stoltz, B. M.; Bercaw, J. E.; Goldberg, K. I. NMR chemical shifts of trace impurities: Common laboratory solvents, organics, and gases in deuterated solvents relevant to the organometallic chemist. *Organometallics* **2010**, *29*, 2176-2179.

(52) Sheldrick, G. Phase annealing in SHELX-90: direct methods for larger structures. *Acta Crystallogr. Sect. A: Fundam. Crystallogr.* **1990**, *46*, 467-473.

(53) Sheldrick, G. A short history of SHELX. *Acta Crystallogr. Sect. A: Fundam. Crystallogr.* **2008**, *64*, 112-122.

(54) Müller, P. Practical suggestions for better crystal structures. *Crystallogr. Rev.* **2009**, *15*, 57-83.

(55) Kuhn, K. M., Grubbs, R. H. A facile preparation of imidazolinium chlorides. *Org. Lett.* **2008**, *10*, 2075-2077.

(56) Leuthäußer, S., Schmidts, V., Thiele, C. M., Plenio, H. π-Face donor properties of N-heterocyclic carbenes in Grubbs II complexes. *Chem.–Eur. J.* **2008**, *14*, 5465-5481.

(57) Türkmen, H., Çetinkaya, B. 1,3-Diarylimidazolidin-2-ylidene (NHC) complexes of Pd(II): Electronic effects on cross-coupling reactions and thermal decompositions. *J. Organomet. Chem.* **2006**, *691*, 3749-3759.

CHAPTER 5. Toward Dynamic and Hierarchically Structured Polymer Gels: An Introduction to Polymer Metal-Organic Cage Gels

Polymer gels, networks of cross-linked polymer chains expanded throughout their entire volume with a fluid,[1] are ubiquitous and versatile materials that derive their utility in large part from their viscoelastic behavior. Nature has relied on polymer gels to execute vital functions: cartilage, one example of a biological polymer gel (biogel), lubricates and diffuses the stress on skeletal joints[2,3]; the extracellular matrix and nuclear pores, examples of micro-/nano-scopic biogels, regulate inter- and intra-cellular molecular trafficking, respectively[4]; mucus serves to both lubricate wet epithilia and also prevent pathogenic entry, while enabling the passage of sperm during ovulation.[4] These are just four of the numerous biogels critical to living systems.[4]

Since Grindlay and Clagett's 1949 invention of formaldehyde-cross-linked poly(vinyl alcohol) "plastic sponge" (now known as Ivalon®) for use in biomedical implants,[5,6] as well as Wichterle and Lim's invention of soft polymer gel contact lenses reported in 1960,[7] synthetic polymer gels have become a critical biomedical materials platform: from scaffolds for cell cultures and tissue engineering to vehicles for drug delivery.[8,9] Yet, despite decades of progress in synthetic polymer network chemistry, we still face the challenge to recapitulate the hierarchical structure and dynamic properties – and thereby functions – of biogels in synthetic materials. Steps toward addressing this challenge will not only improve our understanding of fundamental polymer network structure-function relationships but also translate into advances in healthcare.
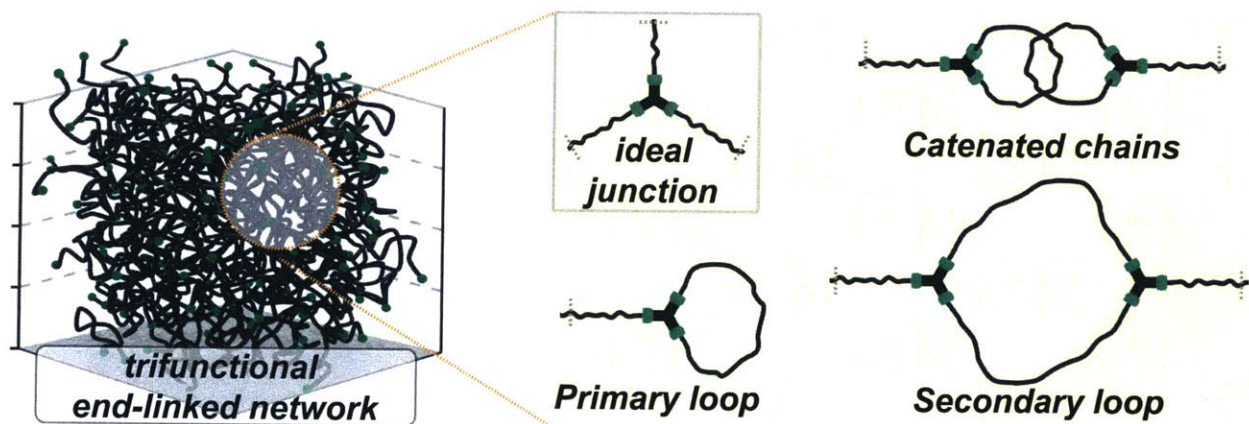
Figure 1. An illustration of a trifunctional end-linked network with ideal junctions and loop or catenated chain defects shown. Note: defects arising from incomplete end-group or cross-linker conversion are not shown.

Among synthetic polymer gels, some of the most well-studied are ones with permanent (i.e. covalently cross-linked) networks also known as chemical gels,[10,11] and among these the structurally most well-defined are end-linked polymer networks,[12,13] in which, as their name suggests, cross-linking takes place at the ends of polymer chains rather than randomly along the

chain. However, even in this subfield of polymer gels, the precise structure of the network that takes into account defects[14] is an active area of research: namely, although experimental quantification of such network defects as primary loops (Figure 1) has been recently accomplished by Johnson and coworkers,[15-17] precise quantification of higher order or catenation defects (Figure 1) and synthetic control of defect content are only beginning to be addressed.[18,19] Solutions to these problems have far-reaching consequences: the more detailed our understanding of junction structures and their defects, the better we can tailor the mechanical properties of polymer gels.

Although traditional covalent cross-linking endows polymer gels with satisfactory mechanical properties for some applications, these gels cannot recapitulate the hierarchical structure or dynamics of a wide range of biogels. To begin to address this challenge, dynamic covalent chemistry[20,21] has been implemented to generate "covalent adaptable networks,"[22-24] with particular attention devoted recently to associative chain-shuffling dynamics.[25-27] Non-covalent chemistry – particularly H-bonding,[28] ionic interactions,[29] metal-ligand coordination[30,31] and combinations thereof[32] – has also been explored for polymer gel synthesis,[11,33] and the union of covalent and non-covalent gelation mechanisms in double-network polymer gels have garnered progressively more interest from the materials science community.[34,35] However, although a wide range of dynamics and mechanics has been captured in these gels, and some physical and chemical principles underlying them have been elucidated,[36-47] simultaneous control of dynamics and hierarchical structure is still in its infancy. Moreover, precise understanding and control of junction defects in such dynamic networks with hierarchical structure is an even more daunting but no less significant task than in covalently cross-linked polymer networks.

Key reported examples of hierarchically assembled dynamic polymer gels could be categorized based on their mechanisms of junction formation: (1) uniform nanoscopic "bundling" of polymer fragments, (2) microphase separation of block copolymers, and (3) polymer chain/nanomaterial association (Figure 2). Tirrell and coworkers pioneered the first approach through the development of telechelic polypeptides with terminal domains, which could assemble into oligomeric coiled-coils.[48] Notably, the stoichiometry of such coiled-coil junctions (i.e., the number of components assembled to form a junction) could be programmed into the terminal polypeptide sequence.[48] The second approach, related closely to the first, entails microphase separation of terminal blocks and mid-blocks of multiblock copolymers to

form micelle-cross-linked polymer gels[33] and has been pioneered independently by Gamarra[49] and Chen[50] and expanded upon by Reynaers,[51] Spontak,[52] and their coworkers in the 1990s. A combination of methods (1) and (2) has been reported recently by Olsen and coworkers,[53] and Rowan and coworkers uncovered a related gelation mechanism in coordination-cross-linked gels: crystallization of metallopolymer chains into nano- or micro-particles that form a gel network through flocculation. Notably, the development of analogous solvent-free supramolecular polymers and block-copolymer polymer assemblies informed the development of the gels, but their disparate dynamic and mechanical properties place them outside the scope of this overview.
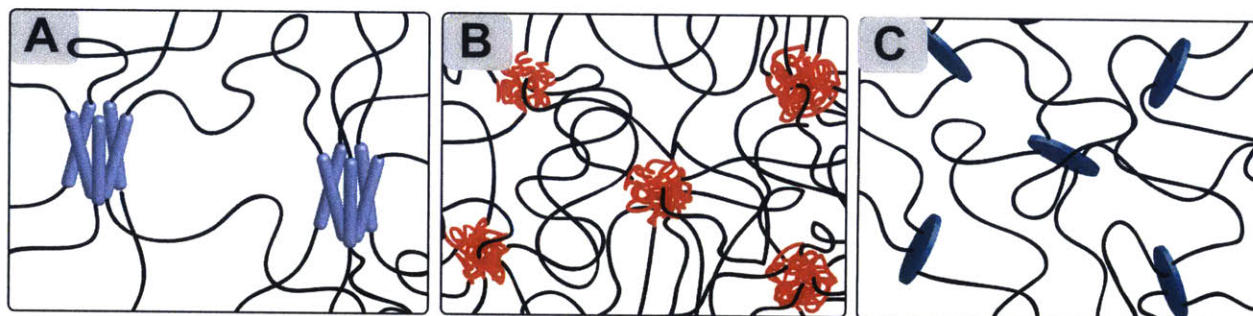
Figure 2. A.–C. Well-studied cross-linking mechanisms of hierachically assembled polymer gel networks: 1 (A), 2 (B), and 3 (C).

In 2002, Haraguchi and Takehisa demonstrated the promise of approach (3):[54] namely, they observed that clay nanoparticle-cross-linked polymer hydrogels had superior extensibility and recovery compared to traditionally cross-linked gels. Major subsequent advances in materials properties (e.g., G') for similar nanocomposite gels were achieved by Chen and Adler,[55] as well as Aida and coworkers,[56] and Hourdet and Petit,[57] among others. In a related pioneering effort, Leibler demonstrated the capability of silica nanoparticles – and suitably functionalized nanomaterials in general – to serve as adhesives for polymer hydrogels.[58]

All of the above gelation mechanisms have their advantages and disadvantages. Approach (1) has the advantage of superb assembly precision, but suffers from limited junction stoichiometry and relatively weak van der Waals interactions involved in the assembly, both of which limit the gels' mechanical properties and range of dynamics. Furthermore, this approach requires protein expression to achieve the desired precision of assembly, which limits not only the scale on which these gels can be produced, but also the scope of junction geometries and functions that can be installed in them. Approaches (2) and (3) have the benefits of a theoretically unlimited junction stoichiometry and the possibility for large-scale inexpensive gel

production. However, they also suffer from lack of precision in – and therefore, fine synthetic control of – junction assembly, which introduces non-uniformity in gel mechanics and dynamics.

Metal coord. geom.	Ligand bite angle →	0°	60°	90°	109.5°	120°
	Linear	M_2L_2	M_3L_3	M_4L_4	M_5L_5	M_6L_6
	Square planar	M_2L_4		M_6L_{12}		$M_{12}L_{24}$

Figure 3. Effect of the ligand bite angle and metal coordination geometry on the stoichiometry of the cages or polygons into which they assemble, as described in references 60 and 65.

From this brief overview of the polymer gel field emerges the conclusion that there is a demand for an alternative – scalable, more broadly and easily tunable, yet precise – mechanism to generate dynamic polymer gels with hierarchical structure. Coordination chemistry offers numerous advantages in this regard because it provides access to a wide range of kinetics and thermodynamics of interactions,[59] and, critically, supports precise and predictable sub-component self-assembly controlled by such parameters as ligand bite angle, metal coordination geometry, and nature of the counterions (Figure 3).[60-65] The vast body of literature, which describes subcomponent self-assembly of metal ions (M) and ligands (L) into metal-organic cages (MOCs, also known as metal-organic polyhedra[66] or MOPs) "M_iL_j" offers numerous possibilities of junctions one can create in polymer gels by merging polymers and MOCs into "polyMOC" gels.[60,61,63-65,67] The broad range of precisely controlled junction composition, stoichiometry, and geometry of MOCs promises to reveal unprecedented properties and structure-function relationships in polyMOC gels.

Prior to the publication of our findings examined in Chapter 6, the mechanism of gelation via MOC assembly has been discussed in only two recent reports, one from the Johnson group[68] and one from Nitschke and coworkers[69]; both of these dealt with junctions of low stoichiometry (M_4L_4) and the cages in these gels were not directly characterized. Inspired by the reports from Fujita and coworkers of robust and uniform assembly of M_nL_{2n} (n = 6, 12, 24) cages from Pd^{2+} salts and bis-pyridine ligands,[65,70,71] we set out to explore the formation and properties of polyMOC gels with junctions at the opposite ends of the stoichiometry spectrum: M_2L_4[72-79] and $M_{12}L_{24}$ (Figure 4).[65,70,71] Hence, the last chapter of this thesis will focus on our development of these polyMOCs and the elaboration of their network structure, mechanical properties, and installation of function through junction engineering.

369
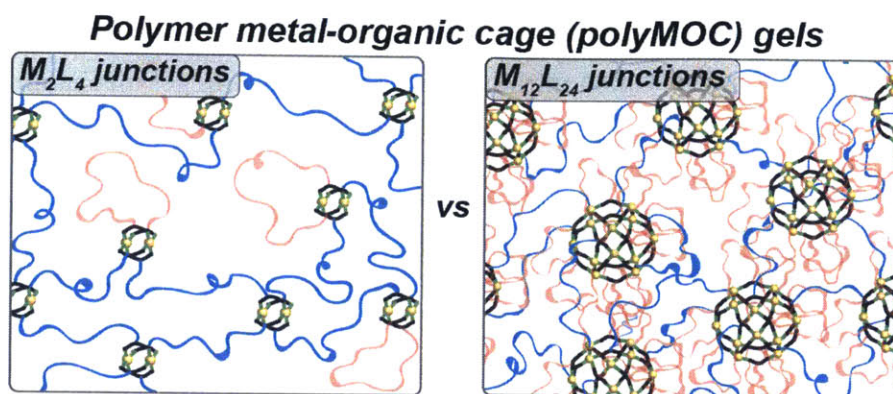
Figure 4. PolyMOC gels designed to have M_2L_4 or $M_{12}L_{24}$ junctions examined in Chapter 6. Primary loops are shown in red, and lastically active chains in blue; ligands and metal ions are in black/green and golden, respectively.

Specifically, Chapter 6 will describe the design and synthesis of these polyMOCs, and their initial computational, spectroscopic, neutron scattering, and rheometry characterization, which reveal both high branch functionality (f, the number of elastically active polymer chains per junction) and high primary loop content in the $M_{12}L_{24}$ cage-linked networks (illustrated in Figure 4).[80] This unusual combination of high loop content and high f enables unprecedented junction engineering, whereby primary loop defects can be replaced with function-bearing ligands without affecting the storage modulus (G') of the gel. The premise of our ongoing work (not included in this thesis), which is being prepared for publication, is the question of how the polymer chain length affects the network structure and defect distribution in polyMOCs.[81] Through the elucidation of this fundamental question via a combination of X-ray and neutron scattering, magic angle spinning nuclear magnetic resonance (MAS NMR) spectroscopy, rheometry, and computation, more complexity in polyMOC network structure is revealed. In this study, we also explore one key consequence of polyMOC structure: relatively high-G' and tough polymer gels can be attained with exceedingly low concentrations of high-f MOC junctions.

5.1 References

(1) McNaught, A. D.; Wilkinson, A. *Iupac. Compendium of Chemical Terminology, 2nd Ed. (the "Gold Book")*; Blackwell Scientific Publications: Oxford, 1997.

(2) Cohen, N. P.; Foster, R. J.; Mow, V. C. Composition and Dynamics of Articular Cartilage: Structure, Function, and Maintaining Healthy State. *J. Orthop. Sports Phys. Ther.* **1998**, *28*, 203-215.

(3) Buckwalter, J. A.; Mankin, H. J.; Grodzinsky, A. J. Articular Cartilage and Osteoarthritis. *Instr. Course Lect. Am. Acad. Orthop. Surg.* **2005**, *54*, 465.

(4) Lieleg, O.; Ribbeck, K. Biological Hydrogels as Selective Diffusion Barriers. *Trends Cell Biol.* **2011**, *21*, 543-551.

(5) Grindlay, J.; Clagett, O. T. In *Proceedings of the staff meetings. Mayo Clinic* 1949; Vol. 24, p 538-538.

(6) Grindlay, J. H.; Waugh, J. M. Plastic Sponge Which Acts as a Framework for Living Tissue: Experimental Studies and Preliminary Report of Use to Reinforce Abdominal Aneurysms. *AMA Arch. Surg.* **1951**, *63*, 288-297.

(7) Wichterle, O.; Lim, D. Hydrophilic Gels for Biological Use. *Nature* **1960**, *185*, 117-118.

(8) Kirschner, C. M.; Anseth, K. S. Hydrogels in Healthcare: From Static to Dynamic Material Microenvironments. *Acta Mater.* **2013**, *61*, 931-944.

(9) Annabi, N.; Tamayol, A.; Uquillas, J. A.; Akbari, M.; Bertassoni, L. E.; Cha, C.; Camci-Unal, G.; Dokmeci, M. R.; Peppas, N. A.; Khademhosseini, A. 25th Anniversary Article: Rational Design and Applications of Hydrogels in Regenerative Medicine. *Adv. Mater.* **2014**, *26*, 85-124.

(10) Flory, P. J. *Principles of Polymer Chemistry*; Cornell University Press, 1953.

(11) Rubinstein, M.; Colby, R. *Polymers Physics*; Oxford, 2003.

(12) Mark, J. E.; Sullivan, J. L. Model Networks of End-Linked Polydimethylsiloxane Chains. I. Comparisons between Experimental and Theoretical Values of the Elastic Modulus and the Equilibrium Degree of Swelling. *J. Chem. Phys.* **1977**, *66*, 1006-1011.

(13) Hild, G. Model Networks Based on 'Endlinking' Processes: Synthesis, Structure and Properties. *Prog. Polym. Sci.* **1998**, *23*, 1019-1149.

(14) Cail, J.; Stepto, R. The Gel Point and Network Formation–Theory and Experiment. *Polym. Bull.* **2007**, *58*, 15-25.

(15) Kawamoto, K.; Zhong, M.; Wang, R.; Olsen, B. D.; Johnson, J. A. Loops Versus Branch Functionality in Model Click Hydrogels. *Macromolecules* **2015**, *48*, 8980-8988.

(16) Zhou, H.; Woo, J.; Cok, A. M.; Wang, M.; Olsen, B. D.; Johnson, J. A. Counting Primary Loops in Polymer Gels. *Proc. Natl. Acad. Sci. USA* **2012**, *109*, 19119-19124.

(17) Zhou, H. X.; Schon, E. M.; Wang, M. Z.; Glassman, M. J.; Liu, J.; Zhong, M. J.; Diaz, D. D.; Olsen, B. D.; Johnson, J. A. Crossover Experiments Applied to Network Formation Reactions: Improved Strategies for Counting Elastically Inactive Molecular Defects in PEG Gels and Hyperbranched Polymers. *J. Am. Chem. Soc.* **2014**, *136*, 9464-9470.

(18) Zhong, M. J.; Wang, R.; Kawamoto, K.; Olsen, B. D.; Johnson, J. A. Quantifying the Impact of Molecular Defects on Polymer Network Elasticity. *Submitted* **2016**.

(19) Gu, Y.; Kawamoto, K.; Zhong, M.; Chen, M.; Hore, M. J. A.; Jordan, A. M.; Korley, L. T. J.; Johnson, J. A. Topological Control of Polymer Networks. *Submitted* **2016**.

(20) Rowan, S. J.; Cantrill, S. J.; Cousins, G. R. L.; Sanders, J. K. M.; Stoddart, J. F. Dynamic Covalent Chemistry. *Angew. Chem. Int. Ed.* **2002**, *41*, 898-952.

371

(21) Jin, Y.; Yu, C.; Denman, R. J.; Zhang, W. Recent Advances in Dynamic Covalent Chemistry. *Chem. Soc. Rev.* **2013**, *42*, 6634-6654.

(22) Scott, T. F.; Schneider, A. D.; Cook, W. D.; Bowman, C. N. Photoinduced Plasticity in Cross-Linked Polymers. *Science* **2005**, *308*, 1615-1617.

(23) Kloxin, C. J.; Scott, T. F.; Adzima, B. J.; Bowman, C. N. Covalent Adaptable Networks (CANs): A Unique Paradigm in Cross-Linked Polymers. *Macromolecules* **2010**, *43*, 2643-2653.

(24) Bowman, C. N.; Kloxin, C. J. Covalent Adaptable Networks: Reversible Bond Structures Incorporated in Polymer Networks. *Angew. Chem. Int. Ed.* **2012**, *51*, 4272-4274.

(25) Montarnal, D.; Capelot, M.; Tournilhac, F.; Leibler, L. Silica-Like Malleable Materials from Permanent Organic Networks. *Science* **2011**, *334*, 965-968.

(26) Denissen, W.; Winne, J. M.; Du Prez, F. E. Vitrimers: Permanent Organic Networks with Glass-Like Fluidity. *Chem. Sci.* **2016**, *7*, 30-38.

(27) Zhou, H.; Johnson, J. A. Photo-Controlled Growth of Telechelic Polymers and End-Linked Polymer Gels. *Angew. Chem. Int. Ed.* **2013**, *52*, 2235-2238.

(28) Lange, R. F. M.; Van Gurp, M.; Meijer, E. W. Hydrogen-Bonded Supramolecular Polymer Networks. *J. Polym. Sci., Part A: Polym. Chem.* **1999**, *37*, 3657-3670.

(29) Lee, K. Y.; Mooney, D. J. Alginate: Properties and Biomedical Applications. *Prog. Polym. Sci.* **2012**, *37*, 106-126.

(30) McKenzie, B. M.; Rowan, S. J. In *Molecular Recognition and Polymers*; John Wiley & Sons, Inc.: 2008, p. 157-178.

(31) Brassinne, J.; Fustin, C.-A.; Gohy, J.-F. Polymer Gels Constructed through Metal–Ligand Coordination. *J. Inorg. Organomet. Polym. Mater.* **2012**, *23*, 24-40.

(32) Nair, K. P.; Breedveld, V.; Weck, M. Multiresponsive Reversible Polymer Networks Based on Hydrogen Bonding and Metal Coordination. *Macromolecules* **2011**, *44*, 3346-3357.

(33) Krishnan, A. S.; Roskov, K. E.; Spontak, R. J. In *Advanced Nanomaterials*; Wiley-VCH Verlag GmbH & Co. KGaA: 2010, p. 791-834.

(34) Gong, J. P. Why Are Double Network Hydrogels So Tough? *Soft Matter* **2010**, *6*, 2583-2590.

(35) Sun, J.-Y.; Zhao, X.; Illeperuma, W. R. K.; Chaudhuri, O.; Oh, K. H.; Mooney, D. J.; Vlassak, J. J.; Suo, Z. Highly Stretchable and Tough Hydrogels. *Nature* **2012**, *489*, 133-136.

(36) Beck, J. B.; Rowan, S. J. Multistimuli, Multiresponsive Metallo-Supramolecular Polymers. *J. Am. Chem. Soc.* **2003**, *125*, 13922-13923.

(37) Zhao, Y.; Beck, J. B.; Rowan, S. J.; Jamieson, A. M. Rheological Behavior of Shear-Responsive Metallo-Supramolecular Gels. *Macromolecules* **2004**, *37*, 3529-3531.

(38) Loveless, D. M.; Jeon, S. L.; Craig, S. L. Rational Control of Viscoelastic Properties in Multicomponent Associative Polymer Networks. *Macromolecules* **2005**, *38*, 10171-10177.

(39) Yount, W. C.; Loveless, D. M.; Craig, S. L. Small-Molecule Dynamics and Mechanisms Underlying the Macroscopic Mechanical Properties of Coordinatively Cross-Linked Polymer Networks. *J. Am. Chem. Soc.* **2005**, *127*, 14488-14496.

(40) Yount, W. C.; Loveless, D. M.; Craig, S. L. Strong Means Slow: Dynamic Contributions to the Bulk Mechanical Properties of Supramolecular Networks. *Angew. Chem. Int. Ed.* **2005**, *44*, 2746-2748.

(41) Weng, W.; Beck, J. B.; Jamieson, A. M.; Rowan, S. J. Understanding the Mechanism of Gelation and Stimuli-Responsive Nature of a Class of Metallo-Supramolecular Gels. *J. Am. Chem. Soc.* **2006**, *128*, 11663-11672.

(42) Weng, W.; Jamieson, A. M.; Rowan, S. J. Structural Origin of the Thixotropic Behavior of a Class of Metallosupramolecular Gels. *Tetrahedron* **2007**, *63*, 7419-7431.

(43) Weng, W. G.; Li, Z.; Jamieson, A. M.; Rowan, S. J. Control of Gel Morphology and Properties of a Class of Metallo-Supramolecular Polymers by Good/Poor Solvent Environments. *Macromolecules* **2009**, *42*, 236-246.

(44) Holten-Andersen, N.; Harrington, M. J.; Birkedal, H.; Lee, B. P.; Messersmith, P. B.; Lee, K. Y. C.; Waite, J. H. Ph-Induced Metal-Ligand Cross-Links Inspired by Mussel Yield Self-Healing Polymer Networks with near-Covalent Elastic Moduli. *Proc. Natl. Acad. Sci. USA* **2011**, *108*, 2651-2655.

(45) Kean, Z. S.; Hawk, J. L.; Lin, S. T.; Zhao, X. H.; Sijbesma, R. P.; Craig, S. L. Increasing the Maximum Achievable Strain of a Covalent Polymer Gel through the Addition of Mechanically Invisible Cross-Links. *Adv. Mater.* **2014**, *26*, 6013-+.

(46) Grindy, S. C.; Learsch, R.; Mozhdehi, D.; Cheng, J.; Barrett, D. G.; Guan, Z.; Messersmith, P. B.; Holten-Andersen, N. Control of Hierarchical Polymer Mechanics with Bioinspired Metal-Coordination Dynamics. *Nat. Mater.* **2015**, *14*, 1210-1216.

(47) Menyo, M. S.; Hawker, C. J.; Waite, J. H. Rate-Dependent Stiffness and Recovery in Interpenetrating Network Hydrogels through Sacrificial Metal Coordination Bonds. *ACS Macro Lett.* **2015**, *4*, 1200-1204.

(48) Petka, W. A.; Harden, J. L.; McGrath, K. P.; Wirtz, D.; Tirrell, D. A. Reversible Hydrogels from Self-Assembling Artificial Proteins. *Science* **1998**, *281*, 389-392.

(49) Gamarra, J. P., Heat resistant gel compositions. U.S. Patent 5149736, Sep. 22, 1992.

(50) Chen, J. Y., Thermoplastic elastomer gelatinous articles. U.S. Patent 5334646, Aug. 2, 1994.

(51) Mischenko, N.; Reynders, K.; Mortensen, K.; Scherrenberg, R.; Fontaine, F.; Graulus, R.; Reynaers, H. Structural Studies of Thermoplastic Triblock Copolymer Gels. *Macromolecules* **1994**, *27*, 2345-2347.

(52) Laurer, J. H.; Bukovnik, R.; Spontak, R. J. Morphological Characteristics of SEBS Thermoplastic Elastomer Gels. *Macromolecules* **1996**, *29*, 5760-5762.

(53) Glassman, M. J.; Chan, J.; Olsen, B. D. Reinforcement of Shear Thinning Protein Hydrogels by Responsive Block Copolymer Self-Assembly. *Adv. Funct. Mater.* **2013**, *23*, 1182-1193.

(54) Haraguchi, K.; Takehisa, T. Nanocomposite Hydrogels: A Unique Organic–Inorganic Network Structure with Extraordinary Mechanical, Optical, and Swelling/De-Swelling Properties. *Adv. Mater.* **2002**, *14*, 1120-1124.

(55) Liu, Y.; Zhu, M.; Liu, X.; Zhang, W.; Sun, B.; Chen, Y.; Adler, H.-J. P. High Clay Content Nanocomposite Hydrogels with Surprising Mechanical Strength and Interesting Deswelling Kinetics. *Polymer* **2006**, *47*, 1-5.

(56) Wang, Q.; Mynar, J. L.; Yoshida, M.; Lee, E.; Lee, M.; Okuro, K.; Kinbara, K.; Aida, T. High-Water-Content Mouldable Hydrogels by Mixing Clay and a Dendritic Molecular Binder. *Nature* **2010**, *463*, 339-343.

(57) Hourdet, D.; Petit, L. In *Macromolecular symposia*; Wiley Online Library: 2010; Vol. 291, p 144-158.

(58) Rose, S.; Prevoteau, A.; Elzière, P.; Hourdet, D.; Marcellan, A.; Leibler, L. Nanoparticle Solutions as Adhesives for Gels and Biological Tissues. *Nature* **2014**, *505*, 382-385.

(59) Cotton, F. A.; Wilkinson, G.; Murillo, C. A.; Bochmann, M.; Grimes, R. *Advanced Inorganic Chemistry*; Wiley New York, 1999; Vol. 5.

(60) Leininger, S.; Olenyuk, B.; Stang, P. J. Self-Assembly of Discrete Cyclic Nanostructures Mediated by Transition Metals. *Chem. Rev. (Washington, DC, U. S.)* **2000**, *100*, 853-908.

(61) Sun, W.-Y.; Yoshizawa, M.; Kusukawa, T.; Fujita, M. Multicomponent Metal–Ligand Self-Assembly. *Curr. Opin. Chem. Biol.* **2002**, *6*, 757-764.

(62) Forgan, R. S.; Sauvage, J.-P.; Stoddart, J. F. Chemical Topology: Complex Molecular Knots, Links, and Entanglements. *Chem. Rev. (Washington, DC, U. S.)* **2011**, *111*, 5434-5464.

(63) Smulders, M. M. J.; Riddell, I. A.; Browne, C.; Nitschke, J. R. Building on Architectural Principles for Three-Dimensional Metallosupramolecular Construction. *Chem. Soc. Rev.* **2013**, *42*, 1728-1754.

(64) Chifotides, H. T.; Dunbar, K. R. Anion–π Interactions in Supramolecular Architectures. *Acc. Chem. Res.* **2013**, *46*, 894-906.

(65) Harris, K.; Fujita, D.; Fujita, M. Giant Hollow M_nL_{2n} Spherical Complexes: Structure, Functionalisation and Applications. *Chem. Commun.* **2013**, *49*, 6703-6712.

(66) Tranchemontagne, D. J.; Ni, Z.; O'Keeffe, M.; Yaghi, O. M. Reticular Chemistry of Metal–Organic Polyhedra. *Angew. Chem. Int. Ed.* **2008**, *47*, 5136-5147.

(67) Ronson, T. K.; Zarra, S.; Black, S. P.; Nitschke, J. R. Metal-Organic Container Molecules through Subcomponent Self-Assembly. *Chem. Commun.* **2013**, *49*, 2476-2490.

(68) Kawamoto, K.; Grindy, S. C.; Liu, J.; Holten-Andersen, N.; Johnson, J. A. Dual Role for 1, 2, 4, 5-Tetrazines in Polymer Networks: Combining Diels–Alder Reactions and Metal Coordination to Generate Functional Supramolecular Gels. *ACS Macro Lett.* **2015**, *4*, 458-461.

(69) Foster, J. A.; Parker, R. M.; Belenguer, A. M.; Kishi, N.; Sutton, S.; Abell, C.; Nitschke, J. R. Differentially Addressable Cavities within Metal–Organic Cage-Cross-Linked Polymeric Hydrogels. *J. Am. Chem. Soc.* **2015**, *137*, 9722-9729.

(70) Tominaga, M.; Suzuki, K.; Kawano, M.; Kusukawa, T.; Ozeki, T.; Shakamoto, S.; Yamaguchi, K.; Fujita, M. Finite, Spherical Coordination Networks That Self-Organize from 36 Small Components. *Angew. Chem., Int. Ed.* **2004**, *43*, 5621-5625.

(71) Sun, Q.-F.; Iwasa, J.; Ogawa, D.; Ishido, Y.; Sato, S.; Ozeki, T.; Sei, Y.; Yamaguchi, K.; Fujita, M. Self-Assembled $M_{24}L_{48}$ Polyhedra and Their Sharp Structural Switch Upon Subtle Ligand Variation. *Science* **2010**, *328*, 1144-1147.

(72) Chand, D. K.; Biradha, K.; Fujita, M. Self-Assembly of a Novel Macrotricyclic Pd(II) Metallocage Encapsulating a Nitrate Ion. *Chem. Commun.* **2001**, 1652-1653.

(73) Owens, T. D.; Hollander, F. J.; Oliver, A. G.; Ellman, J. A. Synthesis, Utility, and Structure of Novel Bis(Sulfinyl)Imidoamidine Ligands for Asymmetric Lewis Acid Catalysis. *J. Am. Chem. Soc.* **2001**, *123*, 1539-1540.

(74) Desmarets, C.; Policar, C.; Chamoreau, L.-M.; Amouri, H. Design, Self-Assembly, and Molecular Structures of 3D Copper(II) Capsules Templated by BF_4^- Guest Anions. *Eur. J. Inorg. Chem.* **2009**, *2009*, 4396-4400.

(75) Liu, H.-K.; Cai, Y.; Luo, W.; Tong, F.; You, C.; Lü, S.; Huang, X.; Ye, H.-Y.; Su, F.; Wang, X. Discrete M_2L_2 Metallacycle and M_2L_4 Cage Frameworks and Anion

Competitive Reactions of Cu_2L_4 Type Receptor. *Inorg. Chem. Commun.* **2009**, *12*, 457-460.

(76)   Liao, P.; Langloss, B. W.; Johnson, A. M.; Knudsen, E. R.; Tham, F. S.; Julian, R. R.; Hooley, R. J. Two-Component Control of Guest Binding in a Self-Assembled Cage Molecule. *Chemical Commun.* **2010**, *46*, 4932-4934.

(77)   Kishi, N.; Li, Z.; Yoza, K.; Akita, M.; Yoshizawa, M. An M_2L_4 Molecular Capsule with an Anthracene Shell: Encapsulation of Large Guests up to 1 nm. *J. Am. Chem. Soc.* **2011**, *133*, 11438-11441.

(78)   Li, Z.; Kishi, N.; Hasegawa, K.; Akita, M.; Yoshizawa, M. Highly Fluorescent M_2L_4 Molecular Capsules with Anthracene Shells. *Chem. Commun.* **2011**, *47*, 8605-8607.

(79)   Li, Z.; Kishi, N.; Yoza, K.; Akita, M.; Yoshizawa, M. Isostructural M_2L_4 Molecular Capsules with Anthracene Shells: Synthesis, Crystal Structures, and Fluorescent Properties. *Chem. Eur. J.* **2012**, *18*, 8358-8365.

(80)   Zhukhovitskiy, A. V.; Zhong, M.; Keeler, E. G.; Michaelis, V. K.; Sun, J. E.; Hore, M. J.; Pochan, D. J.; Griffin, R. G.; Willard, A. P.; Johnson, J. A. Highly Branched and Loop-Rich Gels Via Formation of Metal–Organic Cages Linked by Polymers. *Nat. Chem.* **2016**, *8*, 33-41.

(81)   Zhukhovitskiy, A. V.; Zhao, J.; Hore, M. J. A.; Keeler, E. G.; Alt, E. A.; Zhong, M. J.; Teichen, P.; Willard, A. P.; Johnson, J. A. Ultra-High Branch Functionality and New Levels of Hierarchy in Polymer Gels Through the Self-Assembly of Metal-Organic Cage Junctions. **2016**, *In Preparation.*

CHAPTER 6. Highly Branched and Loop-Rich Gels via Formation of Metal-Organic Cages Linked by Polymers

6.1 Introduction

Coordination chemistry typically features bonds that are intermediate in bond energy between covalent bonds and other non-covalent interactions (e.g., van der Waals interactions and H-bonding).[1] Such bonds have been extensively used for the formation of supramolecular polymer networks/gels[2-17] and metal-organic cages[18-25] and frameworks[26-28] (MOCs and MOFs, respectively); these important classes of materials feature an array of exciting, complementary properties. Materials that incorporate structural features that blend these classes of materials can not only capitalize on their individual positive qualities, but also, by way of synergy, potentially exhibit unprecedented and valuable properties.[29-31]

A key component of any material structure is the network branch functionality, f, which is the average number of bridges that connect network junctions. In gels prepared from flexible polymers, increasing f leads to a direct increase in the elastic modulus.[32] Existing supramolecular metallogels (e.g., based on coordination of Fe^{3+} and catechol derivatives and structural analogues[11,15]) have single metal atoms at their junctions (Figure 1A, left), and these metals can typically only bind to 2–3 ligands. Thus, the ability to tune f in these systems is limited. In sharp contrast, MOCs and the junctions of MOFs are typically comprised of metal-ligand clusters with M_iL_j junction stoichiometry where $j \geq i > 1$. This augmented stoichiometry and increased junction functionality translates into unique cavity structures, but has little impact on viscoelasticity since MOCs and MOFs are generally rigid materials.[33]

With these considerations in mind, we wondered if it would be possible to use multi- metal-ligand supramolecular assembly inspired by MOC synthesis[18-23] to drive gelation and yield polymer metal-organic-cage gels, or polyMOCs, with tunable nano-scale junction structures and enhanced f (Figure 1A, right). Such an approach would be distinct from traditional supramolecular polymerizations[34,35] that generate point-like junctions (Figure 1A, left), or the pre-assembly of stable M_iL_j cages followed by aggregation or weak supramolecular crosslinking of these spectator cages.[36-42] To our knowledge, the concept of gelation driven by multicomponent M_iL_j assembly has been considered in only two reports; both of these focus on low-f materials. First, we described the synthesis of hydrogels with targeted M_4L_4 square junctions via assembly of Fe^{2+} or Ni^{2+} ions with bispyridyl tetrazine ligands bound to the ends of polyethylene glycol (PEG) chains.[43] Though gelation in this system was only possible through multi-metal-ligand assembly, we could not conclusively characterize the putative M_4L_4 clusters,
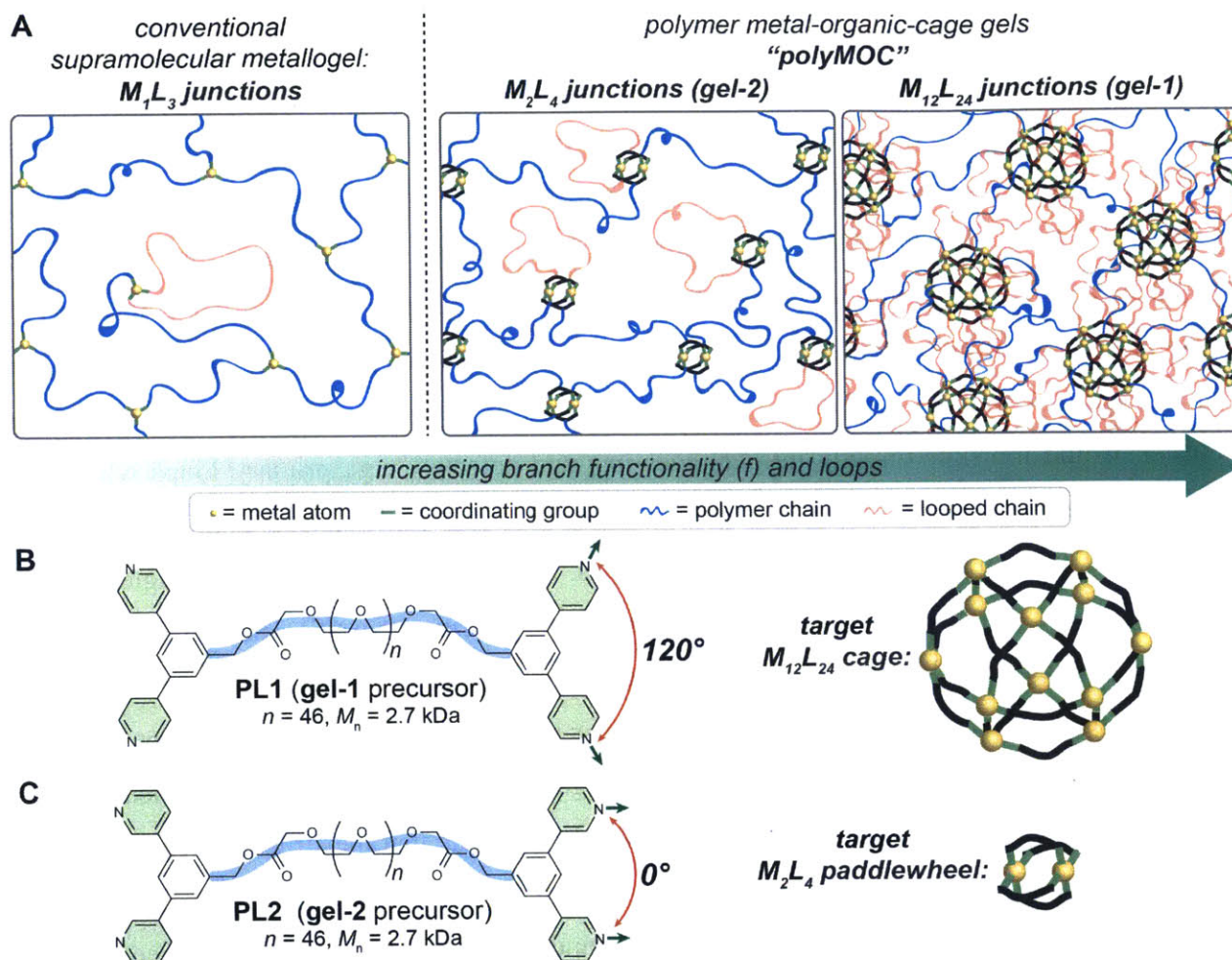
Figure 1. Design of polyMOCs with variable junction structures from isomeric polymer precursors. A. Schematic representations of traditional supramolecular metallogels compared to the polyMOCs with M_2L_4 and $M_{12}L_{24}$ junctions proposed herein. The junction functionality, f, is the average number of chains (shown in blue) emanating from one junction that connect to another unique junction. Loop defects (shown in red) are polymer chains where both ends of the polymer are attached to the same metal atom or metal-ligand cluster. As the number of ligands per junction increases both f and the fraction of looped chains are expected to increase. **B.** Chemical structure of bis-*para*-pyridine-terminated polyethylene glycol (PEG) **PL1** and a schematic of the $M_{12}L_{24}$ cage that is expected to arise from assembly of 24 bis-*para*-pyridine ligands and 12 Pd^{2+} atoms. **C.** Chemical structure of bis-*meta*-pyridine-terminated PEG **PL2** and a schematic of the M_2L_4 paddlewheel that is expected to arise from assembly of 4 bis-*meta*-pyridine ligands and 2 Pd^{2+} atoms. Exposure of **PL1** or **PL2** to Pd^{2+} yields isomeric polyMOCs **gel-1** or **gel-2**, respectively.

and we proposed that a mixture of clusters of different size was likely present. Nitschke and coworkers later reported hydrogels with target M_4L_4 pyramidal junctions prepared from assembly of Fe^{2+} ions and 4,4'-diaminobiphenyl-2,2'-disulfonic acid ligands bound to the ends of PEG.[44] Though small molecule analogues of these ligands did form the target cages in solution, the cages were not directly characterized in the analogous gels; uptake and release of small molecules from the materials suggested the presence of cavities[45] with distinct

environments. Though these examples are encouraging, tuning and enhancing f to enable unprecedented mechanical behaviors in the polyMOC context has not yet been demonstrated.

We began this study with two hypotheses: first, we reasoned that thermal annealing of a mixture of Pd^{2+} ions and PEG terminated with para-bis-pyridyl ligands designed to form $M_{12}L_{24}$ cages[46,47] (**PL1**, Figure 1B) or meta-bis-pyridyl ligands to designed to form M_2L_4 paddlewheels[48,49] (**PL2**, Figure 1C) would generate polyMOC gels **gel-1** and **gel-2**, respectively, with junction structures similar to the target assemblies. Second, we proposed that the difference in average junction size, and the corresponding number of polymer chains connected to each cluster, would translate directly into changes in f and defects – e.g., primary loops where both ligand ends of a single polymer chain are attached to the same junction (red chains, Figure 1A) – that would lead to unique mechanical properties. Herein, we use ^1H magic-angle spinning (MAS) NMR spectroscopy, small-angle neutron scattering (SANS), molecular dynamics simulations, and oscillatory rheometry to test these hypotheses. Our results provide direct evidence for cage assembly in polyMOCs and show that metal-ligand multicomponent assembly-driven gelation programmed by small changes in ligand structure offers a powerful means to tune network structure and mechanical properties. We demonstrate that the structure of **gel-1** (Figure 1A, far right), which features high f and also a large number of loop defects, can be leveraged to selectively replace defects with functional free ligands. Thus, materials with modified junctions can be produced with no impact on mechanical properties, which is not possible in low-f polyMOC **gel-2**.

6.2 Results and Discussion

Solution assembly of free ligands. We first confirmed that bispyridine ligands similar to those on the ends of **PL1** and **PL2** but not bound to polymer (**L1** and **L2**, Figure 2) form the expected $M_{12}L_{24}$ and M_2L_4 assemblies, respectively, in the presence of Pd^{2+}. Information from these studies with "free ligands" and their resulting MOCs is used below to validate the structure of polyMOCs. Exposure of **L1** to $Pd(NO_3)_2 \cdot 2H_2O$ in DMSO-d^6 (0.100 M) at room temperature (RT) provided a heterogeneous mixture with highly broadened ^1H NMR resonances shifted downfield compared to free **L1** (Figure 2A). This mixture transformed into a clear light-yellow solution upon heating for 8 h at 70 °C. The ^1H NMR spectrum of this solution contained one set of ligand-based resonances consistent with a highly symmetric nanoscopic assembly (Figure 2A
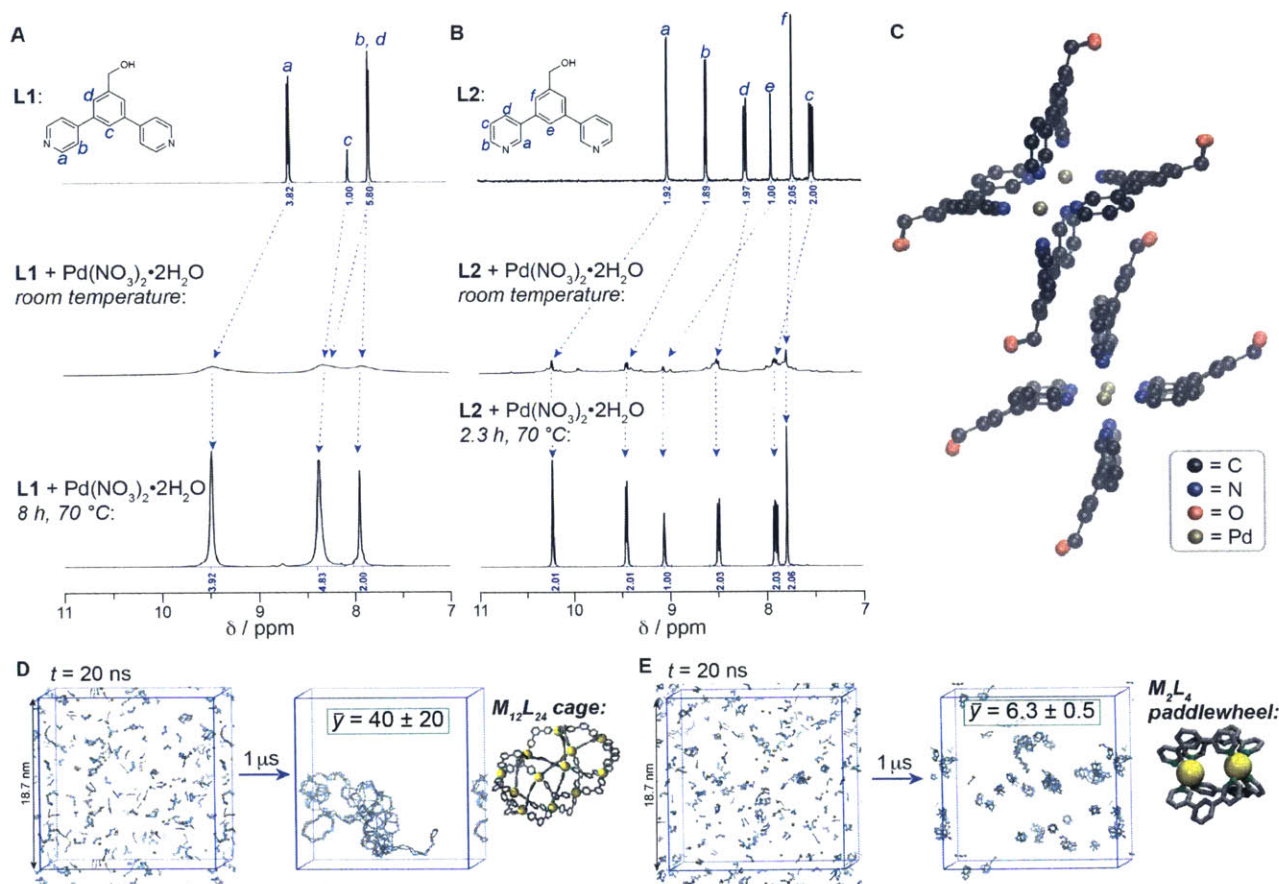
Figure 2. Solution self-assembly of junctions not bound to polymer. a. Aromatic regions of the solution ^{1}H NMR spectra (400 MHz, DMSO-d^6, 25 °C) of, from top to bottom, **L1**, the initial mixture of **L1** and Pd(NO$_3$)$_2$ • 2H$_2$O prepared at room temperature, and the same mixture after thermal annealing. **b.** Aromatic regions of the solution ^{1}H NMR spectra (400 MHz, DMSO-d^6, 25 °C) of, from top to bottom, **L2**, the initial mixture of **L2** and Pd(NO$_3$)$_2$ • 2H$_2$O prepared at room temperature, and the same mixture after thermal annealing. **c.** Single crystal X-ray structure of (**L2**)$_4$Pd^{II}$_2$. Crystals were obtained by vapor diffusion of ethyl acetate into DMSO-d^6 at 23 °C. Note that due to significant disorder the quality of the structure is not suitable for analysis of bond lengths and/or angles. We can confirm the paddlewheel connectivity of the complex as shown. **d.** Snapshots of *in silico* assembly of an **L1** derivative without benzyl alcohol groups and Pd^{2+} after 1 µs at 77 °C initialized from a random configuration. $\bar{y}$ = average number of ligands per cluster. Right: example of a simulated M$_{12}$L$_{24}$ cage. **e.** Snapshots of *in silico* assembly of an **L2** derivative without benzyl alcohol groups and Pd^{2+} after 1 µs at 77 °C initialized from a random configuration. Right: example of a simulated M$_2$L$_4$ cage.

and Experimental). The ^{1}H NMR resonances in the aromatic region were shifted to higher frequency compared to those of **L1**, and the corresponding chemical shifts were virtually identical to those reported by Fujita and coworkers for a similar system.[46]

Upon mixing **L2** with Pd(NO$_3$)$_2$•2H$_2$O in DMSO-d^6 (0.100 M) at RT, many sets of ligand-based resonances were observed in the aromatic region of the ^{1}H NMR spectrum (Figure 2B). Upon annealing for 2 h at 70 °C, this mixture coalesced into a single highly symmetric assembly (Figure 2C and Experimental). Annealing for 8 h at 100 °C afforded an identical spectrum,

implying that the assembly is stable under these conditions. The paddlewheel complex was further characterized by high-resolution electrospray ionization time of flight mass spectrometry (HR ESI-TOF MS); a dominant species with mass/charge (m/z) corresponding to the triply cationic paddlewheel mono-nitrate was observed (see Experimental). Finally, though the quality of our crystallographic data was low, X-ray crystallography confirmed the connectivity of the M_2L_4 paddlewheel complex (Figure 2C).

Molecular dynamics simulations of the assembly of a simplified **L1** without the benzyl alcohol substituent (see Experimental for simulation details) revealed the formation of large clusters after 1 μs with an average number of ligands per cluster, $\bar{y}$, of 40 ± 20 (Figure 2D). In agreement with simulation results from Yoneya and coworkers,[50,51] this result captures early stages of the assembly process; the target $M_{12}L_{24}$ cages are not formed in high yield after 1 μs. Figure 2D (right) shows a representative $M_{12}L_{24}$ assembly obtained from simulation. In the case of **L2**, the simulations yielded $\bar{y}$ = 6.3 ± 0.5 after 1 μs with several of the target M_2L_4 paddlewheels present (Figure 2E). Thus, our simulations suggest that the M_2L_4 paddlewheel forms more readily than the $M_{12}L_{24}$ cage within 1 μs. Collectively, these experimental data and precedents from Fujita and coworkers support the notion that ligands **L1** and **L2** form the target $M_{12}L_{24}$ and M_2L_4 assemblies, respectively, upon thermal annealing.

Formation of polyMOCs. Next we turned to the formation of polyMOCs **gel-1** and **gel2** from polymeric ligands **PL1** and **PL2**, respectively, and Pd^{2+}. Exposure of **PL1** to $Pd(NO_3)_2 \cdot 2H_2O$ in DMSO-d^6 at 23 °C resulted in the immediate formation of an opaque gel (Figure 3A), which suggests the presence of large clusters.[52] The gel was annealed under conditions similar to those used to induce self-assembly of the free ligands; the annealing process was monitored by variable temperature ^1H magic-angle spinning (MAS) NMR (VT ^1H MAS NMR) spectroscopy (Figure 3A and Experimental). Due to the very broad ^1H resonances in the MAS NMR spectrum of **gel-1** (Figure 3A and Experimental), we could not resolve spectral changes upon thermal annealing. However, the aromatic resonances observed for the annealed material (Figure 3A, red spectrum) have the same chemical shifts as those observed in solution ^1H NMR spectra of **L1** assemblies (Figure 2A) and also soluble coordination polymers formed from mixing **PL1** with Pd^{2+} at high dilution followed by annealing (Figure 3A, black spectrum, and Figure 4).
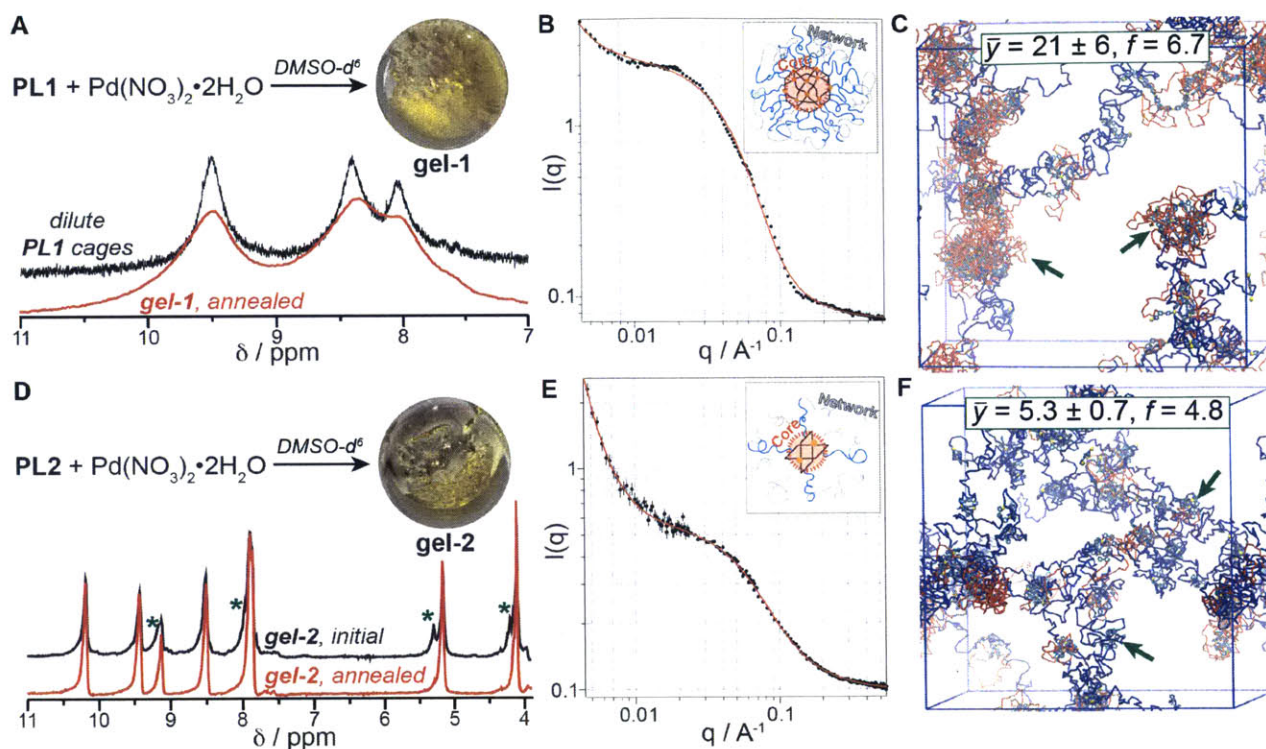
Figure 3. PolyMOC assembly and characterization. A. Synthesis of **gel-1**. In black (*dilute PL1 cages*): aromatic region of the *solution* ^{1}H NMR spectrum of annealed cages with looped PEG chains derived from **1** and Pd^{2+} at high dilution. In red: aromatic region of the ^{1}H MAS spectrum of annealed **gel-1**. **B.** SANS curve (black) for **gel-1** and schematic model used to fit (red) the SANS data. **C.** Snapshot of *in silico* self-assembly of **gel-2** after 1 μs at 77 °C. Looped and non-looped polymer chains are shown in red and blue, respectively. Arrows point to representative loop-rich cluster. **D.** Synthesis of **gel-2**. ^{1}H MAS NMR spectra of **gel-2** before (black) and after (red) annealing. Green asterisks highlight resonances that disappear or sharpen upon annealing. **E.** SANS curve (black) for **gel-2** and schematic model used to fit (red) the SANS data. **F.** Snapshot of *in silico* self-assembly **gel-2** after 1 μs at 77 °C. Arrows point to representative M$_2$L$_4$ junction.

While the majority of junctions in **gel-1** could be the target Pd$_{12}$L$_{24}$ cages (judging from the chemical shift consistency with soluble analogues and symmetric peak shape), we cannot confirm this conclusively from MAS NMR; cage fragments or larger clusters, could yield similar spectra.

SANS experiments were conducted to provide further support for the proposed structure annealed **gel-1** (Figure 3B). The SANS model that best fit the overall scattering curve (Figure 3B, inset schematic) is a summed model of a power law at low scattering angle/larger distances, which is indicative of long-range polymer network structure, and the core-chain model at mid to high scattering angle, which describes the local gel nanostructure (*i.e.*, the polymer-bound junctions). Originally calculated by Hore *et al.*[53] to describe a solid inorganic nanoparticle surrounded by attached polymer chains in a nanocomposite system, the core-chain model well fits the proposed **gel-1** structure of Pd$_{12}$L$_{24}$ cage junctions within a PEG network. The model fit

to the SANS data provides a cage radius of 1.7 ± 0.2 nm with approximately 20 polymer chains emanating from and surrounding the cage core. These values agree well with the expected ~1.8 nm cage radius reported by Fujita and coworkers,[46] and the fact that we would expect 24 chains per cage if every cage formed perfectly. These SANS data provide strong evidence that the structure of **gel-1** is similar to that proposed above (Figure 1A, far right).

Molecular dynamics simulations 1 μs after exposure of **PL1** to Pd^{2+} (see Experimental for simulation details) revealed the presence of large clusters ($\bar{y}$ = 21 ± 6) connected by highly extended polymer chains (Figure 3C). This average
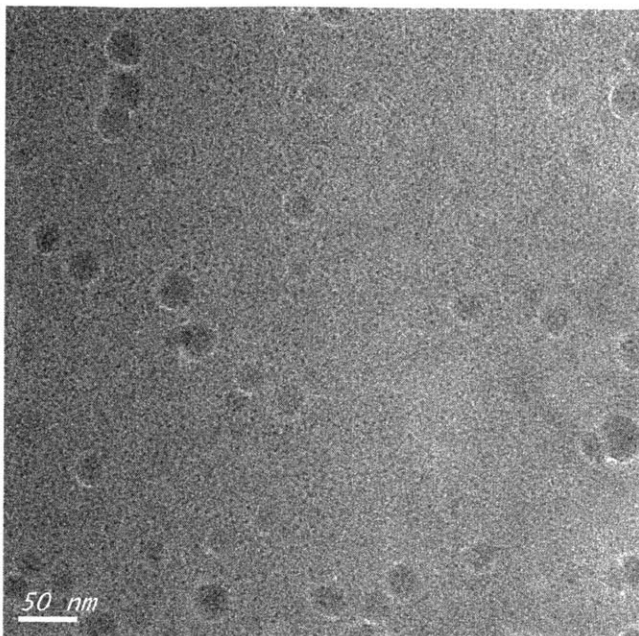
Figure 4. Cryo-TEM micrograph of the solutions of hyperbranched polymer networks, which consist of cages (and clusters of cages) prepared from **PL1** and $Pd(NO_3)_2 \cdot 2H_2O$ at a sufficiently low concentration ([**PL1**] = 4.6 mM) to avoid gelation, dialyzed against Milli-Q® water (see Experimental). The spherical features with a diameter of ~30–40 nm correspond to these clusters of cages.

cluster size – i.e., number of polymers per cluster – agrees quite well with the experimental value observed by SANS, though we stress that, as for the free ligand assembly discussed above, the simulated **gel-1** after 1 μs does not reflect the reality of the thermally annealed network. Instead, we use simulations here to calculate f and the number of looped chains for non-annealed networks; these values will be important for comparison to mechanical property data (*vide infra*). The simulated cluster size distribution in **gel-1** (Figure 5) was quite broad and contained some very large clusters with over 50 ligands (Figure 3C). Given the relatively short polymer chains linking these clusters, a majority of the network chains (68%) are primary loops (Figure 3C, red chains). These chains do not contribute to f, which leads to a calculated f of 6.7. Though this value is clearly well below the maximum possible value of 24, it is nonetheless higher than what is possible for any traditional supramolecular metallogel based on point-like metal junctions. As discussed below, this fact remains true although thermal annealing reduces f and induces even more defect formation.

PolyMOCs formed from **PL2**, **gel-2**, had strikingly different properties compared to **gel-1**.
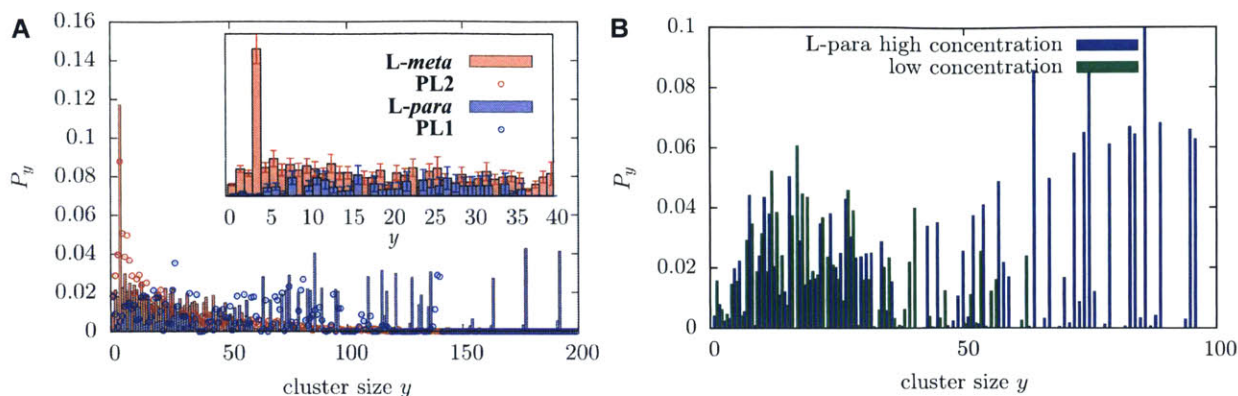
Figure 5. A. Distribution of cluster sizes for systems with **L-*para*** and **L-*meta*** ligands are plotted with blue or red bars, respectively. The data representing polyMOC networks derived from **PL1** and **PL2** are plotted with points using the same colors. **B.** The probability distribution for observing a cluster of size y in a low concentration simulation (system sidelength = 30 nm) is plotted with green boxes. For comparison, the similar distribution for high concentrations (system sidelength = 18.7 nm) is plotted in blue boxes, however scaled so that the normalization is equivalent on the increment of $0 \leq y \leq 50$.

First, **gel-2** was translucent rather than opaque, which immediately suggested the presence of smaller junctions and a more homogeneous network (Figure 3D). In **gel-2**, the MAS NMR spectra revealed a transformation similar to that observed for free ligand **L2**: upon heating for 1 h at 70 °C the ligand-derived resonances coalesced and sharpened into single resonances that mapped closely onto the solution ^{1}H NMR spectrum of the **L2**-based paddlewheels (Figure 3D and Experimental). These data strongly suggest that the network junctions are converted into the target symmetric paddlewheels.

SANS data further supports the structure of **gel-2**. As with **gel-1**, the best fit for the overall scattering curve is a summed model of a power law to describe the network structure and the core-chain model to describe the local nanostructure (Figure 3E). From the fit, the calculated radius of the paddlewheel core in **gel-2** is 0.53 ± 0.05 nm with approximately 4 polymer chains emanating from each paddlewheel core. Again, these values agree quite well with what we expect for the **gel-2** network architecture based on the crystal structure of the paddlewheel complex (Figure 2) and the fact that four polymer chains should be connected to each junction.

As with **gel-1**, we used molecular dynamics simulations of **gel-2** to interrogate the network structure at early stages of formation. In agreement with the data shown for free ligands, which suggests that M_2L_4 paddlewheels form more readily within 1 μs than $M_{12}L_{24}$ cages, simulations of the formation of **gel-2** after 1 μs revealed a preponderance of the target M_2L_4 paddlewheel assembly (Figure 3F). The average cluster size in this case was $\bar{y} = 5.3 \pm 0.7$ ligands; the cluster distribution possessed a peak corresponding to clusters containing 4 ligands (Figure 5A). As

385

expected for the smaller junction size in **gel-2** compared to **gel-1**, only 25% of the polymer chains in **gel-2** were loops. The calculated f for **gel-2** was 4.8, which is greater than 4 due to the presence of some large clusters.

Mechanical Properties of PolyMOCs. Next we used oscillatory rheometry to relate the mechanical properties of **gel-1** and **gel-2** to their network structures. First, the storage and loss moduli (G' and G'', respectively) of **gel-1** (5.9 wt. % in DMSO-d^6, Figure 6A) were studied. Prior to thermal annealing, the high-frequency G' was 12 ± 3 kPa (Figure 6A, black curve, Figure 7A). Based on the phantom network theory of rubber elasticity, which relates G' to f and the mass density of elastically active polymer chains,[32,54] we estimate an f of 6.9 ± 1.6 (see Experimental for details of calculation), which agrees well with the value obtained from simulations (Figure 3C).

Thermal annealing led to a 57% decrease in the high frequency G' value to 5.2 ± 0.3 kPa, which corresponds to an f of 4.1 ± 0.1 (Figure 6A, red curve, Figure 7C; also see Table 1). To rationalize this decrease in f observed upon annealing, we propose that
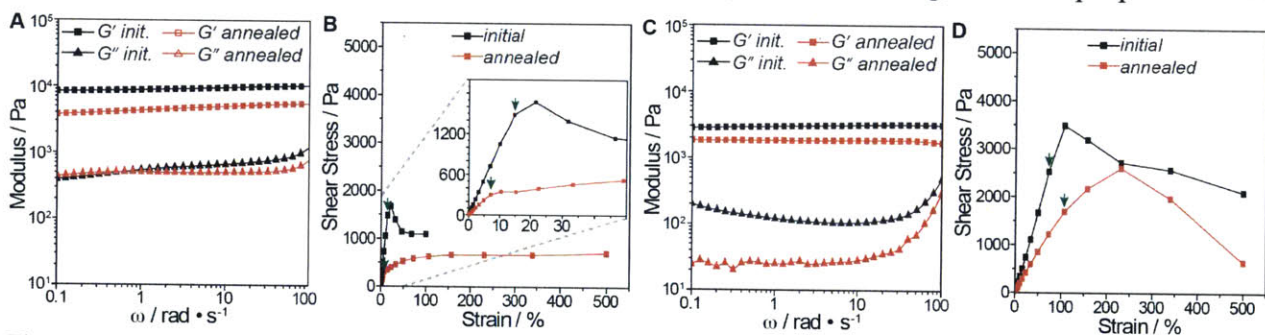
Figure 6. Rheology of polyMOCs at 25 °C. A. Frequency sweeps in oscillatory rheometry of **gel-1** samples at 1.0 % strain amplitude before (black) and after (red) thermal annealing for 4 h at 80 °C. **B.** Stress *vs.* strain plots before (black) and (red) after thermal annealing for **gel-1**. **C.** Frequency sweeps in oscillatory rheometry of **gel-2** samples at 1.0 % strain amplitude before (black) and after (red) thermal annealing for 4 h at 80 °C. **D.** Stress *vs.* strain plots before (black) and after (red) thermal annealing **gel-2**.

annealing drives the fraction of very large clusters (that increase f) in the non-annealed **gel-1** towards the target cluster size of $M_{12}L_{24}$ thus reducing f. Furthermore, because the target $M_{12}L_{24}$ cages cannot effectively pack around each other with relatively short PEG linkers (compared to the cage size) attached to every ligand, the vast majority of the polymers chains must either bridge the same two cages (double loops) or form primary loops. Though neither type of loop cannot be directly measured in these materials at this time,[55,56] the simulation data discussed above for pre-annealed materials suggests that the percentage of primary looped chains can indeed be very high. As we show below, the presence of such a large number of loop
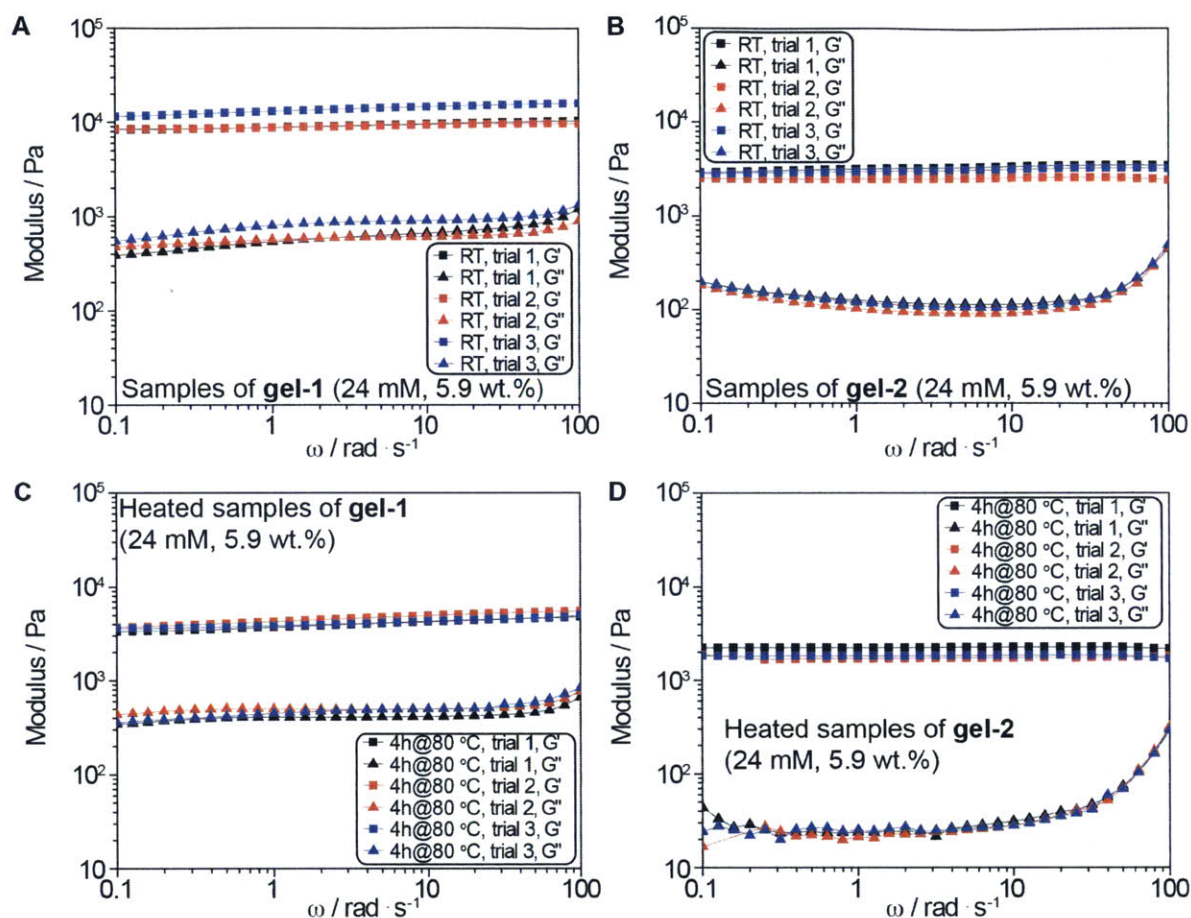
Figure 7. A.–D. Frequency sweeps in oscillatory rheology at 1.0 % strain amplitude for gel-1 ([**PL1**] = 24 mM) before (A) and after annealing for 4 h at 80 °C (B), and the same frequency sweep measurements for gel-2 ([**PL2**] = 24 mM) before (C) and after annealing for 4 h at 80 °C (D).

Table 1. Rheometry characterization of the polyMOC gels via frequency sweeps

Macromer used for gel	G' (100 rad/s), initial / Pa	G'' (100 rad/s), initial / Pa	G' (100 rad/s), annealed /Pa	G'' (100 rad/s), annealed / Pa
PL1	10377	1202.1	4869.4	664.34
PL1	9677.4	895.03	5531	768.5
PL1	16011	1332.7	5090.1	842.28
PL2	3392	440	2160.6	303.51
PL2	2374.1	450.28	1805.5	317.41
PL2	3150.3	486.15	1703.6	292.29

defects provides the opportunity to convert some of these defects into functional species through free ligand replacement, which offers possibilities for functional network design that cannot be realized in materials with low *f* and fewer elastically inactive network defects.
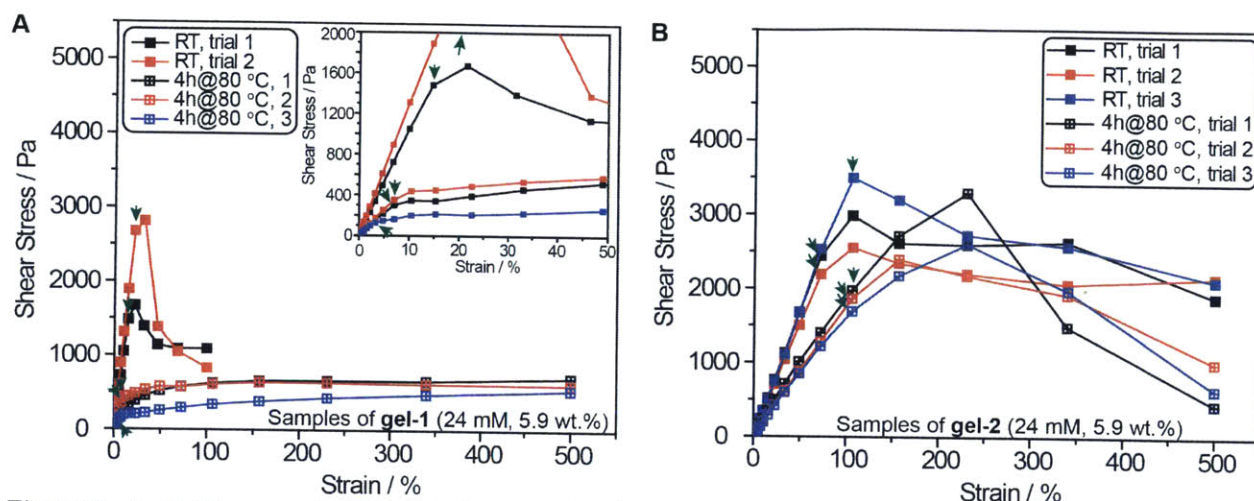
Figure 8. A.–B. Stress *vs.* strain plots before and after thermal annealing for gel-1 ([**PL1**] = 24 mM, (A)) and gel-2 ([**PL2**] = 24 mM, (B)). Green arrows indicate points used for the determination of the yield stresses and strains.

The yield stress of **gel-1** dropped by 87% from 2.1 ± 0.8 kPa to 0.26 ± 0.11 kPa (Figure 6B, Figure 8A and Table 2), and the yield strain decreased from ~18% to ~6.3%, after annealing (Figure 6B, Figure 8A, and Table 2). These results further suggest that **gel-1** consists of large clusters connected by highly extended PEG chains, the latter of which cannot bear larges stresses. In future studies, increasing the PEG chain length could facilitate enhancements in yield stress in **gel-1** analogues with potential decreases in G' offset by a decrease likelihood of primary loop formation.

Table 2. Rheometry characterization of the polyMOC gels via strain sweeps

Macromer used for gel	Yield stress, initial / Pa	Yield strain, initial / %	Yield stress, annealed / Pa	Yield strain, annealed / %
PL1	1480	14.7	298	7.07
PL1	2670	21.5	351	7.07
PL1			142	4.81
PL2	2980	106	1970	106
PL2	2190	72.2	1860	106
PL2	2530	72.2	1690	106

As expected, the mechanical properties of **gel-2** were quite different from **gel-1**. The measured G' for **gel-2** prior to annealing was significantly lower than that measured for **gel-1** (3.0 ± 0.5 kPa, Figure 6c, black curves, Figure 7b, and Table 1). Upon thermal annealing, a 37% decrease in the high frequency G' value to 1.9 ± 0.2 kPa was observed, which, based on phantom network theory, corresponds to an f of 2.13 ± 0.02 (Figure 6C, red curves, Figure 7D, and Table 1). Note that this value is close to the limiting value of 2 below which gelation cannot occur. As described for **gel-1**, we believe that annealing converts the large clusters in **gel-2** to the

target M_2L_4. Since there are fewer large clusters formed initially in **gel-2** compared to **gel-1** (as observed in the simulations above), the corresponding decrease in G' upon annealing is smaller.
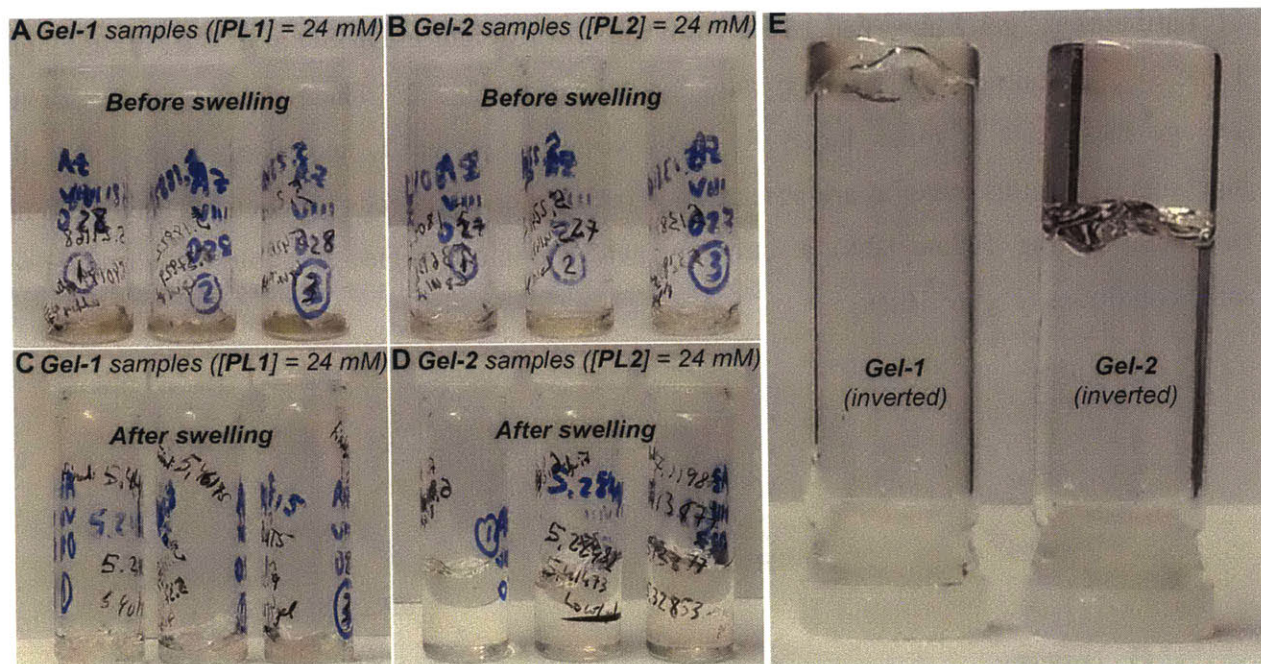
Figure 9. **A.** Three samples of gel-1 ([**PL1**] = 24 mM) in 1-dram vials as prepared after annealing for 4 hours at 80 °C. **B.** Three samples of gel-2 ([**PL2**] = 24 mM) in 1-dram vials as prepared after annealing for 4 hours at 80 °C. **C.** PolyMOC gels shown in panel A after swelling with 3.8 mL DMSO during the course of 5 days and then removing the excess DMSO. **D.** Gels shown in panel B after swelling with 3.8 mL DMSO during the course of 5 days and then removing the excess DMSO. **E.** Inversion test on the swollen polyMOCs confirms that they are still gels.

Table 3. Swelling ratio quantification for the polyMOC gels derived from **PL1** and **PL2**

Macromer used to make the gel	Dry mass (g)	Mass of swollen gel (g)	Swelling ratio
PL1	0.01113	0.23241	20.9
PL1	0.01113	0.27353	24.6
PL1	0.01113	0.25938	23.3
PL2	0.01113	1.71175	154
PL2	0.01113	1.65467	149
PL2	0.01113	1.85764	167

The strain and swelling behavior of **gel-1** and **gel-2** were clear indicators of the emergent bulk properties derived from junction self-assembly. Prior to annealing, the yield stress of **gel-2** (2.6 ± 0.4 kPa, Figure 6D, Figure 8B, and Table 2) was similar to that of **gel-1** (2.1 ± 0.8 kPa). However, while **gel-1** showed an 87% decrease in yield stress after annealing, the yield stress of **gel-2** decreased by only 31% to 1.8 ± 0.1 kPa. Furthermore, while the yield strain of **gel-1** decreased upon annealing (Figure 6D, Figure 8B, and Table 2), the yield strain of **gel-2** *increased*

from ~83% to ~110% (Figure 6D, Figure 8B, and Table 2). **Gel-2** could withstand more than 17-fold greater strain than **gel-1**.

Furthermore, **gel-2** absorbed 157 ± 9 times its own weight in DMSO after 5 d (Figure 9 and Table 3). In contrast, the swelling ratio for **gel-1** was 23 ± 2. These data suggests that the average mesh size is much larger for **gel-2** compared to **gel-1**, and also suggests that the junctions within this material are potentially more dynamic. Indeed, while cuts in **gel-1** did not heal upon heating (Figure 10A), a sample of **gel-2** cut into two pieces visibly healed under the same conditions (Figure 10B).
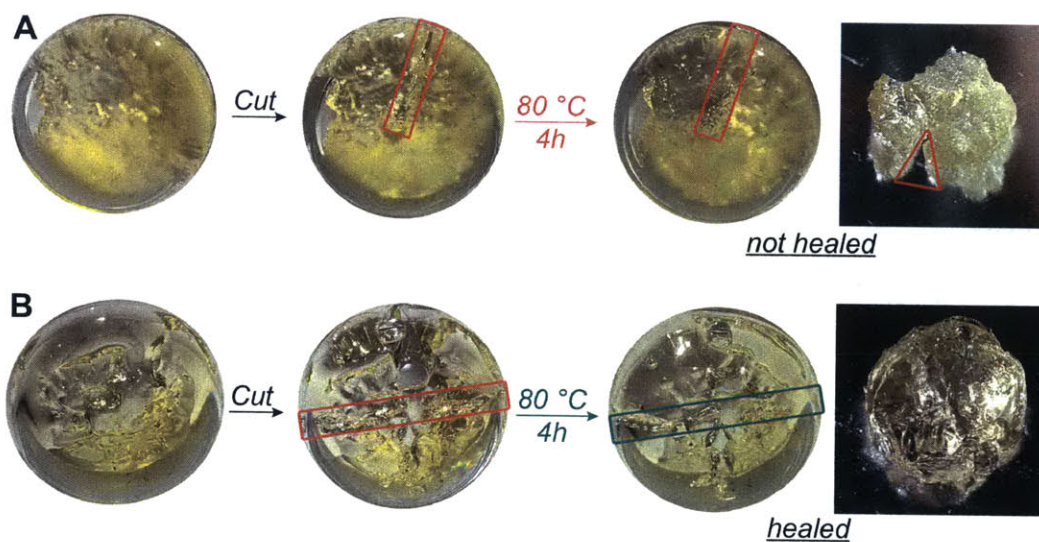
Figure 10. A. Gel-1 in DMSO-d^6 ([**PL1**] = 24 mM) as prepared (left), after cutting into two pieces with a spatula blade (center left, cut region marked with a red box), and after annealing for 4 h at 80 °C (center right), respectively. These photographs were taken from the bottom of a 1-dram vial, which contained the gel. The unhealed cut is easily visualized by separating the two parts of the gel around the cut (highlighted by the red triangle in the photo on the right). **B. Gel-2** in DMSO-d^6 ([**PL2**] = 24 mM) as prepared (left), after cutting into two pieces with a spatula blade (center left, cut region marked with a red box), and after annealing for 4 h at 80 °C (center right), respectively. These photographs were taken from the bottom of a 1-dram vial, which contained the gel. The damage was visibly healed in the region highlighted by the green box; the photo on the right depicts the monolith nature of the healed gel. No solvent was added or pressure applied to facilitate healing.

Loop exchange in high f polyMOC gel-1. The results above highlight how simple polymeric ligand design and the switch from *para* to *meta* bis-pyridine can translate into vastly different polyMOC properties; **gel-1** and **gel-2** behave as though they were different classes of materials (~covalent versus traditional supramolecular gels, respectively). Noting the structure of **gel-1**, which features a large fraction of loops (68% from simulations of pre-annealed networks and 84% from G' measurement and an assumed maximal $f = 24$ and no other defects)

compared to traditional gels, we wondered if it would be possible to selectively replace these loop defects with free ligands (dangling end defects) that contain alternative functionality.

Usually, the mechanical properties of gels (e.g., G') are extremely sensitive to loop and dangling end defects that reduce f; addition of even a small amount of free ligand would dramatically lower G'. Given the large loop fraction of **gel-1**, and the fact that G' is less sensitive to f for networks with increased f, we suspected that incorporation of free ligands into **gel-1**
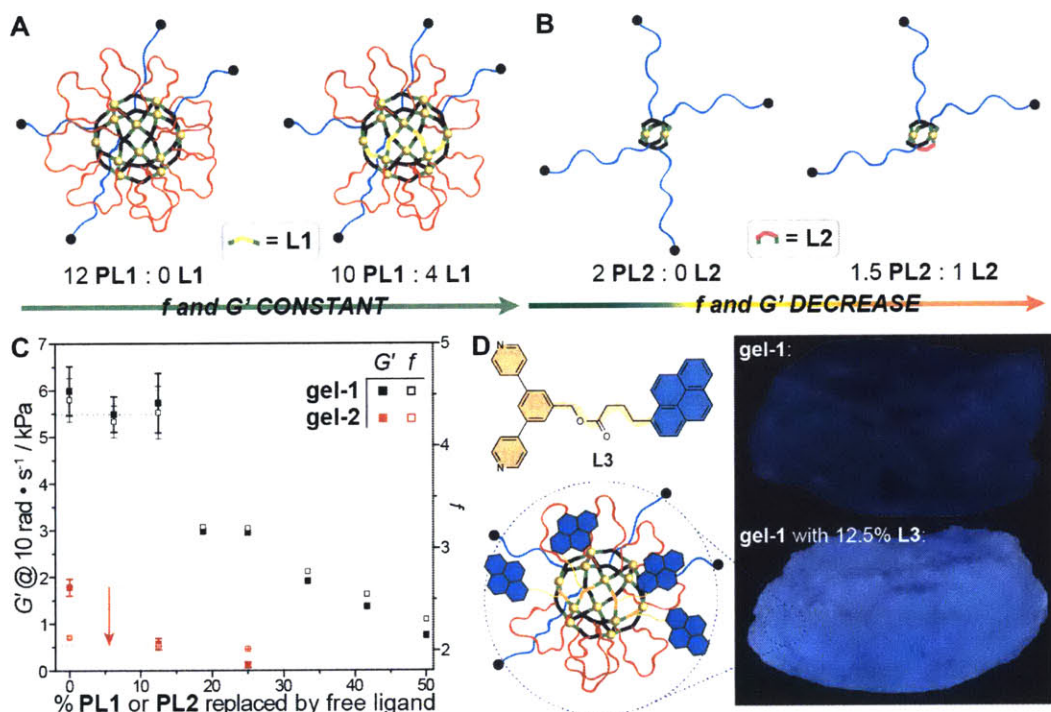
Figure 11. Loop defect exchange in polyMOCs. A. Schematic of representative junctions in polyMOC **gel-1** before (left) and after (after) substitution of **PL1** for 2 equivalents of **L1**. **B.** Schematic of representative junctions in polyMOC **gel-2** before (left) and after (right) substitution of **PL2** for 2 equivalents of **L2**. **C.** The effect of % polymer **PL1** or **PL2** replaced with corresponding free ligands **L1** or **L2** on the G' and calculated f of polyMOCs **gel-1** and **gel-2**, respectively (Table 4). **D.** The structure of pyrene-based ligand **L3** and schematic of representative junction in **gel-1** with 12.5% **L3** added in place of **PL1**. Photographs of **gel-1** (top) and **gel-1** with 12.5 % **PL1** replaced with **L3** after extraction with excess DMSO (bottom). In A, B, and D, primary loops are indicated in red, elastically active chains in blue, **L1/L3** in orange, and L2 in purple.

Table 4. The effect of % macromer replaced on G', G'' and f of polyMOC gels (averages of 3-4 trials)

% Macromer replaced	G'(10 rad/s) of gel-1/ Pa	G"(10 rad/s) of gel-1 / Pa	G'(10 rad/s) of gel-2 / Pa	G"(10 rad/s) of gel-2 / Pa	f of gel-1	f of gel-2
0	5989.8	554.1	1780.1	49.0	4.45	2.12
6.25	5487.0	465.5			4.24	
12.5	5726.2	374.4	561.4	23.1	4.33	2.04
18.75	2974.5	245.6			3.20	
25	2952.8	209.0	111.8	11.4	3.19	2.01
33.333	1909.5	151.6			2.77	
41.67	1355.8	92.2			2.54	
50	740.59	68.4			2.29	

could be possible with minimal or no net change in G' (Figure11A). In contrast, for **gel-2** where f is lower (~2.13) and there are relatively fewer loops (~46% based on G' and assumption of no other defects), the introduction of free ligand should immediately reduce the network connectivity towards the limiting value of $f = 2$. G' in this case should drop precipitously with introduction of free ligand (Figure 11B); such behavior would also be expected in all other traditional gels with low f and few network defects. This junction engineering concept of selective exchange of loop defects with functional dangling ends in a gel, *with no net change in mechanical properties*, would represent a feature of **gel-1** that to our knowledge has not been demonstrated in a polymer network.

To explore this possibility, we measured G' for analogues of **gel-1** and **gel-2** where during the gel preparation (see Experimental for procedure) varying fractions of polymers **PL1** and **PL2** were replaced with 2 equivalents of free ligands **L1** and **L2**, respectively (Figure 11C, filled squares). As before, these G' values were used to calculate f values based on phantom network theory (Figure 11C, open squares, see Experimental for details). When up to 12.5% of **PL1** was replaced with 2 equivalents of **L1**, G' and f were virtually unchanged. Though G' for **gel-1** begins to decrease rapidly as more free ligand is added, even with 50% of **PL1** replaced (network concentration of 3.8 wt. % or 45 mg/mL in DMSO-d^6) the material retained a modulus comparable to traditional supramolecular metallogels with substantially higher polymer content (network concentration of 10 wt. % or 100 mg/mL in water[9]). The f value of **gel-1** with 50% free ligand was 2.29, which is similar to pristine **gel-2** with no free ligand. As predicted, the G' of **gel-2** dropped steeply (by $68 \pm 9\%$) after only 12.5% of **PL2** was replaced, which confirms that low-f network
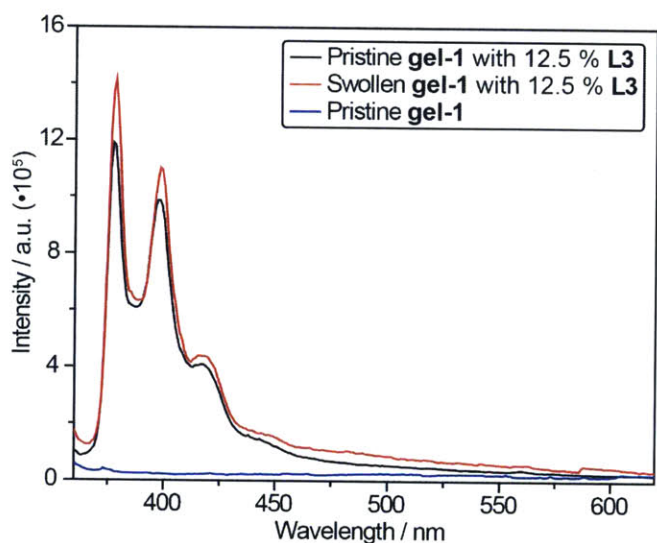
Figure 12. Fluorescence spectra of pristine **gel-1** gel (5.9 wt. %, blue trace), and the same gels with 12.5% **PL1** replaced with **L3** before (black) and after (red trace) swelling with DMSO (~66-fold excess) for 2 d; the "after swelling" fluorescence spectrum (red) has been scaled by the ratio of gel mass before and after swelling (264.5 mg/126.7 mg), since approximately identical amounts of gels were used for the fluorescence measurements (see Experimental).

gel-2 is more sensitive to network defects.

Having established that **gel-1** is much less sensitive to free ligand defects than **gel-2**, we envisioned that additional functionality could be introduced through defect engineering with a functional free ligand (**L3**, Figure 11D). While ligand replacement to introduce functionality has been thoroughly explored in the context of rigid 3D networks (e.g., MOFs[57]), the concept of free ligand addition in place of loop defects in gels is a feature made possible by the structure of **gel-1**. Indeed, replacement of 12.5% of **PL1** with pyrene-based fluorescent ligand **L3** during the gel preparation (see Experimental for details) provided a new polyMOC gel that exhibited blue fluorescence under long-wavelength UV light. This fluorescence persisted after continuous extraction of the gel with DMSO (~66-fold excess) for 2 d (Figure 11D and Figure 12); no detectable **L3** was removed by extraction, which suggests that **L3** is incorporated within the junctions of the polyMOC. Notably, the G' of **L3**-modified **gel-1** was within experimental error of analogous **gel-1** with non-fluorescent ligand **L1** (Figure 13), which confirms that **L3** addition has a negligible impact on the gel mechanical properties. This demonstration of ligand replacement in the junctions of **gel-1** opens exciting avenues for modular polyMOC synthesis; through the use of different free ligands, a range of mechanically uniform materials with distinct properties could be envisaged.
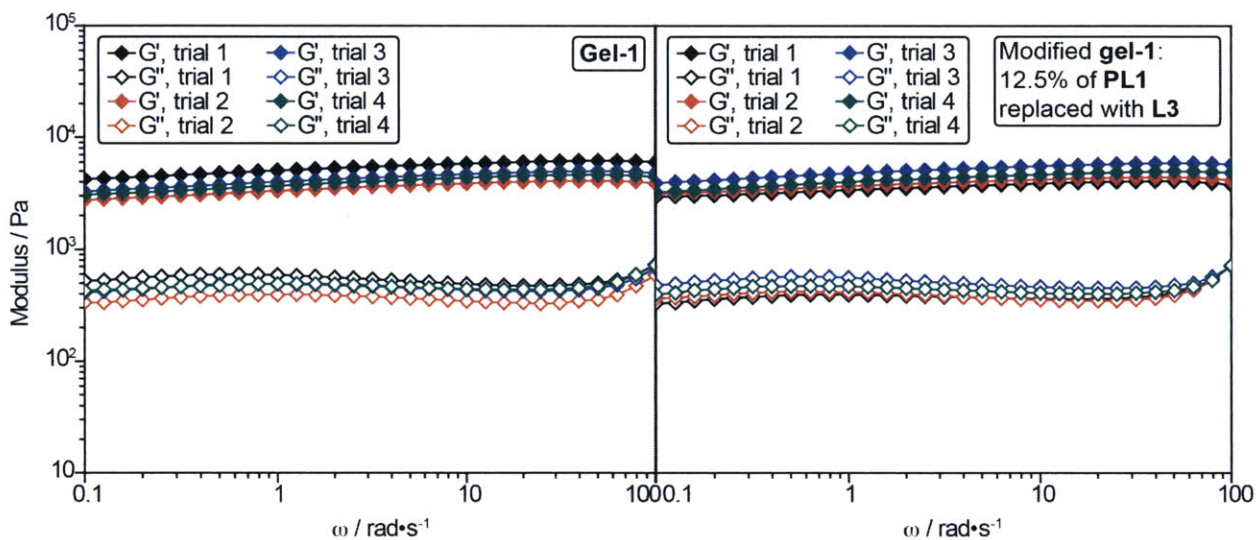
Figure 13. Frequency sweeps in oscillatory rheology at 1.0 % strain amplitude for four different samples of **gel-1** ([**PL1**] = 24 mM) after annealing for 4 h at 80 °C (left), and the same frequency sweep measurements for four different samples **gel-1** with 12.5 % **PL1** replaced with **L3** after annealing for 4 h at 80 °C (right). The G' for **gel-1** gels is 4.7 ± 0.8 kPa, and the G' of the **L3**-modified **gel-1** gels is 4.6 ± 0.7 kPa. Note that a new batch of **PL1** was used for these measurements.

6.3 Conclusions

Herein, we have described a novel class of polymer metal-organic cage – polyMOC – materials that feature self-assembled metal-ligand clusters as junctions connected by flexible polymer chains. A combination of MAS NMR, SANS, simulation, and rheometry were used to study the structure and properties of these materials. These studies show that polyMOCs designed from compositionally identical but isomeric precursors can display a wide range of viscoelastic properties that spans from covalent-like gels to dynamic supramolecular gels. We demonstrate that in polyMOCs with large junctions and a high number loop defects it is possible to selectively replace defects with functional free ligands to imbue the material with novel function (in this case fluorescence) without compromising mechanical integrity. Given the vast array of metal-ligand combinations that are known to provide discrete supramolecular assemblies, and the potential to incorporate many of these within the polyMOC paradigm, we anticipate the development of a range of new polyMOCs with robust, dynamic, and otherwise unprecedented properties.

6.4 Experimental

Materials and Methods

<u>Materials</u>

All non-deuterated solvents, including anhydrous solvents in Sure/Seal™ containers, and polyethylene glycol (PEG, M_n = 2 kDa), and 4-(1-pyrenyl)butyric acid were purchased from Sigma-Aldrich®. Pyridine-3-boronic acid pinacol ester and pyridine-4-boronic acid pinacol ester were purchased from Ark Pharm, Inc. Palladium(II) nitrate dihydrate and tetrakis(triphenylphosphine)palladium were purchased from Strem Chemicals, Inc. All deuterated solvents were purchased from Cambridge Isotope Laboratories, Inc. All other reagents and solvents were purchased from VWR® or Sigma-Aldrich®. All purchased reagents and solvents were used as supplied unless otherwise noted. All air-sensitive reactions were executed using standard Schlenk techniques. All filtration *in vacuo*, unless stated otherwise, was carried out over MAGNA nylon filter disks (Maine Manufacturing, LLC) with 0.45 μm pore size. Spectra/Por® 7 standard regenerated cellulose dialysis tubing (8 kDa molecular weight cut-off (MWCO), 25.5 mm diameter) was purchased from Spectrum® Laboratories.

Chromatography methods

Liquid chromatography–mass spectrometry (LC/MS) were performed on an Agilent 1260 LC system equipped with an Advanced Materials Technology HALO® C18 high performance column. Solvent gradients consisted of mixtures of Milli-Q® water with 0.1% acetic acid (AcOH) and HPLC-grade acetonitrile. Mass spectra were obtained using an Agilent 6130 single quadrupole mass spectrometer.

Preparative high performance liquid chromatography (prep-HPLC) was performed on an Agilent Technologies 1260 Infinity system equipped with a ZORBAX 300SB-C18 PrepHT column (ID x Length = 21.2 x 150 mm; particle size = 5 μm). Eluent flow rate was 20 mL/min, and the eluent composition consisted of mixtures of nano-pure water with 0.1% acetic acid (AcOH) and HPLC-grade acetonitrile. The eluent gradient consisted of a linear ramp from 20% to 60% acetonitrile during 0–18 min, followed by a ramp to 100% acetonitrile during 18–20 min. Polymer samples were dissolved at a concentration of 100 mg/mL, and injected in 1.0 or 0.50 mL volumes. The instrument was controlled using the OpenLAB PrepLC software.

Column chromatography was performed on a Biotage® Isolera One with Accelerated Chromatographic Isolation™ flash chromatography system, using Biotage® KP-Sil SNAP cartridges at the recommended flow rates (e.g., 50 mL/min for 100 g SNAP cartridge).

Gel permeation chromatography (GPC) measurements were performed in tetrahydrofuran (THF) using an Agilent 1260 Infinity system with variable-wavelength diode array (254, 450, and 530 nm) and a refractive index detector, guard column (Agilent PLgel; 5 μm; 50 x 7.5 mm), and three analytical columns (Agilent PLgel; 5 μm; 300 x 7.5 mm; 10^5, 10^4, and 10^3 Å pore sizes). The instrument was calibrated with low-dispersity polystyrene (PS) standards between 1.7 and 3150 kg/mol. All runs were performed at 1.0 mL/min flow rate at 25 °C. The number-average molar mass (M_n), weight-average molar mass (M_w), and dispersity index ($Đ = M_w/M_n$) of **PL1** and **PL2** were calculated by applying the conversion from polystyrene samples described by Sadao and Mori (values of t = 0.916, s = 1.21, derived for PEG, were used for **PL1** and **PL2**).[58]

Solution nuclear magnetic resonance spectroscopy methods

^{1}H nuclear magnetic resonance (^{1}H NMR) and ^{13}C nuclear magnetic resonance (^{13}C NMR) spectra were recorded on two Bruker AVANCE-400 NMR spectrometers (NIH Grant #

1S10RR013886-01). Chemical shifts are expressed in parts per million (ppm), and splitting patterns are designated as s (singlet), d (doublet), t (triplet), m (multiplet), and b (broad). Scalar coupling constants J are reported in Hertz (Hz). MestReNova LITE v5.2.5-4119 software (Mestrelab Research S.L.) was used to analyze the NMR spectra. ^{1}H and ^{13}C NMR spectra were referenced to solvent peaks as reported in literature.[59]

Magic angle spinning nuclear magnetic resonance spectroscopy methods

Variable temperature ^{1}H magic-angle spinning solid-state nuclear magnetic resonance (VT ^{1}H MAS NMR) spectra were recorded on a 11.7 T (500 MHz, ^{1}H) home-built NMR spectrometer (courtesy of Dr. David Ruben, Francis Bitter Magnet Laboratory-MIT). The gel samples immediately after mixing components were loaded via syringe into a 4 mm RevNMR-style zirconia rotor (60 µl fill-volume) which was sealed with a Kel-F cap to reduce the ^{1}H background signal. The spectra were collected using a spinning frequency ($\omega_{r/2\pi}$) of 10 kHz with 128 co-added transients and a recycle delay of 3 seconds. Sample temperatures were varied between 20 and 70 °C and spectra were collected every 5 minutes over a period of eight hours. ^{1}H spectra were referenced to solvent peaks as reported in literature.[59]

Mass spectrometry methods

Vide supra for LC/MS methods.

High-resolution mass spectrometry (HRMS) was obtained using either (1) a Bruker Daltonics® APEXIV 4.7 Tesla Fourier Transform Ion Cyclotron Resonance Mass Spectrometer (FT-ICR-MS) with a direct analysis in real time (DART) or electrospray ionization (ESI) ion sources (NSF Grant #CHE-0234877) or (2) the Bruker Impact HD q-TOF mass spectrometer coupled to a 1290 uHPLC (see ESI-TOF mass spectrum of $Pd_2(L2)_4$ paddlewheels below).

Matrix-assisted laser desorption ionization-time of flight mass spectrometry (MALDI-TOF) was carried out using a Bruker Daltonics® Omniflex® MALDI-TOF instrument, operated using the FlexControl™ version 1.1 software. The data was analyzed using XMass software. The instrument was operated in a reflectron mode (200 ns pulsed ion extraction; reflector voltage = 19.7 kV; lens voltage = 9 kV; detector gain = 20x) with positive ion detection (ion source voltage = 19.0 kV). The laser was operated at a 60-65% intensity at a sampling rate of 1 shot per 1.0 ns, and ~200–1000 shots were averaged to achieve the desired signal-to-noise ratio. The target had a

"Scout 49" geometry. The samples were prepared as follows: first, the matrix solution was prepared by making a saturated solution of α-cyano-4-hydroxycinnamic acid (CHCA) in 1:1 water/acetonitrile with 1% trifluoroacetic acid (TFA). Polymer samples were dissolved at a concentration of 2.5–5 mg/mL in acetonitrile. To 40 μL of the matrix solution was added 4 μL the solution of the polymer sample. 0.5 μL of this solution was spotted in several locations on the MALDI target plate. The reconstituted solution of Calibration Mixture 2 from the Sequazyme™ Peptide Mass Standards Kit (Applied Biosystems, part # P2-314300) was diluted 1:24 (v/v %) with the matrix solution, and 0.5 μL of this solution was spotted over half of the sample spots for each sample on the MALDI target plate. These standards provided for internal mass spectrum calibration. In cases where ionization of the polymer sample was hindered by the presence of the standards, external standard calibration was employed.

Microscopy methods

Cryogenic transmission electron microscopy (cryo-TEM) was performed on holey carbon grids by plunge freezing in liquid ethane, using a Gatan Cryo-Plunge3 instrument, a Gatan Liquid Nitrogen Single Tilt Holder, and a JEOL 2100 FEG microscope. The samples were prepared similarly to the standard preparation of polyMOCs (*vide infra*), except at a low concentration ([**PL1**] = 4.6 mM) to afford soluble hyperbranched network fragments. Thus, **PL1** (6.3 mg, 2.3 μmol) in a 2-mL scintillation vial was dissolved in 350 μL DMSO-d^6, and to it was added a solution of $Pd(NO_3)_2 \cdot 2H_2O$ (0.67 mg, 2.5 μmol) in 150 μL DMSO-d^6 via micropipette; the reaction mixture was heated at 70 °C for 1 d. 200 μL of the resulting solution was then dialyzed against Milli-Q® water (700 mL, 1 d) in a 8 kDa MWCO dialysis tubing (*vide supra*), affording 760 μL of aqueous solution, which was used directly (undiluted) for microscopy.

Molecular dynamics simulation methods

The simulated model system consisted of fully atomistic ligands and metal ions whose interactions were mediated by an implicit solvent. The effect of the implicit solvent is to (**1**) screen electrostatic interactions via a generalized reaction field method,[60] and (**2**) to exert random impulsive forces on the atoms via Langevin dynamics.[61] Following the simulation work presented by Yoneya and Fujita[50,51] we did not explicitly describe the presence of negative counter-ion species and utilized the cationic dummy atom (CaDA) model[62] to describe Pd^{2+} and

the metal-ligand coordination. In the CaDA model metal ligand binding is described empirically through Coulombic interactions between partial charges on the ligand molecules and those on a model Pd^{2+} complex consisting of a neutral Pd core bonded to four dummy atoms, each with a partial charge of $+0.5$ and arranged in a square planar geometry.

Simulations were carried out using GROMACS (version 5.02).[63] For the **L1**-type ligands the inter- and intra-molecular interactions, along with the Ligand-Pd^{2+} van der Waals interactions were described using a standard model force field. The details of the force field, along the associated GROMACS topology files, were adapted directly from simulations of Yoneya and Fujita,[51] which can be found in the Methods sections of reference 51 Therefore, our model of the *para*-substituted bis-pyridine (**L1**) monomers differ from that described in reference 51 only in that our model includes both the repulsive *and* attractive contribution to the short-range Lennard-Jones potential (in reference 51 they use a modified GROMACS package that includes the repulsive-only WCA short range potential). The additional presence of Lennard-Jones attractions in our simulations results in a decrease in overall computational efficiency, but is otherwise expected to have a negligible effect on the results. To model the **L2**-type ligand (the *meta*-substituted bis-pyridine) we modify the **L1** model by exchanging the position of adjacent nitrogen and carbon atoms while retaining the force field parameters and partial charges of the original *para*- substituted ligand (see Figure 14). Reorganizing atoms in this manner allows us to isolate the influence of the Pd-N bite angle on the metal-ligand complexes.
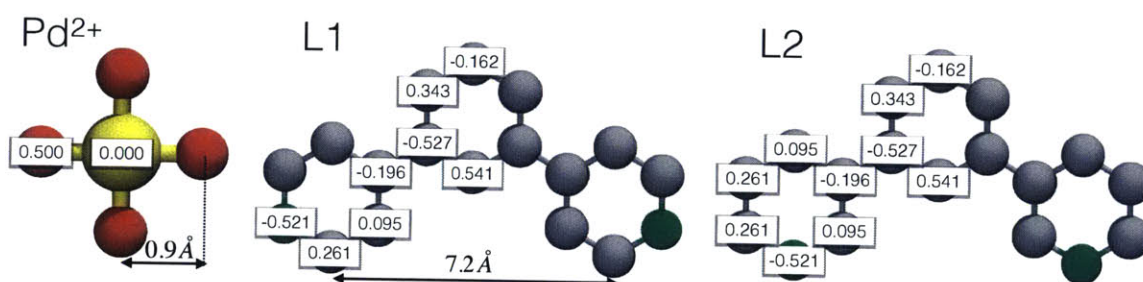
Figure 14. A rendering of the Pd^{2+} complex, the *para*-substituted bis-pyridine ligand (**L-*para***), and the *meta*-substituted bis-pyridine ligand (**L-*meta***). The atoms are labeled with their respective partial charges, given in units of electronic charge.

In the gel-forming system each ligand is bound to a partner ligand via long and flexible polymer chains. An explicit model of such a system dramatically increases the number of atoms being simulated and also introduces a long timescale relaxation process associated with chain entanglement. Here we have utilized an efficient compromise in which the effect of the flexible polymer linker is described implicitly, in the form of a ligand-ligand pair potential. The pair

398

potential is meant to mimic the effect of the polymer linker on the relative positions of connected pairs of ligands. The effect is primarily entropic and is, as we have treated it, directly related to the statistics that govern the end-to-end distance of the isolated polymer.

We modeled the effect of flexible polymer linker through the addition of a pair potential, $w(r)$, acting between the bridging carbon atoms of pairs of ligand molecules (those with partial charge of -0.162 in Figure 14). In particular we took $w(r)$ to be equal to the potential of mean force governing the end-to-end distance of a model polymer linker. This pair potential was generated based on simulations of an idealized version of the PEG linker. Given that the persistence length of PEG, $l = 3.8\text{Å}$,[64] is approximately equal to the monomer size we modeled configurations of the 2.2 kDa linker as a three-dimensional self-avoiding random walk with steps of length l randomly distributed around a unit sphere. By sampling the statistics of this idealized model polymer we determined the end-to-end PMF and tabulated it for use as a user-input pair potential in GROMACS. Figure 15A contains a plot of the potential of mean force used to model the 2.2 kDa linker (Figure 15B).

The potential used to describe the flexible ligand-ligand polymer linker imparts forces that are much smaller than those involved in ligand-metal coordination. The distribution of cluster sizes is therefore quite insensitive to the details of $w(r)$. However, because this potential imposes spatial correlations on specific pairs of ligands, the network-forming properties system can be sensitive to the specific details of $w(r)$. The sensitivity is most pronounced in the statistics of inter-MOC connectivity where the probability for loop formation can be controlled by varying the shape of $w(r)$. For instance, $w(r)$ can be chosen to mimic a very short linker (keeping ligand pairs very close) so that loop formation is enhanced or to mimic a long linker (leveraging the entropic driving force that prevents configurations with very small end-to-end distances) so that loop formation is reduced. Our procedure is approximate but gives rise to ligand-ligand correlations that are in reasonable agreement with our physical expectations.
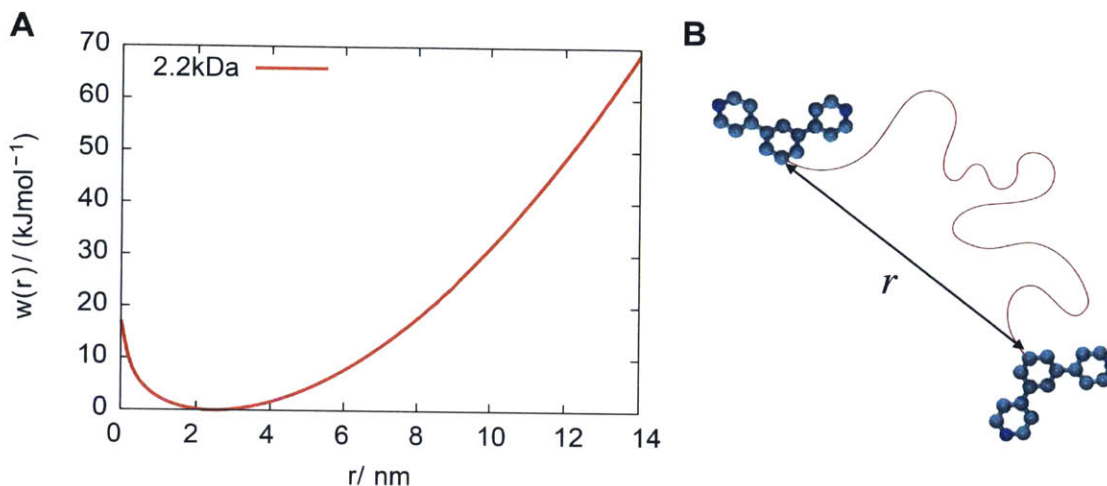
Figure 15. A. The ligand-ligand pair potential used for simulating macromers. **B.** The pair potential acts on the central carbon atoms of two specific ligands.

Simulations consisted of 96 metal ions and 192 ligands (or 96 macromers), enough to form four fully assembled $M_{12}L_{24}$ type clusters, in a cubic, periodically replicated simulation cell with side length 18.7 nm. Initial configurations were generated by randomly distributing ligands and metal ions subject to the constraint that the initial separation between any two species be greater than 1.5 nm. For the polyMOC formation, **PL1** and **PL2** were placed randomly but at an initial fixed distance of 2.6 nm for the 2.2 kDa PEG chain. Simulations were carried out in the NVT ensemble with a 2 fs time step. For each ligand model (4 in total, i.e., **L-para**, **L-meta**, and **PL1** and **PL2**) we generated 20 individual trajectories. Each trajectory consisted of an initial 1 ns equilibration run at a temperature of 500 K, followed by a 1 μs production run at a temperature of 350 K. The details of the implicit solvent and the thermostat were identical to those described in reference 51.

The results presented in Figure 5A indicate that the **L-para** ligands tend to form large and sometimes system-spanning clusters. To explore the effect of concentration on the formation of very large ligand-metal clusters we carried out a set of simulations in which 192 **L-para** ligands and 96 metal ions were placed in a larger periodically replicated cubic cell, one with side length 30 nm. In Figure 5B we present the distribution of cluster sizes, $P(y)$, that emerged from this 'low concentration' simulation compared to that of the high concentration simulation (the latter is an excerpt of the data plotted in Figure 5A). To facilitate a side-by-side comparison, each curve has been normalized over the same increment, specifically $0 \leq y \leq 50$. At low concentration we observe a significantly reduced probability for observing clusters with $y > 50$, and in fact the

distribution of cluster sizes for $y \leq 50$ are quite similar for the low and high concentration simulations. This indicates that the presence of large clusters is either the result of exceeding a percolation threshold in ligand concentration or a preferential stabilization of such clusters due to self-interaction through the periodic boundaries of the system.

Crystallography methods

Low-temperature (100 K) diffraction data (φ- and ω-scans) were collected on a Bruker X8 Kappa Duo four-circle diffractometer coupled to a Smart Apex2 CCD detector, with Mo K_α radiation ($\lambda = 0.71073$ Å) from an $I\mu S$ micro-source. The diffractometer was purchased with the help of funding from the National Science Foundation (NSF) under Grant Number CHE-0946721. The structure was solved by direct methods using SHELXS[65] and refined against F^2 on all data by full-matrix least squares with SHELXL-97[66] following established refinement strategies[67].

The final cif file was checked using the IUCr checkCIF routine, and below, we list the Alerts of level A and B as they appear in the output checkCIF file and the justification for each.

Alert level A

SHFSU01_ALERT_2_A The absolute value of parameter shift to su ratio > 0.20 Absolute value of the parameter shift to su ratio given 6.596 Additional refinement cycles may be required.

Author Response: Structure refinement is not complete. Data are of low quality and so is the structure. Paddlewheel connectivity is confirmed but not much else can be concluded from this structure.

PLAT080_ALERT_2_A Maximum Shift/Error .... 6.60 Why ?

Author Response: Structure refinement is not complete. Data are of low quality and so is the structure. Paddlewheel connectivity is confirmed but not much else can be concluded from this structure.

Alert level B

PLAT201_ALERT_2_B Isotropic non-H Atoms in Main Residue(s) .... 1 Report

Author Response: Structure refinement is not complete. Data are of low quality and so is the structure. Paddlewheel connectivity is confirmed but not much else can be concluded from this structure.

PLAT430_ALERT_2_B Short Inter D...A Contact O10N .. O2A .. 2.74 Ang.

Author Response: Structure refinement is not complete. Data are of low quality and so is the structure. Paddlewheel connectivity is confirmed but not much else can be concluded from this structure.

PLAT601_ALERT_2_B Structure Contains Solvent Accessible VOIDS of . 192 Ang3

Author Response: Structure refinement is not complete. Data are of low quality and so is the structure. Paddlewheel connectivity is confirmed but not much else can be concluded from this structure.

PLAT934_ALERT_3_B Number of (Iobs-Icalc)/SigmaW > 10 Outliers .... 3 check

Author Response: Structure refinement is not complete. Data are of low quality and so is the structure. Paddlewheel connectivity is confirmed but not much else can be concluded from this structure.

PLAT975_ALERT_2_B Check Calcd Residual Density 0.62A From O4S 1.54 eA-3

Author Response: Structure refinement is not complete. Data are of low quality and so is the structure. Paddlewheel connectivity is confirmed but not much else can be concluded from this structure.

Small-angle neutron scattering (SANS) methods

Small-angle neutron scattering (SANS) measurements were performed at the National Institute of Standards and Technology (NIST) Center for Neutron Research (NCNR) (Gaithersburg, MD, USA). The scattered neutron intensity was measured as a function of scattering variable q, where $q = (4\pi/\lambda) \sin (\theta/2)$ and θ is the scattering angle. The beam was monochromated to a wavelength, λ, of 6 Å. Three sample-to-detector distances of 1 m, 4 m, and 13 m were used to cover a total q range of 0.004 to 0.5 Å^{-1}. 400 µL of each sample (gels prepared at 3.54 wt. % of polymer network) was loaded into titanium sample cells with a 1 mm path length. Experiments were performed on the NGB 30 m SANS instrument. Collected data were reduced and analyzed using the SANS macros package provided by the NCNR.[68] The resulting data were placed on an absolute scale and corrected for background electronic noise, detector inhomogeneity, and empty cell scattering using standard techniques.

Scattering data for both samples were fit using a sum of two models, the power law model and the core chain model. The power law model is primarily used to show the presence of

402

a larger entangled network, and describes the scattering intensity as $I(q) = Aq^{-n}$. The core-chain model, due to Hore et al.[53], is a slightly modified version of the reported model.[69] The original Hore core-shell-chain model in reference 69 was used to describe an inorganic iron oxide core with a shell layer of dense polymer brush, surrounded by grafted polymer chains with excluded volume. Here, the shell layer element is omitted but the model remains intact otherwise. In addition, the core in the present system is not inorganic entirely, but a mixed composition of Pd and bis-pyridine ligand. Most importantly, the model does not assume that the chains are Gaussian, and allows the excluded volume of the chains to vary. For this reason, Debye functions are omitted in favor of a more detailed description of polymer chain scattering.

The scattering intensity is calculated from the sum of the spherical core form factor, core-chain form factor correlations, chain-chain correlations, and the form factor of a polymer chain with excluded volume. The form factor amplitude of the spherical core is given by $F_A(q)$,

$$F_A(q) = \left[(\rho_{core} - \rho_{solvent}) V_{core} \frac{3j_1(qr_{core})}{qr_{core}} \right] \tag{0.1}$$

where j_1 is a spherical Bessel function of order 1, r_{core} is the radius of the paddlewheel or cage, V_{core} is the volume of the paddlewheel or cage, ρ_{core} is the scattering length density (SLD) of the paddlewheel or cage, and $\rho_{solvent}$ is the SLD of the solvent.

Scattering from polymer chains is described by the form factor amplitude and form factor of the polymer chains, $F_B(q)$ and $P_B(q)$, respectively. Note that because polymer chains are fractal in nature, the form factor is a separate function from the form factor amplitude. The functions are given by,

$$F_B(q) = \frac{1}{2\nu U^{1/2\nu}} \gamma\left(\frac{1}{2\nu}, U \right) \tag{0.2}$$

$$P_B(q) = \frac{1}{\nu U^{1/2\nu}} \gamma\left(\frac{1}{2\nu}, U \right) - \frac{1}{\nu U^{1/\nu}} \gamma\left(\frac{1}{\nu}, U \right) \tag{0.3}$$

where the lower incomplete gamma function reads

$$\gamma(d,U) = \int_0^U dt (e^{-t} t^{d-1}) \tag{0.4}$$

The parameter $U = q^2 a^2 N^{2\nu}/6$ contains the scattering variable q, the statistical segment length of the polymer chain (a), the degree of polymerization of the chain (N), and the excluded volume parameter ν.

The total macroscopic scattering cross section for N_p/V density of nanoparticles with N_g grafted polymer chains per particle, including the power law term, is then expressed as

$$\frac{d\Sigma(q)}{d\Omega} = Aq^{-n} + \frac{N_p}{V}\left[\begin{array}{l} F_A(q)^2 + N_g V_B (\rho_{chain} - \rho_{solvent})F_A(q)F_B(q) \\ +N_g(N_g - 1)V_B^2(\rho_{chain} - \rho_{solvent})^2 F_B(q)E_A(q)^2 F_B(q) + N_g V_B^2(\rho_{chain} - \rho_{solvent})^2 P_B(q) \end{array}\right]S_I(q) + B \qquad (0.5)$$

where $E_A = j_0(qr_{core})$ is a spherical Bessel function, and B is the constant incoherent background. The radius of gyration for the chains surrounding the paddlewheel or cage is calculated from the parameters of Eq. (0.5) as

$$R_g^{\,2} = \frac{N^{2v}a^2}{(2v+1)(2v+2)} \qquad (0.6)$$

The SLDs for the core of each sample were calculated using an average of the PEG and palladium SLD on the basis of the composition of the two components. Using the NCNR SLD calculator, the bis-pyridine SLD was $1.98 \times 10^{-6} / \text{Å}^2$, the Pd SLD was $4.02 \times 10^{-6} / \text{Å}^2$, and DMSO-d6 had an SLD of $5.28 \times 10^{-6} / \text{Å}^2$. The composition of the components, calculated on the basis of the density and mass for paddlewheel and cage gels (**gel-2** and **gel-1**, respectively), was 70% ligand and 30% Pd yielding an initial SLD of $2.59 \times 10^{-6} / \text{Å}^2$. The initial SLD does not take into account the possible presence of PEG or DMSO within the core, and so is only an initial approximation. The calculated radii, resulting from the core-chain model fits, for the paddlewheel and cage structures were 0.55 ± 0.054 nm and 1.70 ± 0.25 nm, respectively. The calculated number of ligands, also from the core-chain model fits, for the paddlewheel and cage structures, N_g, were approximately 4 and 20, respectively. The excluded volume parameter (v), calculated from the core-chain model fit, for the paddlewheel gel and cage gel, were 0.574 and 0.595, respectively. A value of v that is close to 0.6 is indicative of a swollen polymer chain (*i.e.*, $R_g \sim N^{0.6}$). The radius of gyration (R_g) calculated using Eq (1.6) with paramaters obtained from the core-chain model fits were 0.49 nm and 0.45 nm, respectively, for paddlewheel and cage gel.

70NANB12H239 from NIST, U.S. Department of Commerce. The statements, findings, conclusions, and recommendations are those of the authors and do not necessarily reflect the view of NIST or the U.S. Department of Commerce.

Rheometry methods

Frequency sweep and strain sweep experiments were performed on an Anton Paar MCR 301 rheometer. The rheometer was outfitted with a Peltier heating system with an environmental enclosure for temperature control. A disposable parallel-plate geometry (radius = 12 mm) was used and coupled with a disposable bottom plate, with the typical gap of 1.00 mm between the two plates. Frequency sweep experiments were performed from 0.1 to 100 rad/s at 1% strain, which was first confirmed to be in the linear viscoelastic regime using strain sweep experiments. Gel samples were prepared either on the plate *in situ* or in 1-dram vials (*vide infra*) and subsequently transferred onto the rheometer. Experiments were performed at 25 °C and the evaporation of solvent (DMSO-d^6) was negligible within the typical measurement time (< 1 hour).

Fluorimetry methods

Fluorimetry was carried out using Fluorolog®-3 spectrofluorometer from Jobin Yvon Horiba using the DataMax for Windows™ driving software. The following parameters were used during the fluorimetry: (1) integration time = 0.25 s; (2) increment = 1 nm; (3) excitation wavelength: 340 nm; (4) Detector HV S = 950 V and R = 0 V; bandpass slits: excitation1 = 3.000 nm; emission1 = 5.000 nm. The data was analyzed using OMNIC™ software and plotted in OriginPro 8.5. The samples for fluorimetry were prepared by depositing a fragment of the gel into a cylindrical hole (2 mm diameter x 0.9 mm depth) within a sample holder, sandwiching the sample holder with the gel between two square glass cover slips to stabilize the gel and prevent solvent evaporation, and using the front-face geometry to collect the fluorescence.

Gel swelling methods

Two sets of gels (3 gels per set) were prepared in tared 1-dram vials – one set from macromer **PL1** and the other set from macromer **PL2** – following the general polyMOC synthesis method (*vide infra*), except at 0.500 x the scale: i.e., 10.13 mg of macromer was used

to prepare gels with [macromer] = 24 mM (Figures 9A–B). To each gel was added 3.8 mL DMSO, and the gels were allowed to stand at RT for 5 d, at which time the excess DMSO was removed via syringe, and any residual DMSO was wicked away by gently dabbing the gels in the vials with Kimwipes®. Vial inversion tests confirmed the materials remained in the gel state (Figure 9E). The gels in the vials were weighed, and the swelling ratio for each was determined by diving the mass of the swollen gel by the dry mass of the network (dry mass of the network = mass of macromer + mass of $Pd(NO_3)_2 \cdot 2H_2O$ = 10.13 mg + 1.00 mg = 11.13 mg) (Table 3). Averages and standard deviations were computed for the three trials.

Computations of network branch functionality f from G' via phantom network theory of rubber elasticity[32,54]

A measurement of $G'{\sim}|G|$ (*i.e.*, $G' >> G''$) allows us in principle to compute f in our polyMOCs and thereby validate the conclusions derived from the simulations. The phantom network theory was deemed most appropriate for the analysis of our polyMOCs, because it explicitly relates $|G|$ and f:[32]

$$|G| = \frac{\rho RT}{M_{chain}}\left(\frac{f-2}{f}\right),$$

where ρ is the mass density of the elastically active polymer chains, R is the universal gas constant ($8.31446 \cdot 10^6$ $cm^3 \cdot Pa \cdot K^{-1} \cdot mol^{-1}$), T is the temperature (in this case 298.15 K), M_{chain} is the number-average molecular weight (M_n) of the polymer chain separating the junctions (taken here to be equal to M_n of the macromers = 2700 g/mol).[32] Crucially, ρ is not known *a priori* because an unknown fraction of the polymer chains may form primary loop defects (and therefore not contribute to ρ (dangling chain ends were not observed by NMR and can therefore be ignored). A key realization is that to a first-order approximation (i.e., accounting only for primary loops) ρ scales linearly with the true f of the network – in other words a deviation of f from f_{ideal} by x % is expected to yield the same x % deviation of ρ from ρ_{ideal}. Thus, we have

$$\rho = \frac{f}{f_{ideal}}\rho_{ideal},$$

and substitution of the expression for ρ into the expression for $|G|$ yields

$$|G| = \frac{\rho_{ideal} \cdot RT}{f_{ideal} \cdot M_{chain}} (f - 2).$$

In the case of polyMOCs derived from **PL1** or **PL2**, where no macromer is replaced with free ligand **L1** or **L2**, f_{ideal} is taken to be 24 or 4, respectively, values expected for $M_{12}L_{24}$ or M_2L_4 cages, and consistent with $\bar{y}$ at 1 μs computed above for the corresponding networks (21 ± 6 and 5.3 ± 0.7, *vide supra*). When a fraction r of macromer **PL1** or **PL2** is replaced with **L1** or **L2**, respectively, new f_{ideal} becomes equal to $(1 - r) \cdot (f_{ideal}$ when $r = 0)$ because the free ligands do not contribute to the branch functionality: i.e., $f_{ideal} = (1 - r) \cdot 24$ for **gel-1**, and $f_{ideal} = (1 - r) \cdot 4$ for **gel-2**.

G' and G'' at $\omega = 10$ rad/s were measured for all polyMOCs with varying fractions r of macromer replaced with **L1** or **L2** (Table 4). Thus, when $G' \gg G''$, as is the case for all of our polyMOCs at $\omega = 10$ rad/s, G' can be used in place of $|G|$. Note: for the comparison of f for **gel-1** and **gel-2** before and after annealing, G' at $\omega = 100$ rad/s was utilized. A sample calculation is provided below for a **gel-1** gel where $r = 0.125$. The volume of the gel is the added volume of DMSO-d^6 and the polymer network (the latter was estimated to be the same as that of PEG with $M_n = 2000$, which was measured to be 0.8273 mL/g).

$$G'@10\frac{rad}{s}$$

$$= 4762.1 \text{ Pa} = \frac{\left(\frac{\text{mass of polymer}}{\text{volume of gel}}\right) \cdot 8.31446 \cdot 10^6 \text{ mL} \cdot \text{Pa} \cdot \text{K}^{-1} \cdot \text{mol}^{-1} \cdot 298.15 \text{ K}}{(1 - 0.125) \cdot 24 \cdot 2700\frac{g}{\text{mol}}}$$

$$\cdot (f - 2) = \left(\frac{0.01772 \text{ g}}{0.01772 \text{ g} \cdot 0.8273 \text{ mL/g} + 0.300 \text{ mL}}\right) \cdot 43720.6 \text{ mL} \cdot \text{Pa} \cdot \text{g}^{-1} \cdot (f - 2)$$

$$= 2462.1 \text{ Pa} \cdot (f - 2)$$

$$\therefore f = 2 + \frac{4762.1 \text{ Pa}}{2462.1 \text{ Pa}} = 3.93$$

Synthetic Procedures and Characterization

<u>Modified Syntheses of Previously Reported Compounds</u>

(3,5-di(pyridin-4-yl)phenyl)methanol **L1**.[46] To a 20-mL microwave vial equipped with a magnetic stir-bar were added 3,5-dibromobenzyl alcohol (0.442 g, 1.66 mmol), pyridine-4-boronic acid pinacol ester (0.750 g, 3.66 mmol), potassium carbonate (2.297 g, 16.6 mmol), and

tetrakis(triphenylphosphine)palladium (0.192 g, 0.166), and the vessel was crimped shut, evacuated and refilled with nitrogen three times. To the vessel via syringe were added anhydrous N,N-dimethylformamide (DMF, 13.5 mL) and then de-ionized water (0.280 mL, 15.5 mmol) which had first been sparged with argon for 30 min. The vessel was briefly evacuated until bubbling was observed, and then refilled with nitrogen, and briefly sparged with argon (10-15 sec). The vessel was heated in the oil bath for 60 h at 100 °C, with precipitated palladium black observed after 24 h. At the conclusion of the reaction, the vessel was brought to RT, and the contents of the vessel were filtered *in vacuo* over tightly-packed Celite® 545 on a medium-porosity glass frit, rinsing the flask and Celite with chloroform (3 x 50 mL). The filtrate was subjected to washes with water (5 x 150 mL), followed by drying over Na_2SO_4, filtration over a medium-porosity frit, and concentration *via* rotary evaporation. The crude material was subjected to chromatography on silica gel (CH_2Cl_2/MeOH step gradient: 9.8:2 → 9.5:0.5 → 9:1; **L1** eluted during the second step, R_f = 0.087 in CH_2Cl_2/MeOH = 9.5:0.5). The fractions containing the desired product were combined, concentrated by rotary evaporation, and triturated with CH_2Cl_2 (3 x 1 mL) quickly to remove traces of a co-eluting, but more readily soluble in CH_2Cl_2 impurity. The CH_2Cl_2 rinsings were concentrated by rotary evaporation and triturated with tetrahydrofuran (THF, 4 x 1 mL) quickly. The two portions of triturated solids were combined and dried *in vacuo* affording **L1** (0.2035 g, 46.7 % yield, ≥99% pure by LCMS) as a white to faint-yellow powdery solid. ^{1}H NMR (400 MHz, DMSO-d^6, 25 °C): δ 8.68 (dd, J = 4.5, 1.6 Hz, 4H), 8.06 (t, J = 1.7 Hz, 1H), 7.87-7.80 (m, 6H), 5.40 (t, J = 5.7 Hz, 1H), 4.68 (d, J = 5.4 Hz, 2H). ^{13}C NMR (100 MHz, DMSO-d^6, 25 °C): δ 150.26, 146.75, 144.72, 138.06, 125.58, 123.77, 121.49, 62.57. FT-ICR-DART HRMS: calcd. for $C_{17}H_{14}N_2O$ [M+H]$^+$, most abundant m/z = 263.1179; found, 263.1160.

Polyethylene glycol (PEG)-diacid (M_n = 2.2 kDa) was synthesized following the general protocol disclosed in patent US 8,067,505 B2[70] for the synthesis of PEG diacid from PEG diol, except beginning with PEG-diol (M_n ~ 2.0 kDa) and using sodium tert-butoxide instead of potassium tert-butoxide (the former formed a dispersion in 1:1 tert-butanol/toluene and was transferred via syringe with a 16-gauge needle). Product was isolated as a powdery white solid in 89% (7 g scale) or 93% (3.5 g scale) yields. ^{1}H NMR (400 MHz, DMSO-d^6, 25 °C): δ 13.35–12.01 (b, 2H), 4.01 (s, 4H), 3.71–3.43 (m, 184H). MALDI-TOF: M_n = 2.27 kDa; calcd. for

$C_{98}H_{194}O_{52}$ [M+Na]$^+$, most abundant m/z = 2227.2; found, 2227.2. M_n (^{1}H NMR) = 2.16 kDa. M_n = 2.2 kDa was employed in the calculations for reactions involving this **PEG-diacid**.

Self-assembly of the Pd$_{12}$(L1)$_{24}$ cage and Pd$_2$(L2)$_4$ paddlewheel

Pd$_{12}$(L1)$_{24}$ cage. To a 2-mL vial with **L1** (13.13 mg, 0.05006 mmol) dissolved in 366.7 μL of DMSO-d^6 was added via micropipette a solution of Pd(NO$_3$)$_2$·2H$_2$O (6.67 mg, 0.02503 mmol) in 133.3 μL of DMSO-d^6. The head-space of the vial was briefly purged with argon, the vial was closed with a screw-cap, and the resultant mixture was immediately vortexed, giving rise to a light-yellow liquid with small gelatinous pieces dispersed in it. The mixture was heated at 70 °C for 8 h, during the course of which, it became a light yellow homogeneous solution. ^{1}H NMR indicated quantitative conversion of the components to Pd$_{12}$(L1)$_{24}$ cage assemblies. ^{1}H NMR (400 MHz, DMSO-d^6, 25 °C): δ 9.49 (bs, 96H), 8.38 (bm, 120H), 7.95 (bs, 48H), 5.40 (bs, 24H), 4.57 (bs, 48H). ^{13}C NMR (100 MHz, DMSO-d^6, 25 °C): δ 151.27(b), 149.46, 145.24, 135.01, 127.18(b), 124.34 (b), 62.18.

Pd$_2$(L2)$_4$ paddlewheel. To a standard NMR tube with **L2** (13.13 mg, 0.05006 mmol) dissolved in 366.7 μL of DMSO-d^6 was added via micropipette a solution of Pd(NO$_3$)$_2$·2H$_2$O (6.67 mg, 0.02503 mmol) in 133.3 μL of DMSO-d^6. The resultant mixture was agitated briefly to afford a light-yellow homogeneous solution; the head-space of the NMR tube was briefly purged with argon, and the NMR tube was sealed. The mixture in the NMR tube was heated at 70 °C for 8 h. ^{1}H NMR indicated quantitative conversion of the components to Pd$_2$(L2)$_4$ paddlewheel assemblies. ^{1}H NMR (400 MHz, DMSO-d^6, 25 °C): δ 10.22 (s, 8H), 9.45 (d, J = 5.6 Hz, 8H), 9.06 (s, 4H), 8.49 (d, J = 7.1 Hz, 8H), 7.91 (dd, J = 7.9, 5.9 Hz, 8H), 7.79 (s, 8H), 5.13 (b*), 4.55 (s, 8H). ^{13}C NMR (100 MHz, DMSO-d^6, 25 °C): δ 150.19, 149.23, 145.51, 138.51, 138.38, 134.98, 127.82, 126.02, 124.07, 62.38. FT-ICR-ESI HRMS: calcd. for $C_{36}H_{36}Br_4N_4$ [M − 3(NO$_3^-$)]$^{3+}$, most abundant m/z = 441.4132; found, 441.4141. *The resonance corresponding to the RO<u>H</u> proton is extremely broad and overlapping with nearby peaks, preventing accurate integration.

Synthesis of L2, L3, telechelic PEG macromers PL1 and PL2, and free ligand-substituted polyMOC gels

(3,5-di(pyridin-3-yl)phenyl)methanol **L2**. To a 100-mL round-bottom flask equipped with a magnetic stir-bar were added 3,5-dibromobenzyl alcohol (0.680 g, 2.56 mmol), pyridine-3-boronic acid pinacol ester (1.154 g, 5.63 mmol), potassium carbonate (3.536 g, 25.6 mmol), and tetrakis(triphenylphosphine)palladium (0.295 g, 0.255), and the vessel was sealed with a septum, evacuated and refilled with nitrogen three times. To the vessel via syringe were added anhydrous *N,N*-dimethylformamide (DMF, 20.7 mL) and then de-ionized water (0.430 mL, 23.9 mmol) which had first been sparged with argon for 30 min. The vessel was briefly evacuated until bubbling was observed, and then refilled with nitrogen, and briefly sparged with argon (10–15 sec). The vessel was heated in the oil bath for 60 h at 100 °C, with precipitated palladium black observed after 24 h. At the conclusion of the reaction, the vessel was brought to RT, and the contents of the vessel were filtered *in vacuo* over tightly-packed Celite® 545 on a medium-porosity glass frit, rinsing the flask and Celite with with MeOH (2 mL) and chloroform (3 x 70 mL). The filtrate was subjected to washes with water (4 x 100 mL and 1 x 500 mL), followed by drying over Na_2SO_4, filtration, and concentration *via* rotary evaporation. The remainder was subjected to chromatography on silica gel (CH_2Cl_2/MeOH step gradient: 10:0 → 9.5:0.5 → 9:1; **L2** eluted during the second step, R_f = 0.10 in CH_2Cl_2/MeOH = 9.5:0.5). The fractions containing the pure desired product were combined, concentrated by rotary evaporation, and dried *in vacuo* affording **L2** (0.3284 g, 48.9 % yield, ≥98.5% pure by LCMS) as a white to faint-yellow powdery solid. ^1H NMR (400 MHz, DMSO-d^6, 25 °C): δ 9.01 (dd, J = 2.4, 0.8 Hz, 2H), 8.60 (dd, J = 4.8, 1.6 Hz, 2H), 8.20 (ddd, J = 8.0, 2.4, 1.6 Hz, 2H), 7.93 (t, J = 1.7 Hz, 1H), 7.72 (m, 2H), 7.52 (ddd, J = 8.0, 4.8, 0.8 Hz, 2H), 5.35 (t, J = 5.8 Hz, 1H), 4.67 (d, J = 5.8 Hz, 2H). ^{13}C NMR (100 MHz, DMSO-d^6, 25 °C): δ 148.67, 147.88, 144.51, 137.84, 135.44, 134.37, 124.67, 123.89, 123.85, 62.69. FT-ICR-DART HRMS: calcd. for $C_{17}H_{14}N_2O$ [M+H]$^+$, most abundant *m/z* = 263.1179; found, 263.1176.

3,5-di(pyridin-4-yl)benzyl 4-(pyren-1-yl)butanoate **L3**. To a 1-dram scintillation vial with a magnetic stir-bar were added **L1** (0.0400 g, 0.153 mmol), 4-(1-pyrenyl)butyric acid (0.0440 g, 0.153 mmol), *N*-(3-dimethylaminopropyl)-*N'*-ethylcarbodiimide hydrochloride (EDC·HCl) (0.0380 g, 0.198 mmol), and 4-(dimethylamino)pyridine (DMAP) (0.0048g, 0.040 mmol). The vial was brought into the glove box, and to it was added dichloromethane (DCM, 0.5 mL), and the reaction mixture was sealed and allowed to stir for 24 h. The reaction mixture was then

removed from the glove box and loaded directly onto silica gel packed inside a 2-mL Pasteur pipette for column chromatography, using ethyl acetate as the eluent (R_f of **L3** = 0.10). The fractions containing **L3** were combined, concentrated via rotary evaporation, and subjected to column chromatography using ethyl acetate as the eluent. Rotary evaporation of the combined fractions containing the pure product, followed by drying at 60 °C overnight on the Schlenk line afforded **L3** (0.0687 g, 84.6 %) as a beige-yellow powdery solid. ^{1}H NMR (400 MHz, DCM-d^2, 25 °C): δ 8.66 (dd, J = 4.6, 1.6 Hz, 4H), 8.29 (d, J = 9.3 Hz, 1H), 8.17 (dd, J = 7.6, 1.1, Hz, 1H), 8.14 (dd, J = 7.7, 1.0 Hz, 1H), 8.10 (d, J = 7.8 Hz, 1H), 8.05 (d, J = 9.3 Hz, 1H), 8.03 (s, 2H), 7.99 (t, J = 7.6 Hz, 1H), 7.88—7.83 (m, 2H), 7.72 (d, J = 1.7 Hz, 2H), 7.60 (bd, J = 6.0 Hz, 4H), 5.25 (s, 2H), 3.41 (t, J = 7.6 Hz, 2H), 2.56 (t, J = 7.3 Hz, 2H), 2.23 (tt, J = 7.6, 7.3 Hz, 2H). ^{13}C NMR (100 MHz, DCM-d^2, 25 °C): δ 173.41 (ester carbon), 150.64, 147.80, 139.92, 138.79, 136.25, 131.79, 131.25, 130.35, 129.12, 127.82, 127.78, 127.69, 127.66, 127.07, 126.31, 125.90, 125.37, 125.33, 125.24, 125.19, 125.15, 123.69, 122.08, 65.95, 34.18, 33.01, 27.19. FT-ICR-DART HRMS: calcd. for $C_{37}H_{28}N_2O_2$ [M+H]$^+$, most abundant m/z = 533.2224; found, 533.2216.

PL1. To a 20-mL microwave vial equipped with a magnetic stir-bar were added *finely powdered* **L1** (0.300 g, 1.14 mmol), PEG-diacid (M_n = 2.2 kDa, 0.7741 g, 0.35 mmol), EDC·HCl (0.4336 g, 2.26 mmol), and DMAP (0.0870 g, 0.712), and the vessel was brought into the glove box. To the vessel was added DCM (3.84 mL), ensuring that the solid was washed down the walls of the vial, and the vial was crimped and set to stir at RT. During the first several minutes, most of the solid dissolved, giving rise to a yellow solution. After 25 h, the vessel was removed from the glove box and concentrated *via* rotary evaporation. The product was extracted from the oily mixture with toluene (3 x 2 mL), filtering the extracts through Celite® 545 packed in Pasteur pipettes. The combined extracts were concentrated by rotary evaporation, redissolved in 2 mL toluene, and precipitated into cold (~ -10 – -20 °C) diethyl ether (35 mL). The vial containing the solution of crude product was rinsed with an additional 0.5 mL toluene, and this rinsing was also subjected to precipitation. The precipitation was allowed to proceed overnight at -20 °C, and the precipitated product was collected by filtration *in vacuo*, rinsing with cold diethyl ether (2 x 40 mL, 1 x 100 mL). Quickly, while still cold, the white solid was transferred from the filter disk to a 20-mL scintillation vial and was dried *in vacuo* overnight. The dry solid (~950 mg) was redissolved in water (9.5 mL, 18.2 MΩ•cm at RT, from Milli-Q® system),

411

filtered through a nylon syringe filter with 0.45 μm-pore size, and subjected to prep-HPLC purification. The combined pure fractions were diluted with sat. $NaHCO_{3(aq.)}$ until pH was ~7–8. The aqueous phase was divided into two portions and the product was extracted from each one with DCM (5 x 300 mL). The combined extracts were dried over anhydrous Na_2SO_4, concentrated by rotary evaporation, re-dissolved in 1 mL DCM, and precipitated into cold diethyl ether (35 mL). The vial containing the dissolved pure product was rinsed with an additional 0.5 mL DCM, and this rinsing was also subjected to precipitation. The precipitation was allowed to proceed overnight at -20 °C, and the precipitated product was collected by filtration *in vacuo*, rinsing with cold diethyl ether (2 x 40 mL, 1 x 100 mL). Quickly, while still cold, the white solid was transferred from the filter disk to a 20-mL scintillation vial and was dried *in vacuo* overnight, affording **PL1** (0.3752 g, 40 % yield) as a soft white solid. ^1H NMR (400 MHz, CD_2Cl_2, 25 °C): δ 8.69 (bdd, J = 4.3, 1.4 Hz, 8H), 7.88 (t, J = 1.7 Hz, 2H), 7.73 (d, J = 1.7 Hz, 4H), 7.59 (dd, J = 4.5, 1.7 Hz, 8H), 5.33 (s, 4H), 4.22 (s, 4H), 3.80—3.37 (m, 204H). ^{13}C NMR (100 MHz, CD_2Cl_2, 25 °C): δ 170.55, 150.77, 147.64, 140.04, 138.23, 127.83, 126.09, 122.07, 71.33, 70.90 (b), 70.86, 68.98, 66.19. MALDI-TOF: M_n = 2.7 kDa; calcd. for $C_{132}H_{218}N_4O_{52}$ $[M+H]^+$, most abundant m/z = 2693.5; found, 2693.6. GPC (THF, 25 °C): M_w = 2.83 kDa, M_n = 2.73 kDa (obtained via conversion from values determined via calibration with polystyrene standards); Đ = 1.03. M_n (^1H NMR) = 2.87 kDa. M_n = 2.7 kDa was employed in the calculations for reactions involving **PL1**.

PL2. **PL2** was prepared identically to **PL1**, except using **L2** instead of **L1**. **PL2** was isolated as a soft white solid (0.4208 g, 45 % yield). ^1H NMR (400 MHz, CD_2Cl_2, 25 °C): δ 8.90 (dd, J = 2.3, 0.5 Hz, 4H), 8.62 (dd, J = 4.8, 1.6 Hz, 4H), 7.97 (ddd, J = 7.9, 2.4, 1.7 Hz, 4H), 7.79 (t, J = 1.7 Hz, 2H), 7.65 (d, J = 1.7 Hz, 4H), 7.42 (ddd, J = 7.9, 4.8, 0.8 Hz, 4H), 5.33 (s, 4H), 4.22 (s, 4H), 3.81–3.36 (m, 194H). ^{13}C NMR (100 MHz, CD_2Cl_2, 25 °C): δ 170.56, 149.34, 148.64, 139.64, 138.08, 136.16, 134.83, 127.01, 126.32, 124.03, 71.32, 70.90 (b), 70.85, 68.98, 66.32. MALDI-TOF: M_n = 2.7 kDa; calcd. for $C_{132}H_{218}N_4O_{52}$ $[M+H]^+$, most abundant m/z = 2693.5; found, 2693.8. GPC (THF, 25 °C): M_w = 2.81 kDa, M_n = 2.74 kDa (obtained via conversion from values determined via calibration with polystyrene standards); Đ = 1.03. M_n (^1H NMR) = 2.76 kDa. M_n = 2.7 kDa was employed in the calculations for reactions involving **PL2**.

General synthesis of polyMOCs.

To a 1-dram scintillation vial was added 20.25 mg (7.5 µmol) of macromer (**PL1** or **PL2**) and then 210.0 µL DMSO-d^6. In a 2-mL scintillation vial, a stock solution of Pd(NO$_3$)$_2 \cdot$2H$_2$O in DMSO-d^6 was prepared at a concentration of 11.1 mg Pd(NO$_3$)$_2 \cdot$2H$_2$O per 1.00 mL DMSO-d^6 (after vortexing for ~1 min, a clear orange solution forms). 90 µL of this solution was transferred via micropipette to the solution of the macromer, and gelation was observed immediately, although the gel coloration is inhomogeneous. The headspace of the vial is briefly purged with argon, the vial is sealed, and heated at 80 °C for 4 h to give rise to a homogeneous light-yellow gel (translucent if derived from **PL2**, opaque if derived from **PL1**). Molarity of macromer in the gel (in this case 24 mM) was determined by dividing the number of moles of the macromer used by the *total* volume of the gel, accounting for the non-negligible contribution of the polymer to the total volume.

General synthesis of PolyMOC gels with macromer replaced with free ligand.

The procedure is identical to that used for the synthesis of regular polyMOC gels, except during the preparation of the macromer solution, x% of the macromer was replaced with 2 equivalents of the corresponding *free* ligand to achieve the same total concentration of dipyridine ligands (e.g., when x% = 25%, instead of 20.25 mg of macromer **PL1**, 15.18 mg of **PL1** (0.56 µmol) was combined with 0.98 mg of **L1** (0.38 µmol) in 210.0 µL DMSO-d^6).

413

6.5 Spectra
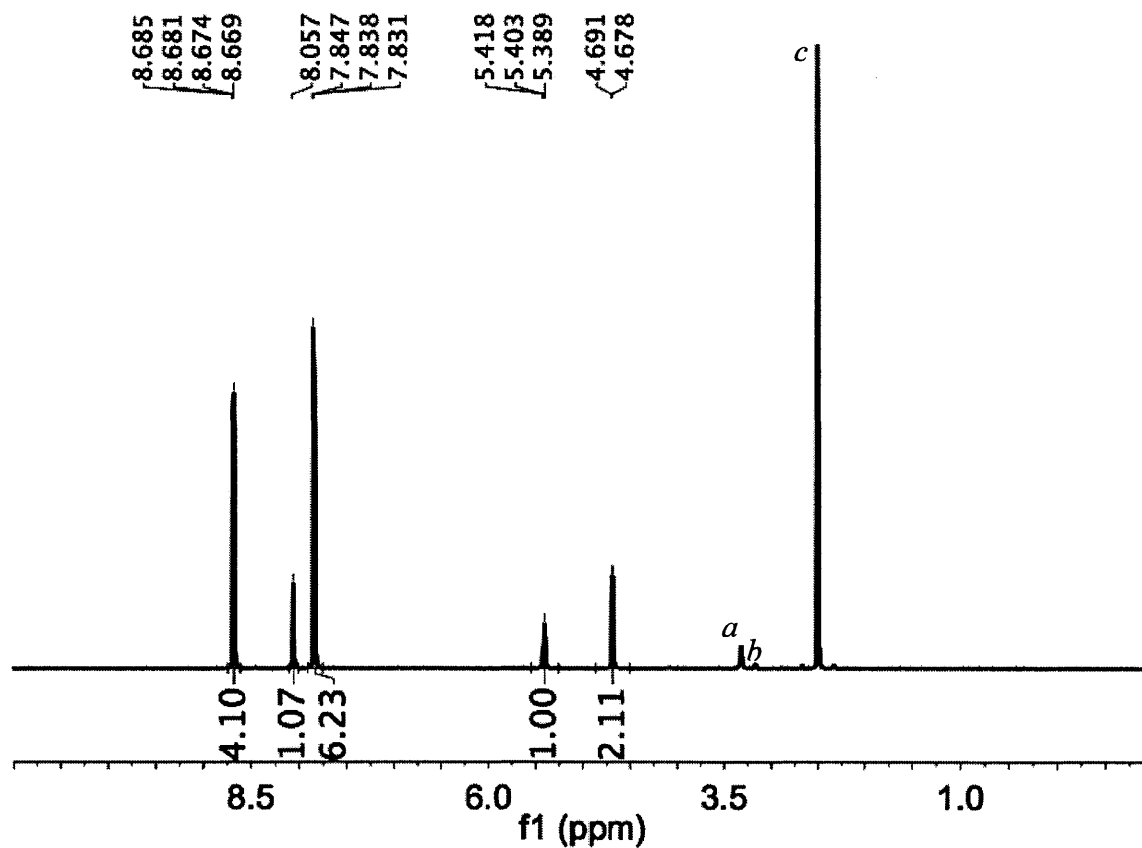
Figure 16. ^{1}H NMR of **L1** at 25 °C in DMSO-d^6. $^{a,\,b,c}$These resonances are due to water (a), methanol (b, ~3%) and residual DMSO-d^5 (c).
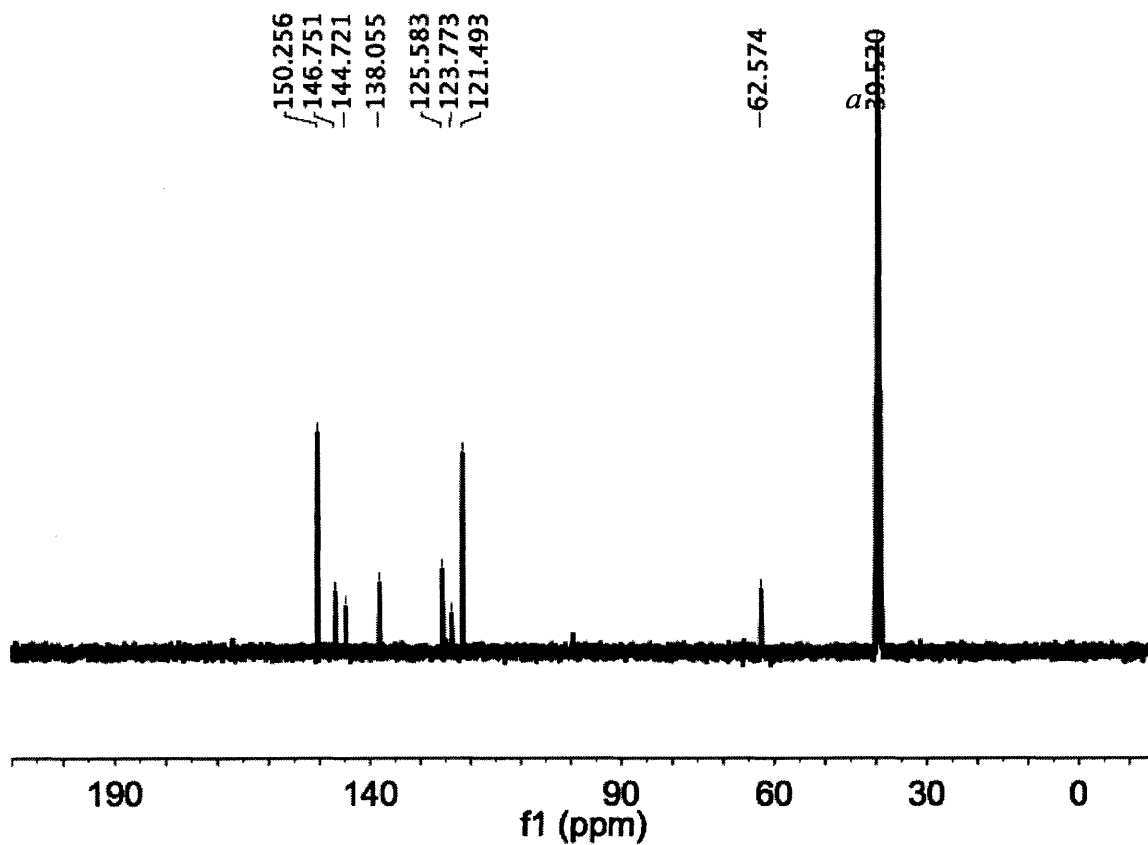
Figure 17. ^{13}C NMR of **L1** at 25 °C in DMSO-d^6. ^{a}This resonance is due to DMSO-d^6.
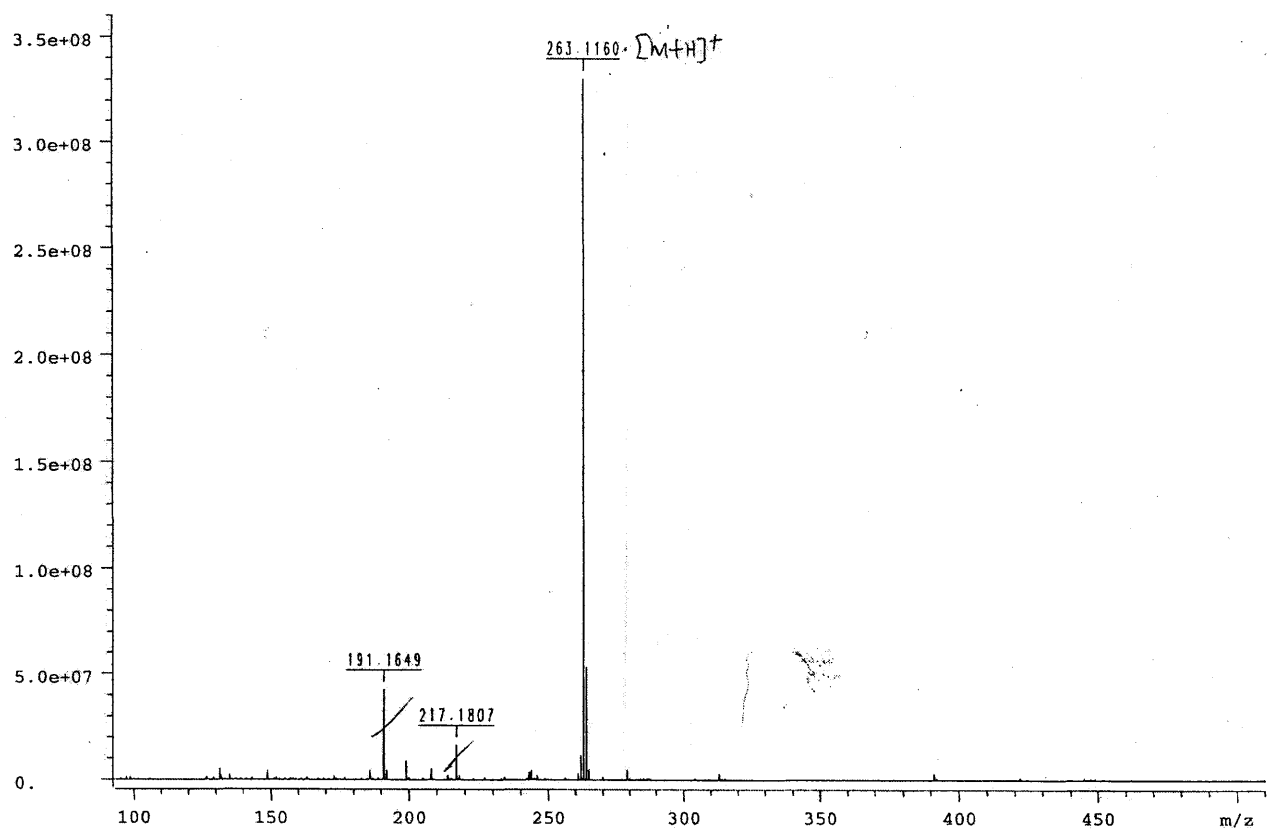
Figure 18. FT-ICR-ESI mass spectrum of **L1**. Peaks marked with slashes correspond to the background signals.
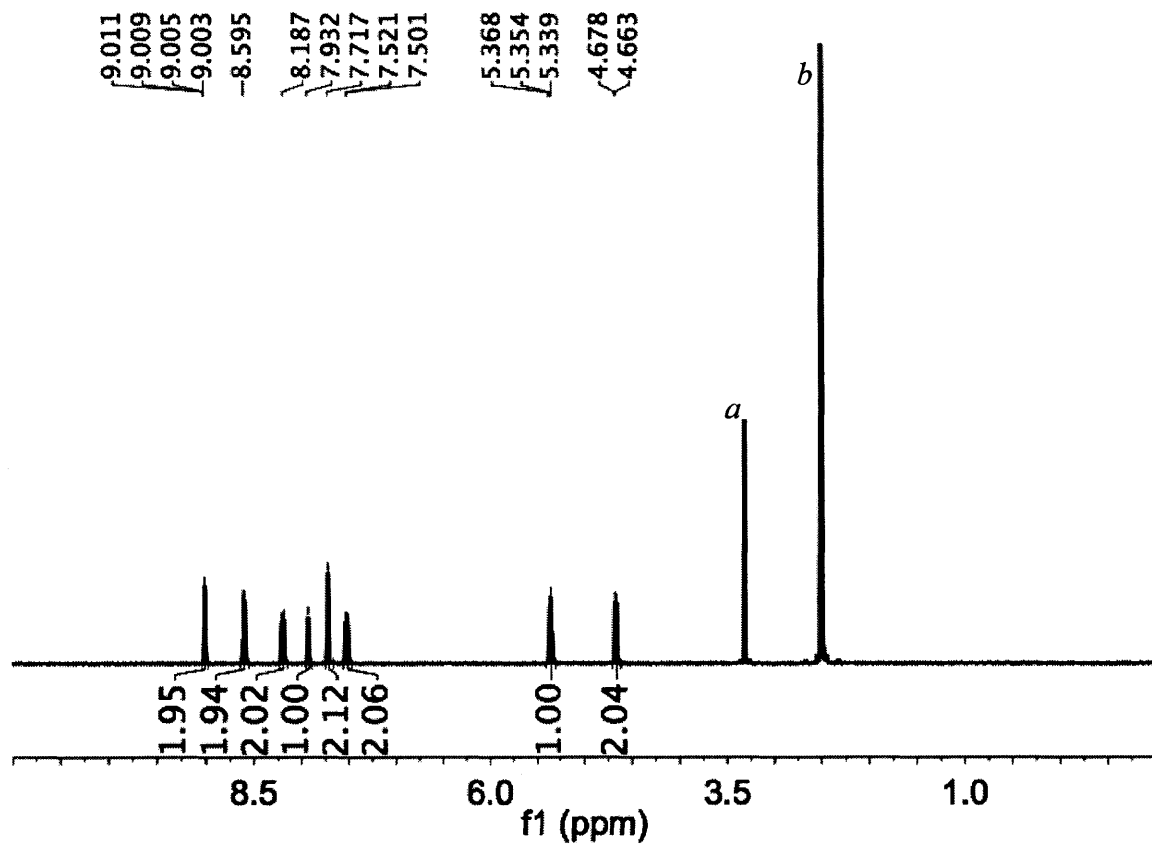
Figure 19. ^{1}H NMR of **L2** at 25 °C in DMSO-d^6. $^{a, b}$These resonances are due to water (a) and residual DMSO-d^5 (b).

417
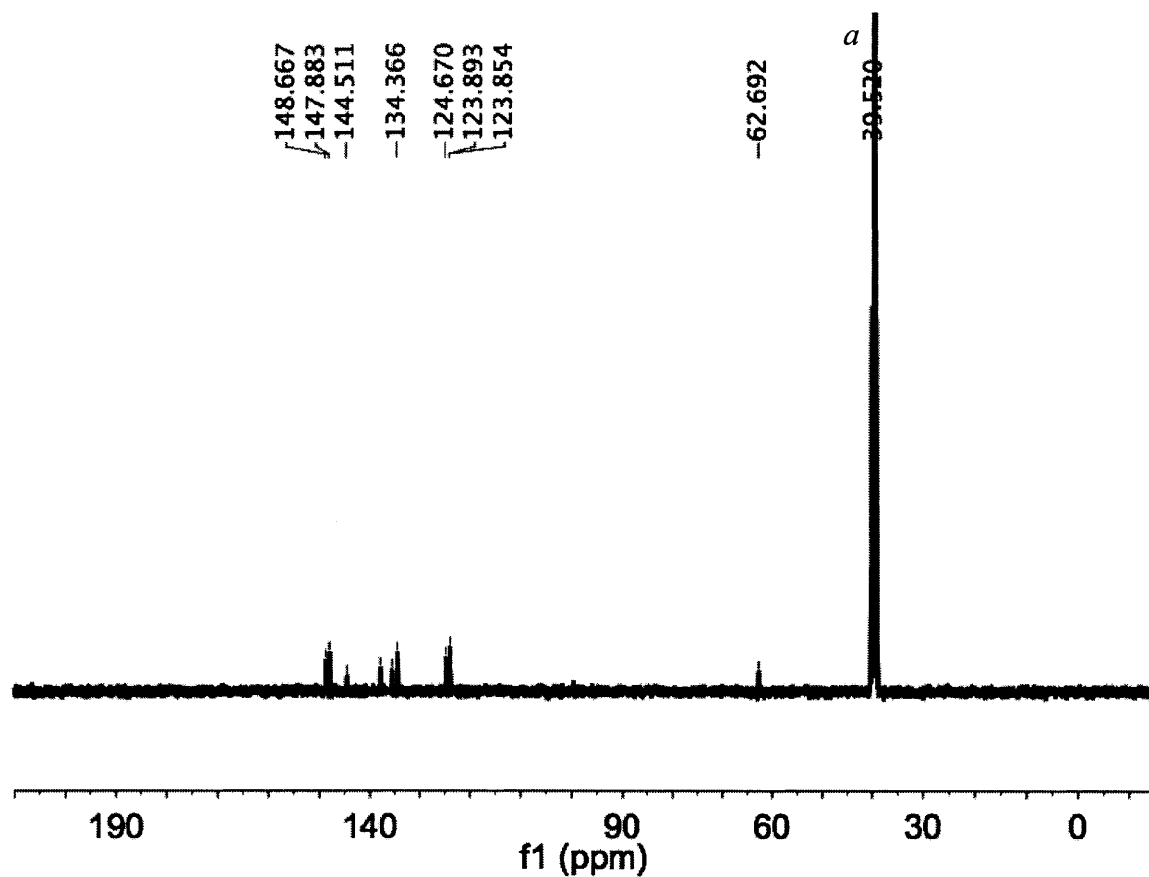
Figure 20. ^{13}C NMR of **L2** at 25 °C in DMSO-d^6. ^{a}This resonance is due to DMSO-d^6.
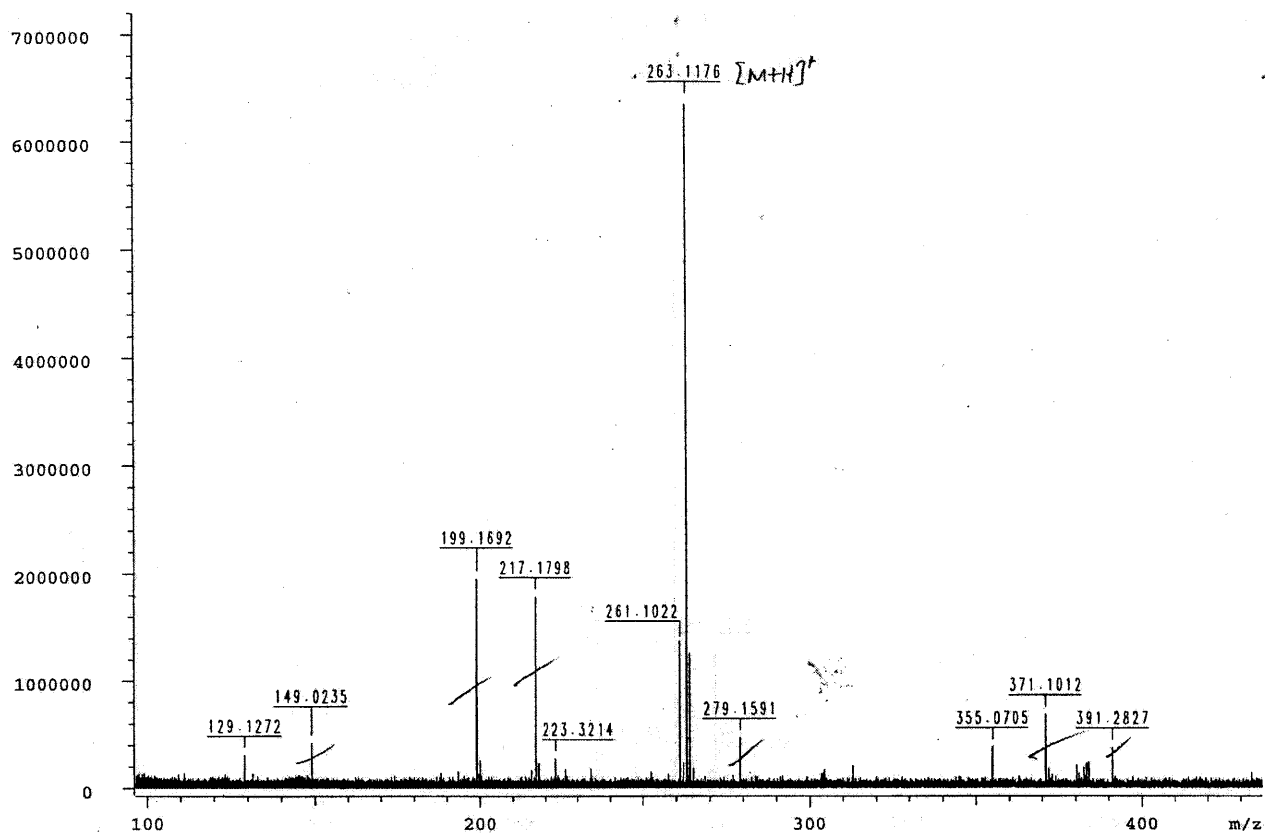
Figure 21. FT-ICR-ESI mass spectrum of **L2**. Peaks marked with slashes correspond to the background signals.
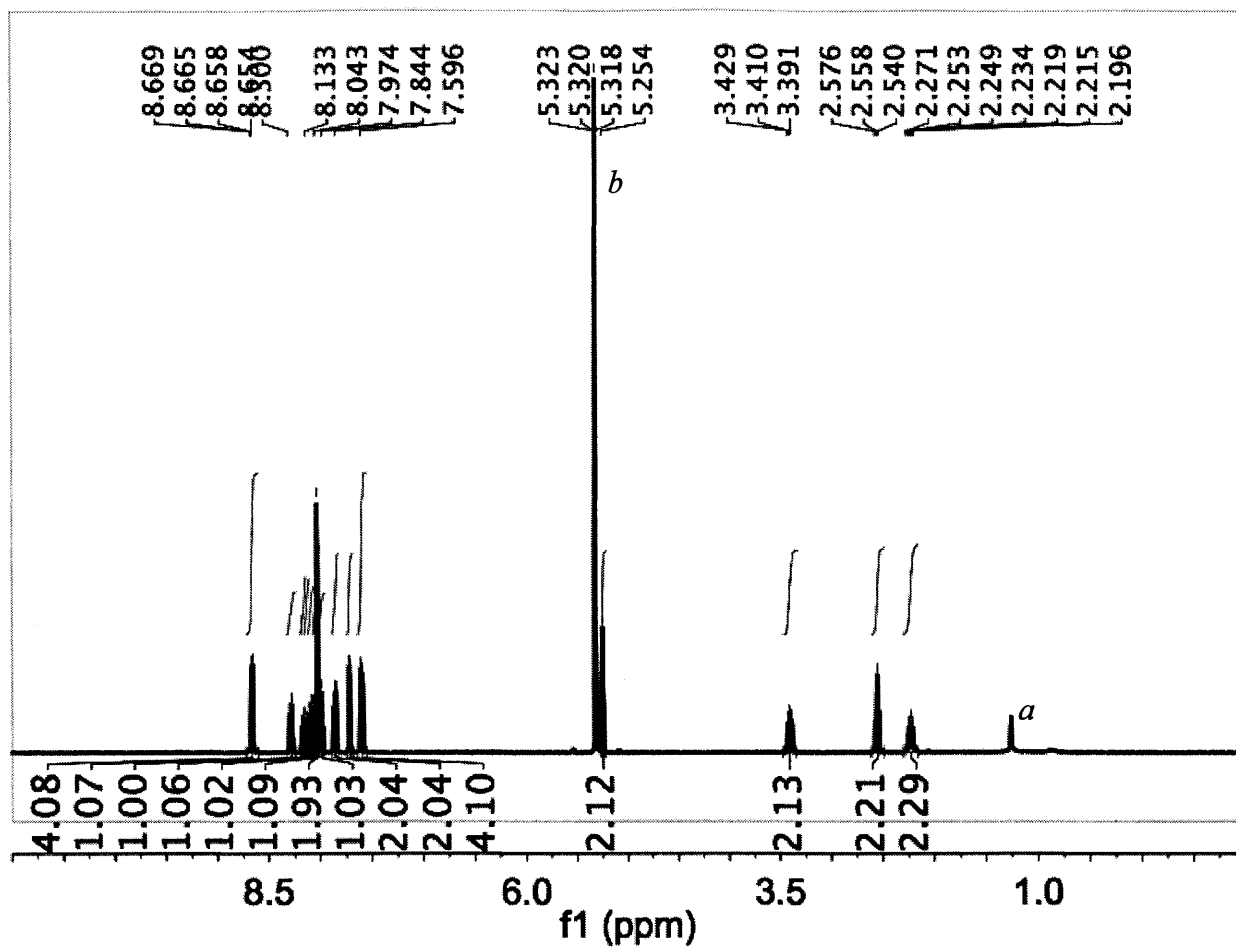
Figure 22. ¹H NMR of **L3** at 25 °C in DCM-d^2. ^{a,b}These resonances are due to H grease (a) and residual DCM-d^1 (b).
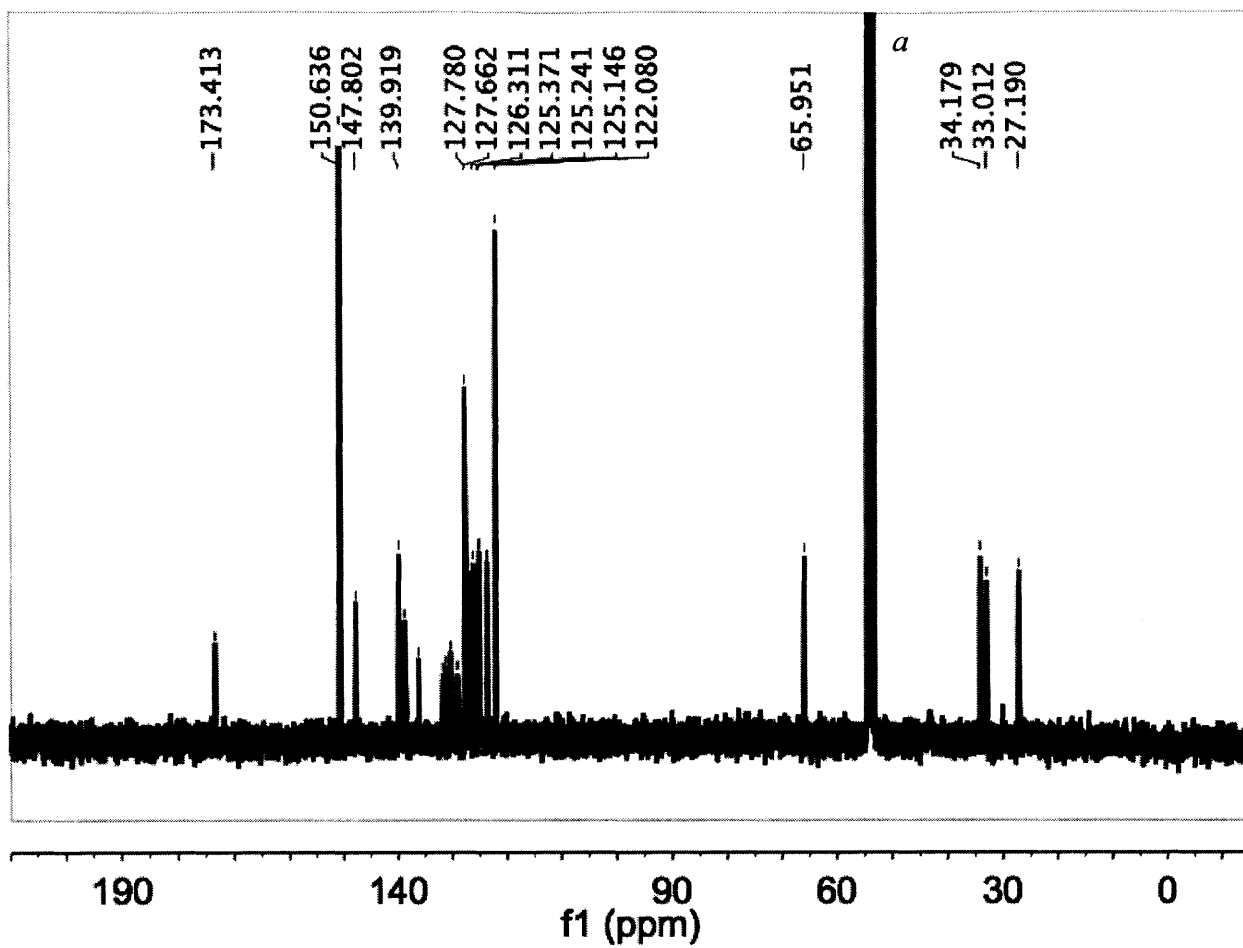
Figure 23. ^{13}C NMR of **L3** at 25 °C in DCM-d^2. ^{a}This resonance is due to DCM-d^2 (a).
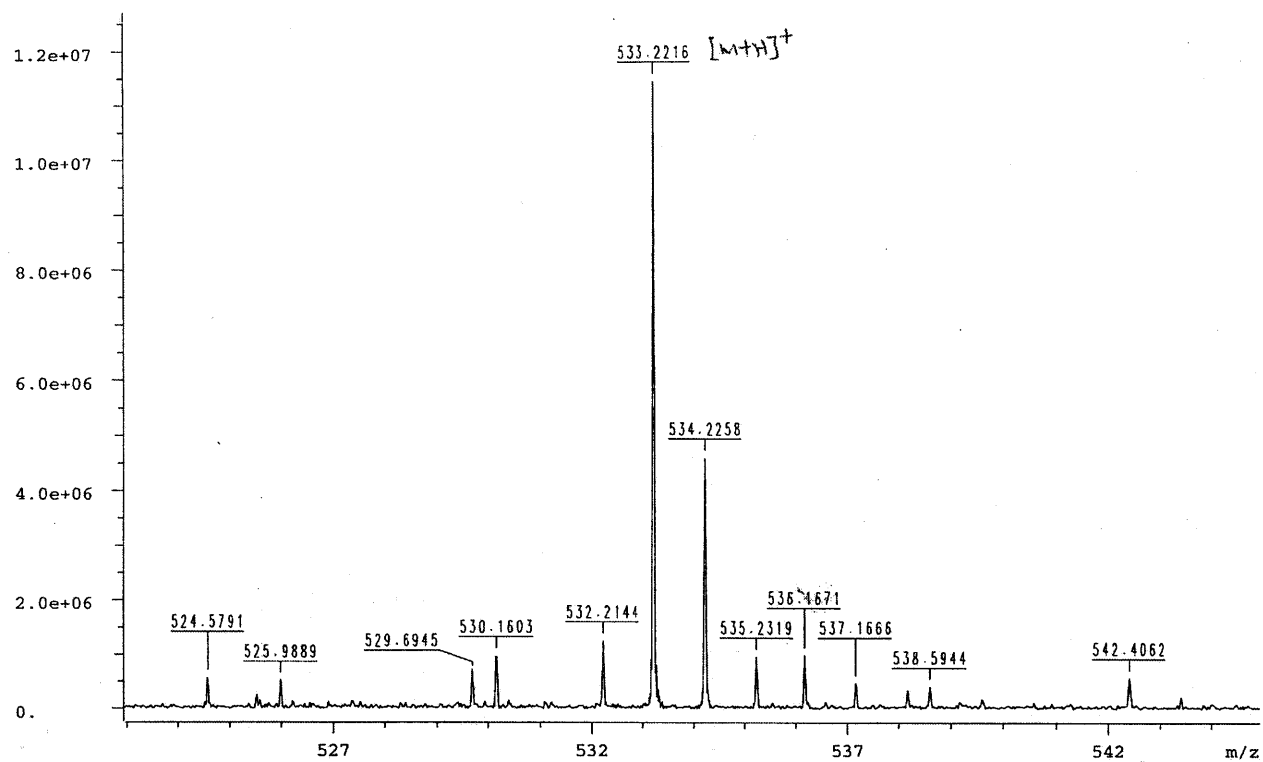
Figure 24. A portion of the FT-ICR-DART mass spectrum of **L3** showing the isotope distribution of the parent ion of **L3** [M+H]$^+$.
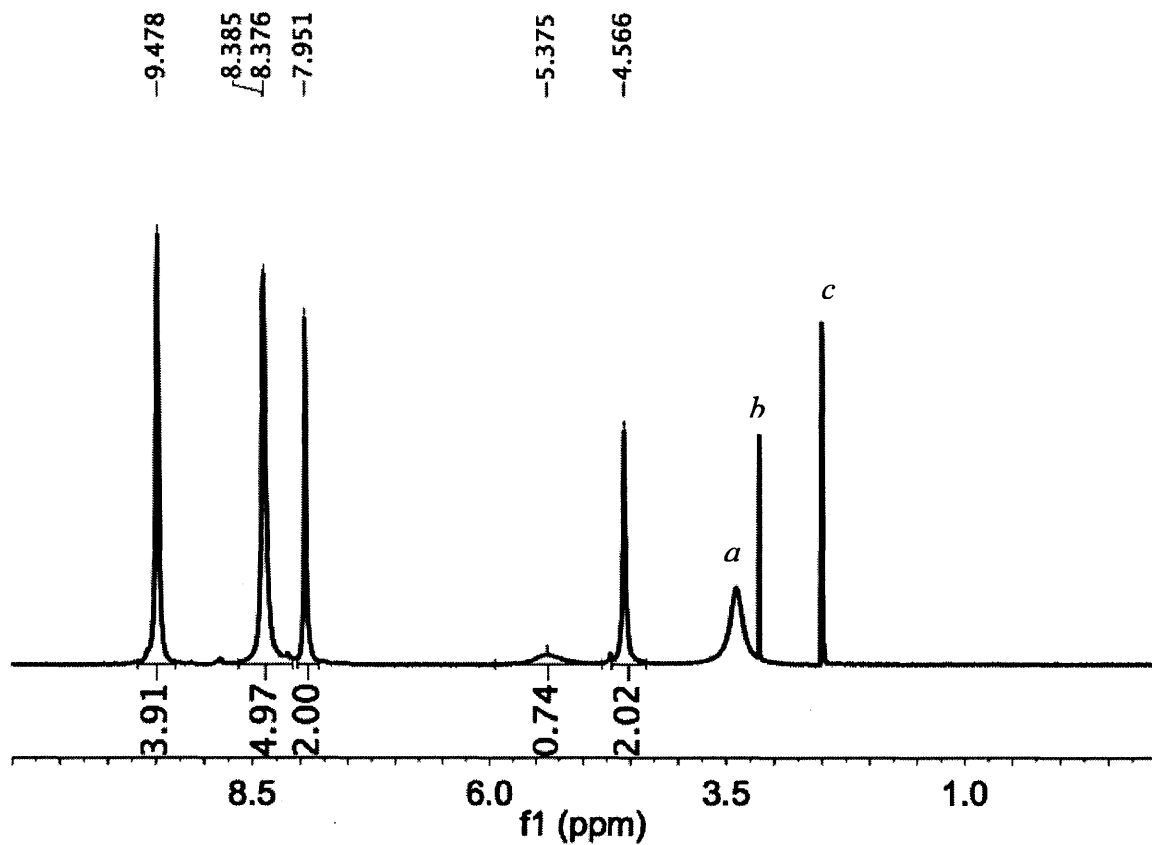
Figure 25. ^{1}H NMR of $Pd_{12}(L1)_{24}$ cage assembly at 25 °C in DMSO-d^6. [a, b, c] These resonances are due to water (a), methanol (b, 2% per **L1**) and residual DMSO-d^5 (c).
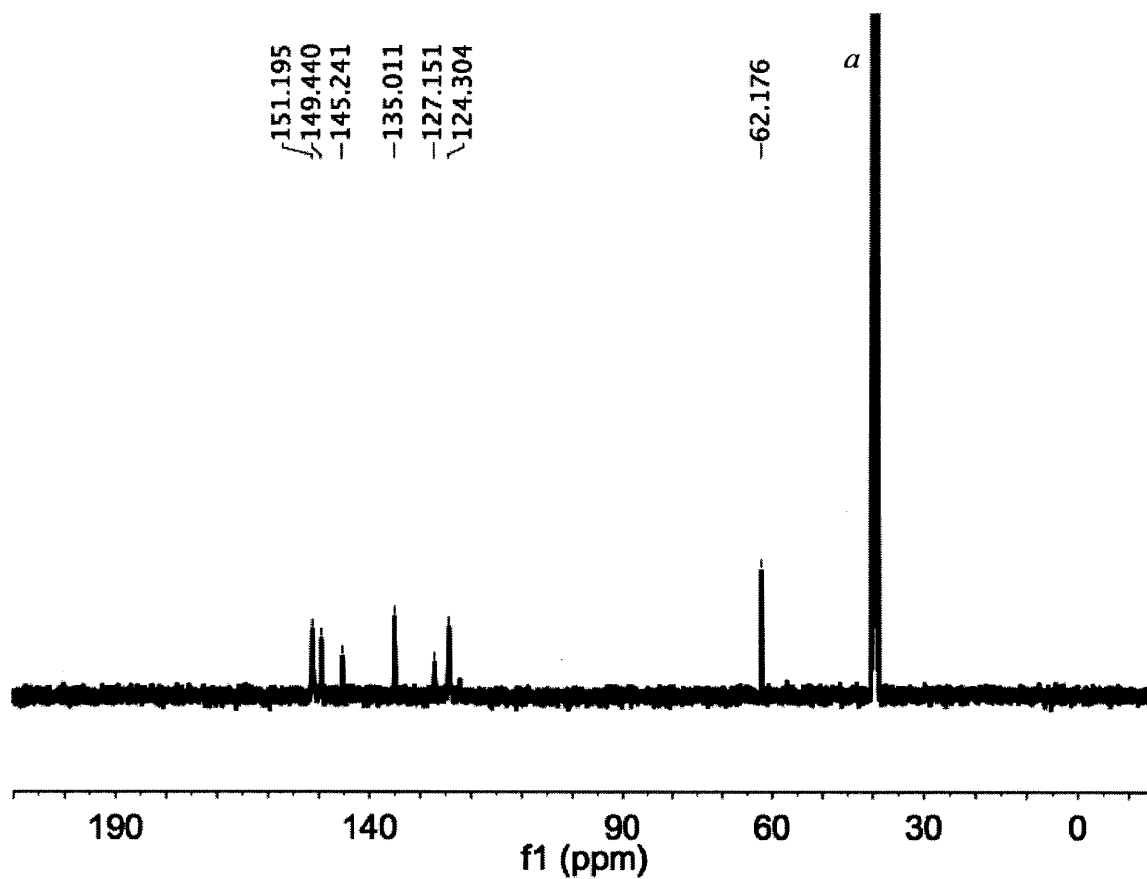
Figure 26. ^{13}C NMR of Pd$_{12}$(**L1**)$_{24}$ cage assembly at 25 °C in DMSO-d^6. ^{a}This resonance is due to DMSO-d^6.

424
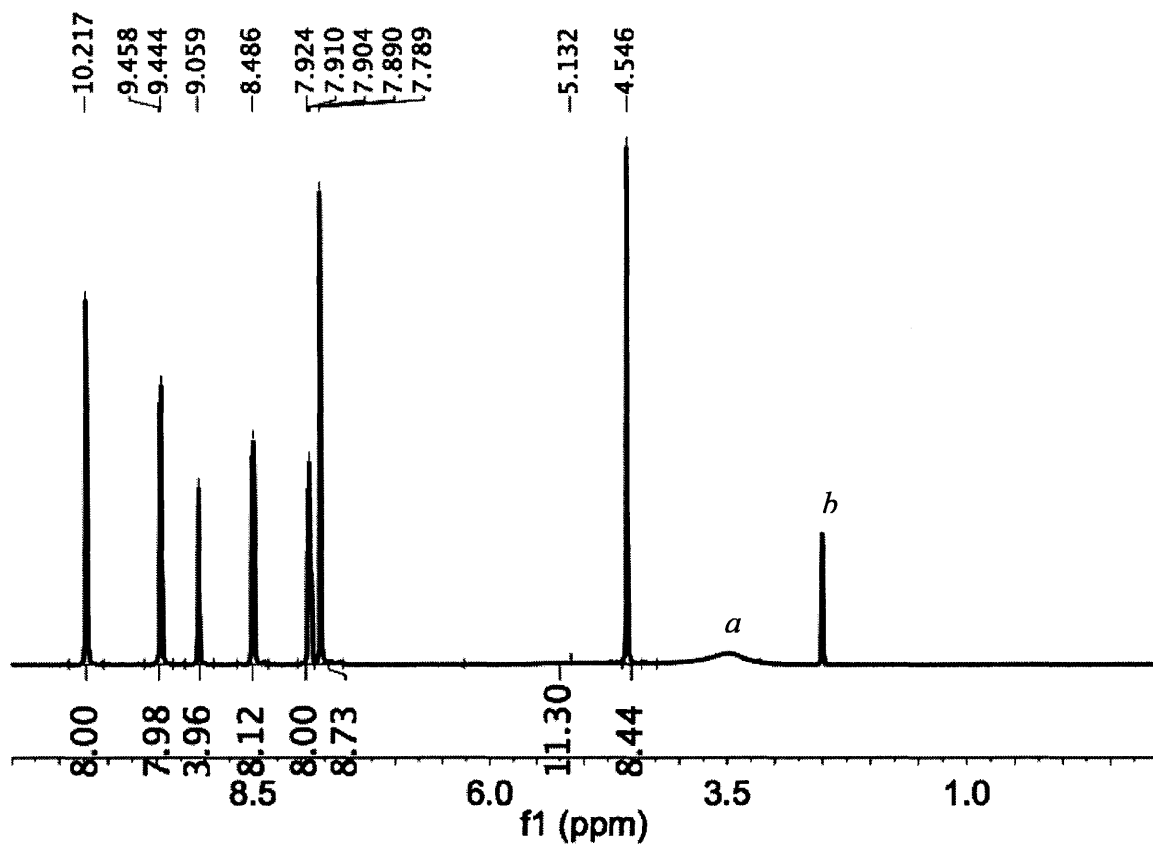
Figure 27. ^{1}H NMR of $Pd_2(L2)_4$ paddlewheel assembly at 25 °C in DMSO-d^6. [a, b]These resonances are due to water (a) and residual DMSO-d^5 (b).
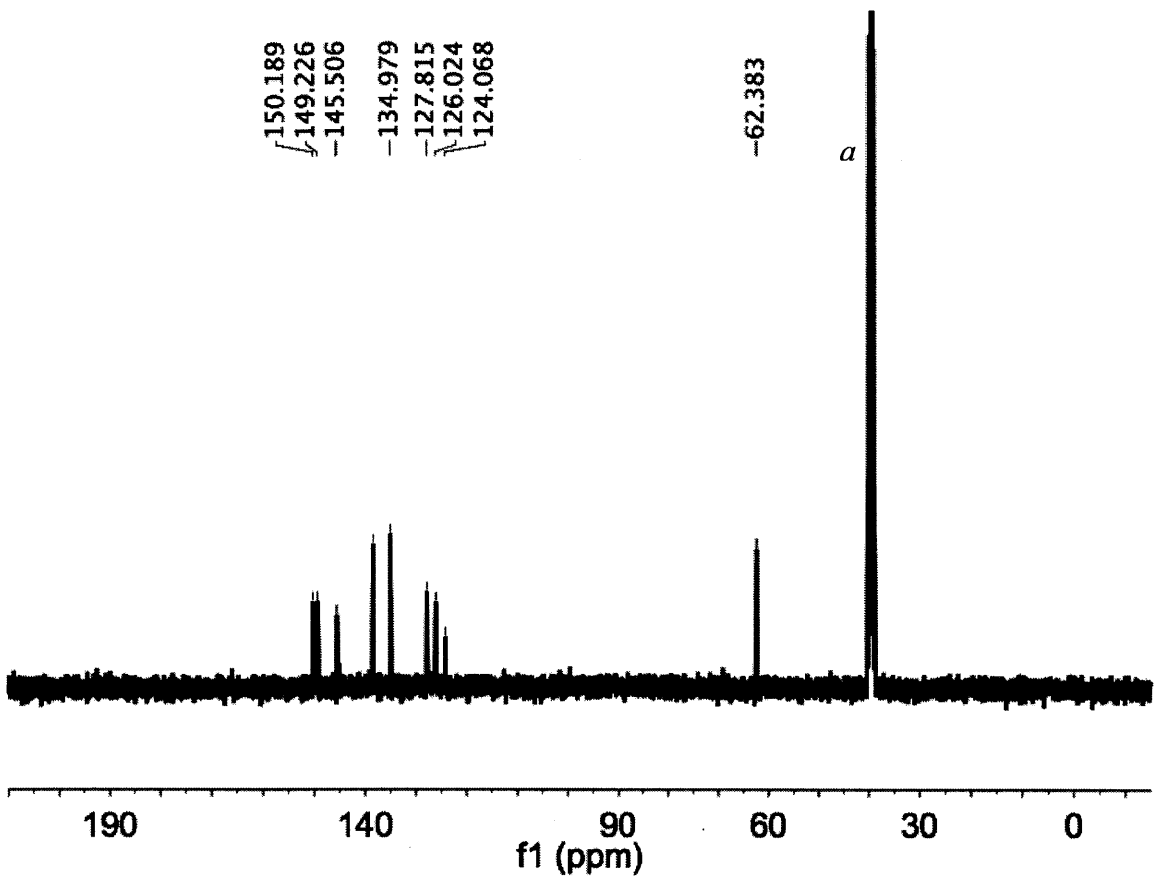
Figure 28. ^{13}C NMR of $Pd_2(L2)_4$ paddlewheel assembly at 25 °C in DMSO-d^6. ^{a}This resonance is due to DMSO-d^6.
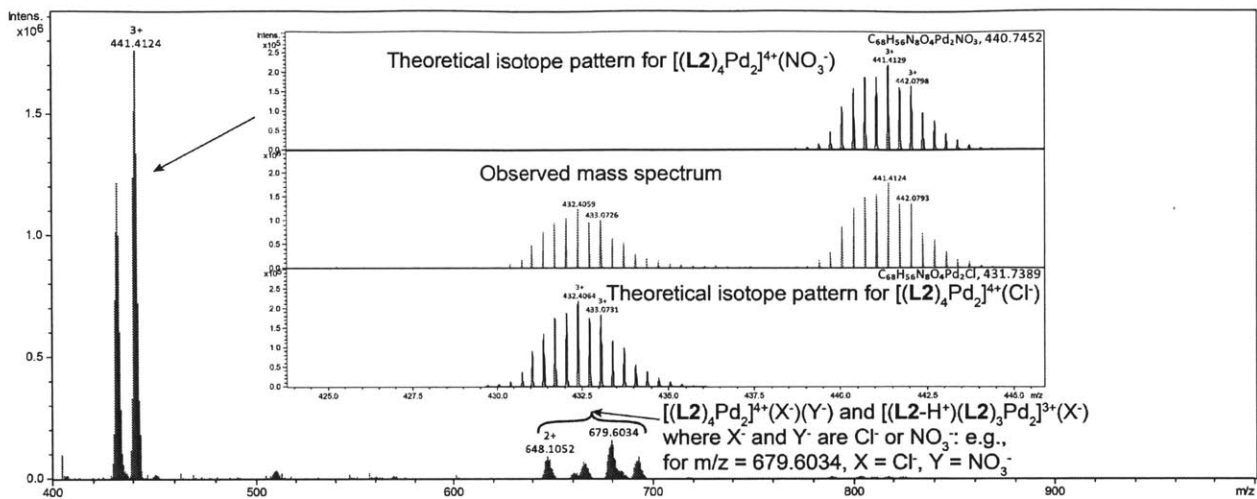
Figure 29. High resolution ESI-TOF mass spectrum of the $Pd_2(L2)_4$ paddlewheel assembly.
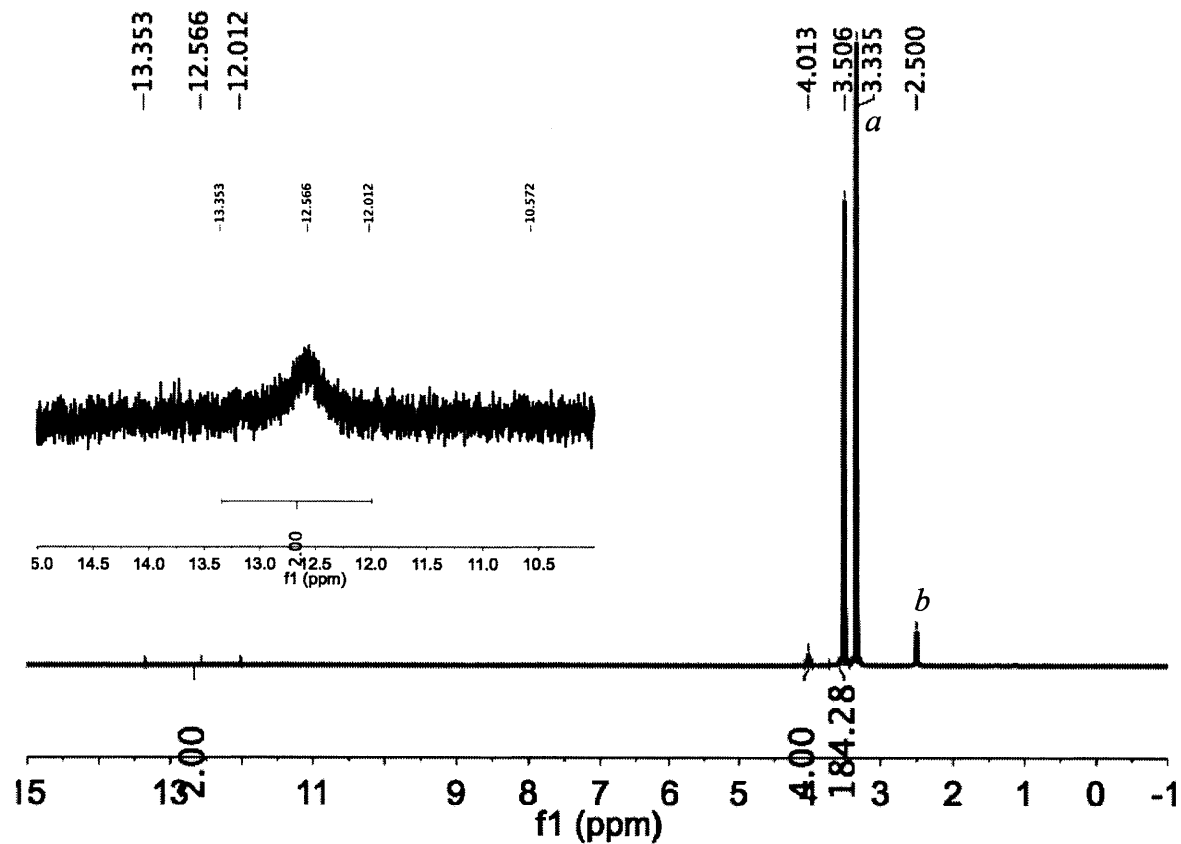
Figure 30. ^{1}H NMR of **PEG-diacid** (M_n=2.2 kDa) at 25 °C in DMSO-d^6. $^{a, b}$These resonances are due to water (a) and residual DMSO-d^5 (b). Inset is the zoomed-in region corresponding to the carboxylic acid proton resonance.
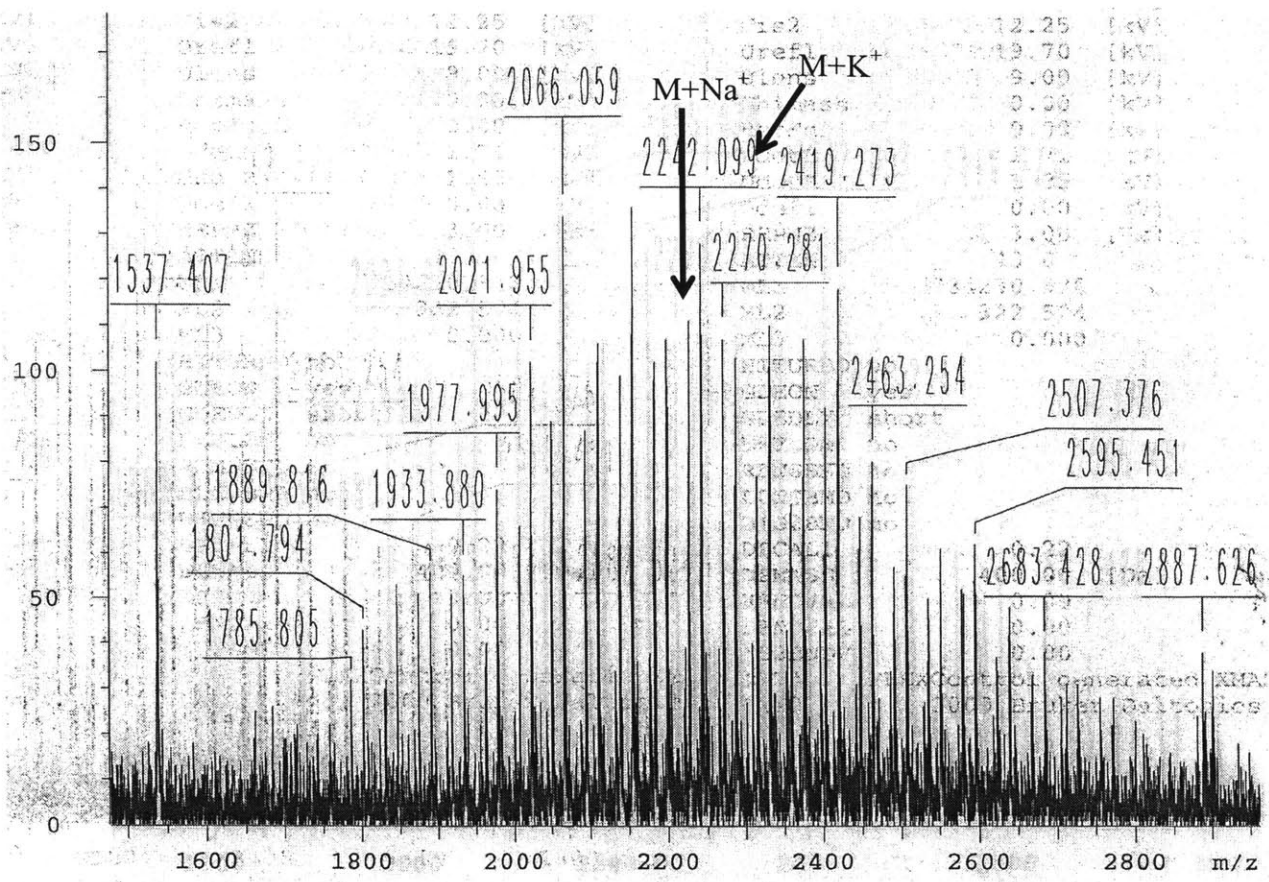
Figure 31. MALDI-TOF mass spectrum of **PEG-diacid** (M_n = 2.2 kDa).
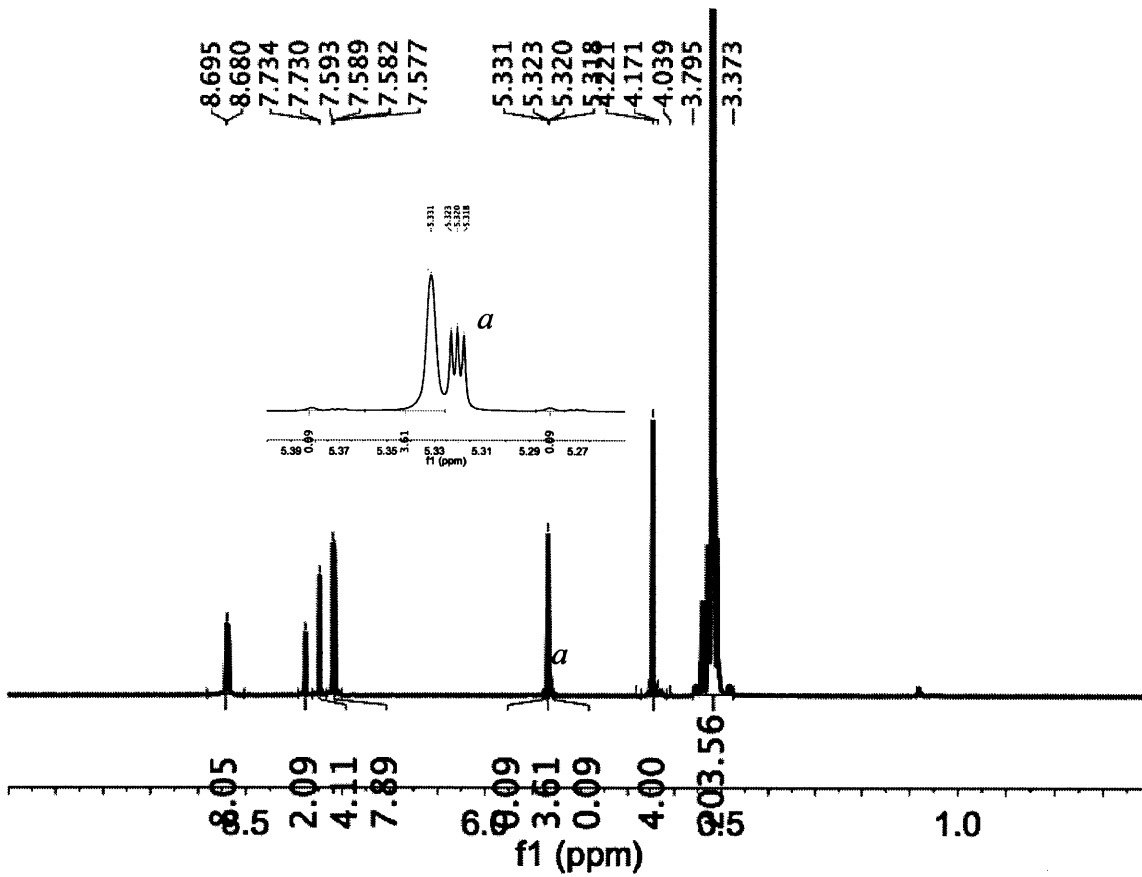
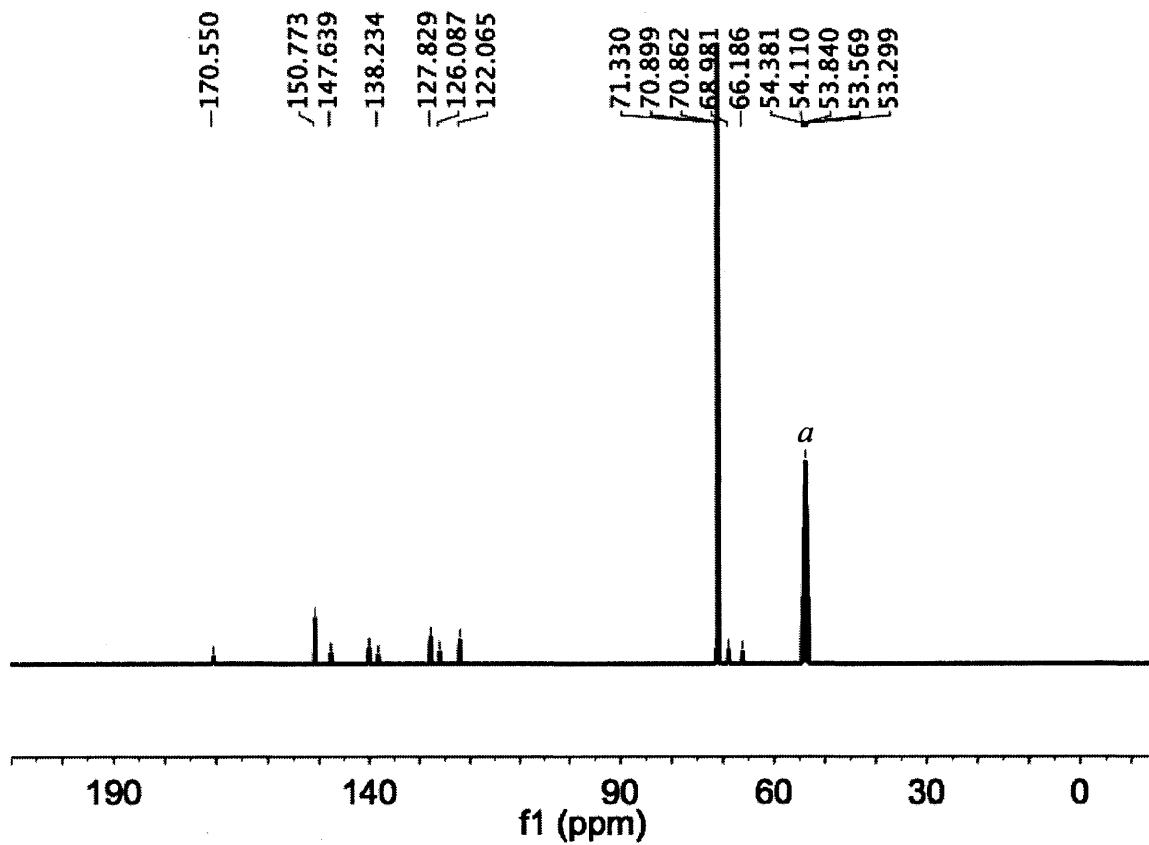**Figure 32.** ^{1}H NMR of **PL1** at 25 °C in CD_2Cl_2. ^{a} This resonance is due to residual $CDHCl_2$ (see inset).

Figure 33. ^{13}C NMR of **PL1** at 25 °C in CD_2Cl_2. ^{a}This resonance is due to CD_2Cl_2.
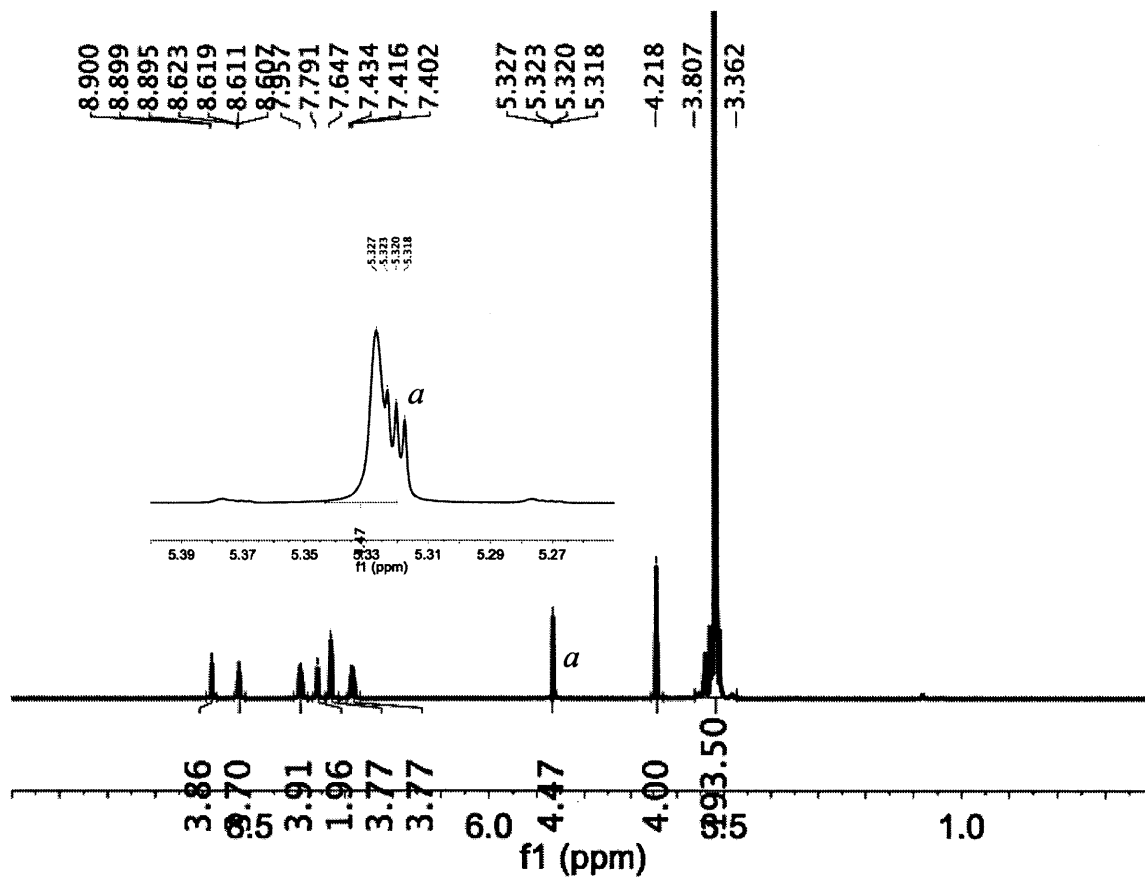
Figure 34. ^{1}H NMR of **PL2** at 25 °C in CD_2Cl_2. ^{a}This resonance is due to residual $CDHCl_2$ (see inset).
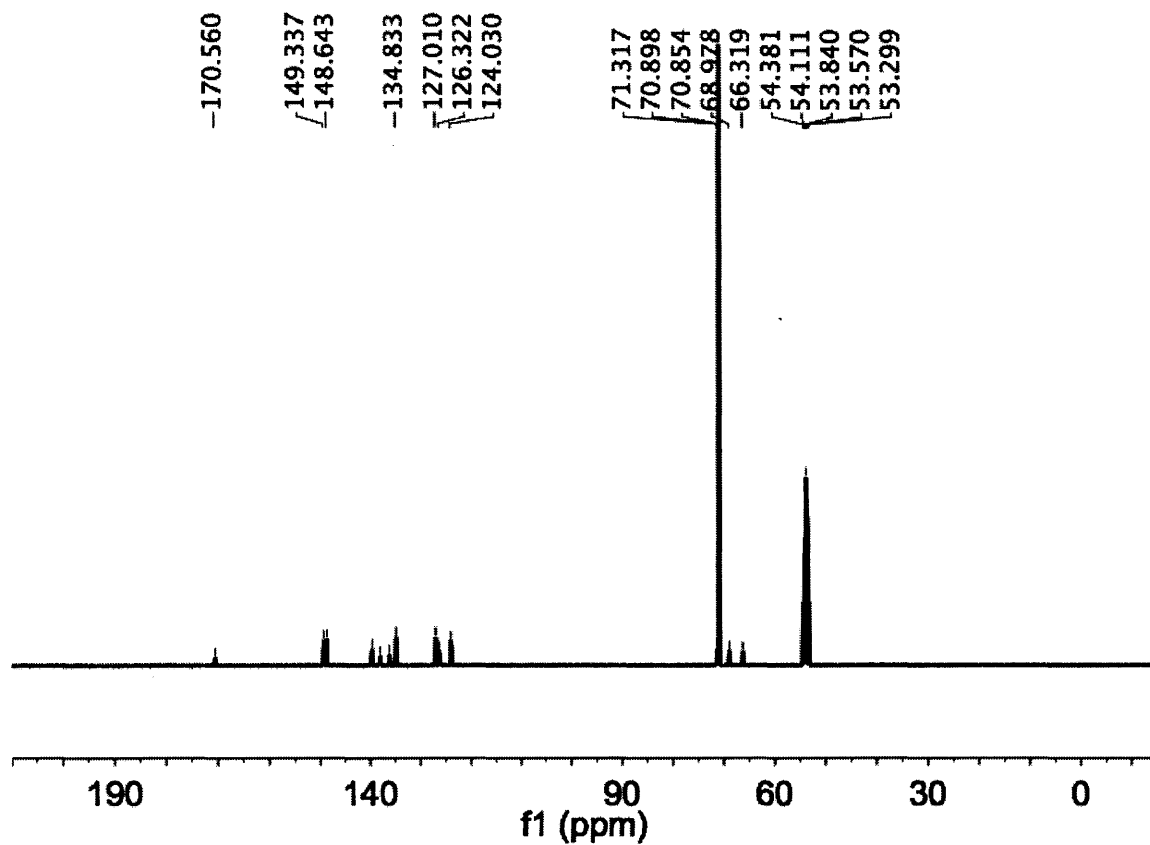
432

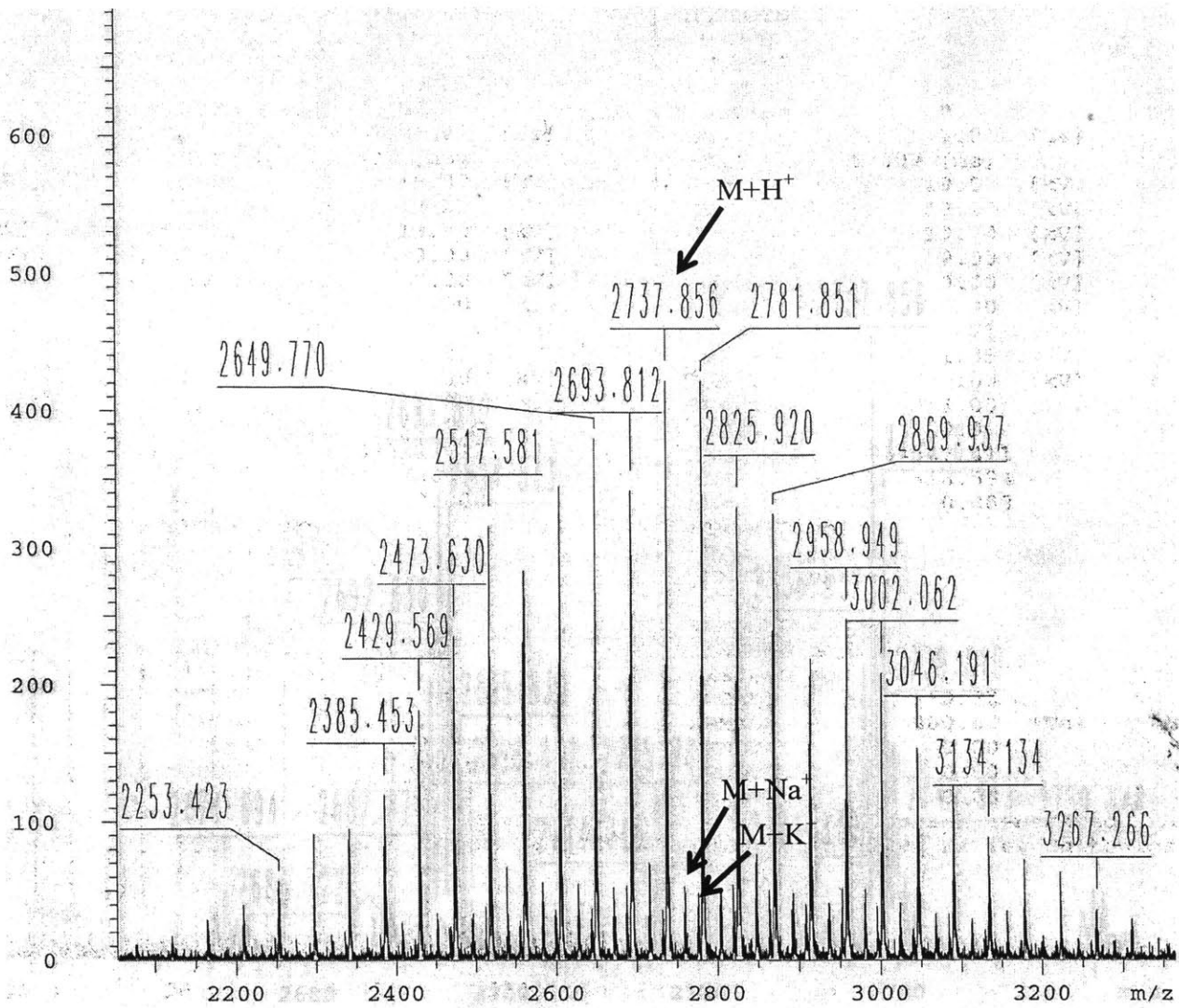**Figure 35.** ^{13}C NMR of **PL2** at 25 °C in CD_2Cl_2. ^{a} This resonance is due to CD_2Cl_2

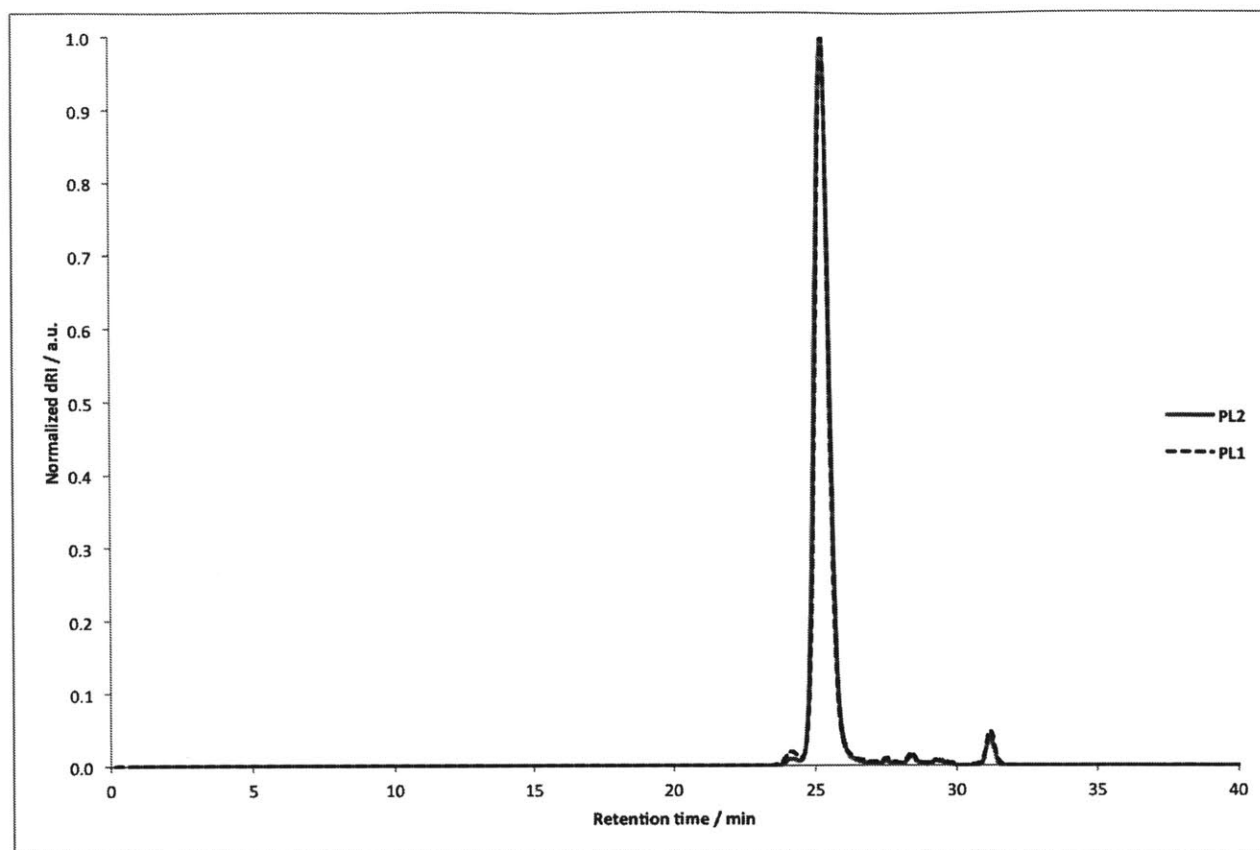**Figure 36.** MALDI-TOF mass spectrum of **PL2**.

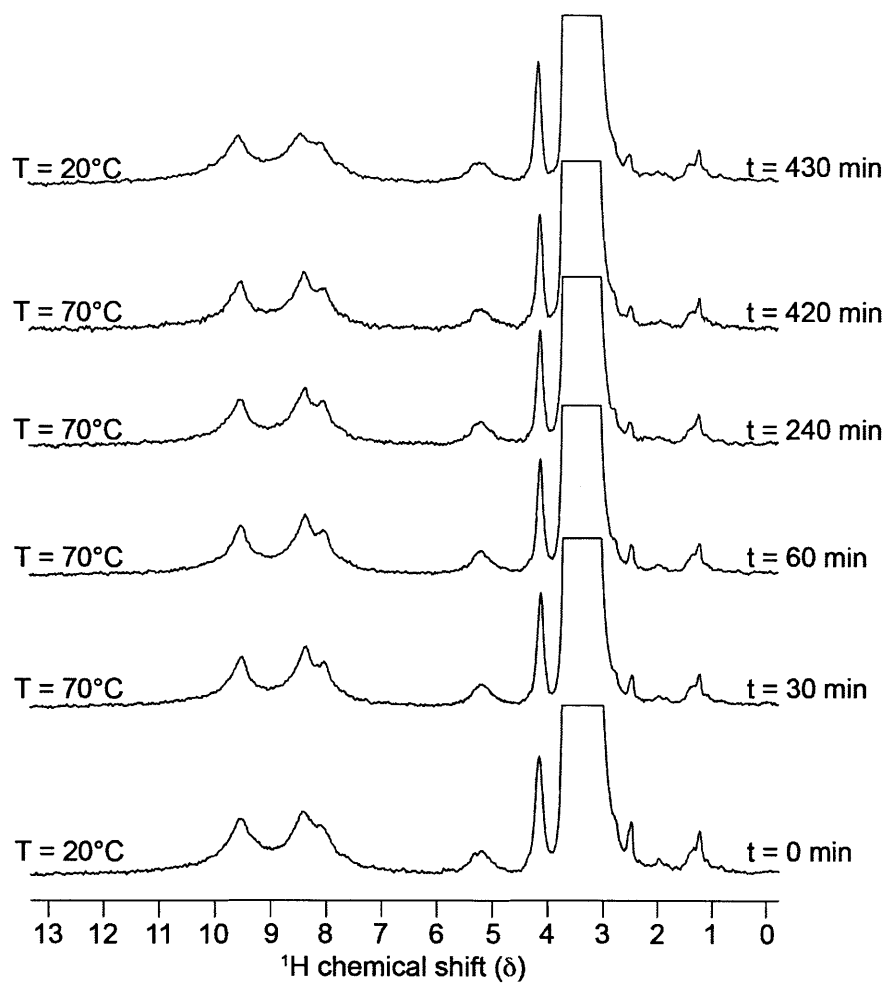**Figure 37.** GPC (THF, 25 °C, *vide supra*) analysis of **PL1** and **PL2**.

Figure 38. VT ^{1}H MAS NMR spectroscopy (500 MHz, DMSO-d^6, $\omega_{r/2}\pi$ = 10 kHz) of the **gel-1** ([**PL1**] = 24 mM) before, during, and after annealing.

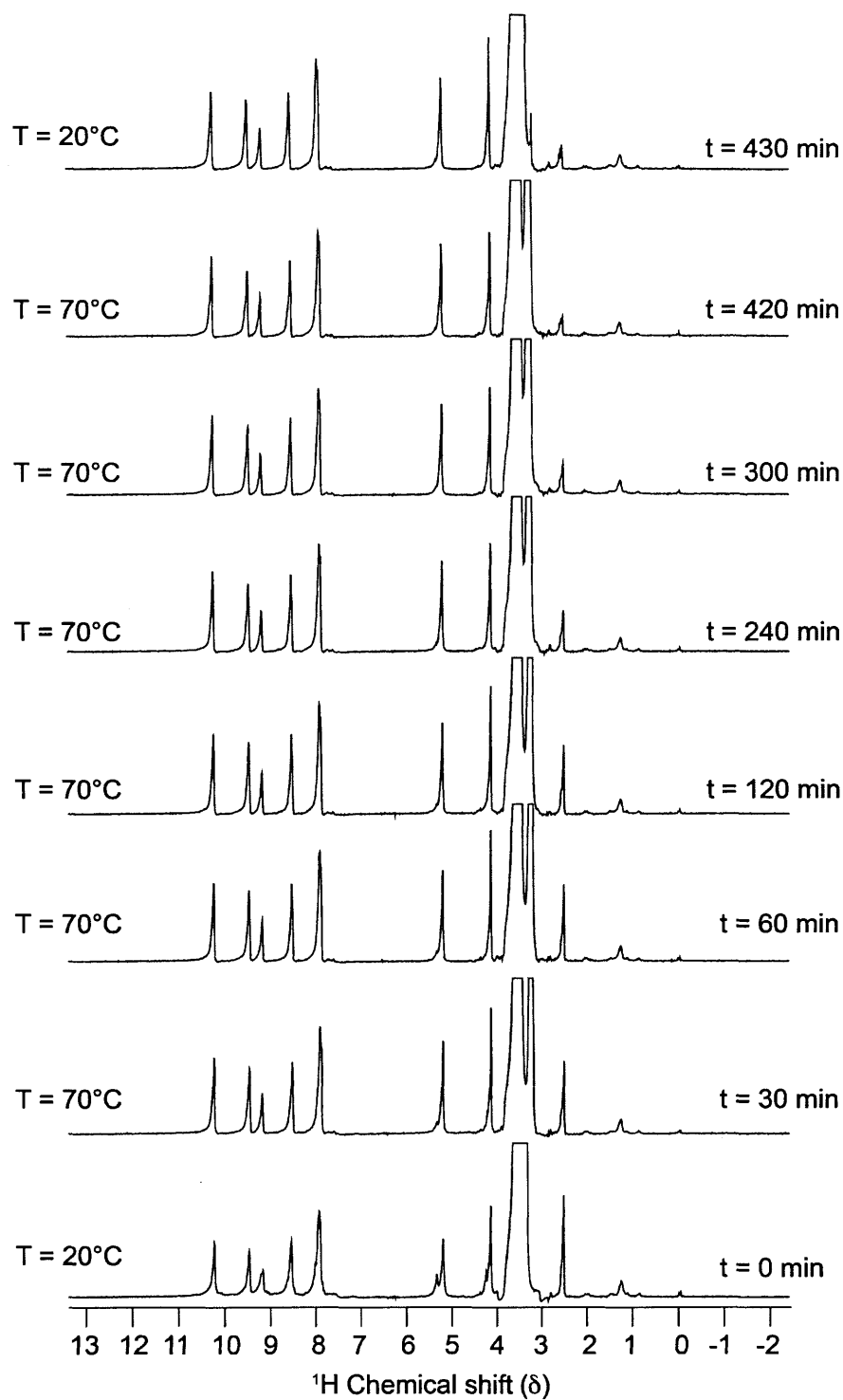**Figure 39.** VT ^{1}H MAS NMR spectroscopy (500 MHz, DMSO-d^6, $\omega_{r/2}\pi$ = 10 kHz) of **gel-2** ([PL2] = 24 mM) before, during, and after annealing.

6.6 References

(1)   Cotton, F. A.; Wilkinson, G.; Murillo, C. A.; Bochmann, M.; Grimes, R. *Advanced Inorganic Chemistry*; Wiley New York, 1999; Vol. 5.

(2)   Braun, D.; Boudevska, H. Reversible Cross-Linking by Complex-Formation - Polymers Containing 2-Hydroxybenzoic Acid Residues. *Eur. Polym. J.* **1976**, *12*, 525-528.

(3)   Xing, B.; Choi, M.-F.; Xu, B. A Stable Metal Coordination Polymer Gel Based on a Calix[4]Arene and Its "Uptake" of Non-Ionic Organic Molecules from the Aqueous Phase. *Chem. Commun.* **2002**, 362-363.

(4)   Beck, J. B.; Rowan, S. J. Multistimuli, Multiresponsive Metallo-Supramolecular Polymers. *J. Am. Chem. Soc.* **2003**, *125*, 13922-13923..

(5)   Pollino, J. M.; Nair, K. P.; Stubbs, L. P.; Adams, J.; Weck, M. Cross-Linked and Functionalized 'Universal Polymer Backbones' Via Simple, Rapid, and Orthogonal Multi-Site Self-Assembly. *Tetrahedron* **2004**, *60,* 7205-7215.

(6)   Loveless, D. M.; Jeon, S. L.; Craig, S. L. Rational Control of Viscoelastic Properties in Multicomponent Associative Polymer Networks. *Macromolecules* **2005**, *38*, 10171-10177.

(7)   Yount, W. C.; Loveless, D. M.; Craig, S. L. Strong Means Slow: Dynamic Contributions to the Bulk Mechanical Properties of Supramolecular Networks. *Angew. Chem., Int. Ed.* **2005**, *44*, 2746-2748.

(8)   Yount, W. C.; Loveless, D. M.; Craig, S. L. Small-Molecule Dynamics and Mechanisms Underlying the Macroscopic Mechanical Properties of Coordinatively Cross-Linked Polymer Networks. *J. Am. Chem. Soc.* **2005**, *127*, 14488-14496.

(9)   Weng, W.; Beck, J. B.; Jamieson, A. M.; Rowan, S. J. Understanding the Mechanism of Gelation and Stimuli-Responsive Nature of a Class of Metallo-Supramolecular Gels. *J. Am. Chem. Soc.* **2006**, *128*, 11663-11672.

(10)   Liu, Y. R.; He, L. S.; Zhang, J. Y.; Wang, X. B.; Su, C. Y. Evolution of Spherical Assemblies to Fibrous Networked Pd(II) Metallogels from a Pyridine-Based Tripodal Ligand and Their Catalytic Property. *Chem. Mater.* **2009**, *21*, 557-563.

(11)   Holten-Andersen, N.; Harrington, M. J.; Birkedal, H.; Lee, B. P.; Messersmith, P. B.; Lee, K. Y. C.; Waite, J. H. pH-Induced Metal-Ligand Cross-Links Inspired by Mussel Yield Self-Healing Polymer Networks with Near-Covalent Elastic Moduli. *Proc. Natl. Acad. Sci. USA* **2011**, *108*, 2651-2655.

(12)   Burnworth, M.; Tang, L.; Kumpfer, J. R.; Duncan, A. J.; Beyer, F. L.; Fiore, G. L.; Rowan, S. J.; Weder, C. Optically Healable Supramolecular Polymers. *Nature* **2011**, *472*, 334-337.

(13)   Zhang, Y.; Zhou, N.; Akella, S.; Kuang, Y.; Kim, D.; Schwartz, A.; Bezpalko, M.; Foxman, B. M.; Fraden, S.; Epstein, I. R.; Xu, B. Active Cross-Linkers That Lead to Active Gels. *Angew. Chem. Int. Ed.* **2013**, *52*, 11494-11498.

(14)   Zhang, J.; Su, C.-Y. Metal-organic gels: From Discrete Metallogelators to Coordination Polymers. *Coord. Chem. Rev.* **2013**, *257*, 1373-1408.

(15)   Menyo, M. S.; Hawker, C. J.; Waite, J. H. Versatile Tuning of Supramolecular Hydrogels Through Metal Complexation of Oxidation-Resistant Catechol-Inspired Ligands. *Soft Matter* **2013**, *9*, 10314-10323.

(16)   Bode, S.; Bose, R. K.; Matthes, S.; Ehrhardt, M.; Seifert, A.; Schacher, F. H.; Paulus, R. M.; Stumpf, S.; Sandmann, B.; Vitz, J.; Winter, A.; Hoeppener, S.; Garcia, S. J.; Spange, S.; van der Zwaag, S.; Hager, M. D.; Schubert, U. S. Self-Healing Metallopolymers

Based on Cadmium Bis(Terpyridine) Complex Containing Polymer Networks. *Polym. Chem.* **2013**, *4*, 4966-4973.

(17) Li, H.; Wu, L. Metallo/Clusto Hybridized Supramolecular Polymers. *Soft Matter* **2014**, *10*, 9038-9053.

(18) Leininger, S.; Olenyuk, B.; Stang, P. J. Self-Assembly of Discrete Cyclic Nanostructures Mediated by Transition Metals. *Chem. Rev.* **2000,***100*, 853-908.

(19) Holliday, B. J.; Mirkin, C. A. Strategies for the Construction of Supramolecular Compounds Through Coordination Chemistry. *Angew. Chem., Int. Ed.* **2001**, *40*, 2022-2043.

(20) Sun, W.-Y.; Yoshizawa, M.; Kusukawa, T.; Fujita, M. Multicomponent Metal–Ligand Self-Assembly. *Curr. Opin. Chem. Biol.* **2002**, *6*, 757-764.

(21) Lehn, J. M. From Supramolecular Chemistry Towards Constitutional Dynamic Chemistry And Adaptive Chemistry. *Chem. Soc. Rev.* **2007**, *36*, 151-160.

(22) Ronson, T. K., Zarra, S., Black, S. P. & Nitschke, J. R. Metal-Organic Container Molecules Through Subcomponent Self-Assembly. *Chem. Commun.* **2013**, *49*, 2476-2490.

(23) Chambron, J.-C.; Sauvage, J.-P. Topologically Complex Molecules Obtained by Transition Metal Templation: It Is the Presentation That Determines the Synthesis Strategy. *New J. Chem.* **2013**, *37*, 49-57.

(24) Harris, K.; Fujita, D.; Fujita, M. Giant Hollow M_nL_{2n} Spherical Complexes: Structure, Functionalisation and Applications. *Chem. Commun.* **49**, 6703-6712 (2013).

(25) McConnell, A. J.; Wood, C. S.; Neelakandan, P. P.; Nitschke, J. R. Stimuli-Responsive Metal–Ligand Assemblies. *Chem. Rev.* **2015**, *115*, 7729-7793.

(26) Zhou, H. C.; Long, J. R.; Yaghi, O. M. Introduction to Metal-Organic Frameworks. *Chem. Rev.* **2012**, *112*, 673-674.

(27) Furukawa, H.; Cordova, K. E.; O'Keeffe, M; Yaghi, O. M. The Chemistry and Applications of Metal-Organic Frameworks. *Science* **2013**, *341*, 974-986.

(28) Furukawa, S.; Reboul, J.; Diring, S.; Sumida, K.; Kitagawa, S. Structuring of Metal-Organic Frameworks at the Mesoscopic/Macroscopic Scale. *Chem. Soc. Rev.* **2014**, *43*, 5700-5734.

(29) Li, L.; Xiang, S.; Cao, S.; Zhang, J.; Ouyang, G.; Chen, L.; Su, C.-Y. A Synthetic Route to Ultralight Hierarchically Micro/Mesoporous Al(III)-Carboxylate Metal-Organic Aerogels. *Nat. Commun.* **2013**, *4*, 1-9.

(30) Zhang, Z.; Nguyen, H. T. H.; Miller, S. A.; Cohen, S. M. PolyMOFs: A Class of Interconvertible Polymer-Metal-Organic-Framework Hybrid Materials. *Angew. Chem. Int. Ed.* **2015**, *54*, 6152-6157.

(31) Reboul, J.; Furukawa, S.; Horike, N.; Tsotsalas, M.; Hirai, K.; Uehara, H.; Kondo, M.; Louvain, N.; Sakata, O.; Kitagawa, S. Mesoscopic Architectures of Porous Coordination Polymers Fabricated by Pseudomorphic Replication. *Nat. Mater.* **2012**, *11*, 717-723.

(32) Rubinstein, M.; Colby, R. H. *Polymer Physics.* (Oxford University Press, 2003).

(33) Horike, S.; Shimomura, S.; Kitagawa, S. Soft Porous Crystals. *Nat. Chem.* **2009**, *1*, 695-704.

(34) Brunsveld, L.; Folmer, B. J. B.; Meijer, E. W.; Sijbesma, R. P. Supramolecular Polymers. *Chem. Rev.* **2001**, *101*, 4071-4097.

(35) Yang, L.; Tan, X.; Wang, Z.; Zhang, X. Supramolecular Polymers: Historical Development, Preparation, Characterization, and Functions. *Chem. Rev.* **2015**, *115*, 7196-7239.

(36) Hardy, J. G.; Cao, X.-Y.; Harrowfield, J.; Lehn, J.-M. Generation of Metallosupramolecular Polymer Gels from Multiply Functionalized Grid-Type Complexes. *New J. Chem.* **2012**, *36*, 668-673.

(37) Li, Y. T.; Zhang, D.; Gai, F.; Zhu, X.; Guo, Y.-n.; Ma, T.; Liu, Y.; Huo, Q. Ionic Self-Assembly of Surface Functionalized Metal–Organic Polyhedra Nanocages and Their Ordered Honeycomb Architecture at the Air/Water Interface. *Chem. Commun.* **2012**, *48*, 7946-7948.

(38) Yan, X.; Li, S.; Pollock, J. B.; Cook, T. R.; Chen, J.; Zhang, Y.; Ji, X.; Yu, Y.; Huang, F.; Stang, P. J. Supramolecular Polymers with Tunable Topologies Via Hierarchical Coordination-Driven Self-Assembly and Hydrogen Bonding Interfaces. *Proc. Natl. Acad. Sci. USA* **2013**, *110*, 15585-15590.

(39) Yan, X.; Li, S.; Cook, T. R.; Ji, X.; Yao, Y.; Pollock, J. B.; Shi, Y.; Yu, G.; Li, J.; Huang, F.; Stang, P. J. Hierarchical Self-Assembly: Well-Defined Supramolecular Nanostructures and Metallohydrogels Via Amphiphilic Discrete Organoplatinum(II) Metallacycles. *J. Am. Chem. Soc.* **2013**, *135*, 14036-14039.

(40) Li, Z.-Y.; Zhang, Y.; Zhang, C.-W.; Chen, L.-J.; Wang, C.; Tan, H.; Yu, Y.; Li, X.; Yang, H.-B. Cross-Linked Supramolecular Polymer Gels Constructed from Discrete Multi-Pillar[5]Arene Metallacycles and Their Multiple Stimuli-Responsive Behavior. *J. Am. Chem. Soc.* **2014**, *136*, 8577-8589.

(41) Yan, X.; Cook, T. R.; Pollock, J. B.; Wei, P.; Zhang, Y.; Yu, Y.; Huang, F.; Stang, P. J. Responsive Supramolecular Polymer Metallogel Constructed by Orthogonal Coordination-Driven Self-Assembly and Host/Guest Interactions. *J. Am. Chem. Soc.* **2014**, *136*, 4460-4463.

(42) Wei, S. C.; Pan, M.; Fan, Y. Z.; Liu, H.; Zhang, J.; Su, C. Y. Creating Coordination-Based Cavities in a Multiresponsive Supramolecular Gel. *Chem. Eur. J.* **2015**, *21*, 7418-7427.

(43) Kawamoto, K.; Grindy, S. C.; Liu, J.; Holten-Andersen, N.; Johnson, J. A. Dual Role for 1,2,4,5-Tetrazines in Polymer Networks: Combining Diels–Alder Reactions and Metal Coordination to Generate Functional Supramolecular Gels. *ACS Macro Lett.* **2015**, *4*, 458-461.

(44) Foster, J. A.; Parker, R. M.; Belenguer, A. M.; Kishi, N.; Sutton, S.; Abell, C.; Nitschke, J. R. Differentially Addressable Cavities within Metal–Organic Cage-Cross-Linked Polymeric Hydrogels. *J. Am. Chem. Soc.* **2015**, *137*, 9722-9729.

(45) Foster, J. A.; Steed, J. W. Exploiting Cavities in Supramolecular Gels. *Angew. Chem., Int. Ed.* **2010**, *49*, 6718-6724.

(46) Tominaga, M.; Suzuki, K.; Kawano, M.; Kusukawa, T.; Ozeki, T.; Shakamoto, S.; Yamaguchi, K.; Fujita, M. Finite, Spherical Coordination Networks That Self-Organize from 36 Small Components. *Angew. Chem. Int. Ed.* **2004**, *43*, 5621-5625.

(47) Sun, Q.-F.; Iwasa, J.; Ogawa, D.; Ishido, Y.; Sato, S.; Ozeki, T.; Sei, Y.; Yamaguchi, K.; Fujita, M. Self-Assembled $M_{24}L_{48}$ Polyhedra and Their Sharp Structural Switch Upon Subtle Ligand Variation. *Science* **2010**, *328*, 1144-1147.

(48) Chand, D. K.; Biradha, K.; Fujita, M. Self-Assembly of a Novel Macrotricyclic Pd(II) Metallocage Encapsulating a Nitrate Ion. *Chem. Commun.* **2001**, 1652-1653.

(49) Liao, P.; Langloss, B. W.; Johnson, A. M.; Knudsen, E. R.; Tham, F. S.; Julian, R. R.; Hooley, R. J. Two-Component Control of Guest Binding in a Self-Assembled Cage Molecule. *Chem. Commun.* **2010**, *46*, 4932-4934.

(50) Yoneya, M.; Yamaguchi, T.; Sato, S.; Fujita, M. Simulation of Metal-Ligand Self-Assembly into Spherical Complex M_6L_8. *J. Am. Chem. Soc.* **2012**, *134*, 14401-14407.

(51) Yoneya, M.; Tsuzuki, S.; Yamaguchi, T.; Sato, S.; Fujita, M. Coordination-Directed Self-Assembly of $M_{12}L_{24}$ Nanocage: Effects of Kinetic Trapping on the Assembly Process. *ACS Nano* **2014**, *8*, 1290-1296.

(52) Shibayama, M. Spatial Inhomogeneity and Dynamic Fluctuations of Polymer Gels. *Macromol. Chem. Phys.* **1998**, *199*, 1-30.

(53) Hore, M. J. A.; Ford, J.; Ohno, K.; Composto, R. J.; Hammouda, B. Direct Measurements of Polymer Brush Conformation Using Small-Angle Neutron Scattering (SANS) From Highly Grafted Iron Oxide Nanoparticles In Homopolymer Melts. *Macromolecules* **2013**, *46*, 9341-9348.

(54) Guth, E.; James, H. M. Elastic and Thermoelastic Properties of Rubber Like Materials. *Ind. Eng. Chem.* **1941**, *33*, 624-629.

(55) Zhou, H.; Woo, J.; Cok, A. M.; Wang, M.; Olsen, B. D.; Johnson, J. A. Counting Primary Loops in Polymer Gels. *Proc. Natl. Acad. Sci. USA* **2012**, *109*, 19119-19124.

(56) Zhou, H. X.; Schon, E. M.; Wang, M. Z.; Glassman, M. J.; Liu, J.; Zhong, M. J.; Diaz, D. D.; Olsen, B. D.; Johnson, J. A. Crossover Experiments Applied to Network Formation Reactions: Improved Strategies for Counting Elastically Inactive Molecular Defects in Peg Gels and Hyperbranched Polymers. *J. Am. Chem. Soc.* **2014**, *136*, 9464-9470.

(57) Deria, P.; Mondloch, J. E.; Karagiaridi, O.; Bury, W.; Hupp, J. T.; Farha, O. K. Beyond Post-Synthesis Modification: Evolution of Metal-Organic Frameworks Via Building Block Replacement. *Chem. Soc. Rev.* **2014**, *43*, 5896-5912.

(58) Mori, S. Calibration of Size Exclusion Chromatography Columns for Determination of Polymer Molecular Weight Distribution. *Anal. Chem.* **1981**, *53*, 1813-1818.

(59) Fulmer, G. R.; Miller, A. J. M.; Sherden, N. H.; Gottlieb, H. E.; Nudelman, A.; Stoltz, B. M.; Bercaw, J. E.; Goldberg, K. I. NMR Chemical Shifts of Trace Impurities: Common Laboratory Solvents, Organics, and Gases in Deuterated Solvents Relevant to the Organometallic Chemist. *Organometallics* **2010**, *29*, 2176-2179.

(60) Tironi, I.; Sperb, R.; Smith, P.; van Gunsteren, W. A Generalized Reaction Field Method for Molecular Dynamics Simulations. *J. Chem. Phys.* **1995**, *102*, 5451-5459.

(61) Yun-Yu, S.; Lu, W.; van Gunsteren, W. On the Approximation of Solvent Effects on the Conformation and Dynamics of Cyclosporin A by Stochastic Dynamics Simulation Techniques. *Mol. Simul.* **1988**, *1*, 369–383.

(62) Pang, Y. Novel Zinc Protein Molecular Dynamics Simulations: Steps Toward Antiangiogenesis for Cancer Treatment. *J. Mol. Model.* **1999**, *5*, 196–202.

(63) Berendsen, H. J. C.; van der Spoel, D.; van Drunen, R. GROMACS: A Message-Passing Parallel Molecular Dynamics Implementation. *Comp. Phys. Comm.* **1995**, *91*, 43-56.

(64) Kienberger, F.; Pastushenko, V. P.; Kada, G.; Gruber, H. J.; Riener, C.; Schindler, H.; Hinterdorfer, P. Static and Dynamical Properties of Single Poly(Ethylene Glycol) Molecules Investigated by Force Spectroscopy. *Single Molecules* **2000**, *1*, 123-128.

(65) Sheldrick, G. Phase Annealing in SHELX-90: Direct Methods for Larger Structures. *Acta Crystallogr. Sect. A* **1990**, *46*, 467-473.

(66) Sheldrick, G. A. Short History of SHELX. *Acta Crystallogr. Sect. A* **2008**, *64*, 112-122.

(67) Müller, P. Practical Suggestions for Better Crystal Structures. *Crystallogr. Rev.* **2009**, *15*, 57-83.

(68) Kline, S. R. Reduction and Analysis of SANS and USANS Data Using IGOR Pro *J. Appl. Cryst.* **2006**, *39*, 895–900.

(69) Hammouda, B. In *Adv. Polym. Sci.*; Springer; 1993; Vol. 106, p. 87-133.

(70) Harris, J. M.; Kozlowski, A.; Guo, L. Method of preparing carboxylic acid functionalized polymers. US Patent 8,067,505, Nov. 29, 2011.

CURRICULUM VITAE

Aleksandr V. Zhukhovitskiy

250 Kendall St., apt. 409
Cambridge, MA 02142
alexzhuk@mit.edu

(847) 899-5153

EDUCATION

Massachusetts Institute of Technology, Cambridge, MA (August 2011 – present)
Ph.D. Candidate
Advisor: Professor Jeremiah A. Johnson

Northwestern University, Evanston, IL (September 2007 – June 2011)
B.A. in the Integrated Science Program, Chemistry, and Mathematics; M.S. in Chemistry
Advisors: Professor SonBinh T. Nguyen (Chemistry), Professor Tobin J. Marks (Chemistry), and Professor Jared Wunsch (Mathematics)

SELECTED RECENT HONORS AND FELLOWSHIPS

- LSRF Fellowship Finalist (2016)
- ACS Division of Organic Chemistry Fellowship (MIT, 2014; declined)
- 2014 Intel PhD Fellowship (MIT, 2014)
- Deshpande Research Grant (MIT, 2012–2014)
- Morse Travel Grant (MIT, Summer of 2012)
- TA award (MIT, 2012)
- Moore Fellowship (MIT, 2011)
- Department Honors in Chemistry (NU, 2011)
- Marple-Schweitzer Memorial Award (NU, 2011)
- NSF Graduate Research Fellowship (2011; declined)
- DoD NDSEG Fellowship (2011)
- Oliver Marcy Scholarship (NU, 2010)
- Goldwater Scholarship (2009)

RELEVANT EXPERIENCE

Doctoral research in Professor Jeremiah Johnson's group, Massachusetts Institute of Technology, Cambridge, MA (November 2011 – present)

I. Fundamental studies of the gold and silicon surface chemistry of N-heterocyclic carbenes (NHCs) and surface-initiation polymerization.

II. Synthesis of novel addressable NHCs and investigation of their reactivity to gain insights into surface modification. Discovery and mechanistic investigation of NHC cycloelimination and the formation of stable NHC-carbodiimide adducts.

III. Synthesis and fundamental studies of polymer metal-organic cage (polyMOC) gels.

These projects involve (1) a wide repertoire of organic reactions for small molecule organic synthesis, (2) structure determination techniques (*e.g.*, 1D/2D NMR spectroscopy, LCMS), (3) polymer synthesis, processing, and analysis (*e.g.*, GPC, MALDI-TOF), and (4) surface characterization (XPS, AFM, QCM-D), (5) nanoparticle characterization (TEM, DLS), (6) rheological studies, (7) SAXS/WAXS, and (7) DFT computations.

Internship in Professor SonBinh Nguyen's group, Northwestern University, Evanston, IL (January 2009– June 2011)

I. Synthesis and ring-opening metathesis polymerization (ROMP) of strained unsaturated lactams and mechanistic studies of the polymerization
Mentor: Emily B. Pentzer (January 2009 – June 2010)

II. Porous organic polymers (POPs) based on phosphorus- and nitrogen-containing building blocks
Mentor: Research Assistant Professor Omar Farha (June 2010 – June 2011)

Summer research in Professor Tobin Marks's group, Northwestern University, Evanston, IL (June – August 2008)

Synthesis and Characterization of a New n-Type Semiconductor Material Based on the Thiophene-Modified Indenofluorene Core.
Mentor: Hakan Usta

PUBLICATIONS AND PATENTS

1. Zhukhovitskiy, A. V.; Mavros, M. G.; Queeney, K. T.; Wu, T.; Van Voorhis, T.; Johnson, J. A. Reactions of Persistent Carbenes with Hydrogen-Terminated Silicon Surfaces. *J. Am. Chem. Soc.* **2016,** *Submitted.*

2. Zhukhovitskiy A. V.; Zhong, M.; Keeler, E. G.; Michaelis, V. K.; Sun, J. E. P.; Hore, M. J. A.; Pochan, D. J.; Griffin, R. G.; Willard, A. P.; Johnson, J. A. Highly Branched and Loop-rich Gels via Formation of Metal-organic Cages Linked by Polymers. *Nat. Chem.* **2016,** *8,* 33-41. **Highlights:** *"Hybrid material flexes its muscles" Chemical and Engineering Progress* 2015, *111, 7.* *"Metal-organic networks go elastic" C&E News* 2015, *November 23rd.* *"Chemists create adaptable metallic-cage gels" MIT News* 2015, *November 17th.* *"Chemists create adaptable metallic-cage gels" Chemeurope.com* 2015, *November 20th.*

3. Zhukhovitskiy A. V.; MacLeod, M. J.; Johnson, J. A. Carbene Ligands in Surface Chemistry: From Stabilization of Discrete Elemental Allotropes to Modification of Nanoscale and Bulk Substrates. *Chem. Rev.* **2015,** *115,* 11503-11532.

4. Zhukhovitskiy, A. V.; Geng, J.; Johnson, J. A. Cycloelimination of Imidazolidin-2-ylidene N-Heterocyclic Carbenes: Mechanism and Insights into the Synthesis of Stable "NHC-CDI" Amidinates. *Chem. Eur. J.* **2015,** *21,* 5685-5688. **Highlight:** "Cover Profile" *Chem. Eur. J.* **2015,** *21,* 5649.

5. Zhukhovitskiy, A. V.; Mavros, M. G.; Van Voorhis, T.; Johnson, J. A. Addressable Carbene Anchors for Gold Surfaces. *J. Am. Chem. Soc.* **2013,** *135,* 7418-7421. **Highlights:** *"Carbene For Gold Surfaces" C&E News: News of the Week* 2013, *91, 11.* *"A New Kind of Chemical Glue" MIT News* 2013, *May 29th.*

6. Burts, A. O.; Li, Y.; Zhukhovitskiy, A. V.; Patel, P. R.; Grubbs, R. H.; Ottaviani, M. F.; Turro, N. J.; Johnson, J. A. Using EPR To Compare PEG-branch-nitroxide 'Bivalent-Brush Polymers' and Traditional PEG Bottle-Brush Polymers: Branching Makes a Difference. *Macromolecules* **2012,** *45,* 8310-8318.

7. Liu, J.; Burts, A. O.; Li, Y.; Zhukhovitskiy, A. V.; Ottaviani, M. F.; Turro, N. J.; Johnson, J. A. 'Brush-First' Method for the Parallel Synthesis of Photocleavable, Nitroxide-Labeled PEG Star Polymers. *J. Am. Chem. Soc.* **2012,** *134,* 16337-16344.

8. Usta, H.; Risko, C.; Wang, Z.; Huang, H.; Deliomeroglu, M. K.; Zhukhovitskiy, A.; Facchetti, A.; Marks, T. J. Design, synthesis, and characterization of ladder-type molecules and polymers. Air-stable, solution-processable n-channel and ambipolar semiconductors for thin-film transistors via experiment and theory. *J. Am. Chem. Soc.* **2009,** *131,* 5586-5608.

9. **Patent:** <u>Zhukhovitskiy, A. V.</u>; Johnson, J. A. Articles And Methods Comprising Persistent Carbenes And Related Compositions. U.S. Patent Application US20140275555 A1, Sept. 18, 2014.

10. **Patent:** Johnson, J. A.; Kawamoto, K.; <u>Zhukhovitskiy, A. V.</u>; Holten-Andersen, N.; Grindy, S. C. PolyMOFs: Hybrid Materials With Combined Gel and MOF Properties Via Metal-Ligand Coordination and Self-Assembly. U.S. Patent Application No. 61/937052, filed on Feb. 7, 2014.

PUBLICATIONS IN PREPARATION

<u>Zhukhovitskiy, A. V.</u>; Zhao, J.; Hore, M. J. A.; Keeler, E. G.; Alt, E. A.; Zhong, M.; Teichen, P.; Griffin, R. G.; Willard, A. P.; Johnson, J. A. Ultra-High Branch Functionality and New Levels of Hierarchy Through the Self-Assembly of Metal-Organic Cage Junctions. **2016. *Manuscript in preparation.***

ACS ABSTRACTS

1. <u>Zhukhovitskiy A. V.</u>; Zhong, M.; Keeler, E. G.; Michaelis, V. K.; Griffin, R. G.; Willard, A. P.; Johnson, J. A. *Suprametallogels: Controlling Gel Properties Through Programmed Metallo-Supramolecular Assembly of Nanocage Junctions.* From Abstract of Papers, 250th ACS National Meeting & Exposition, Boston, MA, United States, August 16–20, 2015, POLY-13.

2. <u>Zhukhovitskiy, A. V.</u>; Johnson, J. A. *Suprametallogels based on Fujita sphere self-assembly.* From Abstracts of Papers, 248th ACS National Meeting & Exposition, San Francisco, CA, United States, August 10–14, 2014, POLY-525.

3. <u>Zhukhovitskiy, A. V.</u>; Johnson, J. A. *Click-o-mers with N-heterocyclic carbenes for sensing metal ions and stabilizing gold nanoparticles.* From Abstracts of Papers, 244th ACS National Meeting & Exposition, Philadelphia, PA, United States, August 19–23, 2012, POLY-94.

4. Pentzer, E. B.; Nguyen, S. T.; <u>Zhukhovitskiy, A. V.</u> *RCM of encapsulated dienes: An efficient strategy for the synthesis of carbonyl-containing cyclic olefins.* From Abstracts of Papers, 239th ACS National Meeting, San Francisco, CA, United States, March 21–25, 2010, INOR-1063.

PRESENTATIONS

1. "Controlling Gel Properties Through Programmed Metallo-Supramolecular Assembly of Nanocage Junctions," National ACS Meeting, Boston, August 16—20, 2015.
2. **Invited:** "Advancing coordination chemistry in materials: Surface functionalization, gelation, and surprises along the way." UMass Amherst 2015 Young Investigator in Materials Research Seminar Series, May 6, 2015.
3. **Invited:** "Advancing coordination chemistry in materials: Surface functionalization, gelation, and surprises along the way." University of Connecticut 2015 Society of Plastics Engineers Seminar Series, April 15, 2015.
4. **Invited:** "Suprametallogels Based on Fujita Sphere Self-Assembly." 2014 Bioinspired Materials Gordon Research Symposium, June 21–22, 2014.
5. "Getting a Better Grip on Surfaces: Addressable N-Heterocyclic Carbenes," Deshpande IdeaStream, April 11, 2014.
6. "Novel applications of metals and ligands in polymer science," PPSM Polymer Day Symposium, MIT, March 12, 2014.
7. "Functionalizable (F-)NHCs and Poly(NHC)s: A Novel Modular Ligand Platform for Gold Nanoparticles and Surfaces," National ACS Meeting, Philadelphia, August 19–23, 2012.

POSTERS

1. "Suprametallogels: Controlling Gel Properties Through Programmed Metallo-supramolecular Assembly of Nanocage Junctions," 44th National Organic Symposium, June 28—July 2, 2015.

2. "Suprametallogels: Controlling Gel Properties Through Programmed Metallo-supramolecular Assembly of Nanocage Junctions," 2015 Polymers Gordon Research Conference, June 14—19, 2015.
3. "Suprametallogels based on Fujita sphere self-assembly," 248th ACS National Meeting & Exposition, San Francisco, CA, August 10—14, 2014.
4. "Functionalizable (F-)NHCs: A Modular Ligand Platform for Gold Surfaces," Boston Symposium on Organic and Bioorganic Chemistry, Sept. 27, 2012.
5. "Synthesis and Characterization of Porous Organic Polymers with Tunable Nucleophilicity and Pore Width for CO_2 Sequestration," Northwestern University 2011 Undergraduate Research Symposium.
6. "Ring-Opening Metathesis Polymerization of Unsaturated Lactams for the Construction of Novel Biodegradable Polymer Scaffolds," Northwestern University 2010 Undergraduate Research Symposium.

MENTORSHIP AND TEACHING

1. Supervised an undergraduate researcher and a high school student in the Johnson Lab during the 2014 – 2015 academic year (MIT).
2. Supervised an undergraduate researcher in the Johnson Lab during the 2013 – 2014 academic year (MIT).
3. Head Teacher Assistant for Organic Chemistry I, Feb. 2012 – May 2012 (MIT). Received a TA award.
4. Teacher Assistant for Organic Chemistry II, Sept. 2011 – Dec. 2011 (MIT).
5. Physics, Chemistry, Mathematics Tutor in the Integrated Science Program (ISP), Nov. 2008 – June 2011 (NU)
6. Teacher Assistant for the Center for Talent Development, Oct. 2007 – Dec. 2007, Oct. 2008 – May 2011 (NU)

SERVICE

1. Environment Health and Safety committee member (Department of Chemistry, MIT, June 2013 – March 2016)
2. Environment Health and Safety representative (Johnson Group, MIT, Nov. 2011 – Dec. 2014)
3. MIT Chemistry Outreach demonstrations at local high schools (2013, 2014, 2015)
4. Cambridge Science Festival chemistry demonstrations (2012, 2013)